Used Fuel Disposal in Crystalline Rocks: FY15 Progress Report

Fuel Cycle Research & Development

Prepared for

U.S. Department of Energy

Used Fuel Disposition

Y. Wang, T. Hadgu, E. Matteo, J. N. Kruichak, M. M. Mills

Sandia National Laboratories

R. Tinnacher, J. Davis

Lawrence Berkeley National Laboratory

H. Viswanathan, S. Chu, T. Dittrich, F. Hyman, S. Karra, N. Makedonska, P. Reimus

Los Alamos National Laboratory

M. Zavarin, P. Zhao, C. Joseph, J. Begg, Z. Dai, A. B. Kersting

Lawrence Livermore National Laboratory

J. Jerden, J. M. Copple, T. Cruse, W. Ebert

Argonne national laboratory

FCT Quality Assurance Program Document

Appendix E
FCT Document Cover Sheet

Name/Title of Deliverable/Milestone	Used Fuel Disposal in Crystalline Rocks: FY15 Progress Report (M2FT-15SN0807071)
Work Package Title and Number	Crystalline Disposal R&D
Work Package WBS Number	FT-15SN080707
Responsible Work Package Manager	Yifeng Wang _(signature)_ (Name/Signature)

Date Submitted   8/13/2015

Quality Rigor Level for Deliverable/Milestone	☒ QRL-3	☐ QRL-2	☐ QRL-1 ☐ Nuclear Data	☐ N/A*

This deliverable was prepared in accordance with   Sandia National Laboratories
(Participant/National Laboratory Name)

QA program which meets the requirements of
      ☒ DOE Order 414.1   ☐ NQA-1-2000

This Deliverable was subjected to:

☐ Technical Review   ☐ Peer Review

Technical Review (TR)   **Peer Review (PR)**
Review Documentation Provided   **Review Documentation Provided**
☐ Signed TR Report or,   ☐ Signed PR Report or,
☐ Signed TR Concurrence Sheet or,   ☐ Signed PR Concurrence Sheet or,
☒ Signature of TR Reviewer(s) below   ☐ Signature of PR Reviewer(s) below
Name and Signature of Reviewers
Carlos Jove-Colon

*Note: In some cases there may be a milestone where an item is being fabricated, maintenance is being performed on a facility, or a document is being issued through a formal document control process where it specifically calls out a formal review of the document. In these cases, documentation (e.g., inspection report, maintenance request, work planning package documentation or the documented review of the issued document through the document control process) of the completion of the activity along with the Document Cover Sheet is sufficient to demonstrate achieving the milestone. QRL for such milestones may be also be marked N/A in the work package provided the work package clearly specifies the requirement to use the Document Cover Sheet and provide supporting documentation.

Used Fuel Disposal in Crystalline Rocks: FY15 Progress Report

EXECUTIVE SUMMARY

The U.S. Department of Energy Office of Nuclear Energy, Office of Fuel Cycle Technology established the Used Fuel Disposition Campaign (UFDC) in fiscal year 2010 (FY10) to conduct the research and development (R&D) activities related to storage, transportation and disposal of used nuclear fuel and high level nuclear waste. The Mission of the UFDC is

> *To identify alternatives and conduct scientific research and technology development to enable storage, transportation and disposal of used nuclear fuel and wastes generated by existing and future nuclear fuel cycles.*

The work package of Crystalline Disposal R&D directly supports the following UFDC objectives:

- Develop a fundamental understanding of disposal system performance in a range of environments for potential wastes that could arise from future nuclear fuel cycle alternatives through theory, simulation, testing, and experimentation.
- Develop a computational modeling capability for the performance of storage and disposal options for a range of fuel cycle alternatives, evolving from generic models to more robust models of performance assessment.

The objective of the Crystalline Disposal R&D Work Package is to advance our understanding of long-term disposal of used fuel in crystalline rocks and to develop necessary experimental and computational capabilities to evaluate various disposal concepts in such media.

FY15 continued to be a successful year in both experimental and modeling arenas in evaluation of used fuel disposal in crystalline rocks. The work covers a wide range of research topics identified in the R&D plan. The major accomplishments are summarized below:

- *Development of Fuel Matrix Degradation Model (FMDM):* Completed a model validation study in which results from the state of the art FMDM were compared to experimental data from international geologic repository programs. Completed conversion of the state of the art FMDM (version 2.3) to Fortran to facilitate integration with the Generic Disposal System Analysis (GDSA) repository Performance Assessment (PA) code PFLOTRAN. Completed preliminary model runs focused on expanding the FMDM to account for corrosion of the used fuel steel canister. Completed scoping experiments investigating the possible poisoning of the Noble Metal Particles (NMP), which are known to catalyze the oxidation of H_2, thus shutting down the oxidative dissolution of used fuel.
- *Thermal limit study of clay materials:* Smectite and illite materials were heated up to 1300 ^{o}C over various time periods. Thermally treated materials were carefully characterized with X-ray diffraction (XRD), BET surface area measurments, cation exchange capacity (CEC) measurements, and particle settling experiments. The results show that mineralogic alteration as a function of heat treatment exerts the greatest control on chemical and physical properties of both illite and smectite clays. Under dry heating, such alteration seems unlikely to occur below temperature 500 ^{o}C. However, thermal treatment under 500 ^{o}C does seem to change surface properties (e.g. surface area) and settling properties of clay particles.

- *Short-term (< 35 days) study of uranium sorption and diffusion in bentonite:* Experimental results from U(VI) sorption experiments with bentonite samples before and after heat treatments suggest a decrease in U(VI) sorption due to heat-induced mineral alterations. This effect could lead to lower U(VI) retardation in comparison to the pristine solids, and potential changes in diffusive U(VI) fluxes. The results from parallel U(VI) through-diffusion experiments in Na-montmorillonite at two alkaline pH conditions (pH 8.75 and 8.95), indicate a relevance of so-called anion exclusion effects, the full or partial exclusion of anionic U(VI) solution species from clay interlayer spaces. Such exclusion affects the diffusion-accessible porosity for U(VI) species predominant under these chemical solution conditions, as well as the resulting U(VI) diffusive fluxes.

- *Long-term (6 years) study of uranium diffusion in bentonite:* For a time period of six years, U(VI) diffusion through compacted MX-80 bentonite was investigated as a function of clay dry bulk density (ρ =1.3, 1.6, 1.9 g/cm^3). Speciation calculations revealed that independent of pore water type and water sampling time the $Ca_2UO_2(CO_3)_3$(aq) complex was always the dominant U(VI) species in solution (83-90%). U(VI) diffused about 2 mm, 1 mm, and 0.7 mm deep in the clay at ρ = 1.3, 1.6, and 1.9 g/cm^3, respectively. The distribution coefficients modeled are very low (K_d = 5.8-2.6$\times$10^{-3} m^3/kg). The K_d values obtained from the long-term experiment is one order of magnitude lower than those from batch sorption measurements. The apparent U(VI) diffusion coefficient determined from the long-term experiment is about two orders lower than obtained from short-term experiments, which may be attributed to a reduction of clay porosity.

- *Study of Pu sorption and desorption in bentonite:* Pu(IV) sorption to industrial grade FEBEX bentonite was studied over the concentration range 10^{-7}–10^{-16} M. Pu(IV) sorption was broadly linear over the 10^{-7}–10^{-16} M concentration ranged during the 120 d experimental period; however, it took up to 100 d to reach sorption equilibrium. A flow cell experiment with Pu(IV) loaded on FEBEX bentonite demonstrated continued desorption of Pu over a 12 day flow period. Comparison with a desorption experiment performed with SWy-1 montmorillonite showed a strong similarity and suggested the importance of montorillonite phases in controlling Pu sorption/desorption reactions on FEBEX bentonite.

- *Colloid stability study:* A study of the dissolution of intrinsic colloids in the presence of montmorillonite at different temperatures was successfully accomplished using a novel experimental setup containing a dialysis device. We showed that the kinetic constants for dissolution were one to two orders of magnitude lower than the apparent diffusion rates across the dialysis membranes. Therefore the dissolution process was the rate-limiting step. Although the presence of clay changes neither the colloids dissolution nor diffusion rates, it can stabilize dissolved Pu species and drive intrinsic Pu colloid dissolution and the formation of more stable pseudo-colloids. Temperature enhances dissolution of intrinsic Pu colloids with activation energy of 28 kJ/mol. Our thermodynamic study shows that the sorption of Pu to montmorillonite is endothermic as a positive change in enthalpy for the sorption has been obtained. The affinity of Pu for montmorillonite increases with increasing temperature and resulting in higher K_ds. Although the fact that intrinsic Pu colloids tend to dissolve in the presence of montmorillonite may limit the migration of intrinsic colloids, the subsequent formation of thermodynamically more stable pseudo-colloids can play important role in Pu transport in the environment over significant temporal and spatial scales.

- *Laboratory investigation of Cs colloid-facilitated transport:* The work demonstrated that a combination of batch sorption/desorption experiments and column transport experiments could be used to effectively parameterize a model describing the colloid-facilitated transport of Cs. Cs partition coefficient estimates onto both the colloids and the stationary media obtained from the batch experiments were used as initial estimates of partition coefficients in the column experiments, and then the column experiment results were used to obtain refined estimates of the number of different sorption sites and the adsorption and desorption rate constants of these sites.

The desorption portion of the column breakthrough curves highlighted the importance of accounting for adsorption-desorption hysteresis (or a very nonlinear adsorption isotherm) of the Cs on the fracture filling materials (FFM) in the model, and this portion of the breakthrough curves also dictated that there be at least two different types of sorption sites on the FFM. The two-site model parameters estimated from the column experiments provided excellent matches to the batch adsorption/desorption data, which provided a measure of assurance in the validity of the model. It was also demonstrated that a relatively simple retardation factor expression could be used to provide a good approximation of colloid-facilitated solute transport under conditions of near-constant mobile colloid concentrations and rapid and reversible solute sorption/desorption onto both the colloids and immobile surfaces.

- *Development and demonstration of Discrete Fracture Network (DFN) model:* A unified description of the dfnWorks suite was developed over the past five years with significant contribution from the Used Fuel Disposition Campaign. The generation and meshing strategy were outlined, a description of the flow solver provided, and the pillars of the particle tracker presented. The ability to resolve flow and transport while retaining fracture geometry allowed for two unique studies of transport in large, kilometer-scale DFN. The first study showed that after a pre-equilibrium region solutes injected under resident conditions could evolve and behave similarly to that injected under flux-weighted conditions. The observation of this evolution was made feasible by the size of the DFN considered and characterizing the physical mechanisms that induced this phenomenon was made possible by retaining the geometry of the fractures rather than using a one-dimensional pipe-network approximation. Similarly, the second study was made possible because the fracture geometry was retained, so in-fracture variability could be incorporated. Other studies have used breakthrough times acquired from single fractures with internal aperture variability, but this study marks the first to resolve Lagrangian based transport in DFN where in-fracture variability is explicitly represented. We found that early breakthrough times and retention curves are influenced by in-fracture aperture variability but the tails of the breakthrough curves are insensitive to these variations.

- *Comparison of Fracture Continuum Model (FCM) with DFN model:* We evaluated the use of the FCM and DFN fracture characterization approaches for modeling of flow and transport in the host rock of a generic crystalline repository. The methodology to establish one-to-one correspondence between DFN and FCM fracture parameters was developed. Benchmark testing was performed for FCM-only modeling, and DFN-FCM modeling comparison using synthetic data. The results were encouraging and showed that both the DFN and FCM methods could be used for modeling flow and transport in crystalline rocks. The results also indicated that further work was needed to bridge differences in results and to exercise both methods under different modeling conditions.

Based on the work accomplished in FY15 and the prior years, the future work is recommended to:
- Focus on two key topics related to deep geologic disposal of used fuel in crystalline rocks: (1) better characterization and understanding of fractured media and fluid flow and transport in such media, and (2) designing effective engineered barrier systems (EBS) for waste isolation. Specific attention will be given to the development of scientifically sound thermal limits for various buffer materials.
- Explore various disposal concepts, for example, borehole disposal vs. drift emplacement, regular waste packages vs. dual purpose canisters (DPCs). Especially, the work will explore potential advantages of crystalline media for the disposal of DPCs, given the high mechanical strength of the rocks.
- Move more towards model demonstrations and applications using data obtained from international collaborations.

- Continue international collaborations, especially with Korea Atomic Research Institute (KAERI), and Sweden Underground Research Lab and through Development of Coupled models and their validation against Experiments (DECOVALEX).
- Closely coordinate with the deep borehole disposal control account. The data obtained and the tools developed in this control account may be transferable to the deep borehole disposal, or vice versa.
- Continue integration with the generic disposal system analysis (GDSA) control account to refine the reference safety case for crystalline media and help to develop a performance assessment (PA) model for the crystalline reference case.

CONTENTS

1.0   GOALS AND OUTLINE

The U.S. Department of Energy Office of Nuclear Energy, Office of Fuel Cycle Technology established the Used Fuel Disposition Campaign (UFDC) in fiscal year 2010 (FY10) to conduct the research and development (R&D) activities related to storage, transportation and disposal of used nuclear fuel and high level nuclear waste. The Mission of the UFDC is

> *To identify alternatives and conduct scientific research and technology development to enable storage, transportation and disposal of used nuclear fuel and wastes generated by existing and future nuclear fuel cycles.*

The work package of Crystalline Disposal R&D directly supports the following UFDC objectives:

- Develop a fundamental understanding of disposal system performance in a range of environments for potential wastes that could arise from future nuclear fuel cycle alternatives through theory, simulation, testing, and experimentation.
- Develop a computational modeling capability for the performance of storage and disposal options for a range of fuel cycle alternatives, evolving from generic models to more robust models of performance assessment.

The objective of the Crystalline Disposal R&D Work Package is to advance our understanding of long-term disposal of used fuel in crystalline rocks and to develop necessary experimental and computational capabilities to evaluate various disposal concepts in such media. FY14 work is aligned with the following considerations and project goals:

- This control account will focus on two key topics related to deep geologic disposal of used fuel in crystalline rocks: (1) better characterization and understanding of fractured media and fluid flow and transport in such media, and (2) designing effective engineered barrier systems (EBS) for waste isolation. Specific attention will be given to the development of scientifically sound thermal limits for various buffer materials.
- Various disposal concepts will be explored, for example, borehole disposal vs. drift emplacement, regular waste packages vs. dual purpose canisters (DPCs). The work will explore possible advantages of crystalline media for the disposal of DPCs, given the high mechanical strength of the rocks.
- The modeling work will move more towards model demonstrations and applications in FY15 and the out years.
- The work planned for this control account will fully leverage international collaborations, especially with Korea Atomic Research Institute (KAERI), Sweden Underground Research Lab and Czech Bedrichov Tunnel Test Facility. At the same time, the control account will also explore the possibility of the development of an underground research lab in the US, with focus on existing mines (e.g., Homestake Mine).
- The data obtained and the tools developed in this control account may be transferable to the deep borehole disposal, or vice versa. It is important to closely coordinate the related activities across the two control accounts.
- Similarly, this control account will help the generic disposal system analysis control account to develop a total system performance assessment model and provide the parameter feeds to the model.

The FY 15 work for the Crystalline Disposal R&D Work Package is structured into the following tasks:

- *Task 1. (ANL) Development of used fuel degradation model:* This task will develop a preliminary model for used fuel degradation model in granitic environments. Due to the budget constraint, this activity will be jointed with the similar effort for the argillite work package. It is believed that a single model can be developed for both granite and argillite media.
- *Task 2. (LANL, SNL, LBNL) Modeling of fluid flow and transport in fractured crystalline rocks:* The task will (1) demonstrate the potential application of a discrete fracture network model to actual field testing data obtained from international collaborations, (2) develop a hydro-chemical model for data interpretation for streaming potential testing to be conducted in KAERI Underground Research Tunnel (KURT), and (3) explore up-scaling techniques to link parameters and process at small-scales to those at scales relevant to performance assessment models.
- *Task 3. (LBNL) Modeling of THMC behaviors in clay-based barrier materials:* The objective of this activity is to develop and apply thermal-hydrological-mechanical-chemical (THMC) modeling capabilities to assess engineering-barrier-system (EBS) responses to different temperatures and pressures, and to evaluate impacts of the interaction between EBS and host rocks.
- *Task 4. (LANL, LLNL, SNL, LBNL) Experimental investigation of radionuclide interactions with natural and engineered materials:* The work will include (1) mechanistic understanding of Pu interactions with representative mineral substrates under granitic chemical conditions, (2) experiments of U and Np sorption on fracture-coating materials, and (3) experiments on uranium and iodide sorption/diffusion in compacted clay and other related materials. One objective of this work will aim to develop new buffer materials through design, for example, the materials that can withstand high thermal perturbations (e.g. caused by the emplacement of dual purpose canisters) without compromising their functionalities as engineered barriers
- *Task 5. (LANL, LLNL, SNL, LBNL) International collaborations:* International collaborations are crucial for the activities proposed for this work package. These collaborations will include: KURT tests, SKB-BRIE tests, CFM tests, DECOVALEX and Mont Terri tests.

This report summarizes work accomplished in FY14 for the Crystalline Disposal R&D Work Package. The report is outlined as follows:

- Chapter 2 documents the development and implementation the Fuel Matrix Degradation Model (FMDM). The work documented is a jointed effort between the Crystalline Work Package and the Argillite Work Package. (Research topics addressed: S2, S3 and P19; see Wang et al., 2014)
- Chapter 3 focuses a preliminary investigation of thermal limits of clay materials as an engineered barrier material. (S2, P21 and P22)
- Chapter 4 summarizes the short-term (<35 days) experimental work on uranium diffusion and retardation in bentonite. (P10, P21 and P22)
- Chapter 5 summarizes a long-term (6 years) investigation of uranium diffusion in bentonite. (P10)
- Chapter 6 focuses on plutonium sorption and desorption in bentonite over a wide range of plutonium concentrations. (P10 and P22)
- Chapter 7 focuses on the stability of Pu colloids in the presence of clay materials and the temperature dependence of this stability. (P11)
- Chapter 8 documents a laboratory study of colloid-facilitated transport of Cs by bentonite colloids in a crystalline rock system. (P10 and P11)
- Chapter 9 presents the work on the development and demonstration of Discrete Fracture Network (DFN) model. (P1)
- Chapter 10 provides a comparison between two modeling approaches for flow and transport in fractured crystalline rocks: DFN model and Fracture Continuum Model (FCM). (P1, P8 and P9)
- Chapter 11 provides a brief description of the relevance of the FY15 work to the DOE Managed High Level Waste (HLW) and Spent Nuclear Fuel (SNF) Research.

- Chapter 12 provides an overall summary of FY15 accomplishment in Crystalline Work Package.

Wang Y. et al., (2014) *Used Fuel Disposal in Crystalline Rocks: Status and FY14 Progress*, FCRD-UFD-2014-000060, SAND2014, Sandia National Laboratories, Albuquerque, NM.

2.   FUEL MATRIX DEGRADATION MODEL AND ITS INTEGRATION WITH PERFORMANCE ASSESSMENTS

2.1   INTRODUCTION

The importance of used nuclear fuel (UNF) degradation in a repository safety case is that the fuel itself is an initial barrier in a multiple-barrier waste isolation system that must be represented in a quantitative safety analysis. The fuel degradation rate is used directly to calculate the radionuclide source term in a safety analysis. High confidence in the performance of the sequential barriers used in a safety case requires an accurate representation of the source term that accounts for fuel degradation and its coupling with other components in engineered barriers. The impact of waste form degradation on the safety analysis could depend on the geologic environment owing to the expected interactions during the relevant performance period and the importance of the ground water composition on the fuel dissolution rate (dissolved oxygen and hydrogen, ligands affecting dissolved concentration limits, secondary phase, etc.).

This chapter documents a continued effort to develop and implement a fundamentals-based process model for the degradation rate of used fuel that can be readily incorporated into the Generic Disposal System Analyses (GDSA) Performance Assessment (PA) code. This model, referred to as the Fuel Matrix Degradation Model (FMDM), was initially based on the Canadian Mixed Potential Model (King and Kolar, 2003), but has since been expanded and customized for the ongoing UFD argillite and crystalline rock disposal work packages.

The continued development and implementation of the FMDM addresses two high level Features, Events, and Processes (FEPs) that are recognized as high R&D priorities for the UFD (Wang et al., 2014). The FEPs addressed by this model are 2.1.02 (waste form) and 2.1.03 (waste container), which correspond to the high priority research topics P19 (Development of waste form degradation model) and P20 (Development of new waste package concepts and models for evaluation of waste package performance for long-term disposal) identified by Wang et al., 2014.

The FMDM calculates the dissolution rate of used fuel based the interfacial corrosion potential (E_{corr}) determined by the kinetic balance between anodic and cathodic half reactions at the fuel/solution boundary. The dissolution rate is relatively fast under oxidizing conditions (high E_{corr}) but decreases dramatically at E_{corr} values lower than the U(IV)/U(VI) threshold (where solubility based, chemical dissolution is dominant). The FMDM accounts for:

- the generation of radiolytic oxidants based on fuel burn-up,
- the catalyzed oxidation of H_2, which protects the fuel from oxidative dissolution,
- the precipitation of secondary phases,
- the complexation of uranyl by carbonate,
- the oxidation of ferrous iron,
- temperature variations (by Arrhenius equations),
- the one-dimensional diffusion of all chemical species.

Of these processes, the catalysis of H_2 oxidation on Nobel Metal Particles (NMP) on the fuel surface and the generation rate of radiolytic oxidants (determined by dose rate, which is related to fuel burn-up) are the most important for determining the degradation rate of the fuel (Jerden et al., 2015).

The dissolution rate calculated by the FMDM accounts for oxidation of the fuel by radiolytic H_2O_2 (and decomposition product O_2), the concentration of which is calculated using an analytical form of the

radiolysis model developed at PNNL (Buck et al., 2014) and the burn-up/dose rate function described in Section 2.2 of this chapter. Fuel oxidation is counteracted by the catalytic oxidation of H_2 on NMP sites that are present on the fuel surface as a distinct phase. The dominant source of H_2 in the repository will be from the anoxic corrosion of steel (Shoesmith, 2008).

As discussed in Section 2.3 below, the FMDM is being extended to include steel corrosion thus providing a realistic kinetic source of H_2 for key interfacial reactions. It was shown in Jerden et al. (2015) that the FMDM accurately reproduces the experimental observation that relatively low concentrations of dissolved H_2 (~0.1mM) can completely inhibit the oxidative dissolution of the fuel. In the absence of oxidative dissolution, the fuel degrades by solubility based chemical dissolution, which is over 4 orders of magnitude slower than oxidative dissolution (Röllin et al., 2001). The FMDM accounts for the surface area of the NMPs and is being extended to account for the effects of species that may poison the catalytic effects of the NMP (see Section 4 below).

The key processes currently accounted for in the FMDM as well as the processes that are to be added in FY 2016 are summarized in Figure 2-1.
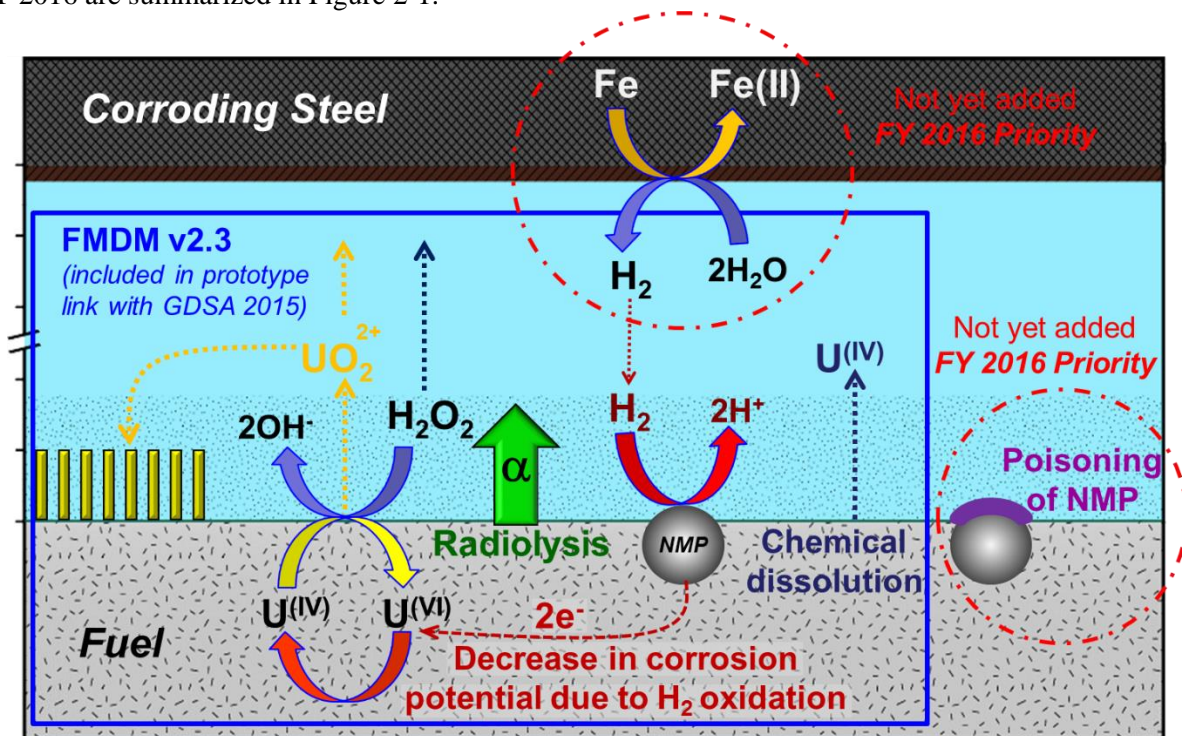
Figure 2-1: Conceptual diagram identifying the key dissolution rate-determining processes in the FMDM and highlighting the FY 2016 priorities.

2.2   FUEL MATRIX DEGRADATION MODEL DEVELOPMENT AND INTEGRATION WITH PFLOTRAN

This section documents model development work that focused on integrating the FMDM with the GDSA PA code PFLOTRAN. This involved the conversion of the FMDM from MATLAB to Fortran and the addition of an analytical function that calculates the dose rate at the fuel surface based on a user specified fuel burnup and fuel age (out of reactor). The Fortran version of the FMDM was integrated with PFLOTRAN to produce a prototype PFLOTRAN-FMDM working model. This integrated code was demonstrated for a scaled-down and simplified repository example, which is described in Section 2.2.3 below.

2.2.1 Conversion of FMDM from MATLAB to Fortran

The first Fortran version of the FMDM [previously referred to as the Mixed Potential Model (MPM)], was completed and distributed to the GDSA team in October 2014 as version number 2.0 and is documented in Jerden et al., 2014. Versions 2.1 and 2.2 were produced and used internally at Argonne but were not distributed. The Fortran FMDM version 2.3 was distributed to the GDSA team in March 2015. The new features of version 2.3 are described in this report.

One of the major changes is that the Fortran FMDM version 2.3 returns the fuel dissolution rate (`fuelDisRate`) in g m^{-2} y^{-1} rather than a matrix of fluxes (as the previous version did). This fuel dissolution rate is equal to the sum of the three interfactial fluxes of uranium leaving the fuel surface: uranyl ion, uranyl tricarbonate and aqueous U(IV) (labled `UO2_2p, UCO3_2n, UO2` in the code).

The other major addition to the FMDM v2.3 is that the dose rate at the fuel surface, which determines the generation rate of radiolytic oxidants, is calculated internally rather than provided as an input to the model. This is accomplished through and analytical dose rate – burnup function that was derived by fitting the burnup – dose rate – age of fuel data of Radulescu 2011 (discussed in Section 2.2.2 below).

The original Fortran FMDM was converted from MATLAB to Fortran 90 for integration with the PFLOTRAN code. The only external library used was LAPACK for its linear algebra solver "`dgesv`" (LAPACK 3.5.0 Windows 32-bit static library). This conversion was a line by line translation of the original MATLAB code. A single call to the FMDM version 2.3 Fortran code requires a call to the subroutine "AMP_step" whose interface is shown below.

```fortran
interface
    subroutine AMP_step ( sTme, conc, initialRun, fuelDisRate, status )
        real ( kind = 8), intent( in )  :: sTme
        real ( kind = 8), intent( inout ),  dimension (:,:) :: conc
        logical ( kind = 4), intent( in ) :: initialRun
        real ( kind = 8), intent(out) :: fuelDisRate
        integer ( kind = 4), intent(out) :: status
    end subroutine
end interface
```

The first time the code is called, initialRun must be set to ".`true.`" and the contents of the concentration matrix "`conc`" are ignored. In this case, the initial concentrations are defaulted to the values returned by the subroutine "`enVals`" in file "AMP_class.f90". In subsequent calls to "AMP_step", the concentration from the previous AMP_step call must be preserved and used as input to the current AMP_step call.

There are eleven components followed by the FMDM version 2.3 Fortran code and the order is defined in the file "AMP_compList. Inc". The first dimension of the concentration matrix is in this order.

`UO2_2p`	[symbol for UO_2^{2+}]
`UCO3_2n`	[symbol for $UO_2(CO_3)_2^{2-}$]
`UO2`	[symbol for $UO_2(aq)$]
`CO3_2n`	[symbol for CO_3^{2-}]
`O2`	[symbol for $O_2(aq)$]
`H2O2`	[symbol for H_2O_2]
`Fe_2p`	[symbol for Fe^{2+}]
`H2`	[symbol for $H_2(aq)$]
`UO2_sld`	[symbol for U(IV) oxide precipitate]
`UO3_sld`	[symbol for U(VI) oxide hydrate precipitate]
`UO4_sld`	[symbol for U(VI) peroxide precipitate]

Figure 2-2 identifies the basic order of calculations within the FMDM, identifies the inputs and outputs from and to PFLOTRAN and indicates the new features of v2.3. This Fortran version of the FMDM has been coupled with PFLOTRAN to form a prototype working integrated model as discussed in Section 2.2.3 below.
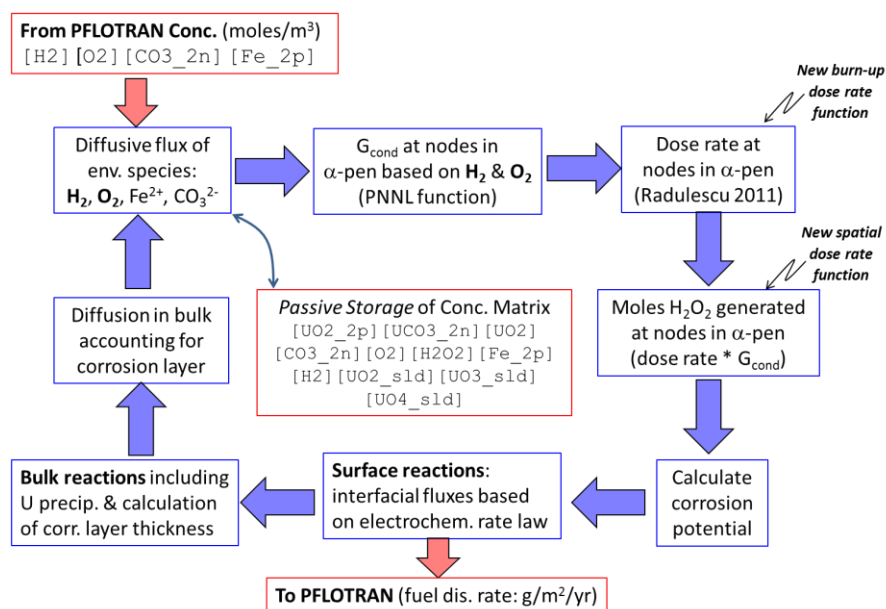
Figure 2-2: Conceptual flow diagram showing the individual calculations within a single time step of the FMDM. Note that the concentrations of all components must be stored and fed back to the FMDM at the beginning of each new time step. G_{cond} refers to the conditional generation value for H_2O_2, which determines the peroxide generation rate within the alpha radiation zone (α-pen). In the FMDM v.2.3 the conditional H_2O_2 generation value is calculated by an analytical function). (G_{cond} is a function of $[H_2]$ and $[O_2]$) derived from sensitivity runs of the PNNL radiolysis model (Buck et al., 2014).

2.2.2 Summary of Technical Changes Made to the FMDM Incorporated into Version 2.3

The following changes are incorporated into the Fortran version 2.3 of the FMDM:

- The does rate function (dose rate as a function of time) was replaced by a function derived from the MCNPX results of Radulescu (2011). The new function calculates the dose rate at the fuel surface as a function of time based on the assumed average burnup of the fuel. The new function is described in Figures 2-3 and 2-4.
- The spatial dose rate function, which calculates the dose rate at nodes within the alpha radiation penetration zone (35 micrometers), was replaced with a new function derived from the MCNPX results of Radulescu 2011. The new function is described in Figure 2-5.

The following is an example section of code showing both the burnup – dose rate function and the spatial dose rate function based on Radulescu (2011). The MATLAB code is shown for clarity – the Fortran implementation is identical except for syntax differences.

```
BU = 60; %Fuel burnup in GWd/MTU
dect = 30; %Decay time of fuel in yr
aof = t/60/60/24/365+dect; %Age of fuel yr

%Relationship between age of fuel, burnup and dose rate (rad0)
%Simple fit from Radulescu 2011 report
 f1=log(aof)*log(aof);
 f2=log(aof);
 f3=1.0/log(aof);
 f4=log(aof)/aof;
 f5=exp(BU/25.26892627636246);
 rad0a = -206.0634818750711-0.7631591788870090*f1...
        +20.97112373957833*f2+678.8463343193430*f3...
        -506.7149017370657*f4+0.1555448893425319*f5;
 rad0 = max(exp(rad0a),5.0e-3);

 %Constant dose rate option
 %rad0 = 1.0; % (J/kg)/s = Gy/s = 100 rad/s

 %Dose rate profile with x
 rCut = exp(-0.14*(lmat*1.0e6)); %Exponential from Radulescu 2011
 %rCut = (max(1 - lmat./penD, 0)); %Linear decrease
 %rCut = lmat <= penD; %Step function

 rad = rad0.*rCut; %Dose rate used to determine H2O2 generation
```
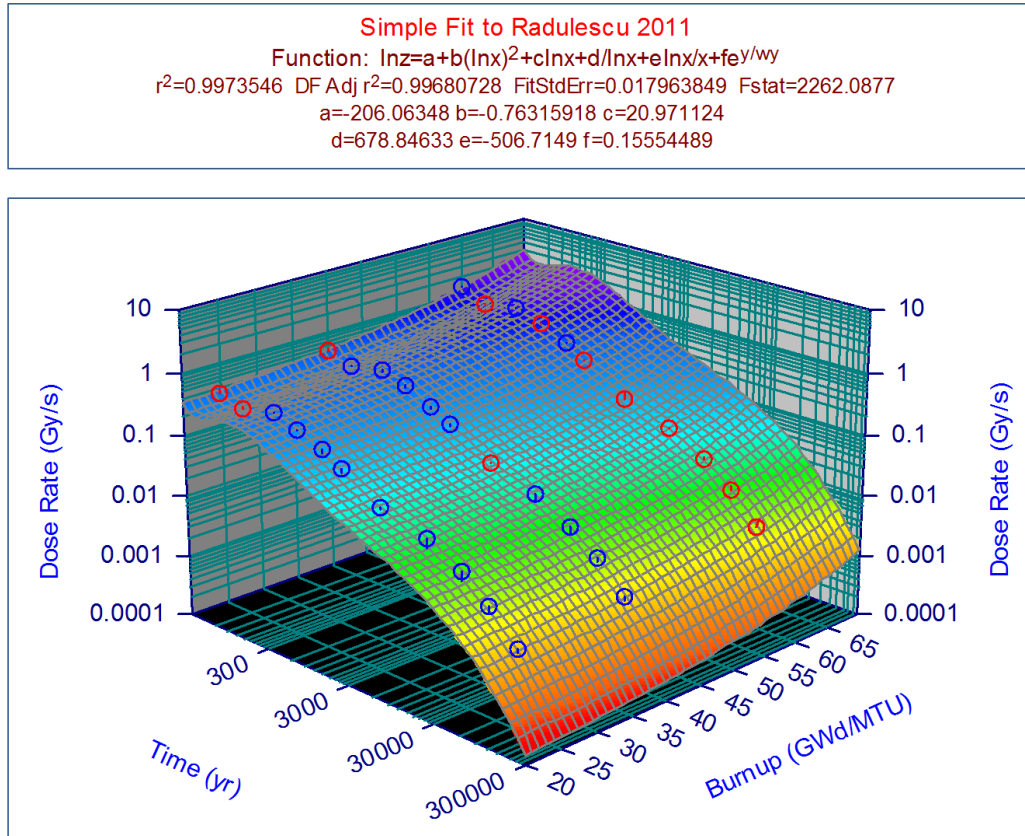
Figure 2-3: The burnup – dose rate function derived from the MCNPX results of Radulescu 2011 as a polynomial fit. The calculation points from Radulescu (2011) are shown as blue and red circles. Blue indicates that the data point falls below the fit surface and red indicates that the data point is above the fit surface. The derived function is shown as the surface: x = time, y = burnup, z = dose rate, where a, b, c, d, e, f and w are all fitting parameters.

Figure 2-4 shows a comparison between the new burnup – dose rate function and the MCNPX results of Radulescu (2011). This figure also shows a comparison between results from the MATLAB version of the FMDM (thin blue line) and the Fortran version (thick red line). This comparison indicates that the Fortran FMDM code accurately reproduces results from the MATLAB FMDM code, which has be validated against experimental data (Jerden et al., 2015).

The results shown in Figure 2-4 indicate that the burnup – dose rate function accurately reproduces the MCNPX results from Radulescu (2011) and that the Fortran and MATLAB versions of the FMDM produce essentially identical results. It is noted that the increase in dose rate from 100 – 200 years in Figure 2-4 corresponds with the ingrowth of Am-241.
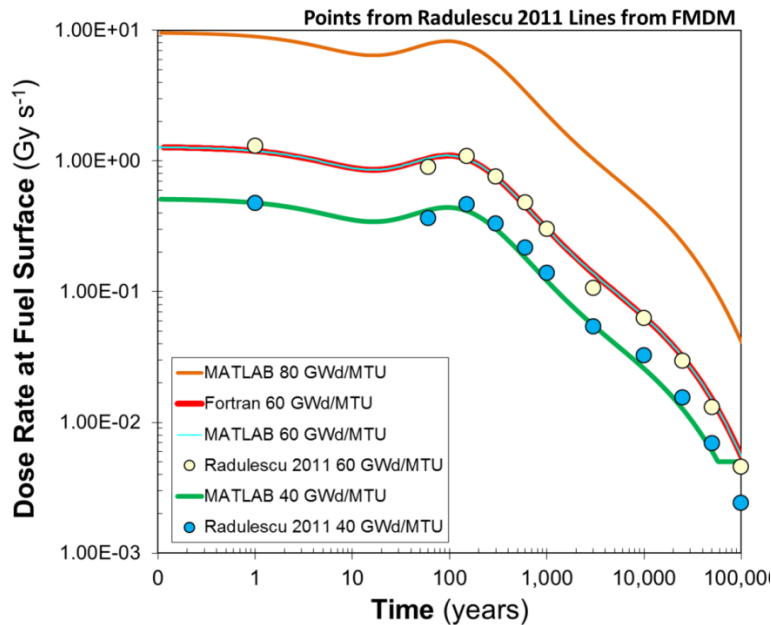
Figure 2-4: shows three types of results: (1) points from Radulescu (2011), (2) dose rate with time from an example simulation with the Fortran FMDM for 60 GWd/MTU (red), (3) dose rate with time from an example simulation with the MATLAB FMDM for 40, 60 and 80 GWd/MTU.

Figure 2-5 compares results from the new spatial dose rate function, which calculates the dose rate at each node within the alpha radiation zone, with the MCNPX of Radulescu 2011. The actual function in the code is:

*Spatial Dose Rate (Gy/hr at x) = Surface Dose Rate (Gy/hr) * exp[-0.14*(x (m)*1.0E+6)]*

The results shown in Figure 2-5 indicate that the spatial dose rate function in the FMDM reasonably represents the spatial dose rate calculations of Radulescu (2011).
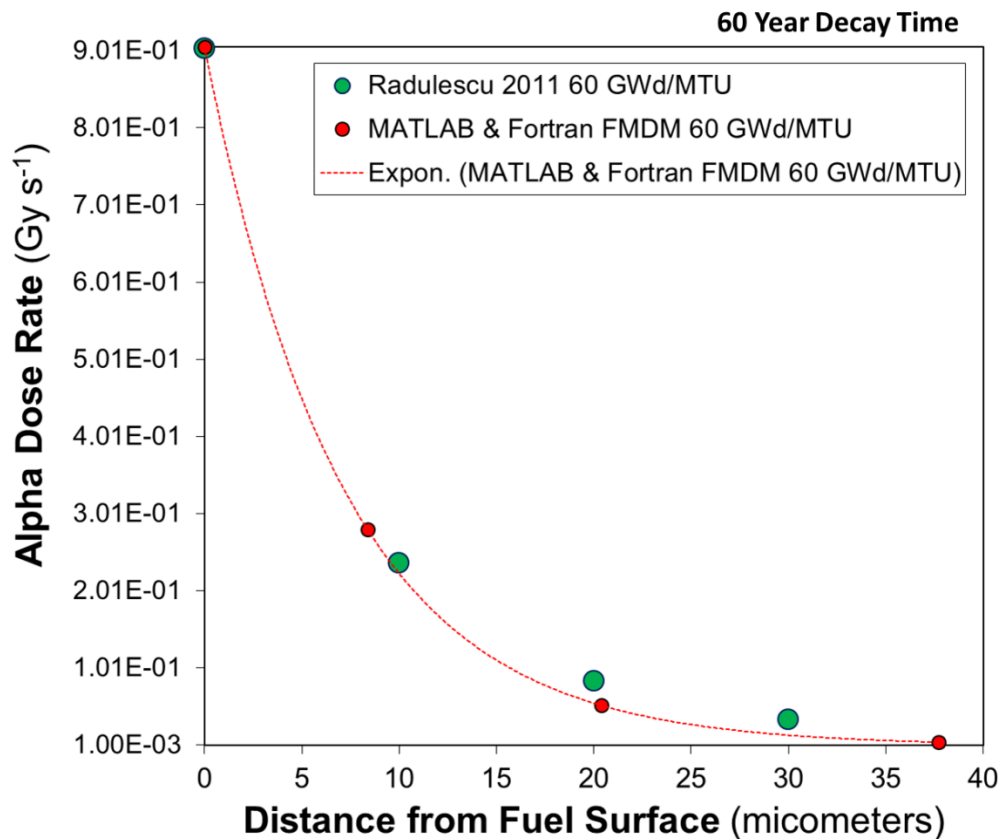
Figure 2-5: Alpha particle dose rate as a function of distance from the fuel surface. The red line is from example simulations with both the MATLAB and Fortran versions of the FMDM. The green points are from MCNPX calculations presented in Radulescu (2011).

Figure 2-6 shows direct comparisons of results from the FMDM MATLAB and Fortran versions (v2.3) for cases in which the H_2 concentration is varied. As shown in previous runs with the MATLAB version, the catalyzed oxidation of H_2 on the NMP surfaces at the fuel/solution inteface dramatically decrease the fuel dissolution rate at H_2 concentrations around 0.01 mM. This is consistent with experimental investigations as discussed in Jerden et al. (2015).

The runs shown in Figure 2-6 were performed to confirm that the H_2 catalysis reactions were accuratly represented in the Fortran version. The results show that the model outputs are essentially identical and that the breaks in the curves for 0.001mM H_2 and 0.01mM H_2 occur in both MATLAB and Fortran versions of the FMDM. The mathematic cause of these breaks or steps in the results is being studied as part of the continuing model development and optimization work. Note: the increase in dissolution rate at 100 -200 years corresponds with the dose rate increase associated with the ingrowth of Am-241.
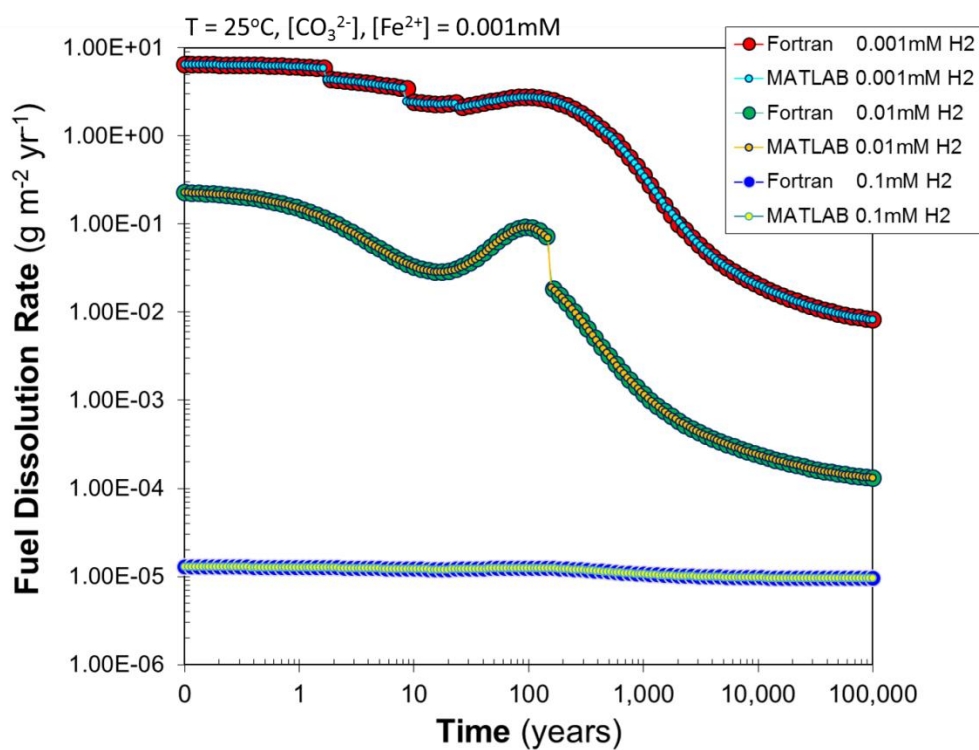
Figure 2-6: Results from three simulation cases performed with both the MATLAB and Fortran versions of the FMDM. For these cases carbonate and iron were held constant at 1.0×10^{-6} molar while H_2 was varied from 1.0×10^{-6} up to 1.0×10^{-4}. The Fortran simulation used 100 time steps, while the MATLAB run used 200 time steps. The results demonstrate that the Fortran and MATLAB versions of the FMDM give identical results.

2.2.3 Demonstration of Prototype Integrated PFLOTRAN – FMDM Model for PA

The method of integration of the FMDM Fortran version 2.3 with PFLOTRAN is summarized in Figure 2-7 (diagrams are from Hammond, 2015). The initial set up that was used to demonstrate the integrated code involved 52 separate 1x1x1 meter fuel bearing cells, each of which degraded at a rate determined by the FMDM (Figure 2-8). For simplicity, the waste container and the fuel cladding were ignored.

Following an initialization step, the PFLOTRAN repository simulation proceeds with energy and mass flow (multiphase flow, heat transfer, reactive transport) calculations, which determine the temperature and solution chemistry inputs for the FMDM (Figure 2-7 top diagram). The fuel burnup and the surface area are currently randomly selected by the code from a relevant range of values. For each time step of the repository simulation, the FMDM returns a fuel dissolution rate for each of the 52 used fuel cells in grams per square meters per year (Figure 2-7 bottom diagram). This is converted to grams per year using the randomized waste form surface area. This rate is then used to calculate the release of a non-sorbing, non-reacting tracer radionuclide (Figure 2-8).

The dimensions and conditions used for this initial demonstration of the integrated PFLOTRAN - FMDM code are as follows:

- Spatial discretization: 101x101x21m with 1m resolution (~214K grid cells)
- Temporal discretization: 100 years with 1 year time step (10^{-6} y initial)
- Waste cell spacing: 5m (X), 20m (Y) between 20-80 m
- Prescribed concentrations: $O_2(aq)$, $H_2(aq)$, HCO_3^-, Fe^{2+} all = 1 mM
- Fuel burnup: 55-65 GWd/MTU (random)
- Total fuel reactive surface area: 0.8-1 m^2 (random)
- Pore water velocity: 1 m/yr (X), 0.14 m/yr (Y)
- Computing performance: 66% of total time (~30 minutes) spent in FMDM

It is important to note that the results of the preliminary run with the PFLOTRAN – FMDM model (Figure 2-8) was for relatively high burnup values and oxidizing conditions. These factors lead to quite high fuel dissolution rates (on the order of $10 - 50$ g m^{-2} yr^{-1}) and thus rapid radionuclide release. The results from an on-going series of runs for anoxic conditions with both high and low H_2 concentrations will reveal the impact of the FMDM H_2 effect on radionuclide mobilization and will be used to confirm that the integrated model correctly represents the stand-alone FMDM process model.

Due to the relatively rapid fuel dissolution rate and probably high reactive surface area values, the mobilization of the tracer radionuclide is relatively rapid; and while, there is some variation in the tracer concentration among individual waste cells (e.g., t_2, Figure 2-8) the overall plume shapes for the four waste cell rows are nearly identical. As mentioned above, results from on-going runs with the integrated model will reveal sensitivities of radionuclide mobilization to key variables such as H_2, O_2 and CO_3^{2-} concentrations. Based on this initial model coupling experience a number of near-term improvements for the integrated code have been identified:

- Increasing flexibility of coupling
- Ability to customize FMDM discretization from PFLOTRAN side
- Incorporating transient surface area
- Updating to FMDM v3.0
- Optimizing FMDM serial performance
- Integration into simulation of a repository with many waste packages

- Adding increasingly mechanistic geochemistry
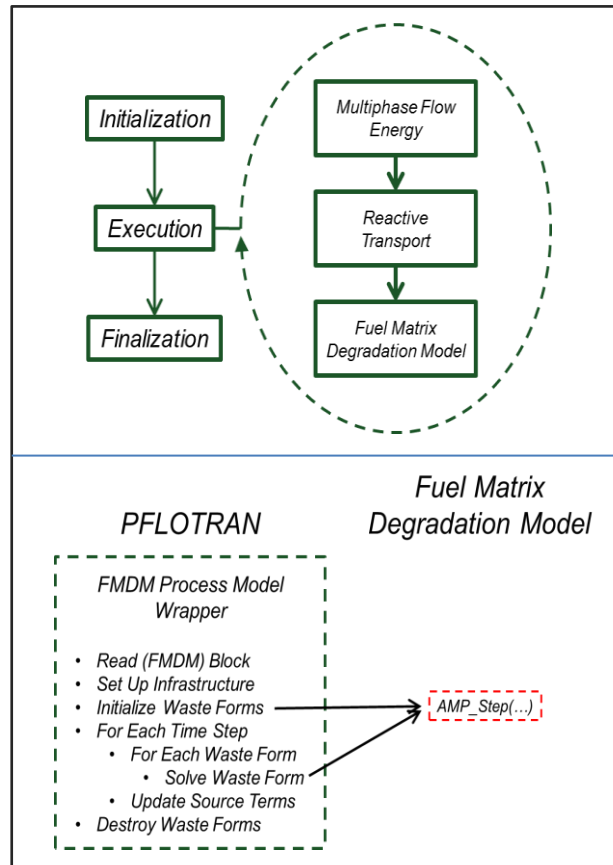
Figure 2-7: Schematic diagrams summarizing the workflow in the prototype PFLOTRAN – FMDM model (from Hammond, 2015).

Figure 2-8: Results from a scaled-down PFLOTRAN repository model in which the FMDM process model has been integrated to determine the dissolution rate of the used fuel and thus the source term of a non-sorbing tracer. The effects of the fuel canister and cladding are ignored. Because this is a prototype model meant only to demonstrate successful model integration, the time scales are left generic (to avoid over-interpretation).

The on-going model integration work is conceptually summarized in Figure 2-9, which shows the overall flows of information between the GDSA code (PFLOTRAN) and the FMDM. The FMDM box identifies what processes are currently included in the integrated model (v2.3), and the new processes that need to be added to bring the FMDM up to date with the recent scientific findings on the dissolution behavior of used nuclear fuel.
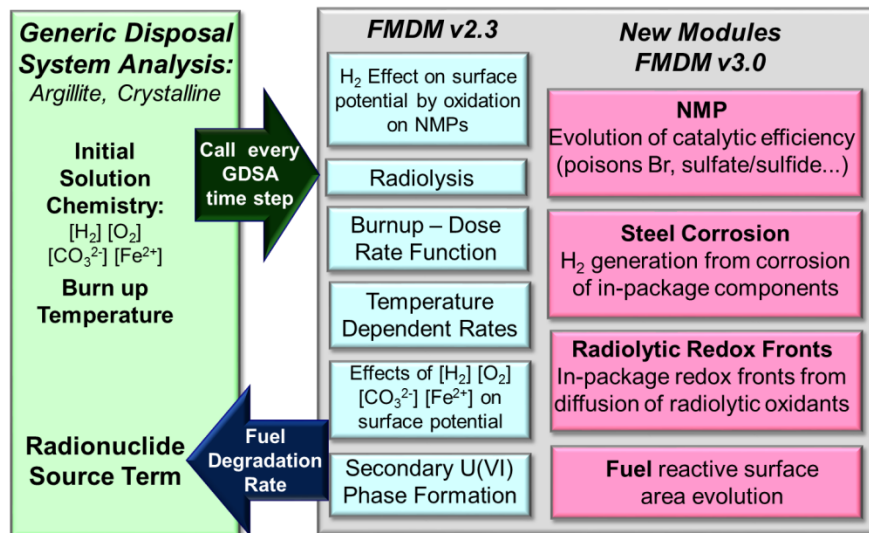
Figure 2-9: Conceptual summary of the flow of information between the GDSA PA model and the FMDM. Processes currently in the FMDM (v2.3) are shown in blue, while new processes that need to be added to bring the FMDM up to date with current scientific findings are shown in pink.

2.3   SCOPING WORK FOR THE DEVELOPMENT OF A CANISTER CORROSION MODEL

The quantification of the long-term corrosion behavior of steels in relevant environmental conditions is central to developing a science-based performance assessment for nuclear waste repositories. The mixed potential theory on which the FMDM is based is ideal for quantifying steel corrosion because it accounts for the fundamental electrochemical mechanisms. Scoping work has thus been initiated to investigate the extension of the FMDM to include the corrosion of a steel surface, which would be located at some distance x from the fuel/NMP surface in the one dimensional FMDM reaction/diffusion domain. That is, the steel corrosion model will have a one-dimensional reaction diffusion layout continuous with the existing FMDM.

As with the FMDM, the steel corrosion model will use mixed potential theory to determine the corrosion rate based on the kinetic balance of all relevant interfacial redox reactions. Homogeneous reactions and diffusion processes that determine the supply of reactants to the steel surface and alteration phase saturation indexes will be taken into account. There are several advantages to this approach of incorporating a steel corrosion model into the FMDM:

- It directly couples fuel degradation and steel corrosion. This is vital, as it has been shown that, even at sub millimolar concentrations, the H_2 produced from the anoxic corrosion of steel can decrease the fuel dissolution rate by over four orders of magnitude (Jerden et al., 2015).

- By directly coupling the fuel and steel degradation, this approach also allows for the quantification of redox fronts that develop within the waste container due to the diffusion of radiolytic oxidants away from the fuel surface and the reactions of these oxidants with the steel surface and the resulting aqueous Fe^{2+} and H_2. This is also important because these redox fronts represent the Eh of the in package solutions in contact with the waste form and waste container internal components.
- This approach will allow the steel corrosion module to be readily implemented into the GDSA PA PFLOTRAN model, as it will be incorporated into the FMDM, a version of which has already been integrated with PA (see Section 2.2.3 above).

The original MPM developed as part of the Canadian repository program, on which the FMDM is based, contained a corroding steel surface (see King and Kolar, 2003). In fact, the earliest version of the FMDM included this corroding steel module, but it was removed so that the modeling efforts could focus on quantifying and optimizing the NMP catalyzed H_2 reactions at the fuel surface. By adding the full steel corrosion module, the extended FMDM could be used to quantify a number of processes that are essential for calculating both container life times and the kinetic interdependencies of fuel and steel corrosion. Specifically, the steel module of the envisioned extended FMDM (version 3.0) would quantify the following processes:

- Selection of passive or active corrosion mechanisms depending on the calculated corrosion potential.
- The generation of H_2 during anoxic corrosion, which has been shown to inhibit the dissolution of used fuel and can lead to alloy embrittlement.
- Production of radiolytic oxidants, which can determine whether a steel corrodes by aerobic or anoxic processes.
- Interactions with porewaters to form iron silicate colloids and surface coatings such as Fe-saponite.
- Sorption of radionuclides to colloidal and fixed steel corrosion products. The model layout and context are shown in the figures at the end of this document.

The conceptual layout of the extended FMDM v3.0 is shown in Figure 2-10. The inputs from the PFLOTRAN PA model would be the same as those discussed in Section 2.2 above. However, the calculated steel dissolution rate (mass per area per time) would be added as and output to PFLOTRAN.
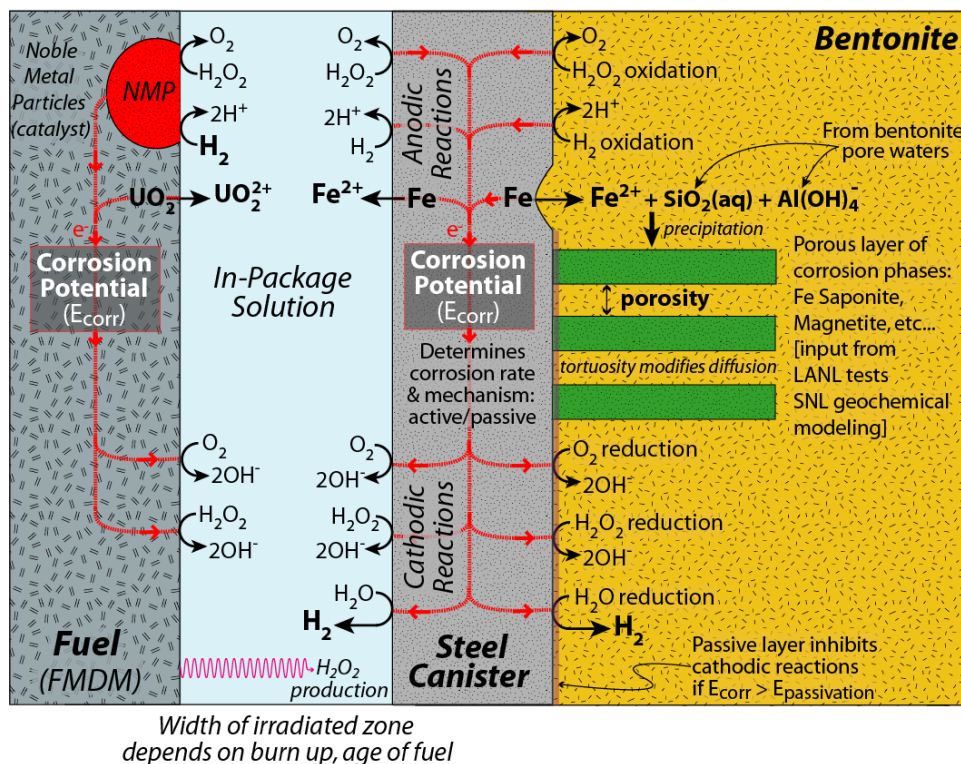
Figure 2-10: Conceptual layout for the extended FMDM version 3.0 that includes a module quantifying steel corrosion (only key interfacial reactions are shown).

As part of this scoping study the older version of the FMDM that contained the steel corrosion module was run for a number of cases to further investigate how the fuel and steel corrosion reactions would influence each other in the context of the model. Example results from these scoping runs are shown in Figure 2-11. The examples show how the diffusion of H_2O_2 away from the alpha radiation zone would set up redox fronts within the solution separating the corroding surfaces (Figure 2-11, top plot). Figure 2-11 also shows a how the concentration profile for H_2 is predicted to evolve (Figure 2-11, bottom plot). The time labels for the profiles in Figure 2-11 are generic because this model is not fully developed and does not include some processes that will effect diffusion rates (e.g., porosity and tortuosity of corrosion layers). That is, the overall shape of the concentration profiles are believed to be accurate, but the absolute time evolution may not be. The overall shape of the concentration profiles and how they change with time are instructive for understanding the inter-dependencies of the two corrosion processes.
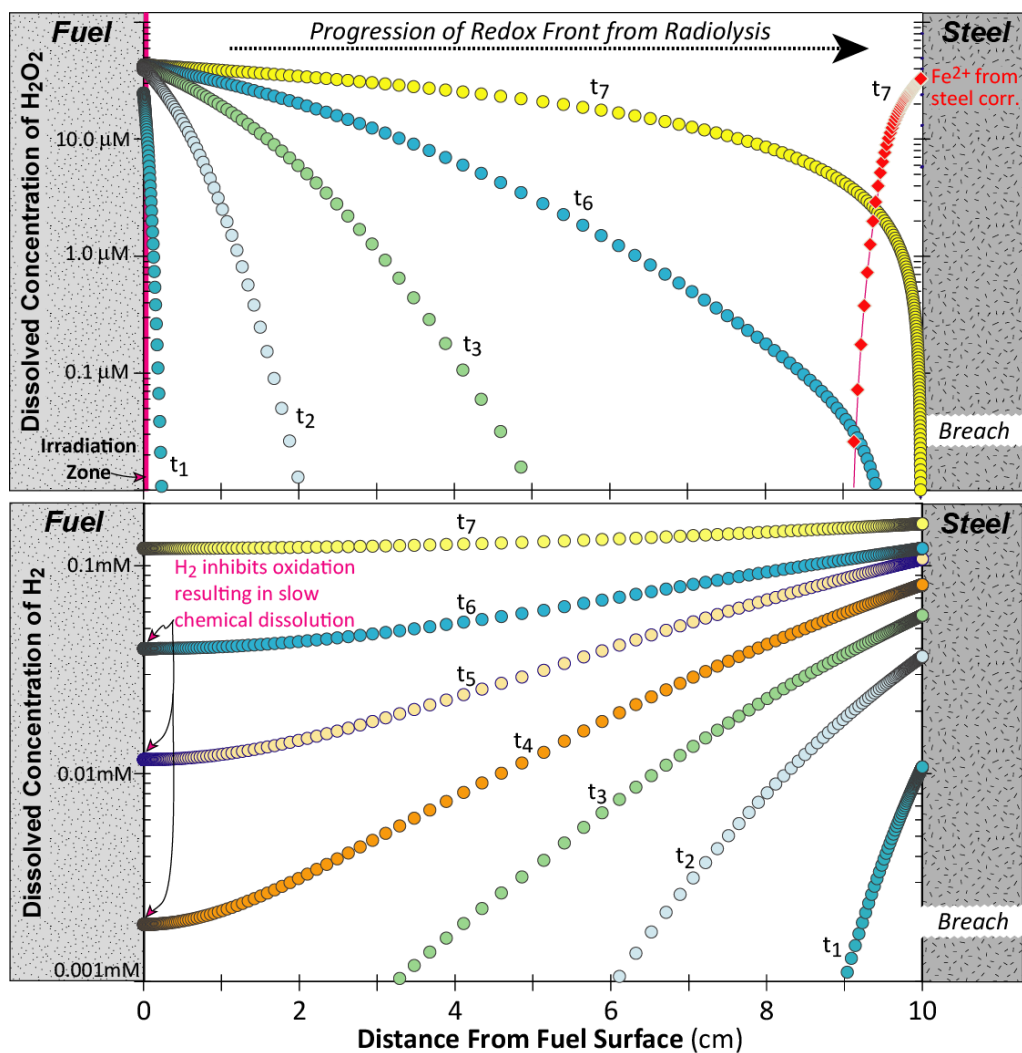
Figure 2-11: Results from an older version of the FMDM that included a corroding steel surface. The top plot shows how H_2O_2 diffusion away from the irradiation zone can set up redox fronts that evolve through time within the in-package solution. The bottom plot shows H_2 concentration profiles with time. Time labels are generic because this model does not include variables known to influence diffusion rates (porosity and tortuosity of corrosion layers). The overall shape of the concentration profiles is accurate, but the absolute time evolution is uncertain.

2.4   RESULTS FROM SCOPING EXPERIMENTS ON POISONING OF NOBLE METAL PARTICLES

In order to ensure that the process models for used fuel degradation and steel corrosion (sections 2.2 and 2.3 above) accurately represent reality within the relevant ranges of repository conditions, the model development efforts need to be coupled with a focused experimental program to quantify key parameters and provide data sets for validation. To this end, the radiological electrochemical testing facilities at Argonne are being used to investigate the interfacial and homogeneous reactions that dominate used fuel degradation.

As shown in Jerden et al. (2015) the catalysis of H_2 oxidation on the NMPs drives the used fuel dissolution rate down by as much as four orders of magnitude when dissolved H_2 concentrations reach approximately 0.1 mM. Because this NMP – H_2 catalysis process plays such a key role in determining the used fuel dissolution rates and its mechanism is not yet fully understood, it is the subject of on-going electrochemical experiments designed to directly inform the process modeling efforts (i.e., the extension of the FMDM to version 3.0).

The experimental set up consists of a 20 mL, three-electrode cell in which the experimental cover gas is continuously bubbled during the experiments (Figure 2-12). Multiple cells (experiments) are run simultaneously within an oven in a radiological laboratory. Multiple power supplies and potentiostats are available so that tests with two or more working electrodes (e.g., NMP and UO_2) can also be performed. The electrodes are characterized pre- and post-experiment by optical and Scanning Electron Microscopy (SEM). The solutions from selected tests are analyzed for electrode constituents (Ru, Mo, Pd, Rh, Tc, U, and other dopants such as REE) by Inductively coupled plasma mass spectrometry (ICP-MS).
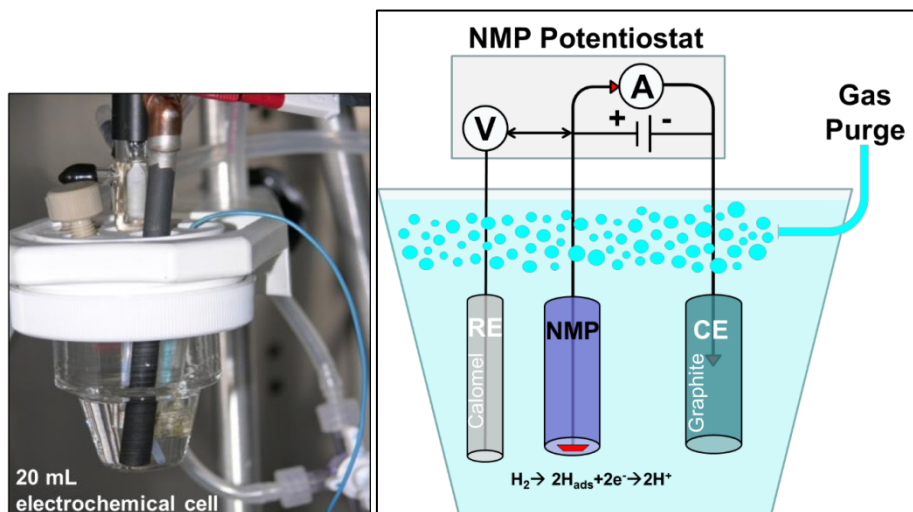
Figure 2-12: Photograph and schematic diagram of the type of cell used for the electrochemical experiments.

The scoping tests performed in FY 2015 focused on the H_2 reactions with a NMP electrode. The electrode was made in house (Argonne) from an alloy produced by Steve Frank at Idaho National Laboratory that closely matches the composition and homogeneity (single alloy phase) of the NMP found in used fuel. The NMP alloy used to make the electrode has a composition of $Ru_{56}Mo_{20}Rh_{11}Pd_{11}Tc_2$ and, based on SEM characterization, appears to be composed of a single phase with perhaps some minor amounts of TcO_2.

One of the most important experimental observations made regarding the role of H_2 in used fuel dissolution is that the presence of halides, particularly Br^-, seems to counteract the H_2 effect (Metz et al., 2008). Although poorly understood, our new results (Figure 2-13) suggest that the NMP surface may be poisoned by halides thus reducing their catalytic efficiency (i.e., counteracting the protective H_2 effect). The poisoning and alteration of the NMP surfaces are not currently accounted for in the FMDM, because these processes are not well understood or quantified. However, due to the importance of the H_2 effect these processes are deemed high priorities for experimental investigations.

To investigate the reaction of H_2 on the NMP electrode scoping tests were performed in which the open circuit potential of the NMP electrode was measured for up to 80 hours in approximately 1 mM NaCl while cover gases of air, Ar or 2% H_2 in Ar were bubbled through the solution. The possible poisoning effect of Br^- was also investigated by performing the 2% H_2 cover gas tests in solutions containing 1 mM NaBr. The pH for all tests remained relatively constant at around 7.0. Typical examples of the results are shown in Figure 2-13.

The results show a pronounced H_2 effect that causes a decrease in the potential of the NMP electrode from greater than 260 mV (vs. SHE) for the air cover gas tests down to less than 100 mV for tests performed with 2% H_2 in Ar as the cover gas. The observation that this large potential drop is not seen when the test is performed in pure Ar indicates that it is due to the H_2 oxidation on the NPM electrode. This shows that, under near neutral conditions, the NMP surface is hosting anodic reactions that can be generalized as:

$$H_2 \rightarrow 2H_{adsorbed} + 2e^- \rightarrow 2H^+ \tag{2-1}$$

As indicated by the green curve in Figure 2-13, the presence of 1 mM Br^- partially counteracts the H_2 effect, shifting the NMP surface potential up by approximately 60 mV. This shows that even over short time frames (minutes) the presence of Br^- has an effect on the NMP – H_2 reaction. This is a significant observation as it identifies a key chemical process that is not currently accounted for in the FMDM.

The implication is that, if repository ground waters contain sufficient Br^-, the H_2 effect, which "protects" the used fuel from dissolution, will be counteracted due to the degradation of NMP catalytic efficiency. This implication was quantified by running the FMDM for a series of cases in which the NMP catalytic efficiency was decremented (Figure 2-14). The results highlight the importance of understanding poisoning or fouling processes that could counteract the NMP catalyzed H_2 effect. More experimental work is needed to quantify these key processes.
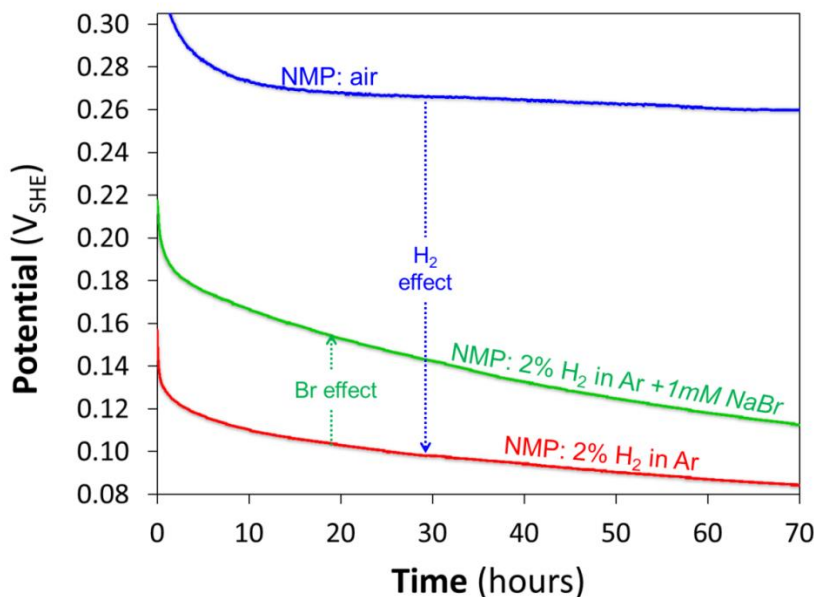
Figure 2-13: Results from scoping electrochemical tests showing the open circuit potential of the $Ru_{56}Mo_{20}Rh_{11}Pd_{11}Tc_2$ (NMP) electrode for three different tests. Note that the presence of Br$^-$ partially counteracts the H$_2$ effect.

It is important to note that even after 70 hours, the open circuit potentials for the NMP have not reached a constant (steady state) value. This indicates that the surface of the electrode may need to be pre-conditioned in the solutions of interest for extended periods of time to achieve steady state with respect to all redox reactions. Future work will involve the thorough surface characterization of the NMP electrode by SEM before and after the experiments to identify any alteration or pitting that may affect the surface reactions.

Future work will also involve a series of electrochemical tests with simulated used fuel that consists of electrically coupled NMP in a UO_2 matrix. These tests will be used to generate a validation data set for the FMDM.

As mentioned above, to quantify the possible poisoning effect of the catalytic NMPs several sensitivity runs were performed with the FMDM v2.3 in which the poisoning process was simulated be decreasing the active NMP surface coverage while the H$_2$ concentration, burnup and temperature were held constant from run to run (Figure 2-14). For these sensitivity runs the fuel burnup was 60 GWd/MTU, the age of the fuel was assumed to be 30 years (out of reactor) and the temperature was held constant at 25°C.

The results show that for a solution containing 1 mM dissolved H$_2$, the presence of 1% surface coverage of NMP leads a greater than 5 orders of magnitude decrease in the dissolution rate relative to the no NMP case. This H$_2$ effect is counteracted by decreasing the active surface area of the NMP. For example, decreasing the NMP surface coverage from 1% to 0.1% causes a an increase of a factor 50 in the predicted dissolution rate, while a decrease to 0.01% results in a dissolution rate increase of around 5 orders of magnitude. These FMDM sensitivity runs are quite preliminary as the mechanism and magnitude of the NMP poisoning process is not yet understood. These results do however underscore the need for continued experimental work to quantify processes that may have a significant effect (orders of magnitude) on the fuel degradation rate and thus radionuclide source term in the PA calculations.
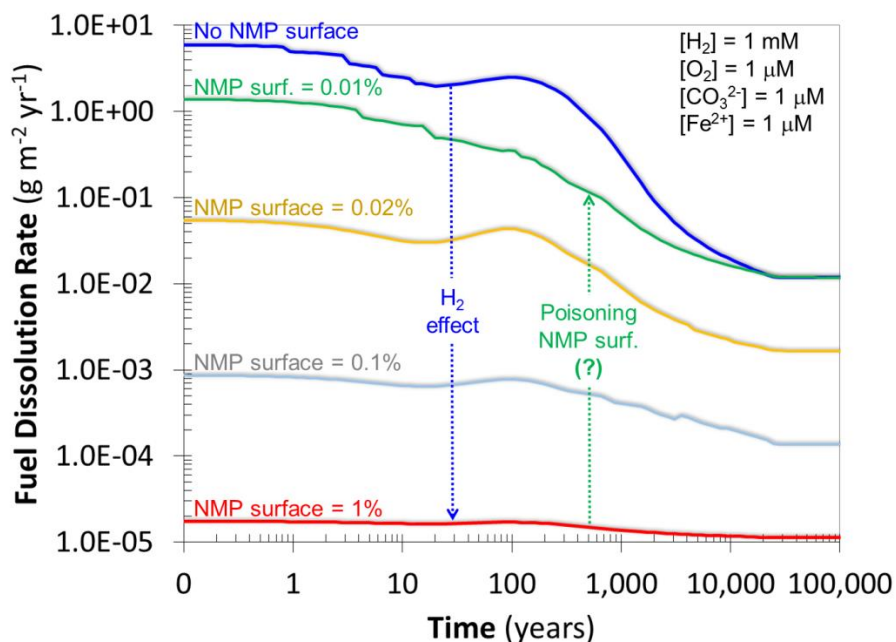
Figure 2-14: Results from the FMDM v2.3 showing the dramatic decrease in fuel dissolution rate caused by the oxidation of H_2 on the NMP and the possible effect of poisoning of the NMP surface (blocking the H_2 oxidation reaction). For these sensitivity runs the fuel burnup was 60 GWd/MTU, the age of the fuel was assumed to be 30 years (out of reactor) and the temperature was held constant at 25°C. The possible poisoning of the NMP surface was accounted for by decreasing the active surface area of the NMP.

2.5   CONCLUSIONS AND FUTURE WORK

The main accomplishments for Argonne's FY2015 work on the Fuel Matrix Degradation Model (FMDM) development project are as follows:

- Completed a model validation study in which results from the state of the art FMDM were compared to experimental data from international geologic repository programs. This study was published in the Journal of Nuclear Materials: "A Multiphase Interfacial Model for the Dissolution of Spent Nuclear Fuel" by J. Jerden, K. Frey and W. Ebert, Volume 462, July 2015, Pages 135-146.
- Completed conversion of the state of the art FMDM (version 2.3) to Fortran to facilitate integration with the Generic Disposal System Analysis (GDSA) repository Performance Assessment (PA) code PFLOTRAN.
- Worked with SNL scientists to complete and test a prototype integrated PFLOTRAN-FMDM repository model for the argillite and crystalline work packages.
- Completed preliminary model runs focused on expanding the FMDM to account for corrosion of the used fuel steel canister.
- Completed scoping experiments investigating the possible poisoning of the Noble Metal Particles (NMP), which are known to catalyze the oxidation of H_2, thus shutting down the oxidative dissolution of used fuel.

The current version of the FMDM has proven effective for quantifying key processes affecting the rate of used fuel degradation; however, the implementation of FMDM within a performance assessment model requires further model development to account for steel corrosion and the possible poisoning of the NMP

phase, which is responsible for the protective H$_2$ effect. Focused experiments are also needed quantify key parameter values and provide data sets for model validation. In order to take advantage of the work that has been done so far on the FMDM, a number of needs have been identified:

- Take next step in integration of FMDM with PFLOTRAN: demonstrate sensitivity of the argillite PA model to key variables in the FMDM such as burnup, surface area and the dissolved concentrations of H$_2$, O$_2$, carbonate and ferrous iron.
- Extend the FMDM to account for the corrosion of the steel waste canister. This will quantify feedbacks between H$_2$ production at the corroding steel surface and the dissolution rate of the used fuel.
- Perform focused electrochemical experiments to determine the effect of halides and other possible poisons on the catalytic efficiency of the NMP. These tests will quantify processes that may counteract the protective H$_2$ effect.

Several specific priorities that have come out of the FMDM – PFLOTRAN integration work are as follows:

- Increasing flexibility of coupling
- Ability to customize FMDM discretization from PFLOTRAN side
- Incorporating transient surface area
- Updating to FMDM v3.0
- Optimizing FMDM serial performance
- Integration into simulation of a repository with many waste packages
- Adding increasingly mechanistic geochemistry

2.6   REFERENCES

Buck E., Jerden, J., Ebert, W., Wittman, R., (2013) C*oupling the Mixed Potential and Radiolysis Models for Used Fuel Degradation,* FCRD-UFD-2013-000290.

Hammond G., (2015) *Generic Disposal System Analysis (GDSA): Coupling of PFLOTRAN to the Fuel Matrix Degradation Model (FMDM),* Slide Presentation*,* Used Fuel Disposition Campaign Annual Working Group Meeting, Las Vegas, NV, June 9-11, 2015

Jerden J. Copple J., Frey K. Ebert W., (2014) Prototype Fortran Version of the Mixed Potential Process Model for Used Fuel Degradation, Used Fuel Disposition Campaign Milestone: M4FT-15AN0806012, October 15, 2014

Jerden J. Frey K. Ebert W., (2015) A Multiphase Interfacial Model for the Dissolution of Spent Nuclear Fuel*, Journal of Nuclear Materials*, 462, 135–146

King F. and Kolar M., (2003). *The Mixed-Potential Model for UO$_2$ Dissolution MPM Versions V1.3 and V1.4*., Ontario Hydro, Nuclear Waste Management Division Report No. 06819-REP-01200-10104 R00.

Metz V., Loida A., Bohnert E., Schild D., Dardenne K., (2008) Effects of Hydrogen and Bromide on the Corrosion of Spent Nuclear Fuel and γ-irradiated UO$_2$(s) in NaCl Brine, *Radiochim. Acta* 96, 637–648

Radulescu, G., (2011) Repository Science/Criticality Analysis, Oak Ridge National Laboratory, Reactor and Nuclear Systems Division, FTOR11UF0334, ORNL/LTR-2011, Oak Ridge National Laboratory, Oak Ridge, TN.

Röllin S., Spahiu K., Eklunda U., (2001), Determination of Dissolution Rates of Spent Fuel in Carbonate Solutions Under Different Redox Conditions with a Flow-through Experiment, *Journal of Nuclear Materials*, 297, 231–243

Wang Y. et al., (2014) *Used Fuel Disposal in Crystalline Rocks: Status and FY14 Progress*, FCRD-UFD-2014-000060, SAND2014, Sandia National Laboratories, Albuquerque, NM.

3.0   INVESTIGATION OF THERMAL EFFECTS ON THE CHEMICAL BEHAVIOR OF CLAYS

3.1   INTRODUCTION

Clay minerals are likely candidates to aid in nuclear waste isolation due to their low permeability, favorable swelling properties, and high cation sorption capacities. Establishing the thermal limit for clay minerals in a nuclear waste repository is a potentially important component of repository design, as flexibility of the heat load within the repository can have a major impact on the selection of repository design. For example, the thermal limit plays a critical role in the time that waste packages would need to cool before being transferred to the repository.

Understanding the chemical and physical changes that occur in clay minerals at various temperatures above the generally recommended thermal limit (of 100 °C) can enable decision-makers with information critical to evaluating the potential trade-offs of increasing the thermal limit within the repository. Most critical is gaining understanding of how varying thermal conditions in the repository will impact radionuclide sorption and transport in clay materials either as engineered barriers or as disposal media.

This study documented in this chapter concludes that mineralogic alteration is the most important factor to consider, in terms of predicting the most salient chemical and physical changes induced by heat treatment of both illite and smectite clays. The amount of clay converted to other silicate phases (Quartz, mullite, etc.) directly determines the amount of change in sorption capacity of both clay-based buffer materials.

Experimental measurements for clay mineral response to thermal loads are critical as direct evidence of material response under thermal load, as well as for parameter input for themal-hydrlogic-mechanical-chemical (THMC) models of repository materials under different thermal loadings. Due to the high sorption potential of clays, in depth understanding of transport and uptake of radionuclides in clay minerals is key. By determining if there are any changes in surface area and cation exchange capacity, as a function of thermal load, this work has the potential to provide key parameters for THMC modeling studies.

3.2   STATE OF THE ART

While the dehydration and dehydroxylation of clay minerals over a range of temperatures from 100 ° C to well over 1000 °C have been studied (Wolters and Emmerich 2007, Muller et al. 2000), focus has been on understanding structural changes during dihydroxylation. Complete dehydration for most clay minerals of interest occurs at temperatures over 500 °C. Other studies involving thermal treatments of clay minerals have mostly focused on clay-type identification (Moore and Reynolds 1997) and heating in conjunction with chemical treatments to enhance dispersion of clay minerals as pillared nanomaterials (de Carvalho Costa et al. 2013) or for applications in catalysis and environmental remediation (Frost and Ding 2003). Onal (2007) studied the simultaneous effect of heat and sulfuric acid treatment on bentonite, and measured CEC and swelling capacity as a function of temperature over a range of 100 °C to 1300 °C. Studies aimed at understanding the thermal effects on clay minerals in the natural environment tend to focus on diagenesis and sedimentology, in which case the interplay between physical structure (e.g., pore evolution, d-spacing) and chemical properties (CEC, anion uptake) are not the main focus.

Studies that have foucused on heat effects on hydrothermal alteration of bentonites that three types of alteration are plausible at temperatures above 100 °C: 1) illitization (Cuadros and Linares 1996, Pusch and Karnaland 1988a), 2) cementation -- by formation of silica minerals, calcite, or sulphate (Pusch et al. 2003), and 3) chloritization (Howard and Roy 1985). While these aforementioned possibilities exist for heat-induced alteration of clay-based materials, the likliehood of repository conditions creating the right chemical, temporal, and thermal conditions to produce such alterations warrants further systematic study (Wersin et al. 2007).

3.3   TECHNICAL APPROACHES

3.3.1   Sample Preparation and Heat Treatments

The clays used all originate from the Clay Mineral Society source clays project at Purdue University. Four clays were used: illite and montmorillonite (ID numbers: IMt-1 and SWy-2, respectively). The clays used were relatively pure. The main purification step used for all of the clays was mechanical separation at 75 microns. The <75 microns size fraction was used in all the experiments presented here.

For each clay, samples of the <75 micron size fraction were individually heated for 2 hours at 100 °C, 200 °C, 300 °C, 400 °C, and 500 °C. Samples were weighed before and after heat treatments to measure weight loss. For select experiements, one of two cooling protocols was used: 1) dessicator-cooled and/or 2) furnace-cooled. After all heat treatments, samples were stored in a desiccator to prevent any post-heat treatment uptake of ambient moisture.

Clay samples of <75 micron size fraction were also heated to 100°C, 500°C, and 800°C and held at these temperatures for 8.5 hours at a ramp time of 2 hours in an open container. Heating experiments were done in closed systems as well by use of parr vessels where moisture could be added to the clay sample. This system was also used for closed-cell dry heating. For closed-cell samples with moisture, a 5:1 solid to solution ratio mixture was prepared.

3.3.2   Surface Area Measurements

Heat treated samples were analyzed by nitrogen adsorption (NAD) using a Micromeritics Tristar 3000 to obtain data for BET surface area. Nitrogen adsorption was performed on all heat treated clay minerals, as well as on untreated samples of each clay type to form a basis of comparison. Due to the heating involved in standard sample preparation protocols for NAD, none of these samples were heated and pumped under vacuum prior to NAD analysis. While this means that the surface areas reported herein may differ significantly from those reported elsewhere, all samples in this study – including untreated (i.e. no heat treatment) – were all handled and prepared in the same manner such that the results are comparable within the scope of this study. The Brunauer, Emmett, and Teller (BET) isotherm was used to determine surface area (herein referred to as "BET surface area").

It is recognized that the BET surface area provides a measurement of the the external surface area (particle-partcile) owing to the fact that the nitrogen does not penetrate the clay interlayer. The methylene blue method of measuring surface area, under circumneutral pH, provides a measure of the total surface area -- edge sites plus basal surfaces (Kahr and Madsen 1995). Internal surface area, then, can be calculated as the difference between the BET surface area and the methylene blue surface area.
Methylene blue adsorption was used to measure the total surface area of the clay minerals in this study. Following a method by Kahr et al. (1995), surface area measurements were made by exposing the clay samples to methylene blue solutions of specific concetrations and measuring the uptake of methylene blue via UV-vis spectroscopy. A calibration curve was first made using methylene blue and water standards

ranging from 10^{-2} to 10^{-9} M. Standards were left on shaker table overnight in a closed container so as to avoid exposure to light, and then centrifuged; 4400 rpm for 1 hour. Absorbance of samples was read using a Beckman Coulter DU 800 UV-Vis at a wavelength of 660nm. A second degree polynomial was used to derive an absorbance curve from the calibration datasets.

The sodium exchanged form of the heated clays (.05 g of montmorillonite, .2g of illite and .2g of illite/smectite) were diluted to a desired concentration with DI water with varying ratios of methylene blue (solution 10mL total).   Clay was suspended in the MB/DI water solution in centrifuge tubes and left on shaker table overnight. Samples were centrifuged at 4400 rpm for one hour and supernate was collected. Supernate absorbance was read using the UV-vis at 660nm. Supernate was also diluted with DI water to 1:10 and 1:100 and ran on the spectrometer.

Using the absorbance measured by the spectrophotometer and the polynomial equation the moles of methylene blue that were sorbed byclay samples were calculated. Graphing the methylene blue added vs the methylene blue absorbed, a "break" point was determined by visual inspection of the location where the absorbance curve reached a constant value.   The surface area of the clays was then calculated assuming a surface area of 130Å^2 for the methylene blue cation (Kahr et al., 1995).

3.3.3   Cation Exchange Capacity (CEC) measurements

Cation exchange capacity was measured using the barium chloride method, as described by Gillman (1979). Heat treated samples were weighed and 0.1M $BaCl_2$ solution was added at a solid to solution mass ratio of ~1:20.   The suspension of clay and $BaCl_2$ solution was then shaken for 24 hours, centrifuged, and sampled (from the supernatant). After removing all of the supernatant for sampling, fresh $BaCl_2$ was added to the clay, which was again shaken, centrifuged, and sampled. This was repeated a third time – all 3 supernatant samples were collected cumulatively (i.e. sequentially added to a single sample collection vial) and analyzed on a Perkin Elmer 8000 series ICP-OES. Each clay sample was prepared and analyzed in triplicate.

3.3.4   Particle Size measurements

Particle size was measured by using a Malvern Zetasizer Nano ZS90. Samples of a 1% mass loading in DI water were made from the heat treated clay of illite and smectite. Each of the samples was suspended by rigorous shaking. Directly following suspension, 3 mL were pipetted into a cuvette, which was placed into the Zetasizer to be analyzed via the particle size module.

3.3.5   Settling Rate Measurements

Three 1% mass loaded samples of smectite clay heated to 100C, 500C, and 800C open for 8 hours were suspended at the same time. They were allowed to settle over time standing vertically with photos being taken at equivalent time intervals.

3.4   TECHNICAL RESULTS

3.4.1   Mass Loss on Heating

Mass loss was measured and percent mass loss was calculated from this data for each of the clays in the study (illite, illite/smectite, and smectite). The results are shown in Figures 3-1 through 3-3. For illite samples, the data suggests that there is only an effect on the 500 °C sample. This difference, however, does correlate with a statistically significant change in internal surface area, but has no significant effect CEC (for more discussion, see technical results section 3.4.2 and 3.4.3 for Surface Area and CEC results). For the smectite, as with the illite/smectite, there is a difference on the order of a few percent between coolong conditions for the 100 °C sample, but this difference correlates with only a slight difference in surface area. There is no statistically significant difference between the two cooling methods for CEC.
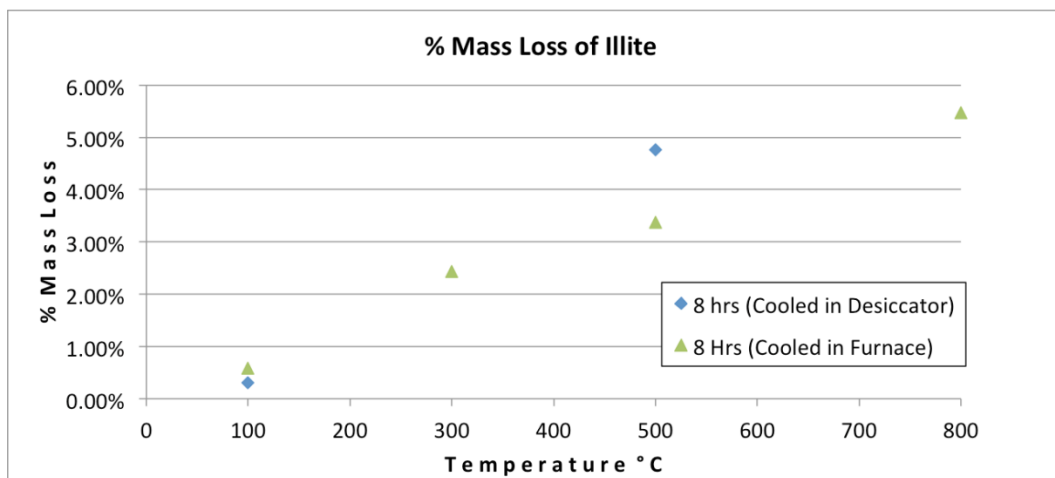
Figure 3-1: Percent mass loss for illite, showing a comparison between cooling methods – dessicator-cooled vs. furnace-cooled. Samples cooled in the dessicator were immediately placed in the dessicator to cool, in theory, unable to re-adsorb moisture during the cooling. Furnace-cooled samples were allowed to cool in the furnace as it cooled, and were potentially subject to ambient moisture level, thus able to re-adsorb some qusantity of moisture released during heating.

Figure 3-2: Percent mass loss for Smectite, showing a comparison between cooling methods – dessicator-cooled vs. furnace-cooled. Samples cooled in the dessicator were immediately placed in the dessicator to cool, in theory, unable to re-adsorb moisture during the cooling. Furnace-cooled samples were allowed to cool in the furnace as it cooled, and were potentially subject to ambient moisture level, thus able to re-adsorb some quantity of moisture released during heating.

3.4.2   Surface Area Measurements

Surface area measurements were made to investigate if changes to internal or external surface area occur during heat treatments. As mentioned in the previous section on mass loss measurement, differences in cooling were also investigated. Total surface area (methylene blue method) and external surface area (BET) were measured and internal surface area was calculated from this data for each of the clays in the study (illite, illite/smectite, and smectite) (Figures 3-4 through 3-6). BET measurements show a slight difference due to cooling conditions, and overall suggest that the external surface begins to decrease as the illite phase tranforms into other mineralogic phases around 500 °C.
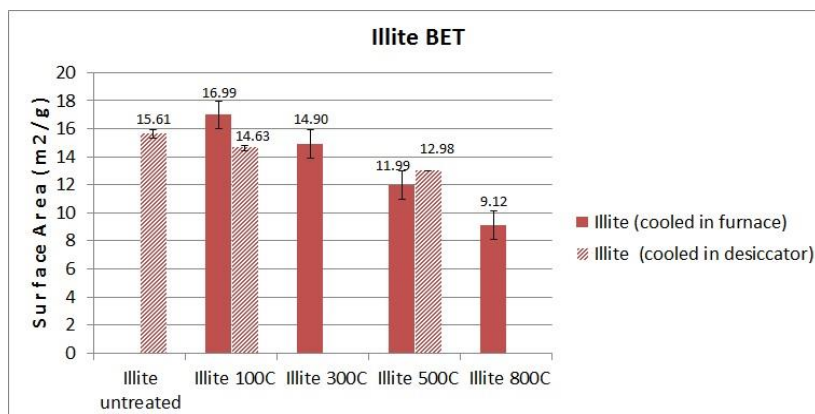
Figure 3-3: External surface of Illite as measured via BET
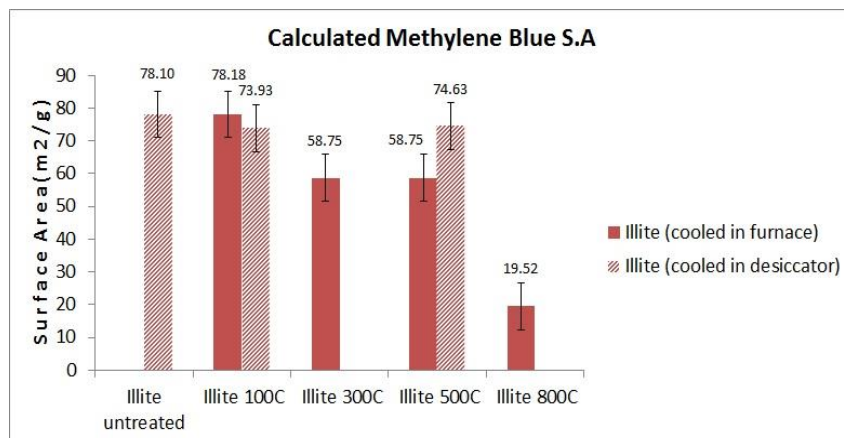
Figure 3-4: Total surface of illite as measured via the methylene blue method

The total surface area measurements show that there is no statistically significant difference induced by cooling method. A significant decrease in total surface area is observed for the 800 °C sample, which correlates to a sharp drop in CEC and a point where all of the illite phase has been transformed into other mineralogic phases (see sections 3.4.3 and 3.4.4). Taken together, we can see that both the internal and external surface areas drop significantly (50%). It can also be inferred that the external surface comprises ~ 20% of the total surface area for the untreated illite samples.
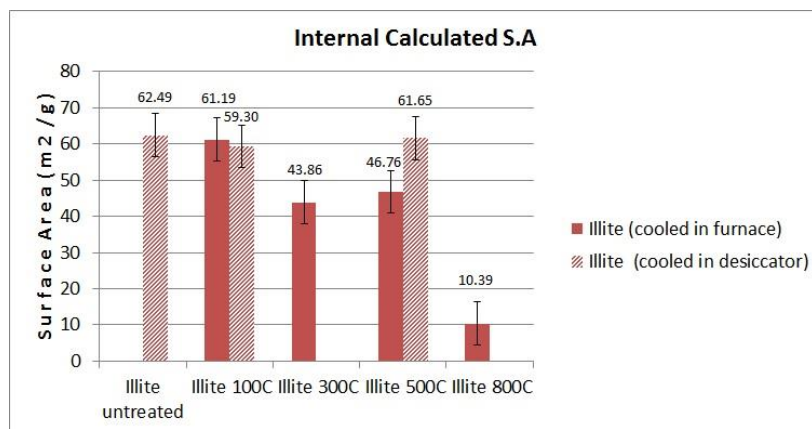
Figure 3-5: Internal surface of illite calculated as the difference between total and external surface areas
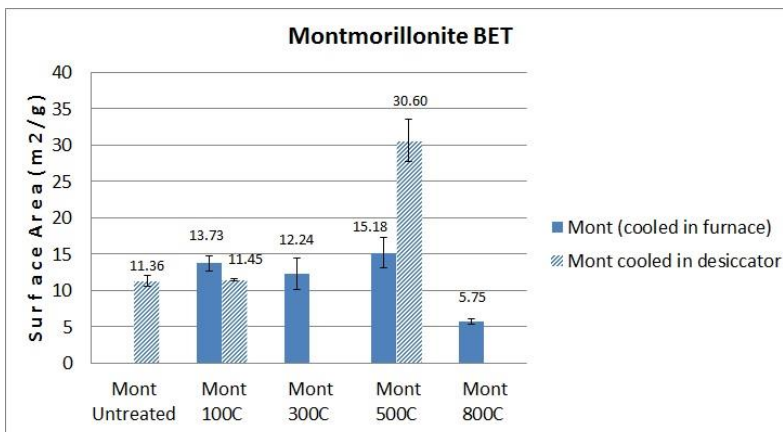
Figure 3-6: External surface of smectite as measured via BET

The results of surface area measurements for smectite samples are shown in Figures 3-7 through 3-9. A comparison between the cooling methods shows that there is a slight statistical difference for 100 °C, and a significant difference for 500 °C. Like the illite samples, the most significant decrease in BET surface occurs at 800 °C, when the smectite phase has transformed to other mineralogic phases (see section 3.4.4). Also, like the illite samples, the CEC data shows a significant change for the 800 °C sample (see section 3.4.3).
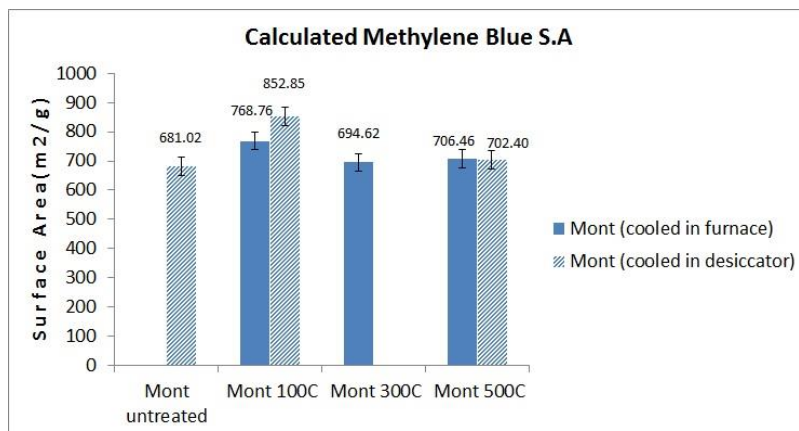
Figure 3-7: Total surface of Smectite as measured via the methylene blue method

Total surface area measurements show virtually no change in total surface area as a function of cooling method or as a function of treatment temperature. Unlike the illite, the smectite surface area is dominated by internal surface area, owing to the fact that the external surface area comprises only ~1.4% of the total surface area for smectite. Total surface area measurements on the smectite for 800 °C were made, however, a clear break-off point (critical to assigning a total surface area value – see section 3.3.2) could not be indentified for the 800 °C sample. Internal surface area measurements show no significant changes as a function of treatment temperature.
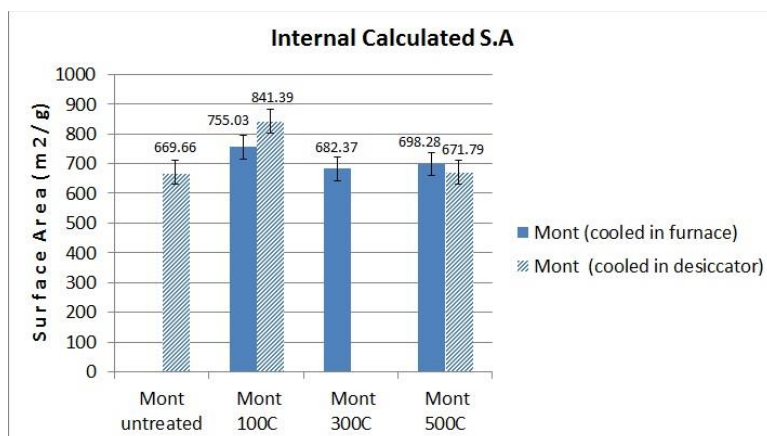
Figure 3-8: Internal surface of smectite calculated as the difference between total and external surface areas

3.4.3   Cation Exchange Capacity (CEC) Measurements

Previous data for the cation exchange measurements suggested that there were some dramatic increases in CEC as a function of heat treatment temperature. However, these results proved to not be reproducible. Given the magnitude of the error of these previous samples when compared to repeatable data presented below, it is presumable that this error was an artifact produced by a dilution error when preparing the samples for elemental analysis.

The current data set suggests that for both illite and smectite, there is no statistically significant change in CEC as a function of heat up to and including 500 °C. For 800 °C, a significant reduction in CEC, 50% and 66%, for illite and smectite respectively, is observed. Figures 3-10 and 3-11 summarize the CEC data for both clays. The color coding in the figures shows the cation composition of exchangeable cations. For both clays, a decrease ion the proportion of exchanged cations for magnesium is observed at 500 °C and above. The XRD data (see section 3.4.4) suggest that this correlates with the formation of $MgSiO_2$ and other Mg-bearing phases that incorporate Mg and render it in an unexchangeable mineral phase.
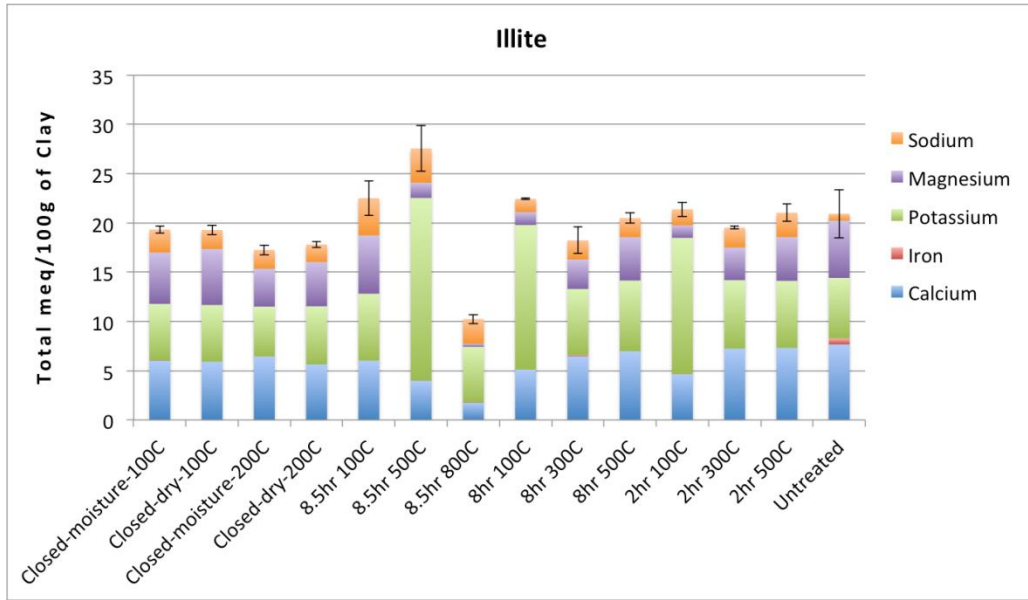
Figure 3-9: Summary of CEC for illite as a function of treatment temperature
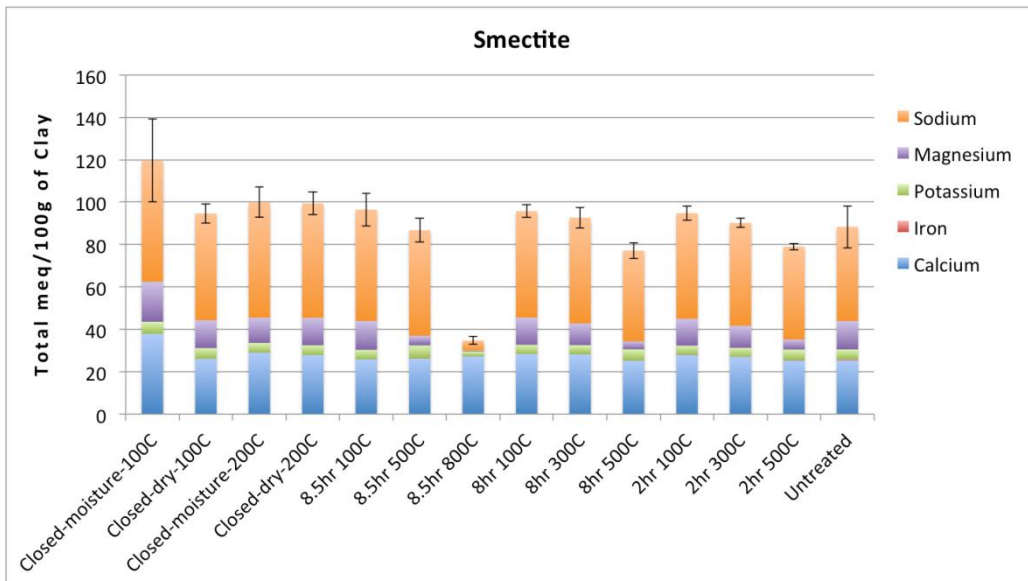
Figure 3-10: Summary of CEC for smectite as a function of treatment temperature

3.4.4 X-Ray Diffraction (XRD) Measurements

Initial XRD data on illite sample shows evidence of quartz, illite/smectite, rutile and possibly a kaolinite phase. The kaolinite phase is less definitive since there is only one major peak to identify this phase in the pattern. The broad peaks of the illite phase suggest a fine crystallite size for this phase and the illite and kaolinite both show a preference for the (00l) peaks which suggests preferred orientation of these mineral phases (not unexpected). There was also evidence of a TiO_2 rutile phase in the XRD data.

X-ray fluorescence (XRF) analysis shows significant concentrations of Si, K, Al, and Fe, with minor and trace constituents of Mg, Ti, Ca, S, Mn and Cr. The Si, Al, and K all can be easily associated with the illite phase. Al and Si can also be attributed to the possible kaolinite phase. Silicon corresponds to the quartz phase. The iron might be associated with the illite, but could also be present in the rutile or quartz phases.
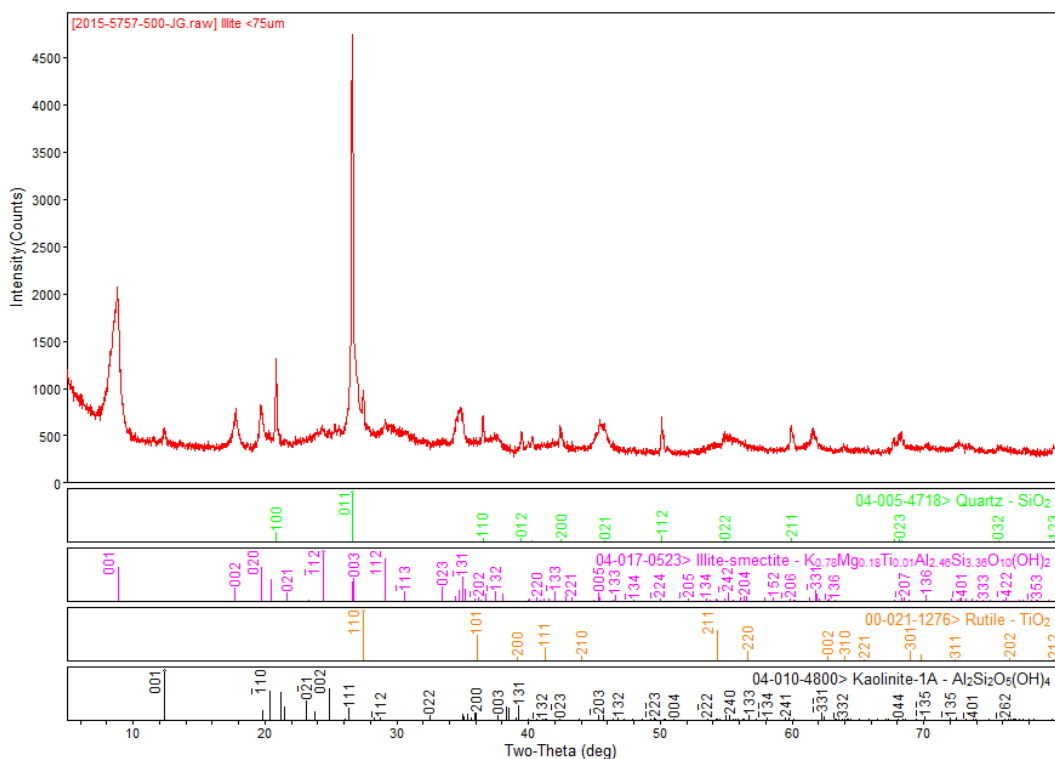
Figure 3-11: Initial XRD data for illite sample (not heat treated)

The high temperature XRD (Figure 3-12) results show evidence of the quartz low-high phase transition at ~500°C. The kaolinite peak also looks to begin to disappear at this point in the pattern. The illite peaks show peak shifting with temperature where the (001) and (002) diffraction planes appear to slightly contract with heating to ~500°C (shifting higher 2q angle with increased temperature), followed by a more significant d-spacing expansion above 500°C. It is not clear if the low-high quartz phase transition is tied to the illite structural behavior or if these changes are coincidental. The illite (020) peak behaves different from the (00l) peaks in that it looks to slightly contract above 500°C. This indicates an

anisotropic thermal expansion behavior of the illite phase likely associated with the layered structure of illite. The illite phase disappears by ~1000°C and the Quartz phase persists up to the maximum temperature of 1300°C, but at a lower concentration. It seems likely that an amorphous phase is forming with the loss of the various crystalline concentrations.

2015-5779-HT XRD
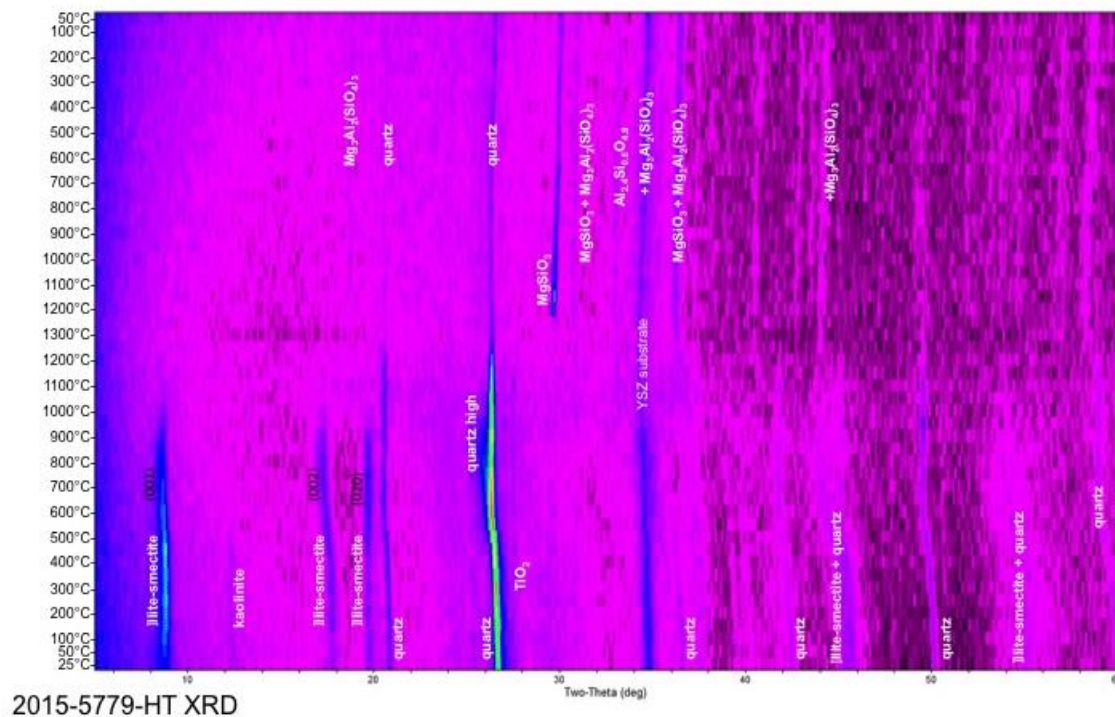
Figure 3-12: Data from high temperature XRD experiment on illite up to 1300 °C, showing transition of mineral phase assemblages with heating and subsequent cooling (moving upward vertically along the y-axis)

Upon cooling, we see the formation of aluminosilicates, magnesium silicates, and Mg-Al silicates. The XRD pattern has significantly changed in regard to crystalline phases after heat treatment, with loss of the illite and kaolin phase, with only the quartz phase remaining in a reduced quantity as compared to the initial concentration.

Initial XRD data for smectite sample show evidence of the presence of quartz, montmorillonite, and possibly a sepiolite phase. The sepiolite phase seems to be a more hydrated phase compared to the montmorillonite phase and it appears that the sepiolite phase decomposes to the montmorillonite phase as the temperature increases above ~100°C, consistent with dehydration. The broad peak of the sepiolite phase suggests a very fine crystallite size for the initial sepiolite compound. The quartz peaks are fairly sharp in the XRD pattern, suggesting a coarser crystallite size.
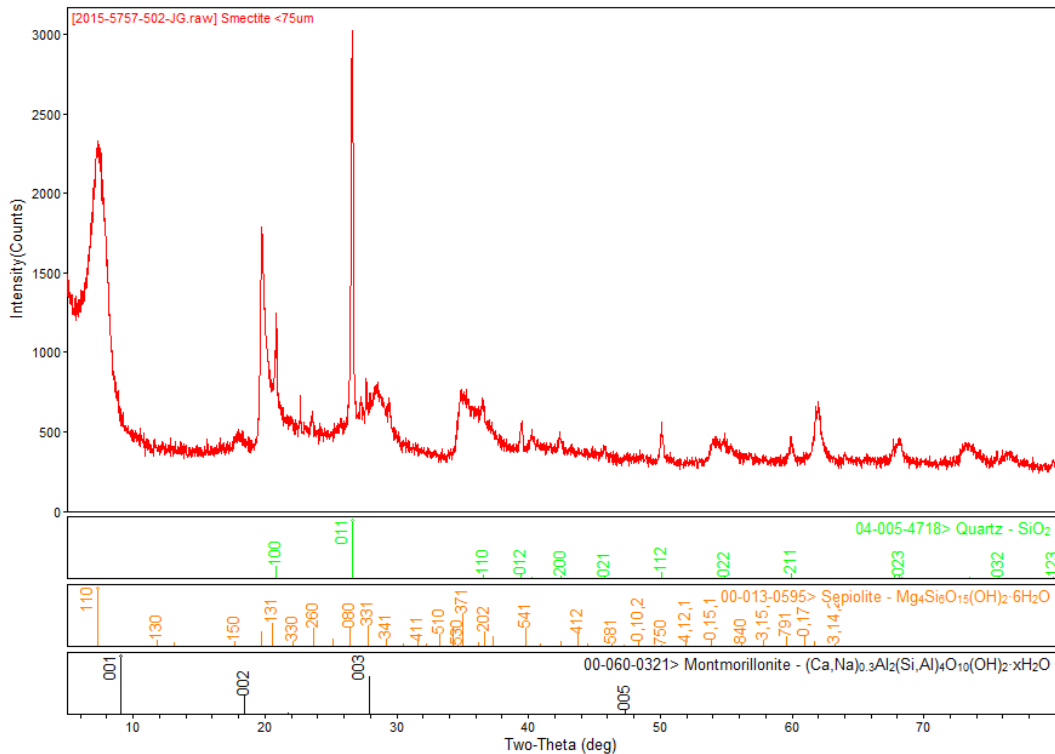
Figure 3-13: Initial XRD data for Smectite sample (not heat treated)

The high temperature XRD results (Figure 3-14) show evidence of the quartz low-high phase transition at ~500°C. After montmorillonite phase has clearly formed above 150°C, it appears to dissipate above 800°C. The montmorillonite peaks show peak shifting with temperature where the (001), (002), and (003) diffraction planes appear to slightly contract with heating to ~500°C (shifting higher 2q angle with increased temperature), followed by a more significant d-spacing expansion above 500°C. It is not clear if the low-high quartz phase transition is tied to the structural behavior of the montmorillonite or if these changes are coincidental. It is unclear if the sepioite phase persists above the 150°C temperature range, or if the montmorillonite phase has peaks in similar positions. The montmorillonite peaks disappear by ~800°C along with the possible formation of a small quantity of $MgSiO_3$. The Quartz phase persists up to approximately 1000°C, where there is a clear phase change to Cristobalite. At 1300°C it appears that all the phases have melted.

Upon cooling, cristobalite reappears at ~1250°C, along with the crystallization of mullite at ~1150°C and another Mg-Al-Silicate Indialite at ~1050°C. The XRD pattern has significantly changed in regard to crystalline phases after heat treatment, with loss of the sepiolite and quartz phase, and showing the formation of cristobalite, mullite, and indialite.

2015-5833-HT XRD
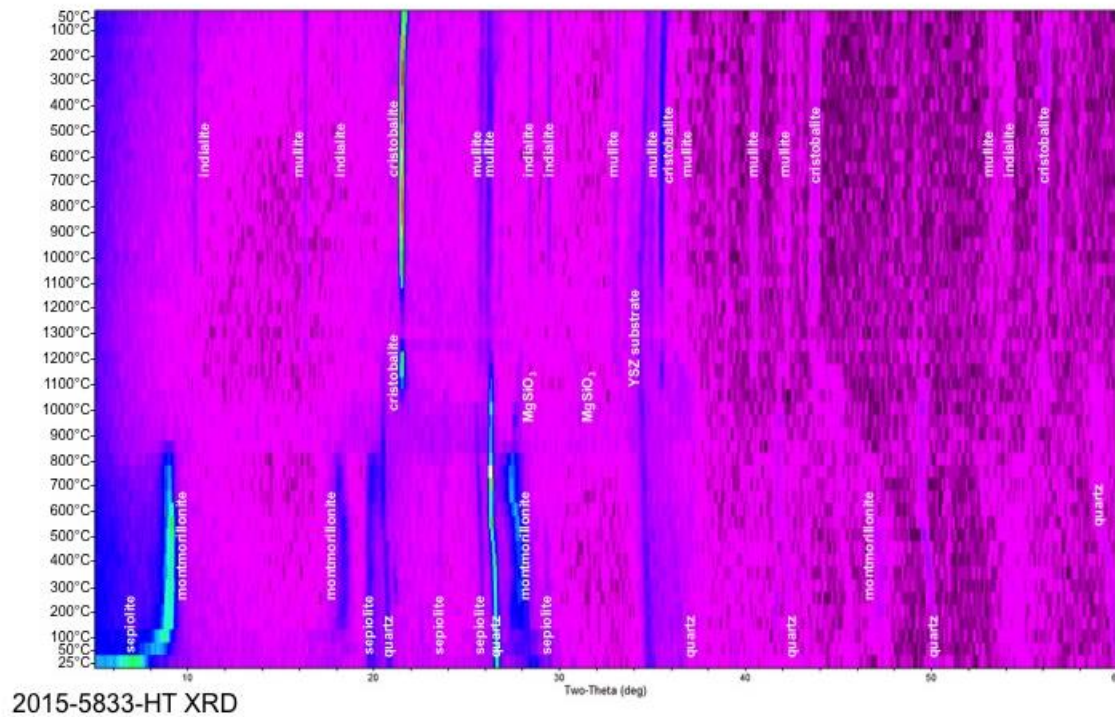
Figure 3-14: Data from high temperature XRD experiment on smectite up to 1300 °C, showing transition of mineral phase assemblages with heating and subsequent cooling (moving upward vertically along the y-axis)

3.4.5   Particle Size Measurements

The results of particle size measurements are shown in Table 3-1. The clay samples treated with different temperatures seems to have similar particle sizes. However, higher temperature treated clays appear to have a much faster settling rate than the lower temperature. This is likely the reason why some samples did not meet quality criteria, since the 3 mL suspended particles were not evenly distributed within the cuvette. It has been observed that the larger particles easily settled to the bottom leaving only the smaller particles suspended for analysis.

Triplicate runs of clays heated to 100°C for 8 hours with no moisture were also run for the particle size measurement consecutively. As can be seen in the table, the particle size diameter reduces after each run allowing for a qualitative interpretation of the settling behavior trend with heat treatment temperature.

Table 3-1: Summary of particle size measurements for different treatments of each clay

Clay	Temperature (°C)	Moisture/ No moisture	System	Z-Ave (d.nm)
Illite	100	moisture	closed	364.7
	100	no moisture	closed	394.2
	100	no moisture	open 2hrs	421.3
	100	no moisture	open 8hrs	384.8
	500	no moisture	open 2hrs	366.7
	500	no moisture	open 8hrs	376.6
	800	no moisture	open 8hrs	361.6
Smectite	100	moisture	closed	477.2
	100	no moisture	closed	539.3
	100	no moisture	open 2hrs	485.7
	100	no moisture	open 8hrs	557.1
	500	no moisture	open 2hrs	***
	500	no moisture	open 8hrs	***
	800	no moisture	open 8hrs	***

***Sample did not meet quality criteria due to settling
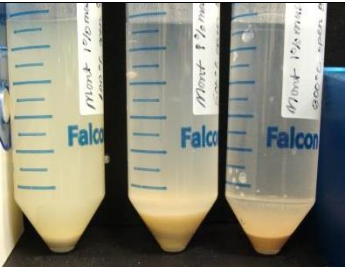
Table 3-2: Summary of particle size values for triplicate runs

Clay	Run #:	Z-Ave (d.nm)	Average (d.nm)
Illite	1	384.8	
	2	379.2	373.6
	3	356.9	
Illite/smectite	1	460.6	
	2	430.5	437.4
	3	421.1	
Smectite	1	557.1	
	2	525.2	534.3
	3	520.5	

3.4.6   Settling Rate Measurement

As shown in the photographs in Table 3-3, the 800°C sample settled at a rate of a few hours while the 100°C and 500°C were still suspended. The 500°C sample deflocculated at a rate faster than the 100°C sample which still had suspended particles after 58 hours.

Table 3-3: Photographs of heat treated smectite clay over time. From left to right: 100°C sample, 500°C sample, 800°C sample

0 minutes		3 hours 20 minutes	
5 minutes		11 hours 45 minutes	
10 minutes		39 hours 45 minutes	
15 minutes		58 hours 45 minutes	

3.5   CONCLUSIONS

Taken together, the surface area, CEC, and XRD results suggest that mineralogic alteration as a function of heat treatment will exert the greatest control on chemical and physical properties of both illite and smectite clays. The most significant changes to both surface area and CEC coincided with significant changes in the mineralogic phase assemblage, i.e., CEC change is directly related to the amount of clay mineral converted to other silicate and aluminosilicate mineralogic phases (e.g., quartz, mullite, etc.). This conclusion suggests a future need to understand smectite to illite transition mechanisms under the relevant and/or likely repository conditions. In addition to temperature, availability of illitizing cations (such as potassium), pressure, and duration of heating are variables that must be better understood to predict how the permeability, swelling capacity, and sorption capacity of clay buffers may evolve under thermal loads in excess of 100 °C.

The particle size and settling mesurements qualitatively suggest that agglomeration of clay particles will occur as a function of thermal heat treatment. As particles aggregate from the effects of heat treatment, large particles settle out, and it appears that the number of smaller, flocculated particles decreases. Most robust methods for quantifying this effect need to be developed and exceuted to fully understand the impact this effect may have in the repository environment.

Future work should focus on understanding of illitization and cementation, as the two most likely and predominant mineralogic alteration pathways for buffer material. Diffusion, permeability, sorption capacity, and swelling measurements of clays altered as such will be important to accurately predicting evolution of buffer behavior under increased thermal load.

3.6   REFERENCES

Cuadros, J., Linares, J., (1996). Experimental kinetic study of the smectite-to-illite transformation. Geochim. Cosmochim. Acta 60, 439–453.

de Carvalho Costa, T. C., J. D. D. Melo, and C. A. Paskocimas. (2013) Thermal and chemical treatments of montmorillonite clay, *Ceramics International*, 301, 5063-5067.

Frost, R. L., and Z. Ding. (2003) Controlled rate thermal analysis and differential scanning calorimetry of sepiolites and palygorskites, *Thermochemica Acta,* 397, 119-128.

Gillman, G., (1979) A proposed method for the measurement of exchange properties of highly weathered soils. *Soil Research*, 17, 129-139.

Howard, J.J., Roy, D.M., (1985). Development of layer charge and kinetics of experimental smectite alteration. Clays Clay Miner. 33, 81–88.

Kahr, G. and F. T. Madsen. (1995) Determiantion of the cation exchange capacity and the surface area of bentonite, illite, and kaolinite by methylene blue adsorption. *Applied Clay Science*, 9, 327-336.

Moore, D. M. and . C. Reynolds. (1997) *X-ray Diffraction and the Identification and Analysis of Clay Minerals.* 2nd Edition, Oxford University Press, NY.

Muller, F., V. Drits, A. Plancon, and J. L. Robert. (2000) Strucutral transformation of 2:! Dioctohedral layer silicates during dehydroxlylation-rehydroxylation reactions, *Clay and Clay Minerals*, 48, 572-585.

Onal. M. (2007) Swelling and cation exchange capacity relationship for the samples obtained by acid activations and heat treatments. *Applied Clay Science*, 37, 74-80.

Pusch, R., Karnland, O., 1988a. Hydrothermal effects on montmorillonite. A preliminary study. SKB Technical Report 88-15, Stockholm, Sweden.

Wersin, P., L. H. Johnson, and I. G. McKinley. (20078) Performance of the bentonite barrier at temperatures beyond 100 °C: A critical review, *Physics and Chemistry of the Earth*, 32, 780-788.

Wolters, F., K. Emmerich. (2007) Thermal reactions of smectites – Relation of dehydroxylation temperature to octahedral structure, *Thermochemica Acta,* 462, 80-88.

4.0 INVESTIGATION OF URANIUM DIFFUSION AND RETARDATION IN BENTONITE

4.1 INTRODUCTION

Nuclear fission produces 14% of the world's electricity supply and could contribute ~15% of CO_2 abatement efforts required to stabilize global CO_2 emissions over the next 50 years (Pacala and Socolow, 2004; Englert et al., 2012). The viability of nuclear energy as a CO_2 abatement technology, however, relies in part on the demonstration that geologic storage facilities can isolate high level radioactive waste (HLRW) on time scales commensurate with the decay of long-lived radioactive fission products and actinides, on the order of 10^6 years. Accurate predictions of repository performance on such long time scales require the development of geophysical models grounded in fundamental knowledge of material properties and constitutive relationships relevant to radionuclide migration in geologic media (Altmann et al., 2012). Depending on the perspective, the radioelements of greatest concern in HLRW storage are those that are present in high abundance (such as uranium), those that are large contributors to the long-term radiotoxic inventory [such as plutonium, americium, curium and neptunium (Kaszuba and Runde, 1999; IAEA, 2004)], or those that have a long half-life and a significant solubility in water: ^{129}I, ^{36}Cl, ^{79}Se, ^{99}Tc, ^{126}Sn, and ^{135}Cs (Altmann, 2008; NEA, 2009).

Most countries with HLRW storage programs are currently investigating clayey media, such as bentonite and shale, for use as engineered barrier systems (EBS) and/or host rocks of geologic repositories (ANDRA, 2005; Delay et al., 2007; Altmann, 2008; Guyonnet et al., 2009; Bock et al., 2010; SKB, 2011; Altmann et al., 2012). At the conditions that would exist in proposed HLRW repositories, clay barriers display very low hydraulic conductivities, the ability to self-seal when fractured, and water and solute mass fluxes that are dominated by molecular diffusion as the primary transport mechanism on time-scales of millions of years (Neuzil, 1986, 1994, 2013; Horseman and Volckaert, 1996; Oscarson et al., 1996; Bock et al., 2010; Mazurek et al., 2011).

Sodium-montmorillonite, the main constituent of bentonite, is a smectite, a 2:1-layer-type dioctahedral phyllosilicate with a large specific surface area (~800 m^2 g^{-1}) and cation exchange capacity (~1 mmol g^{-1}). Each clay layer has a thickness of ~1 nm and carries negatively-charged isomorphic substitutions in its phyllosilicate framework. The aggregation of Na-montmorillonite layers into particles (i.e., stacks of clay layers) results in a complex pore-size distribution including narrow (~1 nm wide) interlayer pores within particles (where diffusion is strongly impacted by clay surfaces) and larger pores between particles (where water may be bulk-liquid-like). Furthermore, Na-montmorillonite provides reactive surface sites for radionuclide sorption reactions, primarily in two forms: (1) cation exchange sites on the planar surfaces of clay layers and (2) surface complexation sites in the form of amphoteric octahedral Al-OH and tetrahedral Si-OH sites on the edges of clay layers making up clay particles. The relevance of a particular type of surface site for contaminant sorption and retardation is strongly dependent on the chemical solution conditions (e.g. ionic strength) and contaminant solution speciation (e.g. with regard to cationic, anionic and neutral species, in a given system).

The diffusion coefficients of water and solutes in clayey media have been extensively studied in conditions relevant to HLRW repositories, particularly in the case of water tracers (HTO), anions (I^-, Br^-, Cl^-, TcO_4^-, SeO_3^{2-}), and alkali and alkaline earth metals (Na^+, Cs^+, Ca^{2+}, Sr^{2+}) (Muurinen et al., 1986; Sato et al., 1992; Kozaki et al., 1996, 1998a; b; Choi and Oscarson, 1996; Kozaki et al., 1999a; b, 2001, 2005, 2008, 2010; Lee et al., 1996; Nakajima et al., 1997; Nakashima, 2000, 2002, 2003, 2006; Molera, 2002; Molera and Eriksen, 2002; Molera et al., 2003; Sato and Suzuki, 2003; Van Loon et al., 2003a; b, 2004a; b, 2005a; b, 2007; Wang, 2003; Jansson and Eriksen, 2004; García-Gutiérrez et al., 2004; Sato and Miyamoto, 2004; Suzuki et al., 2004; García-Gutiérrez et al., 2009; Wang and Liu, 2004; Wang and Tao,

2004; Melkior et al., 2005, 2007, 2009; Nakashima and Mitsumori, 2005; Wang et al., 2005; Appelo and Wersin, 2007; Glaus et al., 2011, 2013; Motellier et al., 2007; Glaus et al., 2007, 2008, 2010; Gonzàlez Sànchez et al., 2008; Descostes et al., 2008; Wersin et al., 2008; Wittebroodt et al., 2008; Jakob et al., 2009; Jougnot et al., 2009; Appelo et al., 2010; Savoye et al., 2010, 2011; Holmboe et al., 2011; Gimmi and Kosakowski, 2011; Loomer et al., 2013; Tachi and Yotsuji, 2014). In comparison, uranium and other strongly-sorbing actinides have been studied less extensively (Bai et al., 2009; F**;** García-Gutiérrez et al., 2003; Joseph et al., 2013; Korichi et al., 2010; Liu et al., 2010; Maes et al., 2002; Muurinen, 1990; Pekala et al., 2009, 2010; Tokunaga et al., 2004) with regards to their diffusive transport behavior in clayey media for a wide range of chemical conditions. Nevertheless, as the basis of nuclear fuel, uranium is one of the primary elements to be considered in environmental risk assessments for nuclear waste repositories. Other radionuclides that are bound in the fuel matrix can only be released at the same rate as uranium dissolves and diffuses through waste containment barriers (Muurinen, 1990). Furthermore, in conceptual studies uranium can serve as a useful analog for other radioactive contaminants, such as Pu, Np, and Am, due to its sorption characteristics, the relevance of uranium-carbonate species for actinide speciation, and the availability of a well-established thermodynamic database describing uranium solution speciation at various chemical conditions. Hence, the characterization of uranium(VI) sorption and diffusion behavior in sodium-montmorillonite and bentonite is the primary focus of this study.

The complexity of the mineralogical structure of montmorillonite, in terms of (1) its pore-size distributions and (2) available surface site types, has important implications for the diffusive transport of radionuclides in bentonite barriers. First, the 'co-existence' of small interlayer pores within particles and larger macropores between clay particles can create two types of clay porosities and diffusion pathways. The relevance of the individual porosities and pathways is strongly dependent on system characteristics, such as the degree of bentonite compaction, chemical solution conditions, and the charge of contaminant species in solution. For instance, a partial or full exclusion of anions from negatively charged clay interlayer spaces can change the effective 'anion-accessible' porosity and decrease the diffusive flux of these solutes under steady state conditions. As a result, diffusive fluxes can vary substantially between cations, anions and uncharged solutes. Furthermore, radionuclides that show dramatic changes in their chemical solution speciation as a function of pH, such as uranium, and are able to form cationic, anionic or uncharged species in solution, are expected to show different diffusive transport behavior under varying chemical solution conditions.

Second, montmorillonite surface site characteristics, and radionuclide sorption affinities for clay surfaces have important implications for diffusive transport as well. While any type of surface reaction results in a retardation of the radionuclide relative to a non-reactive tracer, weak and strong surface reactions can have different net effects on diffusive fluxes under steady state conditions. In case of weak cation exchange reactions, adsorbed cations show a significant mobility in the electric double layer (EDL) (Jenny and Overstreet, 1939; Van Schaik et al., 1966; Nye, 1980; Jakob et al., 2009; Gimmi and Kosakowski, 2011), because of the high, local concentration gradients along the surface. This mobility leads to a 'surface diffusion' of adsorbed cations, in addition to their diffusion in the liquid phase, which, in turn, results in higher total diffusive fluxes under steady state conditions. In contrast, strong sorption reactions, e.g. in the form of surface complexation reactions on edge sites, do not contribute significantly to surface diffusion fluxes under steady state conditions. As a result, the distribution of clay surface sites further complicates the prediction of diffusive fluxes for radionuclides that show substantially different chemical solution speciation as a function of pH. For instance, at low pH conditions, uranium(VI) may be predominantly present as cationic species, sorb onto clay via (potentially weak) cation exchange reactions, and may not be affected by anion exclusion effects. This could cause retardation of uranium(VI) diffusion relative to a non-reactive tracer, but possibly higher diffusive uranium(VI) fluxes compared to the non-reactive tracer or to uranium(VI) diffusion at higher pH conditions. At more alkaline pH, where uranium(VI) is present as anionic species, uranium(VI) is expected to sorb onto montmorillonite in the form of (potentially strong) surface complexation reactions, and be subject to full

or partial anion exclusion from clay interlayer spaces. In this case, uranium(VI) retardation may be coupled with comparable or lower diffusive fluxes relative to non-reactive tracers.

Based on the literature we have reviewed, at present full or partial anion exclusion effects have not been clearly demonstrated experimentally for anionic uranium(VI) species, despite the theoretical understanding of the uranium(VI)-montmorillonite system described above. This is, at least in part, due to the difficulties associated with the experimental approach of so-called uranium(VI) through-diffusion experiments, which monitor the breakthrough and diffusive fluxes of uranium(VI) across a diffusion cell over the course of an experiment. Almost all previously reported uranium(VI)-montmorillonite/bentonite diffusion experiments were based on an evaluation of total uranium(VI) concentrations (dissolved plus sorbed concentrations) as a function of distance in the clay packing after the completion of experiments. While this approach still allows determining apparent uranium diffusion coefficients and sorption distribution coefficients (K_d values) based on the simulation of the concentration profile, the associated model parameters are less constrained, and direct observations of solute retardation, diffusive fluxes, and any potential kinetic effects are not possible. Hence, one of our research goals was to demonstrate that uranium(VI) through-diffusion experiments could be conducted successfully under alkaline conditions.

Furthermore, it should be noted that waste forms, and possibly the presence of concrete in the vicinity of an engineered barrier system (EBS), are likely to create alkaline conditions and concentration gradients in chemical variables (pH, HCO_3^-, Ca^{2+}) within the EBS (Figure 4-1). Hence, it is important to develop conceptual models that can describe uranium(VI) diffusion as a function of chemical solution conditions. Furthermore, an understanding of diffusion rates is needed not only for relevant radionuclides but also predominant earth metals, because the latter elements can affect actinide solution speciation and compete with radionuclides for mineral surface sites. For instance, within engineered clay barriers containing minor amounts of calcite, $Ca_2UO_2(CO_3)_3^0$ is expected to dominate uranium(VI) solution speciation, and hence, control uranium(VI) sorption and diffusion behavior (Kerisit and Liu, 2010; Bradbury and Baeyens, 2011; Joseph et al., 2011). Hence, in an earlier part of this study, we also investigated calcium diffusion behavior in sodium-montmorillonite.

In addition to chemical gradients, gradients in temperature also have to be expected as a function of time and space in the EBS, given the radiation heat produced by the decay of radioactive waste. Besides other factors, an exposure of bentonite and montmorillonite to heat may lead to mineral alterations of the solids, and a possible 'illitization' of montmorillonite, over time (Cheshire et al., 2014; and references therein). Due to the strong dependency of uranium(VI) sorption and diffusion behavior on solid phase characteristics, this creates a strong research need to investigate the potential effects of mineral alterations in bentonite on uranium(VI) sorption/diffusion behavior. For instance, if uranium(VI) sorption affinities to the solids were different for altered than the original minerals, then uranium(VI) transport behavior would be affected by these heat-induced mineral alterations even after EBS temperatures have returned to their original levels.
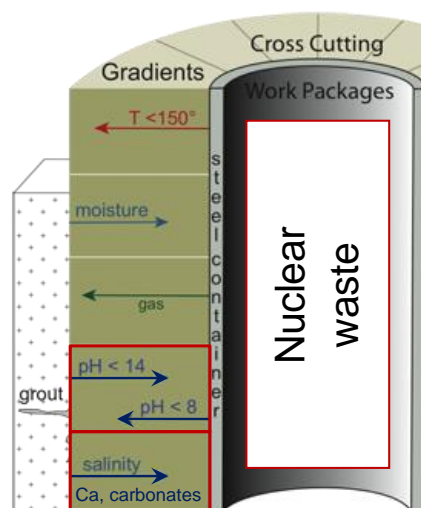
Figure 4-1: Expected gradients in chemical conditions and temperature across the EBS
(Modified after http://www.eng.ox.ac.uk/about-us/jobs/fp/THMC.png/image_preview).

Given these research needs, we can summarize the primary research goals for this study for this fiscal year as follows:

- Evaluate the potential effects of heat-induced mineral alterations in bentonite on uranium(VI) sorption behavior in batch experiments;
- Perform a uranium(VI) through-diffusion experiment to investigate the relevance of full or partial anion-exclusion of uranium(VI) species from Na-montmorillonite interlayer spaces, under alkaline pH conditions.
- Determine uranium(VI) diffusion coefficients in Na-montmorillonite (in the absence of Ca concentration levels affecting uranium(VI) speciation) for their later use in performance assessment models.
- Evaluate effects of uranium(VI) surface complexation reactions on its diffusive transport behavior.
- Demonstrate a successful experimental approach for uranium(VI) through-diffusion experiments, while providing experimental data needed for performance assessment.

4.2 URANIUM(VI) SORPTION EXPERIMENTS

4.2.1 Overview and Goals

Previously, we have performed a series of batch sorption envelope experiments in order to investigate the sorption of uranium(VI) to Na-montmorillonite over a range of chemical solution conditions (pH, calcium and carbonate concentrations, as well as total uranium(VI) concentrations). These data sets are currently used to develop a surface complexation model for this system, which will provide a detailed understanding of uranium (VI)-montmorillonite surface interactions.

For this fiscal year, our goal was to investigate potential impacts of heat-induced mineral alterations in bentonite on uranium(VI) sorption behavior, using previous Na-montmorillonite data as a reference. For this purpose, we obtained 'cooked' and 'uncooked' bentonite samples from Dr. Florie Caporuscio's

research group at Los Alamos National Laboratory. The resulting experimental data will be useful for diffusion and performance assessment models.

4.2.2   Materials

All chemicals used in this study were reagent grade or better. Uranium (VI) solutions contained ^{238}U from a 3.7 $\times 10^{-4}$ M uranyl nitrate stock solution (dilution of 1000 μg/mL Inorganic Ventures ICP-MS Standard). Acids, bases, and salt solutions used in equilibrium and kinetic batch experiments were of TraceSelect grade (Sigma Aldrich) in order to minimize calcium background concentrations. Aqueous solutions were prepared with Nanopure water (Barnstead ultrapure water system). Glassware was cleaned by soaking in acid (10 % (v/v) HCl) for 12 to 24 hours, followed by thorough rinsing with Nanopure water and air-drying.

Three types of solids were compared as reactive surfaces for uranium (VI) sorption reactions, 'cooked' and 'uncooked' bentonite and Na-montmorillonite. 'Cooked' and 'uncooked' bentonite samples were provided by Dr. Florie Caporuscio at Los Alamos National Laboratory. The starting bentonite, used in this heat-treatment, was mined from a reducing horizon in Colony, Wyoming, and represents a Na-montmorillonite with minor amounts of clinoptilolite, feldspars, biotite, cristobalite, quartz and pyrite (Caporuscio et al., 2013; Table 3). This material was exposed to a temperature of 300 °C and a pressure of 150-160 bars for 7 weeks (pH of 6.74, solid-liquid ratio of 5:1). For this heat-treatment, the original composition of the brine in contact with the bentonite contained various concentrations of Ca, Cl, K, Na, Si, sulfate and Sr with a Total Dissolved Solids (TDS) content of 1934 mg/L (Caporuscio et al., 2014; Table 1). Redox conditions were buffered during heat-treatment using a Fe_3O_4-Fe^0 buffer system. An extended mineralogical characterization of the solids before and after heat-treatments allowed for the following conclusions. The post-reaction sample (EBS-12) contained lower fractions of clinoptilolite (13% before, 4% after), pyrite (0.4% before, detected but below quantification limit after) and biotite (3% before, detected but below quantification limit after) than the starting material. At the same time, montmorillonite (72% before, 71% after) and feldspar (9% before, 10% after) fractions remained relatively unchanged (Caporuscio et al., 2013; Table 3). Overall, no 'illitization' of montmorillonite was determined, but the formation of new, amorphous phases was observed, especially the formation of analcime at a fraction of 1% or greater. Both the heat-treated ('cooked' bentonite) and starting material ('uncooked' bentonite) were ground with a Retsch MM 400 ball mill (frequency of 30/sec for 2 minutes) prior to uranium (VI) sorption experiments.

Purified Na-montmorillonite (SWy-2, Clay Minerals Society) served as a reference material for a comparison of uranium (VI) sorption data after 2 days of sorption equilibration. A detailed description of the Na-montmorillonite purification procedure has been provided previously (Rutqvist et al., 2012; Davis et al., 2013). Briefly, pretreatment steps included: the removal of calcite impurities using a 1 M sodium acetate/glacial acetic acid solution (0.564 M) at pH 5; clay equilibration with a 1 M sodium chloride solution; removal of excess salts with Nanopure water; separation of quartz and feldspar impurities from the <2 μm clay fraction by centrifugation; and oven-drying of the purified clay at 45 °C. This purification procedure allowed us to keep calcium background concentrations at or below 88.1μg/l in the reservoir solutions during the calcium bromide through-diffusion experiment, with a contribution of 33.2 μg/L from the background electrolyte itself. (An evaluation of calcium background concentrations for the uranium (VI) through-diffusion experiments is currently ongoing.)

For each solid, a stock suspension of approximately 10 or 20 g/L solids was prepared in Nanopure water, and its exact solid concentration determined by weighing two 10 mL volume fractions before and after drying at 45 °C. A solid concentration of 0.5 g/L was selected for all batch sorption studies, in order to cover a range of U surface concentrations while avoiding complete (i.e. 100%) uranium(VI) sorption.

4.2.3   Experimental Procedure

The effect of pH and equilibration time on uranium(VI) sorption behavior was studied in a series of batch sorption experiments with initial pH values of 4, 4.25, 4.5, 4.75, 5, 5.5, 6, 6.5, 7, 7.5, 7.75, 8, 8.25, 8.5, 8.75, and 9, and equilibration times of 2, 6, 11, 15, and 21 days. All batch sorption experiments were conducted at room temperature (22.5 °C - 23.5 °C), with a nominal total uranium(VI) concentration of 10^{-6} M, a solid concentration of 0.5 g/L, and a total ionic strength of 0.1 M NaCl. The main steps of the experiments included: (1) pre-equilibration of the solids with a background electrolyte solution at the specified pH and chemical solution conditions, (2) uranium (VI) sorption equilibration with the mineral phase, (3) time-dependent sampling and analysis of supernatant fractions after removal of the solid phase by centrifugation, and (4) an evaluation of uranium (VI) wall sorption effects based on an acid-wash procedure.

At the beginning of experiments, aliquots of Nanopure water, solid stock suspensions and a 1M NaCl solution were transferred into sample vials ('50-mL' polycarbonate Oakridge centrifuge tubes) to give the desired solid concentration and ionic strength in the final sample volume of 40 mL. For samples with target pH values of $\geq$ 7.0, increasing amounts of 1M or 0.1M $NaHCO_3$ buffer solutions were added. Solution pH values were adjusted with small volumes of 1, 0.1, 0.01, and 0.001M HCl or NaOH solutions, and closed sample vials pre-equilibrated during shaking for 12 to 24 hours. On the next day, aliquots of uranium (VI) stock solution were added to obtain the final desired total uranium (VI) concentrations. After re-adjustment of pH values, uranium (VI) sorption equilibration was allowed to take place during shaking for specified equilibration times. At specified equilibration times, final pH values were recorded and aliquots of sample suspensions were taken for analysis. For the 2-day and 21-day equilibration period, 11-mL aliquots of sample suspensions were transferred into 15-mL centrifuge vials. These sample fractions were centrifuged on a Beckman Coulter Avanti J-E (JLA 16.250 rotor at 10,000 rpm for 60 minutes), with a calculated particle-size cut-off of 43 nm, and the resulting supernatant solutions were sampled for ICP-MS and Total Inorganic Carbon (TIC) analyses.

Uranium solution concentrations were quantified by ICP-MS after acidification with TraceSelect grade HNO_3. All samples from batch sorption studies were analyzed not only for U solution concentrations, but also calcium background concentrations, as well as elements that could indicate clay dissolution or insufficient solid-liquid separations (Si, Al, Fe, etc.). For the first and last sampling time-points in the experiments with bentonite, supernatant samples were also analyzed for Total Inorganic Carbon (TIC) concentrations using a Shimadzu TOC-V Analyzer. Differences in concentrations of inorganic carbon may occur if trace carbonate minerals dissolved from the bentonite. The latter could potentially have strong influences on uranium (VI) solution speciation and sorption behavior. For 6-, 11-, and 15-day samples, only 3 mL of sample suspensions were removed and centrifuged at 10,000 rpm for 25 minutes, since no TIC analysis was performed for these samples.

For an evaluation of uranium (VI) wall sorption effects, solid phases and remaining sample solutions were discarded at the end of experiments, and vials briefly rinsed with DI-water. Sample vials were then filled with 40 mL of 2% nitric acid solutions (TraceSelect grade) in order to facilitate uranium (VI) desorption from container walls during shaking over approximately 2 weeks. Washing solutions were analyzed for concentrations of desorbed uranium (VI) as described above.

Experimental results for the batch experiments are reported in terms of distribution coefficients (K_d values) and fractions of uranium (VI) sorbed. Distribution coefficients, with units of l/kg, represent the ratio of sorbed (e.g., in mol/kg) over dissolved (e.g., in mol/l) uranium (VI) concentrations after sorption equilibration. Sorbed uranium (VI) fractions were calculated based on concentration differences between (solid-free) standards and (solid-containing) samples.

4.2.4   Results

Figure 4-2 depicts uranium (VI) sorption onto Na-montmorillonite, 'cooked' and 'uncooked' bentonite as a function of pH after a sorption equilibration of 48.5 hours (2-day samples). For both bentonite samples, the fractions of uranium (VI) sorbed are lower than for Na-montmorillonite in the circum-neutral pH region. Furthermore, the heat treatment and resulting mineral alterations in bentonite appear to further decrease uranium (VI) sorption affinities over this pH range.

Furthermore, we observed no significant time-dependent changes in uranium (VI) sorption affinities for any of the bentonite samples (Figure 4-3). Hence, mineral dissolution or degradation reactions with substantial effects on mineral surface characteristics and uranium (VI) solution speciation can be excluded for an experimental time-frame of 21 days.

The latter conclusion is further supported by the fact that no substantial differences were observed for Total Inorganic Carbon (TIC) concentrations between Na-montmorillonite, and 'cooked' and 'uncooked' bentonite samples after 2 days of sorption equilibration, as well as at the end of the 21-day experiments (Figure 4-4). Based on these TIC analysis results, a time-dependent dissolution of a large fraction of carbonate minerals in bentonite samples can be ruled out. Hence, changes in uranium (VI) solution speciation with regard to the formation of uranium (VI)-carbonato complexes are likely not the reason for the observed changes in uranium (VI) sorption behavior.
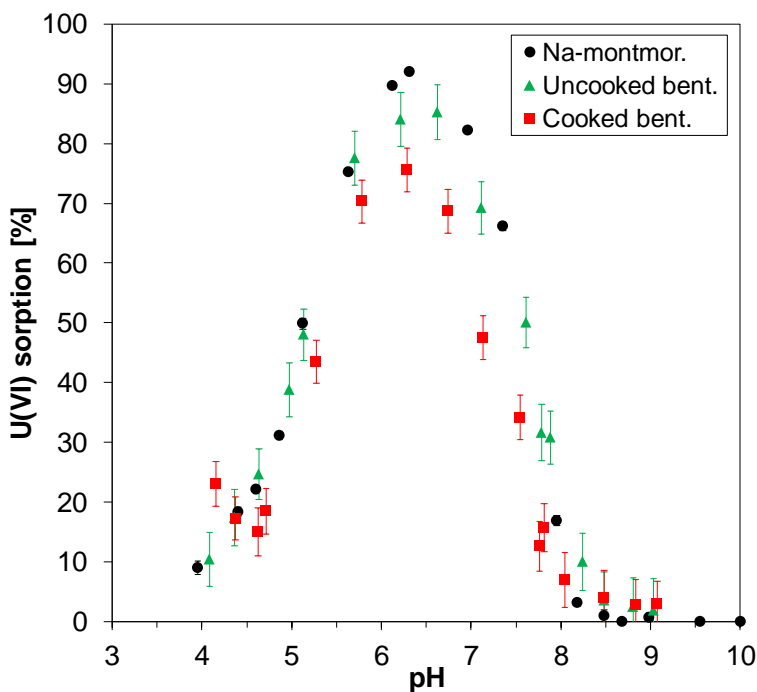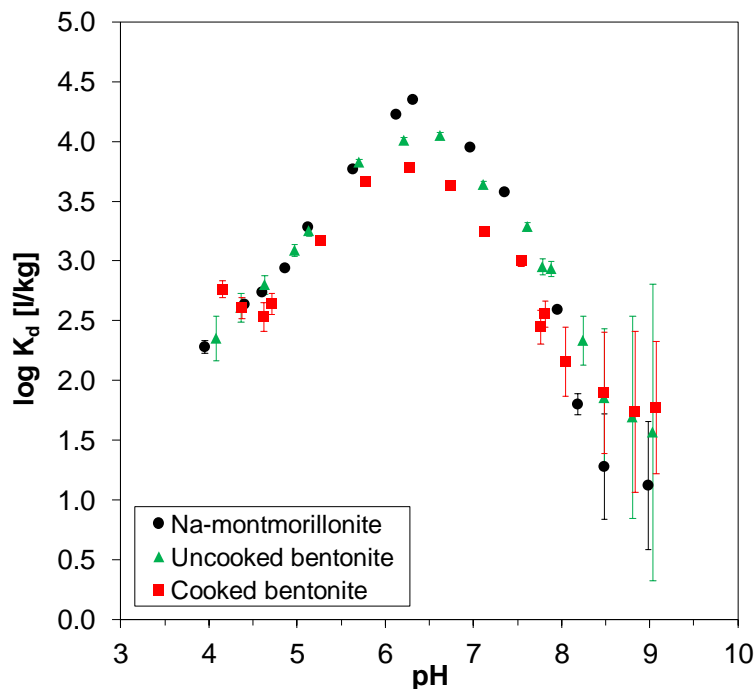
Figure 4-2: Uranium (VI) sorption onto 0.5 g/L sodium-montmorillonite, 'cooked' and 'uncooked' bentonite as a function of pH after sorption equilibration over 48.5 hours (2-day samples). Results are reported in terms of fractions of uranium (VI) sorbed (top) and sorption distribution coefficients (K_d values, bottom).
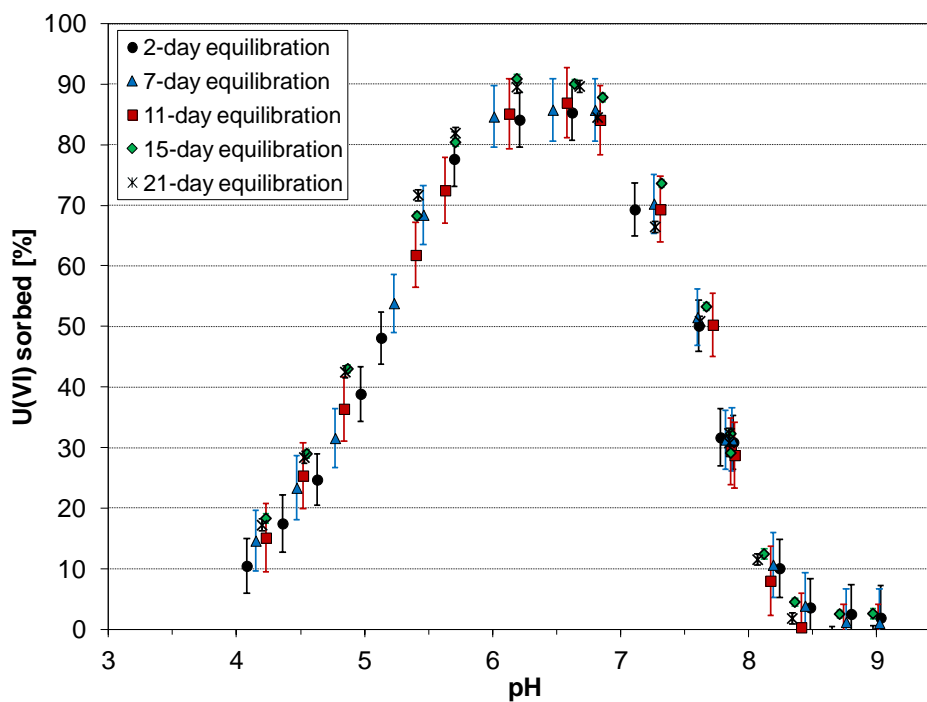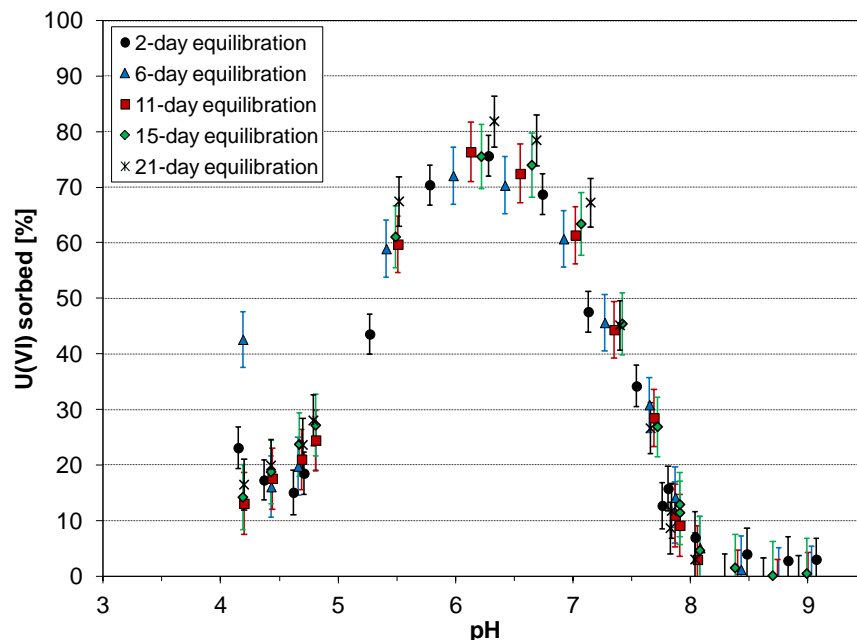
Figure 4-3: Time-dependent uranium (VI) sorption onto 0.5 g/L of 'cooked' and 'uncooked' bentonite samples as a function of pH and over a total sorption equilibration of 21 days. Error bars reflect analytical uncertainties for the analysis of uranium solution concentrations by ICP-MS analysis.
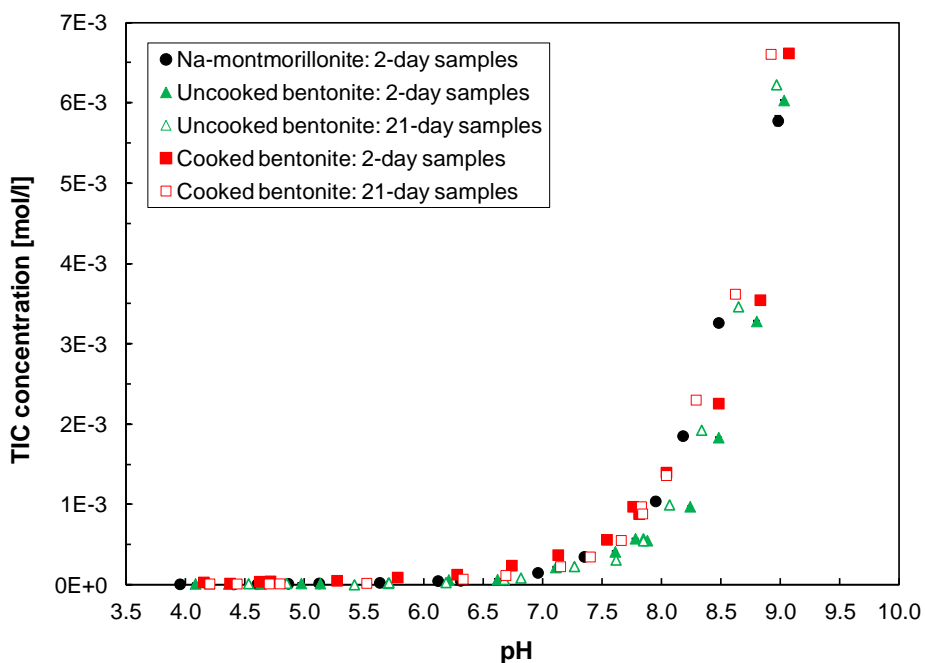
Figure 4-4: Comparison of Total Inorganic Carbon (TIC) concentrations in Na-montmorillonite, 'cooked' and 'uncooked' bentonite suspensions during uranium(VI) sorption experiments.

4.3   DIFFUSION EXPERIMENTS

4.3.1   Overview and Goals

As described in detail previously (Davis et al., 2013; Rutqvist et al., 2014), our first diffusion experiment focused on the diffusive transport of calcium bromide in purified Na-montmorillonite at a low degree of compaction (dry density of 0.79 kg/l). This experiment allowed us: (1) to test our experimental approach with non-radioactive solutes prior to uranium (VI) diffusion experiments; (2) to determine diffusion coefficients for calcium (and bromide) for their later incorporation in performance assessment models, which is motivated by the strong influence of Ca on uranium(VI) solution speciation; and (3) to examine the ability of existing pore-scale conceptual models to link molecular and macroscopic scale data on adsorption and diffusion in compacted smectite. A brief summary of results for that experiment and associated modeling/simulations, and the implications of these findings for uranium (VI) diffusion in Na-montmorillonite, are provided below. Additional details can be found in a previous report (Rutqvist et al., 2014) and a companion manuscript (Tinnacher et al., in review for publication in *Geochimica et Cosmochimica Acta*).

This year, two parallel uranium (VI) diffusion experiments were begun using a very similar experimental protocol, purified Na-montmorillonite, and a comparable low degree of clay compaction. With these uranium(VI) diffusion experiments, we are pursuing the following goals: (1) to determine uranium(VI) diffusion coefficients in Na-montmorillonite (with Ca concentration levels too low to affect uranium(VI) speciation) for their later use in performance assessment models; (2) to investigate the role of full or partial anion exclusion of negatively-charged uranium(VI) solution species from montmorillonite interlayer spaces; (3) to evaluate effects of uranium(VI) sorption reactions on its diffusive transport behavior; and (4) to demonstrate an experimental approach for uranium(VI) through-diffusion experiments and provide relevant experimental data that is otherwise not accessible. We provide a summary of the currently available experimental data for the uranium (VI) diffusion experiments in Section 4.3.4. A detailed interpretation of the experimental results, however, which is dependent on the simulation of diffusion data after the completion of the experiment, will be reported at a later point in time.

4.3.2   Key Findings from Calcium Bromide Diffusion Experiment

One of the goals of this study was to examine the ability of existing pore scale conceptual models to link molecular and macroscopic scale data on adsorption and diffusion in compacted smectite. For this purpose, macroscopic scale measurements of the adsorption and diffusion of calcium, bromide, and tritiated water (HTO) in Na-montmorillonite were modeled using a multi-component reactive transport approach while testing a variety of conceptual models of pore scale properties (adsorption and diffusion in individual pores). Molecular dynamics (MD) simulations were carried out under conditions similar to those of our macroscopic scale diffusion experiments to help constrain the pore scale models.

Our evaluation of pore scale models based on experimental and modeling results suggests that *single porosity* pore scale models are consistent with results from pore scale MD simulations, but not with macroscopic, experimental data. Among the tested conceptual models, a *dual porosity* model, which allows for a distinction between bulk liquid and diffuse ion swarm (DIS) waters, provides the best overall agreement with all results. Furthermore, our results also indicate that the pore size distribution of our compacted clay cannot be unimodal, and that Na and Ca ions adsorbed in the Stern layer retain a significant mobility. Hence, for the future development of conceptual diffusion models, an introduction of Stern layer diffusion (in addition to diffusion in bulk liquid water and DIS water) needs to be considered.

4.3.3 Materials and Methods for Uranium (VI) Diffusion Experiments

Uranium(VI) diffusion experiments involved a series of steps which can be summarized as follows: (1) the purification of a commercially-available Source Clay from the Clay Minerals Society (Na-montmorillonite, SWy-2) in order to minimize calcium background concentrations and quartz/feldspar impurities in the solid; (2) the purification of an in-house uranium-233 stock solution to remove accumulated daughter products and provide a known chemical solution matrix of the stock; (3) the equilibration of the purified Na-montmorillonite with background electrolyte solutions at the specified pH conditions in batch mode; (4) dry-packing of the pH-equilibration montmorillonite samples into diffusion cells followed by the saturation of the clay packings with background electrolyte solutions at the specified, target pH conditions; (5) tracer tests with tritiated water (HTO) to determine the total porosities of the clay packings in each cell; and (6) the actual uranium(VI) through-diffusion experiments.

Purification of Uranium-233 Stock Solution: We selected uranium-233 as the tracer for uranium (VI) diffusion experiments due to its short half-life relative to other uranium isotopes. This allows for better detection limits of low uranium (VI) concentrations in solution, a relatively straight-forward and fast analysis by liquid scintillation counting, and hence a close and timely monitoring of diffusive fluxes over the course of diffusion experiments. As commercially available U-233 was too expensive, we utilized an existing in-house U-233 stock solution provided by Dr. Heino Nitsche (Nuclear Sciences Division, Lawrence Berkeley National Laboratory, deceased). However, a purification of this in-house stock was necessary in order to remove accumulated daughter products (Th-229, Ra-225, Ac-225), and to ensure that U-233 was present as uranium (VI) and in a known chemical solution matrix.

The purification procedure was based on the separation of uranium from impurities using an Eichrom UTEVA resin column (2-mL cartridges, 50-100 μm UTEVA resin, Eichrom P/N: UT-R50-S), while largely following the recommendations provided in Method ACW02, Rev. 1.4 (Uranium in Water) by Eichrom Technologies, LLC. During the procedure, resin columns were positioned in an Eichrom column rack (P/N AC-103) and connected to 2-mL NORM-JECT Luer sterile syringes, serving as solution reservoirs.

All acids and other chemicals used in the procedure were of TraceSelect Grade. New, acid-washed Savillex PFA vials were used to contain acids and other solutions. Furthermore, a nitric acid (3 M)-aluminum nitrate (1 M) solution was purified from known impurities of natural uranium in aluminum nitrate prior to its use in the procedure, as described in the following. A 2-mL UTEVA resin column was first conditioned with 7 mL of 3 M nitric acid in small volume increments (1 or 2 mL). Then, the nitric acid (3 M)-aluminum nitrate (1 M) solution was loaded onto the conditioned column in 2 mL increments and the purified solution, drained by gravity, collected in a fresh, clean vial.

The original U-233 stock solution (5 mL, 25 μCi total, nominal activity) was carefully dried in a Savillex PFA vial on a hot plate. The glass vial, previously containing the original stock, was rinsed with 4 mL, and then 2-times 3 mL of 5 M nitric acid. After each rinse, the individual rinse solutions were dried in the same Savillex vial. Then, U-233 was redissolved in 10 mL of 5 M nitric acid, and dried again. Finally, U-233 was dissolved in 10 mL of 3 M nitric acid-1 M aluminum nitrate solution plus 1 mL of 3.5 M $NaNO_2$. The latter was added to ensure a +6 oxidation state of U-233 in the final, purified stock.

A new 2-mL UTEVA resin column was preconditioned with 4-times 2 mL of 3 M nitric acid. Then, the solution containing U-233 was loaded onto the column in 2 mL increments, and the column effluent, which is expected to contain Ra-225, Ac-225 and possibly other impurities, collected as waste. Up to the loading of the U-233 solution, all solutions were eluted from the resin column by gravity. However, after this step, gravity-based flow-rates decreased and solutions had to be gently loaded by hand with syringes (2-mL NORM-JECT Luer sterile syringes), while ensuring sufficiently slow flow-rates (~1 mL/min.).

Next, the Savillex vial, used to dry the original U-233 stock, was rinsed with 3-times 2 mL of 3 M HNO_3, and the rinse solutions loaded onto the UTEVA column as well. This was followed by column rinses with three different types of solutions, all added in small volume increments: (1) 5 mL of 3 M HNO_3, (2) 15 mL of 8 M HNO_3, and (3) 5 mL of 9 M HCl. With the last rinse, the column resin was converted to the chloride system, and some Np and Th is expected to be removed in the process. During all of these rinses, column effluents were collected as waste. In the next step, Th-229 was removed from the column by eluting with 7-times 3 mL of 5 M HCl-0.05 M oxalic acid.

Finally, the purified U-233 was eluted from the column into three separate Savillex vials, using 5-times 2 mL of 1 M HCl (stock #1), 5-times 2 mL of 1 M HCl (stock #2), 5-times 2 mL of 0.5 M HCl (stock #3). Exact volumes of the eluted stock solutions were calculated based on weight differences before and after filling of the vials. Liquid scintillation counting (PerkinElmer Liquid Scintillation Analyzer Tri-Carb 2900TR; Ultima Gold XR liquid scintillation cocktail) of small volumes of each stock (5, 10 and 15 µL) determined specific activities of 0.61 µCi/mL (stock #1), 1.61 µCi/mL (stock #2) and 0.30 µCi/mL (stock #3) of U-233. The recovery of U-233 during the purification procedure was estimated at 100%.

Clay Equilibration with Desired pH-Conditions in Batch Mode: As stated above, our goal was to evaluate both, the potential influence of anion exclusion effects and uranium (VI) sorption reactions on uranium (VI) diffusion behavior in through-diffusion experiments. This required a careful selection of the experimental conditions, such as solution pH, total uranium (VI) concentrations and degree of clay compaction, in order to ensure a breakthrough of uranium (VI) within reasonable experimental time-frames.

With regard to pH, the selected target pH conditions should ensure: (1) a predominance of anionic uranium (VI) species in solution in order to investigate potential anion exclusion effects; and (2) a sufficiently low uranium (VI) sorption affinity to montmorillonite in order to avoid strong uranium (VI) retardation that would exceed reasonable experimental time-frames. For the latter, we determined, based on preliminary calculations, that a target range of log K_d values between 0.7 and 1 [l/kg] (K_d=5-10 [l/kg]) would be appropriate. The first requirement leads to the selection of alkaline pH conditions (Figure 4-5). The second criterion further narrows the pH range to values between 8 and 9 (Figure 4-6). Hence, we decided to perform two parallel diffusion experiments at target pH values of pH-8.75 and pH-8.95, with the assumption that interactions between the clay and pH-adjusted electrolyte solutions could potentially lower the pH further, given our experience from the previous calcium bromide diffusion experiment.
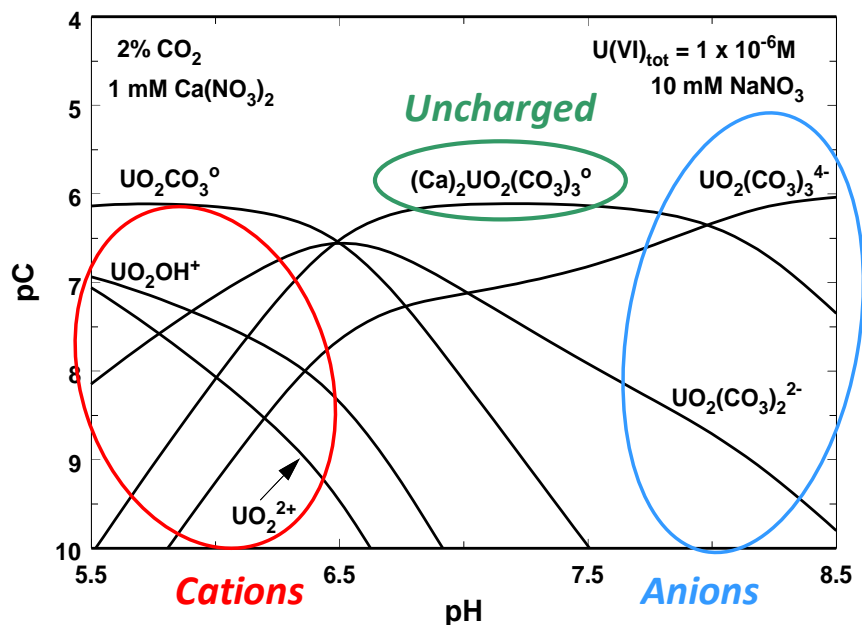
Figure 4-5: Distribution of cationic, anionic and neutral uranium (VI) species as a function of pH in a solution in equilibrium with a gas phase containing 2% CO_2.
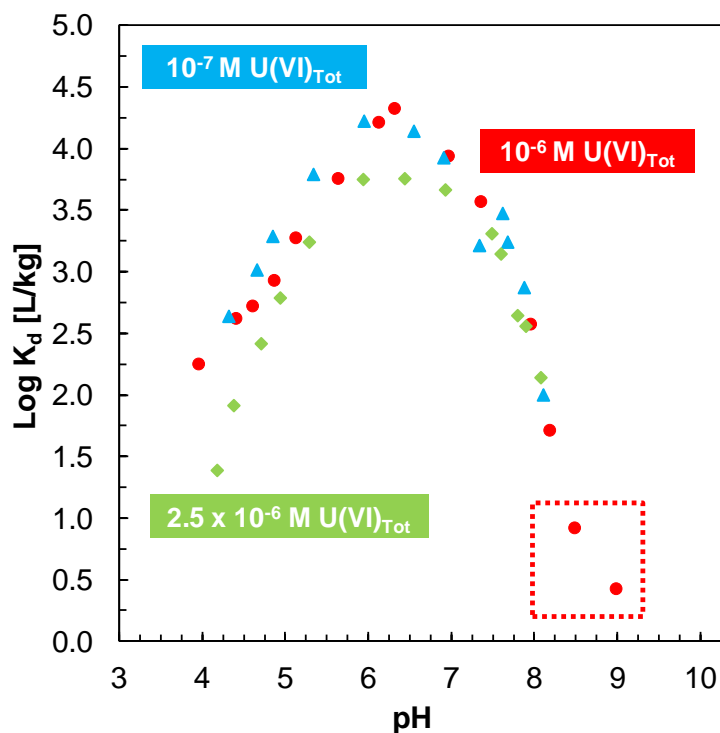
Figure 4-6: Results from previous uranium (VI) batch sorption experiments with Na-montmorillonite that were used to select appropriate pH conditions for uranium(VI) diffusion experiments.

The specific compositions of background electrolyte solutions at pH 8.75 and 8.95 and a total ionic strength of 0.1 M were based on aqueous speciation calculations, taking into account the ionic strength contributions of the buffer (sodium bicarbonate) and the base (sodium hydroxide) to be added for initial pH adjustments. Two-liter electrolyte solutions were prepared using high-purity chemicals (Fluka TraceSelect NaCl and NaOH; Alfa Aesar Puratronic $NaHCO_3$). After an initial equilibration of solutions with atmospheric CO_2 over two days, the pH was further adjusted by adding small volumes of high-purity HCl or NaOH.

Dry, purified Na-montmorillonite was pre-equilibrated with the background electrolyte solutions at the specified pH-conditions (pH-8.75 and pH-8.95) in batch mode in order to accelerate the equilibration process. For this purpose, six aliquots of approximately 1 gram of Na-montmorillonite were added to six acid-washed 40-mL polycarbonate centrifuge vials (Oakridge tubes). After adding 33 mL of pH-adjusted background electrolyte solutions to each vial (three vials per pH condition), the clay was first mixed by hand and then on a rotary shaker over four days. Afterwards, the pH values of the clay suspensions were recorded, and the clay separated from solutions in two consecutive centrifugations (Avanti J-E centrifuge, JA-17 rotor, 16,000 rpm for 33 minutes each). After re-combining all clay fractions in the original polycarbonate vials, 20 mL of fresh background electrolyte solutions were added to each individual vial, and the clay mixing and equilibration steps repeated.

This series of steps was repeated further for a total number of 10 equilibration steps over three weeks (individual equilibration times of 4, 0.8, 0.8, 1, 3.8, 0.9, 1, 0.9, 2.9, and 1 days). (Over this time-frame, the pH values in electrolyte solutions not in contact with clay remained stable.) Afterwards, three pH fine-adjustments were performed by adding small volumes of HCl and NaOH solutions directly to the individual vials over three days, while allowing for system equilibration over about one day after each adjustment. An overview of the changing pH conditions after each equilibration or adjustment step is provided in Figure 4-7.
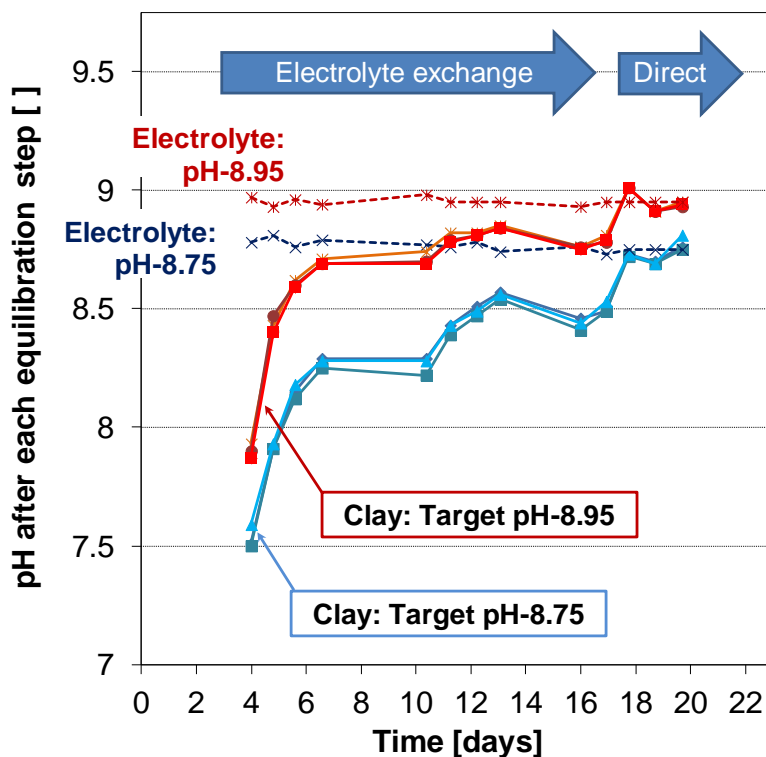
Figure 4-7: Overview of pH-equilibration of Na-montmorillonite in preparation for uranium(VI) diffusion experiments. Blue arrows indicate changes in the equilibration procedure from the exchange of background electrolyte solutions to a direct pH adjustment with HCl and NaOH solutions.

Once the pH conditions in the suspensions appeared to remain stable, the clay samples were isolated from solutions by centrifugation as described above, and dried in a convection oven at 45 °C over five days. After grinding of the dry clay samples in a Retsch MM 400 ball mill (frequency of 30/sec for 2 minutes), the pH-equilibrated samples were ready for their use in later uranium (VI) diffusion experiments.

Experimental Setup for Uranium(VI) Diffusion Experiments: The uranium (VI) through-diffusion experiments largely followed procedures previously described in the literature (Molera and Eriksen, 2002; Van Loon et al., 2003a;b). The experimental setup consists of a set of two diffusion cells, each connected to high- and low-concentration reservoirs, and a peristaltic pump (4-8). All experimental solutions were repeatedly adjusted to the target pH values of pH 8.75 and 8.95 using small volumes of acid/base solutions (TraceSelect grade NaOH and HCl) while equilibrating with atmospheric CO_2, prior to their contact with the mineral phase.
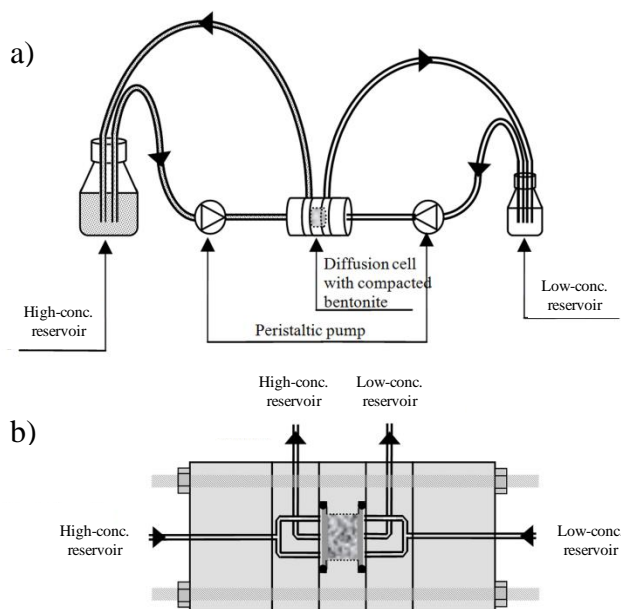
Figure 4-8: Schematic of the experimental apparatus for uranium (VI) diffusion studies.

At the beginning of the experiment, dry, pH-adjusted Na-montmorillonite samples were packed into the diffusion cells (PEEK; D=1.0 cm, L=0.5 cm; Alltech 2 μm stainless-steel frits, P/N 721825) by hand with the goal to obtain a dry bulk density of approximately 0.8 kg dm^{-3}. The clay was carefully compacted with a custom-made PEEK rod, and then saturated with the individual background electrolyte solutions (0.1 M NaCl, pH-8.75 or pH-8.95) by circulating electrolyte solutions for about 3 ½ weeks (two 200-mL reservoirs per cell; estimated flow rate of 0.78 mL min^{-1}). The exact dry densities of the clay packings (0.77 kg dm^{-3} for both cells) were calculated after determining the water content of the clay samples based on drying at 150 °C for approximately five days.

After clay saturation, tracer tests with tritiated water (HTO) were initiated by replacing the reservoir solutions with 200 mL of background electrolytes at pH-8.75 or pH-8.95 containing ~24 nCi/mL (~890 Bq mL^{-1}) HTO (high-concentration reservoirs) on one end of each diffusion cell, and 20 mL reservoirs containing fresh, HTO-free electrolyte solutions (low-concentration reservoirs) on the opposite ends. Over the following weeks, the circulation of solutions was continued at the same flow rate. Electrolyte solutions in the low-concentration reservoirs were repeatedly replaced in order to maintain a nearly constant concentration gradient between the high- and low-concentration reservoirs. The exchanged low-concentration reservoir vials were weighed to correct for volume losses due to evaporation. Solutions were sampled for tritium analysis by liquid scintillation counting (PerkinElmer Liquid Scintillation Analyzer Tri-Carb 2900TR; Ultima Gold XR liquid scintillation cocktail), and their solution pH values were recorded. This procedure was continued until a series of data points had been collected under steady-state conditions for HTO diffusive fluxes.

The solutions in the high-concentration reservoirs were then replaced with HTO-free background electrolyte solutions at pH-8.75 and pH-8.95 containing a nominal concentration of 2.5 × 10^{-6} M uranium(VI) in the form of the U-233 tracer (exact concentrations were 2.36 × 10^{-6} M U-233 or 5.35 nCi/mL = 198 Bq/mL for pH-8.75, and 2.34 × 10^{-6} M U-233 or 5.30 nCi/mL = 196 Bq/mL for pH-8.95). Again, low-concentration reservoir solutions were continuously replaced, and uranium-233 and tritium activities analyzed (PerkinElmer Liquid Scintillation Analyzer Tri-Carb 2900TR; Ultima Gold XR liquid

scintillation cocktail), with the goal to collect a sufficient number of data points under steady-state conditions for uranium (VI) diffusive fluxes in each system. In addition, the pH values in low-concentration reservoir solutions were measured. Furthermore, samples from low-concentration reservoir solutions were preserved for a later ICP-MS analysis of a series of elements that could either be relevant for uranium(VI) solution speciation or indicate any potential montmorillonite degradation, as wells as for alkalinity titrations (both analyses currently in progress).

It is important to note that, with the replacement of HTO high-concentration reservoir solutions with U-233 high-concentration reservoir solutions, we essentially started an 'out-diffusion' experiment for tritium. At the end of the tritium tracer test, and after reaching steady-state conditions, a linear HTO concentration profile had been established across the clay packing in the diffusion cell. By replacing the high-concentration reservoir with a HTO-free solution and continuously exchanging low-concentration reservoir solutions during the uranium (VI) diffusion experiments, new concentration gradients between HTO in the diffusion cells and the reservoir solutions are established. Hence, HTO diffuses out of the cells in both directions, and is accumulated in both the high- and low-concentration reservoir solutions. As a result, low HTO concentrations are detected in low-concentration reservoir solutions during the uranium (VI) diffusion experiments. These 'out-diffusion' data for HTO will allow us to further constrain total porosity values that are inferred from simulations of HTO through-diffusion data.

Last, given the high importance of pH for uranium (VI) solution speciation and sorption behavior, we performed two additional pH measurements at two other points in the experimental setup during uranium (VI) diffusion, besides the values collected for low-concentration reservoir solutions. First, a small pH probe was directly immersed into the two high-concentration reservoir solutions containing U-233 over the course of the experiment. In addition, we collected small volumes (3-5 mL) of 'flow-back' solutions, which are high-concentration reservoir solutions that had been in contact with the clay packings in the diffusion cells and were flowing back into the high-concentration reservoirs. After these pH measurements, collected solution fractions were returned to their respective reservoirs. These additional measurements were taken in order to check whether the pH values directly recorded in high-concentration reservoir solutions actually represented the conditions of solutions in contact with the clay packings. This consideration is based on the large dilution effects occurring in high-concentration reservoirs during the circulations of solutions (200 mL of reservoir volume versus 0.78 mL min^{-1} flow-rate for the circulating solution). However, both of these types of measurements were performed much less frequently in order to minimize any potential disturbances to the experiments.

4.3.4   Results

pH Monitoring Data for Uranium(VI) Diffusion Experiments: In Figure 4-9, we provide a summary of pH monitoring data recorded during the HTO tracer tests and over the course of the (ongoing) uranium(VI) diffusion experiments. It appears that the contact of background electrolyte solutions with the clay packings causes a slight drop in pH in both systems. However, other than this initial pH drop, the pH conditions are reasonably stable over time and across the individual diffusion cells in both systems. Hence, the pH pre-equilibration step in batch mode allowed for a reasonable stabilization of pH conditions in later diffusion experiments. The latter will simplify the simulation and interpretation of diffusion data, given the strong dependence of uranium (VI) solution speciation and sorption behavior on pH.
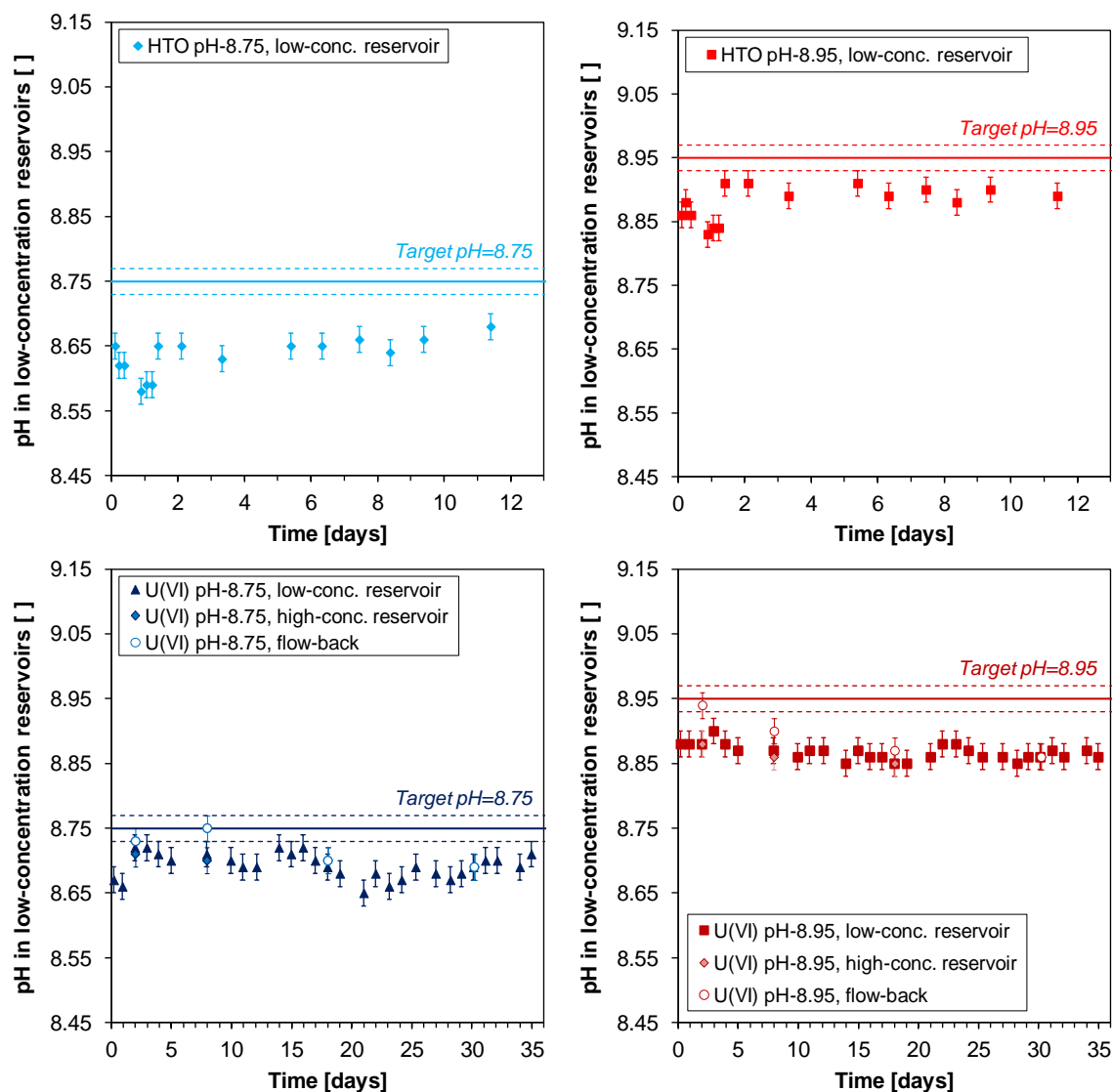
Figure 4-9: pH monitoring data for HTO tracer test and uranium(VI) diffusion experiments.

The pH values in 'flow-back' solutions appear to be slightly higher and closer to target pH values than in high-concentration reservoir solution at early time-points in the experiment. However, otherwise no apparent trends regarding pH differences between high-concentration reservoir solutions and flow-back solutions were observed.

Tritium Tracer Tests: Normalized mass flux densities reaching the low-concentration reservoir (J_N in m day^{-1}) were calculated with the following expression:

$$J_N = \frac{C_{low}}{C_{high}} \frac{V_{low}}{A \Delta t}$$

(4-1)

where C_{low} is the concentration of the species of interest measured in the low-concentration reservoir at a sampling event, C_{high} is the constant concentration in the high-concentration reservoir, Δt is the time interval since the previous sampling event (in days), A is the cross sectional area available for diffusion (0.785 cm^2), and V_{low} is the volume of the low-concentration reservoir (about 20 mL). (With the exchange of low-concentration reservoir solutions, C_{low} is initially zero at the beginning of each individual time interval.)

Figure 4-10 depicts the results for normalized HTO fluxes recorded during the HTO tracer tests (HTO through-diffusion data) and the (ongoing) uranium(VI) diffusion experiments (HTO out-diffusion data), respectively. Based on the results for HTO through-diffusion (Figure 4-10, top), we can conclude that the total porosity of the clay packing in the pH-8.75 system is slightly higher than for the pH-8.95 system. This agrees well with our estimated dry density values for the two cells, with 0.766 and 0.772 kg dm^{-3} for pH-8.75 and pH-8.95 systems, respectively. Slightly higher dry densities and degrees of clay compaction would result in slightly lower total porosities of the clay packing. A later simulation of both types of experimental data sets will allows us to determine the total porosity and water diffusion coefficients in each system.

Uranium (VI) Through-Diffusion: Based on currently available data, observed normalized fluxes for uranium(VI) are about one order of magnitude lower than fluxes for tritiated water (Figure 4-11). Furthermore, under both pH conditions, uranium (VI) breakthrough is retarded relative to the non-reactive tracer tritium, with a greater retardation at target pH-8.75 than pH-8.95. The latter is in good agreement with uranium (VI) sorption data, which indicate higher uranium(VI) sorption affinities and K_d values at pH-8.75 than pH-8.95.

Given that the currently observed uranium (VI) fluxes are substantially lower than for HTO, we assume at this point that this will also be the case under steady-state conditions for uranium (VI) fluxes. Hence, a significant contribution of uranium (VI) surface diffusion to the total fluxes, and a strong influence of weak uranium (VI) sorption reactions, e.g. in the form of cation exchange reactions, can most likely be ruled out for these systems. Last, there seems to be a stronger kinetic component for uranium (VI) sorption reactions at pH-8.75 than at pH-8.95 (Figure 4-12), since the time-frames required to reach steady-state conditions appear to be different for these two systems. This indicates a potential overall rate dependence on the aqueous speciation of uranium (VI), perhaps related to the dissociation kinetics of different aqueous uranium (VI) complexes prior to the formation of uranium(VI) surface complexes at montmorillonite edge sites.
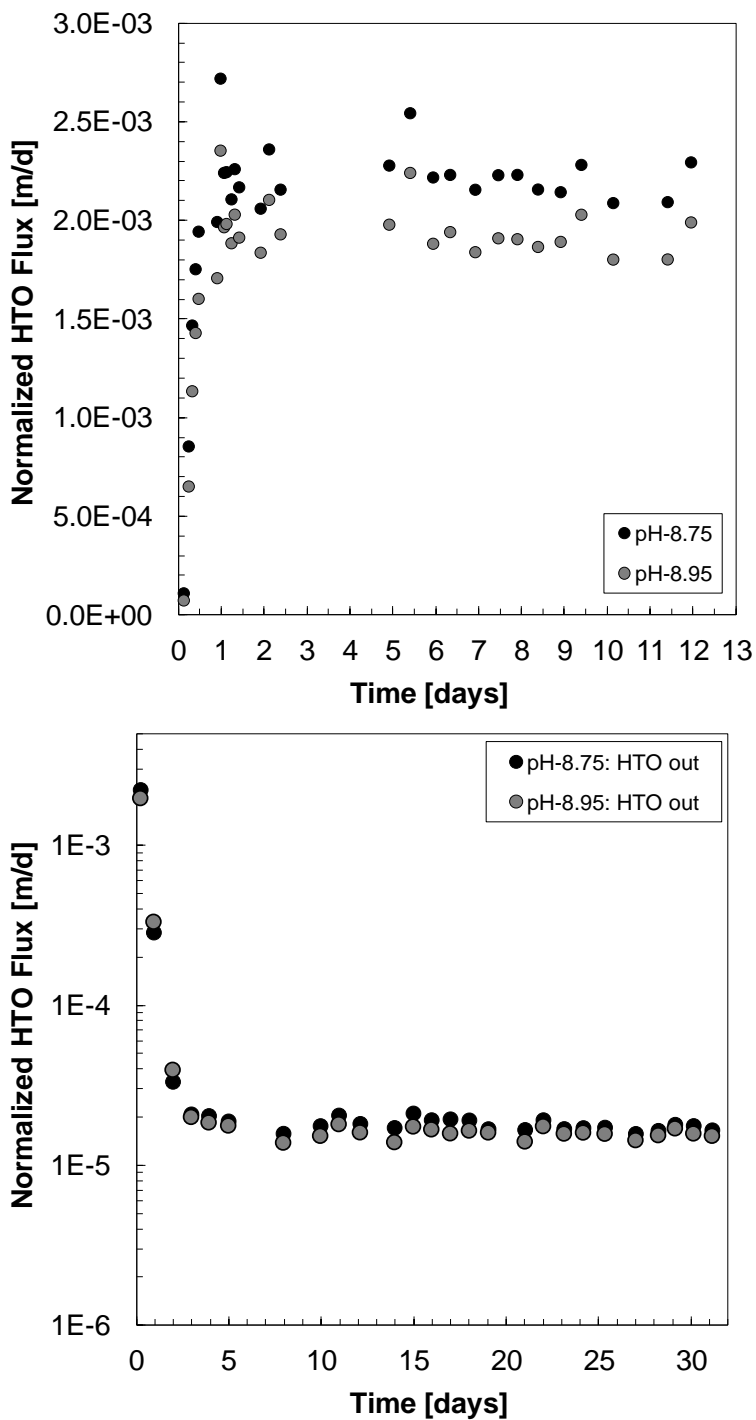
Figure 4-10: Normalized HTO diffusive fluxes in low-concentration reservoirs during HTO tracer tests (HTO through-diffusion experiments, top) and uranium (VI) through-diffusion experiments (HTO out-diffusion experiments, bottom) at target pH values of 8.75 and 8.95.
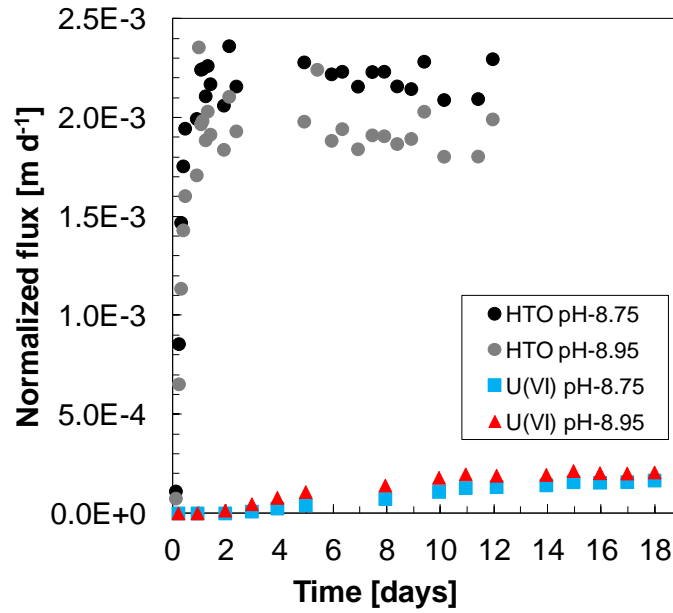
Figure 4-11: Comparison of normalized diffusive fluxes for tritiated water (HTO) and uranium (VI) at target pH values of 8.75 and 8.95.
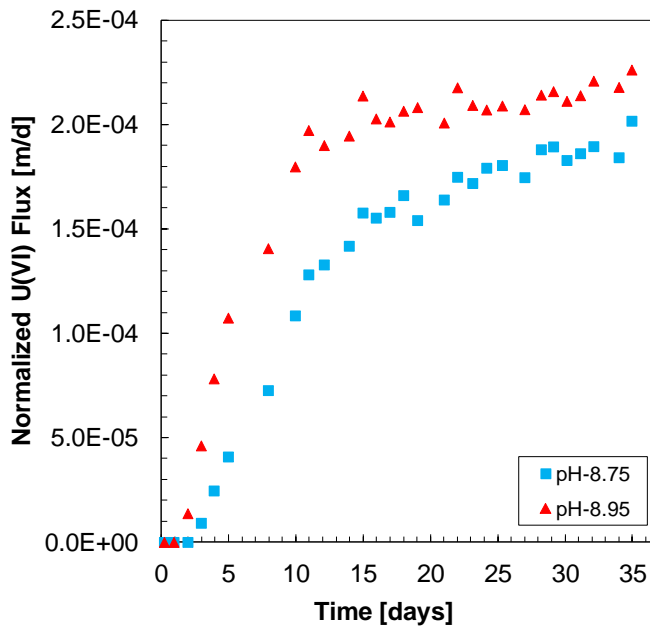
Figure 4-12: Normalized uranium(VI) diffusive fluxes during uranium (VI) through-diffusion experiments at target pH values of 8.75 and 8.95.

4.4 FUTURE WORK

The following tasks are planned for the upcoming year:

1) Continue data collection and analysis for the ongoing uranium(VI) diffusion experiment in purified Na-montmorillonite until a sufficient number of data points has been collected under steady-state conditions for diffusive uranium (VI) fluxes at both pH conditions.
2) Simulation of the uranium (VI) diffusion data in collaboration with modelers, with the goal to elucidate the following research questions: (a) the potential influence of anion exclusion effects, and (b) the relevance of uranium (VI) cation exchange versus surface complexation reactions for the diffusive transport behavior of uranium (VI) under alkaline conditions.

An evaluation of these questions is needed in order to develop realistic conceptual models for diffusion process models in conjunction with performance assessment models. In addition, the determination of uranium (VI) diffusion coefficients, resulting from the simulations of these data sets, will directly provide input parameters for later performance models. The latter, however, requires that future performance assessment models are capable of tracking changes in aqueous compositions over time and space.

While the data from the current uranium (VI) – Na-montmorillonite diffusion experiments at alkaline pH conditions will represent an important step towards the development of a realistic, conceptual uranium (VI)-diffusion model, we are also proposing a new set of parallel diffusion experiments in Na-montmorillonite. These experiments will be performed under acidic pH conditions, with pH values specifically selected to show similar uranium (VI) sorption distribution coefficients (K_d values) as in the current experiments under alkaline pH. At low pH, uranium(VI) is primarily present in the form of cationic solution species, which are expected to sorb onto montmorillonite in the form of (weak) cation exchange reactions. Hence, given our current understanding of these systems, this should result in comparable uranium (VI) retardation, as observed under alkaline conditions, but significantly higher diffusive fluxes of uranium(VI). Experimental evidence supporting this hypothesis is strongly needed in order to allow for a realistic prediction of uranium (VI) mobility at a range of pH conditions.

Furthermore, additional uranium (VI) diffusion experiments are planned for different types of solids, namely 'cooked' and 'uncooked' bentonite samples. Current data describing uranium(VI) sorption behavior to these solids suggest a decrease in uranium(VI) sorption after the exposure of bentonite to heat, which may also affect uranium(VI) retardation during diffusion in these systems. Prior to performing this new set of diffusion experiments, we will characterize uranium (VI) sorption behavior to a series of other heat-treated bentonite/clay samples. For instance, uranium(VI) sorption experiments with bentonite samples from the FEBEX heater test will allow us to evaluate if a substantially longer exposure to heat (over years versus weeks), but at a lower temperature (100 °C versus 300 °C), increases or decreases the observed temperature effects on uranium(VI) sorption behavior. Furthermore, we will use heat-treated Opalinus Clay samples for additional comparisons. Typically, Opalinus Clay contains small fractions of pyrite, which are known to lead to a surface reduction of uranium (VI) to uranium (IV), at least under anaerobic conditions (e.g., Bruggeman and Maes, 2010), potentially resulting in a higher apparent fraction of uranium sorbed. Our goal is to investigate whether a potential decrease in the pyrite fraction due to heat-treatment could cause a change in uranium sorption characteristics. We will collaborate with Dr. Liange Zheng (LBNL) and Dr. Florie Caporuscio at Los Alamos National Laboratory in order to obtain these bentonite and clay samples.

Given the time-consuming nature of diffusion experiments, the results from this series of uranium (VI) sorption experiments will allow us to select a solid phase that is expected to cause the biggest differences in uranium (VI) diffusion behavior relative to Na-montmorillonite, as well as the appropriate system conditions for these experiments.

4.5   REFERENCES

Altmann, S., 2008. 'Geo'chemical research: A key building block for nuclear waste disposal safety cases. *J. Contam. Hydrol.* 102, 174–179.

Altmann, S., Tournassat, C., Goutelard, F., Parneix, J.-C., Gimmi, T., Maes, N., 2012. Diffusion-driven transport in clayrock formations. *Appl. Geochem.* 27, 463–478.

ANDRA, 2005. Référentiel du comportement des radionucléides et des toxiques chimiques d'un stockage dans le Callovo-Oxfordien jusqu'à l'Homme. (No. Dossier 2005 Argile). Dossier 2005 Argile. Agence Nationale pour la gestion des déchets radioactifs, Châtenay-Malabry, France.

Appelo, C.A.J., Van Loon, L.R., Wersin, P., 2010. Multicomponent diffusion of a suite of tracers (HTO, Cl, Br, I, Na, Sr, Cs) in a single sample of Opalinus Clay. *Geochim. Cosmochim. Acta* 74, 1201–1219.

Appelo, C.A.J., Wersin, P., 2007. Multicomponent diffusion modeling in clay systems with application to the diffusion of tritium, iodide, and sodium in Opalinus clay. *Env. Sci. Tech.* 41, 5002–5007.

Bai, J., C. X. Liu and W. P. Ball 2009. Study of Sorption-Retarded U(VI) Diffusion in Hanford Silt/Clay Material. Environmental Science & Technology 43 (20): 7706-7711.

Bock, H., Dehandschutter, B., Martin, C.D., Mazurek, M., De Haller, A., Skoczylas, F., Davy, C., 2010. Self-sealing fractures in argillaceous formations in the context of geological disposal of radioactive was (No. 6184). Nuclear energy agency, organisation for economic co-operation and development.

Bradbury, M.H., Baeyens, B., 2011. Predictive sorption modelling of Ni(II), Co(II), Eu(IIII), Th(IV) and U(VI) on MX-80 bentonite and Opalinus Clay: A "bottom-up" approach. *Appl. Clay Sci.* 52, 27–33.

Brown, P.L., Haworth, A., Sharland, S.M., Tweed, C.J. 1991. Modelling studies of the sorption of radionuclides in the far field of nuclear waste repository. *Radiochim. Acta*, 52/53, 439-443.

Bruggeman, C., Maes, N., 2010. Uptake of uranium(VI) by pyrite under Boom Clay conditions: Influence of dissolved organic carbon. *Environ. Sci. Technol.*, 44, 4210-4216.

Caporuscio, F.A., Cheshire, M.C., Rearick, M.S., McCarney, M.K., Jove-Colon, C. 2013. EBS Report - LANL Experimental update of buffer/backfill at elevated P,T. DOE Report number: FCRD-UFD-2013-000207.

Caporuscio, F.A., Cheshire, M.C., Rearick, M.S., Jove-Colon, C. 2014. LANL Argillite EBS Experimental Program 2014. FCRD-UFD-2014-000491.

Cheshire, M.C., Caporuscio, F.A., Rearick, M.S., Jove-Colon, C., McCarney, M.K. 2014. Bentonite evolution at elevated pressures and temperatures: An experimental study for generic nuclear repository designs. *American Mineralogist*, 99, 1662-1675.

Choi, J.-W., Oscarson, D., 1996. Diffusive transport through compacted Na-and Ca-bentonite. *J. Contam. Hydrol.* 22, 189–202.

Davis, J., Rutqvist, J., Steefel, C., Tinnacher, R., Vilarrasa, V., Zheng, L., Bourg, I., Liu H.-H., Birkholzer, J. Investigation of Reactive Transport and Coupled THM Processes in EBS: FY13 Report, Lawrence Berkeley National Laboratory, DOE Used Fuel Disposition Campaign, FCRD-UFD-2013-000216. (2013).

Delay, J., Vinsot, A., Krieguer, J.-M., Rebours, H., Armand, G., 2007. Making of the underground scientific experimental programme at the Meuse/Haute-Marne underground research laboratory, North Eastern France. *Phys. Chem. Earth, Parts A/B/C* 32, 2–18.

Descostes, M., Blin, V., Bazer-Bachi, F., Meier, P., Grenut, B., Radwan, J., Schlegel, M.L., Buschaert, S., Coelho, D., Tevissen, E., 2008. Diffusion of anionic species in Callovo-Oxfordian argillites and Oxfordian limestones (Meuse/Haute-Marne, France). *Appl. Geochem.* 23, 655–677.

Englert, M., Krall, L., Ewing, R.C., 2012. Is nuclear fission a sustainable source of energy? *MRS bulletin* 37, 417–424.

García-Gutiérrez, M., J. L. Cormenzana, T. Missana, M. Mingarro and U. Alonso 2003. Analysis of uranium diffusion coefficients in compacted FEBEX bentonite. Scientific Basis for Nuclear Waste Management XXVII, Kalmar, Sweden, Materials Research Society.

García-Gutiérrez, M., Cormenzana, J.L., Missana, T., Mingarro, M., 2004. Diffusion coefficients and accessible porosity for HTO and ^{36}Cl in compacted FEBEX bentonite. *Appl. Clay Sci.* 26, 65–73.

Gimmi, T., Kosakowski, G., 2011. How mobile are sorbed cations in clays and clay rocks? *Env. Sci. Tech.* 45, 1443–1449.

Glaus, M., Baeyens, B., Bradbury, M.H., Jakob, A., Van Loon, L.R., Yaroshchuk, A., 2007. Diffusion of ^{22}Na and ^{85}Sr in montmorillonite: evidence of interlayer diffusion being the dominant pathway at high compaction. *Environ. Sci. Technol.* 41, 478–485.

Glaus, M.A., Birgersson, M., Karnland, O., Van Loon, L.R., 2013. Seeming steady-state uphill diffusion of ^{22}Na$^+$ in compacted montmorillonite. *Env. Sci. Tech.* 47, 11522–11527.

Glaus, M.A., Frick, S., Rosse, R., Van Loon, L.R., 2010. Comparative study of tracer diffusion of HTO, Na-22(+) and Cl-36(-) in compacted kaolinite, illite and montmorillonite. *Geochim. Cosmochim. Acta* 74, 1999–2010.

Glaus, M.A., Frick, S., Rossé, R., Van Loon, L.R., 2011. Consistent interpretation of the results of through-, out-diffusion and tracer profile analysis for trace anion diffusion in compacted montmorillonite. *J. Contam. Hydrol.* 123, 1–10.

Glaus, M.A., Müller, W., Van Loon, L.R., 2008. Diffusion of iodide and iodate through Opalinus Clay: Monitoring of the redox state using an anion chromatographic technique. *Appl. Geochem.* 23, 3612–3619.

Gonzàlez Sànchez, F., Van Loon, L.R., Gimmi, T., Jakob, A., Glaus, M.A., Diamond, L.W., 2008. Self-diffusion of water and its dependence on temperature and ionic strength in highly compacted montmorillonite, illite and kaolinite. *Appl. Geochem.* 23, 3840–3851.

Guyonnet, D., Touze-Foltz, N., Norotte, V., Pothier, C., Didier, G., Gailhanou, H., Blanc, P., Warmont, F., 2009. Performance-based indicators for controlling geosynthetic clay liners in landfill applications. *Geotext. Geomembranes* 27, 321–331.

Holmboe, M., Karin Norrfors, K., Jonsson, M., Wold, S., 2011. Effect of textgreekg-radiation on radionuclide retention in compacted bentonite. *Radiat. Phys. Chem.* 80, 1371–1377.

Horseman, S.T., Volckaert, G., 1996. Disposal of radioactive wastes in argillaceous formations. *Geological Society, London, Engineering Geology Special Publications* 11, 179–191.

IAEA, 2004. Implications of partitioning and transmutation in radioactive waste management, *Technical reports series*. International Atomic Energy Agency, Vienna.

Jakob, A., Pfingsten, W., Van Loon, L.R., 2009. Effects of sorption competition on caesium diffusion through compacted argillaceous rock. *Geochim. Cosmochim. Acta* 73, 2441–2456.

Jansson, M., Eriksen, T.E., 2004. In situ anion diffusion experiments using radiotracers. *J. Contam. Hydrol.* 68, 183–192.

Jenny, H., Overstreet, R., 1939. Surface Migration of Ions and Contact Exchange. *J. Phys. Chem.* 43, 1185–1196.

Joseph, C., Schmeide, K., Sachs, S., Brendler, V., Geipel, G., Bernhard, G., 2011. Sorption of uranium (VI) onto Opalinus Clay in the absence and presence of humic acid in Opalinus Clay pore water. *Chem. Geol.* 284, 240–250.

Joseph, C., Van Loon, L.R., Jakob, A., Steudtner, R., Schmeide, K., Sachs, S., Berhard, G. 2013. Diffusion of U(VI) in Opalinus Clay: influence of temperature and humic acid. *Geochim. Cosmochim. Acta*, 109, 74-89.

Jougnot, D., Revil, A., Leroy, P., 2009. Diffusion of ionic tracers in the Callovo-Oxfordian clay-rock using the Donnan equilibrium model and the formation factor. *Geochim. Cosmochim. Acta* 73, 2712–2726.

Kaszuba, J.P., Runde, W.H., 1999. The aqueous geochemistry of neptunium: Dynamic control of soluble concentrations with applications to nuclear waste disposal. *Env. Sci. Tech.* 33, 4427–4433.

Kerisit, S., Liu, C., 2010. Molecular simulation of the diffusion of uranyl carbonate species in aqueous solution. *Geochim. Cosmochim. Acta* 74, 4937–4952.

Korichi, S., A. Bensmaili and M. Keddam 2010. Reactive Diffusion of Uranium in Compacted Clay: Evaluation of Diffusion Coefficients by a Kinetic Approach. Defect and Diffusion Forum 297-301: 275-280.

Kozaki, T., Fujishima, A., Saito, N., Sato, S., Ohashi, H., 2005. Effects of dry density and exchangeable cations on the diffusion process of sodium ions in compacted montmorillonite. *Eng. Geol.* 81, 246–254.

Kozaki, T., Fujishima, A., Sato, S., Ohashi, H., 1998a. Self-diffusion of sodium ions in compacted montmorillonite. *Nucl. Technol.* 121, 63–69.

Kozaki, T., Inada, K., Sato, S., Ohashi, H., 2001. Diffusion mechanism of chloride ions in sodium montmorillonite. *J. Contam. Hydrol.* 47, 159–170.

Kozaki, T., Liu, J.H., Sato, S., 2008. Diffusion mechanism of sodium ions in compacted montmorillonite under different NaCl concentration. *Phys. Chem. Earth, Parts A/B/C* 33, 957–961.

Kozaki, T., Saito, N., Fujishima, A., Sato, S., Ohashi, H., 1998b. Activation energy for diffusion of chloride ions in compacted sodium montmorillonite. *J. Contam. Hydrol.* 35, 67–75.

Kozaki, T., Sato, H., Fujishima, A., Saito, N., Sato, S., Ohashi, H., 1996. Effect of dry density on activation energy for diffusion of strontium in compacted sodium montmorillonite. In: *MRS Proceedings*. Cambridge Univ Press, p. 893.

Kozaki, T., Sato, H., Sato, S., Ohashi, H., 1999a. Diffusion mechanism of cesium ions in compacted montmorillonite. *Eng. Geol.* 54, 223–230.

Kozaki, T., Sato, Y., Nakajima, M., Kato, H., Sato, S., Ohashi, H., 1999b. Effect of particle size on the diffusion behavior of some radionuclides in compacted bentonite. *J. Nucl. Mater.* 270, 265–272.

Kozaki, T., Sawaguchi, T., Fujishima, A., Sato, S., 2010. Effect of exchangeable cations on apparent diffusion of Ca^{2+} ions in Na-and Ca-montmorillonite mixtures. *Phys. Chem. Earth, Parts A/B/C* 35, 254–258.

Lee, J.O., Cho, W.J., Hahn, P.S., Lee, K.J., 1996. Effect of dry density on Sr-90 diffusion in a compacted Ca-bentonite for a backfill of radioactive waste repository. *Ann. Nucl. Energy* 23, 727–738.

Loomer, D.B., Scott, L., Al, T.A., Mayer, K.U., Bea, S., 2013. Diffusion–reaction studies in low permeability shale using X-ray radiography with cesium. *Appl. Geochem.* 39, 49–58.

Liu, C., L. Zhong and J. M. Zachara 2010. Uranium(VI) diffusion in low-permeability subsurface materials. Radiochimica Acta 98 (9-11): 719-726.

Maes, N., H. Moors, L. Wang, G. Delecaut, P. De Canniere and M. Put 2002. The use of electromigration as a qualitative technique to study the migration behaviour and speciation of uranium in the Boom Clay. Radiochimica Acta 90 (9-11): 741-746.

Mazurek, M., Alt-Epping, P., Bath, A., Gimmi, T., Niklaus Waber, H., Buschaert, S., Cannière, P.D., De Craen, M., Gautschi, A., Savoye, S., Vinsot, A., Wemaere, I., Wouters, L., 2011. Natural tracer profiles across argillaceous formations. *Appl. Geochem.* 26, 1035–1064.

Melkior, T., Gaucher, E.C., Brouard, C., Yahiaoui, S., Thoby, D., Clinard, C., Ferrage, E., Guyonnet, D., Tournassat, C., Coelho, D., 2009. Na^+ and HTO diffusion in compacted bentonite: Effect of surface chemistry and related texture. *J. Hydrol.* 370, 9–20.

Melkior, T., Yahiaoui, S., Motellier, S., Thoby, D., Tevissen, E., 2005. Cesium sorption and diffusion in Bure mudrock samples. *Appl. Clay Sci.* 29, 172–186.

Melkior, T., Yahiaoui, S., Thoby, D., Motellier, S., Barthes, V., 2007. Diffusion coefficients of alkaline cations in Bure mudrock. *Phys. Chem. Earth, Parts A/B/C* 32, 453–462.

Molera, M., 2002. On the sorption and diffusion of radionuclides in Bentonite Clay. Ph. D. thesis, Royal Institute of Technolgy, Stockholm.

Molera, M., Eriksen, T., 2002. Diffusion of $^{22}Na^+$, $^{85}Sr^{2+}$, $^{134}Cs^+$ and $^{57}Co^{2+}$ in bentonite clay compacted to different densities: experiments and modeling. *Radiochim. Acta* 90, 753–760.

Molera, M., Eriksen, T., Jansson, M., 2003. Anion diffusion pathways in bentonite clay compacted to different dry densities. *Appl. Clay Sci.* 23, 69–76.

Motellier, S., Devol-Brown, I., Savoye, S., Thoby, D., Alberto, J.-C., 2007. Evaluation of tritiated water diffusion through the Toarcian clayey formation of the Tournemire experimental site (France). *J. Contam. Hydrol.* 94, 99–108.

Muurinen, A., Penitä-Hiltunen, P., Rantanen, J., 1986. Diffusion Mecflanisms of Srrontium and Cesium in Compacrtd Sodium Bentonite. In: *MRS Proceedings*. Cambridge Univ Press, p. 803.

Muurinen, A. 1990. Diffusion of uranium in compacted sodium bentonite. Engineering Geology 28 (3-4): 359-367.

Nakajima, M., Kozaki, T., Kato, H., Sato, S., Ohashi, H., 1997. The dependence of the diffusion coefficients of 3H and Cs on grain size in compacted montmorillonite. In: *MRS Proceedings*. Cambridge Univ Press, p. 947.

Nakashima, Y., 2000. The use of X-ray CT to measure diffusion coefficients of heavy ions in water-saturated porous media. *Eng. Geol.* 56, 11–17.

Nakashima, Y., 2002. Diffusion of H_2O and I^- in expandable mica and montmorillonite gels: contribution of bound H_2O. *Clays Clay Miner.* 50, 1–10.

Nakashima, Y., 2003. Diffusivity measurement of heavy ions in Wyoming montmorillonite gels by X-ray computed tomography. *J. Contam. Hydrol.* 61, 147–156.

Nakashima, Y., 2006. H_2O self-diffusion coefficient of water-rich MX80 bentonite gels. *Clay Miner.* 41, 659–668.

Nakashima, Y., Mitsumori, F., 2005. H_2O self-diffusion restricted by clay platelets with immobilized bound H_2O layers: PGSE NMR study of water-rich saponite gels. *Appl. Clay Sci.* 28, 209–221.

NEA, 2009. Mobile fission and activation products in nuclear waste disposal. NEA Report No. 6310, NEA, OECD (Nuclear Energy Agency, Organisation for Economic Co-operation and Development).

Neuzil, C.E., 1986. Groundwater flow in low-permeability environments. *Water Resour. Res.* 22, 1163–1195.

Neuzil, C.E., 1994. How permeable are clays and shales? *Water Resour. Res.* 30, 145–150.

Neuzil, C.E., 2013. Can shale safely host US nuclear waste? *EOS, Trans. Am. Geophys. Union* 94, 261–262.

Nye, P.H., 1980. Diffusion of ions and uncharged solutes in soils and soil clays. *Adv. Agron.* 31, 225–272.

Oscarson, D.W., Dixon, D.A., Hume, H.B., 1996. Mass transport through defected bentonite plugs. *Appl. Clay Sci.* 11, 127–142.

Pacala, S., Socolow, R., 2004. Stabilization wedges: solving the climate problem for the next 50 years with current technologies. *Science* 305, 968–972.

Pekala, M., D. K. A. Jan, H. N. Waber, T. Gimmi and P. Alt-Epping 2009. Transport of U-234 in the Opalinus Clay on centimetre to decimetre scales. Applied Geochemistry 24 (1): 138-152.

Pekala, M., J. D. Kramers and H. N. Waber 2010. $^{234}U/^{238}U$ activity ratio disequilibrium technique for studying uranium mobility in the Opalinus Clay at Mont Terri, Switzerland. Applied Radiation and Isotopes 68 (6): 984-992.

Rutqvist, J., Steefel, C., Davis, J., Bourg, I., Tinnacher, R., Galindez, J., Holmboe, M., Birkholzer, J., Liu, H.H. Investigation of Reactive Transport and Coupled THM Processes in EBS: FY12 Report, Lawrence Berkeley National Laboratory, DOE Used Fuel Disposition Campaign, FCRD-UFD-2012-000125. (2012).

Rutqvist, J., Davis, J., Zheng, L., Vilarrasa, V., Houseworth, J., Birkholzer, J., Investigation of Reactive Coupled THM Processes and Reactive Transport: FY14 Report, Lawrence Berkeley National Laboratory, DOE Used Fuel Disposition Campaign, FCRD-UFD-2014-000497. (2014).

Sato, H., Ashida, T., Kohara, Y., Yui, M., Sasaki, N., 1992. Effect of dry density on diffusion of some radionuclides in compacted sodium bentonite. *J. Nucl. Sci. Technol.* 29, 873–882.

Sato, H., Miyamoto, S., 2004. Diffusion behaviour of selenite and hydroselenide in compacted bentonite. *Appl. Clay Sci.* 26, 47–55.

Sato, H., Suzuki, S., 2003. Fundamental study on the effect of an orientation of clay particles on diffusion pathway in compacted bentonite. *Appl. Clay Sci.* 23, 51–60.

Savoye, S., Goutelard, F., Beaucaire, C., Charles, Y., Fayette, A., Herbette, M., Larabi, Y., Coelho, D., 2011. Effect of temperature on the containment properties of argillaceous rocks: The case study of Callovo–Oxfordian claystones. *J. Contam. Hydrol.* 125, 102–112.

Savoye, S., Page, J., Puente, C., Imbert, C., Coelho, D., 2010. New experimental approach for studying diffusion through an intact and unsaturated medium: a case study with Callovo-Oxfordian argillite. *Env. Sci. Tech.* 44, 3698–3704.

SKB, 2011. Long-term safety for the final repository for spent nuclear fuel at Forsmark. Main report of the SR-Site project. Volume I. SKB - TR-11-01.

Suzuki, S., Sato, H., Ishidera, T., Fujii, N., 2004. Study on anisotropy of effective diffusion coefficient and activation energy for deuterated water in compacted sodium bentonite. *J. Contam. Hydrol.* 68, 23–37.

Tachi, Y., Yotsuji, K., 2014. Diffusion and sorption of Cs^+, Na^+, I^- and HTO in compacted sodium montmorillonite as a function of porewater salinity: Integrated sorption and diffusion model. *Geochim. Cosmochim. Acta* 132, 75–93.

Tokunaga, T. K., J. M. Wan, J. Pena, S. R. Sutton and M. Newville 2004. Hexavalent uranium diffusion into soils from concentrated acidic and alkaline solutions. Environmental Science & Technology 38 (11): 3056-3062.

Van Loon, L.R., Baeyens, B., Bradbury, M.H., 2005a. Diffusion and retention of sodium and strontium in Opalinus clay: Comparison of sorption data from diffusion and batch sorption measurements, and geochemical calculations. *Appl. Geochem.* 20, 2351–2363.

Van Loon, L.R., Glaus, M.A., Müller, W., 2007. Anion exclusion effects in compacted bentonites: Towards a better understanding of anion diffusion. *Appl. Geochem.* 22, 2536–2552.

Van Loon, L.R., Müller, W., Iijima, K., 2005b. Activation energies of the self-diffusion of HTO, 22Na+ and 36Cl- in a highly compacted argillaceous rock (Opalinus Clay). *Appl. Geochem.* 20, 961–972.

Van Loon, L.R., Soler, J.M., Bradbury, M.H., 2003a. Diffusion of HTO, $^{36}Cl^-$ and $^{125}I^-$ in Opalinus Clay samples from Mont Terri: Effect of confining pressure. *J. Contam. Hydrol.* 61, 73–83.

Van Loon, L.R., Soler, J.M., Jakob, A., Bradbury, M.H., 2003b. Effect of confining pressure on the diffusion of HTO, 36Cl- and 125I- in a layered argillaceous rock (Opalinus Clay): diffusion perpendicular to the fabric. *Appl. Geochem.* 18, 1653–1662.

Van Loon, L.R., Soler, J.M., Muller, W., Bradbury, M.H., 2004a. Anisotropic diffusion in layered argillaceous rocks: a case study with Opalinus Clay. *Env. Sci. Tech.* 38, 5721–5728.

Van Loon, L.R., Wersin, P., Soler, J.M., Eikenberg, J., Gimmi, T., Hernan, P., Dewonck, S., Savoye, S., 2004b. In-situ diffusion of HTO, $^{22}Na^+$, Cs^+ and I^- in Opalinus Clay at the Mont Terri underground rock laboratory. *Radiochim. Acta* 92, 757–763.

Van Schaik, J., Kemper, W., 1966. Chloride diffusion in clay-water systems. *Soil Sci. Soc. Am. J.* 30, 22–25.

Wang, X., Liu, X., 2004. Effect of pH and concentration on the diffusion of radiostrontium in compacted bentonite—a capillary experimental study. *Appl. Radiat. Isot.* 61, 1413–1418.

Wang, X., Tan, X., Chen, C., Chen, L., 2005. The concentration and pH dependent diffusion of ^{137}Cs in compacted bentonite by using capillary method. *J. Nucl. Mater.* 345, 184–191.

Wang, X., Tao, Z., 2004. Diffusion of $^{99}TcO4^-$ in compacted bentonite: Effect of pH, concentration, density and contact time. *J. Radioanal. Nucl. Chem.* 260, 305–309.

Wang, X.K., 2003. Diffusion of ^{137}Cs in compacted bentonite: Effect of pH and concentration. *J. Radioanal. Nucl. Chem.* 258, 315–319.

Wersin, P., Soler, J.M., Van Loon, L., Eikenberg, J., Baeyens, B., Grolimund, D., Gimmi, T., Dewonck, S., 2008. Diffusion of HTO, Br^-, I^-, Cs^+, $^{85}Sr^{2+}$ and $^{60}Co^{2+}$ in a clay formation: Results and modelling from an in situ experiment in Opalinus Clay. *Appl. Geochem.* 23, 678–691.

Wittebroodt, C., Savoye, S., Gouze, P., 2008. Influence of initial iodide concentration on the iodide uptake by the argillite of Tournemire. *Phys. Chem. Earth, Parts A/B/C* 33, 943–948.

5.0   LONG-TERM DIFFUSION OF U(VI) IN BENTONITE: DEPENDENCE ON DENSITY

5.1   INTRODUCTION

High-level nuclear waste (HLW) mainly resulting from worldwide energy production by nuclear power plants presents a highly chemo- and radiotoxic risk to the environment. The main strategy of waste management is to place the waste in containers and to store them safely in deep geological formations such as salt domes, crystalline rock, and clay rock. The prevention of radionuclide entry to the ecosphere needs to be maintained until their radioactivity is decayed to the natural radiotoxicity level (about one million years). Independent of the chosen host rock in most of the nuclear waste repository designs currently under development, the clay rock bentonite is discussed as material used to backfill the drilled cavities after disposal of the waste containers. This bentonite will acquire different densities depending on the level of confinement (Keto et al., 2007). Typically, bentonite dry bulk densities between 1.5 and 1.8 g/cm^3 can be reached.

For risk assessment, it has to be known if the radionuclides can be mobilized within the repository and transported into the surrounding geo- and biosphere if there is sudden water ingress. For this, the respective retardation factors of the radionuclides migrating through, and interacting with, the different barriers in the system have to be determined under environmentally relevant conditions. Waste-released radionuclides can be retarded by the surrounding barriers (e.g., waste container, backfill material, host rock) in several ways such as sorption, surface precipitation, or molecular diffusion. In many cases it is not possible to attribute the retention of the radionuclide migration to only one interaction process. For instance, the interaction of U(VI) with the natural clay rock Opalinus Clay, which is discussed as potential host rock for a nuclear waste repository, was studied by batch sorption (Joseph et al., 2011) and diffusion experiments (Joseph et al., 2013b). Finally, molecular diffusion was identified as the decisive retardation process.

Many studies focus on the radionuclide diffusion through bentonite since this barrier interacts with the migrating radionuclides before the host rock. In particular, the influence of the bentonite density on the radionuclide diffusion was studied for tritiated water (HTO) (Brockmann, 2006; Sato et al., 1992), $^{90}Sr^{2+}$ (Kim et al., 1993; Sato et al., 1992), $^{99}TcO_4^-$ (Sato et al., 1992), $^{129}I^-$ (Sato et al., 1992), $^{137}Cs^+$ (Brockmann, 2006; Kim et al., 1993; Sato et al., 1992), $^{36}Cl^-$ (Kim et al., 1993; Van Loon et al., 2007b), $^{237}Np(V)$ (Kozai et al., 2001; Sato et al., 1992), and $^{241}Am(III)$ (Sato et al., 1992). The general observation of all studies was that the effective diffusion coefficient, D_e, decreases with increasing density.

Uranium, in particular the isotopes ^{238}U (half-life, $t_{1/2} = 4.468 \times 10^9$ a) and ^{235}U ($t_{1/2} = 7.038 \times 10^8$ a), represents the main fraction of disposed spent nuclear fuel rods and consequently, is the main radiologic component of HLW. In general, uranium is stored in the oxidation state IV in the form of UO_2, which is under repository-relevant conditions insoluble and immobile. However, several oxidation processes can occur and U(IV) can be partly transformed to U(VI) (Bruno et al., 2004), which forms mainly mobile species.

For the uranium diffusion through bentonite, several studies can be found in the literature (Table 5-1). Generally, the experiments are performed for less than one year, except the study of Ramebäck et al. (1998). There the uranium release from spent UO_2 fuel and its following migration through compacted MX-80 bentonite was investigated for 74 months. Independent of the experimental time period applied, the diffusion results obtained by such studies shall be used to model the diffusion of radionuclides on a longer time frame with regard to safety assessment. This bears the question if the values obtained in short-

term experiments are also valid for longer time periods or if other factors may influence the diffusion with time.

Table 5-1: Literature selection of experimental conditions (t: time; ρ: dry bulk density) and corresponding diffusion parameters determined (D_a: apparent diffusion coefficient; K_d: distribution coefficient) for the uranium diffusion through compacted bentonite/montmorillonite.

t , days	ρ, g/cm^3	D_a, m^2/s	K_d, m^3/kg	Reference
62	2.0	3.4×10^{-12}; 6.4×10^{-13}; 2.7×10^{-13}	0.093	(Torstenfelt and Allard, 1986)
48; 85	0.9	$1.16 - 2.3\times10^{-12}$	$0.047 - 0.310$	(Wang et al., 2005)
90	1.6	$3\times10^{-15} - 6.6\times10^{-14}$	$0.0013 - 0.0023$	(Glaus and Van Loon, 2012)
29 – 121	0.8 – 1.8	$3.7\times10^{-12} - 3.1\times10^{-14}$	$0.01 - 0.1$	(Idemitsu et al., 1996)
279	1.65	$4\times10^{-14} - 1\times10^{-13}$	$0.006 - 0.021$	(Garcia-Gutierrez et al., 2004)
90 – 2220	2.0	$1.9\times10^{-13} - 1.6\times10^{-14}$	–	(Ramebäck et al., 1998)

Some of the studies presented in Table 6 were performed at lower bentonite densities than expected to be present in a repository (Wang et al., 2005). Often simple background electrolytes such as water (Garcia-Gutierrez et al., 2004; Idemitsu et al., 1996) or $NaClO_4$ (Wang et al., 2005) were used. In previous studies, the approach of Crank (1975) was applied to fit the uranium profiles and to determine the diffusion coefficients (Idemitsu et al., 1996; Wang et al., 2005). It describes the diffusion as a semi-infinite medium with the assumption that the upstream boundary reservoir is kept at a constant concentration. A variety of modeling software is available to describe more complex systems under variable boundary conditions and to determine respective diffusion parameters (Comsol, 2014; Steefel, 2011).

Besides the nature of the tracer (size, charge, oxidation state) and the composition of the solution (type of ions, level of salinity), the dry density of compacted bentonite affects the diffusion-accessible pore space or effective porosity, ε_{eff} [-], in diffusion experiments (Van Loon et al., 2007b). The effective porosity influences the effective diffusion coefficient of the diffusing species, D_e [m^2/s]. A common method to describe this relation and consequently to predict diffusion parameters in materials with known porosity is the application of an empirical formula analogous to Archie's law (Boving and Grathwohl, 2001):

$$D_e = \varepsilon_{eff}^{m} \cdot D_w \tag{5-1}$$

where D_w [m^2/s] is the diffusion coefficient of the tracer in water and m [-] is an empirical constant also known as the cementation factor of sedimentary rocks. The constant m depends on the properties of the porous material and is not influenced by temperature or sorption of the tracer on the porous medium.

In the present study, the diffusion of HTO and U(VI) through compacted bentonite was investigated as a function of dry density (ρ = 1.3, 1.6, 1.9 g/cm^3) at room temperature under ambient conditions. Based on HTO diffusion experiments, values for ε_{eff} at the respective dry density were determined. In the case of the U(VI) diffusion, the experiments were conducted for six years. As background electrolyte, synthetic bentonite model pore water (Van Loon et al., 2007a) was used. Using such a complex salt system offers the opportunity to perform experiments under more realistic conditions, in particular, towards the present diffusing uranium species. Speciation modeling based on the present conditions in the reservoir solutions was performed. The solutions were also analyzed for their biological contaminants, since microbial growth was observed over the duration of the experiment. To determine the diffusion parameters based on the collected experimental data the modeling codes CrunchFlow2011 (Steefel, 2011) and COMSOL

Multiphysics® 5.0 (Comsol, 2014), and the parameter optimization software PEST (Doherty, 2003) were applied. The relation between the resulting fitting values of ε_{eff} (HTO) and D_e (HTO, U(VI)) were analyzed according to the Archie's law analog and empirical constants were determined.

5.2   EXPERIMENTAL

5.2.1   Materials and Solutions

In the diffusion experiments, natural Na-bentonite MX-80 from Wyoming, USA was used. Herbert and Moog (2002) determined its mineralogy as follows: ~90% montmorillonite, 4% quartz, 2% muscovite, 2% calcite, < 2% cristobalite, and < 1% pyrite. In this study, the bentonite was provided as granulate by Süd-Chemie AG (Munich, Germany). The N_2-BET specific surface area was 15.7 m^2/g (Coulter SA 3100, Beckman Coulter, Fullerton, USA). The bentonite was characterized using X-ray fluorescence (XRF; mod. Tiger S8, Bruker, Billerica, MA, USA). The results are shown in Table 5-2. The natural uranium content was measured by inductively coupled plasma–mass spectrometry (ICP–MS, Thermo Scientific™ iCAP™ Q, Thermo Electron Corp., Waltham, MA, USA) after digestion of bentonite samples with HNO_3, HCl, and HF on a hot plate. The uranium content amounted to 13 ± 0.1 ppm.

Table 5-2: Composition of the MX-80 batch used in the diffusion experiments determined by XRF (only compounds > 1 wt.% are shown; error = 2σ).

Compound	wt.%
SiO_2	63.0 ± 0.2
Al_2O_3	18.7 ± 0.1
Fe_2O_3	8.58 ± 0.01
CaO	4.36 ± 0.02
MgO	1.84 ± 0.04
SO_3	1.32 ± 0.02

Synthetic pore water was used in diffusion experiments (pH 8, $I = 0.3$ M, (Van Loon et al., 2007a)). Its composition was calculated at the Paul Scherrer Institute based on the inventory of the soluble salts of the bentonite, the cation loading of the surface, $\varepsilon_{eff}(Cl^-)$, and several saturation phases in the bentonite (Bradbury and Baeyens, 2003b). In this study, the bulk dry densities 1.3 g/cm^3, 1.6 g/cm^3, and 1.9 g/cm^3 were investigated. The modeled compositions of the respective pore waters with their ionic strength, I, are summarized in Table 5-3. The solutions were prepared under ambient conditions in Milli-Q water (18 MΩ; mod. Milli-RO/Milli-Q-System, Millipore, Schwalbach, Germany). The pH was measured using a laboratory pH meter (mod. inoLab pH 720, WTW, Weilheim, Germany) with a BlueLine 16 pH microelectrode (SI Analytics, Mainz, Germany), calibrated using standard buffers (WTW) at pH 7 and 9, and adjusted to pH 8 in the solutions using diluted NaOH (*p.a.*, Merck, Darmstadt, Germany) and HCl (*p.a.*, Merck).

Table 5-3: Composition of the model pore water in dependence on dry bulk density (Van Loon et al., 2007a).

ρ / g/cm^3	1.3	1.6	1.9
$\varepsilon_{eff}(Cl^-)$	0.122	0.044	0.019
$p(CO_2)$ / bar	-3.42	-3.47	-3.65
Na / M	1.83×10^{-1}	2.07×10^{-1}	2.54×10^{-1}
K / M	2.7×10^{-3}	3.1×10^{-3}	3.7×10^{-3}
Mg / M	1.0×10^{-2}	1.2×10^{-2}	1.5×10^{-2}
Ca / M	9.2×10^{-3}	9.8×10^{-3}	1.2×10^{-2}
Sr / M	8.1×10^{-5}	8.6×10^{-5}	1.1×10^{-4}
Cl / M	1.81×10^{-2}	6.18×10^{-2}	1.7×10^{-2}
SO$_4$ / M	1.02×10^{-1}	9.5×10^{-2}	7.1×10^{-2}
C$_{inorg}$ / M	8.9×10^{-4}	8.0×10^{-4}	5.5×10^{-4}
F / M	2.2×10^{-4}	2.2×10^{-4}	1.9×10^{-4}
Si / M	1.8×10^{-4}	1.8×10^{-4}	1.8×10^{-4}
I / M	0.26	0.29	0.33

A HTO solution (1.2 MBq/mL; Eckert & Ziegler, Valencia, CA, USA), and a depleted UO_2Cl_2 solution in 0.005 M HCl (5×10^{-4} M) were used as stock solutions to adjust the initial concentrations of $C_0(HTO) = 500$ Bq/mL (= 2.2×10^{-10} M) and $C_0(U(VI)) = 1\times10^{-6}$ M in the source reservoir solutions for the respective diffusion experiments.

5.2.2   Experimental Set-Up

High-grade stainless steel diffusion cells (design described in detail in Van Loon et al. (2003)) were used in the diffusion experiments to resist the high swelling pressure of the bentonite. In total, four diffusion cells were filled with MX-80, one diffusion cell for each dry density studied (1.3, 1.6, 1.9 g/cm^3), and one blank cell (1.6 g/cm^3) to monitor the fraction of natural uranium leached out from the bentonite by contact with the background electrolyte. The required amount of MX-80 was compacted in a cylindrical sample holder between two stainless steel filter plates (316L, pore diameter: 0.01 mm; MOTT industrial division, Farmington, USA). The dimensions of the MX-80 samples and filters are shown in Table 5-4. The diffusion cells were closed by tightening the screws at the diffusion cell end plates. To compress the bentonite to dry densities of 1.6 and 1.9 g/cm^3 in the predefined volume of the sample holder, a uniaxial pressure testing machine (Amsler Prüfsysteme AG, Neftenbach, Switzerland) with a constant tension rate of 1 MPa/min was used. The cells containing bentonite at dry densities of 1.3 and 1.6 g/cm^3 were equipped with miniature ring load cells (mod. 8438, Burster Präzisionsmesstechnik GmbH & Co. KG, Gernsbach, Germany) to measure the swelling pressure in the compacted MX-80. Previous measurements showed that at 1.9 g/cm^3 the initial load on the load cell due to the compaction of MX-80 is too high for any additional load measurements (Brockmann, 2006) and thus, the respective diffusion cell was not equipped with a ring load cell. The measured signal of the load cells was converted to millivolts by a one-channel analog input/output module (mod. ADAM 4016, Advantech Corporation, Taipei, Taiwan). Prior to the filling with bentonite, calibration curves of the load cells up to a pressure of 30 MPa were recorded. For that, the empty diffusion cells were filled with water using a high-performance liquid chromatography (HPLC) pump (mod. K-501, Knauer, Berlin, Germany) and a flow rate of 0.05 mL/min.

Table 5-4: Dimensions of the filters and the MX-80 samples.

Parameter	Value
Filters Length	1.55×10^{-3} m
Diameter	25.4×10^{-3} m
MX-80 Length	5.3×10^{-3} m
Diameter	25.7×10^{-3} m
Cross-sectional area	5.19×10^{-4} m^2

All experiments were performed under ambient conditions at room temperature. In the first instance, the respective synthetic pore water was pumped through the confined bentonite samples only at one end plate of the diffusion cells with a stepwise increase of the hydraulic pressure (cf. Appendix Table A.1) provided by the HPLC pump with a flow rate of 0.05 mL/min. After breakthrough of the pore water at the opposite end plate, the percolation was continued until several pore volumes had been exchanged. Then, the HPLC pump was disconnected and the diffusion cells were coupled with a peristaltic pump (mod. Ecoline, Ismatec, IDEX Health & Science, Glattbrugg, Switzerland) and a source and receiving reservoir, respectively, filled with the according synthetic pore water. This experimental set-up was described previously (Brockmann, 2006; Trepte, 2004).

The bentonite samples were conditioned by circulation of the respective background electrolyte through the end plates of the diffusion cells for three to four weeks. Subsequently, the solutions in the source and receiving reservoirs were replaced by fresh ones, whereby, the source reservoir solutions contained the tracer and the receiving reservoir solutions were tracer-free. Consequently, the tracer diffusion started. At first, HTO through- and out-diffusion experiments were performed as described by Brockmann (2006) in order to determine values for ε_{eff} of the MX-80 samples in dependence on dry density. After that, the U(VI) diffusion started. During the duration of the experiments, the pH in the reservoirs was not readjusted.

All diffusion experiments performed were designed at constant boundary conditions. In the case of the HTO diffusion experiments, the source and receiving reservoir solutions were collected in separate reservoirs after passing the end plate of the diffusion cells to prevent tracer solutions from recirculation. The receiving reservoir solutions were regularly exchanged and analyzed. In case of the U(VI) diffusion experiments, both the source and receiving reservoir solutions were recirculated. The U(VI) concentration in the solutions was regularly analyzed. The receiving reservoir solutions were replaced by fresh solution when their U(VI) concentration exceeded 1% of the initial U(VI) concentration in the source reservoir.

After 2457 days (~6 years), the U(VI) diffusion experiment was stopped and the clay samples were removed from the cells. For this, the cylindrical sample holders containing the MX-80 in different dry densities were shock frozen in liquid N$_2$. The bentonite samples were carefully extracted and placed on a 1 mm-thin bed of quartz sand (*p.a.*, Merck) each in a polytetrafluoroethylene (PTFE) cylinder manufactured at Helmholtz-Zentrum Dresden-Rossendorf (HZDR). Thereby, the bentonite side which was contacted with the source reservoir solution during the diffusion experiment faced the sand. The bentonite was dried in a drying cabinet overnight at 60°C. The next day, the bentonite samples were combined with a stainless steel drilling sample holder (made at HZDR) using a "water-clear" epoxy casting resin and hardener (ρ_S = 1.25 g/cm^3; R&G Faserverbundwerkstoffe GmbH, Waldenbuch, Germany; cf. Fig. 5-1). After hardening of the resin for one day the PTFE cylinder was opened with a saw. From the fixed bentonite samples the U(VI) diffusion profiles were determined with the help of the abrasive peeling technique (Van Loon and Eikenberg, 2005). The peeled layers were extracted for U(VI)

content by 1 M HNO_3 (*p.a.*, Roth, Karlsruhe, Germany) and analyzed. This method has been applied in a number of earlier experiments (Joseph et al., 2013b; Sachs et al., 2007).
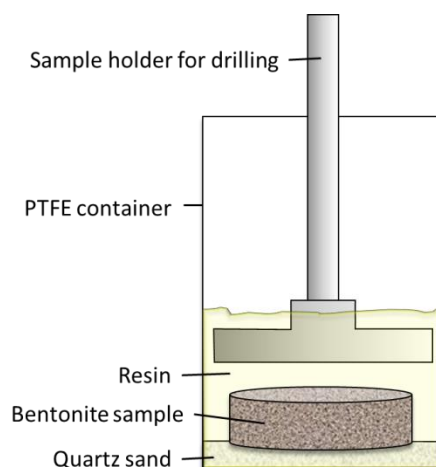
Figure 5-1: Set-up for combination of the bentonite sample with the stainless steel sample holder for drilling.

5.2.3   Characterization of the Reservoir Solutions

The composition of the solutions was analyzed with ICP–MS (mod. ELAN 6000, Perkin Elmer, Boston, USA), atomic absorption spectroscopy (AAS; mod. AAS-4100, Perkin Elmer), and ion chromatography (IC; mod. IC separation center 733, Metrohm, Herisau, Switzerland). The total inorganic carbon content was measured using a multi N/C 2100 analyzer (Analytik Jena, Jena, Germany) as difference of the total carbon (TC) and total organic carbon (TOC). The HTO activity was determined by liquid scintillation counting (LSC; mod. 1414 WIN Spectral Low-Level α/β, Perkin Elmer Wallac GmbH, Freiburg, Germany) using Ultima Gold™ (Perkin Elmer) as scintillation cocktail. The U(VI) concentration in the source and receiving reservoir solutions as well as in the extracts was measured with ICP–MS. In the evaluation of the experiment, the concentration values were decay corrected.

At the end of the diffusion experiment, the solutions were filtered (0.45-μm MF-Millipore membrane filter, EMD Millipore, Billerica, MA, USA; cf. Appendix Table A.2) for identification of the bacterial and eukaryotic inhabitants in selected reservoir solutions. The DNA of the filtered microorganisms was isolated using the RapidWater® DNA isolation kit (Mo Bio Laboratories Inc., Carlsbad, CA, USA) according to the manufacturer's recommendations. A 10-minute incubation step at 65 °C was added prior to bead beating to aid lysis of fungi and algae species present in solution. The PCR reaction mix contained one iQ™ supermix (Bio-Rad, Hercules, CA, USA), 0.2 μM of each of the following primers, and 4–20 ng genomic DNA as template. The universal bacterial primers GM3 (5´-AGAGTTTGATCMTGGC-3´) and GM4 (5´-TACCTTGTTACGACTT-3´) were used to amplify nearly the entire bacterial 16S rDNA gene (Muyzer et al., 1995). PCR conditions were: 5 min at 94 °C, 35 cycles of 1 min at 94 °C, 1 min at 42 °C, and 3 min at 72 °C, followed by a final elongation at 72 °C for 30 min. The universal eukaryotic primers NS1 (5'-GTAGTCATATGCTTGTCTC-3') and NS2 (5'-GGCTGCTGGCACCAGACTTGC-3') were used to amplify a region close to the 5' of the 18S rDNA gene; equivalent to a 555 bp fragment in *Saccharomyces cerevisiae* (White et al., 1990). The primers

applied cover 52 of 59 phyla (White et al., 1990), no set of phyla was preferred. PCR conditions were: 5 min at 94 °C, 35 cycles of 1 min at 94 °C, 1 min at 44 °C, and 2 min at 72 °C, followed by a final elongation at 72 °C for 30 min.

Amplified rDNA was run on a 1% agarose gel electrophoresis in a 1X Tris-acetate-EDTA buffer. Bands were excised using a sterile razor, and DNA was purified using the NucleoSpin® PCR cleanup and gel extraction kit (Clontech Laboratories, Inc., Mountain View, CA, USA). Purified rDNA fragments were ligated into pCR®2.1-TOPO® vectors (Life Technologies, Grand Island, NY, USA) and transformed into Stellar™ chemically competent *Escherichia coli* (Clontech Laboratories, Inc.). Plasmid DNA extraction and sequencing were performed by Elim Biopharmaceuticals (Hayward, CA, USA). The rDNA sequences were taxonomically classified using SINA (Pruesse et al., 2012) with the minimal identity within query sequence set to 0.9 and default settings for all other parameters.

5.2.4   Theoretical Background

The species investigated, HTO and U(VI), were assumed to migrate via molecular diffusion through bentonite. The theoretical background of molecular diffusion is given in (Van Loon et al., 2003). The diffusion process through a porous medium is defined by Fick's first law:

$$J = -D_e \cdot \frac{\partial c}{\partial x} \qquad\qquad (5\text{-}2)$$

where the diffusive flux J [mol/(m^2·s)] of a solute is equal to the effective diffusion coefficient times the negative concentration gradient (with c [mol/m^3] as tracer concentration in the mobile phase and x [m] as spatial coordinate). The change of concentration with time, t [s], is expressed by Fick's second law:

$$\frac{\partial c}{\partial t} = D_a \cdot \frac{\partial^2 c}{\partial x^2} \qquad\qquad (5\text{-}3)$$

Thereby, D_a [m^2/s] denotes the apparent diffusion coefficient. Both diffusion coefficients are linked by the rock capacity factor α [–] according to:

$$D_a = \frac{D_e}{\alpha} \qquad\qquad (5\text{-}4)$$

The rock capacity factor is defined as:

$$\alpha = \varepsilon_{eff} + \rho \cdot K_d \qquad\qquad (5\text{-}5)$$

where ρ [kg/m^3] is the dry bulk density and K_d [m^3/kg] the sorption distribution coefficient. For non-sorbing tracers such as HTO with $K_d = 0$, it is assumed that α is equal to ε_{eff}. In contrast to D_e, D_a considers the tracer sorption on the clay. In addition, D_e is correlated to the diffusion coefficient of a species in water by:

$$D_e = \frac{\varepsilon \cdot \delta}{\tau^2} \cdot D_w \qquad\qquad (5\text{-}6)$$

with δ constrictivity, which describes the relation between the size of the respective diffusing species and the present pore size, and τ as tortuosity, which describes to which degree the diffusion path is curved and twisted. In CrunchFlow2011 (Steefel, 2011), this relation is defined as:

$$D_e = \varepsilon_{\text{eff}} \cdot \tau \cdot D_w \tag{5-7}$$

with $\tau \leq 1$.

5.2.5   CrunchFlow2011 Implementation

From a chemical point of view, our CrunchFlow2011 simulations of U(VI) interaction with solid phases were reduced to simple K_d models. Only the following primary species were considered: HTO and UO_2^{2+}, as respective migrating species; Cl^- for charge balance; >SiOH and >FeOH, as generic surface species for U(VI) sorption onto clay and stainless steel filter plates, respectively, and no activity correction.

The HTO diffusion experiments were performed to determine ε_{eff}(HTO) diffusion as a function of clay bulk density. It was assumed that HTO does not interact with the clay and filter surfaces, thus, no HTO sorption was simulated. For modeling of the U(VI) diffusion, the pre-determined ε_{eff}(HTO) values were incorporated in the model assuming that these are equal to the ε_{eff}(U(VI)) values. Of course, the real ε_{eff}(U(VI)) values could be smaller based on the size of the U(VI) species molecule but cannot be determined by this experiment or by modeling. The K_d values for the U(VI) sorption on the bentonite samples were determined by fitting the binding site concentration of quartz, [>SiOH]. How these parameters are connected to each other can be seen in Eq. 26. A log K value for the UO_2^{2+} sorption onto quartz was fitted to achieve a K_d value for the sorption of $Ca_2UO_2(CO_3)_3$(aq) to opalinus clay of 0.0222 kg/m^3 (Joseph et al., 2011) assuming a specific surface area (SSA) of 100 m^2/g (montmorillonite; Payne et al., 2011) and a binding site density of 2.31 sites/nm^2 (= $3.8 \cdot 10^{-6}$ mol/m^2; (Pabalan et al., 1998)).

$$\log K = \log \left(\frac{[> \text{SiOH}]}{K_d} \cdot \text{SSA} \right) \tag{5-8}$$

The U(VI) sorption on the stainless steel filter plates was determined after the stop of the diffusion experiment by acid extraction with 1 M HNO_3 for one week. With increasing clay bulk density and changes in the pore water composition the U(VI), sorption on the filters increased. The filter sorption was incorporated in the model by defining a log K (>FeOHUO$_2^{2+}$) and assuming a specific surface area of 50 m^2/g (goethite; Turner and Sassman, 1996) and a binding site density, [>FeOH], of 3.8×10^{-6} mol/m^2. The resulting K_d values measured and the log K values calculated are shown in the Appendix Table A.3.

For both, the HTO and U(VI) diffusion modeling, the CrunchFlow2011 model was composed of source reservoir, stainless steel filter, bentonite sample, stainless steel filter, and receiving reservoir. Each part was considered as homogeneous. In case of the HTO diffusion through bentonite a one-dimensional model was applied. The source reservoir was considered as exterior node and thus, not incorporated in the discretization. The two filter sections were separated in 10 nodes; each part had a length of 0.16×10^{-3} m. The clay section was composed of 200 nodes of 0.0265×10^{-3} m length. The receiving reservoir was described by only one node with a length of 0.15×10^{-3} m. Generally, the length of this last node is defined over the volume of the receiving reservoir solution (~200 mL in average). This would lead to a cell length of 0.39 m (considering the cross-sectional area given in Table 5-4). To reach a better continuity between the nodes during the modeling process the node length was artificially decreased to the length of the filter

nodes. To compensate this size change the porosity of the receiving reservoir condition was artificially increased to 2600. Since the source reservoir was an exterior node, its porosity was set to 1.0.

During the performance of the U(VI) diffusion experiment [238]U was detected in the receiving reservoir solution. This was attributed to the continuous dissolution of natural uranium contained in the clay due to pore water contact. The receiving reservoir solution was regularly replaced by fresh pore water. In addition, there were several events where no circulation of solution through the diffusion cell end plates took place (e.g., tubing exchange, broken pump) during the six years the diffusion experiment was conducted. Both the number of solution replacements and the conservatively estimated total stops are summarized in Table 5-5.

Table 5-5: Amount of replacements of the receiving reservoir solutions and total duration of no solution circulation (conservative estimation) through the diffusion cell end plates for the U(VI) diffusion through MX-80 bentonite as a function of dry bulk density investigated.

ρ / g/cm^3	1.3	1.6	1.9
No. of replacements	35	20	20
Total stops / days	61	298	302

For modeling of the U(VI) diffusion in bentonite, a series of input files was used to take into account (i) the regular exchange of the receiving reservoir solution and (ii) unplanned stops of pore water circulation. Due to this and for reasons of consistency it was necessary to define a two-dimensional model (cf. Fig. 5-2). In the x-dimension, the discretization in this model was similar to that one used to model the HTO diffusion, except that the source reservoir was no longer an exterior node and that the clay section was discretized into 1060 nodes to effectively match the U sampling intervals. The volume of the pore water in the reservoirs was assumed to be 200 mL (source) and 50 mL (receiving), thus, their porosities were increased artificially to 2600 and 643 in the input files, respectively. In y-dimension three nodes with an equal length of 519×10^{-3} m were defined considering the cross-sectional area and assuming that each row of nodes represents the model of the whole experimental set-up.
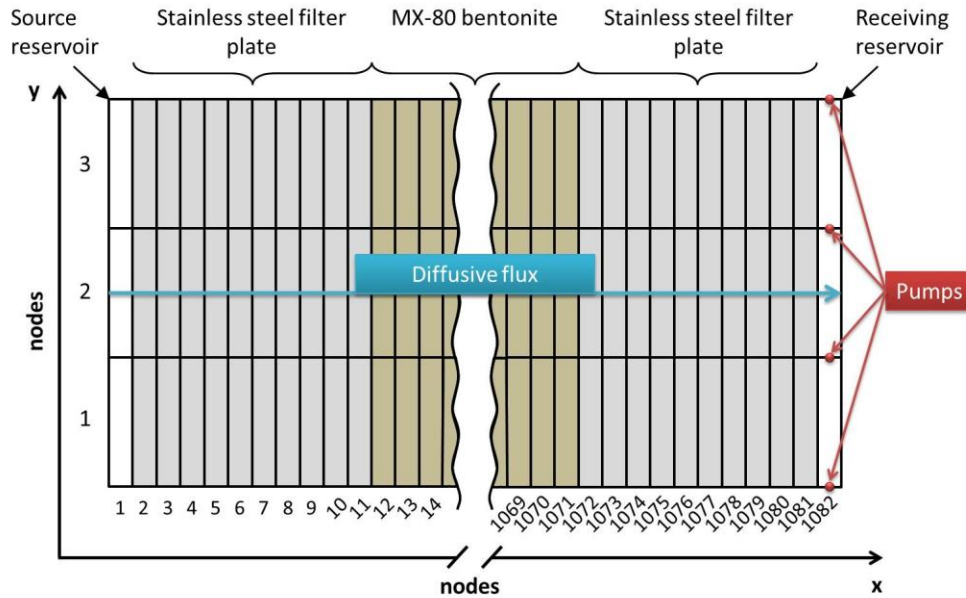
Figure 5-2: Conceptional description of the two-dimensional model used to simulate the U(VI) diffusion with CrunchFlow2011.

The exchange of the receiving reservoir solution was incorporated in the U(VI) diffusion model by virtual pumps which were placed on the exterior frame of the receiving reservoir nodes in y-dimension (cf. Fig. 5-2). At specified time points the pumps were switched on for a model time period of one day. Then, fresh receiving reservoir solution was pumped through the receiving reservoir nodes perpendicular to the direction of the diffusive flux to achieve a 6 pore volume exchange of the receiving reservoir.

In the case of the HTO and U(VI) modeling, constant conditions (Eq. 5-9) at the source reservoir boundary were assumed. For the receiving reservoir boundary, the increase of the HTO and U(VI) concentration with time in the respective receiving reservoir solutions were considered (Eq. 5-10).

$$c(x = 0, t > 0) = c_0 = \text{const.} \tag{5-9}$$

$$c(x = L, t > 0) = f_L(t) \tag{5-10}$$

whereby L [m] denotes the thickness of the system filter/clay/filter. During HTO diffusion modeling the filters, the bentonite and the receiving reservoir solution were regarded as initially free of tracer, whereas for U(VI) diffusion modeling, an initial uranium concentration, c_{initial}, was assumed.

As D_w(HTO) the value of Glaus et al. (2008) with $D_w = 2.2 \times 10^{-9}$ m^2/s and as D_w(U(VI)) the value published for Ca$_2$UO$_2$(CO$_3$)$_3$(aq) by Kerisit and Liu (2010) with $D_w = 4.6 \times 10^{-10}$ m^2/s were used. For each condition, a tortuosity was assigned. The tortuosities of the source and receiving reservoir solution (if part of discretization) were set to 1.0. The filter tortuosity was calculated based on Eq. 25. In the case of HTO, D_w(HTO), ε_{eff}(filter), and the D_e value for HTO diffusing through stainless steel filter plates ($D_f = 2.3 \times 10^{-10}$ m^2/s; (Glaus et al., 2008)) were used. In the case of U(VI), D_f was estimated by $D_f = D_w/10$ (Glaus et al., 2008). The clay tortuosity was in both model approaches a fitting parameter. A summary of the parameters kept constant in both models independent of the density investigated is shown in Table 5-6.

Table 5-6: Overview of the parameters used in the CrunchFlow2011 input files for modeling the HTO and U(VI) diffusion through bentonite independent of the dry bulk density investigated.

Condition	Parameter	Value in the	
		HTO model	**U(VI) model**
Overall	t / d	13.05	2457
	D_w / m^2/s	2.2×10^{-9}	4.6×10^{-10}
Source reservoir	ε_{eff}	1.0	2600
	τ	-	1.0
Stainless steel filter plates	ρ_S / g/cm^3	5.27	5.27
	ε_{eff}	0.3	0.3
	τ	0.35	0.33
MX-80 bentonite	ρ_S / g/cm^3	2.65	- [a]
Receiving reservoir	ε_{eff}	2600	643
	τ	1.0	1.0

[a] varied in dependence on ε(HTO) and ρ

For comparison with the experimental data, in case of the HTO diffusion, the HTO concentration in the node of the receiving reservoir on specified time points (the experimental sampling days) was determined. In the case of the U(VI) diffusion, two output files were relevant for comparison with the experimentally obtained profile and outflow data: (1) The uranium content in the clay as a function of distance at the end of the diffusion experiment and (2) the U(VI) concentration in the receiving reservoir at the time points where the solution was replaced.

5.2.6 PEST Estimation

The PEST estimation code (Doherty, 2003) was used to minimize the differences between the data of the CrunchFlow2011 output files and the experimental diffusion data by changing pre-defined CrunchFlow2011 input parameters. Crucial for reaching convergence in the fitting routine was the definition of the weighting factors for the experimental data. For fitting the HTO diffusion the weighting factor was $1/\Delta c$, where Δc [M] describes the uncertainty of the measured HTO concentration. For the U(VI) profile fit the weighting factor was $1/d$, where d denotes the distance to the clay edge [mm]. For the fit of the U(VI) outflow in the receiving reservoir solution, $1/c$ was used as the weighting factor, where c denotes the U(VI) concentration in the receiving reservoir at the time points of the solution replacement. The relevant diffusion parameters and their fitting equivalents for HTO and U(VI) diffusion modeling are shown in Table 5-7, whereby c(U(VI))$_{BG}$ denotes the background U(VI) concentration in the clay.

Table 5-7: Overview of the diffusion parameters and their fitting equivalents varied in the MX-80 bentonite in the CrunchFlow2011 input files using the PEST optimization code.

Model	HTO outflow		U(VI) profile			U(VI) outflow [a]
Diffusion parameter	D_e	ε_{eff}	K_d	-	D_e, D_a	D_e, D_a
Fitting equivalent	τ	ε_{eff}	[>SiOH]	c(U(VI))$_{BG} \tau$		τ

[a] Only one parameter was fitted due to the strong correlation between τ, [>SiOH], and c(U(VI))$_{BG}$.

5.2.7   COMSOL Multiphysics® 5.0

To confirm the parameter fitting obtained by CrunchFlow2011 and PEST, COMSOL Multiphysics® 5.0 (Comsol, 2014) was used. Here, a one-dimensional model consisting of source reservoir, filter, clay, filter, and receiving reservoir was defined using an extremely fine mesh (maximum element size: 8.4×10^{-5} m) to simulate both the HTO and U(VI) diffusion. Thereby, the same input parameters as for the CrunchFlow2011 modeling were used, except that the already optimized values for the diffusion-relevant parameters were incorporated. No chemical species had to be defined, since the molecular diffusion through a porous medium was investigated from the physical point of view only. The regular replacements of the receiving reservoir solution and the irregular pump stops were not considered in the model. Again, the time evolution of the HTO flux and the accumulated concentration of HTO and U(VI) in the receiving reservoir solution as well as the U(VI) profile in the clay at the end of the diffusion experiment were extracted from the model and compared with the respective experimental data.

5.2.8   Experimental Uncertainties

The experimental uncertainties of the values for the diffusive HTO flux and the accumulated diffused HTO activity in the receiving reservoir solution resulted from the uncertainty of the parameters required to calculate these values (cf. (Van Loon and Soler, 2004)). In the case of U(VI) diffusion profiles, the experimental uncertainty of the diffusion depth is given by the average of the individual distance measurement at four points of the clay sample. The uncertainties of the diffusion parameters resulted from the uncertainties of their fitting equivalents (cf. Table 5-7), which were provided by PEST after the fitting procedure in the form of 95% confidence limits. The impact of the drying procedure to prepare the samples for abrasive peeling on the samples' dimensions and dry densities and consequently, on the diffusion parameters were investigated by CrunchFlow2011 modeling. It was assumed that the dry bulk density decreases by 10% and the diameter of the sample increases or decreases by 10%. No significant influence on the resulting diffusion parameters was observed.

5.3   RESULTS AND DISCUSSION

5.3.1   Swelling Behavior of Bentonite

In the beginning of the experiments the bentonite samples were conditioned with pore water (cf. Table 5-3). The associated load cells measured the swelling pressure of the MX-80 samples as a function of time during this saturation process. The results for the diffusion cells with ρ of 1.3 and 1.6 g/cm^3 are shown in Figure 5-3.
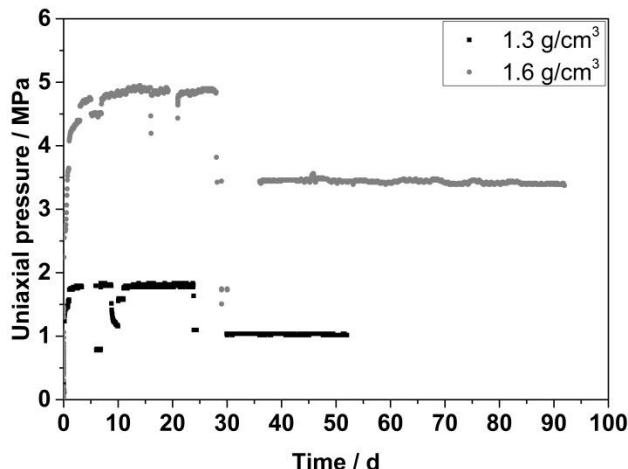
Figure 5-3: Swelling pressure measured for the diffusion cells with ρ = 1.3 and 1.6 g/cm^3 as a function of time.

At 1.3 g/cm^3 and 1.6 g/cm^3, swelling pressure reached equilibrium within 30 days at about 1 MPa and within 35 days at about 3.5 MPa, respectively. The intense drops of pressure before equilibrium establishment can be attributed to changes in the hydraulic pressure of the HPLC pump (cf. Appendix Table A.1). Lee et al. (2012) investigated the swelling pressure of Ca-bentonite as a function of dry density, ionic strength, and time. Under comparable conditions as used in this study they observed that the steady state region was reached after 20 days which agrees well with the present results. It was assumed that after the respective time periods the bentonite samples were fully saturated with pore water and the HTO and U(VI) diffusion experiments were started.

5.3.2   Aqueous U(VI) Speciation

Table 5-8 summarizes the composition of the experimentally prepared pore water in the source reservoir in the first and the last year of the diffusion experiment for all three dry bulk densities investigated.

Table 5-8: Composition of the source reservoir solutions in the first and the last year of the U(VI) diffusion experiment as well as the main aqueous U(VI) species calculated for the listed conditions.

	$1.3\ \text{g/cm}^3$		$1.6\ \text{g/cm}^3$		$1.9\ \text{g/cm}^3$	
	$t = 191$ d	$t = 2401$ d	$t = 191$ d	$t = 2401$ d	$t = 191$ d	$t = 2401$ d
c / M						
U [a]	1.1×10^{-6}	1.1×10^{-6}	1.1×10^{-6}	1.1×10^{-6}	1.1×10^{-6}	1.2×10^{-6}
Na [a]	2.0×10^{-1}	2.2×10^{-1}	2.2×10^{-1}	2.8×10^{-1}	2.7×10^{-1}	3.2×10^{-1}
K [a]	3.2×10^{-3}	3.2×10^{-3}	3.6×10^{-3}	4.0×10^{-3}	4.4×10^{-3}	4.6×10^{-3}
Mg [b]	1.1×10^{-2}	1.2×10^{-2}	1.2×10^{-2}	1.5×10^{-2}	1.6×10^{-2}	1.8×10^{-2}
Ca [b]	9.2×10^{-3}	1.1×10^{-2}	8.9×10^{-3}	1.4×10^{-2}	1.2×10^{-2}	1.5×10^{-2}
Sr [a]	8.6×10^{-5}	9.5×10^{-5}	8.2×10^{-5}	1.1×10^{-4}	1.1×10^{-4}	1.3×10^{-4}
Si [a]	n.d. [e]	5.3×10^{-4}	n.d.	3.9×10^{-4}	n.d.	3.7×10^{-4}
Cl^- [c]	1.9×10^{-2}	2.1×10^{-2}	6.4×10^{-2}	7.8×10^{-2}	1.7×10^{-1}	2.1×10^{-1}
SO_4^{2-} [c]	1.1×10^{-1}	1.2×10^{-1}	1.1×10^{-1}	1.2×10^{-1}	6.7×10^{-2}	8.8×10^{-2}
C_{inorg} [d]	9.7×10^{-4}	9.7×10^{-4}	8.7×10^{-4}	6.0×10^{-4}	5.2×10^{-4}	6.2×10^{-4}
F^- [c]	2.3×10^{-4}	2.5×10^{-4}	2.3×10^{-4}	3.5×10^{-4}	2.0×10^{-4}	2.6×10^{-4}
I	0.28	0.31	0.30	0.37	0.32	0.41
Aqueous U(VI) species distribution / % [f]						
$Ca_2UO_2(CO_3)_3(aq)$	85.5	87.5	83.7	89.1	89.9	90.4
$UO_2(CO_3)_3^{4-}$	9.4	8.2	10.6	7.3	5.4	6.1
$MgUO_2(CO_3)_3^{2-}$	3.2	2.4	3.9	2.4	3.1	2.6
$CaUO_2(CO_3)_3^{2-}$	1.2	1.1	1.2			

[a] ICP–MS (error: ±10%) [b] AAS (error: ±2%) [c] IC (error: ±3-10%)

[d] TC – TOC (error: ±3%) [e] n.d. = not determined [f] only species ≥ 1% shown

The comparison of the composition and ionic strength of the solutions shows that their salinity increased with time. This can be attributed partly to water evaporation over the long time period the experiment was conducted. Within this time the source reservoir solutions were never exchanged. However, all reservoir solutions were replaced by fresh ones at $t = 2401$ days. The experiment was stopped at $t = 2457$ days. The composition of these solutions is summarized in Table A.4.

To interpret the diffusion results it has to be known which U(VI) species dominates the solution. Based on the composition of the source reservoir solutions, U(VI) speciation was calculated using the speciation code "The Geochemist's Workbench® 8.0" (Bethke and Yeakel, 2010) and the thermodynamic data compiled in Guillaumont et al. (2003b) including the data for the alkaline earth tricarbonato complexes with U(VI) (Bernhard et al., 2001; Dong and Brooks, 2006). The speciation results are presented in Table 5-8. The $Ca_2UO_2(CO_3)_3$(aq) complex dominates the speciation in all solutions and consequently, can be assumed to be the main diffusing U(VI) compound under the present conditions.

Since the $Ca_2UO_2(CO_3)_3$(aq) complex is a neutral species, it will be not repulsed by the negatively charged clay surface and the main part of the interparticle space would be accessible. Bernhart et al. (2001) investigated this complex by extended X-ray absorption fine-structure spectroscopy. Based on their results an average diameter between 10-11 Å for the non-hydrated complex can be assumed taking into account the radii of calcium and oxygen. The question arises if this complex also has access to the interlayers of the montmorillonite fraction of MX-80, which can have distances from 2 to 10 Å (Bradbury and Baeyens, 2002; Keren and Shainberg, 1975) depending on how many water layers are present. In this study, ε_{eff} of HTO is used in the U(VI) diffusion model, although one can expect that ε_{eff} of U(VI) is smaller than HTO regarding the size of $Ca_2UO_2(CO_3)_3$(aq) which leads to higher steric hindrance. However, as previously discussed (Joseph et al., 2013b), the used value of ε_{eff} has no significant impact on the modeled U(VI) diffusion parameters, since the U(VI) sorption onto the clay is dominating (cf. Eq. 5-5).

5.3.3   Biological Contaminants

Despite the presence of NaF ($c \approx 2\times10^{-4}$ M) and the oligotrophic nature of the reservoir solutions, contaminating eukaryotic and prokaryotic microorganisms were detected within each reservoir, including those tracered with 1×10^{-6} M U(VI). To identify the most abundant contaminating microorganisms and determine whether the presence of U(VI) influenced the diversity of microbial contaminants, a subset of 16S and 18S rDNA was sequenced from all source reservoir solutions and one receiving reservoir (cell 1.9 g/cm^3). Surprisingly, the majority of bacteria were heterotrophs (cf. Appendix Table A.5), despite the low levels of dissolved organic carbon. Exceptions include the green sulfur family *Chlorobiales* that are photoautotrophs.

The comparison of the prokaryotic diversity in the source and receiving reservoir solution of cell 1.9 g/cm^3 shows that bacteria from the *Planctomyces* genus and *Rhodospirillales* order can be found in both solutions. The *Planctomyces* genus even dominates the diversity in both samples. Otherwise, there are also prokaryotic families only present in the source or receiving reservoir solution. That leads to the conclusion that the solutions should be regarded as independent. Their prokaryotic diversity cannot be attributed to spores or microorganisms that were originally contained in the bentonite clay sample since all diffusion cells contained compacted MX-80 from the same batch.

The prokaryotic diversity of the blank cell solution differs from those of the solutions tracered with U(VI). Although members of the family *Planctomycetaceae* represent the largest fraction of bacterial contaminants in the blank cell solution and can be found in the source reservoir solutions of the cells 1.6 and 1.9 g/cm^3, there is an interesting difference at the genus level. The *pir4 lineage* dominates in the blank cell solution, but is not found in the solution containing U(VI). There, the *Planctomyces* genus

dominates in the solutions. There are also several members of the phylum *Actinobacteria* that are only present in the blank solution (e.g., *Ilumatobacter*, *Nocardioidaceae*, *Gaiellales*). Thus, the presence of U(VI) may have selected against growth of some bacterial species.

Of particular note, six of seven 16S rDNA clone sequences of the phylum *Actinobacteria*, identified in the 1.6 g/cm^3 cell source reservoir solution, have 99% sequence similarity to an uncultured isolate (WC2_55) that was found in a low-level radioactive waste site at the Idaho National Laboratory (Field et al., 2010). Furthermore, isolates with the highest sequence similarity to the additional seventh clone were identified in environments contaminated by heavy metals and mining operations (These sequences have been deposited in the GenBank but not included in a publication to date.).

The phyla from *Proteobacteria*, *Chloroflexi*, *Actinobacteria*, *Acidobacteria*, *Chlorobium*, and *Planctomycetes* identified in this study were also found in subsurface sediments from uranium-contaminated sites in Tennessee (Akob et al., 2007; Barns et al., 2007) and Colorado (Barns et al., 2007). Amongst others, representatives of the *Proteobacteria* and *Acidobacteria* phylum were identified in uranium and heavy metal-contaminated soils and mine waste piles at former uranium mining and milling sites in Bulgaria (Radeva et al., 2013) and in samples from several uranium mining wastes in Germany and the United States (Radeva and Selenska-Pobell, 2005). *Proteobacteria* were found in the pore water of Opalinus Clay samples (Stroes-Gascoyne et al., 2011). At longer times scales, i.e. after ten years of interaction, *Actinobacteria* and *Proteobacteria* were identified at the iron/clay interface between re-compacted argillite and steel coupons (Urios et al., 2013). These studies show the ubiquitous presence of the identified prokaryotic species at uranium contaminated soils, hence, also in this experiment.

In the case of the eukaryotic diversity in all reservoir solutions investigated, fungi species (*Ascomycota* phylum) were identified (cf. Appendix Table A.6). In particular, between the source and receiving reservoir solutions of cell 1.9 g/cm^3 no additional similarities could be found.

The eukaryotic diversity at relatively high U(VI) concentrations differs from that with background level U(VI) concentrations. In all three source reservoir solutions tracered with U(VI), representatives of the green algae phylum *Chlorophyta* were the largest or second largest fraction in the analyzed plasmids. Only at lower U(VI) concentrations were representatives of the *Stramenopiles* phylum identified and these represented the dominant fraction, suggesting that this phylum may not have an appropriate defense mechanism towards relatively high levels of uranium.

Algae are particularly well known for excretion of organic compounds that can seed heterotrophic growth. Intriguingly, reservoirs with a high abundance of algae (i.e., source and receiving reservoir cell 1.9 g/cm^3, blank cell) also have high levels of *Planctomyces*, which could suggest a potential synthrophic relationship as previously described (Pizzetti et al., 2011). Jasrotia et al. (2014) found *Ascomycota* in a subsurface environment contaminated with uranium at the watershed scale at Oak Ridge, Tennessee. Amongst others, *Amoebae*, *Fungi*, and *Stramenopiles* taxes were identified in the eukaryotic community in biofilms formed in an acid mine drainage in the underground uranium mine Königstein (Saxony, Germany) (Zirnstein et al., 2012). These species seem to have a well-performing survival mechanism to overcome the chemotoxic effect of the present uranium. For *Stramenopiles* this finding stands in contrast to the conclusion in the present study. Probably, the difference in pH ((Zirnstein et al., 2012): pH 2.86 ± 0.05; this study: pH 8) has an impact on its survival mechanism.

In this study it is assumed that the various prokaryotic and eukaryotic species present in the reservoir solutions have no impact on the uranium diffusion path. The solutions were regularly filtered. In addition, the tubing between the solutions and the diffusion cells was regularly exchanged to guarantee the unhindered flow of the solutions through the endplates of the diffusion cells. The filtered solutions showed still a U(VI) concentration of about 1×10^{-6} M. Thus, a biotransformation of the U(VI) to insoluble

uranium species can be excluded. However, it cannot be ruled out that the detected microorganisms release organic compounds to the pore water solutions, which can affect the U(VI) speciation. The TOC levels were determined for each solution (cf. Appendix Tables A.5 and A.6), but the organic compounds were not analyzed in more detail.

5.3.4   HTO Diffusion Through MX-80 as a Function of Clay Bulk Density

Before the U(VI) diffusion experiments were started a HTO diffusion experiment was conducted to determine the HTO transport porosity and to determine if the applied experimental set-up delivers parameter values which are comparable to literature data. Table 5-9 summarizes the HTO diffusion parameters used in, and obtained by, fitting of the experimental results for the three investigated dry bulk densities.

As expected, ε_{eff} and τ decrease with increasing MX-80 dry density since the diffusion available pore space becomes smaller as well as the diffusion path more curved with increasing clay compaction in the diffusion cell. Both parameters contribute to the decrease of D_e with increasing density. The unusual high porosity at $\rho = 1.6$ g/cm^3 seems to be an outlier. Probably, it can be attributed to phase heterogeneities in the clay sample caused by the HPLC pump during the saturation process. The comparison of the results with literature values shows a quite good agreement, in particular with the values from (Glaus et al., 2010) obtained for $\rho = 1.9$ g/cm^3. Figure 5-4 shows the relation between the values of D_e and ε_{eff} obtained in this study. The data were fitted using Archie's law analog (Eq. 5-1) with D_w(HTO) (Table 5-9).
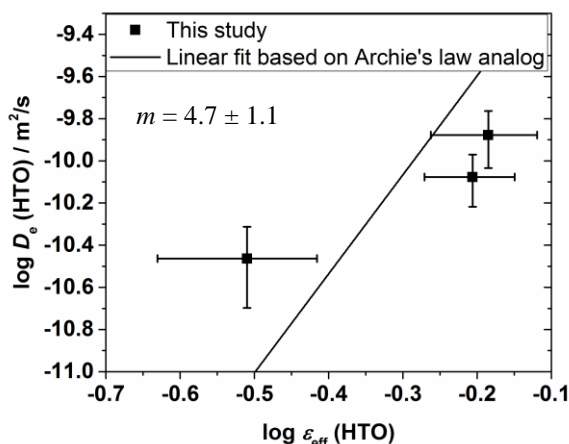
Figure 5-4: Relation between D_e and ε_{eff} for the HTO diffusion through MX-80 bentonite.

Table 5-9: Parameter values of the HTO diffusion through bentonite obtained in this study and found in literature as a function of dry bulk density.

ρ / g/cm^3 Parameter	1.3	1.6	1.9
c_0 / M	2.25×10^{-10}	2.24×10^{-10}	2.20×10^{-10}
ε_{eff} / $-$	0.65 ± 0.11	0.62 ± 0.09	0.31 ± 0.08
τ / $\times10^{-2}$	9.2 ± 1.4	6.1 ± 0.7	4.8 ± 0.9
D_e / $\times10^{-11}$ m^2/s	13.2 ± 4.1	8.4 ± 2.2	3.4 ± 1.4
ε_{eff} / $-$ [a]	0.38 ± 0.05 / 0.41 ± 0.06		
D_e / $\times10^{-11}$ m^2/s [a]	1.7 ± 0.2 / 1.9 ± 0.2		
ε_{eff} / $-$ [b]	0.44 ± 0.02	0.40 ± 0.02 / 0.35 ± 0.02	
D_e / $\times10^{-11}$ m^2/s [b]	11.2 ± 0.6	5.9 ± 0.3 / 5.2 ± 0.4	

[a] Values from (Glaus et al., 2010) obtained for compacted Na-montmorillonite at $I =$ 0.1 M and 1 M NaClO$_4$.
[b] Values from (Wu et al., 2012) obtained for GMZ bentonite at dry densities of 1.6, 1.8, and 2.0 g/cm^3.

The empirical constant resulting from the linear fit agrees well with the cementation factor of 4.5 ± 1.0 determined by Wu et al. (2012) for the HTO diffusion through GMZ bentonite using D_w(HTO) of 2.3×10^{-9} m^2/s. Instead of using D_w(HTO), Glaus et al. (2010) defined this factor as fitting parameter called A in their investigation of the HTO diffusion through compacted Na-montmorillonite. They obtained values of $A = 9.8\times10^{-11}$ m^2/s and $m = 1.81$. If such a free fit is applied to the data in the present study, values of $A = (2.1 \pm 0.8)\times10^{-10}$ m^2/s and $m = 1.6 \pm 0.6$ result. The cementation factor can be confirmed. The discrepancy in A can be attributed to the outlier at 1.6 g/cm^3. The agreement with literature values proves the applicability of the present experimental set-up. Thus, the diffusion studies were continued with U(VI).

5.3.5 U(VI) Diffusion in MX-80 as a Function of Clay Bulk Density

In Figure 5-5, the uranium depth profiles for the U(VI) diffusion into MX-80 as a function of dry density are presented together with the best fit curves of the CrunchFlow modeling. In addition, the uranium profile of the blank diffusion cell is depicted. Its maximal uranium concentration is used as guidance for the natural uranium level in all MX-80 samples investigated. Based on this comparison it can be seen that the added uranium diffuses about 2 mm, 1 mm, and 0.7 mm into the clay at ρ = 1.3, 1.6, and 1.9 g/cm^3, respectively.
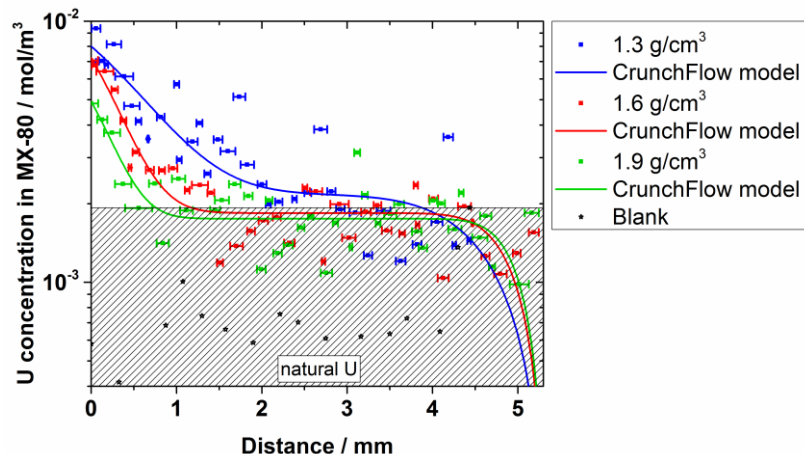
Figure 5-5: Concentration depth profile of uranium in MX-80 as a function of clay dry density.

The drop of the modeled uranium concentration in MX-80 at a depth of about 5 mm results from the leaching of natural uranium from the clay rock and its transport to the adjacent receiving reservoir solution, which was considered in the model. For example, the experimentally determined U(VI) concentration in the receiving reservoir solution of cell 1.6 g/cm^3 is presented in Figure 5-5 which also highlights the time points of solution replacement. For consistency, the data of the U(VI) outflow of the blank cell are also shown. Since both sets of data points are in the same order of magnitude, the measured U(VI) in the receiving reservoir of cell 1.6 g/cm^3 can be clearly attributed to natural uranium leached out of MX-80 and not to the diffused, experimentally added U(VI) tracer. Obviously, the CrunchFlow model using the profile fit parameters does not fit the experimental observations (straight lines in the model curves are the considered time periods of no solution circulation (cf. Table 5-5)).

In a second fit approach, instead of the uranium profile, the experimentally determined U(VI) outflow was fitted for each dry density. A quite good agreement between experiment and model data was achieved (cf. Fig. 5-6). Consequently, the corresponding U(VI) model profiles are no longer in agreement with the experimental data (cf. Appendix Fig. A1). This discrepancy shows that the in- and outflow of U(VI) in MX-80 has to be regarded independently in this study.
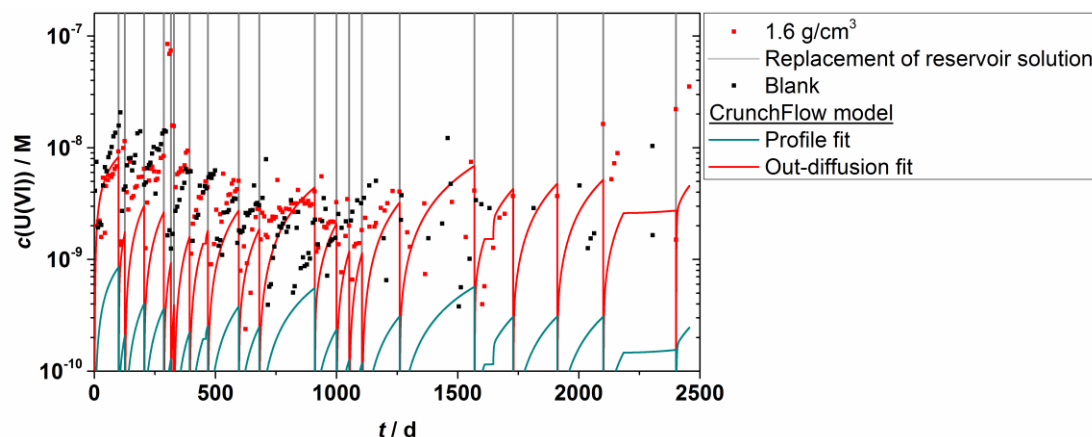
Figure 5-6: U(VI) concentration in the receiving reservoir solution of diffusion cell 1.6 g/cm^3 as a function of time. CrunchFlow model data obtained by fitting the uranium depth profile in MX-80 and the uranium out-diffusion in the receiving reservoir.

Table 5-10 summarizes the diffusion parameter values used in and obtained by modeling and fitting of the U(VI) diffusion depth profiles and the U(VI) concentration evolutions in the receiving reservoir solutions as a function of the dry density. The K_d values obtained are very low. This can be explained by the present U(VI) speciation (cf. Table 13). The neutral $Ca_2UO_2(CO_3)_3(aq)$ complex is dominating the source reservoir solutions and is known to sorb only weakly onto clay (Joseph et al., 2011). In addition, $UO_2(CO_3)_3^{4-}$, the second dominant species in solution, is regarded as non-sorbing species (Joseph et al., 2013a; Křepelová et al., 2006) since it will be repulsed by the negatively charged clay surface. The obtained K_d values are all in the same order of magnitude (vary by a factor of two) and tend to lower values with increasing ρ. The K_d variance may be attributed to small changes in the composition of the pore waters used in the three diffusion experiments. Due to the decreases in K_d and ε_{eff}, α decreases with increasing ρ (cf. Eq. 5-5). The low Kd values suggest that U(VI) reduction to U(IV) was negligible in these experiments.

Table 5-10: Parameter values of the U(VI) diffusion in MX-80 based on modeling the uranium depth profile in the clay and the uranium out-diffusion in the receiving reservoir as a function of dry bulk density.

ρ / g/cm³	1.3		1.6		1.9	
Fit of	profile	out-diffusion	profile	out-diffusion	profile	out-diffusion
Parameter						
ρ_S / g/cm³		3.75		4.24		2.75
ε_{eff} / −		0.65 ± 0.11		0.62 ± 0.09	0.31 ± 0.08	
$c(U(VI))_{initial}$ / M [a]		3.87×10⁻¹⁰	4.2×10⁻¹²		4.2×10⁻¹²	
$c(U(VI))_{BG}$ / ×10⁻⁷ M	3 ± 1		2.4 ± 0.3		3.4 ± 1.0	
[>SiOH] / ×10⁻⁷ mol/m²	10 ± 1		7.5 ± 0.4		4.4 ± 1.4	
K_d / ×10⁻³ m³/kg		5.8 ± 0.6	4.4 ± 0.2		2.6 ± 0.8	
α / −			8.2 ± 0.8	7.6 ± 0.4	5.2 ± 1.5	
τ / ×10⁻⁵	5.4 ± 3.4 1.5 ± 1.6	59 ± 20	340 ± 80	1.6 ± 0.4		77 ± 25
D_e / ×10⁻¹⁵ m²/s	16 ± 10 2.1 ± 2.3		1030 ± 240 83 ± 28		4.5 ± 1.2	220 ± 70
D_a / ×10⁻¹⁶ m²/s	20 ± 11 4.0 ± 3.5		1200 ± 300 160 ± 50		5.9 ± 1.2	290 ± 90

[a] Initial uranium concentration assumed in the filters and the receiving reservoir based on the minimal uranium concentration measured in the respective receiving reservoir.

Table 5-11 shows a multitude of published K_d values for U(VI) sorption onto bentonite and montmorillonite which can be explained by the different conditions used in the respective experiments. The K_d values from the present study differ from the values obtained by diffusion experiments published by (Wang et al., 2005) by about one order of magnitude. They studied U(VI) diffusion through MX-80 as a function of U(VI) concentration and time under a slightly lower pH and ionic strength than used in the present study which leads to a different U(VI) speciation and sorption behavior. Probably, $(UO_2)_2CO_3(OH)_3^-$ is the dominant U(VI) species in solution which is known to sorb more strongly on clay than $Ca_2UO_2(CO_3)_3(aq)$ (Joseph et al., 2013a; Křepelová et al., 2006) and thus higher K_d values were obtained. (Glaus and Van Loon, 2012) investigated U(VI) diffusion through compacted montmorillonite in NaClO₄ in the presence of calcium and carbonate ions as a function of the NaClO₄ ionic strength. In this case, besides the $Ca_2UO_2(CO_3)_3(aq)$ complex, a relatively large fraction of the different negatively charged uranyl carbonato complexes are present in solution, which, as mentioned before, sorb even less than the $Ca_2UO_2(CO_3)_3(aq)$ complex. Thus, slightly smaller K_d values are obtained. However, the values differ from the K_d values presented in this study only by a factor of three which can be regarded as in very good agreement.

Table 5-11: Selection of K_d values from the literature obtained by diffusion as well as batch sorption experiments.

	Clay type	Background electrolyte	pH	[U(VI)] M	K_d ×10⁻³ m³/kg	Reference
Obtained by diffusion experiments [a] ρ / g/cm³						
0.953	MX-80	0.1 M NaClO₄	7	1×10⁻⁶	92	[b]
0.996	MX-80	0.1 M NaClO₄	7	1×10⁻⁶	51	[b]
1.6	mont [c]	0.1; 0.5 M [d]	8.6-9	6×10⁻⁵	1.3; 1.6	[e]
Obtained by batch sorption experiments [a] S/L ratio / g/L [f]						
2.5	MX-80	1.3 pore water 1.6 pore water 1.9 pore water	8	1×10⁻⁶	13 ± 1.5 39 ± 1 39 ± 0.9	[g]
10	MX-80	synthetic groundwater (0.008 M)	8.2	2.1×10⁻⁷	93	[h]
0.32-13.5	MX-80	model pore water (0.7 M)	7.6	1×10⁻⁶- 3×10⁻⁸	28 (average)	[i]

[a] If more than one K_d is published in a literature source, these K_d values are taken whose experimental conditions are most similar to the conditions used in the present study.
[b] (Wang et al., 2005)
[c] mont = montmorillonite
[d] varying NaClO₄ + 1×10⁻² M CHES buffer + 1×10⁻³ M C$_{inorg}$ + 1×10⁻⁴ M Ca²⁺
[e] (Glaus and Van Loon, 2012)
[f] S/L ratio = solid-to-liquid ratio
[g] (Nebelung and Brendler, 2009)
[h] (Allard et al., 1982)
[i] (Bradbury and Baeyens, 2011)

Bradbury and Baeyens (2003a) suggested that a comparison between K_d data from intact and dispersed systems is only meaningful when the same water conditions are present. Thus, the batch sorption K_d values published by Nebelung and Brandler (2009) provide the best comparison with the K_d values obtained by diffusion experiments in this study, since the same MX-80 batch, pore waters, and initial U(VI) concentration were used. Their K_d values are about one order of magnitude higher than the K_d values obtained by diffusion. The reason could be that more binding sites are accessible for U(VI) during a batch sorption experiment, where the powder clay is mixed with the U(VI) solution, than in a diffusion experiment, where the only binding sites accessible for U(VI) interaction are those on the source reservoir side of the compacted clay cylinder and those that surround the individual diffusion path. In addition, since a much smaller S/L ratio was applied in the batch sorption experiments than in the diffusion experiments, possibly, the pore water is not in equilibrium with the small amount of solid and minerals can precipitate on the micromolar level. U(VI) can be either incorporated in these precipitates or can sorb on the newly formed mineral phases(Allard et al., 1982; Bradbury and Baeyens, 2011; Pabalan and Turner, 1997)(Allard et al., 1982; Bradbury and Baeyens, 2011; Pabalan and Turner, 1997)(Allard et al., 1982; Bradbury and Baeyens, 2011; Pabalan and Turner, 1997)(Allard et al., 1982; Bradbury and Baeyens, 2011; Pabalan and Turner, 1997)(Allard et al., 1982; Bradbury and Baeyens, 2011; Pabalan and Turner, 1997)(Allard et al., 1982; Bradbury and Baeyens, 2011; Pabalan and Turner, 1997)(Allard et al., 1982; Bradbury and Baeyens, 2011; Pabalan and Turner, 1997)(Allard et al., 1982; Bradbury and

Baeyens, 2011; Pabalan and Turner, 1997). The dependence of K_d on the S/L ratio was already described in previous studies for the U(VI) sorption onto clay (Joseph et al., 2011) and soils (Zheng et al., 2003), where it was attributed to the calcium carbonate content in the solid. (Zheng et al., 2003) defined a formula to calculate the appropriate S/L ratio for sorption experiments with calcareous soils. If this formula is applied to the present conditions a S/L ratio of at least 7.5 g/L results. In the case of Allard et al. (1982) and Bradbury and Baeyens (2011) an appropriate high S/L ratio was used, but the batch sorption experiments were conducted with different background electrolytes (ionic strength, composition) than applied in the present experiments which has an impact the U(VI) sorption behavior.

By fitting the uranium profile in the clay, about two orders of magnitude lower tortuosities were obtained than by fitting the uranium outflow in the receiving reservoir solution. These lead to two orders of magnitude lower D_e and D_a values which points to a slower U(VI) in-diffusion than out-diffusion in the investigated system. The comparison with literature D_a values (cf. Fig. 5-7) reveals that the profile fit results are about two orders of magnitude smaller than any reported D_a value for the U(VI) diffusion through bentonite so far, but the outflow fit results agree quite well with the values reported by Idemitsu et al. (1996) and Gaus and Van Loon (2012).
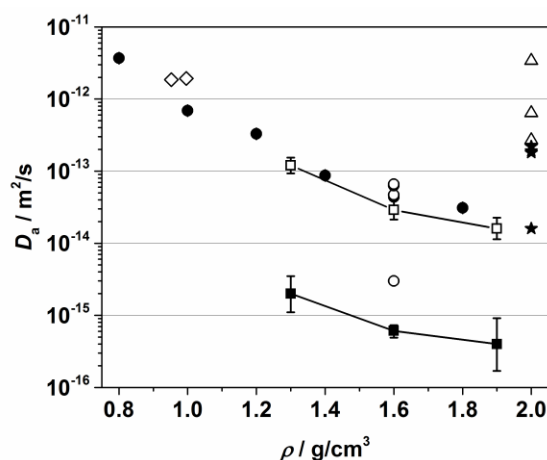
Figure 5-7: Comparison of D_a values obtained in this study by fitting of the uranium profiles in the MX-80 (■) and the uranium out-diffusion into the receiving reservoir solutions (□) with literature values as a function of dry density: (Δ) (Torstenfelt and Allard, 1986); (●) (Idemitsu et al., 1996); (★) (Ramebäck et al., 1998); (◊) (Wang et al., 2005); (○) (Glaus and Van Loon, 2012). Lines were drawn for visual reasons.

Idemitsu et al. (1996) investigated the uranium diffusion through two bentonite clays (Kunigel V1, Kunipia F) as a function of dry density at pH 8-10 in deionized water for 29-121 days. In Figure 5-7 only the diffusion results for Kunipia F are shown because its composition is similar to that of MX-80. Glaus and Van Loon (2012) investigated the diffusion through compacted montmorillonite as a function of ionic strength using ^{233}U(VI) as diffusing tracer. The smallest D_a value was obtained at $I = 0.1$ M NaClO$_4$ and lies close to the profile fit results in the present study. Glaus and Van Loon (2012) interpreted the uranium diffusion behavior under their conditions as "anion-like". They observed a change in the profile from a sharp decline with strong tailing to a profile with a smaller decrease without tailing with increasing ionic strength which is characteristic for an increase of D_a. The uranium profiles in the present study are influenced by the natural ^{238}U background. Thus, no clear statement concerning a tailing or rather any "anion-like" diffusion behavior can be made.

Torstenfelt and Allard (1986) studied the U(VI) diffusion through MX-80 for 62 days (artificial groundwater, pH 8.8-9, I = 0.035 M). They also observed a tailing of the [233]U profile at higher diffusion distances. They assumed that there are three different U(VI) fractions or species diffusing through the clay and defined a respective D_a value for each species. However, each of their species showed at least a one order of magnitude higher D_a value at 2 g/cm^{3} than resulted in the present study at lower dry densities. This difference could be due to a different uranium speciation with a larger fraction of anionic U(VI) species in solution or the applied diffusion set-up.

Rameback et al. (1998) performed a complex long-term diffusion experiment using spent UO_2 fuel as uranium source material. Unfortunately, the temperature was not monitored during the experiment. Although it can be expected that it is elevated due to radioactive decay of the radionuclides present. This would directly affect the U(VI) migration behavior and significantly increase the resulting D_e values. However, their diffusion cells were stopped and the profiles were analyzed at different time points. The first D_a value determined after 3 months of diffusion lies close to one of the D_a values of Torstenfelt and Allard (1986). The longest time period investigated amounted to 74 months (~6 years) which is close to the duration of the diffusion experiment which was conducted in the present study. Rameback et al. (1998) observed that the D_a values decreased with time by about one order of magnitude (cf. Fig. 12) and concluded that the system at shorter time scales may not be in equilibrium. This behavior of diffusing U(VI) could be reflected by the results in the present study. The two orders of magnitude big difference to the D_a values of Rameback et al. (1998) could be a temperature effect. Wang et al. (2005) also performed time-dependent diffusion experiments but at times shorter than a year (maximal 85 days). No decrease of the D_a values was observed. This is an additional indication that the change of D_a with time becomes obvious only in long-term experiments.

The question arises as to what causes this retardation of U(VI) migration within the MX-80. Rameback et al. (1998) proposed consideration of sorption kinetics with regard to surface redox reactions, leading on the longer time scale to surface precipitation of UO_2 and thus to an immobilization of the diffusing tracer. Although in this study the diffusion experiments were conducted under aerobic conditions, a redox reaction within the clay core, for instance, with the Fe(II) species, cannot be ruled out and thus is regarded as one possible retardation scenario. However, we would expect that the reduction of U(VI) to U(IV) would lead to a higher apparent Kd which was not observed in our simulations. Thus, reduction of U(VI) to U(IV) appears to be an unlikely explanation for the lower apparent diffusivities observed here.

Xiong et al. (2014) created a meso-scale model to describe the diffusion of species through porous media and investigated $Ca_2UO_2(CO_3)_3$(aq) diffusion through bentonite. They obtained similar D_a values as published by Wang et al. (2005). However, they pointed out that the pore space connectivity is dependent on the size and sorption properties of a diffusing species and showed that with progression of the diffusion process, the pore connectivity decreases due to sorption of the diffusing species onto throat walls. In the long-term, as sorption proceeds, this leads to a decrease of the D_a values. Compared to Wang et al. (2005), one order of magnitude smaller K_d values were obtained in this study (cf. Tables 5-5 and 5-6), thus the sorption and subsequent blocking of diffusion paths may have a smaller contribution to the retardation process observed in the present study. The work of Singer et al. (2014) confirms experimentally the blocking of pores by sorption. They investigated U(VI) batch sorption and diffusion kinetics in meso-porous silica as a function of time, initial U(VI) concentration, and solution composition (pH, calcium and carbonate presence) and found that the kinetics were strongly concentration-dependent. At c_0(U(VI)) = 1×10^{-5} M, after a particular time point they observed precipitation of a uranium-bearing phase within the silica pores and assumed that the initial diffusion and sorption was thermodynamically controlled by the aqueous U(VI) speciation, but the subsequent precipitation was kinetically controlled by continuous sorption of the respective U(VI) species near the pore openings which led to a so-called bottle-

neck effect. However, at $c_0(U(VI)) = 1\times10^{-6}$ M, the U(VI) concentration also used in the present diffusion study, no precipitation was observed. But does this mean that the formation of a uranium-containing precipitate in the MX-80 pores may not occur? The experiment of Singer et al. (2014) was conducted for 336 h (two weeks) and not for about six years as in the present study. If it is a precipitation reaction with relatively slow kinetics, a blocking of pores would become obvious only in long-term experiments. Thus, it cannot be excluded for the U(VI) diffusion through MX-80 bentonite.

Keller et al. (2015) investigated the evolution of the interparticle pore space of MX-80 used in a long-term (over two years) part-time heated (about one year) experiment. They found that due to the filling of the pore space with a so-called clay-gel or colloidal gel the interparticle porosity of the clay decreased below the percolation threshold for gas. Consequently, the pore connectivity decreased substantially. Thus, gas transport through the interparticle pore space was excluded. However, such a change in porosity and pore connectivity may not only be relevant for gas transport. It also could significantly affect the molecular diffusion of slow-migrating tracers like U(VI).

In the long term, all scenarios described would hinder or even stop the U(VI) diffusion through MX-80 bentonite. Thus, they can be responsible, or at least contribute, to the observed retardation of the U(VI) migration. However, in all cases the leaching or out-diffusion of natural U(VI) would not be affected.

Since the investigation of the in-diffusion of U(VI) delivered diffusion parameter values which are obviously biased by retarding effects, for determination of the Archie's law constants, only the data obtained by fitting the U(VI) out-diffusion were used. In Fig. 5-8 the relation between $D_e(U(VI))$ and $\varepsilon_{eff}(HTO)$ is plotted and fitted by Archie's law analog using $D_w(U(VI))$ (cf. Table 5-11). An empirical constant of 9.7 ± 2.5 for the U(VI) diffusion out of MX-80 bentonite was determined. To the best of the author's knowledge, this is the first time an Archie's law analog constant for the U(VI) / bentonite system is reported.
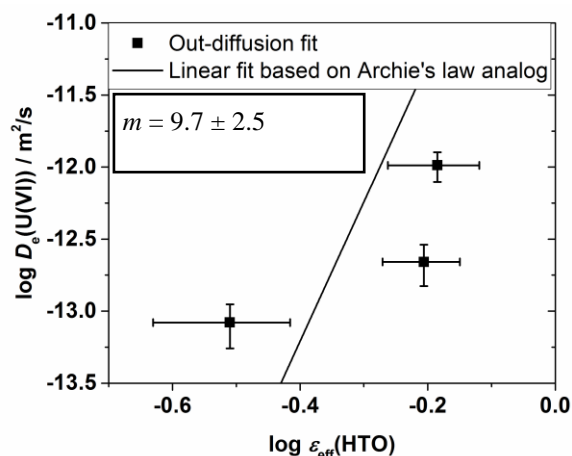
Figure 5-8: Relation between D_e and ε_{eff} for the U(VI) out-diffusion from MX-80 into the receiving reservoir solution.

Recently, Van Loon (2014) discussed the limits of Archie's law analog by collecting and comparing D_e and respective ε_{eff} values for several diffusing tracers. He found that for $\varepsilon_{eff} \leq 0.1$, the Archie's law analog is not able to describe appropriately the relation between D_e and ε_{eff} for various sedimentary rocks. He proposed a small variation of Archie's law analog, the so-called extended Archie's law (cf. Eq.5-11), to reproduce the data and consequently, to predict D_e values also for systems with smaller porosities.

$$D_e = \varepsilon_{\text{eff}}^{m1} \cdot D_w + \varepsilon_{\text{eff}}^{m2} \cdot B \qquad\qquad (5\text{-}11)$$

where B, $m1$, $m2$ are empirical factors.

Van Loon (2014) used Eq. (5-11) to estimate D_e values for various tracers, host rocks, and compacted bentonite. For bentonite a total porosity of 0.36 was assumed, which is close to the ε_{eff} of the MX-80 dry density 1.9 g/cm^3 investigated in this study. The Archie's parameters were defined with $m1 = 2.4$, $m2 = 1.0$ and $B = 1\times10^{-11}$ m^2/s. For U(IV+VI), a neutral diffusing species was assumed, meaning the whole total porosity was accessible for diffusion. Using a D_w value of 7.5×10^{-10} m^2/s, slightly higher than in this study, a D_e value of 6.8×10^{-11} m^2/s was estimated (upper boundary: 1.8×10^{-10} m^2/s; lower boundary: 3.8×10^{-11} m^2/s). This value is over one order of magnitude higher than any D_e value obtained in the current study for the out-diffusion of U(VI). Thus, the extended Archie's law significantly overestimates U(VI) diffusion through compacted bentonite. Either ε_{eff} for U(VI) is substantially smaller, or the extended Archie's law in this form is not applicable to the U(VI) / MX-80 system.

5.4   CONCLUSIONS

For a time period of six years, U(VI) diffusion through compacted MX-80 bentonite was investigated as a function of clay dry bulk density ($\rho =1.3$, 1.6, 1.9 g/cm^3). Speciation calculations revealed that independent of pore water type and water sampling time the $Ca_2UO_2(CO_3)_3$(aq) complex was always the dominant U(VI) species in solution (83-90%). This neutral complex was assumed to be the main diffusing U(VI) species in the system. As effective transport porosity, ε_{eff}, the value for HTO was assumed in the U(VI) diffusion model, although one can expect that ε_{eff}(U(VI)) is smaller than ε_{eff}(HTO) regarding to the size of the molecules and their respective access to the clay interlayers. However, the used value of ε_{eff} has no significant impact on the modeled U(VI) diffusion parameters, since the U(VI) sorption onto the clay is dominating.

Under consideration of the natural uranium background in MX-80 it was estimated that U(VI) diffused about 2 mm, 1 mm, and 0.7 mm deep in the clay at $\rho = 1.3$, 1.6, and 1.9 g/cm^3, respectively. The distribution coefficients modeled are very low ($K_d = 5.8\text{-}2.6\times10^{-3}$ m^3/kg). This can be attributed to $Ca_2UO_2(CO_3)_3$(aq) which is known to sorb only weakly onto clay. For the same system, batch sorption experiments were performed using a solid-to-liquid ratio of 2.5 g/L (Nebelung and Brendler, 2009). The K_d values obtained were about one order of magnitude higher than the K_d values of the present study. Probably, the S/L ratio was too small. Such a dependence of K_d on the S/L ratio was previously described for U(VI) sorption onto clay (Joseph et al., 2011). However, the K_d values of the present study differ only by a factor of three from the K_d values published by Glaus and Van Loon (2012) for U(VI) diffusion through compacted montmorillonite in calcareous NaClO$_4$ solutions for $I = 0.1$ M, 0.5 M, which can be regarded as in very good agreement.

For determination of the apparent U(VI) diffusion coefficient, D_a, two fitting approaches were applied. 1) Fitting of the uranium depth profiles: about two orders of magnitude lower D_a values were obtained than any published D_a value so far, in particular, for "short-term" diffusion studies conducted for less than one year. 2) Fitting of the out-diffusion of natural uranium into the receiving reservoir solution: D_a values are in very good agreement with literature data (Glaus and Van Loon, 2012; Idemitsu et al., 1996). This discrepancy shows that the in- and out-diffusion of U(VI) in MX-80 has to be regarded independently in this study.

The reason for these substantial different results could be a reduction of clay porosity far below the percolation threshold by formation of a clay-gel in the pores after longer time scales as just recently reported for MX-80 (Keller et al., 2015), which leads to a decrease in pore connectivity and would hinder or even stop the through-diffusion of U(VI). However, the out-diffusion or leaching of U(VI) from the

clay would still be possible. The experiments show the value of long-term diffusion experiments, since migration determining processes may occur or be visible only at longer time frames. In addition, it shows the excellent retention capacity of bentonite for weakly sorbing U(VI) species.

5.5   REFERENCES

Included in Chapter 7.

5.6 APPENDIX

Table A.1: Steps of hydraulic pressure exerted on the MX-80 in the diffusion cells during saturation process.

1.3 g/cm³		1.6 g/cm³		1.9 g/cm³	
Time period / d	p / MPa	Time period / d	p / MPa	Time period / d	p / MPa
1	0.4-0.5	1	0.9-1.0	1	0.9-1.0
7	0.7-0.8	2	1.9-2.0	1	1.9-2.0
		21	2.4-2.5	4	2.4-2.5
				0.25	2.9-3.0
				29	3.4-3.5

Table A.2: Filtered volumes of the reservoir solutions for microbial analysis at $t = 2401$ d..

1.3 g/cm³	1.6 g/cm³	1.9 g/cm³		Blank
source / mL	source / mL	source / mL	receiving / mL	source / mL
175 + 125 [a]	200	265	17 [b]	10 [b]

[a] For 18S RNA and 16S RNA analysis, respectively.
[b] Entire solution remaining at the end of the diffusion experiment.

Table A.3: Experimentally determined K_d values for the U(VI) sorption on the stainless steel filter plates, the according log K values for the respective UO_2^{2+} surface complex formed on the filters assumed in the model database, and the resulting capacity factor, α, as a function of clay dry bulk density.

ρ / kg/m³	K_d(filter) / m³/kg	log K (>FeOHUO$_2^{2+}$)	α (filter)
1300	0.0008	-0.600915605	3.08
1600	0.0024	-1.096735999	8.99
1900	0.0048	-1.401759154	17.85

Table A.4: Composition of the source reservoir solutions at $t = 2401$ d (fresh solution) and $t = 2457$ d of the U(VI) diffusion experiment as well as the main aqueous U(VI) species calculated for the listed conditions.

	1.3 g/cm^3		1.6 g/cm^3		1.9 g/cm^3	
	$t = 2401$ d	$t = 2457$ d	$t = 2401$ d	$t = 2457$ d	$t = 2401$ d	$t = 2457$ d
c / M						
U [a]	1.3×10^{-6}	1.1×10^{-6}	1.1×10^{-6}	7.8×10^{-7}	1.1×10^{-6}	9.2×10^{-7}
Na [a]	1.8×10^{-1}	1.4×10^{-1}	2.1×10^{-1}	1.6×10^{-1}	2.6×10^{-1}	1.9×10^{-1}
K [a]	2.6×10^{-3}	2.0×10^{-3}	2.9×10^{-3}	2.3×10^{-3}	3.4×10^{-3}	2.7×10^{-3}
Mg [b]	9.6×10^{-3}	7.4×10^{-3}	1.2×10^{-2}	8.9×10^{-3}	1.5×10^{-2}	1.1×10^{-2}
Ca [b]	9.3×10^{-3}	6.9×10^{-3}	9.4×10^{-3}	7.5×10^{-3}	1.2×10^{-2}	8.8×10^{-3}
Sr [a]	7.8×10^{-5}	6.0×10^{-5}	8.3×10^{-5}	6.3×10^{-5}	1.0×10^{-4}	7.8×10^{-5}
Si [a]	1.2×10^{-5}	4.6×10^{-5}	9.5×10^{-6}	4.0×10^{-5}	9.7×10^{-6}	2.2×10^{-5}
Cl$^-$ [c]	1.8×10^{-2}	n.d. [e]	5.9×10^{-2}	n.d.	1.7×10^{-1}	n.d.
SO$_4$$^{2-}$ [c]	1.0×10^{-1}	n.d.	9.6×10^{-2}	n.d.	7.0×10^{-2}	n.d.
C$_{inorg}$ [d]	8.7×10^{-4}	n.d.	7.4×10^{-4}	n.d.	5.0×10^{-4}	n.d.
F$^-$ [c]	1.9×10^{-4}	n.d.	2.1×10^{-4}	n.d.	1.7×10^{-4}	n.d.
I	0.26	n.d.	0.29	n.d.	0.33	n.d.
Aqueous U(VI) species distribution / % [f]						
Ca$_2$UO$_2$(CO$_3$)$_3$(aq)	87.3	-	86.0	-	89.6	-
UO$_2$(CO$_3$)$_3$$^{4-}$	8.1	-	8.6	-	6.0	-
MgUO$_2$(CO$_3$)$_3$$^{2-}$	2.7	-	3.3	-	2.9	-
CaUO$_2$(CO$_3$)$_3$$^{2-}$	1.1	-	1.1	-		

[a] ICP–MS (error: ±10%) [b] AAS (error: ±2%) [c] IC (error: ±3-10%)

[d] TC – TOC (error: ±3%) [e] n.d. = not determined [f] only species $\geq$ 1% shown

Table A.5: Classification of the extracted subsets of 16S rDNA in some of the reservoir solutions at t = 2401 d.

Sequence number	SINA alignment score	Identity [a]	Gene base pairs [b]	Taxonomic classification
Source reservoir 1.3 g/cm³ (TOC: 30.4 mg/L)				
1	0.995275	99.6617	1478	Bacteria; Actinobacteria; Actinobacteria; Micrococcales; Microbacteriaceae; Microbacterium;
2	0.991891	96.3583	1474	Bacteria; Chlorobi; Chlorobia; Chlorobiales; SJA-28;
3	0.996122	96.2912	1453	Bacteria; Chloroflexi; Anaerolineae; Anaerolineales; Anaerolineaceae; uncultured;
4	0.988642	99.1435	1444	Bacteria; Proteobacteria; Alphaproteobacteria; Rhizobiales; Rhizobiaceae; Rhizobium;
5	0.993977	98.6343	1421	Bacteria; Proteobacteria; Alphaproteobacteria; Caulobacterales; Caulobacteraceae; Brevundimonas;
6	0.916514	84.318	1456	Bacteria; Proteobacteria; Alphaproteobacteria; Rhodospirillales; Rhodospirillaceae; uncultured;
7	0.994048	98.2001	1447	Bacteria; Proteobacteria; Alphaproteobacteria; Sphingomonadales; Sphingomonadaceae; Sphingobium;
Source reservoir 1.6 g/cm³ (TOC: 71.2 mg/L)				
1	0.994832	96.2888	1480	Bacteria; Acidobacteria; Acidobacteria; Subgroup 4; Family Incertae Sedis; Blastocatella;
2	0.995184	97.1705	1481	Bacteria; Actinobacteria; Actinobacteria; Micrococcales; Microbacteriaceae;
3	0.989163	97.9914	697	Bacteria; Actinobacteria; Actinobacteria; Micrococcales; Microbacteriaceae;
4	0.994939	97.2414	1482	Bacteria; Actinobacteria; Actinobacteria; Micrococcales; Microbacteriaceae;
5	0.99941	97.4465	1481	Bacteria; Actinobacteria; Actinobacteria; Micrococcales; Microbacteriaceae;
6	0.998331	97.3775	1481	Bacteria; Actinobacteria; Actinobacteria; Micrococcales; Microbacteriaceae;
7	0.999058	97.4144	1481	Bacteria; Actinobacteria; Actinobacteria; Micrococcales; Microbacteriaceae;
8	0.99941	97.5155	1481	Bacteria; Actinobacteria; Actinobacteria; Micrococcales; Microbacteriaceae;
9	0.957789	85.9422	1483	Bacteria; Planctomycetes; Planctomycetacia; Planctomycetales; Planctomycetaceae; Planctomyces;
10	0.958302	85.8425	1483	Bacteria; Planctomycetes; Planctomycetacia; Planctomycetales; Planctomycetaceae; Planctomyces;
11	0.959896	85.9422	1483	Bacteria; Planctomycetes; Planctomycetacia; Planctomycetales; Planctomycetaceae; Planctomyces;
12	0.998232	99.2409	1448	Bacteria; Proteobacteria; Alphaproteobacteria; Rhodospirillales;
13	0.996117	94.3515	1442	Bacteria; Proteobacteria; Alphaproteobacteria; Caulobacterales; Caulobacteraceae; Phenylobacterium;

Table A.5 (continued):   Classification of the extracted subsets of 16S rDNA in some of the reservoir solutions at $t = 2401$ d.

Sequence number	SINA alignment score	Identity [a]	Gene base pairs [b]	Taxonomic classification
				Source reservoir 1.9 g/cm³ (TOC: 13.8 mg/L)
1	0.956615	85.9422	1483	Bacteria; Planctomycetes; Planctomycetacia; Planctomycetales; Planctomycetaceae; Planctomyces;
2	0.978713	96.0358	861	Bacteria; Planctomycetes; Planctomycetacia; Planctomycetales; Planctomycetaceae; Planctomyces;
3	0.959648	85.9422	1483	Bacteria; Planctomycetes; Planctomycetacia; Planctomycetales; Planctomycetaceae; Planctomyces;
4	0.994544	99.1426	1482	Bacteria; Planctomycetes; Planctomycetacia; Planctomycetales; Planctomycetaceae; uncultured;
5	0.987073	97.2678	1478	Bacteria; Planctomycetes; Planctomycetacia; Planctomycetales; Planctomycetaceae; Planctomyces;
6	0.985868	97.1897	1540	Bacteria; Planctomycetes; Planctomycetacia; Planctomycetales; Planctomycetaceae; Planctomyces;
7	0.985091	97.1116	1478	Bacteria; Planctomycetes; Planctomycetacia; Planctomycetales; Planctomycetaceae; Planctomyces;
8	0.996453	99.3103	1448	Bacteria; Proteobacteria; Alphaproteobacteria; Rhodospirillales;
9	0.990316	98.3425	1446	Bacteria; Proteobacteria; Alphaproteobacteria; Rhizobiales; Methylobacteriaceae; uncultured;
10	0.995982	95.7547	861	Bacteria; Proteobacteria; Deltaproteobacteria; Sh765B-TzT-29;
11	0.996177	96.6465	1521	Bacteria; Proteobacteria; Deltaproteobacteria; Sh765B-TzT-29;
12	0.993285	96.3783	1521	Bacteria; Proteobacteria; Deltaproteobacteria; Sh765B-TzT-29;
13	0.992335	96.2441	1528	Bacteria; Proteobacteria; Deltaproteobacteria; Sh765B-TzT-29;
14	0.996864	96.6465	1521	Bacteria; Proteobacteria; Deltaproteobacteria; Sh765B-TzT-29;
15	0.994749	96.5795	1520	Bacteria; Proteobacteria; Deltaproteobacteria; Sh765B-TzT-29;
				Receiving reservoir 1.9 g/cm³ (TOC: 12.4 mg/L)
1	0.994984	96.4936	1481	Bacteria; Acidobacteria; Acidobacteria; Subgroup 4; Family Incertae Sedis; Blastocatella;
2	0.997053	96.4912	1480	Bacteria; Acidobacteria; Acidobacteria; Subgroup 4; Family Incertae Sedis; Blastocatella;
3	0.991193	96.3583	1474	Bacteria; Chlorobi; Chlorobia; Chlorobiales; SJA-28;
4	0.989999	96.1398	1474	Bacteria; Chlorobi; Chlorobia; Chlorobiales; SJA-28;
5	0.992331	96.4312	1474	Bacteria; Chlorobi; Chlorobia; Chlorobiales; SJA-28;
6	0.987478	97.2678	1478	Bacteria; Planctomycetes; Planctomycetacia; Planctomycetales; Planctomycetaceae; Planctomyces;
7	0.957186	85.9422	1483	Bacteria; Planctomycetes; Planctomycetacia; Planctomycetales; Planctomycetaceae; Planctomyces;

Table A.5 (continued):   Classification of the extracted subsets of 16S rDNA in some of the reservoir solutions at $t = 2401$ d.

Sequence number	SINA alignment score	Identity [a]	Gene base pairs [b]	Taxonomic classification
8	0.988288	97.2678	1416	Bacteria; Planctomycetes; Planctomycetacia; Planctomycetales; Planctomycetaceae; Planctomyces;
9	0.988669	97.3458	1478	Bacteria; Planctomycetes; Planctomycetacia; Planctomycetales; Planctomycetaceae; Planctomyces;
10	0.97735	88.563	1450	Bacteria; Planctomycetes; Phycisphaerae; Phycisphaerales; Phycisphaeraceae; SM1A02;
11	0.984449	97.1116	1478	Bacteria; Planctomycetes; Planctomycetacia; Planctomycetales; Planctomycetaceae; Planctomyces;
12	0.983618	97.1116	1478	Bacteria; Planctomycetes; Planctomycetacia; Planctomycetales; Planctomycetaceae; Planctomyces;
13	0.98784	97.3458	1478	Bacteria; Planctomycetes; Planctomycetacia; Planctomycetales; Planctomycetaceae; Planctomyces;
14	0.998198	99.0997	1444	Bacteria; Proteobacteria; Alphaproteobacteria; Rhodospirillales; Rhodospirillaceae; Ferrovibrio;
15	0.993439	94.8052	1459	Bacteria; Proteobacteria; Alphaproteobacteria; Rhodospirillales; Rhodospirillaceae; uncultured;
Source reservoir blank (TOC: 9.46 mg/L)				
1	0.973816	88.817	1505	Bacteria; Actinobacteria; Thermoleophilia; Gaiellales; uncultured;
7	0.992813	96.9466	1477	Bacteria; Actinobacteria; Acidimicrobiia; Acidimicrobiales; Acidimicrobiaceae; Ilumatobacter;
2	0.979708	97.1066	1477	Bacteria; Actinobacteria; Actinobacteria; Corynebacteriales; Mycobacteriaceae; Mycobacterium;
9	0.985871	96.1273	1474	Bacteria; Actinobacteria; Actinobacteria; Propionibacteriales; Nocardioidaceae;
4	0.991824	96.6019	1461	Bacteria; Chloroflexi; Caldilineae; Caldilineales; Caldilineaceae; uncultured;
3	0.96176	85.8425	1482	Bacteria; Planctomycetes; Planctomycetacia; Planctomycetales; Planctomycetaceae; Planctomyces;
5	0.976667	95.9533	1480	Bacteria; Planctomycetes; Planctomycetacia; Planctomycetales; Planctomycetaceae; Pir4 lineage;
6	0.968724	92.8287	1498	Bacteria; Planctomycetes; Planctomycetacia; Planctomycetales; Planctomycetaceae; Pir4 lineage;
8	0.982095	93.6255	1498	Bacteria; Planctomycetes; Planctomycetacia; Planctomycetales; Planctomycetaceae; Pir4 lineage;
10	0.969645	93.1206	1498	Bacteria; Planctomycetes; Planctomycetacia; Planctomycetales; Planctomycetaceae; Pir4 lineage;

[a] The highest identity the aligned sequence has with any sequence in the alignment seed.

[b] The number of base pairs within the small subunit.

Table A.6: Classification of the extracted subsets of 18S rDNA in some of the reservoir solutions at t = 2401 d.

Sequence number	SINA alignment score	Identity [a]	Gene base pairs [b]	Taxonomic classification
Source reservoir 1.3 g/cm³ (TOC: 30.4 mg/L)				
1	0.990453	99.3559	621	Eukaryota; Amoebozoa; Discosea; Longamoebia; Centramoebida; Acanthamoeba;
2	0.995935	99.6779	620	Eukaryota; Amoebozoa; Discosea; Longamoebia; Centramoebida; Acanthamoeba;
3	0.976368	96.4093	555	Eukaryota; Archaeplastida; Chloroplastida; Chlorophyta; Trebouxiophyceae;
4	0.970769	96.0503	555	Eukaryota; Archaeplastida; Chloroplastida; Chlorophyta; Trebouxiophyceae;
5	0.976368	96.4093	555	Eukaryota; Archaeplastida; Chloroplastida; Chlorophyta; Trebouxiophyceae;
6	0.881533	79.4816	459	Eukaryota; Excavata; Malawimonas;
7	0.99265	97.2763	549	Eukaryota; Opisthokonta; Nucletmycea; Fungi; Dikarya; Ascomycota; Pezizomycotina; Eurotiomycetes;
8	0.99265	97.2763	549	Eukaryota; Opisthokonta; Nucletmycea; Fungi; Dikarya; Ascomycota; Pezizomycotina; Eurotiomycetes;
9	0.992668	97.0817	549	Eukaryota; Opisthokonta; Nucletmycea; Fungi; Dikarya; Ascomycota; Pezizomycotina; Eurotiomycetes;
10	0.989928	97.4708	549	Eukaryota; Opisthokonta; Nucletmycea; Fungi; Dikarya; Ascomycota; Pezizomycotina; Eurotiomycetes;
11	0.989928	97.4708	549	Eukaryota; Opisthokonta; Nucletmycea; Fungi; Dikarya; Ascomycota; Pezizomycotina; Eurotiomycetes;
12	0.989928	97.4708	549	Eukaryota; Opisthokonta; Nucletmycea; Fungi; Dikarya; Ascomycota; Pezizomycotina; Eurotiomycetes;
13	0.989925	97.2763	549	Eukaryota; Opisthokonta; Nucletmycea; Fungi; Dikarya; Ascomycota; Pezizomycotina; Eurotiomycetes;
14	0.972734	96.7245	549	Eukaryota; Opisthokonta; Nucletmycea; Fungi; Dikarya; Ascomycota; Pezizomycotina; Sordariomycetes; Hypocreomycetidae; Hypocreales;
15	0.99256	98.9796	552	Eukaryota; Opisthokonta; Nucletmycea; Fungi; Dikarya; Ascomycota; Pezizomycotina; Leotiomycetes; Leotiomycetidae;
Source reservoir 1.6 g/cm³ (TOC: 71.2 mg/L)				
1	0.957817	93.8959	555	Eukaryota; Archaeplastida; Chloroplastida; Chlorophyta; Trebouxiophyceae;
2	0.976368	96.4093	555	Eukaryota; Archaeplastida; Chloroplastida; Chlorophyta; Trebouxiophyceae;
3	0.998402	98.5428	549	Eukaryota; Opisthokonta; Nucletmycea; Fungi; Dikarya; Ascomycota; Pezizomycotina; Eurotiomycetes; Chaetothyriomycetidae; Chaetothyriales;

Table A.6 (continued): Classification of the extracted subsets of 18S rDNA in some of the reservoir solutions at $t = 2401$ d.

Sequence number	SINA alignment score	Identity [a]	Gene base pairs [b]	Taxonomic classification
5	0.995577	98.1785	549	Eukaryota; Opisthokonta; Nucletmycea; Fungi; Dikarya; Ascomycota; Pezizomycotina; Eurotiomycetes; Chaetothyriomycetidae; Chaetothyriales;
6	0.998402	98.5428	549	Eukaryota; Opisthokonta; Nucletmycea; Fungi; Dikarya; Ascomycota; Pezizomycotina; Eurotiomycetes; Chaetothyriomycetidae; Chaetothyriales;
7	0.992764	98.1785	549	Eukaryota; Opisthokonta; Nucletmycea; Fungi; Dikarya; Ascomycota; Pezizomycotina; Eurotiomycetes; Chaetothyriomycetidae; Chaetothyriales;
8	0.995555	98.5428	549	Eukaryota; Opisthokonta; Nucletmycea; Fungi; Dikarya; Ascomycota; Pezizomycotina; Eurotiomycetes; Chaetothyriomycetidae; Chaetothyriales;
9	0.998402	98.5428	549	Eukaryota; Opisthokonta; Nucletmycea; Fungi; Dikarya; Ascomycota; Pezizomycotina; Eurotiomycetes; Chaetothyriomycetidae; Chaetothyriales;
10	0.98797	97.4708	549	Eukaryota; Opisthokonta; Nucletmycea; Fungi; Dikarya; Ascomycota; Pezizomycotina; Eurotiomycetes;
11	0.998402	98.5428	549	Eukaryota; Opisthokonta; Nucletmycea; Fungi; Dikarya; Ascomycota; Pezizomycotina; Eurotiomycetes; Chaetothyriomycetidae; Chaetothyriales;
12	0.99624	98.3607	549	Eukaryota; Opisthokonta; Nucletmycea; Fungi; Dikarya; Ascomycota; Pezizomycotina; Eurotiomycetes; Chaetothyriomycetidae; Chaetothyriales;
13	0.983933	95.1087	549	Eukaryota; Opisthokonta; Nucletmycea; Fungi; Dikarya; Ascomycota; Pezizomycotina; Sordariomycetes; Hypocreomycetidae; Hypocreales;
14	0.990089	97.8221	550	Eukaryota; Opisthokonta; Nucletmycea; Fungi; Dikarya; Ascomycota; Pezizomycotina; Sordariomycetes; Hypocreomycetidae; Hypocreales;

Source reservoir 1.9 g/cm^3 (TOC: 13.8 mg/L)

Sequence number	SINA alignment score	Identity [a]	Gene base pairs [b]	Taxonomic classification
1	0.976368	96.4093	555	Eukaryota; Archaeplastida; Chloroplastida; Chlorophyta; Trebouxiophyceae;
2	0.976368	96.4093	555	Eukaryota; Archaeplastida; Chloroplastida; Chlorophyta; Trebouxiophyceae;
3	0.976368	96.4093	555	Eukaryota; Archaeplastida; Chloroplastida; Chlorophyta; Trebouxiophyceae;
4	0.976368	96.4093	555	Eukaryota; Archaeplastida; Chloroplastida; Chlorophyta; Trebouxiophyceae;

Table A.6 (continued): Classification of the extracted subsets of 18S rDNA in some of the reservoir solutions at t = 2401 d.

Sequence number	SINA alignment score	Identity [a]	Gene base pairs [b]	Taxonomic classification
5	0.973758	96.2298	555	Eukaryota; Archaeplastida; Chloroplastida; Chlorophyta; Trebouxiophyceae;
6	0.97075	96.0503	555	Eukaryota; Archaeplastida; Chloroplastida; Chlorophyta; Trebouxiophyceae;
7	0.973527	96.2298	555	Eukaryota; Archaeplastida; Chloroplastida; Chlorophyta; Trebouxiophyceae;
8	0.976368	96.4093	555	Eukaryota; Archaeplastida; Chloroplastida; Chlorophyta; Trebouxiophyceae;
9	0.987091	97.2763	549	Eukaryota; Opisthokonta; Nucletmycea; Fungi; Dikarya; Ascomycota; Pezizomycotina; Eurotiomycetes;
10	0.993291	98.0072	550	Eukaryota; Opisthokonta; Nucletmycea; Fungi; Dikarya; Basidiomycota; Ustilaginomycotina; Exobasidiomycetes; Exobasidiomycetidae;
11	0.984719	96.036	552	Eukaryota; Opisthokonta; Nucletmycea; Fungi; Dikarya; Basidiomycota;

Receiving reservoir 1.9 g/cm^3 (TOC: 12.4 mg/L)

Sequence number	SINA alignment score	Identity [a]	Gene base pairs [b]	Taxonomic classification
1	0.989928	97.4708	549	Eukaryota; Opisthokonta; Nucletmycea; Fungi; Dikarya; Ascomycota; Pezizomycotina; Eurotiomycetes;
2	0.98424	97.0817	549	Eukaryota; Opisthokonta; Nucletmycea; Fungi; Dikarya; Ascomycota; Pezizomycotina; Eurotiomycetes;
3	0.989928	97.4708	549	Eukaryota; Opisthokonta; Nucletmycea; Fungi; Dikarya; Ascomycota; Pezizomycotina; Eurotiomycetes;
4	0.989928	97.4708	549	Eukaryota; Opisthokonta; Nucletmycea; Fungi; Dikarya; Ascomycota; Pezizomycotina; Eurotiomycetes;
5	0.970755	93.4702	553	Eukaryota; SAR; Stramenopiles;
6	0.96952	94.0298	553	Eukaryota; SAR; Stramenopiles;
7	0.970755	93.4702	553	Eukaryota; SAR; Stramenopiles;
8	0.967364	92.7374	553	Eukaryota; SAR; Stramenopiles;
9	0.970755	93.4702	553	Eukaryota; SAR; Stramenopiles;
10	0.970755	93.4702	553	Eukaryota; SAR; Stramenopiles;
11	0.970345	93.8433	553	Eukaryota; SAR; Stramenopiles; Chrysophyceae;

Source reservoir blank (TOC: 9.46 mg/L)

Sequence number	SINA alignment score	Identity [a]	Gene base pairs [b]	Taxonomic classification
1	0.951908	95.9742	608	Eukaryota; Amoebozoa; Discosea; Longamoebia; Centramoebida; Acanthamoeba;
2	0	100	621	Eukaryota; Amoebozoa; Discosea; Longamoebia; Centramoebida; Acanthamoeba;
3	0	100	621	Eukaryota; Amoebozoa; Discosea; Longamoebia; Centramoebida; Acanthamoeba;

Table A.6 (continued): Classification of the extracted subsets of 18S rDNA in some of the reservoir solutions at $t = 2401$ d.

Sequence number	SINA alignment score	Identity [a]	Gene base pairs [b]	Taxonomic classification
4	0 100	621		Eukaryota; Amoebozoa; Discosea; Longamoebia; Centramoebida; Acanthamoeba;
5	0.973563	96.2298	555	Eukaryota; Archaeplastida; Chloroplastida; Chlorophyta; Trebouxiophyceae;
6	0.984804	96.1315	551	Eukaryota; Opisthokonta; Nucletmycea; Fungi; Dikarya; Ascomycota; Pezizomycotina; Eurotiomycetes;
7	0.970213	92.9236	553	Eukaryota; SAR; Stramenopiles;
8	0.970755	93.4702	553	Eukaryota; SAR; Stramenopiles;
9	0.970755	93.4702	553	Eukaryota; SAR; Stramenopiles;
10	0.967749	93.2836	553	Eukaryota; SAR; Stramenopiles;
11	0.970755	93.4702	553	Eukaryota; SAR; Stramenopiles;

[a] The highest identity the aligned sequence has with any sequence in the alignment seed.

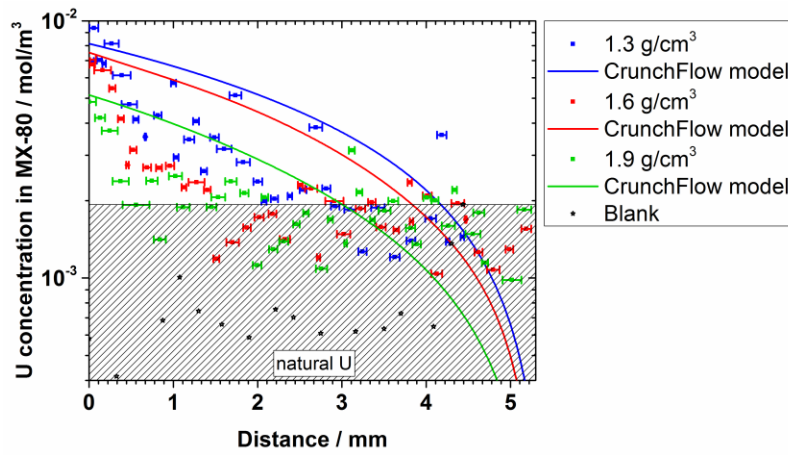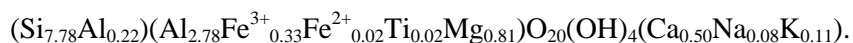[b] The number of base pairs within the small subunit.

Figure A1: Concentration depth profile of uranium in MX-80 as a function of clay dry density. CrunchFlow model data obtained by fitting the uranium outflow in the receiving reservoir.

6.0 SORPTION AND DESORPTION OF PLUTONIUM BY BENTONITE

6.1 INTRODUCTION

Permanent interment in a deep geological repository is seen as the most viable option for radioactive waste disposal in many countries with a civilian nuclear fuel program (Iaea, 1995). Conceptually, the repository scenario comprises a geological barrier (host rock) combined with engineering barriers that aim to contain the radionuclides until they have decayed below harmful levels. The waste itself will likely be contained in steel canisters surrounded by a layer of compacted clay. The efficacy of this disposal option is related to its capacity to confine radioactivity and isolate it from the biosphere (Dozol et al., 1993).

Due to its swelling properties, plasticity, ion exchange and sorption behavior, and sealing capability, bentonite is considered a good candidate for backfill material (Guven, 1990). Traditionally, the term bentonite refers to aluminum phyllosilicate clays derived from the devitrification and chemical alteration of glassy volcanic ash or tuff (Ross and Shannon, 1926). However, the term has been used to describe smectite-rich materials, regardless of origin (Grim, 1968). The smectite mineral group includes a number of 2:1 layer silicates, the most common of which is montmorillonite. Montmorillonites constitute a large proportion of bentonite mineralogy (65-90 wt %) with the result that the two names are often used synonymously, although the former is a clay mineral and the latter a clay rock (Grauer, 1986). Montmorillonite can display significant morphological and chemical differences depending on its provenance (Guven, 1988). ENRESA, the body responsible for the management of Spanish radioactive waste, has proposed FEBEX bentonite from Cortijo de Archidona in Almeria, Spain for use in its repositories. As a result, the physiochemical properties of this clay rock have been well studied, particularly in an extensive experimental program performed at the National Cooperative for the Disposal of Radioactive Waste's (Nagra) Grimsel Test Site in Switzerland. The FEBEX bentonite has a high smectite content (93 $\pm$ 2 %) with quartz (2 $\pm$ 1%), plagioclase (3 $\pm$ 1 %), cristobalite (2 $\pm$ 1 %), potassium feldspar, calcite and tridymite as accessory minerals (Missana et al., 2004). The less than 2 μm fraction (after Ca homoionization) of this bentonite is composed of >99% smectite with the structural formula (Fernandez et al., 2004):

$$(Si_{7.78}Al_{0.22})(Al_{2.78}Fe^{3+}_{0.33}Fe^{2+}_{0.02}Ti_{0.02}Mg_{0.81})O_{20}(OH)_4(Ca_{0.50}Na_{0.08}K_{0.11}).$$

Due to their long half-lives and toxicity, the isotopes ^{239}Pu (2.41 $\times$ 10^4 y) and ^{240}Pu (6.56 $\times$ 10^3 y) are expected to contribute significantly to the total hazardous inventory in a waste repository scenario (Schwenk-Ferrero, 2013). Despite several decades of study, our understanding of how Pu migrates in subsurface environments is far from complete due to the wide array of factors which can significantly influence its mobility. These include Pu redox processes (Choppin, 1991; Sanchez et al., 1985), colloid-facilitated transport processes (Kersting et al., 1999; Novikov et al., 2006), solubility effects (Efurd et al., 1998; Neck et al., 2007c), sorption/desorption rates and affinities for natural mineral surfaces (Powell et al., 2004; Zavarin et al., 2012), and interactions with natural organic matter (including bacteria) (Icopini et al., 2009; Zhao et al., 2011). Pu exhibits a complex redox chemistry in natural waters with four oxidation states (VI, V, IV, III) potentially stable and with each oxidation state displaying a unique solubility (Neck et al., 2007c) and mineral sorption affinity (Begg et al., 2013; Keeney-Kennicutt and Morse, 1985; Sanchez et al., 1985; Silva and Nitsche, 1995). Pu(IV) and Pu(V) are the more common species under mildly oxic environmental conditions and also represent the oxidation states with the lowest (Pu(V)) and

highest (Pu(IV)) affinities for mineral surfaces (Choppin, 2007; Kaplan et al., 2007; Silva and Nitsche, 1995).

Mineral-colloid facilitated transport is thought to be a significant contributor to Pu migration in the subsurface (Kersting et al., 1999; Novikov et al., 2006; Santschi et al., 2002). One of the concerns with the use of bentonite as a backfill material in a repository is that it can form colloids, which may enhance the migration of radionuclide species that are sorbed to them (Geckeis et al., 2004). As a result, attention has been focused on the interaction between Pu and bentonite colloids (Huber et al., 2011; Missana et al., 2008). Previous work on FEBEX bentonite has shown that colloids with a hydrodynamic size of 250 ± 50 nm have an XRD pattern consistent with an aluminum-rich dioctahedral smectite with no significant impurities (Missana et al., 2004).

The sorption of Pu species to Khakassiya bentonite and SWy-1 montmorillonite has been found to exhibit pH and ionic strength dependency, indicating that both ion-exchange and surface complexation processes are occurring (Sabodina et al., 2006; Zavarin et al., 2012). However, surface complexation processes will dominate at neutral to alkaline pHs. Smectite minerals have been shown to have a high sorption affinity for Pu. For example, Pu(V) partitioning to Yucca Mountain tuffs found a ubiquitous and preferential association of Pu with smectite minerals (Vaniman et al., 1995). Further, Pu(IV) K_d values from 10,000 to 40,000 mL g^{-1} have been reported for smectite-rich sediments from Lithuania in the pH range 5 to 12 (Lujaniene et al., 2007). Missana et al. (2008) studied the sorption of Pu(IV) to FEBEX bentonite *colloids* (>99% smectite) at pH 9.5 and reported log K_d values of 5.37 ± 0.18. Pu(IV) sorption to FEBEX bentonite *colloids* under anaerobic conditions at pH 9.6, resulted in log R_d values (a term equivalent to K_d but without the assumption of equilibrium) of 5 and 5.9 after one and three weeks of sorption time, respectively (Nagra, 2006). The increase in R_d values with time was attributed to the presence of a small amount (~ 5 %) of Pu(VI) in the spike solution which was slowly reduced to Pu(IV) on the mineral surface (Nagra, 2006).

In a recent study, we examined the long term sorption behavior of Pu(IV) and Pu(V) on SWy-1 Na-montmorillonite under aerobic conditions. After 30 d equilibration, calculated log K_d values for Pu(IV) and Pu(V) were 4.25 ± 0.15 and 3.57 ± 0.18, respectively (Begg et al., 2013). However, following one year of equilibration, calculated log K_d values in the Pu(V) experiments had increased to 4.32 ± 0.15, similar to those calculated for Pu(IV) after 30 d. The convergence of K_d values for Pu(IV) and Pu(V) was attributed to the slow reduction of Pu(V) on the montmorillonite surface causing increased uptake of Pu(V). This finding highlights the need to ensure that experimental studies used to inform predictive transport models accurately encapsulate long term environmental behaviors.

Several recent studies have indicated that actinide concentration can affect their sorption to mineral surfaces (Hixon and Powell, 2014; Missana et al., 2008; Snow et al., 2013). In the case of Pu(IV), its low solubility at circumneutral pH means that sorption may demonstrate an apparent concentration dependence as solubility limits are reached. For example, the study of Pu(IV) sorption to bentonite colloids (>99% smectite) observed that sorption was linear for initial Pu concentrations of $1 \times 10^{-8} - 1 \times 10^{-7}$ M but at higher concentrations precipitation of Pu was evidenced by a sharp increase in the isotherm slope (Missana et al., 2008). Concentration dependent sorption behavior may also be observed at low actinide concentrations: work with goethite and Np(V) found that K_d values differed by an order of magnitude at solution concentrations below 10^{-11} M compared to higher concentrations. This behavior was attributed to the existence of different adsorption sites on the mineral with different adsorption affinities for

Np (Snow et al., 2013). These examples of concentration dependent behavior of actinides indicate that there may be a difference between the sorption behavior of Pu at the concentrations found in contaminated subsurface waters (10^{-12}–10^{-20} M) (Dai et al., 2005; Kersting et al., 1999; Novikov et al., 2006; Penrose et al., 1990) and concentrations typically used in laboratory experiments (10^{-7}–10^{-11} M Pu). Although a primary assumption of reactive transport models, the validity of extrapolating Pu-mineral sorption behavior from relatively high concentration laboratory experiments to the low concentrations found in many field settings has not been widely tested. Pu desorption reactions have been far less well studied than sorption reactions. This is problematic because application of thermodynamic equilibrium parameters in field transport models which incorrectly represent desorption processes are likely to be flawed (Artinger et al., 2002). One of the pertinent issues for Pu, especially given the evidence that its mobility may be enhanced by mineral-colloid facilitated transport, is whether there is equality in sorption and desorption behavior (Kersting et al., 1999). Differences in behavior may be caused by aging processes, hysteresis effects, and irreversible sorption, amongst others (Tinnacher et al., 2011). A study of Pu(IV) sorption to Callovo-Oxfordian argillite found that after seven days' desorption, Pu K_d values were of the same order of magnitude as they were following a seventy four day adsorption period, indicating sorption reversibility (Latrille et al., 2006). Similarly, Lu et al. (2003) investigated Pu interaction with montmorillonite and found that with a 20 day adsorption period and a 32 day desorption period, similar K_d values were obtained for both adsorption and desorption steps.

The aim of the current work is two-fold: to provide information on Pu sorption/desorption to/from industrial grade FEBEX bentonite, a potential repository backfill material, and to determine if the linearity observed for Pu(V) sorption to a pure Na-montmorillonite (Begg et al., 2013) extends to Pu(IV) sorption to a multi-component clay rock material. We investigate the sorption behavior of Pu(IV) to FEBEX bentonite across a wide range of initial concentrations (10^{-7}–10^{-16} M) over a 120 d period. In addition, we perform long term (10 month) sorption experiments with Pu(V) to compare with the slow apparent rates of reduction previously observed for Pu(V) on montmorillonite (Begg et al., 2013). The results of these experiments demonstrate the apparent control that the montmorillonite component in bentonite exerts on the sorption behavior of Pu, provides long term sorption data for industrial grade FEBEX bentonite, and validates the extrapolation of Pu(IV) experiments performed at concentrations of 10^{-9}–10^{-11} M Pu to much lower concentrations typically found in the environment at timescales relevant for groundwater transport.

6.2   MATERIALS AND METHODS

6.2.1   Bentonite Preparation

Unless stated otherwise, all solutions were prepared using ultrapure water (Milli-Q Gradient System, >18 MΩ·cm) and ACS grade chemicals without further purification. The FEBEX bentonite was ground in a mortar and pestle and sieved to <63 μm to minimize clay heterogeneity. The clay was then homo-ionized in 1 M NaCl solution for 7 days and dialyzed in MQ H_2O to remove excess salts. As experiments were performed to characterize the behavior of Pu in the presence of bulk bentonite, no further treatment was performed. A portion of the bentonite suspension was dried, the clay lightly ground, and its surface area measured ($N_2(g)$-BET Quadrasorb SI). The surface area of the prepared bentonite was 25.2 ± 1.0 $m^2\,g^{-1}$.

The solids were re-suspended in a 0.7 mM $NaHCO_3$/5 mM NaCl buffer solution (pH 8) to make a suspension with a bentonite concentration of ~ 5 g L^{-1}. This buffer solution was chosen so as to

allow comparison with previous experiments performed with SWy-1 Na-montmorillonite (Begg et al., 2013). Gravimetric analysis of the dried mass of the solid in triplicate 5 mL aliquots of the suspension returned a standard error of 1.2%, indicating homogeneity in the stock suspension and providing confidence in the amount of solid added to experiments. The stock suspension was allowed to equilibrate under aerobic conditions for several days prior to the start of sorption experiments.

6.2.2   Pu Stock Solutions

Three different Pu stock solutions were used in the sorption experiments in order to facilitate measurement over the wide range of Pu concentrations investigated. A ^{242}Pu stock (15.8% ^{238}Pu, 5.1% $^{239+240}$Pu, 79.1% ^{242}Pu by activity) and a ^{238}Pu stock (98.8% ^{238}Pu, 0.11% ^{241}Pu, and 0.1% ^{239}Pu by activity) were used in experiments with initial concentrations of 10^{-7}–10^{-11} M. A New Brunswick Laboratory (NBL) Pu reference material CRM-137 (33.5% ^{238}Pu, 35.3% ^{239}Pu, 31.3% ^{240}Pu by activity) was used in experiments with initial Pu concentrations $\leq 10^{-11}$ M. A table of the different stocks used, including their oxidation state, where measured, is given in the Appendix Table A1.

The Pu stock solutions were purified using anion exchange resin (BioRad AG 1 × 8, 100-200 mesh) pre-conditioned with 8 M HNO$_3$. Prior to loading on the resin, Pu was reacted with NaNO$_2$ to reduce it to Pu(IV). The Pu was loaded on the resin in 8 M HNO$_3$, washed with 3 column volumes of 8 M HNO$_3$, and then eluted in 1 M or 0.1 M HCl (Powell et al., 2011). For experiments using Pu(IV), the oxidation state of the Pu stocks was checked with a LaF$_3$ precipitation method (Kobashi and Choppin, 1988) and found to be > 92% Pu(III)/(IV) (Table A1). Subsequent stock dilutions were made using 0.1 M HCl, with select analysis indicating that this did not significantly alter the oxidation state of the Pu. For experiments starting with Pu(V), the Pu(IV) stripped from the columns was converted to Pu(VI) either electrochemically (^{242}Pu stocks) or by heating in HNO$_3$ (^{238}Pu stocks), adjusting to pH 3 with NaOH, spiking with 0.05 M hydrogen peroxide and gently heating to produce Pu(V). To remove any Pu(VI) remaining in solution, the stocks were diluted in 0.7 mM NaHCO$_3$/5 mM NaCl buffer solution to achieve a circumneutral pH and contacted with 10 g/L high surface area SiO$_2$, which will preferentially adsorb Pu(VI), before being phase separated for use in experiments (Orlandini et al., 1986). Pu(V) stocks were <3% Pu(III)/(IV) by LaF$_3$ precipitation. Final Pu concentration in the stock solutions was determined by liquid scintillation counting (LSC; Packard Tri-Carb TR2900 LSA and Ultima Gold cocktail).

6.2.3   Plutonium Batch Sorption Experiments

Sorption experiments were performed over a wide range of initial Pu(IV) concentrations (10^{-7}–10^{-16} M). In the following description we use the nominal terms *high concentration* to refer to experiments initially spiked to Pu concentrations of 10^{-7}–10^{-11} M and *low concentration* for experiments initially spiked to Pu concentrations of 10^{-11}–10^{-16} M. The two types of experiments were performed in separate laboratories in order to minimize any potential contamination of the *low concentration* samples.

All Pu(IV) and Pu(V) batch sorption experiments were performed under air in 0.7 mM NaHCO$_3$/5 mM NaCl buffer solution (pH 8) with 1 g L^{-1} FEBEX bentonite. These experimental conditions were chosen to achieve consistency with previous experiments using SWy-1 Na-montmorillonite (Begg et al., 2013). Pu(IV) and Pu(V) aqueous speciation for initial Pu concentrations of 10^{-10} M in the buffer solution were calculated using the Geochemist's

Workbench family of codes and thermodynamic data from Guillaumont et al. (2003a). The results are shown in Appendix Figure A1. Batch experiments were conducted in either 50 mL Nalgene Oak Ridge polycarbonate centrifuge tubes (*high concentration*) or 500 mL Nalgene bottles (*low concentration*). Higher volumes were required in *low concentration* experiments to achieve the low detection limits afforded by accelerator mass spectrometry (AMS). Pu(IV) sorption experiments were performed at *low concentrations* and *high concentrations*, while Pu(V) experiments were performed only at *high concentrations*. For Pu(IV) experiments, where the Pu stock was in 0.1 M HCl, dilute NaOH was added to the samples immediately prior to spiking in order to neutralize the acidity associated with the Pu(IV) spike. This was not necessary for Pu(V) experiments where the pH of the stock was circumneutral. Bentonite blanks (with no Pu) and Pu spiked blanks (with no bentonite; select concentrations) were run in parallel. The results of the mineral free experiments are included in the Appendix. The pH of each experiment was checked (Orion 920A with calibrated electrode) and adjusted to pH 8.0 ± 0.2 using dilute NaOH or HCl within 10 minutes of spiking. Measurement of pH over the course of the experiments indicated that the drift in pH was less than 0.2 pH units. Samples were placed on an orbital shaker at 125 rpm at room temperature for the duration of the experiment. Experiments were kept in the dark in order to minimize photo-catalyzed reactions that may directly or indirectly affect the redox speciation of Pu (Mccubbin and Leonard, 1996; Powell et al., 2005).

At each time point, samples were centrifuged to achieve a 50 nm size cut off. No further attempts at size fractionation were made. We note that centrifugation can potentially remove not only Pu sorbed on bentonite but also any Pu precipitates with a particle size greater than 50 nm. Thus, the apparent sorption determined based on centrifugation could, in fact, represent a combination of Pu sorption, Pu precipitation, as well as Pu surface precipitation on the bentonite particle surfaces. However, in the *low concentration* experiments, we consider the formation of Pu precipitates/polymers to be thermodynamically unfavorable. For *high concentration* samples, aliquots of both the suspension and the supernatant were removed and counted via LSC. In *low concentration* experiments, aliquots of supernatant were acidified to 2% HNO_3 and analyzed using AMS (10-MeV tandem accelerator at the Center for Accelerator Mass Spectrometry (CAMS), Lawrence Livermore National Laboratory, CA). AMS is an ultra-sensitive analytical technique that can quantify long-lived radionuclides at ultra-low concentrations and routinely achieves instrumental backgrounds of 10^5 atoms for actinide elements (Marchetti et al., 2005). AMS analysis has been reported previously and included isotope dilution using a non-isobarically interfering isotope of ^{242}Pu (99.99% ^{242}Pu) (Marchetti et al., 2005).

6.2.4   Plutonium Desorption Flow Cell Experiments

A stirred flow cell experiment was performed at pH 8 to examine the desorption of Pu(IV) from bentonite. The flow cell set up was similar to that described previously for Np(V) and goethite and Pu(IV) and goethite (Begg et al., 2014; Tinnacher et al., 2011). The flow cell was made of Teflon®, with a 20 mL hemispherical chamber and fitted with a 100 nm pore size Millipore polycarbonate filter. A diagram of the flow cell is shown in Appendix Figure A2. Prior to use, the cell was washed with 10% HCl and MQ water. To sorb Pu on the clay, Pu(IV) at 3×10^{-10} M was equilibrated with 1 g L^{-1} bentonite for 21 days. After this equilibration period, an aliquot of the spiked suspension was centrifuged (25 000 $\times$ *g*, 2 h; 50 nm cut-off) and the concentration of the Pu in the supernatant measured. A 20 mL aliquot of bentonite suspension was loaded into the flow cell with a stir bar included to ensure ideal mixing conditions. In previous flow cell work with SWy-1 Na-montmorillonite, ^{3}H was used as a conservative tracer to test if ideal mixing conditions existed. A plot of the decline in ^{3}H concentration and a theoretical non-reactive species

is shown in Appendix Figure A3. The similarity between the calculated and observed curves demonstrates that the flow cell experiment is ideally mixed when the stir bar is operational.

Atmosphere-equilibrated, Pu free, 0.7 mM $NaHCO_3$/5 mM NaCl buffer solution at pH 8 was flowed through the cell at an initial rate of 0.4 mL min^{-1} (average retention time of ~ 50 minutes). Effluent fractions were collected on a Spectra/Chrom CF-1 fraction collector and the volumes determined gravimetrically. Periodic pH measurements of the effluent were performed to ensure that the experiment remained at pH 8. Collected fractions were acidified with 2% HNO_3 prior to Pu analysis. Pu concentration in the effluent fractions was determined via liquid scintillation counting. The total timescale of the flow cell experiment was 12 days.

6.3   RESULTS AND DISCUSSION

6.3.1   Pu(IV) Sorption to Bentonite

The sorption of Pu(IV) to bentonite was studied over an initial Pu concentration range of 10^{-7}–10^{-16} M. The resulting sorption isotherm after 120 d equilibration is shown in Figure 6-1. To determine if sorption equilibrium was achieved in the experiment, samples at 10^{-10} and 10^{-7} M were sampled after 67 d, 100 d and 120 d. The results of this sampling are shown in the inset in Figure 6-1. The similarity in the aqueous Pu concentrations at 100 d and 120 d versus 67 d indicate that sorption equilibrium was reached by 120 d. The slow approach to sorption equilibrium is consistent with previous studies on Pu(IV) sorption to clay and may reflect the presence of small amounts of Pu(V) in the initial stock solution, although we cannot discount other aging processes such as Pu polymerization/precipitation reactions, particularly in the higher concentration sample (Begg et al., 2013; Nagra, 2006). Furthermore, unintended changes in Pu oxidation state may be exacerbated when an acidic Pu(IV) stock is spiked into a circumneutral pH solution under oxic conditions. In the Appendix, Figure A4 shows oxidation state analysis of a parallel experiment where a mineral-free, pH 8 solution was spiked with a >97% Pu(III)/(IV) stock solution (4.48×10^{-7} M) to a concentration of 3×10^{-10} M. Both LaF_3 and solvent extraction analysis of the aqueous Pu indicate that 1 h after spiking, approximately 30% of the Pu(III)/(IV) had been oxidized to Pu(V)/(VI). LaF_3 analysis over 6 d showed no appreciable change in Pu oxidation state from the 1 h values while no significant Pu was lost from solution over this short time period.
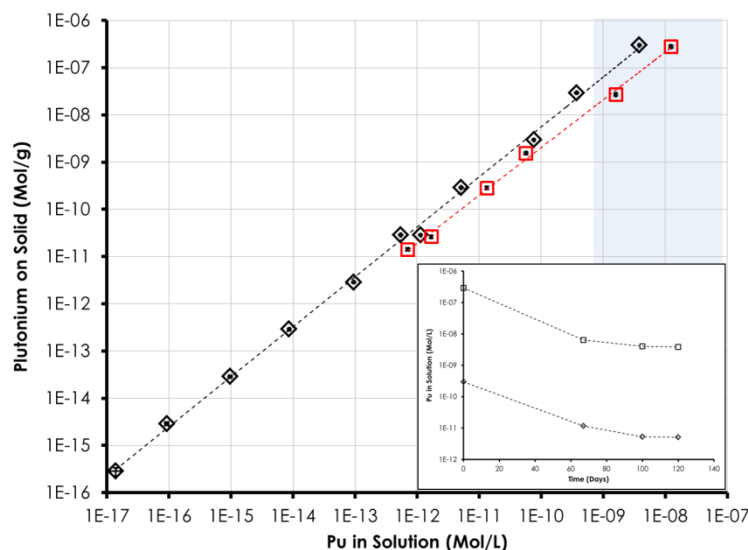
Figure 6-1: 120 d Pu(IV) sorption isotherm for FEBEX bentonite (1 g L^{-1}) in 0.7 mM NaHCO$_3$, 5 mM NaCl buffer solution at pH 8 (black diamonds). Inset shows time series data for experiments at 10^{-7} and 10^{-10} M initial Pu(IV) to indicate apparent adsorption equilibrium at 120 d. Also shown are data for 30 d Pu(IV) adsorption isotherm for SWy-1 Na-montmorillonite (1 g L^{-1}) in 0.7 mM NaHCO$_3$, 5 mM NaCl buffer solution at pH 8 (red squares) (Begg et al., 2013). Lines are shown to guide the eye only. Blue shaded area represents expected concentration for Pu(IV) colloid formation (Neck et al., 2007c). Error bars based on LSC counting uncertainties (1σ) for bentonite experiments and 1σ for quadruplicate montmorillonite experiments are within range of the symbols used.

After 120 d equilibration, the sorption of Pu(IV) to bentonite was broadly linear over the ten orders of magnitude concentration range tested (Figure 6-1). Our result shows that on timescales of months, Pu(IV) exhibits similar apparent sorption behavior to bentonite at the higher concentrations used in typical laboratory experiments (10^{-7}–10^{-11} M) as it does at concentrations typically found in contaminated environments ($\leq$10^{-12} M). This result complements previously published linear sorption behavior observed for Pu(V) on SWy-1 Na-montmorillonite over a similar Pu concentration range (Begg et al., 2013). A log-log slope for Pu(IV) sorption to bentonite was calculated and found to be 1.06 ± 0.01 (1 S.E.). A value greater than 1 suggests that surface precipitation (or, indeed, bulk precipitation in our case) of Pu may be occurring (Dzombak and Morel, 1993). The expected concentration range for Pu(IV) intrinsic colloid formation at pH 8 is highlighted in blue in Figure 6-1 (Neck et al., 2007c). The highest two concentrations used in the current isotherm experiment fall within the expected range for Pu(IV) colloid formation (Neck et al., 2007c). Thus the isotherm slope, in combination with the known solubility of Pu(IV) suggest that surface polymerization/precipitation/surface precipitation processes are occurring in the two highest Pu concentration samples (initial Pu(IV) 10^{-7} and 10^{-8} M) (Neck et al., 2007c). This is consistent with Pu-goethite sorption data of Kersting et al. (2011) that exhibited substantial Pu precipitation effects only above 10^{-8} M Pu. Although the effects of precipitation/polymerization appear to be relatively small when examined across 10 orders of magnitude in Pu concentration and on a log scale, they may nonetheless affect the

sorption behavior of Pu. Accordingly, we recommend that future experiments investigating Pu(IV) environmental *ad*sorption behavior are performed at concentrations $<10^{-9}$ M.

As the isotherm slope is close to unity, sorption can be considered Langmuirian in behavior. However, unlike traditional Langmuir plots which exhibit a flattening of the isotherm as mineral surface sites become saturated, the data remain largely linear at higher concentrations. Previously, Missana and Garcia-Gutierrez (2007) calculated the strong site concentration on bentonite colloids to be 6.1×10^{-8} mol m^{-2}. Given that the experiments were performed with 1 g L^{-1} clay with a surface area of 25 m^2 g^{-1} this would suggest a strong site concentration of 1.54×10^{-6} mol L^{-1} which exceeds the highest Pu concentration used (10^{-7} M). As a result, strong site saturation effects are not expected or observed in our experiments. Indeed, we suggest that polymerization/precipitation/surface precipitation effects will become prominent before saturation of strong sites occurs.

Previous work with Pu(IV) and hematite has identified a concentration dependence to the rate of Pu(IV) sorption over a 2 d period (Romanchuk et al., 2011). A one-step, fast adsorption was seen in experiments with 10^{-14} M Pu compared to a two-step adsorption (fast initial sorption followed by slower uptake) at 10^{-10} M Pu. The fast sorption step was attributed to the adsorption of monomeric Pu(IV) while the slower step was hypothesized to be caused either by diffusion to micropores in the mineral or by the formation of polymeric Pu(IV) species (Romanchuk et al., 2011). Our current work with clays indicates that regardless of initial sorption rates, the apparent extent of Pu(IV) sorption to bentonite appears broadly independent of initial concentration for the 10^{-7}–10^{-16} M range on timescales relevant to groundwater transport scenarios. However, some small signs of Pu precipitation are present in our highest concentration samples and the importance of such reactions is acknowledged.

Log K$_d$ values from the Pu(IV) bentonite sorption isotherm at 120 d range from 4.3 – 4.9 mL/g. There was a slight increase in calculated log K$_d$ values as a function of Pu(IV) concentration. We attribute this to Pu(IV) intrinsic colloid formation and/or other precipitation processes at the higher concentrations, as discussed previously, rather than the result of concentration-dependent, high sorption affinity sites on the clay (that would exhibit an inverse relationship between K$_d$ and Pu(IV) concentration). The log K$_d$ values observed in this experiment are lower than values for Pu(IV) sorption to bentonite colloids of 5-5.9 measured by Geckeis et al. (2004) and 5.39 ± 0.18 measured by Missana et al. (2008). However, these previous experiments were performed at pH 9.5 – 9.6, used bentonite colloids of ~200 - 280 nm (which are expected to be entirely composed of montmorillonite) and were performed under anaerobic conditions (Huber et al., 2011). The K$_d$ values observed here likely reflect the contribution of Pu(V), which sorbs weakly to montmorillonite and reduces slowly to Pu(IV) under aerobic conditions (Zavarin et al., 2012). Anaerobic conditions expected in certain repository scenarios are likely to promote greater Pu(IV) stability relative to the aerobic conditions examined herein.

Also shown in Figure 6-1 is the 30 d sorption isotherm for Pu(IV) on SWy-1 Na-montmorillonite previously reported in Begg et al. (1982). Comparison of the Pu(IV) sorption isotherms for montmorillonite and bentonite shows they are very similar in terms of slope and the extent of Pu sorption. These results show that Pu sorption by a bulk bentonite (92% montmorillonite) is comparable to sorption to pure montmorillonite. However, a slightly higher sorption affinity of Pu(IV) for bentonite than montmorillonite is observed and is more marked at the two highest Pu concentrations. Given that the current work suggests that sorption equilibrium is not achieved until after 67 d (Figure 6-1 inset), we suggest that this difference is in part due to the different equilibration period in the two experiments: 30 d for montmorillonite and 120 d for bentonite.

Indeed, interpolation of bentonite K_d values for the experiment at 10^{-10} M Pu(IV) suggests a 30 d log K_d of 4.1 compared to 4.3 in the equivalent montmorillonite experiment.

6.3.2   Pu(V) Sorption to Bentonite

The sorption rate of Pu(V) to FEBEX bentonite was studied in triplicate over a 30 day period using an initial concentration of 10^{-10} M (Figure 6-2). Also plotted in Figure 6-2 is the sorption of Pu(V) to SWy-1 Na-montmorillonite at an initial concentration of 10^{-9} M reported previously (Begg et al., 2013). Both sorption plots show a similar time dependence, suggesting that the montmorillonite component of the bentonite controls the sorption of Pu(V). The sorption of Pu(V) by bentonite shows an initial rapid uptake with 49.5% $\pm$ 0.7 % removed in the first 48 h. This is followed by a slower uptake over the rest of the experiment with 13.4 $\pm$ 1.6 % Pu remaining in solution at 30 d. Applying the first order rate model previously used to describe Pu(V) sorption to SWy-1 montmorillonite to the bentonite-Pu(V) sorption data leads to a surface area normalized sorption rate of $10^{-3.5}$ L m^{-2} h^{-1} which compares quite favorably with $10^{-2.8}$ L m^{-2} h^{-1} calculated for montmorillonite (Begg et al., 2013).
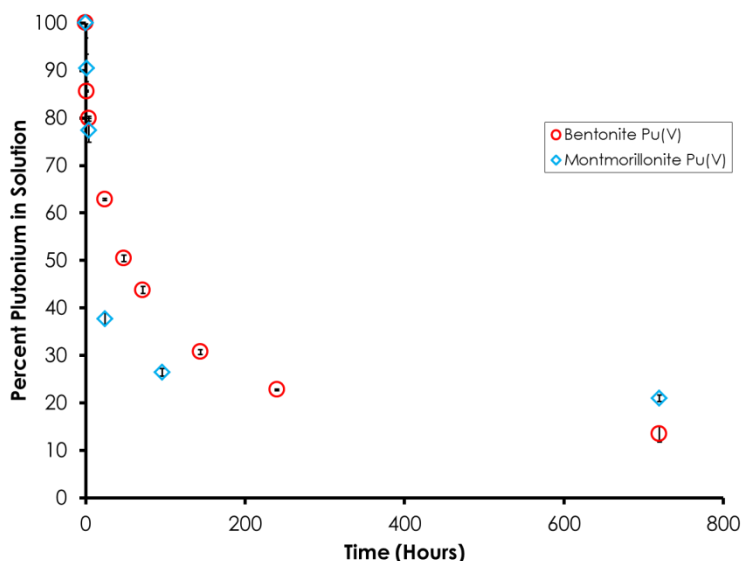
Figure 6-2: Sorption of Pu(V) to FEBEX bentonite (1 g L^{-1}; red circles) and SWy-1 Na-montmorillonite (1 g L^{-1}; blue diamonds) plotted as percentage of Pu removed from solution vs time. Initial Pu concentrations were 10^{-10} M for bentonite and 10^{-9} M for montmorillonite. Error bars based on 1σ for triplicate bentonite experiments and 1σ for quadruplicate montmorillonite experiments.

The long-term (greater than 30 d) sorption of Pu(V) to bentonite was also studied over an initial concentration range of 10^{-7}–10^{-11} M Pu. Samples were analyzed after 30, 120 and 300 d. At 30 days, the isotherm appears linear on a log-log plot with slope of 0.92 $\pm$ 0.03 (Figure 6-3). However, the slope of 0.92 indicates that sorption is, in fact, non-linear and appears to exhibit a Freundlich behavior (i.e. S = K_fC^n with n = 0.92). However, as these data do not reflect an equilibrium state and sorption is affected by surface mediated reduction rates, the apparent non-linearity most likely reflects a concentration dependence on the surface mediated reduction of

Pu(V). This is consistent with the findings of Hixon and Powell (2014) who observed a concentration rate dependence for Pu(V) reduction on hematite between 10^{-8} and 10^{-6} M. At 120 d, the isotherm is truly linear with a log-log slope of 1.03 ± 0.03. Further, the position of the isotherm has shifted between the two time points, indicating that sorption of Pu from the aqueous phase has continued over the time period between 30 d and 120 d. At 300 d, the isotherm is linear (1.02 ± 0.001), with a further small shift in position relative to the 120 d isotherm.
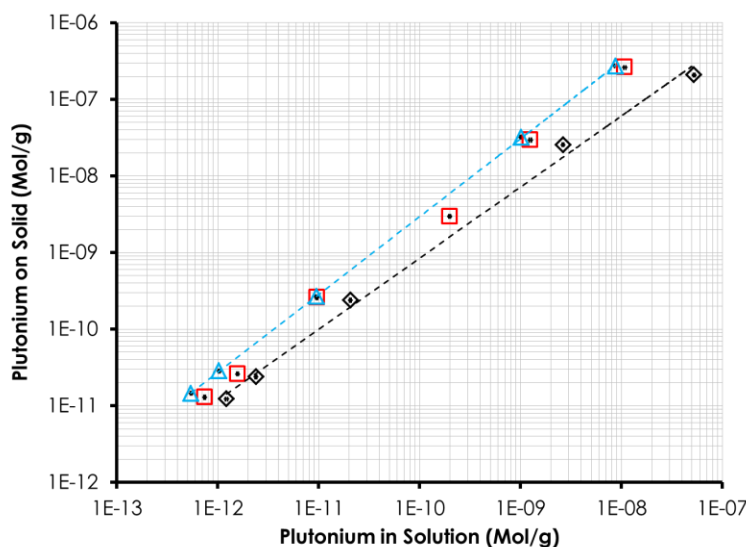
Figure 6-3: Pu(V) sorption isotherm for FEBEX bentonite (1 g L^{-1}) in 0.7 mM NaHCO$_3$, 5 mM NaCl buffer solution at pH 8. Different symbols represent sampling at different time points: 30 d (black diamonds), 120 d (red squares), 300 d (blue triangles). Lines are to guide the eye only. Error bars based on LSC counting uncertainties (1σ) are within range of symbols used.

The Pu(V) sorption data for 30 d and 300 d is compared to the 120 d Pu(IV) sorption data in Figure 6-4. Over the course of the experiment, the position of the Pu(V) sorption data moves towards the 120 d Pu(IV) sorption data. This observation is consistent with the idea that kinetically limited reduction of Pu(V) on the mineral surface is responsible for the slow, continued uptake of Pu(V) (Begg et al., 2013). Log K_d values for Pu(V) sorption to bentonite after 300 days were 4.42 ± 0.03. The similarity of the K_d values of both Pu(IV) and Pu(V) over these long timescales demonstrates a convergence of the sorption behavior of Pu on bentonite regardless of initial oxidation state.
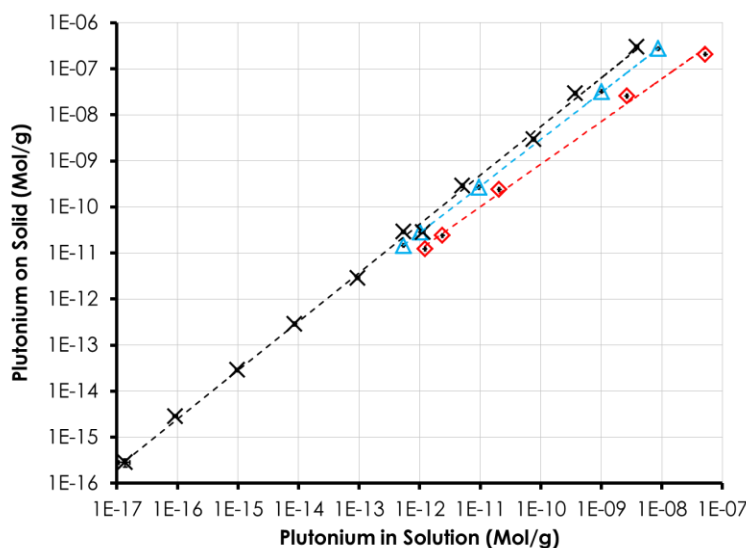
Figure 6-4: Sorption of Pu(V) to FEBEX bentonite (1 g L^{-1}, pH 8) at 30 d (red diamonds) and 300 d (blue triangles), compared with Pu(IV) sorption to FEBEX bentonite (1 g L^{-1}, pH 8) at 120 d (black crosses). Lines are to guide the eye only. Error bars based on LSC counting uncertainties (1σ) are within range of symbols used.

By assuming that the slow uptake of Pu from solution seen in the Pu(V) isotherm was due to the slow reduction of Pu(V) on the clay surface, the data from the 30 d, 120 d, and 300 d time points were used to estimate the apparent reduction rate. By using these last three data points, we hope to better isolate the reduction process from the early time sorption of Pu(V) (Begg et al., 2013). Apparent first order reduction rates were calculated from the slope of the plot of ln(C) versus time. The average surface normalized apparent reduction rate for these experiments was $10^{-5.3\pm1.3}$ L m^{-2} h^{-1}. Interestingly, when the same calculation was applied to the Pu(IV) data collected at 10^{-10} M for 67, 100 and 120 d, the calculated rate was $10^{-4.6\pm0.7}$ L m^{-2} h^{-1}. The similarity between the values further suggests that the long term uptake observed in Pu(IV) experiments was due to reduction of residual Pu(V) in solution.

The oxidation state of Pu in solution was monitored for bentonite experiments performed at 10^{-10} M and 10^{-8} M Pu(V) using LaF$_3$ precipitation (Appendix Figure A5). In both experiments, the percentage of Pu(V)/(VI) in solution declined between 30 and 120 days. At 300 d, the percent Pu(V)/(VI) in solution was ~33 at both 10^{-10} M and 10^{-8} M, respectively. In contrast, in mineral free Pu(V) experiments, LaF$_3$ analysis showed that the Pu remaining in solution after 300 days was dominated by Pu(V)/(VI) (96 ± 10% and 75 ± 18% for experiments at 10^{-10} and 10^{-8} M, respectively). This difference in oxidation state indicates that interaction of Pu(V) with mineral surfaces results not only in surface mediated reduction of Pu(V) but also leads to a difference in oxidation state distribution in solution. This change in the oxidation state of solution Pu in the presence of bentonite indicates that a solid:solution sorption equilibrium is established with respect to both Pu(V) and Pu(IV) under the present experimental conditions. This is in accordance with the recently proposed model for Pu(V) oxidation state distribution in the solid/aqueous phase following sorption on Savannah River sediments (Powell et al., 2014).

6.3.3   Desorption of Pu from Bentonite

A flow cell experiment was performed to investigate the desorption of Pu from bentonite. Prior to desorption, Pu(IV) at an initial concentration of 3×10^{-10} M was equilibrated with 1 g L^{-1} bentonite in 0.7 mM NaHCO$_3$/5 mM NaCl buffer solution at pH 8 for 21 days under aerobic conditions. After this period, the calculated log K$_d$ for Pu(IV) sorption was 4.1, which is consistent with the sorption behavior of the Pu(IV) isotherm experiment performed at 10^{-10} M (4.4 at 67 d, 4.8 at 120 d).

The desorption of Pu from bentonite is plotted in terms of the cumulative fraction of total Pu desorbed in Figure 6-5. Also included in this plot are the data from a parallel experiment at pH 8 performed with SWy-1 Na-montmorillonite. Much (but not all) of the sharp increase in the cumulative desorbed Pu between 0 and ~ 2.5 chamber volumes (cv) in both plots represents removal of aqueous Pu remaining in solution following the sorption period. This Pu is displaced from the flow cell over the course of several cv (i.e. tailing). Comparison of a theoretical non-reactive tracer dilution curve under the initial flow conditions with the observed Pu concentrations in the bentonite experiment shows that the two curves begin to deviate within 1.2 cv (Appendix Figure A6). The deviation demonstrates an excess of Pu in the effluent from that which would be expected by dilution alone, indicating that Pu desorption from bentonite contributes significantly to the overall Pu breakthrough after just one chamber volume.
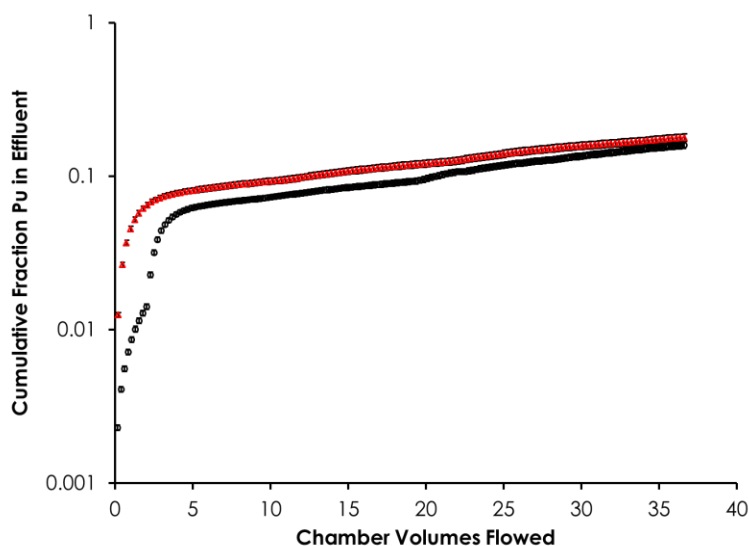

Figure 6-5: Cumulative fraction of Pu removed from bentonite (black circles) and montmorillonite (red triangles) flow cell experiments. Error bars based on LSC counting uncertainties (1σ) are within range of symbols used.

Both the shape of the plots and the final amounts of Pu desorbed are very similar for FEBEX bentonite and SWy-1 montmorillonite. This behavior is not unexpected in the context of the similarity of Pu sorption behavior between bentonite and montmorillonite. This plot further suggests that it is the montmorillonite component of the FEBEX bentonite that is controlling the desorption behavior of Pu in this experiment. The slope of the cumulative desorption plot for both

bentonite and montmorillonite continues to rise over the duration of the experiment, indicating that Pu is still being desorbed from the mineral surfaces at the termination of the flow period.

We calculated an apparent log K_d at the end of the flow cell experiment of 6.0 based on the Pu concentration in the final collected effluent fraction, accounting for the net removal of 16.5 % of the Pu from the system (Figure 6-5), and assuming no change in solid: solution ratio. This K_d value is much larger than the values in the Pu(IV) sorption experiments after 120 d equilibration (4.3 – 4.9). This indicates that on the timescale of the flow portion of the experiment (chamber residence time < 1 d) desorption of Pu appears to be rate limited. Following the cessation of the 12 d flow cell desorption experiment, the Pu-bentonite suspension was allowed to equilibrate under no-flow conditions (0.0 mL min^{-1}) for two months. After 60 d, the log K_d was calculated to be 4.8, which is in good agreement with the 120 d sorption K_d values. This similarity indicates Pu-bentonite sorption reversibility over extended time periods. The slow approach to apparent desorption equilibrium in these experiments (i.e. on timescales greater than 1 d) is consistent with previous work looking at Pu desorption from montmorillonite, bentonite colloids and argillites (Huber et al., 2011; Latrille et al., 2006; Lu et al., 2003). The slow desorption kinetics observed here highlight the need to consider both desorption rates and desorption equilibrium conditions when predicting Pu transport.

Oxidation state analysis using LaF_3 precipitation was performed on flow cell effluent during the flow period, after remnant aqueous Pu from the sorption step had been removed from the cell. The analysis indicated that the desorbed Pu was predominantly in the Pu(V)/(VI) oxidation state (90 ± 10%). This would suggest that in the short term, desorption of Pu(V) from the mineral surface is favored over Pu(IV). Further, given that Pu(IV) was initially adsorbed on the bentonite and is expected to be favored on the mineral surface, this result also suggests that the oxidation of Pu(IV) to Pu(V) is important for the desorption of Pu. However we cannot verify this without direct oxidation state analysis of Pu on the mineral surface. If Pu(IV) oxidation is involved in the desorption reaction, Pu desorption rates may be substantially lower under anoxic conditions where Pu(IV) oxidation is inhibited. Such an inhibition may further exacerbate mineral-colloid facilitated transport under anoxic repository conditions. Interestingly, oxidation state analysis of the Pu supernatant after the 2 month post flow cell equilibration period indicated that the aqueous Pu was predominantly Pu(IV). This suggests that changes in Pu oxidation state are responsible for differences in short term and long term desorption behavior of Pu from bentonite.

6.4   CONCLUSIONS

We investigated the sorption behavior of Pu(IV) to FEBEX bentonite over the concentration range 10^{-7}–10^{-16} M to determine if Pu sorption behavior at concentrations used in typical laboratory experiments (10^{-7}–10^{-11} M) was comparable to typical environmental concentrations ($\leq 10^{-12}$ M). On the timescale of months, the affinity of Pu(IV) for bentonite appears to be independent of concentration. However, slight non-linear behavior suggests that polymerization/precipitation reactions contribute to the apparent sorption at Pu(IV) concentrations $\geq 10^{-8}$ M. The sorption behavior of Pu(IV) to FEBEX bentonite is very similar to that previously observed for Pu(IV) sorption to colloidal SWy-1 Na-montmorillonite.

Pu(V) sorption to bentonite is also linear. However, Pu(V) sorption exhibits a much more significant time-dependence. The time-dependence is indicative of rate limited reduction of Pu(V) on clay minerals. The reduction rate constants determined based on these data agree with previously published reduction rates of Pu(V) on SWy-1 montmorillonite. The favorable

comparison between Pu(IV) and Pu(V) behavior in the presence of FEBEX bentonite and SWy-1 Na-montmorillonite highlights the dominant role of montorillonite phases in controlling Pu sorption/desorption reactions on FEBEX bentonite.

The kinetics of desorption will be of key importance for predicting the mobility of Pu in groundwater environments, especially if Pu is associated with colloidal mineral phases. Pu oxidation state changes appear to influence the differences in desorption behavior observed at short and long timescales. The observation that after 2 months of desorption the K_d value was similar to the K_d value observed after 21 d sorption indicates rate-limited yet truly reversible Pu sorption under these experimental conditions.

These experiments were performed under aerobic conditions and Pu(IV) reoxidation appears to play an important role in the observed desorption behavior.   Aerobic conditions may not be present in all nuclear waste repository scenarios (e.g. Duro et al., 2014). As a result, future work should build on these results by examining Pu sorption/desorption behavior across a wider range of geochemical conditions.

6.5   REFERENCES

Included in Chapter 7.

6.6   APPENDIX

Table A1.

Name	Isotopic composition		
238	98.8% ^{238}Pu 0.11% ^{241}Pu 0.1% ^{239}Pu		

Stock Concentration (M)	Medium	% Pu(III)/(IV) ± 10%	Experiment
1.05E-06	1 N HCl	92	Pu(IV) Isotherm 10^{-9}
1.09E-07	0.1 N HCl	n.d.*	Pu(IV) Isotherm 10^{-10}
1.04E-08	0.1 N HCl	100	Pu(IV) Isotherm 10^{-11}
4.48E-08	0.1 N HCl	99	Flow Cell 10^{-10}
1.15E-08	0.7 mM NaHCO$_3$, 5 mM NaCl	2	Pu(V) isotherm 10^{-9}-10^{-11}

Name	Isotopic composition		
242	15.8% ^{238}Pu 5.1% $^{239+240}$Pu 79.1% ^{242}Pu		

Stock Concentration (M)	Medium	% Pu(III)/(IV) ± 10%	Experiment
2.67E-05	0.1 N HCl	100	Pu(IV) Isotherm 10^{-7}-10^{-8}
2.29E-06	0.7 mM NaHCO$_3$, 5 mM NaCl	3	Pu(V) isotherm 10^{-7}-10^{-8}

Name	Isotopic composition		
CRM	33.5% ^{238}Pu 35.3% ^{239}Pu 31.3% ^{240}Pu		

Stock Concentration (M)	Medium	% Pu(III)/(IV) ± 10%	Experiment
2.81E-07	0.1 N HCl	97	Top stock only
3.75E-08	0.1 N HCl	98	Pu(IV) Isotherm 10^{-11}-10^{-12}
3.60E-10	0.1 N HCl	n.d	Pu(IV) Isotherm 10^{-13}-10^{-14}
3.65E-12	0.1 N HCl	n.d.	Pu(IV) Isotherm 10^{-15}-10^{-16}

* n.d. = not determined
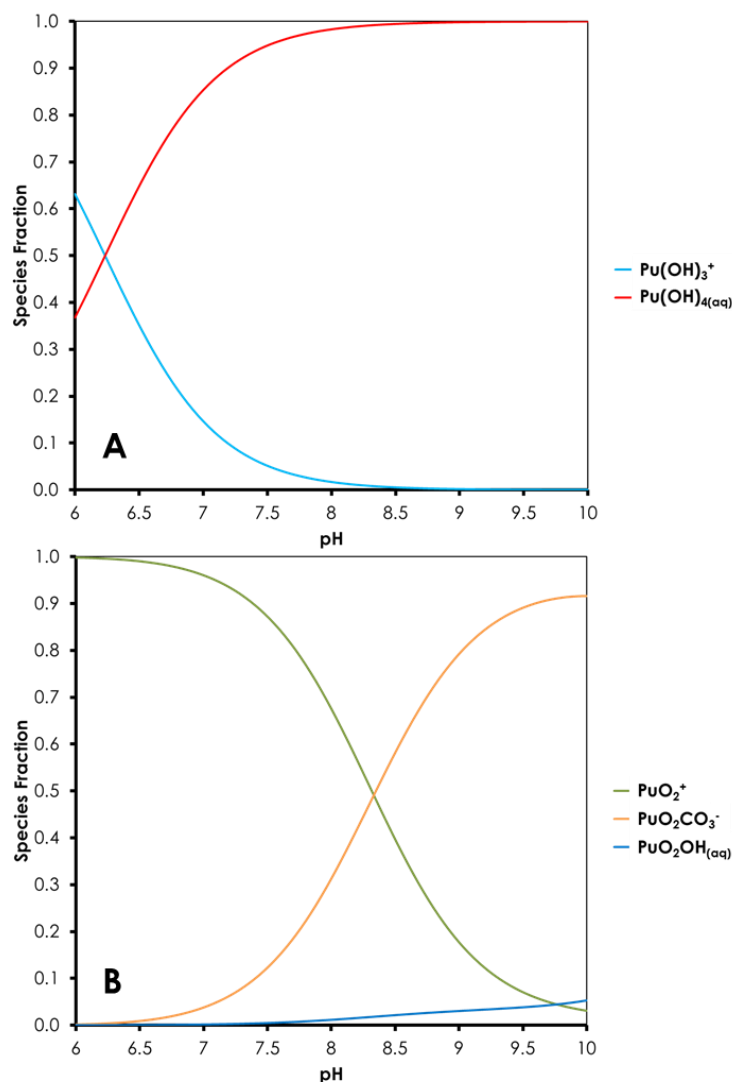
Figure A1: Predicted speciation of Pu(IV) (A) and Pu(V) (B) in experimental systems used in this study ([Pu] 10^{-10} M; 0.7 mM NaHCO$_3$, 5 mM NaCl buffer solution at pH 8). Calculations performed using thermodynamic constants from Guillaumont et al. (2003a). Other species which were accounted for but were not significant over this pH range were Pu(CO$_3$)$^{4-}$, Pu(CO$_3$)$_5^{6-}$, Pu(OH)$^{2+}$, Pu(OH)$_3^+$, Pu^{4+}, PuCl^{3+} and PuOH^{3+} for Pu(IV) and PuO$_2$(CO$_3$)$_3^{5-}$ for Pu(V). Figure modified from Figure S1 in Begg et al. (1982).

Mineral Free Experiments

Mineral free experiments were performed with initial Pu(IV) concentrations of 10^{-8}, 10^{-9} and 10^{-11} M Pu(IV). Measurement of the aqueous phase (i.e. with no centrifuging) within 1 d of spiking and again after 120 d showed that 60-75 % of Pu was lost from the bulk solution over this time period. Interestingly, LaF$_3$ analysis of the 10^{-10} M Pu(IV) mineral free experiment performed after 120 d indicated that the dominant oxidation state in the solution was Pu(V)/(VI). These results indicate that either precipitation of Pu(IV) colloids followed by sorption to container walls or sorption of monomeric Pu(IV) to container walls will occur in the absence of a mineral surface under the experimental conditions investigated. However, in the *high concentration* experiments

performed with bentonite measurement of the bulk suspension phase indicated that Pu sorption to container walls was insignificant in the presence of the mineral and that container wall sorption will not affect our measurement of Pu sorption by bentonite.

Mineral free Pu(V) experiments were performed at initial concentrations of 10^{-10} and 10^{-8} M. A loss of Pu from solution was observed in both experiments with 73% and 36% remaining in solution in the 10^{-10} M and 10^{-8} M Pu(V) experiments, respectively, after 300 d. It is likely that Pu precipitation/sorption to the container walls is responsible for this loss of Pu from solution. This is consistent with previous work that has shown the solubility of Pu(V) in natural waters at circumneutral pH to be in the range of 10^{-6} – 10^{-9} M. Further, previous work in our lab has observed similar differences in the behavior of aqueous Pu(V) in mineral free experiments at concentrations of 10^{-6} and 10^{-9} M.(Begg et al., 2013; Neck et al., 2007c; Nitsche and Edelstein, 1985; Runde et al., 2002a)
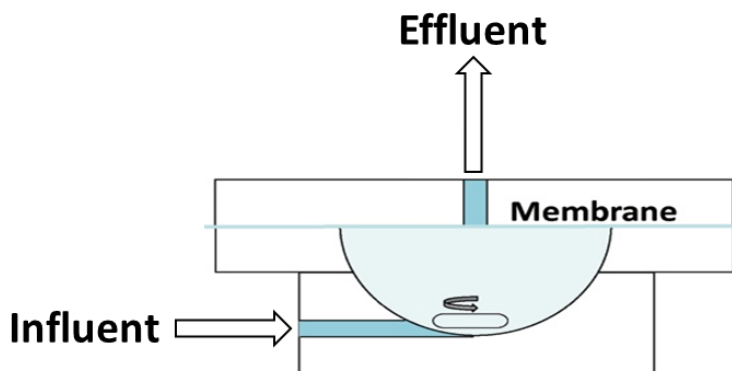
Figure A2: Flow cell set up. Cell provided by Dr Brian Powell (Environmental Engineering and Earth Sciences, Clemson University). Figure modified from Begg et al. (2014).
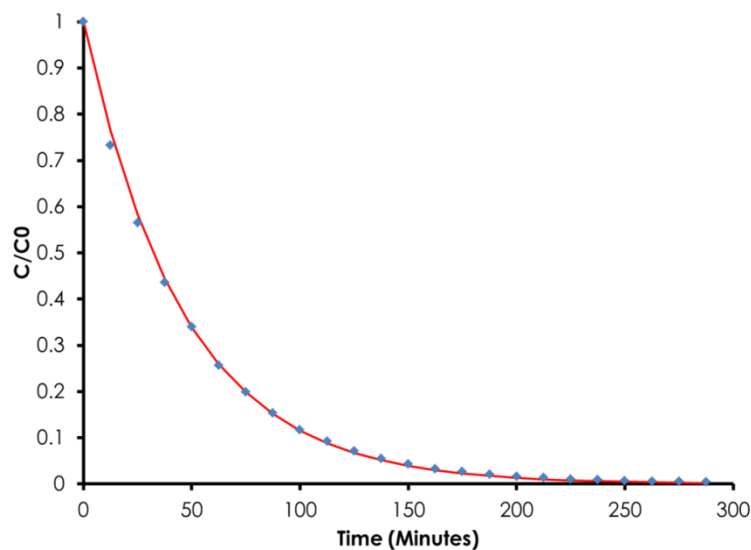
Figure A3: ^{3}H effluent profile from flow-cell experiment performed with montmorillonite. Data points represent measured fraction of ^{3}H in effluent. Solid line represents theoretical non-reactive tracer . Flow rate = 0.4 mL min^{-1}, cell volume = 20 mL.
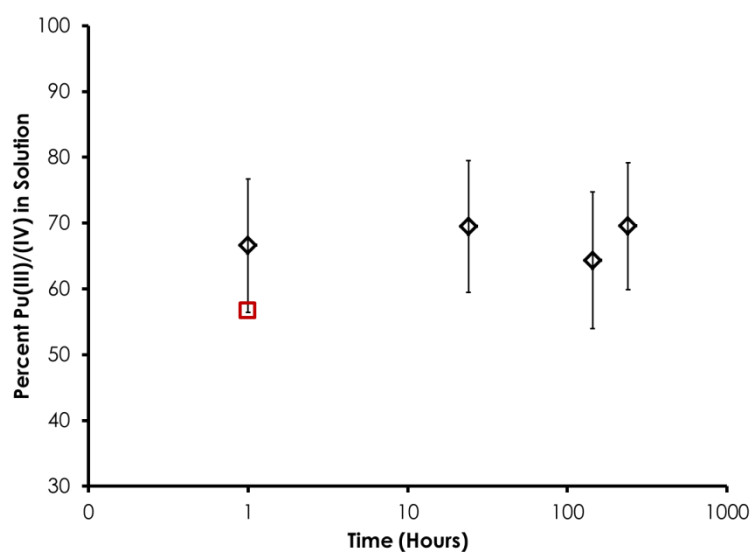

Figure A4: Percent Pu(III)/(IV) of solution Pu $(3 \times 10^{-10}$ M) in 0.7 mM NaHCO$_3$, 5 mM NaCl buffer (pH 8) as measured by LaF$_3$ precipitation (diamonds). Also shown is percent Pu(IV) in solution as measured by solvent extraction at 1 h (square). Original Pu(IV) stock solution was > 97% Pu(III)/(IV) (LaF$_3$). Error bars are an estimated absolute 10% value and are intended to reflect the difference between the solvent extraction and LaF$_3$ precipitation techniques. Note y-axis starts at 30%.
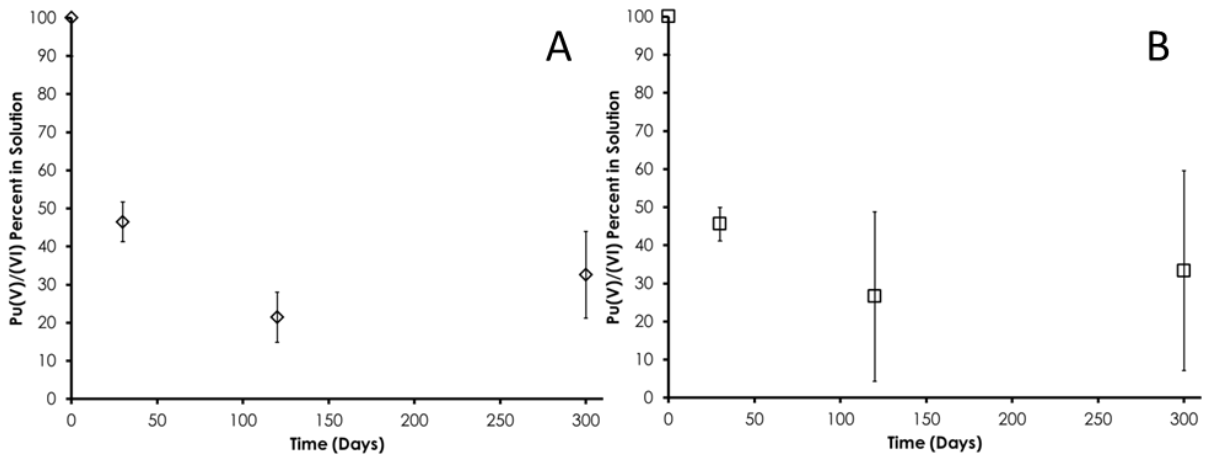
Figure A5: Changes in percent Pu(V)/(VI) in solution for Pu(V) isotherm experiments performed at initial concentrations of 10^{-10} M (A) and 10^{-8}M (B). Error bars based on LSC counting uncertainties (1☐).
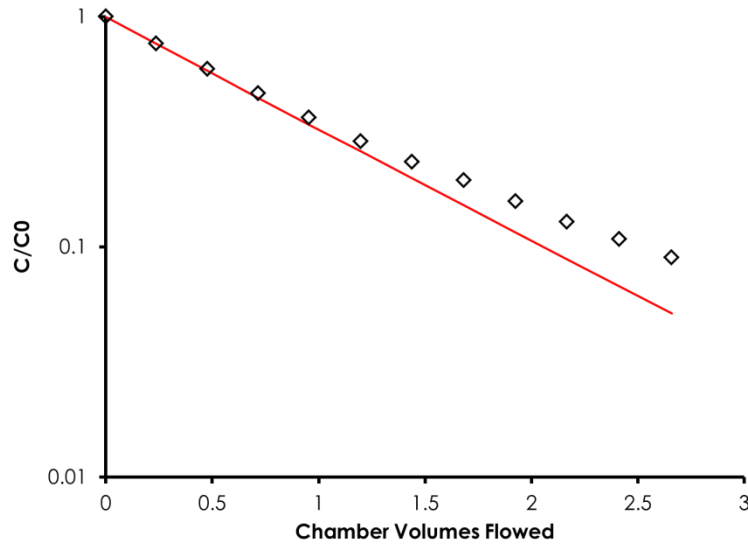

Figure A6: Comparison of expected effluent concentration of a theoretical non-reactive tracer expressed as a fraction of total tracer (red line) versus measured effluent concentration of Pu in bentonite flow cell experiment expressed as a fraction of total Pu.

7.0   DISSOLUTION OF PLUTONIUM INTRINSIC COLLOIDS IN THE PRESENCE OF CLAY AND AS A FUNCTION OF TEMPERATURE

7.1   INTRODUCTION

The large volumes of plutonium (Pu) designated for storage in high-level nuclear waste repositories are predicted to impact repository performance under certain scenarios (Kaszuba and Runde, 1999; Management, 2002). The dissolution of Pu in the waste forms will likely control the release of Pu to the environment as intrinsic or pseudo-colloids (Kersting, 2013; Walther and Denecke, 2013). Colloid facilitated Pu transport has been reported on the scale of kilometers at sites both in the US (Kersting et al., 1999; Santschi et al., 2002) and Russia (Novikov et al., 2006). Despite the recognized importance of colloid-facilitated Pu transport, geochemical and biochemical mechanisms controlling Pu colloid formation and stability over the range of concentrations expected in the environment have not been identified. In particular, kinetic information under environmental conditions is lacking. The temperature in the vicinity of radiological waste packages is expected to be elevated over an extended time period. Thus, understanding Pu behavior at elevated temperatures is necessary. The paucity of thermodynamic and kinetic data regarding temperature dependence limits the efficacy of current transport model predictions (Altmaier et al., 2013; Rao et al., 2011; Zavarin et al., 2014).

Pu can be associated with the colloidal fraction of groundwater in two forms. Pu can either form an intrinsic colloid or sorb to existing mineral, organic, or microbial colloids to form pseudo-colloids. At high concentrations where the solubility product is exceeded, Pu will precipitate and form Pu intrinsic colloids and precipitates (Neck et al., 2007c; Neck and Kim, 2001). Transport of Pu intrinsic colloids is controlled by its stability (both physical and chemical). At low concentrations, Pu will sorb onto inorganic or organic colloids, resulting in the formation of pseudo-colloids. Transport of Pu pseudo-colloids is determined by the Pu sorption/desorption kinetics. Both forms of Pu colloids may exist simultaneously under some subsurface conditions.
The identity of naturally occurring mineral colloids will be a function of the host rock mineralogy. Among the most ubiquitous mineral colloids are aluminosilicate clays that are commonly observed as mobile colloids due to their inherently small particle size and prevalence as alteration minerals from original host rock material (Kersting et al., 1999). Clays are known to sorb Pu (Begg et al., 2013; Bertetti et al., 1998; Keeney-Kennicutt and Morse, 1985; Kozai et al., 1996; Kozai et al., 1993; Lujaniene et al., 2007; Powell et al., 2004; Powell et al., 2005; Powell et al., 2008; Sabodina et al., 2006; Sanchez et al., 1985; Turner et al., 1998). The proposed use of bentonite within some engineered barrier system scenarios for high-level nuclear waste repositories provides additional importance to understanding Pu interaction with aluminosilicate clays (Sabodina et al., 2006). Aluminosilicate clays may represent a key phase that will control transport of Pu pseudo-colloids in repository near and far fields.

Batch sorption has been the most common method used to measure the affinity of a contaminant for a mineral surface. Data obtained from a conventional sorption experiment are the concentrations of the contaminant in the liquid phase before and after sorption. Filtration and/or centrifugation are used to separate solids from liquid after equilibrium is reached. The quantity sorbed is calculated based on the difference of the total and aqueous concentrations. However, if the contaminant is involved in multiple processes (i.e., sorption, colloids formation and/or precipitation), these individual processes cannot isolated or identified from the batch sorption data alone.

In order to distinguish between precipitated, colloidal, and sorbed species, we employed dialysis membranes to segregate intrinsic colloids from pseudo-colloids. Dialysis membranes are commonly used to separate suspended solutes or particles of different dimensions in a liquid mixture. Desirable size separation by dialysis can be achieved by selecting an appropriate membrane pore-size molecular weight cutoff (MWCO). Membrane pore sizes of ≤5 kilo Daltons (kDa) (approximately equivalent to ≤2 nm) can provide reasonable separation of aqueous and colloidal species. In the present study, we examined the stability of Pu intrinsic colloids relative to pseudo-colloids using a novel experimental design and modeling approaches. We employed dialysis membranes to segregate intrinsic colloids (2~5 nm) from montmorillonite colloids (>100 nm) and allow aqueous Pu to interact with both colloidal phases. Using the dialysis membrane approach, we monitored the dissolution of intrinsic colloids in the absence and presence of montmorillonite. The data provide new insights into the stability of intrinsic colloids in the presence of clay at 25 and 80°C.

7.2   MATERIALS AND METHODS

7.2.1   Pu Stock and Intrinsic Colloid Preparation

All reagents were of analytical grade or better and used as received. De-ionized water from a Barnstead Milli‑Q (MQ) water purification system (18.2 MΩ cm) was used for all procedures and solution preparation. Pu stock solutions with two different Pu isotopic ratios were used. A relatively pure alpha-emitting ^{238}Pu stock solution was used in low and intermediate Pu concentration experiments. The ^{238}Pu, ^{239}Pu, ^{240}Pu, and ^{241}Pu mass percent in the stock was 76.8%, 21.0%, 2.0%, and 0.14%, respectively. The major isotope contributing to alpha activity in this stock was ^{238}Pu (~99.9% by activity). The second Pu stock solution, used in the high Pu concentration experiments, was a ^{242}Pu solution spiked with ~1% of the ^{238}Pu stock. The ^{238}Pu, ^{239}Pu, ^{240}Pu, ^{241}Pu, and ^{242}Pu mass percent in this stock was 0.75%, 0.21%, 0.13%, 0.04%, and 98.87%, respectively. The major isotopes contributing to alpha activity in this stock were ^{238}Pu (96.8%) and ^{242}Pu (2.9%). Both Pu stock solutions were purified using AG$^{®}$1×8 100-200 mesh anion exchange resin from Bio-Rad Laboratories, and filtered through an Amicon Ultra 0.5 mL centrifugal filter with membrane MWCO of 3 kDa (EMD Millipore). The oxidation state of Pu(IV) was confirmed using both UV-Vis and solvent extraction. The aqueous Pu(IV) starting solution was prepared by spiking the acidic stock solution into a pH 8 buffer solution (5 mM NaCl/0.7 mM NaHCO$_3$) and gradually adding microliters of NaOH (1 N or 6 N) to readjust the pH to 8. The Pu intrinsic colloids were prepared by neutralizing the aqueous Pu(IV) stocks using NaOH and adjusting solution to pH 9-10. After aging for more than a week, the intrinsic colloids were centrifuged at an RCF of 9168 for 1 h and the supernatant removed. The intrinsic colloid particle size cut-off based on centrifugation was 14 nm. However, the average particle size of the intrinsic colloids was 30 nm and composed of aggregated PuO$_2$ crystallites ranging in size from 2.5 to 4.5 nm (Figure 7-1). An intrinsic colloid stock solution was prepared by re-suspending the intrinsic colloids in MQ water. The intrinsic colloid starting solutions were prepared by spiking the intrinsic colloid stock solution into a pH 8 buffer solution without further pH adjustment. Pu concentrations in samples were analyzed by a PerkinElmer Tri-Carb 2900TR Liquid Scintillation Analyzer. The fraction of aqueous Pu in the intrinsic colloid stock solution, based on 3 kDa MWCO, was 1 to 3%.
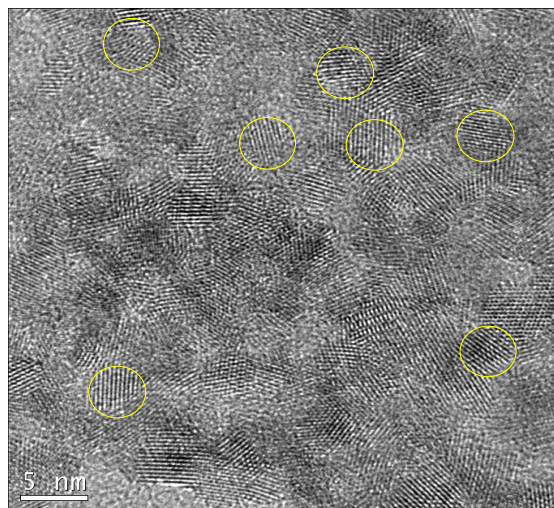
Figure 7-1: TEM image of PuO_2 intrinsic colloids. Several individual PuO_2 crystallites are highlighted by yellow circles. The measured average particle sizes was 3.5 nm with a range of 2.5-4.5 nm.

7.2.2   Montmorillonite

SWy-1 montmorillonite (Clay Minerals Society) was pre-treated using 1 mM HCl (to dissolve any carbonate minerals) followed by addition of 0.1% of H_2O_2 (to oxidize organic contaminants and reduced metals (e.g., Fe^{2+}). The pre-treated montmorillonite was centrifuged to remove excess liquid, and the wet paste was transferred to a 6 to 8 kDa MWCO dialysis tube suspended in 0.01 M NaCl solution to produce a homoionic Na-montmorillonite. The clay minerals were dialyzed for seven days, and the NaCl solution was changed at least once per day. The clay minerals were then suspended in MQ water and centrifuged to obtain particle sizes from 50 nm to 2 μm. The wet solids were dried at 40°C until a constant weight was obtained. A stock montmorillonite suspension was made by mixing 4 g of dried montmorillonite in 400 mL of pH 8 buffer solution (10 g L^{-1}). Quadrasorb SI surface area analyzer (QuantaChrome Instruments) was used for BET measurements. The surface area of montmorillonite measured by $N_2(g)$-BET was 31.5 ± 0.2 m^2 g^{-1}, which is comparable to the reported value of 31.8 m^2 g^{-1} (Clay Minerals Society).

7.2.3   Dissolution Experiments

Intrinsic colloid stability was evaluated using the experimental design shown in Figure 7-2. Briefly, intrinsic colloids are placed inside the dialysis bag, while the clay colloids are placed outside the dialysis bag. Thus, the colloidal montmorillonite is isolated from the intrinsic colloids while exchange of truly aqueous (non-colloidal) ions between both solid phases is permitted. Pu detected outside the dialysis bag over time represents dissolved Pu species that diffused across the dialysis membrane. In the presence of montmorillonite, the dissolved Pu can either remain in solution or sorb to montmorillonite. The dissolution rate of intrinsic colloids is expected to be a function of its solubility, surface area, solution composition, pH and temperature. The sorption rate of Pu to montmorillonite is affected by similar processes.
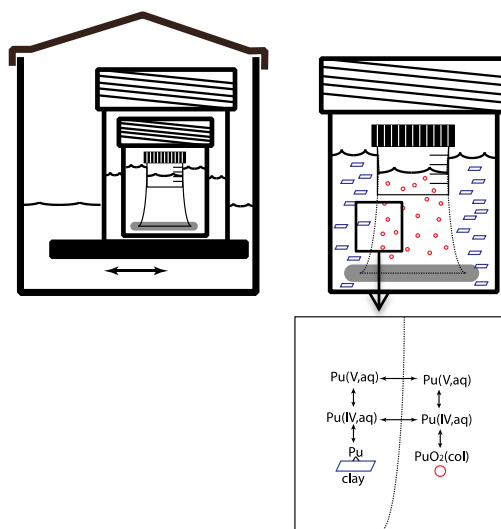
Figure 7-2: Experimental design using dialysis membrane to separate Pu intrinsic colloids (placed inside dialysis tubing) from mineral colloids (placed outside the tubing). For Pu-montmorillonite sorption to occur, intrinsic colloids must dissolve and diffuse through the membrane.

A total of 16 experiments (excluding a control blank) were performed to test the experimental design and quantify dissolution of intrinsic colloids in the presence of montmorillonite. The dialysis membrane used was Spectra/Por® 7 standard RC pre-treated dialysis tubing with a MWCO of 1 kDa (Spectrum Laboratories, Inc). The experiments were performed at two temperatures, 25°C (8 experiments) and 80°C (8 experiments) to evaluate the effect of temperature. At each temperature, Pu was added either as an aqueous species (to test simple diffusion and sorption of Pu) or as an intrinsic colloid (to test intrinsic colloid dissolution, diffusion and sorption of Pu). The initial Pu concentrations bracketed the PuO_2(am, hyd) solubility ($\sim 5 \times 10^{-9}$ M) (Neck et al., 2007c). In addition, montmorillonite-free solutions (spiked blanks) with initial Pu concentrations below and near PuO_2(am, hyd) solubility were used to compare with sorption experiments and evaluate Pu loss to container walls and dialysis membranes.

All experiments were conducted in 450 mL Teflon jars with air-tight closures. 225 mL of pH 8 buffer solution was mixed with 25 mL of montmorillonite stock suspension to yield 250 mL of a 1 g L^{-1} montmorillonite suspension. A sealed dialysis tubing containing 30 mL of either aqueous Pu or intrinsic colloids was then placed in the 250 mL pH buffer solution with or without montmorillonite. The 450 mL Teflon jars were submerged in 1 L Teflon containers filled with MQ water to minimize evaporative losses and provide secondary containment to the radioactive samples. Over the course of the experiment, the 25°C samples were placed on a top-loading orbital shaker, and the 80°C samples were submerged in an Innova 3100 water bath shaker (New Brunswick Scientific). All samples were shaken at an orbital speed of 100 rpm during experiments.
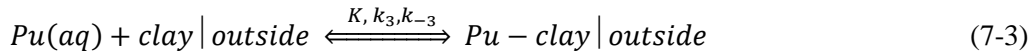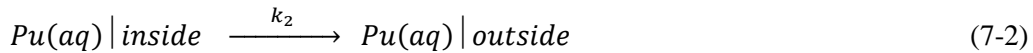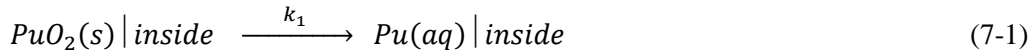
Each experiment was sampled as a function of time over a three-month period. At each sampling interval, aliquots of the montmorillonite suspension were collected, centrifuged and analyzed for total Pu, supernatant Pu, and solution pH. Alternatively, aqueous Pu was determined by

measuring the filtrate Pu concentration after filtering the suspension through 3kDa MWCO centrifugal filters. The montmorillonite concentration in the suspension was also measured based on light scattering at a wavelength range of 300−500 nm using a Cary 500 Scan UV-Vis-NIR spectrophotometer (Varian). The pH of the clay suspension was monitored and maintained at pH 8 ± 0.5 at all times.

7.3   RESULTS AND DISCUSSION

7.3.1   Kinetics

The formation of Pu-montmorillonite pseudo-colloids in this system involves a series of processes including intrinsic colloid dissolution, Pu(IV)/Pu(V) redox reactions, aqueous Pu diffusion, and sorption. Some of the processes are parallel and others are sequential. To simplify the kinetics comparison, we focus on the essential processes, which follow a sequential order: Pu intrinsic colloids dissolve to produce aqueous Pu inside the dialysis membrane (Eq. 7-1); the aqueous Pu is transported across the membrane (Eq. 7-2), and aqueous Pu sorbs onto clay that is placed outside of the dialysis membrane (Eq. 7-3):

$$PuO_2(s) \big| inside \quad \xrightarrow{k_1} \quad Pu(aq) \big| inside \tag{7-1}$$

$$Pu(aq) \big| inside \quad \xrightarrow{k_2} \quad Pu(aq) \big| outside \tag{7-2}$$

$$Pu(aq) + clay \big| outside \quad \xleftrightarrow{K, k_3, k_{-3}} \quad Pu - clay \big| outside \tag{7-3}$$

where k_1 and k_2 represent apparent kinetic constants, $K = k_3/k_{-3}$ is the sorption equilibrium constant, and k_3 and k_{-3} are the sorption and desorption rate constants.

A pseudo 1st order reaction model was used for all three reactions (i.e. rate constant units of d^{-1}). As a result, kinetic rate constants can be compared directly to determine the rate limiting step. However, it should be noted that a true dissolution rate constant is typically normalized to surface area. Similarly, k_2 reflects the apparent diffusion coefficient of Pu under these experimental conditions, including the configuration/dimensions of the dialysis systems, the number of membrane pores and their sizes, and shaker speed used in the experiments. Thus, the apparent diffusion coefficient is not intended to reflect the true diffusivity in water. Aqueous Pu and intrinsic colloid experiments allow us to determine k_1 and k_2. By analyzing concentrations of total and aqueous Pu in the clay suspension, we can also obtain the equilibrium constant K.

7.3.2   Apparent Diffusion in the System

To determine the rates of apparent diffusion in our experiments, ^3H and aqueous Pu(V) were placed inside a dialysis bag and the solution outside dialysis bag was sampled as a function of time and monitored for Pu and ^3H (i.e. Eq. 7-2). The concentrations of ^3H or Pu inside the dialysis bag as a function of time can be described by:

$$\frac{dC_{in}}{dt} = -k_2(C_{in} - C_{out}) \tag{7-4}$$

where C_{in} and C_{out} are ^{3}H or Pu concentrations (in mol L^{-1}) inside and outside of the dialysis bag, respectively, and k_2 is the rate constant for diffusion across the dialysis membrane. Assuming C_{out}=0 at t=0, the ^{3}H or Pu concentration outside of the dialysis bag can be described by

$$C_{out} = (C_{in}^o - C_{in}) * \frac{V_{in}}{V_{out}}$$ (7-5)

where V_{in} and V_{out} (L) are the solution volumes inside and outside of dialysis bag and C_{in}^0 is the concentration (mol L^{-1}) inside the dialysis bag at time zero. Combining Eq. 7-4 and 7-5 and integrating leads to the following equation

$$C_{in} = C_{in}^o \left(\frac{V_{in}}{V_{in}+V_{out}}\right) + Ae^{-k_2\left(\frac{V_{in}+V_{out}}{V_{out}}\right)t}.$$ (7-6)

Replacing C_{in} in Eq. 5 with Eq. 6, rearranging the terms, and assuming that C_{out}=0 at t=0 and $C_{out} = C_{in} \times V_{in}/(V_{in}+V_{out})$ at $t \rightarrow \infty$, we obtain:

$$C_{out} = \frac{V_{in}}{V_{out}+V_{in}} C_{in}^o \left[1 - e^{-k_2^* t}\right]$$ (7-7)

where k_2^* is the apparent diffusion rate constant (d^{-1}).

The data obtained from diffusion experiments are plotted in Fig. 7-3. The fitted rate constant was 40 d^{-1} for tritium at both temperatures. The fitted rate constant for Pu(V) at 25°C was 25 day^{-1}. At 80°C, the short term (<0.1 d) Pu(V) data was fit to a rate constant of 30 d^{-1}. However, Pu concentrations decreased at later times. The decrease may reflect slow sorption to container walls, sorption to the dialysis membrane, and/or oxidation/reduction of Pu(V). All fitted rate constants are listed in Table 7-1. The fitted rate constants indicate that diffusion of aqueous species across the dialysis membrane will occur on time scale of <<1 day.
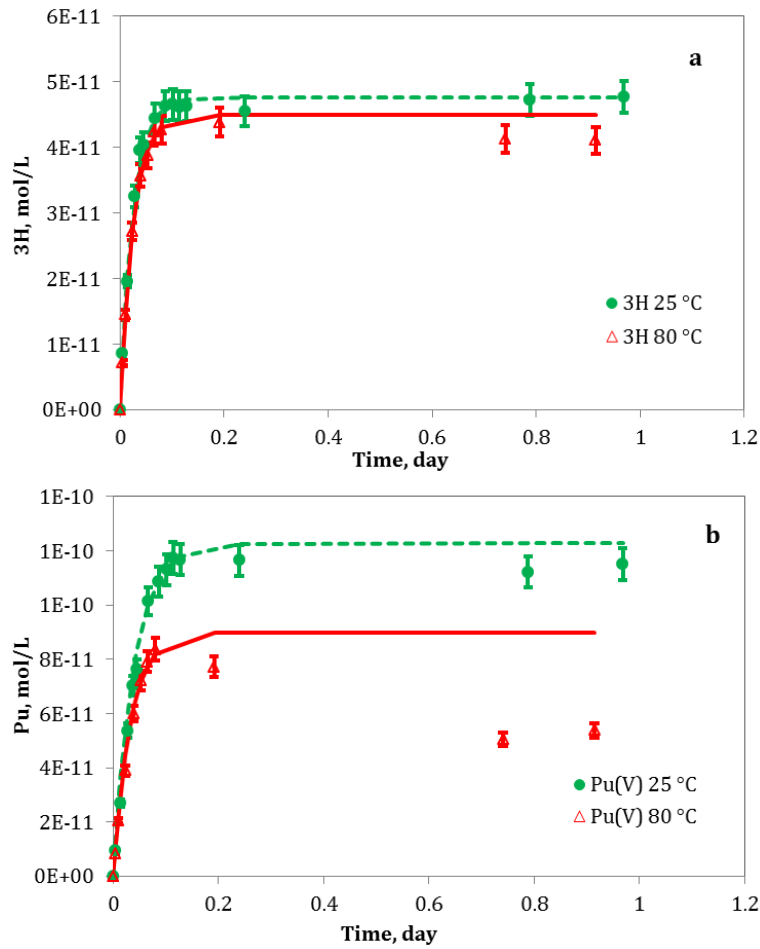
Figure 7-3: Diffusion of (a) ^{3}H and (b) Pu(V) as function of time at 25°C and 80°C and associated diffusion model fits.

Table 7-1: Experimental conditions and fitted apparent diffusion rate constants for Pu(V) and ^{3}H diffusion experiments.

Expt	T	Pu(V)	^{3}H	k_2
	°C	---- mol L^{-1} ---		d^{-1}
1	25	1.2E-9	4.4E-10	25,40*
2	80	1.2E-9	4.4E-10	30,40*

* Pu(V) and ^{3}H rate constants, respectively.

* V_{in} = 30 mL, V_{out} = 250 mL

7.3.3   Kinetics of Intrinsic Colloid Dissolution

In these experiments (Table 7-2), intrinsic Pu colloids were placed inside the dialysis bag, which was suspended in a clay suspension. The clay suspension was sampled as a function of time and the concentration of total and aqueous Pu was monitored. If the total Pu concentration in the clay suspension is used to evaluate the system (assuming Pu sorption to montmorillonite is an equilibrium process), then the system can be approximated by a simple chain reaction of first order rate laws. The rate law for mineral dissolution can be described by the following equation (Maher et al., 2006):

$$R = k_{dis} \cdot A \cdot \beta(a) \cdot f(\Delta G) \tag{7-8}$$

where k_{dis} is the rate constant in mol m^{-2} s^{-1}, A (in m^2) is the mineral surface area in contact with the aqueous solution. $\beta(a)$ is a function of various factors (e.g., pH, inhibitors or catalysts) that affect the dissolution. $f(\Delta G)$ is a dependence of rate on Gibbs free energy ΔG. In our experiments, the surface area A is proportional to PuO$_2$ colloids concentration in the dialysis bag: $A = C_{in}^0 V_{in} SSA$. The value of 4×10^4 m^2/mol used for the specific surface area (*SSA)* is calculated using an average particle size of 3.5 nm and density of 11.5 g/cm^3 for the PuO$_2$ colloids.

For the sake of simplicity and direct comparison between dissolution of PuO$_2$ colloids and diffusion of aqueous species, we used 1st order reactions for both Pu colloid dissolution and diffusion. If the kinetics can be described as two first order chain reactions, the Pu concentration in montmorillonite suspension is governed by the following equation (Lasaga, 1998):

$$C_{out} = \frac{V_{in}}{V_{out}+V_{in}} C_{in}^o \left[1 + \frac{k_1 \exp(-k_2 t) - k_2 \exp(-k_1 t)}{k_2 - k_1}\right] \tag{7-9}$$

where C_{out} in mol L^{-1} represents the total Pu concentration in clay suspension as a function of time (t, d), k_1 and k_2 (d^{-1}) are apparent rate constants of dissolution and diffusion processes, respectively. In the case where rate constants k_1 and k_2 differ by orders of magnitude, the rate-limiting process can be identified and the model further simplified to a first order rate model. The experimental data are plotted in Figure 7-4 and the fitted first order rate constants are summarized in Table 7-2. The first order rate constants for the dissolution of intrinsic colloids ranged from 0.025-0.40 d^{-1} at 25°C and 0.15-0.30 d^{-1} at 80°C, one to two orders of magnitude lower than the rate constants determined in the diffusion experiments. Thus, it appears that intrinsic colloid dissolution is the rate-limiting step.
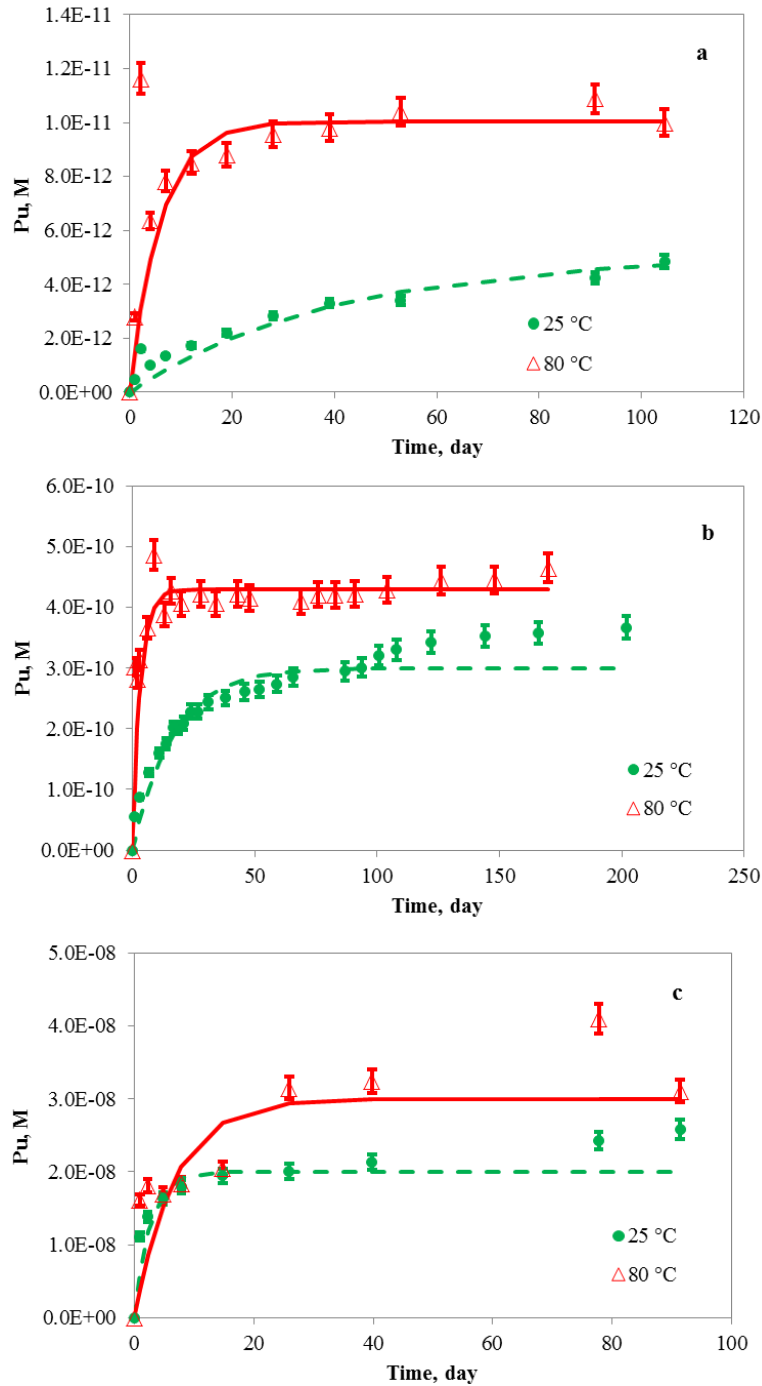
Figure 7-4: Dissolution and diffusion of Pu colloids in the presence of clay at 25 and 80°C. Lines are fitted curves using psuedo1[st] order reaction model. Initial Pu colloids concentrations were 1.1×10^{-10} mol L^{-1} (4a), 8.3×10^{-9} mol L^{-1} (4b), and 1.9×10^{-6} mol L^{-1} (4c).

Table 7-2: Experimental conditions and fitted apparent diffusion rate constants for Pu intrinsic colloid/montmorillonite experiments.

Expt	Temp	Pu coll.	k_1	k_s	Pu in clay
	°C	mol L^{-1}	d^{-1}	mol m^{-2} s^{-1}	%
1	25	1.1E-10	0.025	7.2E-12	45
2		8.3E-9	0.06	1.7E-11	33
3		1.9E-6	0.4	1.1E-10	10
4	80	1.1E-10	0.17	4.9E-11	88
5		5.7E-9	0.3	8.6E-11	70
6		1.9E-6	0.15	4.3E-11	15

* Vin = 30 mL, Vout = 250 mL, 1 g/L montmorillonite

The surface area normalized dissolution rate constant, k_s (mol m^{-2} s^{-1}), can be calculated using the following equation:

$$k_s = \frac{k_1}{SSA}$$

(7-10)

Furthermore, the lifetime of PuO$_2$ colloids can be estimated using (Lasaga, 1998):

$$t_{lifetime} = \frac{r_o}{k_s \bar{V}}$$

(7-11)

where r_o is the initial average radius of PuO$_2$ (1.75 nm) and $\bar{V}$ is the molar volume of the colloids. The logk_s (mol m^{-2} s^{-1}) values obtained in these experiments were -10 to -11 which results in a lifetime range of <1 to 4 months. The logk_s of montmorillonite is in the range of -14 to -18 (Golubev et al., 2006; Huertas et al., 2001; Rozalén et al., 2009; Rozalén et al., 2008). These lower dissolution rates combined with their much larger particle sizes, lead to much longer lifetimes (thousands to millions of years). However, the lifetime of Pu on these montmorillonite colloids is not known.

In a heterogeneous system and at constant pressure and temperature, the overall dissolution rate of a metal oxide can be described as the sum of the rates of proton-promoted, hydroxide-promoted, ligand-promoted and reductant or oxidant-promoted (if appropriate) dissolution. In other words, the dissolution rate is actually the sum of all the parallel dissolution rates of different metal centers (Afonso and Stumm, 1992; Hocsman et al., 2006; Kohler et al., 2003; Lasaga and Luttge, 2004; Stumm, 1997). We cannot distinguish between these processes here. However, the dissolution rate clearly increases with the intrinsic Pu colloid concentration, as would be expected for a surface-controlled dissolution process.

In the high intrinsic colloid concentration samples, the overall rates may have decreased significantly towards to the end of experiments as the system approached equilibrium (Lasaga, 1981; Lasaga and Luttge, 2004). The impact of solution saturation can explain the decrease in kinetic constant obtained in the highest Pu concentration experiment at 80℃ (Table 7-2).

7.3.4   Sorption Kinetics in the Aqueous Pu(IV)-Montmorillonite System

Four experiments were performed using aqueous Pu(IV) in the presence of montmorillonite (Table 7-3). The purpose of these experiments was to investigate Pu speciation effects on diffusion. The experimental data are plotted along with fitting curves in Figure 7-5. The fast rates (30 d^{-1}) observed at 25℃ suggest that these experiments were diffusion controlled. However, the rate constants obtained from the 80℃ experiments were much lower (0.15-0.2 d^{-1}) and similar to those obtained from intrinsic colloid experiments. In fact, these rate constants are 200 times slower than that observed at 25℃. This suggests that aqueous Pu(IV) species hydrolyzed to form intrinsic Pu colloids or PuO_2 solids at 80℃. Once these intrinsic Pu colloids formed inside the dialysis bag, they slowly dissolved and diffused across the membrane. The intrinsic colloids dissolution was thermodynamically controlled. Hydrolysis of Pu(IV) is endothermic and, as a result, high temperatures will favor the formation of intrinsic Pu colloids (Cleveland, 1979). In addition, the ionization constant of water, K_w, increases with temperature which can lead to a 30 $\times$ increase in hydroxide concentration at pH 8 between 25 and 80℃. This will also enhance Pu(IV) hydrolysis. Endothermic hydrolysis behavior of aqueous Pu and other actinide species has been reported in numerous studies (Altmaier et al., 2013; Rao et al., 2004; Rao et al., 2011; Runde et al., 2002b).
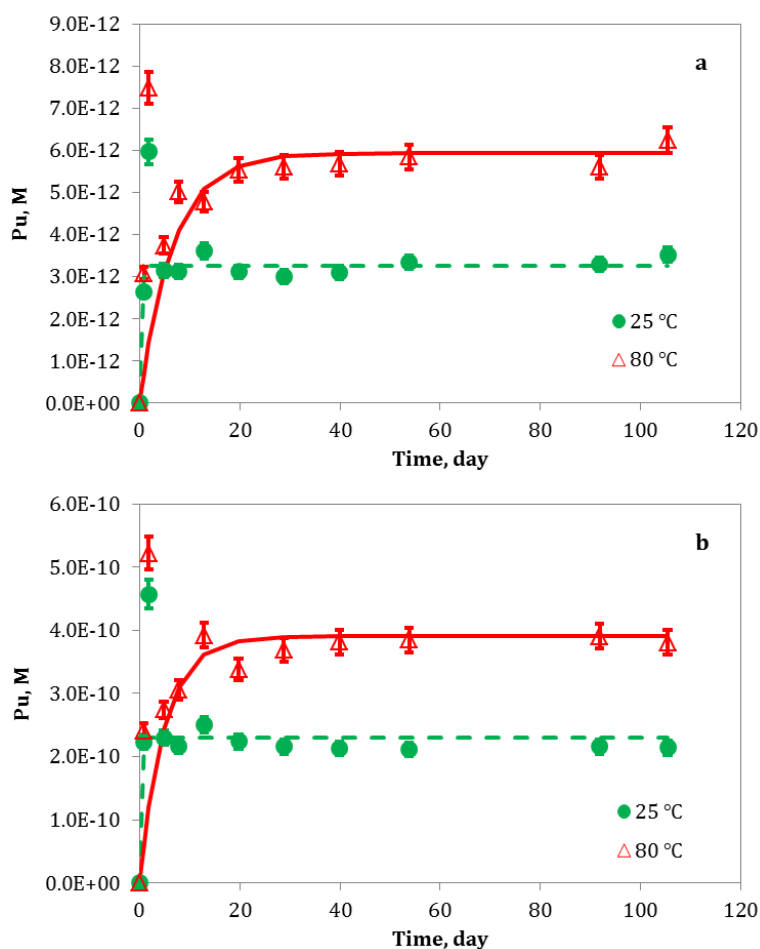
Figure 7-5: Kinetics of the aqueous Pu(IV)-montmorillonite system at 25 and 80°C. Lines are fitted curves using psuedo1st order kinetic model. Initial Pu concentrations of 5.5×10^{-11} mol L^{-1} (5a) and 5.8×10^{-9} mol L^{-1} (5b).
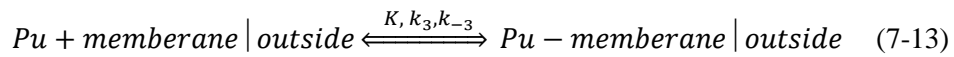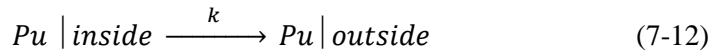
Table 7-3: Experimental conditions and fitted apparent diffusion rate constants for aqueous Pu(IV)-montmorillonite experiments.

Expt	Temp	Pu(IV),aq	k_1	k_2	k_s	Pu in clay
	°C	mol L^{-1}	d^{-1}	d^{-1}	mol m^{-2} s^{-1}	%
1	25	5.5E-11		30		55
2		5.8E-9		30		37
3	80	5.5E-11	0.15		4.3E-11	100
4		5.8E-9	0.2		5.7E-11	63

* Vin = 30 mL, Vout = 250 mL, 1 g/L montmorillonite

7.3.5   Kinetics in the Absence of Montmorillonite

Four experiments using both intrinsic colloids and aqueous Pu(IV) were performed in the absence of montmorillonite. These experiments served as control experiments to evaluate the sorption of Pu to the container walls, dialysis membrane and other materials. The experimental data are plotted along with fitting curves in Figure 7- 6. At 25°C, Pu concentrations in the solution outside of the dialysis bag were initially higher than at 80 °C, and then decreased over time, indicating there was significant sorption to the dialysis bag and/or container wall over time. To first order, the processes in this system can be described as a 1st order diffusion/dissolution reaction followed by a rate limited sorption reaction:

$$Pu \mid inside \xrightarrow{\quad k \quad} Pu \mid outside \qquad\qquad (7\text{-}12)$$

$$Pu + memberane \mid outside \xleftrightarrow{\quad K, k_3, k_{-3} \quad} Pu - memberane \mid outside \quad (7\text{-}13)$$

The Pu concentration outside of the dialysis bag as a function of time is governed by (Lasaga, 1998):

$$C_{out} = \frac{V_{in}}{V_{out}} C_{in}^o \left[1 - \exp(-kt) - \frac{k_3}{k_3 + k_{-3}} \left(1 + \frac{k*\exp(-(k_3 + k_{-3})t) - (k_3 + k_{-3})\exp(-kt)}{k_3 + k_{-3} - k} \right) \right] \quad (7\text{-}14)$$

where k represents kinetic constant of either PuO_2 dissolution or aqueous Pu(aq) diffusion across the membrane; $K = k_3/k_{-3}$ is the sorption equilibrium constant, and k_3 and k_{-3} are the sorption and desorption rate constants.

Table 7-4 lists the curve fitting results and shows that rate constants are consistent with the ones obtained from dissolution or diffusion experiments depending upon Pu initial speciation and experimental temperatures. In the intrinsic colloid system, rate constants were 0.06 and 0.3 day^{-1} for experiments performed at 25 and 80°C, respectively. These values match k_1 values obtained in the intrinsic colloid-montmorillonite experiments, suggesting that kinetics were again governed by PuO_2 dissolution. In the aqueous Pu(IV) experiments, the rates constants were 30 and 0.3 d^{-1} in the 25 and 80°C experiments, respectively. The 30 d^{-1} rate constant matches aqueous Pu(IV) diffusion rate constants, indicating that the diffusion process was controlling the system. Thus, we can conclude that the presence of clay impacts neither diffusion rates of Pu species nor dissolution rates of intrinsic Pu colloids. At elevated temperature, the 0.3 day^{-1} rate constant matches those obtained from intrinsic Pu colloid dissolutions experiments with or without clay, suggesting that aqueous Pu(IV) underwent fast hydrolysis to form intrinsic Pu colloids, whose dissolution became a rate-limiting step governing the observed kinetics. Although the presence of clay doesn't affect the kinetics of these systems, it stabilizes Pu and increased the total amount of Pu on the outside of the dialysis membrane.
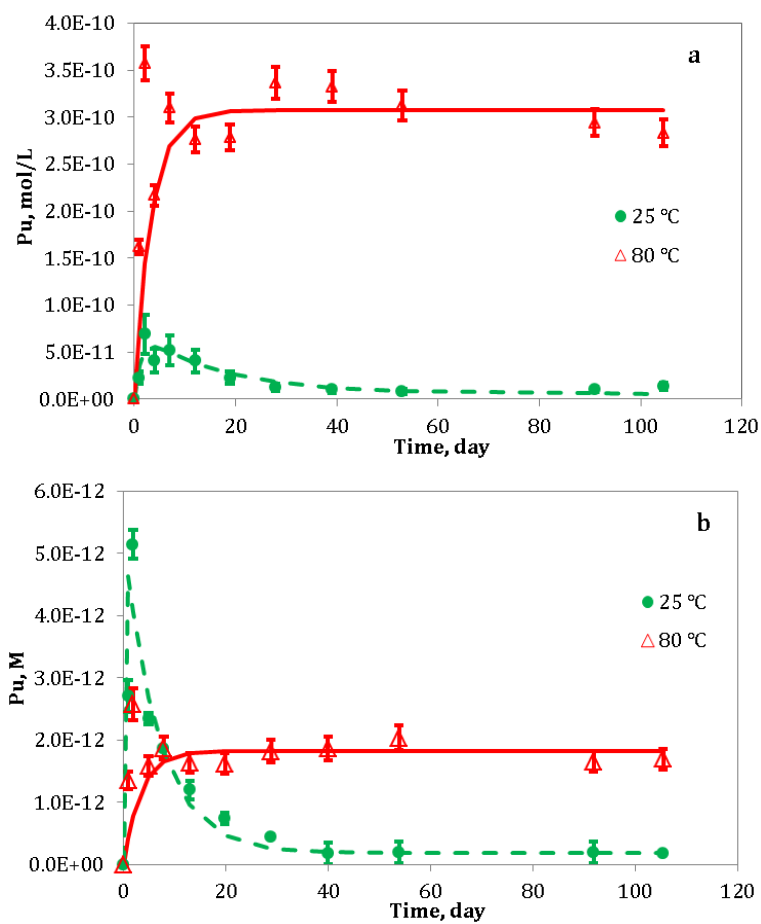
Figure 7-6: Pu concentrations outside the dialysis membrane for intrinsic colloid and aqueous Pu(IV) experiments in the absence of montmorillonite at 25 and 80°C. Lines are fitted curves using kinetics model pseudo 1st order dissolution/diffusion and rate-limited sorption/desorption. Intrinsic colloid (6a) and aqueous Pu(IV) (6b).

Table 7-4: Experimental conditions and fitted apparent diffusion rate constants for intrinsic colloids and aqueous Pu(IV) experiments in the absence of montmorillonite.

Temp	Pu intrinsic colloids	Pu(IV, aq)	k	k_3	k_{-3}	$K = k_3/k_{-3}$	Pu in clay suspension
°C	--- mol L^{-1} ---		-------- d^{-1} --------				%
25	7.8E-9		0.06	0.8	0.005	160	2
80	7.8E-9		0.3	20	0.8	25	35
25		5.5E-11	30	0.14	0.005	28	3
80		5.5E-11	0.3	0.002	0.03	0.007	28

* Vin = 30 mL, Vout = 225 mL.

7.3.6   Dependence on Temperature

High temperature can enhance Pu(IV) hydrolysis as the process is endothermic (Altmaier et al., 2013; Cleveland, 1979). In addition, a significant increase in water ionization due to a decrease in pK_w (~12.5) at 80°C also drives reaction towards Pu(IV) hydrolysis. As a result, the solubility of Pu colloids under our experimental conditions appeared to decrease at higher temperature. Pu(IV) solubility decreasing in J-13 and UE-25p #1 groundwaters in the vicinity of Yucca Mountain, NV at elevated temperatures has also been reported despite possible existence of higher oxidation states of Pu(V, VI) and/or multi solid phases controlling Pu solubility (Efurd et al., 1998; Nitsche et al., 1993; Nitsche et al., 1994; Runde et al., 2002b).

In general, the dissolution of a solid in an aqueous solution contains two essential steps: the chemical reactions occurring at the solid surface and the transport of dissolved species to and from the surface. The kinetics of the dissolution can be controlled by surface chemical reactions, transport of soluble species to and from the surface, or a combination of both processes (Berner, 1981). The values of the dissolution activation energy (E_a) not only provide important temperature dependence of the rates, but also offer important clues to the dissolution mechanisms. Transport-controlled processes in fluid media typically are associated with diffusion activation energies, whose E_a values are of <21 kJ mol^{-1}. The processes controlled by chemical reactions on solid surfaces would have values of E_a> 42 kJ mol^{-1} due to the involvement of breaking bonds in crystals (Lasaga, 1998). However, it has been observed that most of the activation energies (E_a) for wide variety of mineral dissolutions/alteration processes lie in the intermediate range 21-42 kJ mol^{-1}, suggesting that their dissolution was controlled by both mass transport and surface reactions (Hocsman et al., 2006). It is also possible that the catalytic effect of adsorption on surfaces or surface defects may reduce the activation energies to this intermediate energy range (Lasaga and Gibbs, 1990; Xiao and Lasaga, 1994).

The temperature dependence of rate constant is often assumed to follow the Arrhenius equation:

$$k_1 = \boldsymbol{A_{diss}}\, exp(-\frac{E_a}{RT}) \tag{7-15}$$

The activation energy (Ea) can be calculated using rate constants at two different temperatures:

$$\ln\left[\frac{k_1(T_2)}{k_1(T_1)}\right] = -\frac{E_a}{R}\left(\frac{1}{T_2} - \frac{1}{T_1}\right) \tag{7-16}$$

where A_{diss} is the pre-exponential factor, which is a constant for a given reaction, $k_1(T_1)$ and, $k_1(T_2)$ are the dissolution rate constant k_1 at absolute temperatures T_1 and T_2 in kelvin, respectively, E_a is the activation energy for the reaction in J mole^{-1}, and R = 8.314 J mol^{-1} K^{-1} is the gas constant.

We used k_1 values obtained from low Pu colloid concentration experiments, in which the systems were far from solution equilibrium, to calculate an apparent E_a. The average of apparent activation energy (E_a) for PuO$_2$ colloids dissolution process was 28 kJ mol^{-1}. This intermediate value may indicate that the dissolution process of intrinsic colloids is controlled by the combination of both surface reaction and mass transport at the surface (Hocsman et al., 2006). A theoretical generalization proposed by Berner (Berner, 1978; Berner, 1981) stated that dissolution of minerals with low solubility is more likely to be controlled by reactions at sites on the surface, whereas dissolutions of highly soluble minerals are controlled by material transport either from or to aqueous solution or through protective surface layers.

7.3.7   Temperature Dependence of Pu Sorption to Montmorillonite

The K$_d$s for Pu-montmorillonite can be calculated using the measured Pu activity on montmorillonite and in the supernatant. The resulting K$_d$s from various experiments are plotted in Figure 7. Many factors including Pu speciation, oxidation state, and temperature can impact K$_d$s. Generally, K$_d$s obtained from intrinsic colloid experiments tend to initially have lower values than those obtained from aqueous Pu(IV) experiments. However, K$_d$s from intrinsic colloid experiments tend to increase with time to approach values from aqueous Pu(IV) experiments. This phenomenon can be explained by the change in Pu oxidation states over time. Pu(V) is the predominant species formed as a result of intrinsic Pu colloid dissolution and this oxidation state exhibits a weaker sorption to clay relative to Pu(IV) (Altmaier et al., 2013; Begg et al., 2014; Neck et al., 2007a; Neck et al., 2007b). Over time, Pu(V) tends to reduce to Pu(IV) on the montmorillonite surface which leads to an increasing K$_d$ (Begg et al., 2013). Figure 7 also shows that the K$_d$ increases with increasing of temperature which implies that the sorption process is endothermic and that higher temperatures lead to greater Pu sorption to montmorillonite.

The van't Hoff equation as expressed in eq. 7-17 and Gibbs free energy as described in eq. 7-18 can be used to calculate the changes in enthalpy ($\Delta H°$, J mol^{-1}), entropy ($\Delta S°$, J mol^{-1} K^{-1}) and Gibbs free energy ($\Delta G°$, J mol^{-1}) of Pu-clay sorption at standard atmospheric pressure:

$$lnK_d = -\frac{\Delta H°}{RT} + \frac{\Delta S°}{R} \tag{7-17}$$

$$\Delta G° = \Delta H° - T\Delta S° \tag{7-18}$$

where T is the absolute temperature in kelvin and $R = 8.314$ J mol^{-1} K^{-1} is the gas constant.
The calculated thermodynamic parameters are summarized in Table 7-5. The positive value of $\Delta H°$ (38 kJ mol^{-1}) confirms the endothermic nature of the Pu-montmorillonite sorption, and negative values of $\Delta G°$ indicate that the sorption reaction is spontaneous. A more negative value of $\Delta G°$ obtained from elevated temperature confirms that the formed Pu pseudo-colloids are more

stable at higher temperature. However, as described in the following paragraph, the thermodynamic parameters derived from these experiments are only approximate since redox conditions, pH, and Pu oxidation states were not strictly controlled.
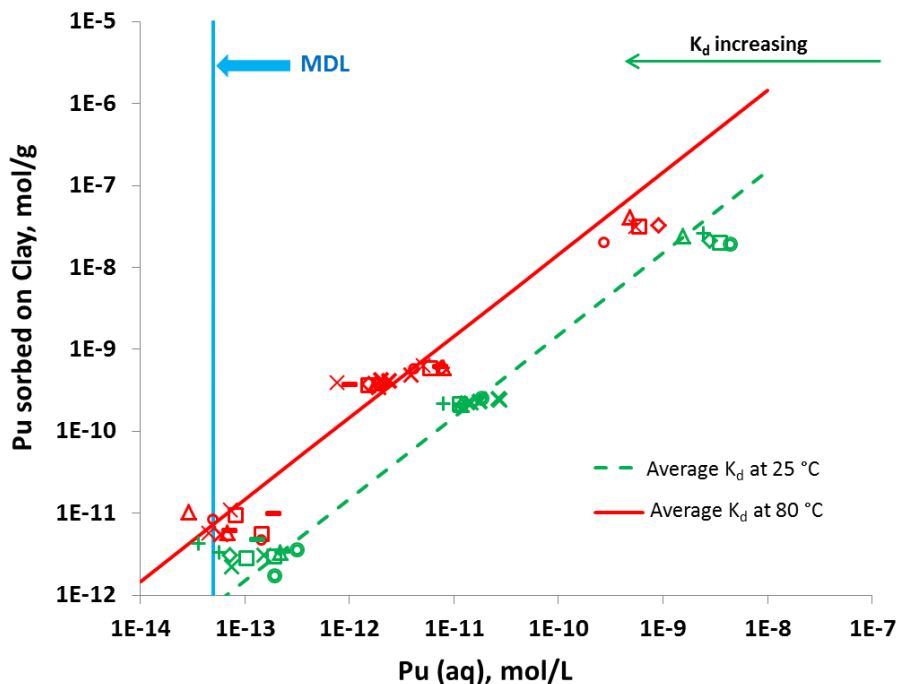

Figure 7-7: Pu-montmorillonite K_ds from intrinsic colloid and aqueous Pu(IV) experiments with montmorillonite at 25 and 80°C. Lines represent the average K_ds obtained from intrinsic colloid-montmorillonite and aqueous Pu(IV)-montmorillonite experiments.

At the termination of the experiments, Pu oxidation state distribution in the supernatants of both intrinsic colloid suspension and pseudo-colloid suspensions were analyzed using solvent extraction (Figure 7-8). We show that in the pseudo-colloid suspensions, higher oxidation states Pu(V) and Pu(VI) were the predominant aqueous species at 25°C, while Pu(IV) was more prevalent at 80°C (Figure 7-8a). This suggests that elevated temperatures led to more reducing solution conditions. This may, in part, explain the higher K_ds at 80°C. On the other hand, in the intrinsic colloid suspensions, Pu(IV) concentration was much higher at 25°C than that at 80°C. In the absence of clay, oxidizing Pu(IV) to higher oxidation states by oxygen in the air is enhanced at higher temperature. Although the Pu oxidation state distribution changed at different temperatures and colloidal solutions, and they made significant impact on the Pu sorption behavior, the processes controlling Pu speciation in solution or on mineral surface is not yet clear and requires further investigation.
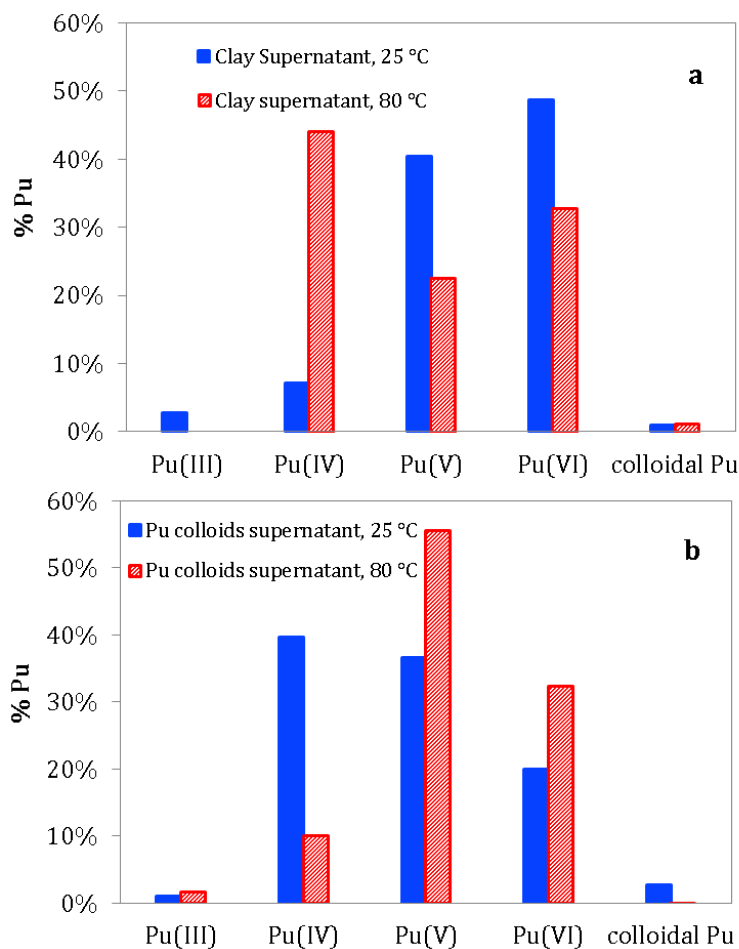
Figure 7-8: Pu oxidation state distributions in the aqueous phase at 25 and 80°C in montmorillonite suspensions (8a) and intrinsic colloid suspensions (8b).

Table 7-5: Thermodynamic parameters for sorption of Pu to montmorillonite at 25 and 80°C

Temp	Average K_d mL g^{-1}	T K	$\Delta H°$ kJ mol^{-1}	$\Delta S°$ kJ mol^{-1} K^{-1}	$T\Delta S°$ kJ mol^{-1}	$\Delta G°$ kJ mol^{-1}
25 °C	1.50E+04	298.15	36.1	0.20	59.9	-23.8
80 °C	1.45E+05	353.15	36.1	0.20	71.1	-34.9

7.4   CONCLUSIONS

A study of the dissolution of intrinsic colloids in the presence of montmorillonite at different temperatures was successfully accomplished using a novel experimental setup containing a dialysis device. This device enables us to separate two solid phases. The kinetics of a series of processes including Pu intrinsic colloid dissolution were modeled using a series of 1st order reactions. We show that the kinetic constants for dissolution were one to two orders of magnitude lower than the apparent diffusion rates across the dialysis membranes. Therefore the dissolution

process was the rate-limiting step. Although the presence of clay changes neither the colloids dissolution nor diffusion rates, it can stabilize dissolved Pu species and drive intrinsic Pu colloid dissolution and the formation of more stable pseudo-colloids. Temperature enhances dissolution of intrinsic Pu colloids by overcoming a moderate activation energy (28 kJ mol^{-1}). Our thermodynamic study shows that the sorption of Pu to montmorillonite is endothermic as a positive change in enthalpy for the sorption has been obtained. The affinity of Pu for montmorillonite increases with increasing temperature and resulting in higher K_ds. Although the fact that intrinsic Pu colloids tend to dissolve in the presence of montmorillonite may limit the migration of intrinsic colloids, the subsequent formation of thermodynamically more stable pseudo-colloids can play important role in Pu transport in the environment over significant temporal and spatial scales.

7.5   REFERENCES

Afonso, M. D. and Stumm, W., 1992. Reductive Dissolution of Iron(Iii) (Hydr)Oxides by Hydrogen-Sulfide. *Langmuir* **8**, 1671-1675.

Akob, D. M., Mills, H. J., and Kostka, J. E., 2007. Metabolically active microbial communities in uranium-contaminated subsurface sediments. *Fems Microbiology Ecology* **59**, 95-107.

Allard, B., Olofsson, U., Torstenfelt, B., Kipatsi, H., and Andersson, K., 1982. Sorption of actinides in well-defined oxidation states on geologic media. *Mater. Res. Soc. Symp. Proc.* **11**, 775-82.

Altmaier, M., Gaona, X., and Fanghaenel, T., 2013. Recent Advances in Aqueous Actinide Chemistry and Thermodynamics. *Chem Rev* **113**, 901-943.

Artinger, R., Schuessler, W., Schaefer, T., and Kim, J. I., 2002. A kinetic study of Am(III)/humic colloid interactions. *Environ Sci Technol* **36**, 4358-4363.

Barns, S. M., Cain, E. C., Sommerville, L., and Kuske, C. R., 2007. Acidobactetia phylum sequences in uranium-contaminated subsurface sediments greatly expand the known diversity within the phylum. *Applied and Environmental Microbiology* **73**, 3113-3116.

Begg, J. D., Zavarin, M., and Kersting, A. B., 2014. Plutonium Desorption from Mineral Surfaces at Environmental Concentrations of Hydrogen Peroxide. *Environ Sci Technol* **48**, 6201-6210.

Begg, J. D., Zavarin, M., Tumey, S. J., and Kersting, A. B., 2015. Plutonium sorption and desorption behavior on bentonite. *Journal of Environmental Radioactivity* **141**, 106-114.

Begg, J. D., Zavarin, M., Zhao, P. H., Tumey, S. J., Powell, B., and Kersting, A. B., 2013. Pu(V) and Pu(IV) Sorption to Montmorillonite. *Environ Sci Technol* **47**, 5146-5153.

Berner, R. A., 1978. RATE CONTROL OF MINERAL DISSOLUTION UNDER EARTH SURFACE CONDITIONS. *American Journal of Science* **278**, 1235-1252.

Berner, R. A., 1981. Kinetics of Weathering and Diagenesis. In: Lasaga, A. C. and Kirkpatrick, R. J. Eds.), *Kinetics of Geochemical Processes*. BookCrafters, Inc., Chelsea, Michigan

Bernhard, G., Geipel, G., Reich, T., Brendler, V., Amayri, S., and Nitsche, H., 2001. Uranyl(VI) carbonate complex formation: Validation of the $Ca_2UO_2(CO_3)_3$(aq.) species. *Radiochim Acta* **89**, 511-518.

Bertetti, F. P., Pabalan, R. T., and Almendarez, M. G., 1998. Studies on neptunium(V) sorption on quartz, clinoptilolite, montmorillonite, and a-alumina. In: Jenne, E. A. (Ed.), *Adsorption of Metals by Geomedia*. Academic Press, San Diego.

Bethke, C. M. and Yeakel, S., 2010. The Geochemist's Workbench®. Hydrogeology Program, University of Illinois, Urbana, Illinois.

Boving, T. B. and Grathwohl, P., 2001. Tracer diffusion coefficients in sedimentary rocks: correlation to porosity and hydraulic conductivity. *Journal of Contaminant Hydrology* **53**, 85-100.

Bradbury, M. H. and Baeyens, B., 2002. Porewater chemistry in compacted re-saturated MX-80 bentonite: Physico-chemical characterisation and geochemical modelling*PSI Bericht Nr. 02-10*. Paul Scherrer Institute, Villigen PSI.

Bradbury, M. H. and Baeyens, B., 2003a. A comparison of apparent diffusion coefficients measured in compacted Kunigel V1 bentonite with those calculated from batch sorption measurements and D_e(HTO) data: a case study for Cs(I), Ni(II), Sm(III), Am(III), Zr(IV) and Np(V)*PSI Report 03-02*. Paul Scherrer Institut, Laboratory for Waste Management, Villigen PSI.

Bradbury, M. H. and Baeyens, B., 2003b. Porewater chemistry in compacted re-saturated MX-80 bentonite. *Journal of Contaminant Hydrology* **61**, 329-338.

Bradbury, M. H. and Baeyens, B., 2011. Physico-chemical characterisation data and sorption measurements of Cs, Ni, Eu, Th, U, Cl, I and Se on MX-80 bentonite*Technical Report 09-08*. Nagra, Wettingen.

Brockmann, S., 2006. Migration of caesium in bentonite: Influence of the pore water composition. Practical Report, Hochschule für Technik und Wirtschaft & Forschungszentrum Rossendorf.

Bruno, J., Arcos, D., Cera, E., Duro, L., and Grivé, M., 2004. Modelling near- and far-field processes in nuclear waste management. In: Grieré, R. and Stille, P. Eds.), *Energy, waste, and the environment: a geochemical perspective*. Geological Society, London.

Choppin, G. R., 1991. Redox speciation of plutonium in natural waters. *J Radioan Nucl Ch Ar* **147**, 109-116.

Choppin, G. R., 2007. Actinide speciation in the environment. *Journal of Radioanalytical and Nuclear Chemistry* **273**, 695-703.

Cleveland, J. M., 1979. The Chemistry of Plutonium. American Nuclear Society, La Grange Park.

COMSOL, 2014. COMSOL Multiphysics®. COMSOL, Inc., Burlington.

Crank, J., 1975. *The mathematics of diffusion*. Oxford University Press Inc., New York.

Dai, M. H., Buesseler, K., and Pike, S. M., 2005. Plutonium in groundwater at the 100K-Area of the US DOE Hanford site. *Journal of Contaminant Hydrology* **76**, 167-189.

Doherty, J., 2003. PEST*Model-independent parameter estimation and uncertainty analysis*. Watermark Numerical Computing, Brisbane.

Dong, W. M. and Brooks, S. C., 2006. Determination of the formation constants of ternary complexes of uranyl and carbonate with alkaline earth metals (Mg^{2+}, Ca^{2+}, Sr^{2+}, and Ba^{2+}) using anion exchange method. *Environ Sci Technol* **40**, 4689-4695.

Dozol, M., Hagemann, R., Hoffman, D. C., Adloff, J. P., Vongunten, H. R., Foos, J., Kasprzak, K. S., Liu, Y. F., Zvara, I., Ache, H. J., Das, H. A., Hagemann, R. J. C., Herrmann, G., Karol, P., Maenhaut, W., Nakahara, H., Sakanoue, M., Tetlow, J. A., Baro, G. B., Fardy, J. J., Benes, P., Roessler, K., Roth, E., Burger, K., Steinnes, E., Kostanski, M. J., Peisach, M., Liljenzin, J. O., Aras, N. K., Myasoedov, B. F., and Holden, N. E., 1993. Radionuclide migration in groundwaters - Review of the behavior of actinides (Technical report) *Pure and Applied Chemistry* **65**, 1081-1102.

Duro, L., Domènech, C., Grivé, M., Roman-Ross, G., Bruno, J., and Källström, K., 2014. Assessment of the evolution of the redox conditions in a low and intermediate level nuclear waste repository (SFR1, Sweden). *Applied Geochemistry* **49**, 192-205.

Dzombak, D. A. and Morel, F. M. M., 1993. Surface complexation modeling: hydrous ferric oxide. Wiley-Interscience, New York.

Efurd, D. W., Runde, W., Banar, J. C., Janecky, D. R., Kaszuba, J. P., Palmer, P. D., Roensch, F. R., and Tait, C. D., 1998. Neptunium and plutonium solubilities in a Yucca Mountain groundwater. *Environ Sci Technol* **32**, 3893-3900.

Fernandez, A. M., Baeyens, B., Bradbury, M., and Rivas, P., 2004. Analysis of the porewater chemical composition of a Spanish compacted bentonite used in an engineered barrier. *Physics and Chemistry of the Earth* **29**, 105-118.

Field, E. K., D'Imperio, S., Miller, A. R., VanEngelen, M. R., Gerlach, R., Lee, B. D., Apel, W. A., and Peyton, B. M., 2010. Application of molecular techniques to elucidate the influence of cellulosic waste on the bacterial community structure at a simulated low-level-radioactive-waste site. *Applied and Environmental Microbiology* **76**, 3106-3115.

Garcia-Gutierrez, M., Cormenzana, J. L., Missana, T., Mingarro, M., and Alonso, U., 2004. Analysis of uranium diffusion coefficients in compacted FEBEX bentonite. *Mater. Res. Soc. Symp. Proc.* **807**, 603-608.

Geckeis, H., Schafer, T., Hauser, W., Rabung, T., Missana, T., Degueldre, C., Mori, A., Eikenberg, J., Fierz, T., and Alexander, W. R., 2004. Results of the colloid and radionuclide retention experiment (CRR) at the Grimsel Test Site (GTS), Switzerland - impact of reaction kinetics and speciation on radionuclide migration. *Radiochim Acta* **92**, 765-774.

Glaus, M. A., Frick, S., Rosse, R., and Van Loon, L. R., 2010. Comparative study of tracer diffusion of HTO, $^{22}Na^+$ and $^{36}Cl^-$ in compacted kaolinite, illite and montmorillonite. *Geochimica et Cosmochimica Acta* **74**, 1999-2010.

Glaus, M. A., Rossé, R., Van Loon, L. R., and Yaroshchuk, A. E., 2008. Tracer diffusion in sintered stainless steel filters: measurement of effective diffusion coefficients and implications for diffusion studies with compacted clays. *Clays and Clay Minerals* **56**, 677-685.

Glaus, M. A. and Van Loon, L. R., 2012. Diffusive behaviour of charged uranyl complexes in compacted montmorillonite*Clays in Natural & Engineered Barriers for Radioactive Waste Confinement - 5th International Meeting*. Andra, Montpellier.

Golubev, S. V., Bauer, A., and Pokrovsky, O. S., 2006. Effect of pH and organic ligands on the kinetics of smectite dissolution at 25 °C. *Geochimica Et Cosmochimica Acta* **70**, 4436-4451.

Grauer, R., 1986. Bentonite as a backfill material in the high-level waste repository: Chemical aspects*EIR Bericht Nr. 576, Nagra Technical Report NTB 86-12E*. Paul Scherrer Institut, Villigen, Switzerland and Nagra, Wettingen, Switzerland.

Grim, R. E., 1968. *Clay mineralogy*. McGraw Hill.

Guillaumont, R., Fanghanel, T., Neck, V., Fuger, J., Palmer, D. A., Grenthe, I., and Rand, M. H., 2003a. Update on the chemical thermodynamics of uranium, neptunium, plutonium, americium, and technetium. In: Mompean, F. J., Illemassene, M., Domenech-Orti, C., and Said, K. B. Eds.)*Chemical Thermodynamics*. Elsevier, Amsterdam.

Guillaumont, R., Fanghänel, T., Neck, V., Fuger, J., Palmer, D. A., Grenthe, I., and Rand, M. H., 2003b. *Update on the Chemical Thermodynamics of Uranium, Neptunium, Plutonium, Americium and Technetium (OECD/NEA, ed.)*. Elsevier, Amsterdam.

Guven, N., 1988. Smectites. *Reviews in Mineralogy and Geochemistry* **19**, 497-559.

Guven, N., 1990. Longevity of bentonite as buffer material in a nuclear-waste repository. *Engineering Geology* **28**, 233-247.

Herbert, H.-J. and Moog, H. C., 2002. Untersuchungen zur Quellung von Bentoniten in hochsalinaren Lösungen-Abschlussbericht*GRS-179*. Gesellschaft für Anlagen- und Reaktorsicherheit.

Hixon, A. E. and Powell, B. A., 2014. Observed changes in the mechanism and rates of Pu(V) reduction on hematite as a function of total plutonium concentration. *Environ Sci Technol* **48**, 9255-9262.

Hocsman, A., Di Nezo, S., Charlet, L., and Avena, M., 2006. On the mechanisms of dissolution of montroydite [HgO(s)]: Dependence of the dissolution rate on pH, temperature, and stirring rate. *Journal of Colloid and Interface Science* **297**, 696-704.

Huber, F., Kunze, P., Geckeis, H., and Schafer, T., 2011. Sorption reversibility kinetics in the ternary system radionuclide-bentonite colloids/nanoparticles-granite fracture filling material. *Applied Geochemistry* **26**, 2226-2237.

Huertas, F. J., Caballero, E., Jiménez de Cisneros, C., Huertas, F., and Linares, J., 2001. Kinetics of montmorillonite dissolution in granitic solutions. *Applied Geochemistry* **16**, 397-407.

IAEA, 1995. Principles of Radioactive Waste Management*Safety Series* IAEA, Vienna.

Icopini, G. A., Lack, J. G., Hersman, L. E., Neu, M. P., and Boukhalfa, H., 2009. Plutonium(V/VI) reduction by the metal-reducing Bacteria Geobacter metallireducens GS-15 and Shewanella oneidensis MR-1. *Applied and Environmental Microbiology* **75**, 3641-3647.

Idemitsu, K., Tachi, Y., Furuya, H., Inagaki, Y., and Arima, T., 1996. Diffusion of uranium in compacted bentonites in the reducing condition with corrosion products of iron. *Mater. Res. Soc. Symp. Proc.* **412**, 683-90.

Jasrotia, P., Green, S. J., Canion, A., Overholt, W. A., Prakash, O., Wafula, D., Hubbard, D., Watson, D. B., Schadt, C. W., Brooks, S. C., and Kostka, J. E., 2014. Watershed-scale fungal community characterization along a pH gradient in a subsurface environment cocontaminated with uranium and nitrate. *Applied and Environmental Microbiology* **80**, 1810-1820.

Joseph, C., Schmeide, K., Sachs, S., Brendler, V., Geipel, G., and Bernhard, G., 2011. Sorption of uranium(VI) onto Opalinus Clay in the absence and presence of humic acid in Opalinus Clay pore water. *Chemical Geology* **284**, 240-250.

Joseph, C., Stockmann, M., Schmeide, K., Sachs, S., Brendler, V., and Bernhard, G., 2013a. Sorption of U(VI) onto Opalinus Clay: Effects of pH and humic acid. *Applied Geochemistry* **36**, 104-117.

Joseph, C., Van Loon, L. R., Jakob, A., Steudtner, R., Schmeide, K., Sachs, S., and Bernhard, G., 2013b. Diffusion of U(VI) in Opalinus Clay: Influence of temperature and humic acid. *Geochimica et Cosmochimica Acta* **109**, 74-89.

Kaplan, D. I., Powell, B. A., Duff, M. C., Demirkanli, D. I., Denham, M., Fjeld, R. A., and Molz, F. J., 2007. Influence of sources on plutonium mobility and oxidation state transformations in vadose zone sediments. *Environ Sci Technol* **41**, 7417-7423.

Kaszuba, J. P. and Runde, W. H., 1999. The aqueous geochemistry of neptunium: Dynamic control of soluble concentrations with applications to nuclear waste disposal. *Environ Sci Technol* **33**, 4427-4433.

Keeney-Kennicutt, W. L. and Morse, J. W., 1985. The redox chemistry of Pu(V)O2+ interaction with common mineral surfaces in dilute solutions and seawater. *Geochimica Et Cosmochimica Acta* **49**, 2577-2588.

Keller, L. M., Holzer, L., Gasser, P., Erni, R., and Rossell, M. D., 2015. Intergranular pore space evolution in MX80 bentonite during a long-term experiment. *Applied Clay Science* **104**, 150-159.

Keren, R. and Shainberg, I., 1975. Water-vapor isotherms and heat of immersion of Na/Ca-montmorillonite systems - I: Homoionic clay. *Clays and Clay Minerals* **23**, 193-200.

Kerisit, S. and Liu, C. X., 2010. Molecular simulation of the diffusion of uranyl carbonate species in aqueous solution. *Geochimica et Cosmochimica Acta* **74**, 4937-4952.

Kersting, A. B., 2013. Plutonium Transport in the Environment. *Inorganic Chemistry* **52**, 3533-3546.

Kersting, A. B., Efurd, D. W., Finnegan, D. L., Rokop, D. J., Smith, D. K., and Thompson, J. L., 1999. Migration of plutonium in ground water at the Nevada Test Site. *Nature* **397**, 56-59.

Kersting, A. B., Zavarin, M., Powell, B. A., Moser, D., Carroll, S. A., Maxwell, R., Dai, Z., Williams, R., Tumey, S., Zhao, P., Tinnacher, R., Huang, P., Kips, R., Mason, H., Begg, J., Fisher, J., Simpkins, L., Zimmerman, T., Jablonski, J., and Snow, M., 2011. LLNL SFA FY11 Program Management and Performance Report: Environmental Transport of Plutonium.

Keto, P., Gunnarsson, D., Johannesson, L.-E., and Hansen, J., 2007. Assessment of backfilling materials and methods for deposition tunnels*Clays in Natural & Engineered Barriers for Radioactive Waste Confinement*. Andra, Lille.

Kim, H. T., Suk, T. W., Park, S. H., and Lee, C. S., 1993. Diffusivities for ions through compacted sodium-bentonite with varying dry bulk density. *Waste Manage. (N. Y.)* **13**, 303-8.

Kobashi, A. and Choppin, G. R., 1988. A study of techniques for separating plutonium in different oxidation states. *Radiochim. Acta* **43**, 211-215.

Kohler, S. J., Dufaud, F., and Oelkers, E. H., 2003. An experimental study of illite dissolution kinetics as a function of pH from 1.4 to 12.4 and temperature from 5 to 50 degrees C. *Geochimica Et Cosmochimica Acta* **67**, 3583-3594.

Kozai, N., Inada, K., Kozaki, T., Sato, S., Ohashi, H., and Banba, T., 2001. Apparent diffusion coefficients and chemical species of neptunium(V) in compacted Na-montmorillonite. *Journal of Contaminant Hydrology* **47**, 149-158.

Kozai, N., Ohnuko, T., Matsumoto, J., Banba, T., and Ito, Y., 1996. A study of the specific sorption of neptunium(V) on smectite in low pH solution. *Radiochim. Acta* **75**, 149-158.

Kozai, N., Ohnuky, T., and Muraoka, S., 1993. Sorption characteristics of neptunium by sodium-smectite. *J. Nuclear Sci. Tech.* **30**, 1153-1159.

Křepelová, A., Sachs, S., and Bernhard, G., 2006. Uranium(VI) sorption onto kaolinite in the presence and absence of humic acid. *Radiochim Acta* **94**, 825-833.

Lasaga, A. C., 1981. Transition State Theory. In: Lasaga, A. C. and Kirkpatrick, R. J. Eds.), *Kinetics of Geochemical Processes*. BookCrafters, Inc., Chelsea, Michigan

Lasaga, A. C., 1998. *Kinetic Theory in the Earth Sciences*. Princeton University Press, Princeton, NJ.

Lasaga, A. C. and Gibbs, G. V., 1990. ABINITIO QUANTUM-MECHANICAL CALCULATIONS OF WATER-ROCK INTERACTIONS - ADSORPTION AND HYDROLYSIS REACTIONS. *American Journal of Science* **290**, 263-295.

Lasaga, A. C. and Luttge, A., 2004. Mineralogical approaches to fundamental crystal dissolution kinetics. *American Mineralogist* **89**, 527-540.

Latrille, C., Ly, J., and Herbette, M., 2006. Retention of Sn(IV) and Pu(IV) onto four argillites from the Callovo-Oxfordian level at Bure (France) from eight equilibrated sedimentary waters. *Radiochim Acta* **94**, 421-427.

Lee, J. O., Lim, J. G., Kang, I. M., and Kwon, S., 2012. Swelling pressures of compacted Ca-bentonite. *Engineering Geology* **129–130**, 20-26.

Lu, N. P., Reimus, P. W., Parker, G. R., Conca, J. L., and Triay, I. R., 2003. Sorption kinetics and impact of temperature, ionic strength and colloid concentration on the adsorption of plutonium-239 by inorganic colloids. *Radiochim Acta* **91**, 713-720.

Lujaniene, G., Motiejunas, S., and Sapolaite, J., 2007. Sorption of Cs, Pu and Am on clay minerals. *Journal of Radioanalytical and Nuclear Chemistry* **274**, 345-353.

Maher, K., Steefel, C. I., DePaolo, D. J., and Viani, B. E., 2006. The mineral dissolution rate conundrum: Insights from reactive transport modeling of U isotopes and pore fluid chemistry in marine sediments. *Geochimica Et Cosmochimica Acta* **70**, 337-363.

Management, O. o. C. R. W., 2002. Yucca Mountain Science and Engineering Report: Technical Information Supporting Site Recommendation Consideration. U.S. Department of Energy.

Marchetti, A. A., Brown, T. A., Cox, C. C., Hamilton, T. F., and Martinelli, R. E., 2005. Accelerator mass spectrometry of actinides. *Journal of Radioanalytical and Nuclear Chemistry* **263**, 483-487.

McCubbin, D. and Leonard, K. S., 1996. Photochemical dissolution of radionuclides from marine sediments. *Mar Chem* **55**, 399-408.

Missana, T., Alonso, U., Garcia-Gutierrez, M., and Mingarro, M., 2008. Role of bentonite colloids on europium and plutonium migration in a granite fracture. *Applied Geochemistry* **23**, 1484-1497.

Missana, T. and Garcia-Gutierrez, M., 2007. Adsorption of bivalent ions (Ca(II), Sr(II) and Co(II)) onto FEBEX bentonite. *Physics and Chemistry of the Earth* **32**, 559-567.

Missana, T., Garcia-Gutierrez, M., and Alonso, U., 2004. Kinetics and irreversibility of cesium and uranium sorption onto bentonite colloids in a deep granitic environment. *Applied Clay Science* **26**, 137-150.

Muyzer, G., Teske, A., Wirsen, C. O., and Jannasch, H. W., 1995. Phylogenetic relationships of *Thiomicrospira* species and their identification in deep-sea hydrothermal vent samples by denaturing gradient gel electrophoresis of 16S rDNA fragments. *Archives of Microbiology* **164**, 165-172.

NAGRA, 2006. The CRR Final Project Report Series II: Supporting Laboratory Experiments with Radionuclides and Bentonite Colloids. Technical Report 03-02. In: Missana, T. and Geckeis, H. Eds.). Nagra, Wettingen, Switzerland

Nebelung, C. and Brendler, V., 2009. Uranium(VI) sorption on montmorillonite and bentonite: Prediction and experiments. In: Bernhard, G. (Ed.),*Annual Report 2008, FZD-511*. Forschungszentrum Dresden-Rossendorf, Institut für Radiochemie, Dresden.

Neck, V., Altmaier, M., and Fanghaenel, T., 2007a. Thermodynamic data for hydrous and anhydrous PuO2+x(S). *Journal of Alloys and Compounds* **444**, 464-469.

Neck, V., Altmaier, M., and Fanghanel, T., 2007b. Solubility of plutonium hydroxides/hydrous oxides under reducing conditions and in the presence of oxygen. *Cr Chim* **10**, 959-977.

Neck, V., Altmaier, M., Seibert, A., Yun, J. I., Marquardt, C. M., and Fanghanel, T., 2007c. Solubility and redox reactions of Pu(IV) hydrous oxide: Evidence for the formation of PuO(2+x)(s, hyd). *Radiochim Acta* **95**, 193-207.

Neck, V. and Kim, J. I., 2001. Solubility and hydrolysis of tetravalent actinides. *Radiochim Acta* **89**, 1-16.

Nitsche, H. and Edelstein, N. M., 1985. Solubilities and speciation of selected transuranium ions. A comparison of a non-complexing solution with a groundwater from the Nevada Tuff Site. *Radiochim Acta* **39**, 23-33.

Nitsche, H., Gatti, R. C., Standifer, E. M., Lee, S. C., Muller, A., Prussin, T., Deinhammer, R. S., Maurer, H., Becraft, K., Leung, S., and Carpenter, S. A., 1993. Measured solubilites and speciations of neptunium, plutonium, and americium in a typical groundwater (J-13) from the Yucca Mountain region. Los Alamos National Laboratory, Los Alamos, NM.

Nitsche, H., Roberts, K., Prussin, T., Muller, A., Becraft, K., Keeney, D., Carpenter, S. A., and Gatti, R. C., 1994. Measured solubilities and speciations from oversaturation experiments of neptunium, plutonium, and americium in UE-25p #1 well from the Yucca Mountain region. Los Alamos National Laboratory, Los Alamos.

Novikov, A. P., Kalmykov, S. N., Utsunomiya, S., Ewing, R. C., Horreard, F., Merkulov, A., Clark, S. B., Tkachev, V. V., and Myasoedov, B. F., 2006. Colloid transport of plutonium in the far-field of the Mayak Production Association, Russia. *Science* **314**, 638-641.

Orlandini, K. A., Penrose, W. R., and Nelson, D. M., 1986. Pu(V) as the stable form of oxidized plutonium in natural waters. *Mar Chem* **18**, 49-57.

Pabalan, R. T. and Turner, D. R., 1997. Uranium(VI) sorption on montmorillonite: Experimental and surface complexation modeling study. *Aquatic Geochemistry* **2**, 203-226.

Pabalan, R. T., Turner, D. R., Bertetti, F. P., and Prikryl, J. D., 1998. Uranium(VI) sorption onto selected mineral surfaces. In: Jenne, E. A. (Ed.), *Adsorption of metals by geomedia: Variables, mechanisms, and model applications*. Academic Press, San Diego.

Payne, T. E., Brendler, V., Comarmond, M. J., and Nebelung, C., 2011. Assessment of surface area normalisation for interpreting distribution coefficients (K_d) for uranium sorption. *Journal of Environmental Radioactivity* **102**, 888-895.

Penrose, W. R., Polzer, W. L., Essington, E. H., Nelson, D. M., and Orlandini, K. A., 1990. Mobility of plutonium and americium through a shallow aquifer in a semiarid region. *Environ Sci Technol* **24**, 228-234.

Pizzetti, I., Fuchs, B. M., Gerdts, G., Wichels, A., Wiltshire, K. H., and Amann, R., 2011. Temporal variability of coastal *Planctomycetes* clades at kabeltonne station, North Sea. *Applied and Environmental Microbiology* **77**, 5009-5017.

Powell, B. A., Dai, Z. R., Zavarin, M., Zhao, P. H., and Kersting, A. B., 2011. Stabilization of plutonium nano-colloids by epitaxial distortion on mineral surfaces. *Environ Sci Technol* **45**, 2698-2703.

Powell, B. A., Fjeld, R. A., Kaplan, D. I., Coates, J. T., and Serkiz, S. M., 2004. Pu(V)O2+ adsorption and reduction by synthetic magnetite (Fe3O4). *Environ Sci Technol* **38**, 6016-6024.

Powell, B. A., Fjeld, R. A., Kaplan, D. I., Coates, J. T., and Serkiz, S. M., 2005. Pu(V)O2+ adsorption and reduction by synthetic hematite and goethite. *Environ Sci Technol* **39**, 2107-2114.

Powell, B. A., Kaplan, D. I., Serkiz, S. M., Coates, J. T., and Fjeld, R. A., 2014. Pu(V) transport through Savannah River Site soils - an evaluation of a conceptual model of surface-mediated reduction to Pu (IV). *Journal of Environmental Radioactivity* **131**, 47-56.

Powell, B. A., Kersting, A. B., and Zavarin, M., 2008. Sorption and Desorption Rates of Neptunium and Plutonium on Goethite. In: Zavarin, M., Kersting, A. B., Lindvall, R. E., and Rose, T. P. Eds.), *Hydrologic Resources Management Program and Underground Test Area Project, FY 2006 Progress Report*. Lawrence Livermore National Laboratory, Livermore, CA.

Pruesse, E., Peplies, J., and Glöckner, F. O., 2012. SINA: Accurate high-throughput multiple sequence alignment of ribosomal RNA genes. *Bioinformatics* **28**, 1823-1829.

Radeva, G., Kenarova, A., Bachvarova, V., Flemming, K., Popov, I., Vassilev, D., and Selenska-Pobell, S., 2013. Bacterial diversity at abandoned uranium mining and milling sites in Bulgaria as revealed by 16S rRNA genetic diversity study. *Water Air and Soil Pollution* **224**, 1-14.

Radeva, G. and Selenska-Pobell, S., 2005. Bacterial diversity in water samples from uranium wastes as demonstrated by 16S rDNA and ribosomal intergenic spacer amplification retrievals. *Canadian Journal of Microbiology* **51**, 910-923.

Ramebäck, H., Skålberg, M., Eklund, U. B., Kjellberg, L., and Werme, L., 1998. Mobility of U, Np, Pu, Am and Cm from spent nuclear fuel into bentonite clay. *Radiochim Acta* **82**, 167-171.

Rao, L. F., Srinivasan, T. G., Garnov, A. Y., Zanonato, P. L., Di Bernardo, P., and Bismondo, A., 2004. Hydrolysis of neptunium(V) at variable temperatures (10-85 degrees C). *Geochimica Et Cosmochimica Acta* **68**, 4821-4830.

Rao, L. F., Tian, G. X., Di Bernardo, P., and Zanonato, P., 2011. Hydrolysis of Plutonium(VI) at Variable Temperatures (283-343 K). *Chem-Eur J* **17**, 10985-10993.

Romanchuk, A. Y., Kalmykov, S. N., and Aliev, R. A., 2011. Plutonium sorption onto hematite colloids at femto- and nanomolar concentrations. *Radiochim Acta* **99**, 137-144.

Ross, C. S. and Shannon, E. V., 1926. The minerals of bentonite and related clays and their physical properties. *Journal of the American Ceramic Society* **9**, 77-96.

Rozalén, M., Brady, P. V., and Huertas, F. J., 2009. Surface chemistry of K-montmorillonite: Ionic strength, temperature dependence and dissolution kinetics. *Journal of Colloid and Interface Science* **333**, 474-484.

Rozalén, M. L., Huertas, F. J., Brady, P. V., Cama, J., García-Palma, S., and Linares, J., 2008. Experimental study of the effect of pH on the kinetics of montmorillonite dissolution at 25 °C. *Geochimica Et Cosmochimica Acta* **72**, 4224-4253.

Runde, W., Conradson, S. D., Efurd, D. W., Lu, N. P., VanPelt, C. E., and Tait, C. D., 2002a. Solubility and sorption of redox-sensitive radionuclides (Np, Pu) in J-13 water from the Yucca Mountain site: comparison between experiment and theory. *Applied Geochemistry* **17**, 837-853.

Runde, W., Conradson, S. D., Wes Efurd, D., Lu, N., VanPelt, C. E., and Tait, C. D., 2002b. Solubility and sorption of redox-sensitive radionuclides (Np, Pu) in J-13 water from the Yucca Mountain site: comparison between experiment and theory. *Applied Geochemistry* **17**, 837-853.

Sabodina, M. N., Kalmykov, S. N., Sapozhnikov, Y. A., and Zakharova, E. V., 2006. Neptunium, plutonium and ^{137}Cs sorption by bentonite clays and their speciation in pore waters. *Journal of Radioanalytical and Nuclear Chemistry* **270**, 349-355.

Sachs, S., Křepelová, A., Schmeide, K., Koban, A., Günther, A., Mibus, J., Brendler, V., Geipel, G., and Bernhard, G., 2007. Joint Project: Migration of actinides in the system clay, humic substance, aquifer - Migration behavior of actinides (uranium, neptunium) in clays: Characterization and quantification of the influence of humic substances*Wissenschaftlich-Technische Berichte, FZD-460*. Forschungszentrum Dresden-Rossendorf, Dresden.

Sanchez, A. L., Murray, J. W., and Sibley, T. H., 1985. The adsorption of plutonium IV and plutonium V on goethite. *Geochimica et Cosmochimica Acta* **49**, 2297-2307.

Santschi, P. H., Roberts, K. A., and Guo, L. D., 2002. Organic mature of colloidal actinides transported in surface water environments. *Environ Sci Technol* **36**, 3711-3719.

Sato, H., Ashida, T., Kohara, Y., Yui, M., and Sasaki, N., 1992. Effect of dry density on diffusion of some radionuclides in compacted sodium bentonite. *J. Nucl. Sci. Technol.* **29**, 873-882.

Schwenk-Ferrero, A., 2013. German spent nuclear fuel legacy: Characteristics and high-level waste management issues. *Science and Technology of Nuclear Installations* **2013**, 11.

Silva, R. J. and Nitsche, H., 1995. Actinide environmental chemistry. *Radiochim Acta* **70-1**, 377-396.

Singer, D. M., Guo, H., and Davis, J. A., 2014. U(VI) and Sr(II) batch sorption and diffusion kinetics into mesoporous silica (MCM-41). *Chemical Geology* **390**, 152-163.

Snow, M. S., Zhao, P. H., Dai, Z. R., Kersting, A. B., and Zavarin, M., 2013. Neptunium(V) sorption to goethite at attomolar to micromolar concentrations using radiometric methods. *Journal of Colloid and Interface Science* **390**, 176-182.

Steefel, C., 2011. CrunchFlow*Software for modeling multicomponent reactive flow and transport*. Lawrence Berkeley National Laboratory, Berkeley, CA.

Stroes-Gascoyne, S., Sergeant, C., Schippers, A., Hamon, C. J., Nèble, S., Vesvres, M. H., Barsotti, V., Poulain, S., and Le Marrec, C., 2011. Biogeochemical processes in a clay formation *in situ* experiment: Part D – Microbial analyses – Synthesis of results. *Applied Geochemistry* **26**, 980-989.

Stumm, W., 1997. Reactivity at the mineral-water interface: dissolution and inhibition. *Colloids and Surfaces A: Physicochemical and Engineering Aspects* **120**, 143-166.

Tinnacher, R. M., Zavarin, M., Powell, B. A., and Kersting, A. B., 2011. Kinetics of neptunium(V) sorption and desorption on goethite: An experimental and modeling study. *Geochimica et Cosmochimica Acta* **75**, 6584-6599.

Torstenfelt, B. and Allard, B., 1986. Migration of fission products and actinides in compacted bentonite*SKB Technical Report 86-14*. Swedish nuclear fuel and waste management CO, Stockholm.

Trepte, P., 2004. Diffusion of tritiated water (HTO) through compacted bentonite samples: Effect of sample thickness. Practical report, Hochschule für Technik und Wirtschaft Dresden & Forschungszentrum Rossendorf.

Turner, D. R., Pabalan, R. T., and Bertetti, F. P., 1998. Neptunium(V) sorption on montmorillonite: An experimental and surface complexation modeling study. *Clays and Clay Minerals* **46**, 256-269.

Turner, D. R. and Sassman, S. A., 1996. Approaches to sorption modeling for high-level waste performance assessment. *Journal of Contaminant Hydrology* **21**, 311-332.

Urios, L., Marsal, F., Pellegrini, D., and Magot, M., 2013. Microbial diversity at iron-clay interfaces after 10 years of interaction inside a deep argillite geological formation (Tournemire, France). *Geomicrobiol. J.* **30**, 442-453.

Van Loon, L. R., 2014. Effective diffusion coefficients and porosity values for argillaceous rocks and bentonite: Measured and estimated values for the provisional safety analyses for SGT-E2*Technical Report 12-03*. Nagra, Wettingen.

Van Loon, L. R., Baeyens, B., Glaus, M. A., Bradbury, M. H., Müller, W., and Schaible, A., 2007a. NF-PRO Report, Contract Number: FI6W-CT-2003-02389, RTD Component: 2, Work Package: 2.5*Deliverable (D-N°: 2.5.20), Reporting period: 01/01/04 - 31/12/07*. European Commission - Community Research.

Van Loon, L. R. and Eikenberg, J., 2005. A high-resolution abrasive method for determining diffusion profiles of sorbing radionuclides in dense argillaceous rocks. *Applied Radiation and Isotopes* **63**, 11-21.

Van Loon, L. R., Glaus, M. A., and Müller, W., 2007b. Anion exclusion effects in compacted bentonites: Towards a better understanding of anion diffusion. *Applied Geochemistry* **22**, 2536-2552.

Van Loon, L. R. and Soler, J. M., 2004. Diffusion of HTO, $^{36}Cl^-$, $^{125}I^-$, and $^{22}Na^+$ in Opalinus Clay: Effect of Confining Pressure, Sample Orientation, Sample Depth and Temperature*PSI-Bericht 04-03*. Paul Scherrer Institute, Villigen PSI.

Van Loon, L. R., Soler, J. M., Jakob, A., and Bradbury, M. H., 2003. Effect of confining pressure on the diffusion of HTO, $^{36}Cl^-$ and $^{125}I^-$ in a layered argillaceous rock (Opalinus Clay): diffusion perpendicular to the fabric. *Applied Geochemistry* **18**, 1653-1662.

Vaniman, D., Furlano, A., Chipera, S., Thompson, J., and Triay, I., 1995. Microautoradiography in studies of Pu(V) sorption by trace and fracture minerals in tuff. *MRS Proceedings* **412**, 639-646.

Walther, C. and Denecke, M. A., 2013. Actinide Colloids and Particles of Environmental Concern. *Chem Rev* **113**, 995-1015.

Wang, X. K., Chen, C. L., Zhou, X., Tan, X. L., and Hu, W. P., 2005. Diffusion and sorption of U(VI) in compacted bentonite studied by a capillary method. *Radiochim Acta* **93**, 273-278.

White, T. J., Bruns, T., Lee, S., and Taylor, J., 1990. *Amplification and direct sequencing of fungal ribosomal RNA genes for phylogenetics*. Academic Press, San Diego, California, USA; London, England, UK.

Wu, T., Dai, W., Xiao, G. P., Shu, F. J., Yao, J., and Li, J. Y., 2012. Influence of dry density on HTO diffusion in GMZ bentonite. *J. Radioanal. Nucl. Chem.* **292**, 853-857.

Xiao, Y. T. and Lasaga, A. C., 1994. AB-INITIO QUANTUM-MECHANICAL STUDIES OF THE KINETICS AND MECHANISMS OF SILICATE DISSOLUTION - H+(H3O+) CATALYSIS. *Geochimica Et Cosmochimica Acta* **58**, 5379-5400.

Xiong, Q., Jivkov, A. P., and Yates, J. R., 2014. Discrete modelling of contaminant diffusion in porous media with sorption. *Microporous Mesoporous Mater.* **185**, 51-60.

Zavarin, M., Powell, B. A., Bourbin, M., Zhao, P. H., and Kersting, A. B., 2012. Np(V) and Pu(V) ion exchange and surface-mediated reduction mechanisms on montmorillonite. *Environ Sci Technol* **46**, 2692-2698.

Zavarin, M., Zhao, P. H., Dai, Z. R., and Kersting, A. B., 2014. Plutonium sorption and precipitation in the presence of goethite at 25 and 80 degrees C. *Radiochim Acta* **102**, 983-997.

Zhao, P. H., Zavarin, M., Leif, R. N., Powell, B. A., Singleton, M. J., Lindvall, R. E., and Kersting, A. B., 2011. Mobilization of actinides by dissolved organic compounds at the Nevada Test Site. *Applied Geochemistry* **26**, 308-318.

Zheng, Z. P., Tokunaga, T. K., and Wan, J. M., 2003. Influence of calcium carbonate on U(VI) sorption to soils. *Environ Sci Technol* **37**, 5603-5608.

Zirnstein, I., Arnold, T., Krawczyk-Bärsch, E., Jenk, U., Bernhard, G., and Röske, I., 2012. Eukaryotic life in biofilms formed in a uranium mine. *MicrobiologyOpen* **1**, 83-94.

8.0   LABORATORY INVESTIGATION OF COLLOID-FACILITATED TRANSPORT OF CESIUM BY BENTONITE COLLOIDS IN A CRYSTALLINE ROCK SYSTEM

8.1   INTRODUCTION

The most likely mechanism for strongly-adsorbing radionuclides to be transported significant distances in groundwater after being released from waste packages in a high-level nuclear waste repository is by colloid-facilitated transport. Barring a strong association with mobile colloids, strongly-adsorbing radionuclides are generally predicted to have negligible impact on dose estimates in repository risk assessments because they aren't expected to transport far enough to reach potential receptors. The objective of this study was to quantify the potential for colloid-facilitated transport of one strongly-adsorbing radionuclide, cesium (as ^{137}Cs), through a weathered fractured granodiorite system. Cs was adsorbed to bentonite clay colloids before injection through columns packed with geologic media to provide estimates of desorption rate constants (from colloids) and other parameters that are important for performance assessment calculations. While our studies focused on a specific crystalline rock system, the method(s) we developed can, in principle, be applied to any geologic setting in which colloid-facilitated transport in groundwater is a potential mechanism for radionuclide release to the accessible environment. The methods are intended to especially provide insights into upscaling of colloid-facilitated radionuclide transport predictions in time and space.

For this study, we selected a fractured/weathered granodiorite at the Grimsel Test Site (GTS) in Switzerland as a model crystalline rock repository system because the system has been thoroughly studied (e.g., Geckeis et al., 2004; Huber et al., 2011), and field experiments involving radionuclides have already been conducted at this site (Geckeis et al., 2004; Möri, 2004; Wang et al., 2013; Dittrich et al.., 2014). Working on this system provides a unique opportunity to compare lab experimental results with field-scale observations.

Field experiments and observations in a shear zone at the GTS have shown that Cs transport in a fractured crystalline environment can be enhanced by the presence of bentonite colloids (Geckeis et al., 2004; Möri, 2004; Wang et al., 2013). In an experiment conducted at the GTS in 2002 as part of the a Colloid and Radionuclide Retardation (CRR) project, a significant fraction (~60%) of ^{137}Cs associated with colloids transported essentially conservatively in a dipole tracer test conducted between two boreholes completed in the shear zone. The mean conservative tracer residence time in this experiment was on the order of 2 hours, with peak tracer concentrations occurring in about 70 minutes. Interestingly, a second peak of ^{137}Cs, accounting for less than 10% of the injected mass, was observed at about 100 times longer than the first peak. This peak likely reflected the retardation of dissolved ^{137}Cs that was not associated with the colloids (or had become dissociated from the colloids during transport through the shear zone), as the colloid concentrations had essentially declined to background long before this peak was observed (Geckeis et al., 2004; Möri, 2004). In 2012, a second colloid-facilitated transport experiment involving ^{137}Cs was conducted at the GTS under the Colloids Formation and Migration (CFM) project (Wang et al., 2013). This experiment was conducted in a different dipole than the 2002 test (between a borehole and the access tunnel wall) and with a mean residence time of about 34 hours. In this experiment, the ^{137}Cs recovery was only about 10% and the breakthrough curve closely matched the shape of the bentonite colloid breakthrough curve, indicating that the observed ^{137}Cs was essentially all associated with the colloids. A second ^{137}Cs peak was not observed in this experiment, although this may have been because the experiment was not

conducted long enough to observe such a peak. A second peak would have taken about a year to arrive if the delay relative to the first peak was the same as in the 2002 experiment.

Laboratory experiments to evaluate the association of Cs with bentonite or smectite colloids have been conducted by several research groups (Murali and Mathur, 2002; Missana et al., 2004; Geckeis et al., 2004; Kurosawa et al., 2004; Iijima et al., 2010). The experiments of Missana et al. (2004), Geckeis et al. (2004) and Iijima et al. (2010) focused on the Grimsel system, although the bentonite colloids used by Iijima et al. (2010) were derived from a different bentonite source. These experiments, and in particular the work of Missana et al. (2004), have shown that Cs sorption to GTS bentonite colloids has a nonlinear dependence on Cs concentrations and that desorption of at least a portion of the sorbed Cs is slow and potentially incomplete (partial sorption irreversibility).   The dependence of Cs partition coefficients (K_d values) onto the bentonite colloids as a function of Cs concentration measured by Missana et al. (2004) is reproduced in Figure 8-1. In general, the work of the other research groups mentioned above are in reasonable agreement with Missana et al. (2004) when the Cs concentrations in the respective experiments are considered.
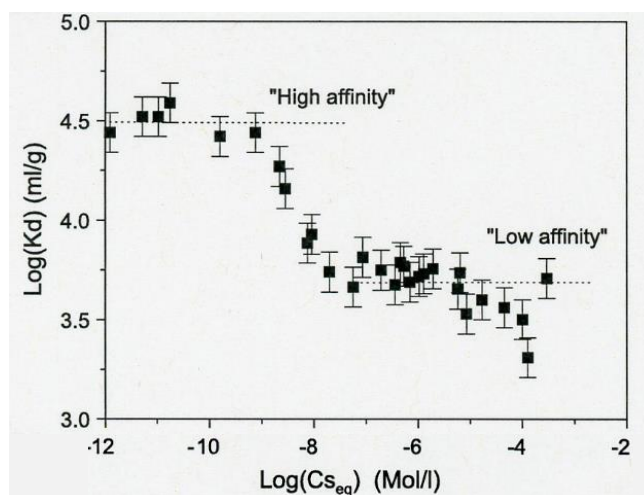
Figure 8-1: Batch adsorption K_d values for ^{137}Cs on same bentonite colloids as used in this study in GTS groundwater as a function of Cs concentration (reproduced from Missana et al., 2004).

In this study, we conducted both batch and column transport experiments to refine and parameterize a colloid-facilitated transport model and to provide insight into potential colloid-facilitated transport of Cs isotopes in a crystalline rock repository. The batch experiments included both Cs adsorption and desorption experiments onto fracture fill material (FFM) obtained from the GTS shear zone. We also measured the partitioning of Cs onto colloids that were prepared from the same bentonite that was used in the GTS field experiments (also the same bentonite used by Missana et al., 2004). The starting concentration of Cs in these experiments was not varied, but rather was kept the same as the injection solutions for the column experiments so that we could compare the batch test parameters with parameters derived from the column experiments. Column experiments were conducted with (1) Cs injected without colloids, (2) Cs injected pre-sorbed onto colloids with the colloid pulse ending at the same time as the Cs pulse, and (3) Cs injected pre-sorbed onto colloids with the colloids continuously fed through the column after the Cs pulse had ended.

An update of work conducted for the Colloids Formation and Migration Project at the Grimsel Test Site is not included in this report other than to say that the majority of the work over the past 1-1/2 years has involved the emplacement and subsequent long-term monitoring of a radionuclide-doped bentonite plug into a borehole at the GTS that intersects the flowing shear zone in which previous colloid-facilitated radionuclide transport experiments were conducted. The emplacement of the doped bentonite was accomplished in May 2014, and since then monitoring has indicated that the bentonite rapidly (within about 2 weeks) swelled to fill and pressurize the emplacement interval (between two packers instrumented with pressure sensors) and that a small amount of the conservative dye tracer included with the doped bentonite has appeared at both a near-field monitoring borehole (located several cm from the main emplacement hole) and at the access tunnel wall where a surface packer is being used as a controlled hydrologic sink. It also appears that the near-field monitoring borehole is registering a slight increase in groundwater turbidity, which suggests the appearance of colloids eroding from the bentonite plug. These results are all very preliminary, and as a courtesy to the CFM project participants, it would not be appropriate to present them in written form for the first time in this report.

8.2   STATE OF THE ART

The current state of the art in conducting colloid-facilitated contaminant/radionuclide transport experiments and in modeling colloid-facilitated transport has been addressed at length in the literature. Excellent reviews are provided by Grolimund et al. (2007), Bertetti et al. (2006), Kanti and Khilar (2006), Grolimund and Borkovec (2005), Painter et al., (2002), and Kersting and Reimus (2003). These reviews cite many earlier efforts. Modeling of colloid-facilitated contaminant transport has progressed very little in the past 20 years, but incremental advances have been made in parameterizing models and reducing uncertainty in model predictions by designing and conducting experiments that better interrogate the processes that result in colloid-facilitated transport over long time and distance scales (i.e., slow desorption colloids and slow or reversible colloid filtration). For example, in Dittrich et al. (2014 and 2015a), we introduced a method of reinjecting effluent from colloid-facilitated radionuclide transport column experiments into subsequent columns to allow better interrogation of slow desorption kinetics from colloids, which are very important for predicting colloid-facilitated transport in upscaled systems. In this study, we build on that approach and apply it to a study of the colloid-facilitated transport of Cs.

8.3   TECHNICAL APPROACHES (MATERIALS AND METHODS)

We conducted a series of batch adsorption and desorption experiments, as well as three flow-through experiments in small columns to evaluate the colloid-facilitated transport of Cs in the shear zone at the GTS. The materials and methods are described in this section.

Groundwater: The groundwater used in all experiments was synthetic shear zone water (SZW) that matched the water chemistry of the water in the shear zone at the Grimsel Test Site. The SZW was prepared by adding analytical grade reagents to filtered, high-purity water (> 18 MΩ cm resistivity) according to the concentrations of constituents listed in Table 8-1.

The ionic strength (0.66 mM) was calculated from the added reagents and a pH of 8.0 was measured the solution equilibrated with the atmosphere in Los Alamos, NM (2,231 m above sea level). The carbonate concentration listed in Table 3-1 is as prepared, not after equilibration with the atmosphere.

Table 8-1: Synthetic shear zone water constituents.

Constituent	mg/L
Na	14.97
K	0.20
Mg	0.02
Ca	5.60
Cl	5.67
SO_4	5.85
F	6.00
Si	9.96
$CO_3 + HCO_3$	20.06
Ionic Strength	0.66 mM
pH	8.0

Geologic Media: Weathered fracture fill material, or FFM (also known as fault gouge), was collected by coring the MI shear zone at the Grimsel Test Site (GTS) in Switzerland. The shear zone is not currently exposed in the CFM tunnel (where the field transport experiments were conducted), so the material was collected in an adjacent tunnel. The shear zone occurs where a fracture in the granite rock had been exposed to hydrothermal solutions and was altered over time. Samples were shipped to Los Alamos National Laboratory in pieces ranging from micron size up to 10-15 cm long. Due to the small quantity of material available, all pieces less than 1 cm in size were combined and crushed using a percussion mortar, sieved into 75-150, 150-355, and 355-500 μm size fractions, and thoroughly rinsed in high-purity water to removal all fines. The samples were then rinsed with synthetic Grimsel shear zone water (SZW) until the electrical conductivity of solution in contact with the material for 24 hours was within 5% of the electrical conductivity of the SZW. Samples were then oven dried for 12 hours at 60 °C and stored in glass jars. Optical microscope (Wild Heerbrugg, M420) photographs of the 150-355 μm size fraction of the FFM and the unaltered granodiorite matrix show that the FFM appears to have a larger fraction of dark grains (Figure 8-2).

The mineralogy of the granodiorite and FFM were determined by quantitative x-ray diffraction (QXRD) at Los Alamos. Table 8-2 lists the major fractions for the unaltered granodiorite, a scraping from the shear zone surface and a bulk sample of the crushed FFM that we used for all experiments discussed in this report.
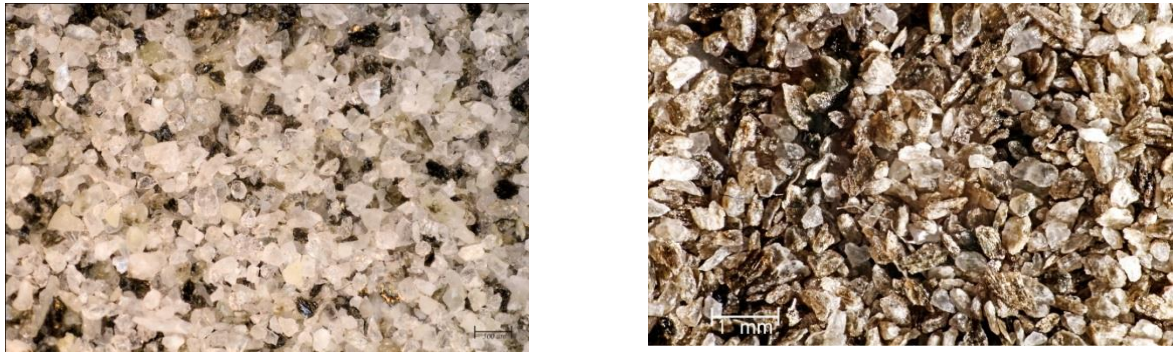
Figure 8-2: Microphotographs of crushed and sieved Grimsel granodiorite (left) and fracture fill material (right) in the 150-355 μm size fraction (from Dittrich and Reimus, 2015 and Dittrich et al., 2015a).

Table 8-2: Quantitative X-ray diffraction interpretation (wt%) of Grimsel granodiorite, shear zone surface, and bulk FFM materials.

Mineral	Granodiorite	Shear Zone Surface	FFM
Quartz	32	18	13
Microcline	10	8	5
Albite	42	44	34
Biotite	5	11	31
Chlorite	1	--	
Muscovite	10	19	16
Epidote	<1	--	--
Smectite	--	--	1
Calcite	--	<1	<1

Table 8-3: Bulk chemical analysis of granodiorite and FFM materials by X-ray fluorescence analysis (wt%).

Constituent	Granodiorite bulk	FFM bulk	Detection Limits
fuse ratio	7:1	7:1	7:1
Na_2O	4.01	3.15	0.0451
MgO	0.725	4.28	0.0300
$Al2O_3$	14.0	14.3	0.0313
SiO_2	70.9	63.4	0.1507
P_2O_5	0.115	0.124	0.0049
K_2O	4.22	4.90	0.0112
CaO	1.90	1.03	0.0084
TiO_2	0.436	0.491	0.0092
MnO	0.081	0.086	0.0252
$Fe2O_3$	3.10	3.83	0.0041
V	29	41	13
Cr	bdl	bdl	10
Co	bdl	bdl	15
Ni	bdl	bdl	5
Cu	bdl	bdl	5
Zn	31	53	5
Ge	bdl	bdl	24
As	bdl	bdl	15
Rb	110	192	4
Sr	135	71	5
Zr	217	236	6
Ba	403	372	19
W	bdl	bdl	43
U	bdl	bdl	4
LOI	0.35	4.28	
total	99.931	99.970	

bdl = below detection limit
LOI = loss on ignition

Table 8-3 shows the bulk chemical analysis of the granodiorite and bulk FFM by x-ray florescence spectroscopy. The main differences between the unaltered granodiorite and FFM were a significant enrichment in Mg, minor enrichment in K and Fe, and minor depletions of Si, Na, and Ca in the FFM relative to the parent granodiorite.

The surface area of the FFM was determined by the BET method with krypton gas (Micromeritics Analytical Services) and was measured as 0.23 m^2 g^{-1} for the 150-355 μm size fraction used in all experiments.

Bentonite Colloids: Bentonite colloids were processed from a brick of compressed bentonite from the Corijo de Archidona deposit (Almeria, Spain) that was shipped to us by our colleagues from the Grimsel Test Site in Switzerland. This material is also called FEBEX bentonite because it was used in the Full-scale high-level waste Engineered Barriers EXperiment at the GTS, which goes by the acronym FEBEX. The major mineralogy of this bentonite, as determined by quantitative XRD by our European colleagues, is given in Table 8-4. Samples of the brick were crushed in a ceramic mortar and pestle and sieved to retain the size fraction less than 75 μm. The bentonite colloids were sodium saturated to enable comparison of our results with other published results (Huber et al., 2011). 50 g of material was added to 1 L of 1 M NaCl and was placed on a shaker table for 7 days. The supernatant was decanted and the removed liquid was replaced with new 1 M NaCl and placed on the shaker for 7 additional days. This process was repeated 3 times and the solution conductivity was measured (VWR Series 500, Model 2052 meter and VWR 525 conductivity dip cell/electrode, Model 23198-020) to ensure completeness of the exchange process. The resulting suspension was settled and the supernatant was decanted and replaced with SZW. This process was repeated 6 times until the conductivity of the supernatant was reduced below 2.5 mS/cm and the colloids did not readily settle. The suspension was then placed in a sonic bath for 30 min, centrifuged for 12 hr, and the supernatant removed and replaced with SZW. This process was repeated 10 times until the resulting conductivity of the bentonite suspension was within 1% of the SZW. Various steps of the process are depicted in Figure 2-3.

The suspension was then diluted to 1 g L^{-1} with SZW and was settled in 1 L graduated cylinders for 2 weeks to obtain a stable experimental suspension. The top 700 mL was decanted and Stokes' Law was applied to calculate a theoretical maximum particle size of less than 1 μm. The final stock suspension was then passed through a 0.8-μm filter to remove any larger particles. A single particle counter was used to measure the particle size distribution of the stock suspension. Very few particles larger than 220 μm were present (Figure 8-4).

The concentration of the stock suspension was calculated to be (1540 mg L^{-1}) by drying 25 mL of suspension on a watch glass (in triplicate) and determining the weight difference after drying. The stock suspension was diluted to 100 mg L^{-1} and was stored in a sealed glass bottle. Surface area of the dried colloids was measured by the BET method with nitrogen gas to be 56.1 m^2 g^{-1}.

Table 8-4: Quantitative X-ray diffraction interpretation (wt%) of FEBEX bentonite.

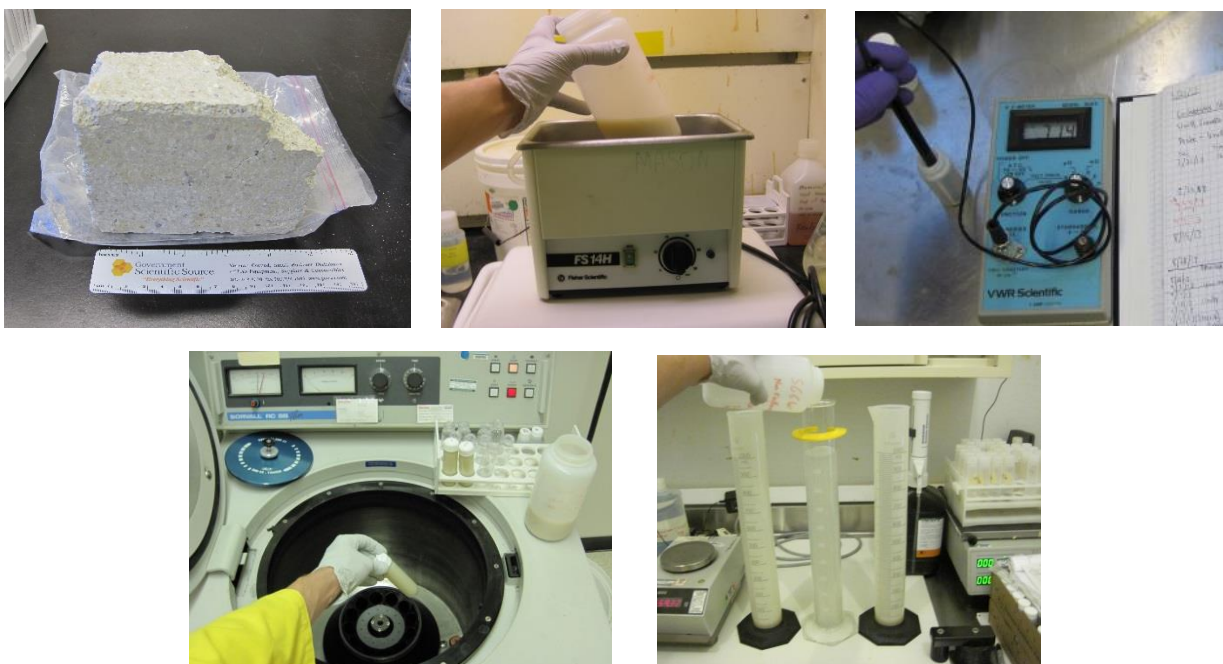| Mineral	Bentonite
Quartz	2 ± 1
Plagioclase (Na, Ca)	3 ± 1
Cristobalite	2 ± 1
Feldspars	Trace
Smectite	92 ± 3
Calcite	1 ± 0.5

Figure 8-3: Various steps in preparation of colloid suspension from FEBEX bentonite brick.
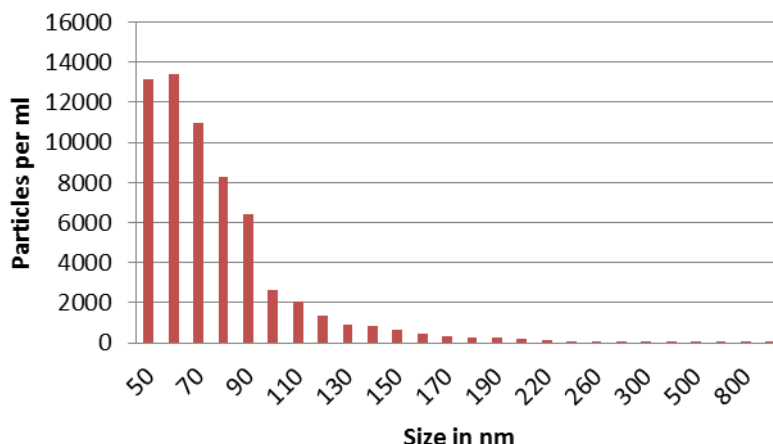
Figure 8-4: Particle size distribution of FEBEX bentonite colloid suspension as measured by a single particle counter. Note that the concentration scale on the y-axis does not account for sample dilution in the final suspension used in the experiments.

Cesium and Tritiated Water: The Cs used in all experiments was taken from a [137]CsCl stock in 0.1 M HCl (Eckert and Ziegler). The stock solution contained 3.056 μCi of [137]Cs (referenced to 10/1/2011) in 100 ml of aqueous solution, corresponding to a concentration of 2.6e-9 M [137]Cs. The solution contained 10 μg/ml, or 7.5e-5 M, of carrier (nonradioactive) Cs. When the SZW with 100 mg/L of suspended bentonite colloids was initially spiked with a small amount of this solution, NaOH was added to the suspension to neutralize the HCl from the stock solution and re-establish the pH of 8. This NaOH addition resulted in exceeding the ionic strength threshold for colloid stability, which led to the colloids aggregating and settling to the bottom of the container. The colloids were resuspended by decanting off most of the supernatant and adding enough fresh SZW to re-establish the 100 mg/L colloid concentration (and also to re-establish the unaltered or only slightly-altered Na and Cl concentrations in the SZW). The resulting solution was sonicated to re-disperse the colloids, and after sonication and settling, the colloid size distribution was found to be essentially indistinguishable from the original size distribution shown in Figure 8-4. After this procedure, the ^{137}Cs concentration in the suspension was about 3e-11 M, and the total Cs concentration was inferred to be ~9e-7 M. This process was repeated for subsequent batches of Cs-spiked colloid suspensions. The suspensions were allowed to equilibrate for at least 1 week. All suspensions were stored in Teflon® bottles until used in experiments.

Tritium in the form of tritiated water ([3]HHO) was added to the Cs and bentonite suspensions and was used as a conservative tracer to provide groundwater residence times and dispersivities in the column experiments.

Analytical Measurements: [137]Cs and tritium concentrations were measured by liquid scintillation counting, or LSC (Perkin Elmer Tri-Carb 2550) with energy ranges of 0-15 keV for tritium and 15-225 keV for [137]Cs (energies uncorrected for quenching). A 1 mL aliquot of sample was combined with 5 mL of deionized water and 14 mL of liquid scintillation cocktail (Packard, Ultima Gold AB) in a polypropylene scintillation vial to yield 20 mL total. The vial was vigorously shaken for at least 15 seconds to ensure mixing between the cocktail and the sample, and samples were counted for two 15 minute increments and the results were averaged. The

transformed index of an external [133]Ba standard (tSIE) was used to correct for variable quenching of the samples, especially with respect to tritium.

Total ^{137}Cs concentrations were measured with uncentrifuged column effluent and dissolved ^{137}Cs was measured by centrifuging the sample at 15,000 RPM for 12 hours and then analyzing 1 mL of the supernatant for ^{137}Cs concentration. Colloid-associated ^{137}Cs was then calculated as the difference between the total and dissolved ^{137}Cs concentration for each sample.

pH of the solutions, suspensions, and breakthrough experiment samples were measured using a pH meter (Orion, Model 290) and a glass pH electrode (Fisher, AccupHast) calibrated with 4.01, 7.00, and 9.01 pH buffer solutions (Ricca Chemical Corp.).

Colloid concentrations of the bentonite suspensions in the column breakthrough experiments were measured using turbidimetry. The turbidimeter (Hach, 2100N) was calibrated with standards (0.1, 1, 5, 10, 20, 40, 60, 80, 100 mg L^{-1}) and the same 12 mm borosilicate glass test tube was used for every measurement to reduce error from test tube variability. Colloid concentrations were calculated using a correlation function derived to relate colloid concentration with the measured NTU (nephelometric turbidity units) of the samples.

Batch Experiments: Batch adsorption and desorption experiments were conducted to evaluate the interaction of Cs with crushed FFM that was used in the column experiments. The experiments were performed in duplicate in polycarbonate centrifuge tubes, and a control experiment without the FFM was also conducted to allow corrections for any interaction of the Cs with the centrifuge tube walls. All sorption experiments were conducted using colloid-free SZW spiked with ^{137}Cs to the same concentration as in the colloid suspensions (with appropriate dilution with SZW to match the Na and Cl concentrations). In the reactors containing FFM, 20 ml of ^{137}Cs-spiked colloid-free SZW was placed in contact with 0.25 g of the FFM. The sorption experiments were conducted for ~70 hours, with samples collected from the centrifuge tubes after 2.5 and 30 min, and also after 3.1, 5.25, 20.3, 40.6 and 68.9 hr. All but approximately 1 ml of the remaining solution was then decanted off, and 20 ml of ^{137}Cs-free SZW was added to start duplicate desorption experiments (with a control as well). In the desorption experiments, samples were collected after 1, 7, 22 and 48 min, and also after 3.7, 6.1, 21.5, 46.1 and 70 hrs. All but 1 ml of the remaining solution was then again decanted off and 20 ml of ^{137}Cs-free SZW was added to start a second desorption step/experiment. However, for this step, one of the centrifuge tubes containing FFM received SZW that contained suspended colloids at 100 mg/L while the other received colloid-free SZW. In these desorption experiments, samples were collected after 1, 10, 20, 45, 70 min, and also after 3.6, 5.75, 21.4, 28.6, 48.5, 76 and 142 hrs.

Formal sorption and desorption experiments were not conducted to evaluate ^{137}Cs partitioning between the bentonite colloids and the SZW, but this partitioning was measured numerous times throughout the course of the study, and the ^{137}Cs was consistently found to be about 23-25% associated with the colloids and 75-77% in the solution phase. This result translates to a partition coefficient, or K_d value, of approximately 3700 ml/g, which is consistent with the results of Missana et al. (2004) for concentrations exceeding about 1e-8 M Cs (see Figure 8-1).

Column Transport Experiments: Column transport experiments were conducted by eluting Cs and bentonite suspensions through columns packed with FFM in the 150-355 μm size range. Small columns were constructed from 1.5 cm lengths of 0.95 cm diameter Teflon® tubing (Dittrich et al., 2015b). The ends of the tubes were tapped to accept Teflon® compression fittings. The inside openings were covered with a small disk of 75 μm PEEK screen to retain the column

material while providing minimum resistance to flow and causing negligible straining of colloids. Teflon® tubing (1/16ᵗʰ-inch ID) and 3-way polycarbonate stopcocks were used to connect the columns to 60 mL polypropylene syringes (Becton Dickinson) installed on syringe pumps (KD Scientific, Model 100). 3-way stopcocks allowed for refilling syringes and switching suspensions or solutions while minimizing flow and pressure disturbances that may affect colloid retention. Flow was directed upward to help maintain saturation and to minimize the potential for air bubbles collecting in the columns. An additional length of 1/16ᵗʰ-inch ID Teflon® tubing was connected to the top (outlet side) of the column and directed column effluent to a fraction collector (Gilson, FC-220) filled with 13×100 mm polystyrene test tubes. The fraction collector was enclosed in an acrylic plastic chamber with evaporation pans filled with deionized water to minimize evaporation before sample analysis. Figure 8-5 shows a picture of the column experiment setup.

Columns were packed with 1.5 g of dry FFM, resulting in a porosity of approximately 0.4 and a bulk density of about 1.6 g/cm³. The columns were initially flushed at ~0.3 ml/hr with ^{137}Cs-, ^{3}HHO-, and colloid-free SZW for 7 days and the pH was monitored to ensure effluent pH stabilized within 0.1 pH units of the influent solution (pH 8.0 ± 0.1) before the start of a radionuclide/colloid injection.

Figure 8-5: Photos of column experiment setup with three 1.5-cm-long columns running in parallel with syringe pumps, tubing, and fraction collector.

To begin each breakthrough experiment, the background solution was switched to either a bentonite suspension in SZW (100 mg/L bentonite) that contained ^{3}HHO and ^{137}Cs (3e-11 M ^{137}Cs, 9e-7 M total Cs) or to colloid-free SZW containing the same concentrations of ^{3}HHO and ^{137}Cs. Two identical columns were used; one received the ^{137}Cs-spiked colloid suspension and the other received the colloid-free spiked solution. The flow rates through the columns were nominally ~0.28 ml/hr. Syringes were refilled several times during the experiment and were eventually changed to SZW free of ^{3}HHO, ^{137}Cs, and bentonite colloids to observe the flushing of the colloids and ^{137}Cs from the columns. Samples were collected at 12 hr intervals and the sample mass was weighed with a digital balance (Mettler, PL1200) and subtracted from the empty test tube weight to calculate the actual flow rates. Total and dissolved ^{137}Cs activity, tritium activity, and colloid concentrations were measured for every sample early in the breakthroughs and then less often as the experiments progressed.

Once the ^{137}Cs concentration in the effluent from the column injected with the colloid suspension reached the inlet ^{137}Cs concentration, the effluent that wasn't used for radionuclide or colloid analyses was stored in a Teflon® bottle for re-use. This combined effluent was then injected into another FFM-filled column that had not been previously exposed to colloids or [137]Cs. The same procedure was followed as the other two columns except that after the injection solution was exhausted, the solution in the syringes was changed to [3]HHO- and ^{137}Cs-free SZW that contained suspended colloids at the same concentration as the combined effluent injected at the beginning of the experiment. Thus, while the injection of [3]HHO and Cs ceased, the injection of colloids continued without interruption for the remainder of the experiment.

At the end of each column experiment, a 0.1 M HCl solution was flushed through the column to desorb any ^{137}Cs remaining in the column and attempt to close the Cs mass balance for the experiment.

Control column experiments containing no FFM but with all the other experimental components were also conducted to evaluate interaction of Cs with any of the components other than the FFM, and it was found that interactions were negligible, so the results of these experiments are not presented in this report.

Interpretive Modeling: The batch experiments were interpreted by simply calculating ^{137}Cs partition coefficients near the end of the experiments for either adsorption or desorption. The partition coefficients were calculated as:

Adsorption: $$K_d = \frac{V}{M}\frac{(C_0 - C)}{C} \tag{8-1}$$

Desorption: $$K_d = \frac{V_{des}}{M}\frac{[(C_0 - C)_{ads}V_{ads} + C_{ads}V_{res,ads} - CV_{des}]}{CV_{des}} \text{ or } K_d = \frac{V_{des}}{M}\frac{S}{C} \tag{8-2}$$

where, V = volume of solution, ml
   M = mass of FFM or colloids, g
   C = concentration at end of experiment, mol/ml
   C_0 = concentration at beginning of experiment, mol/ml
   S = concentration on FFM or colloids, mol/g (calculated using data from previous step)
   ads = subscript for adsorption step
   des = subscript for desorption step
   $V_{res,ads}$ = volume of residual solution remaining behind after adsorption step, ml

The adsorption and desorption rate constants were not estimated from the batch experiments because the rates were observed to be very rapid – so much so that they were thought to be potentially limited by mass transfer rates in the batch reactors, especially considering the large volume to solid mass ratios in the centrifuge tubes. Also, when sorption site capacities are allowed to vary, estimates of rate constants from batch experiments are notoriously nonunique (a smaller site capacity and faster rate constants will often yield equally good fits to a data set as a larger site capacity and smaller rate constants). Thus, rather than attempt to estimate rate constants from the batch experiments, the rate constants were estimated by interpreting the column experiment data, and then the rates deduced from the columns were used to do a forward prediction of the batch sorption/desorption experiments. The forward batch experiment model was embodied in a Fortran program that allowed multiple sites with different rate constants and adsorption capacities (Dittrich et al., 2014). The governing equations of the model were:

Solution: $\dfrac{\partial c}{\partial t} = \dfrac{M}{V}\left[-\sum_i k_{fi}c\left(1 - \dfrac{s_i}{s_{mi}}\right) + \sum_i k_{ri}s_i\right]$ (8-3)

Solids: $\dfrac{\partial s_i}{\partial t} = k_{fi}c\left(1 - \dfrac{s_i}{s_{mi}}\right) - k_{ri}s_i$ (8-4)

where, c = concentration in aqueous phase, mol/ml
 s_i = concentration on surface sorption site i, mol/g
 t = time, hr
 k_{fi} = adsorption rate constant for sorption site i, ml/g-hr
 k_{ri} = desorption rate constant for site i, hr^{-1}
 s_{mi} = surface site density (maximum adsorption capacity) for sorption site i, mol/g
  M = mass of solids, g
 V = volume of solution, ml.

In addition to solving equations (8-3) and (8-4), the batch model allowed the volume of solution in the reactor to be changed at specified times to simulate sampling, and it also allowed for a specified volume of Cs-free water to be added to the reactor to simulate the start of the desorption phase of the experiments. Equations (8-3) and (8-4) were solved using a 4th-order Runge-Kutta algorithm.

The model used to interpret the column transport experiments was also embodied in a Fortran program that was described previously in Dittrich et al. (2014). Although the model allows for dual-porosity transport (including diffusion into a stagnant secondary porosity that has sorption properties), it was found that the model matches to the column breakthrough curves were not improved by including a secondary porosity, so the secondary porosity features of the model are not described below.

Colloid Transport in Flowing Porosity:

Mobile: $\dfrac{\partial C_{col}}{\partial t} + v_f\dfrac{\partial C_{col}}{\partial x} - D_c\dfrac{\partial^2 C_{col}}{\partial x^2} + k_{fc}C_{col} - k_{rc}S_{col} + k_{fci}C_{col} - P_{col} = 0$

(8-5)

Immobile:

$\dfrac{\partial S_{col}}{\partial t} - k_{fc}C_{col} + k_{rc}S_{col} - k_{fci}C_{col} = 0$ (8-6)

Solute Transport in Flowing Porosity:

$\dfrac{\partial C}{\partial t} + v_f\dfrac{\partial C}{\partial x} - D_f\dfrac{\partial^2 C}{\partial x^2} + k_{1f}CC_{col}\left(1 - \dfrac{C_1}{C_{col}S_1^0}\right) + k_{2f}CC_{col}\left(1 - \dfrac{C_2}{C_{col}S_2^0}\right) +$

$\left(\dfrac{\rho_f}{\eta}\right)\left[\sum_i k_{fi}C\left(1 - \dfrac{S_i}{S_{mi}}\right) - \sum_i k_{ri}S_i\right] + k_{1f}CS_{col}\left(1 - \dfrac{C_{filt,1}}{S_{col}S_1^0}\right) + k_{2f}CS_{col}\left(1 - \dfrac{C_{filt,2}}{S_{col}S_2^0}\right) -$ (8-7)

$k_{1b}C_1 - k_{2r}C_2 - k_{1b}C_{filt,1} - k_{2r}C_{filt,2} = 0$

Solute Transport on mobile colloids while adsorbed to colloid sites 1 and 2:

$$\frac{\partial C_1}{\partial t} + v_f \frac{\partial C_1}{\partial x} - D_c \frac{\partial^2 C_1}{\partial x^2} - k_{1f} C C_{col}\left(1 - \frac{C_1}{C_{col}S_1^0}\right) - k_{rc} C_{filt,1} +$$

$$k_{1r} C_1 + k_{fc} C_1 - P_{col} S_a = 0$$

(2- 8)

$$\frac{\partial C_2}{\partial t} + v_f \frac{\partial C_2}{\partial x} - D_c \frac{\partial^2 C_2}{\partial x^2} - k_{2f} C C_{col}\left(1 - \frac{C_2}{C_{col}S_2^0}\right) - k_{rc} C_{filt,2} +$$

$$k_{2r} C_2 + k_{fc} C_2 - P_{col} S_b = 0$$

(2- 9)

Immobile Solute in Fractures (sorption sites a and b):

$$\frac{\partial S_i}{\partial t} - \sum_i k_{fi} C\left(1 - \frac{S_i}{S_{mi}}\right) + \sum_i k_{ri} S_i = 0$$

(2-10)

Immobile Solute adorbed onto Immobile Colloids in Fractures (colloid sites 1 and 2):

$$\frac{\partial C_{filt,1}}{\partial t} - k_{1f} C S_{col}\left(1 - \frac{C_{filt,1}}{S_{col}S_1^0}\right) - (k_{fc} + k_{fci})C_1 + k_{rc} C_{filt,1} + k_{1r} C_{filt,1} = 0$$

(2-11)

$$\frac{\partial C_{filt,2}}{\partial t} - k_{2f} C S_{col}\left(1 - \frac{C_{filt,2}}{S_{col}S_2^0}\right) - (k_{fc} + k_{fci})C_2 + k_{rc} C_{filt,2} + k_{2r} C_{filt,2} = 0$$

(2-12)

where, C_{col} = concentration of colloids in solute phase, mol/cm^3
S_{col} = colloid concentration on media surfaces, mol/cm^3
C = solution concentration of solute in flowing porosity, mol/cm^3
S_i = sorbed concentration of solute on media surface site i, mol/g
C_1 = concentration of solute sorbed to site 1 on mobile colloids, mol/cm^3
C_2 = concentration of solute sorbed to site 2 on mobile colloids, mol/cm^3
$C_{filt,1}$ = concentration of solute sorbed to site 1 on immobile colloids, mol/cm^3
$C_{filt,2}$ = concentration of solute sorbed to site 2 on immobile colloids, mol/cm^3
P_{col} = colloid production rate in flowing porosity, g/cm^3-hr
v_f = fluid velocity in flowing porosity, cm/hr
D_f = solute dispersion coefficient in flowing porosity, cm^2/hr
D_c = colloid dispersion coefficient in flowing porosity, cm^2/hr
ρ_f = effective bulk density within flowing porosity, g/cm^3
η = porosity in flow domain
k_{fc} = colloid filtration rate constant (1/hr) = λv_f, where λ = filtration coefficient (1/cm)
k_{rc} = reverse colloid filtration (detachment) rate constant, 1/hr
k_{fci} = irreversible colloid filtration rate constant, 1/hr
k_{fi} = rate constant for sorption of solute onto media surface site i, ml/g-hr
k_{ri} = rate constant for desorption of solute from media surface site i, 1/hr
k_{1f} = rate constant for sorption of solute onto colloid surface site 1, ml/g-hr
k_{1r} = rate constant for desorption of solute from colloid surface site 1, 1/hr
k_{2f} = rate constant for sorption of solute onto colloid surface site 2, ml/g-hr
k_{2r} = rate constant for desorption of solute from colloid surface site 2, 1/hr

S_1^0 = maximum solute capacity on colloid sorption site 1, mol/g colloid
S_2^0 = maximum solute capacity on colloid sorption site 2, mol/g colloid
S_{mi} = maximum solute capacity on media sorption site i, mol/g solid

The model allows for up to 5 different types of sorption sites, with different rate constants and sorption capacities, to be specified on the immobile media surfaces (the FFM), but it only allows for 2 different types of sorption sites on the colloids. Both reversible and irreversible colloid filtration can be simulated, although the bentonite colloids in this study transported essentially conservatively through the 1.5-cm columns, so the filtration rate constants were set to zero and filtration was effectively ignored.

The column modeling procedure involved first using the ^{3}HHO breakthrough curves to obtain estimates of the mean residence time and dispersivity in the columns, and then these parameters were assumed to apply to the transport of colloids and Cs through the columns. Rapid and reversible adsorption of the Cs onto the colloids was assumed based on observations that the Cs partitioning to the colloids occurred as rapidly as could be measured when ^{137}Cs-spiked suspensions were prepared. The ratios of adsorption rate constants to desorption rate constants for the Cs on both the colloids and the FFM were constrained by the partitioning observed in the batch experiments, but the rate constants themselves were allowed to vary to match the observed breakthrough curves. Further details of the procedure are provided in the next section.

8.4   TECHNICAL RESULTS

8.4.1   Batch Experiment Results

The results of batch adsorption experiments of the Cs onto the FFM are shown in Figure 8-6. The duplicate FFM experiments are in excellent agreement, and the control experiment shows no evidence of any interaction of Cs with the centrifuge tubes. The partition coefficient, or K_d value, at the end of the experiment is calculated (eq. 8-1) to be approximately 51 ml/g. This value is much lower than the K_d value of ~3600 ml/g calculated for Cs partitioning to the bentonite colloids, but when one considers the much larger specific surface area of the colloids vs. the FFM (56.1 m^2/g vs. 0.23 m^2/g), the Cs partition coefficient on a surface area basis is actually slightly larger for the FFM than for the colloids: 220 ml/m^2 for the FFM vs. 64 ml/m^2 for the colloids. The model curves shown in Figure 8-6 were generated using the batch adsorption model with the sorption and desorption rate constants that provided the best matches to the column data, so they were not optimized to offer the best fits to the batch data. It is apparent that the parameters yielding a good match to the column data also provided reasonably good matches to the batch data, particularly in the case of the two-site model.

The results of the two desorption experiments evaluating Cs desorption from the FFM are shown in Figures 8-7 and 8-8, respectively. Figure 8-7 shows that the duplicate experiments are again in excellent agreement. The K_d value at the end of this experiment is calculated (eq. 8-2) to be approximately 200 ml/g, or nearly 4 times greater than the K_d value at the end of the adsorption experiment. This result indicates that there is some adsorption-desorption hysteresis, with at least a portion of the adsorbed Cs not readily desorbing from the FFM or desorbing at a slower rate than the remainder of the Cs. This result might also be interpreted as an indication of a nonlinear adsorption isotherm, as the Cs concentration in solution at the end of the desorption experiment is about a factor of 5.5 lower than at the end of the adsorption experiment. Either way, it appears that Cs was desorbed preferentially from weaker sorption sites and the Cs remaining on the FFM after desorption is, on average, more strongly associated with the FFM than the Cs at the end of

the adsorption experiment. As in the case of Figure 8-6, the model curves in Figure 8-7 show the desorption of Cs from the FFM predicted using the model parameters that provided good matches to the column transport data. They are not optimized fits to the batch desorption data.
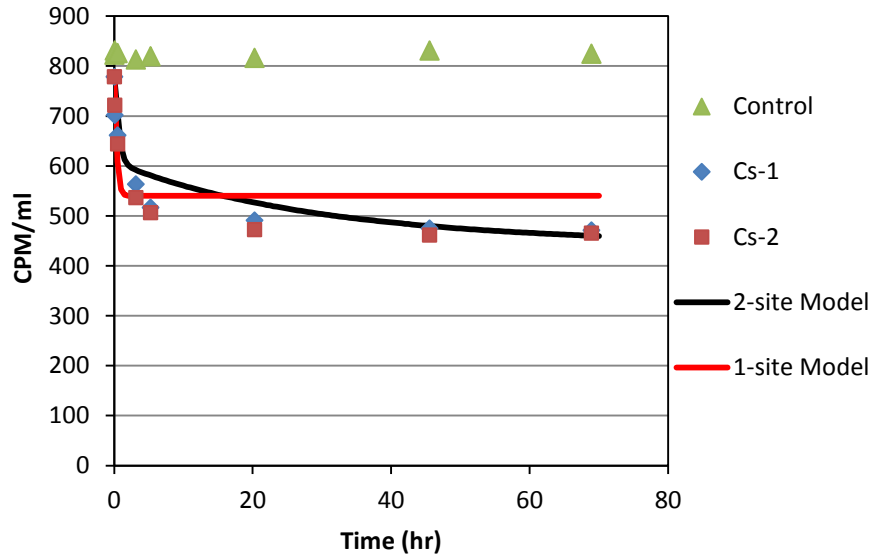

Figure 8-6: Results of batch adsorption experiment of ^{137}Cs onto FFM in SGW. 800 CPM/ml (starting concentration) corresponds to about 3e-11 M ^{137}Cs and about 9e-7 M total Cs. The one-site and two-site model curves were generated using the best-fitting parameters for the column experiments and do not represent fits to the batch data.
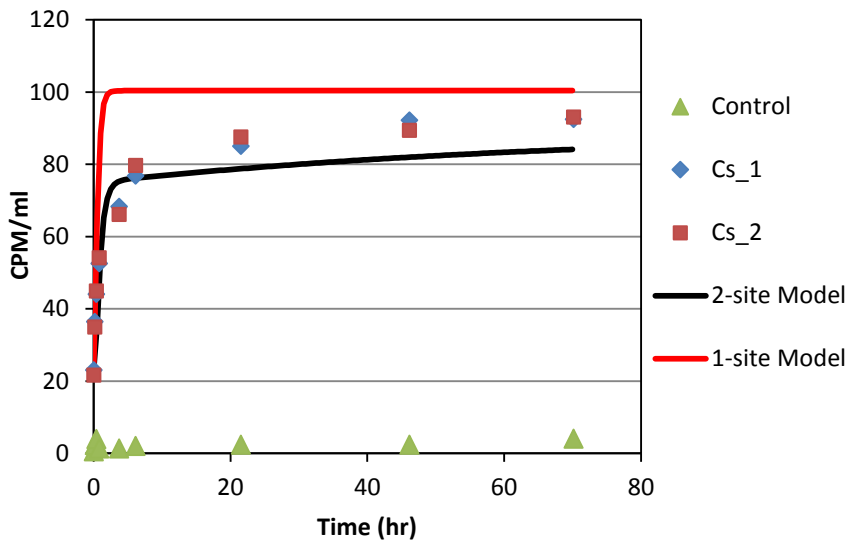
Figure 8-7: Results of batch experiment of first desorption step of ^{137}Cs from FFM in SGW. The one-site and two-site model curves were generated using the best-fitting parameters for the column experiments and do not represent fits to the batch data.

In Figure 8-8, there is a difference between the two desorption curves because the desorption solution added to one of the centrifuge tubes included Cs-free bentonite colloids at ~100 mg/L while the other solution was colloid-free SZW. The data points for the experiment with colloids are measurements of samples that were not centrifuged to remove the colloidal fraction of Cs, so these data represent dissolved plus colloidal Cs concentrations. It is apparent that more of the Cs desorbed from the FFM when the colloids were present. Furthermore, if one assumes that 25% of the solution-phase Cs in the colloid experiment is associated with the colloids (consistent with Cs partitioning to colloids in the absence of FFM), the concentration of dissolved Cs is nearly the same at the end of both experiments. The Cs-FFM K_d value at the end of this experiment is calculated to be approximately 320 ml/g, or nearly 6.5 times greater than the K_d value at the end of the adsorption experiment, and about 60% greater than at the end of the first desorption experiment. This result indicates that as successively more Cs is desorbed from the FFM, the remaining adsorbed Cs is, on average, more and more strongly associated with the FFM. Note that model curves are not shown in Figure 8-8 because the column experiments did not include the equivalent of a second desorption step.
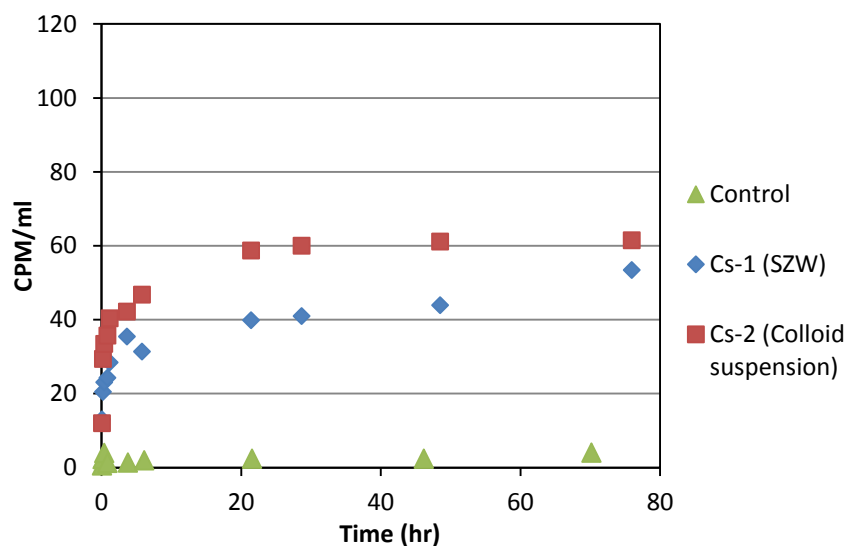
Figure 8-8: Results of batch experiment of second desorption step of ^{137}Cs from FFM in SGW (starting with FFM remaining after first desorption step shown in Figure 8-7). Note that the Cs-1 experiment involved desorption in colloid-free SZW, while Cs-2 involved desorption in SZW containing 100 mg/L of bentonite colloids. Model curves are not shown because there was no column experiment that corresponded to s second desorption step. The y-axis scale is the same as in Figure 8-7 to allow comparison of the amounts of ^{137}Cs desorbed.

Collectively, the batch experiment results suggest that there are multiple sorption sites on the FFM with different sorption and desorption rate constants and likely different sorption capacities. The batch data do not support a highly-refined determination of the rate constants and capacities of the different types of sites, but they certainly support the use of multiple sites when matching the column experiment data, which is important because it was found that the column data were much better matched when multiple sites were assumed.

8.4.2   Column Experiment Results

Figure 8-9 shows the Cs breakthrough curves in the FFM column experiments with and without colloids in the injection pulse. It is immediately apparent that the colloids transported through the column without significant filtration, as the colloid concentration jumped to its injection concentration (C/Co = 1) after one pore volume and remained there until the injection pulse ended. This result greatly simplified the modeling of the experiments, making it possible to assume a colloid filtration rate constant of zero. The mean water residence time in the columns, as determined from the ^{3}HHO breakthrough curves was approximately 1.5 hours, and the column Peclet number (column length divided by longitudinal dispersivity) was estimated to be around 100. Neither of these parameters were tightly constrained by the data because of the extremely rapid breakthrough of the ^{3}HHO, which resulted in only one to three samples being collected that contained C/Co values between 0 and 1.0.

The model fits to the Cs breakthrough curves in Figure 8-9 assume only a single type of sorption site on both the FFM and the colloids. However, the FFM sorption site was allowed to have a different desorption rate constant once the Cs and colloid injection pulse ended so that the hysteretic sorption behavior could be simulated. Changing the desorption rate constant effectively changed the K_d value because the K_d value is the ratio of the adsorption to the desorption rate constants. This adjustment is consistent with the hysteretic behavior observed in the batch sorption and desorption tests; in fact, it was initially assumed that the K_d values during adsorption and desorption in the column experiments were equal to the values deduced from the corresponding batch tests (with the desorption K_d value taken to be the K_d value observed at the end of the first batch desorption experiment, not the second one). These values were adjusted only slightly to achieve better matches to the column data.
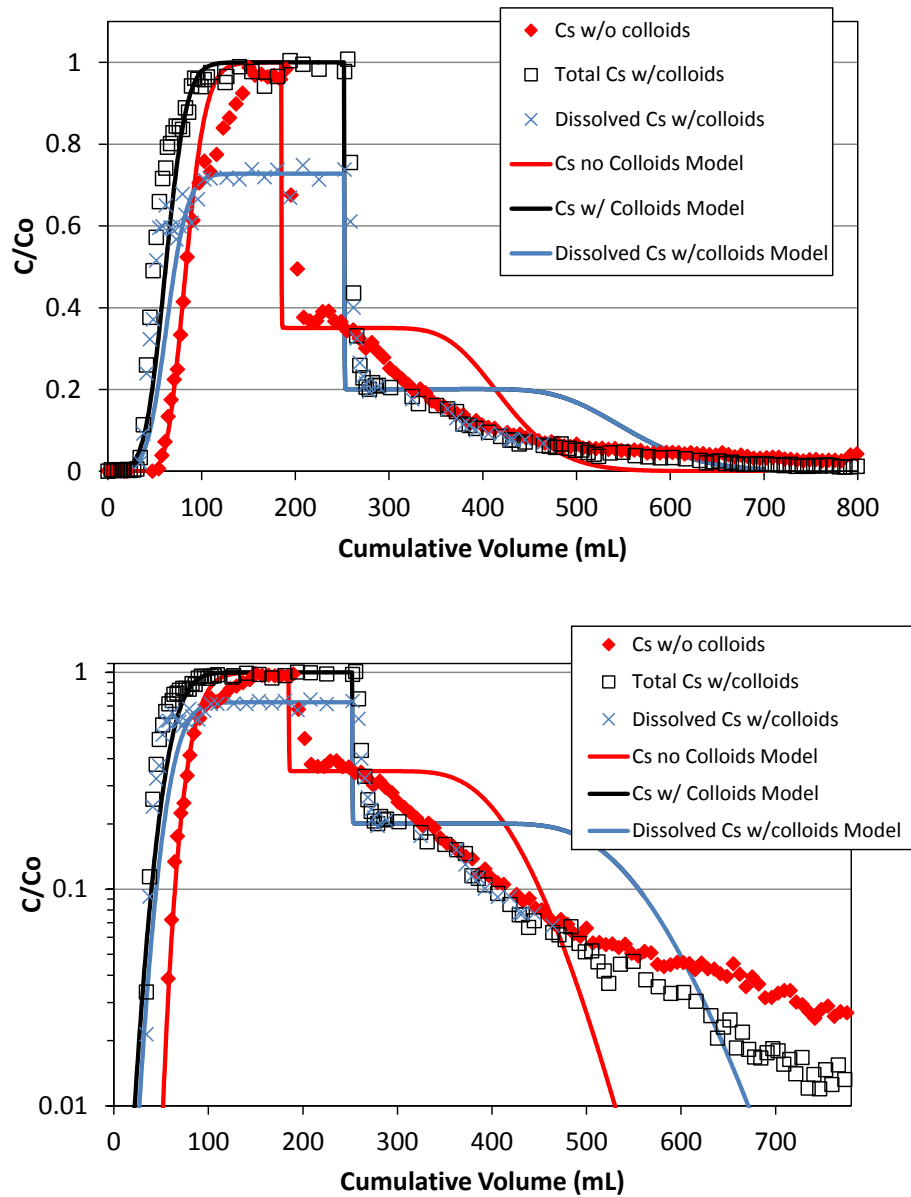
Figure 8-9: Normalized breakthough curves of ^{137}Cs in column experiments with and without colloids in the injection pulse (top – linear concentration scale; bottom - log concentration scale). Lines are model matches to the data assuming only a single type of sorption site on both the colloids and the FFM. Note that the injection pulses ended when the model curves show sudden drops in concentration. [3]HHO and colloid breakthrough curves are not shown, but the colloids essentially mirrored the [3]HHO curves and showed no evidence of any filtration. Model parameters are listed in Tables 8-5 and 8-6.

It is apparent in Figure 8-9 that while the initial arrival and rising portion of the Cs breakthrough curves were matched reasonably well with a single sorption site, the desorption portions of the curves were poorly matched. The observed sudden drop in concentration at the end of the injection pulse can be matched quite well by adjusting the desorption rate constant. However, the larger desorption K_d value also results in a relatively steady concentration plateau for a much longer time than observed in the data, and then there is a much more rapid decline in concentration than the observed late-time tailing behavior. It should be noted that the K_d value for Cs partitioning to the bentonite colloids was fixed in all column simulations to be exactly that observed in the prepared colloid suspensions, i.e., 3700 ml/g. The rate constants for Cs partitioning to the colloids were allowed to vary to achieve better fits to the column data, but the ratio of the rate constants was fixed to be equal to the observed K_d value. The main constraint was that the rates had to exceed a lower threshold to avoid unrealistically early breakthrough of colloid-associated Cs.

As the model curves of Figure 8-9 suggest, it was not possible to obtain a reasonable match to the Cs tailing behavior in the column experiments using a single sorption site. Decreasing the desorption K_d value resulted in increasing the height of the concentration plateau, shortening the plateau, and steepening the eventual decline in concentration relative to the curves shown in Figure 8-9. Increasing the desorption K_d value had the opposite effect: it lowered and lengthened the plateau, and although it decreased the steepness of the eventual concentration decline, the decline was still considerably faster than the observed data. Attempts to manipulate the adsorption and desorption rate constants while keeping their ratios the same (i.e., keeping K_d values fixed) only marginally improved the matches to the desorption portion of the breakthrough curves, but it degraded the matches to the rising portion of the curves. The adsorption and desorption rate constants yielding the model curves of Figure 8-9 were used to obtain the one-site model curves for the batch experiments shown in Figures 8-6 and 8-7. It is apparent that these values provided reasonably good approximate matches to the batch data, although the rate constants that were assumed in the column experiments to avoid early breakthrough of Cs were clearly too fast to match the batch data.

Figure 8-10 shows the results of matching a two-site model (on both the FFM and colloids) to the column experiment Cs breakthrough curves with and without colloids present in the injection pulse. It is obvious that the two-site model offers a significant improvement over the one-site model, especially during the desorption portion of the column experiments. The inclusion of a second site with slower adsorption and desorption kinetics than the first site allows the Cs tailing behavior to be much better matched than when only a single site is allowed. Some discrepancies between the model and data remain in the early part of the desorption portion of the breakthrough curves, but these could be reduced by including a third sorption site on the FFM. We did not attempt to include a third site because we felt that the two-site model effectively captured the main features of the breakthrough curves. The adsorption and desorption rate constants and the sorption site capacities on the FFM yielding the model curves of Figure 8-10 are listed in Table 8-5. The one-site model parameters corresponding to the curves of Figure 8-9 are also listed in Table 8-5. The parameters of Table 8-5 were used to obtain the batch experiment model curves of Figures 8-6 and 8-7. It is apparent in Figures 8-6 and 8-7 that the two-site model parameters yielding good matches to the column transport data provided much better matches to the batch data than the one-site model parameters.

The colloid sorption site parameters assumed in all the model runs to interpret the column experiments are listed in Table 8-6. In the case where only a single sorption site on the colloids was assumed (Figure 8-9), the parameters for the second site were set to zero, but the same

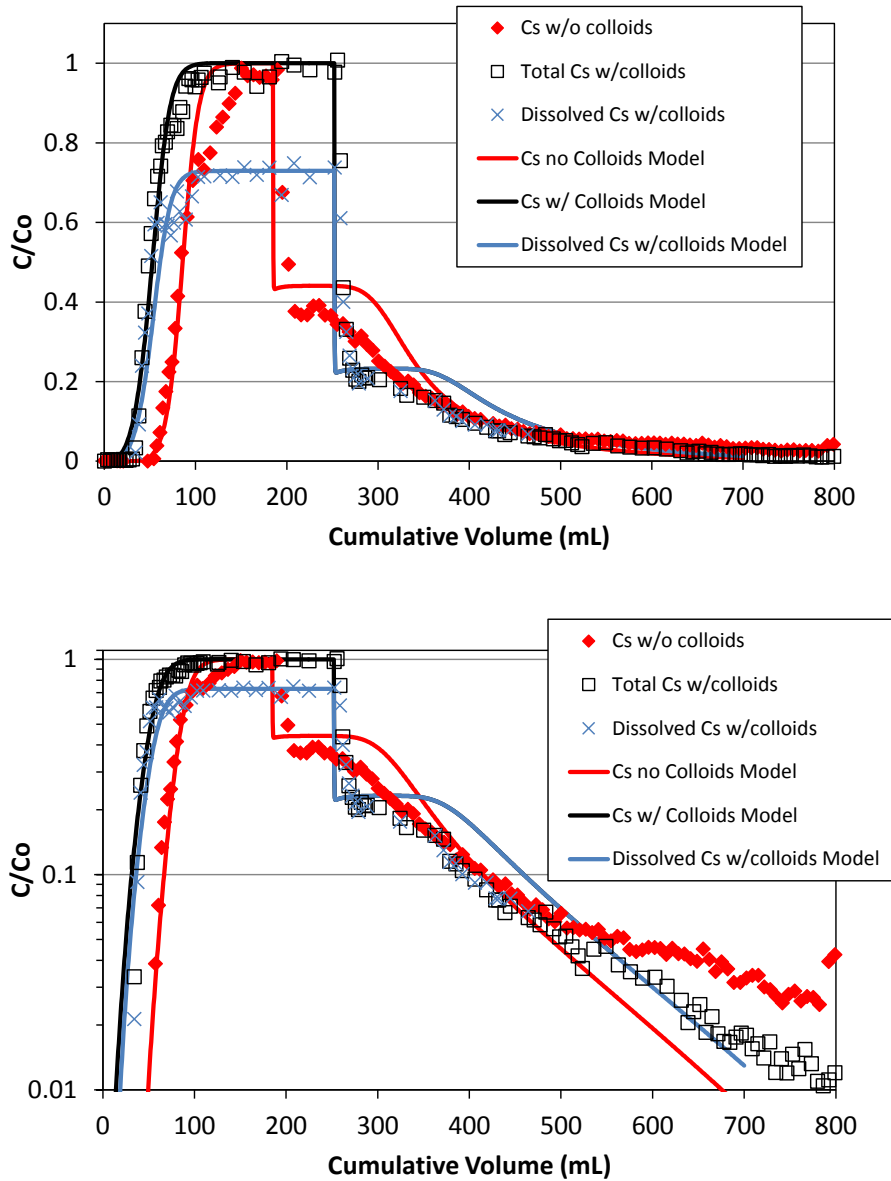parameters were used for the first site regardless of whether a second site was assumed to be present or not.

Figure 8-10: Normalized breakthough curves of Figure 8-9 showing model matches to the data assuming two types of sorption sites on both the colloids and the FFM. Model parameters are listed in Tables 8-5 and 8-6.

It is worthwhile to make a couple of comments about the two-site model parameters of Tables 8-5 and 8-6. First, while a second sorption site is assumed on the colloids, this site has negligible impact on the model results because the capacity of the site is extremely small relative to the Cs concentrations in the experiments. The parameters of the second site were chosen to be consistent with the results of Missana et al. (2004), who noted a strong Cs sorption site with very low capacity on FEBEX bentonite colloids in Grimsel groundwater, which was not apparent until Cs concentrations decreased below about 1e-8 M (Figure 8-1). The effective K_d values on the colloids as a function of Cs concentration using the two-site model parameters of Table 8-6 is shown in Figure 8-11; the similarity of this figure to Figure 8-1 is readily apparent.

Table 8-5: FFM sorption parameters yielding the model curves shown in Figures 8-9, 8-10, and 8-12

Cs Transport with No Colloids						
	Figure 8-9 (1 site)		**Figure 8-10 (2 sites)**		**Figure 8-12 (2 sites)**	
Parameter	**Ads.**	**Des.**	**Ads.**	**Des.**	**Ads.**	**Des.**
Sorption rate constant, 1st site (ml/g-hr)	102	102	50	50	--	--
Desorption rate constant, 1st site (1/hr)	2	0.7	1.4	0.6	--	--
Max. site capacity, 1st site (mol/g)	1e-5	1e-5	1e-5	1e-5	--	--
Sorption rate constant, 2nd site (ml/g-hr)	--	--	1.02	1.02	--	--
Desorption rate constant, 2nd site (1/hr)	--	--	0.014	0.008	--	--
Max. site capacity, 2nd site (mol/g)	--	--	4e-8	4e-8	--	--
Cs Transport with Colloids						
	Figure 8-9 (1 site)		**Figure 8-10 (2 sites)**		**Figure 8-12 (2 sites)**	
Parameter	**Ads.**	**Des.**	**Ads.**	**Des.**	**Ads.**	**Des.**
Sorption rate constant, 1st site (ml/g-hr)	102	102	50	50	50	50
Desorption rate constant, 1st site (1/hr)	2	0.55	2	0.6	2	0.8
Max. site capacity, 1st site (mol/g)	1e-5	1e-5	1e-5	1e-5	1e-5	1e-5
Sorption rate constant, 2nd site (ml/g-hr)	--	--	1.02	1.02	1.02	1.02
Desorption rate constant, 2nd site (1/hr)	--	--	0.02	0.008	0.02	0.011
Max. site capacity, 2nd site (mol/g)	--	--	4e-8	4e-8	4e-8	4e-8

Note: Grey-shaded cells highlight increases in desorption rate constants in the presence of colloids during the adsorption phase of Figure 8-10 experiments (when colloids were present during adsorption phase), and green-shaded cells highlight increases in desorption rate constants in the presence of colloids during the desorption phase of Figure 8-12 experiment (vs. Figure 8-10 experiment where colloids were not present during desorption). Rate constants for the 1-site model (Figure 8-9) were adjusted to achieve good matches to the data without consideration of the presence or absence of colloids.

Table 8-6: Colloid sorption parameters used in all model simulations.

Parameter	Value
Sorption rate constant, 1st site (ml/g-hr)	29600
Desorption rate constant, 1st site (1/hr)	8
Max. site capacity, 1st site (mol/g)	1e-3
Sorption rate constant, 2nd site (ml/g-hr)	59200
Desorption rate constant, 2nd site (1/hr)	0.4
Max. site capacity, 2nd site (mol/g)	6e-8
K_d value, 1st site	3700
K_d value, 2nd site	148000

A second comment about the two-site model parameters of Tables 8-5 and 8-6 is that slightly larger desorption rate constants from the FFM (Table 8-6) were assumed during the adsorption portion of the column experiment with colloids than during the adsorption portion of the experiment without colloids. This adjustment was not arbitrary; it was made to honor the larger apparent desorption rate of Cs from the FFM in the presence of colloids than in the absence of colloids in the second batch desorption experiment (Figure 8-8). The relative difference in the desorption rate constants was approximately the same as that necessary to explain the difference in the two desorption data sets of Figure 8-8.
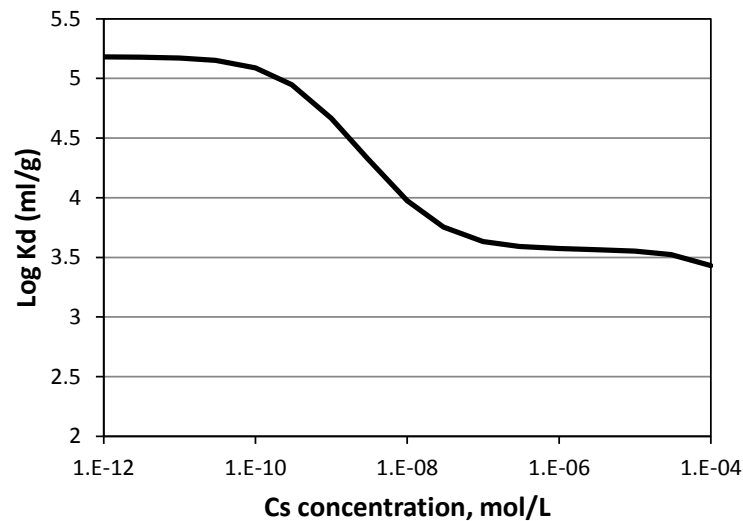
Figure 8-11: Cs K_d values on colloids as a function of Cs concentration using the sorption parameters of Table 8-6.

Figure 8-12 shows the breakthrough curves in the experiment in which a portion of the effluent from the column experiment containing colloids was injected into a second column. In this experiment, colloids continued to be injected after the end of the Cs injection pulse. This experiment was not modeled using a one-site model but rather was modeled using the same two-site model parameters as in the first column experiment involving colloids. The only difference in the model parameters between the two experiments was that a slightly larger Cs desorption rate

constant from the FFM was assumed during the desorption portion of the second experiment to account for the increased desorption rate from the FFM in the presence of colloids (there were no colloids present during the desorption portion of the first experiment). It is apparent that there is good agreement between the model and data without any adjustment of the model parameters obtained from the first colloid experiment (other than the desorption rate constant adjustment to account for the presence of colloids during tailing in the second experiment). However, it is also apparent that if the model had been extended to longer times, it would have been necessary to include a third sorption site on the FFM to effectively capture the late-time tailing behavior.

An intriguing result of the second experiment was that the ratio of dissolved Cs to total Cs exiting the column became increasingly smaller as the tailing portion of the experiment progressed. Figure 8-13 shows this ratio as a function of eluted volume during the experiment, and Figure 8-14 shows the fraction as a function of total Cs concentration exiting the column, irrespective of time or volume eluted. These results are consistent with a second and stronger sorption site on the colloids that is just beginning to exert its influence as Cs concentrations decrease late in the experiment. That is, it is consistent with the results of Missana et al. (2004) that show evidence for a strong sorption site with low site abundance on the bentonite colloids that is apparent only at low Cs concentrations. The model curves of Figure 8-12 actually reflect a minor decrease in the ratio of dissolved to total Cs late in the experiment because of the inclusion of a second stronger sorption site on the colloids, but this decrease is not nearly as large as that observed in the experimental data.

Figure 2-15 shows the Cs recoveries as a function of volume eluted in each of the three column experiments. Over 90% of the Cs was recovered during each of the experiments, with the mass balance being closed to within a few percent by the final 0.1 M HCl flush. This flush confirmed that there was a small amount of remaining Cs in the columns at the end of each experiment.
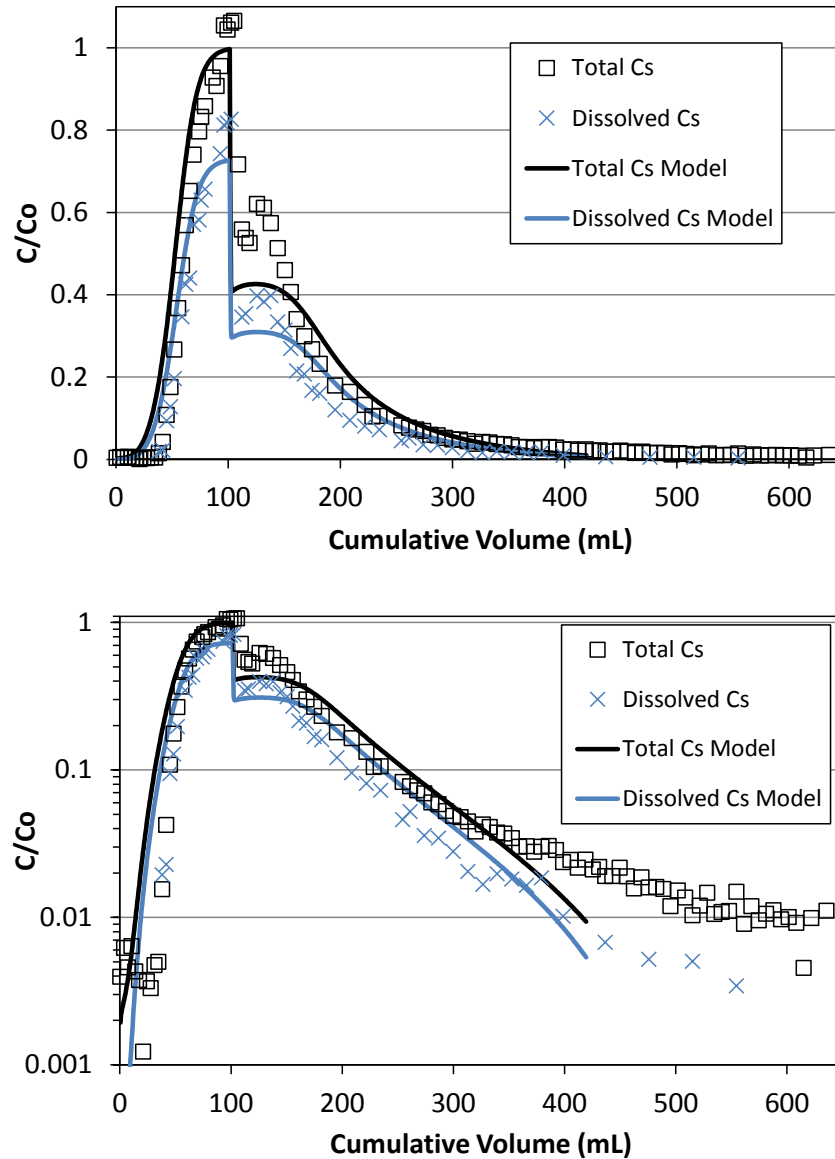
Figure 8-12: Normalized breakthough curves of ^{137}Cs in column experiment in which a portion of the effluent from the experiment with colloids shown in Figures 8-9 and 10-10 was passed through another column. Colloids continued to be injected through the column even after the Cs pulse had ended. Lines are model matches to the data assuming two types of sorption sites on both the colloids and the FFM. Note that the Cs injection pulse ended when the two model curves show sudden drops in concentration. [3]HHO and colloid breakthrough curves are not shown, but the colloids essentially mirrored the [3]HHO curves and showed no evidence of any filtration. Model parameters are listed in Tables 8-5 and 8-6.
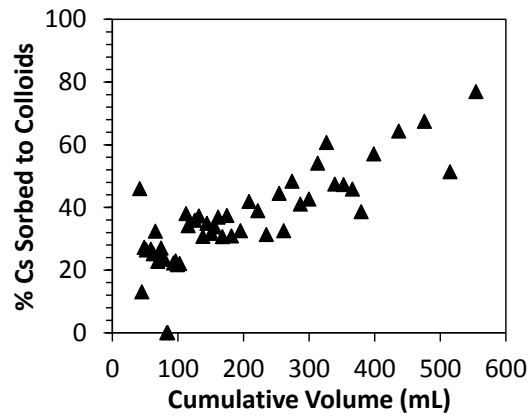
Figure 8-13: Fraction of Cs sorbed to colloids a function volume eluted in the experiments of Figure 8-12.
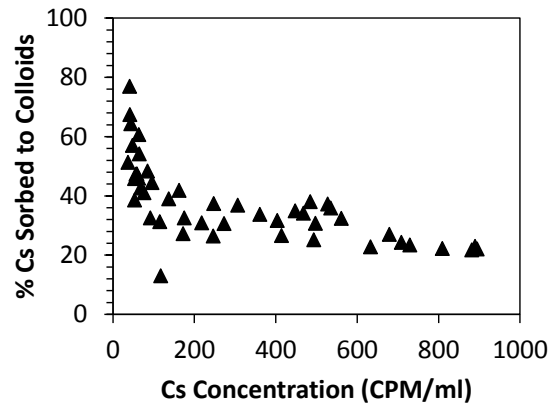
Figure 8-14: Fraction of Cs sorbed to colloids a function of Cs concentration in the experiments of Figure 8-12. Note that 50 CPM/ml is equivalent to about 5e-8 M total Cs concentration.
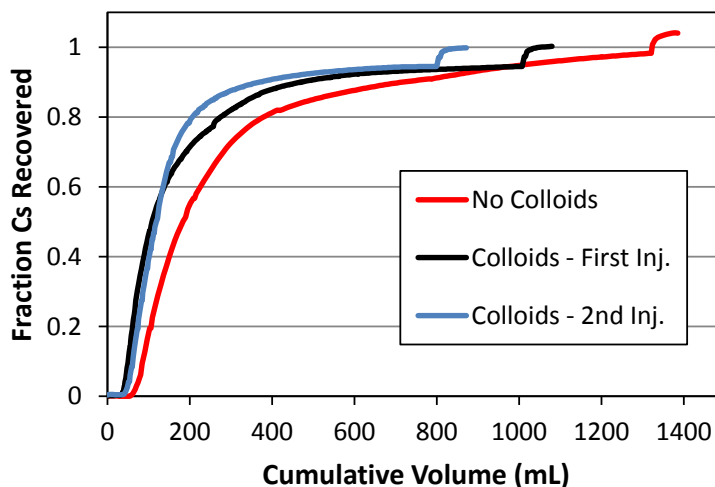
Figure 8-15: Fraction of Cs recovered in each of the column experiments.

8.4.3   Implications for Repository Performance Assessments

The implications of the batch and column experiments in this study are that Cs radioisotopes appear unlikely to transport over significant time and distance scales in association with bentonite colloids *unless* steady-state mobile colloid concentrations are quite high.   Although Cs partitioning to the bentonite colloids is quite strong, the sorption process appears to be reversible, with the desorption kinetics being rapid enough that Cs would be expected to completely dissociate from mobile colloids over long time and distance scales that are relevant to repository performance assessments.   We hasten to point out that greater facilitation of Cs transport by bentonite colloids would be expected if Cs concentrations were lower than in our experiments because of the stronger partitioning of Cs to the colloids at lower concentrations (observed by Missana et al., 2004, and also evident at late times in our second Cs/colloid column experiment). This greater Cs partitioning and slower desorption rates from bentonite colloids at lower Cs concentrations may have been responsible for the much greater apparent (relative to our experiments) colloid-facilitated transport of Cs in a 2012 GTS field transport experiment (described in Wang et al., 2013), and in a 2002 GTS field experiment (Geckeis et al., 2004; Möri, 2004).   In those field experiments, which were conducted in nominally the same geochemical system as our experiments, the colloid concentrations were comparable to ours (~100 mg/L), but the Cs concentrations were less than 1e-9 M, as opposed to about 1e-6 M in our experiments. The much lower Cs concentrations (due to the lack of non-radioactive carrier Cs associated with the ^{137}Cs) would have resulted in significantly stronger Cs partitioning to the colloids than in our experiments because of the much greater influence of the low-abundance strong sorption sites on the colloids at these lower Cs concentrations.

Under our experimental conditions of near-equilibrium Cs partitioning to both colloids and stationary media, as well as the nearly constant mobile colloid concentrations, the 1-D transport equation describing colloid-facilitated solute transport can be reduced to:

$$\frac{\partial C}{\partial t} + v_f \frac{\partial C}{\partial x} - D_c \frac{\partial^2 C}{\partial x^2} + \frac{\rho_f}{\eta} K_d \frac{\partial C}{\partial t} + K_c C_{col} \frac{\partial C}{\partial t} + v_f K_c C_{col} \frac{\partial C}{\partial x} = 0$$

(8-13)

which can be further simplified to:

$$\left(1 + \frac{\rho_f}{\eta} K_d + K_c C_{col}\right)\frac{\partial C}{\partial t} + \left(1 + K_c C_{col}\right)v_f \frac{\partial C}{\partial x} - D_c \frac{\partial^2 C}{\partial x^2} = 0$$

(8-14)

where K_c = equilibrium partition coefficient of the solute to the colloids, ml/g.

Equation (8-14) implies an effective solute velocity of $\left(1 + K_c C_{col}\right)v_f$ with a retardation factor of $1 + \frac{\rho_f}{\eta} K_d + K_c C_{col}$, so the overall effective retardation factor of the solute in the presence of the colloids, R_c, becomes:

$$R_C = \frac{1 + \frac{\rho_f}{\eta} K_d + K_c C_{col}}{1 + K_c C_{col}}$$

(8-15)

Figure 8-16 shows the result of applying this simple expression in an analytical solution of 1-D advection-dispersion equation to predict the rising portion of the breakthrough curves of Figures 8-9 and 8-10. The measured values of K_d and K_c from the batch sorption experiments and the known colloid concentrations in the column experiments were used to calculate the colloid-facilitated transport retardation factor (eq. 8-15) and also the solute-only retardation factor, $R = 1 + \frac{\rho_f}{\eta} K_d$. It is apparent that these simple retardation factors provide good predictions of the Cs breakthroughs in the column experiments. The analytical solution cannot be used to predict the desorption portion of the breakthrough curves because of the sorption-desorption hysteresis. Nevertheless, when solute partitioning to mobile colloids and immobile surfaces are fast and colloid concentrations are relatively constant, the retardation factor of eq. (8-15) can serve as a good approximation to estimate the potential for colloid-facilitated transport. Typically the value of $K_c C_{col}$ will be small compared to the value of $\frac{\rho_f}{\eta} K_d$ in the numerator of eq. (8-15) (in our experiments $K_c C_{col}$ was ~0.37 compared to about 200 for $\frac{\rho_f}{\eta} K_d$) because C_{col} is usually very small relative to $\frac{\rho_f}{\eta}$, so the main effect of the presence of colloids is in the denominator of eq. (8-15), where $K_c C_{col}$ must be greater than about 0.1 to have a significant impact on solute transport relative to transport in the absence of colloids.
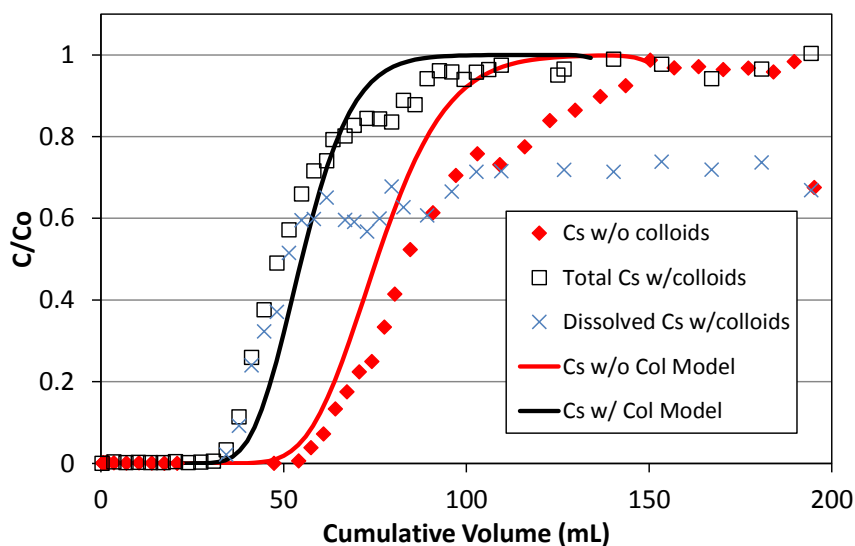
Figure 8-16: Predictions of the rising portion of the Cs breakthrough curves of Figures 8-9 and 8-10 using eq. (8-15) as a retardation factor for colloid-facilitated transport in an analytical solution of 1-D advection-dispersion equation. The K_d and K_c values from the batch experiments were used in eq. (8-15).

8.5   CONCLUSIONS AND FUTURE WORK

In this study, we demonstrate how a combination of batch sorption/desorption experiments and column transport experiments were used to effectively parameterize a model describing the colloid-facilitated transport of Cs in the Grimsel granodiorite/FFM system. Cs partition coefficient estimates onto both the colloids and the stationary media obtained from the batch experiments were used as initial estimates of partition coefficients in the column experiments, and then the column experiment results were used to obtain refined estimates of the number of different sorption sites and the adsorption and desorption rate constants of the sites. The desorption portion of the column breakthrough curves highlighted the importance of accounting for adsorption-desorption hysteresis (or a very nonlinear adsorption isotherm) of the Cs on the FFM in the model, and this portion of the breakthrough curves also dictated that there be at least two different types of sorption sites on the FFM. In the end, the two-site model parameters estimated from the column experiments provided excellent matches to the batch adsorption/desorption data, which provided a measure of assurance in the validity of the model.

It was also demonstrated how a relatively simple retardation factor expression could be used to provide a good approximation of colloid-facilitated solute transport under conditions of near-constant mobile colloid concentrations and rapid and reversible solute sorption/desorption onto both the colloids and immobile surfaces. This expression provided a very good approximation to the column breakthrough curves using the partition coefficients observed in the batch experiments and the known colloid concentrations in the column experiments.

For future work, the model developed in this study will be applied to do a forward prediction of the Cs breakthrough curve in the 2012 colloid-facilitated transport experiment at the GTS. A previous interpretation of this experiment (Wang et al., 2013) indicated that Cs transported much

differently than in the laboratory experiments of this study. Desorption of Cs from the colloids in the field test was much slower than in the laboratory tests, resulting in an essentially unretarded breakthrough of a fraction of the injected Cs. There was no unretarded Cs transport in the lab column experiments despite the fact that the lab experiments had shorter residence times than in the field. The Cs partition coefficient to the colloids that provided a good match to the field Cs breakthrough curve was larger than for the stronger of the two sites in the laboratory-based model. However, it must be kept in mind that the Cs concentrations in the field experiment were lower than in the laboratory experiments by about three orders of magnitude, which would have increased the influence of the stronger sorption sites on the colloids. A goal of the future effort will be to refine the model and model parameters developed here to allow the model to explain both the laboratory and field Cs transport data. The key to this effort will be making adjustments to the parameters of the stronger of the two sorption sites on the colloids so that the strong site can account for essentially all of the Cs transport observed in the field test while the weaker site still accounts for most of the Cs transport observed in the laboratory tests. It may also be necessary to introduce an additional site to the model.

Additional future work for the Used Fuel Disposition Campaign (UFDC) in FY 2016 will include a comprehensive evaluation report on the state of knowledge of colloid-facilitated radionuclide transport as it applies to repository performance assessments. This effort will include interactions with performance assessment modelers on the project to develop an approach to efficiently account for colloid-facilitated transport in repository performance assessments. The evaluation report will include a summary of the results from this study as well as previous work in the UFDC program on the colloid-facilitated transport of americium in the Grimsel granodiorite system and the association of plutonium with intrinsic colloids (efforts at Lawrence Livermore National Laboratory), and it will also summarize and incorporate the results of field colloid-facilitated transport experiments at the GTS. The report will also draw heavily from numerous studies conducted outside the UFDC over the past 20+ years. A major emphasis of the report will be on how the collective observations and knowledge of colloid-facilitated radionuclide transport can be effectively upscaled to time and distance scales relevant to repository performance assessments.

8.6   REFERENCES

Bertetti, F.P., Klar, R.V., and Vaught, M.M. (2006) *Colloid-Facilitated Transport of Radionuclides in Natural Groundwater Systems – Literature Rreview.* Report prepared for U.S. Nuclear Regulatory Commission by Center for Nuclear Waste Regulatory Analysis, San Antonio, TX.

Dittrich, T. Gable, C.W., Hyman, J., Karra, S., Makedonska, N., Painter, S.L. and Reimus, P.W. (2014) Crystalline and Crystalline International Disposal Activities, Chapters 4 and 6, *FCRD-UFD-2014-000495*, prepared for Used Fuel Disposition Campaign of Fuel Cycle Research and Development, Los Alamos National Laboratory, Los Alamos, NM.

Dittrich, T.M. and Reimus, P.W. (2015) Uranium transport in a crushed granodiorite: Experiments and reactive transport modeling. *J. Contam. Hydrol*. 175-176, 44-59. doi: 10.1016/j.jconhyd.2015.02.004.

Dittrich, T.M., Boukhalfa, H., Ware, S.D., and Reimus, P.W. (2015a) Laboratory investigation of the role of desorption kinetics on americium transport associated with bentonite colloids. *J. Environ. Radioactiv.* 148, 170-182. doi: 10.1016/j.jenvrad.2015.07.001.

Dittrich, T.M., Ware, S.D., and Reimus, P.W. (2015b) Mini-columns for conducting breakthrough experiments: Design and construction. *LA-UR-15-24392*; Los Alamos National Laboratory, Los Alamos, NM. doi: 10.2172/1184604.

Geckeis, H., Schäfer, T., Hauser, W., Rabung, Th., Missana, T., Degueldre, C., Möri, A., Eikenberg, J., Fierz, Th., and Alexander, W. (2004) Results of the colloid and radionuclide retention experiment (CRR) at the Grimsel Test Site (GTS), Switzerland – impact of reaction kinetics and speciation on radionuclide migration. *Radiochim. Acta,.* 92, 765-774.

Grolimund, D., Barmettler, K., and Borkevic, M. (2007) Colloid-facilitated transport in natural porous media: Fundamental phenomena and modelling, in *Colloid Transport in Porous Media*, Frimmel, F., von der Kammer, F, and Flemming, H-C., eds., Springer, Berlin, Germany.

Grolimund, D., and Borkevic, M. (2005) Colloid-facilitated transport of strongly sorbing contaminants in natural porous media: Mathematical modeling and laboratory column experiments, *Environ. Sci. Technol.*, 39, 6378-6386.

Huber, F., Kunze, P., Geckeis, H., and Schäfer, T. (2011) Sorption reversibility kinetics in the ternarysystem radiocuclide-bentonite colloids/nanoparticles-granite fracture filling material. *Appl. Geochem.,* 26, 2226-2237.

Iijima, K., Tomura, T., Tobita, M., and Suzuki, Y. (2010) Distribution of Cs and Am in the solution- bentonite colloids-granite ternary system: effect of addition order and sorption reversibility. *Radiochim. Acta* 98, 729-736.

Iijima, K., Shoji, Y., and Tomura, T. (2008) Sorption behavior of americium onto bentonite colloid. *Radiochim. Acta,* 96, 721-730.

Kanti, S.T. and Khilar, K.C. (2006) Review on subsurface colloids and colloid-associated contaminant transport in saturated porous media, *Adv. Colloid. Interface Sci.*, 119(2-3), 71-96.

Kersting, A. B. and P. W. Reimus, eds. 2003. "Colloid-Facilitated Transport of Low-Solubility Radionuclides: A Field, Experimental, and Modeling Investigation," *UCRL-ID-149688*, Lawrence Livermore National Laboratory, Livermore, CA.

Murali, M., and Mathur, J. (2002) Sorption characterisitics of Am(III), Sr(II) and Cs(I) on bentonite and granite. *J. Radioanal. Nucl. Ch*. 254(1), 129-136.

Painter, S., Cvetkovic, V., Pickett, D. and Turner, D.R. (2002) Significance of kinetics for sorption on inorganic colloids: Modeling and experiment interpretation issues, *Environ. Sci. Technol.*, 36, 5369-5375.

Wang, Y., et al. (2013) Natural System Evaluation and Tool Development – International Collaborations: FY13 Progress Report, Used Fuel Disposition Campaign Milestone Report *FCRD-UFD-2013-000628*; Chapter 2, Interpretations of Colloid-Facilitated Transport Experiments at the Grimsel Test Site from 2008 through 2012.

9.0   DEVELOPMENT AND DEMONSTRATION OF DISCRETE FRACTURE NETWORK MODEL

9.1   INTRODUCTION

In this document we report recent technical and scientific developments of the Los Alamos National Laboratory computational suite, dfnWorks, for simulating flow and transport in fractured rocks such as the Crystalline rocks that are the focus of this work package. dfnWorks can be used to stochastically generate three-dimensional discrete fracture networks where fracture geometry is retained and flow and transport are simulated therein without using one-dimensional pipe network approximations. In the first section of this report, we outline the dfnWorks suite, to highlight the novel and important aspects of the suite. The most significant technical advances over the past year have been i) the full-integration with the massively parallel flow solver, PFLOTRAN (Lichtner et al 2015) and ii) the completion of a Lagrangian transport simulator to determine pathlines through the resulting steady state flow field (Makedonska et al. 2015). We also describe the generation and meshing strategy that made these technical advances feasible.

In the subsequent sections, we describe two unique studies that these technical achievements made possible. In the first study a DFN model loosely based on the Forsmark site characterization provided by (SKB, 2011) is adopted to generate an ensemble of DFN in cubic kilometer domains. Then we compared the influence of different initial boundary conditions on the asymptotic behavior of passive transport, Section 9.3. We determined that after a pre-equilibrium region solutes injected under resident conditions evolve and behave similarly to that injected under flux-weighted conditions. The principal results required unique aspects of the dfnWorks suite, namely i) the parallel solver PFLOTRAN allowed for simulating flow through large networks, approximately five thousand fractures with roughly nine millions computational cells, in an efficient manner, ii) the retention of explicit fracture geometry allowed us to link flow and transport behavior to fracture statistics and iii) the particle tracking routine made it easy to account for various boundary conditions. In the second study, we study the influence of in-fracture aperture variability on breakthrough times and retention. dfnWorks retains the explicit fracture geometry, rather than using a one-dimensional pipe-network approximation, and each cell in the computational mesh can be assigned a unique fracture aperture/transmissivity determined using a correlated random field. We compare transport through DFN realizations with a) random aperture variation and b) various correlation lengths in the random aperture field. We find that early breakthrough times and retention curves are influenced by in-fracture aperture variability but the tails of the breakthrough curves are insensitive to these variations.

The studies presented in this report set the stage for two topics that we plan to study extensively going forward. First, we plan to work with the performance assessment team on the Used Fuel Disposition Campaign to determine when the DFN formulation is appropriate for their performance assessment studies. Second, with DOE now a member of the Swedish Task Force we are planning to using DFN tools to contribute to Task 9A, "Force on Modeling of Groundwater Flow and Transport of Solutes".

9.2   DFNWORKS

9.2.1   Introduction

Discrete fracture network (DFN) modeling is a promising alternative to continuum approaches for simulating flow and transport through sparsely fractured rocks in the subsurface. In contrast to continuum methodologies, e.g., stochastic continuum (Neuman 2005) and dual/multiple continuum (Lichtner et al. 2015), where effective parameters are used to include the influence of the fractures on the flow, in the DFN approach, geologic field investigations are used to create a network of fractures where the geometry and properties of individual fractures are explicitly represented as lines in two dimensions or planar polygons in three dimensions. These generated networks are meshed for computation and the governing equations are numerically integrated to simulate flow. Examples of the various DFN methodologies and their applications are found in (Cacas et al. 1990, Berrone et al. 2013, Dreuzy et al, 2004, Dreuzy et al. 2012, Dershowitz, 2014, Erhel et al. 2009, Mustapha et al. 2007, Pichot et al. 2010, 2012, Xu et al. 2006).

The primary challenge in using the DFN methodology is creating an efficient and scalable workflow. The choice to include the detailed geometry of the fractures and the connectivity of the fracture network allows for a more accurate representation of physical phenomenon and robust predictive simulation of flow and transport through fractured rocks compared to continuum approaches. However, these advantages come at an enormous computational cost, especially when attempting to simulate transport through large networks of fractures. This challenge can be broken down into three main obstacles: i) generation of a high quality computational mesh representation of three-dimensional fracture network, ii) solving the governing equations on that mesh in a computationally efficient manner, and iii) simulating transport through the resulting flow field.

In this chapter, we describe the DFNWORKS high-performance computational suite that overcomes each of these obstacles in a unique fashion. Developed at Los Alamos National Laboratory over the past five years, DFNWORKS provides a novel workflow to model flow and transport in three-dimensional fractured media at scales ranging from millimeters to kilometers. One DFNWORKS simulation is shown in Fig. 9-1. The fracture network contains approximately nine hundred fractures sampled from three fracture families, with different mean radii, mean orientation, and distribution of fracture lengths. The network is created and meshed using DFNGEN, which combines the feature rejection algorithm for meshing (Hyman et al. 2014) methodology to stochastically generate three-dimensional DFNs on the basis of site specific data with the LAGRIT (LaGriT, 2013) meshing toolbox to create a high resolution computational mesh representation of the DFN. Constant pressure boundary conditions are applied to the left and right faces of the network to drive flow through the network, and steady-state conditions are determined by numerically integrating the governing flow equations using DFNFLOW, which utilizes the massively parallel subsurface flow and reactive transport code PFLOTRAN (Lichtner et al. 2015). Transport through the DFN is simulated by adopting a Lagrangian approach within DFNTRANS, which is an extension of the of the WALKABOUT particle tracking method (Painter et al. 2012) to determine pathlines through the DFN (Makedonska et al. 2015). Particle trajectories, shown in orange and red, start from a short line source on a single fracture on the inlet plane and disperse from one another as they pass through the network, and exit the domain on numerous fractures. Importantly, all but the network generation can be carried out in parallel, which allows DFNWORKS to be applied to extremely large networks.

In Sec. 9.2.2 we describe each of these pillars of DFNWORKS (DFNGEN, DFNFLOW, DFNTRANS) which make simulations similar to Fig. 9-1 feasible. We conclude with some remarks about the suite and discuss some extensions of the method in Sec. 9.2.3.

9.2.2   DFNWORKS Description

An overview of the entire DFNWORKS workflow is illustrated in Figure 9-2. The workflow has three principal pieces (DFNGEN, DFNFLOW, DFNTRANS) which can be broken down into six primary aspects. The input for DFNWORKS is a fractured site characterization that provides distributions of fracture orientations, radius, and spatial locations. DFNGEN: 1) FRAM - Create DFN: Using the fractured site characterization networks are constructed using the feature rejection algorithm for meshing. 2) LAGRIT - Mesh DFN: The LAGRIT meshing tool box is used to create a conforming Delaunay triangulation of the network. DFN-FLOW: 3) Convert Mesh to PFLOTRAN input: Control volume information is formatted for PFLOTRAN. 4) Compute Pressure Solution: The steady-state pressure solution in the DFN is obtained using PFLOTRAN. DFNTRANS: 5) Reconstruct Local Velocity Field: Darcy fluxes obtained using DFNFLOW are used to reconstruct the local velocity field, which is used for particle tracking on the DFN. 6) Lagrangian Transport Simulation: An extension of the WALKABOUT method is used to determine pathlines through the network and simulate transport.

Figure 9-3 illustrates the utility of the DFNWORKS workflow with a simple two fracture network, a rectangular fracture is intersected by an elliptical fracture. Figure 9-3.a overlays the mesh on the two fracture system and the fractures are colored by the distance of the computational cell from the line of intersection. Near the intersection, the mesh is refined to accurately resolve the gradients in the pressure and velocity field, which are much higher near fracture intersections than far away. Away from the intersection the mesh is coarsened to decrease computational requirements. Figure 9-3.b shows the steady-state pressure solution, the gradient is aligned with the x-axis, and yellow lines are pressure contours. The pressure contours on the elliptical fracture show there is a pressure gradient and therefore flow is occurring on this dead-end fracture, it is not connect to the domain boundary or another fracture other than principal fracture. A pipe-network representations that preserves the topology of the DFN while disregarding the detailed geometry of the fractures, a common practice in many DFN simulations, (e.g., Joyce et al. 2014), would eliminate this dead-end fracture from the network, thereby disregarding the influence of flow in the elliptical fracture on transport. Figure 9-3.c shows that the influence of flow in this fracture on transport is non- negligible and how the simplifying assumption missing important transport properties. Here, fractures are colored by x coordinate of gradient of the pressure field, which is the fluid velocity in the x direction, and black lines are particle trajectories passing through the DFN. The non-uniformity of the trajectories results in a distribution of particle travel times that exhibits longitudinal dispersion. Using the simplifying pipe- network approximations, the breakthrough curve would be a step function with no dispersion or tail, which will lead to incorrect upscaled models for transport. Although this is a sample two fracture example, it serves to demonstrate the importance of both the geometry and topology of these networks. The workflow outlined in Fig. 9-2 allows DFNWORKS to retain the explicit geometry and topology so upscaled flow and transport properties do not suffer from these elimination artifacts, and does so in a parallel manner.

In the rest of this section, we describe the different pieces of the DFNWORKS framework in the order that they are implemented during the workflow. We start with the generation method DFNGEN, move on to the flow solver DFNFLOW, and close this section by describing the particle tracking algorithm DFNTRANS which was explained in details in UFD report, FCRD-UFD-2014-

000059,   of 2014, "Modeling Fluid Flow in Natural Systems: Model Validation and Demonstration".
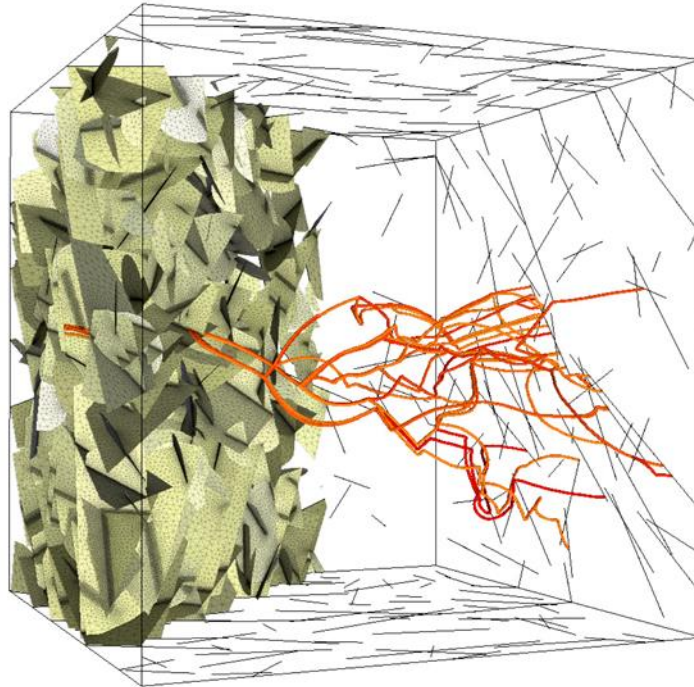

Figure 9-1: Sample fracture network and particle trajectories in a DFNWORKS simulation. The network is created and meshed using DFNGEN, which combines the feature rejection algorithm for meshing (Hyman et al. 2014) to stochastically generate three-dimensional DFNs on the basis of site specific data with the LAGRIT meshing toolbox to create a high resolution computational mesh representation of the DFN that conforms to the lines of intersections between fractures in an intrinsically parallel fashion. Constant pressure boundary conditions are applied to the left and right faces of the network to drive flow through the network, and steady-state conditions are determined by numerically integrating the governing flow equations using DFNFLOW, which utilizes the massively parallel subsurface flow and reactive transport code PFLOTRAN. Transport through the DFN is simulated by adopting a Lagrangian approach within DFNTRANS, which is an extension of the of the WALKABOUT particle tracking method (Painter et al. 2012) to determine pathlines through the DFN. Particle trajectories, shown in orange and red, start from a short line source on a single fracture on the inlet plane and disperse from one another as they pass through the network, and exit the domain on numerous fractures.
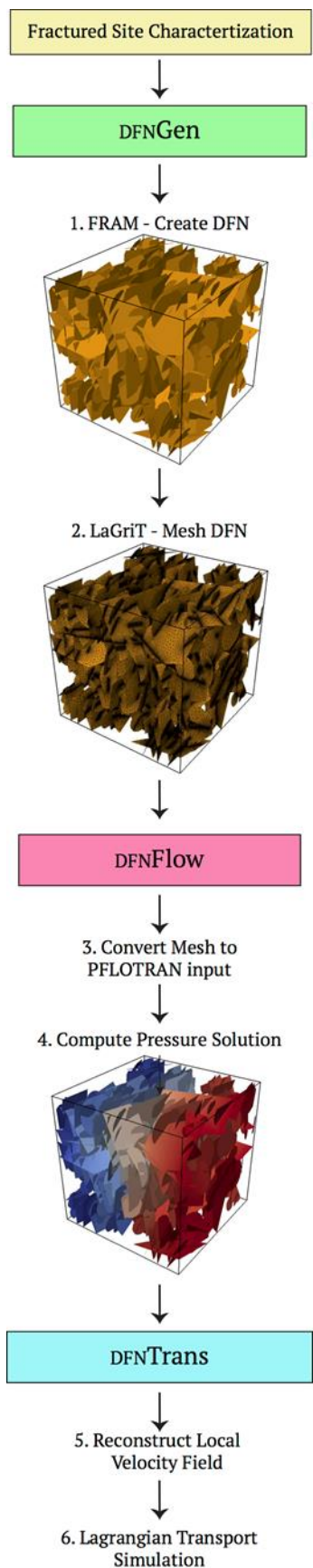
Figure 9-2: DFNWORKS Workflow. From top: The input for DFNWORKS is a fractured site characterization that provides distributions of fracture orientations, radius, and spatial locations. DFNGEN: 1) FRAM - Create DFN: Using the fractured site characterization that networks are constructed using the feature rejection algorithm for meshing. 2) LAGRIT - Mesh DFN: The LAGRIT meshing tool box is used to create a conforming Delaunay triangulation of the network. DFNFLOW: 3) Convert Mesh to PFLOTRAN input: Control volume information is formatted for pflotran. 4) Compute Pressure Solution: The steady-state pressure solution in the DFN is obtained using pflotran. dfnTrans: 5) Reconstruct Local Velocity Field: Darcy fluxes obtained using dfnFlow are used to reconstruct the local velocity field, which is used for particle tracking on the DFN. 6) Lagrangian Transport Simulation: An extension of the walkabout method is used to determine pathlines through the network and simulate transport.

a)

b)

c)

Figure 9-3: Two fracture DFN demonstrating the utility of the DFNWORKS suite. (a) Conforming Delaunay mesh on the two fracture system. The fractures are colored by the distance of the computational cell from the line of intersection. Away from the intersection the mesh is coarsened to preserve computational resources. (b) Steady- state pressure solution, the gradient is aligned with the x-axis, and yellow lines are pressure contours. The pressure contours on the elliptical fracture show there is a pressure gradient and therefore flow is occurring on this dead-end fracture, it is not connect to the domain boundary (or another fracture other than principal fracture. (c) Fractures are colored by x coordinate of gradient of the pressure field, which is the fluid velocity in the x direction, and black lines are particle trajectories passing through the DFN. The non-uniformity of the trajectories results in a distribution of particle travel times that exhibits longitudinal dispersion. Using the simplifying pipe-network approximations, the breakthrough curve would be a step function with no dispersion or tail, which will lead to incorrect upscaled models for transport.

DFNGEN: The Feature Rejection Algorithm for Meshing

Each three-dimensional DFN is generated and meshed using the feature rejection algorithm for meshing (FRAM) methodology of Hyman et al., (Hyman et al. 2014). Each DFN is constructed so that all features in the network, e.g., length of intersections between fractures; distance between lines of intersection of a fracture, are larger than a user-defined minimum length scale. This restriction provides a firm lower bound on the required mesh resolution, and special care is taken so that prescribed geological statistics are not affected by this restriction. Once the DFN is generated, the LAGRIT (LaGriT, 2013) meshing toolbox is used to create a high resolution computational mesh representation of the DFN in parallel. An algorithm for conforming Delaunay triangulation is implemented so that meshes along intersections coincide and Voronoi control volumes suitable for finite volume solvers such as FEHM (Zyvoloski, 2007), TOUGH2 (Pruess, 1999), and the fully parallelized PFLOTRAN (Lichtner et al. 2015) are produced. Because the mesh conforms to fracture intersections, the method does not require solving additional systems of linear equations, which is needed if a non-conforming mesh is used (Berrone et al. 2013, Pichot et al. 2010, 2012). Key features of FRAM are that it is fully automated, meaning that throughout the procedure no adjustments of the mesh are performed to improve the mesh quality, and it's flexible, any statistical survey of a fracture site may be used in the generation of fractures, thereby allowing it to generate realistic DFNs that mimic natural fracture sites. In this section, we provide a brief description of FRAM and refer the interested reader to Hyman et al., (Hyman et al. 2014) for a complete description of the method.

Network Generation and Meshing

The principal issue in meshing a DFN is that to resolve a tiny feature in the network, the edges of the mesh surrounding the feature must be the size of the feature or smaller, if the physics are to be properly resolved. Various methods have been proposed to address this issue, and others, associated with meshing a DFN. In one methodology, pathological cases that degrade mesh quality, e.g., an arbitrarily short line of intersection between two fractures, are systematically removed after an unconstrained fracture network is generated and meshed (Mustapha and Mustapha 2007, Mustapha and Dimitrakopoulos 2011, 2011, Maryska et al. 2005, Erhel et al. 2009). However, such adjustments can deform the network, resulting in fractures that may no longer be planar. Another methodology does not require the mesh to coincide at the line of intersection, and the difficulty is pushed forward by the inclusion of additional linear systems that must be solved to impose continuity of pressure and flux along fracture intersections (Benedetto et al. 2014, Berrone et al. 2013, Pichot et al. 2010, 2012). These additional linear systems make this methodology computationally more expensive when solving for flow than when the meshes are forced to align. In addition, a non-aligned grid at fracture intersections may complicate solute transport calculations.

In contrast to these methods, DFNGEN uses FRAM to constrain the generation of the network so that it only contains features greater than or equal to a user-prescribed minimum length scale h. Each fracture in our DFN is a planar straight-line graph (PSLG) made up of the set of line segments that represent the boundary of the fracture and the line segments that represent where other fractures intersect it. Given a set of PSLGs $\mathcal{X}$ with arbitrary orientation in R^3, one can define a *local feature size at a point p* as the radius of the smallest sphere centered at p that intersects two non-incident vertices of segments of $\mathcal{X}$ (Ruppert 1995). In a three-dimensional DFN, examples of a measurable feature include: the length of the line of intersection between two fractures, the distance from the end of a fracture intersection that is interior to the polygon

boundary to the polygon boundary, and the distance between two fracture intersection line segments. During the generation process, we require that the DFN never generate a fracture with a feature of size less than h, which provides a firm lower bound on the required resolution of the mesh. When the resulting network is meshed, all features can be resolved by generating triangular cell edges with a minimum length slightly less than h.

By constraining the network so that all features in the network are greater than h, FRAM ensures that pathological cases which degrade mesh quality are not present in the network. Under these conditions, a conforming Delaunay triangulation algorithm (Mount and Gable, 2001) can be used to ensure that the line of intersection between any two fractures is preserved in the mesh so long as the lines of intersection are discretized in steps less than h. The conforming Delaunay triangulation algorithm procedure results in meshes that are coincident along the common line of intersection between fractures. Because computational control volumes (Voronoi polygons) are based on vertices and the triangular meshes are coincident along intersections, the Voronoi cells also conform at the fracture boundaries. This results in Voronoi control volumes that span both of the intersecting fractures. However, the neighbors of these Voronoi cells are still two-dimensional. The need to check for a feature size less than h means that the fracture generation process is computationally more demanding than methods that do not impose the minimum feature size constraint. The tradeoff is a streamlined/parallelized process of mesh generation, numerical integration of the pressure solution, and simplifying particle tracking through the resulting flow field.

Mesh Examples

In figure 9-4 three intersecting fractures show the intersecting conforming Delaunay triangulations. Two of the fractures are colored by distance from lines of intersections (traces) with each other and other fractures that intersect these fractures, and the other is semi-transparent for clarity. The mesh is optionally coarsened away from intersections with pressure gradients will be lower. The inclusion of the semi- transparent fracture illustrates how FRAM creates a mesh that adheres to multiple intersections on the surface of a single fracture. Two additional fractures intersect the elliptical fracture, and intersect one another on the surface of that fracture, as shown by the intersecting white colored regions. The inset shows that the Delaunay mesh conforms all of these lines of intersection.
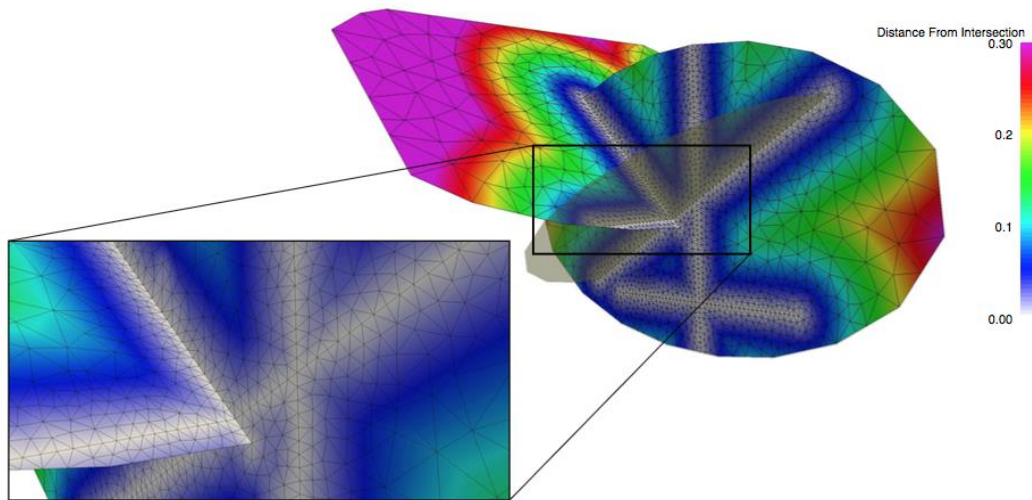
Figure 9-4: Three intersecting fractures show the intersecting conforming Delaunay triangulations. Two of the fractures are colored by distance from lines of intersections (traces) between fractures, and the other is semi-transparent. The mesh is optionally coarsened away from intersections with pressure gradients will be lower. The inclusion of the semi-transparent fracture illustrates how FRAM creates a mesh that adheres to multiple intersections on the surface of a single fracture. Two additional fractures intersect the elliptical fracture, and intersect one another on the surface of that fracture, as shown by the intersecting white colored regions. The inset shows that the Delaunay mesh conforms all of these lines of intersection.

CELLS N

$id_1\, x_1\, y_1\, z_1\, volume_1$

$id_2\, x_2\, y_2\, z_2\, volume_2$

…

…

$id_N\, x_N\, y_N\, z_N\, volume_N$

CONNECTIONS M

$id_{up,\,1}\, id_{dn,\,1}\, x_1\, y_1\, z_1\, area_1$

$id_{up,\,2}\, id_{dn,\,2}\, x_2\, y_2\, z_2\, area_2$

…

…

$id_{up,\,M}\, id_{dn,\,M}\, x_M\, y_M\, z_M\, area_M$

Figure 9-5: Explicit grid format in PFLOTRAN that is used to read the DFN mesh. N is the number grid cells and M is the total number of internal connections between grid cells. In the first block under CELLS, id_i, x_i, y_i, z_i are the cell id, x-coordinate, y-coordinate and z-coordinate of the i-th grid cell, respectively. In the second block under CONNECTIONS, $id_{up,j}$, $id_{dn,j}$, x_j, y_j, z_j, $area_j$ are the upwind grid cell id of the j-th connection, downwind grid cell id of the j-th connection, Coordinates of the face between the j-th connection and the area of the face between the j-th connection, respectively.

Remarks about FRAM

Decisions about the minimum length scale h that will be represented in a DFN are made a priori; which is typically the case in scientific computing and not unique to FRAM. When adopting the FRAM methodology the choice of the h will be reflected in the generated network. If h is chosen to large with respect to fracture and domain size, then it will be difficult to generate a DFN that meets the density requirements. If h is chosen too small, then computational cost associated with meshing and solving the governing equations will increase. The choice of h should be made so that all physical phenomena of interest are greater than h, so they can be well resolved by the computational mesh, while limiting computational expenses. The tradeoff between spatial resolution and computational expediency inherent in the choice of h in FRAM is the familiar tradeoff in most branches of scientific computing.

Due to the rejection nature of FRAM some of the desired distributions in the network, e.g. fracture length, will not be properly represented due to over rejection unless certain criteria are met. For example, larger fractures generate more measurable features in the network than smaller ones and can be rejected a disproportionate amount. However, modifying the procedure by which fracture

lengths are sampled can alleviate the issue of bias in the represented fracture length distribution. This is only necessary when sampling from a distribution with a broad range of lengths, such as a truncated power law distribution. An alternative solution is decreasing h to loosen the acceptation criteria. In the limit of $h \rightarrow 0$, all prescribed distributions will be recovered exactly because no fractures are rejected. Details about these procedures are in (Hyman et al. 2014).

DFNFLOW: Flow Solver

Once the DFN is generated and meshed using DFNGEN, Voronoi control volumes, the dual mesh of the Delaunay triangulation, are computed. Then a Python script processes the LAGRIT output into an unstructured grid format compatible with the massively parallel subsurface flow code PFLOTRAN. Modifications were made to PFLOTRAN to read the unstructured Voronoi mesh and to perform calculations on the Voronoi mesh. The format to read Voronoi meshes involves locations of the Voronoi cell-centers, the connectivity of the cell-centers and the cell areas, and is referred to as explicit unstructured grid format (see Fig. 9-5). This explicit unstructured grid format can be used to read any generalized n-faced polygonal meshes. The permeability in each Voronoi cell is based on the local aperture of the fracture. These values are computed using a Python script and read into PFLOTRAN. Using this information, PFLOTRAN determines the steady-state pressure field within the DFN using a two-point flux based finite volume scheme. By using a control volume based discretization for flow, local mass balance is ensured, and by using a Voronoi mesh, the accuracy of the flux evaluation is maintained (Zyvoloski and Vesselinov, 2006). PFLOTRAN returns the groundwater fluxes (Darcy velocities) at the edges of the Voronoi control volumes. These fluxes are then used in DFNTRANS for velocity reconstruction and particle tracking. In the next part of this section, a brief description of PFLOTRAN is presented. The reader is referred to (Mills et al. 2007, Hammond et al. 2012, 2014) for details of PFLOTRAN implementation and its parallel performance.

PFLOTRAN (Lichtner et al. 20150) is an open-source, massively parallel, multiscale and multiphysics code for subsurface and surface processes. The code is the result of a multiple DOE national laboratory effort with core developers from LANL, SNL, LBNL and ORNL, with users and contributors from universities and other research facilities all over the world. PFLOTRAN is built on top of PETSc (Portable, Extensible Toolkit for Scientific Computation) (Balay et al. 2014) framework and incorporates PETSc's parallel data structures, linear and non-linear solvers, and relies on domain decomposition for parallelism, and was originally developed as part of the Department of Energy SciDAC-2 groundwater program. This foundation has allowed PFLOTRAN to run simulations with billions of degrees of freedom on over 100,000 processor cores. The code solves a system of nonlinear partial differential equations that model non-isothermal multiphase flow, reactive transport and geomechanics in porous media. Equations describing multiple continua (for matrix-fracture interactions) and non-isothermal surface flow are also solved. The code is written in object-oriented Fortran 2003 (base and derived classes) which gives the flexibility to: a) add new process models and couple with existing process models, and b) couple with other external codes that use PETSc and drive the coupling with PFLOTRAN as the master. To reduce I/O bottlenecks, PFLOTRAN also has parallel I/O modules built and outputs data in Tecplot ASCII as well as the binary HDF5 formats. The HDF5 output can be visualized using the HPC toolkits such as VisIt and Paraview. PFLOTRAN can run on a wide range of architectures ranging from multi-core laptops and clusters to petascale leadership-class supercomputers. PFLOTRAN applications are related to areas in energy, climate and nuclear including nuclear waste disposal (Makedonska et al. 2015), CO_2 sequestration (Lichtner and Karra, 2014, Lu and Lichtner, 2007), enhanced geothermal systems (Lichtner and Karra, 2014), groundwater

contamination (Hammond and Lichtner, 2010), hydraulic fracturing (Karra et al. 2015, Middleton et al.2015), induced seismicity (Karra et al. 2013) and Arctic hydrology and climate (Karra et al. 2014, Mills et al. 2012). PFLOTRAN can be downloaded from http://bitbucket.org/pflotran.

The subsurface flow processes currently available in PFLOTRAN include single-phase variably-saturated flow (Richards equation), non-isothermal two-phase water-supercritical CO_2, general mode that allows modeling multiphase flow of any two component systems, thermal-hydrologic coupled heat and mass conservation and three-phase ice-liquid-vapor (water) flow for Arctic applications. Any of these flow modes can be coupled to multicomponent reactive transport equations using either a global implicit algorithm or operator splitting. The multicomponent reactive transport processes include aqueous complexation, sorption, mineral precipitation/dissolution, and microbially-mediated biodegradation. Because these flow processes are already available in PFLOTRAN , they can all be used DFN simulations with little extended effort on behave of the user. Additionally, PFLOTRAN can be controlled from Python using the PyFLOTRAN (karra and Kitay, 2015) interface that provides Python classes and methods for easy modification of PFLOTRAN input file. This allows for a streamlined workflow from pre-processing to post-processing in Python, and usage of Python scripting tools and packages for directory hierarchy, multiple processing and error checking.

DNFTRANS: Particle Tracking

Particle tracking method is a method for resolving solute transport using control volume flow solutions obtained from flow solver (dfnFlow) on the unstructured mesh generated using dfnGen. We adopt a Lagrangian approach and represent a non-reactive conservative solute as a collection of indivisible passive tracer particles. Particle tracking methods: a) provide a wealth of information about the local flow field, b) do not suffer from numerical dispersion, which is inherent in the discretization of advection-dispersion equations, and c) allow for the computation of each particle trajectory to be preformed in an intrinsically parallel fashion if particles are not allowed to interact with one another or the fracture network. However, particle tracking on a DFN poses unique challenges that arise from both the quality of the flow solution, the unstructured mesh representation of the DFN, and the physical phenomena of interest. The flow solutions obtained from dfnFlow are locally mass conserving, so the particle tracking method does not suffer from the problems inherent in using Galerkin fnite element codes, (e.g., Dershowitz, 2014, Mustapha et al. 2011, Elsworth 1986, Geier 2011, Hartley et al. 2004, Outters and Shuttle, 2000), where experience has shown that particles can become stuck in cells that exhibit unphysical stagnant regions because the flow solution does not conserve mass locally. Because the primary interest of particle tracking is simulation of mass transport, these stuck particles, representing a loss of mass in the system due to numerical artifacts, limit the usefulness of flow field provided by finite element methods (Geier 2011). The coupling of dfnTrans with finite volume codes ensures that all particles released into these DFN will eventually exit the system, and do so without incorporating additional pipe-network simplifications (Cacas et al. 1990, Dershowitz and Fidelibus, 1999).

In this section, we highlight the most important details of the method, namely: (i) the reconstruction of velocities on each vertex of the computational mesh and (ii) the unique approach taken to address mass transport through fractures intersections. A comprehensive explanation of dfnTrans and details concerning its implementation can be found in Makedonska et al., (Makedonska et al. 2015).

Reconstruction of Velocity Field

The pathline followed by a particle is obtained by numerically integrating the trajectory equation, $\mathbf{x} = \mathbf{v}(\mathbf{x}(t))$, with initial position $\mathbf{x}(0) = \mathbf{x}$. Here, $\mathbf{v}$ is the Eulerian velocity vector that must be defined at every point in the fracture network. However, the control volume flow solution provides a set of scalar quantities that are approximations to the normal component of Darcy flux integrated over each edge of each control volume cell, rather than the required continuous velocity field.
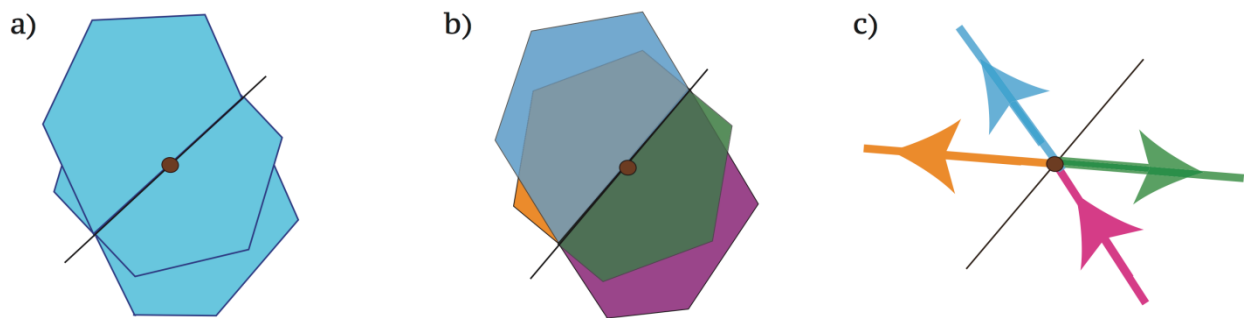
Figure 9-6: Illustration of the technique used to reconstruct flow velocities along the line of intersection between two fractures. a) A control volume along a line of intersection between two fractures. Fluxes are defined on faces of the control volume cells. b) The control volume is spilt into four sub-polygons using the line of intersection. The green and orange sub-polygons are on one fracture and the blue and purple are on another. c) The flow velocities are reconstructed on each of the split polygons, here arrows indicate inflow/outflow. In this example, the flux into the control volume occurs through the purple sub-volume and outflow occurs through the remaining sub-polygons.

To address this issue Painter et al. (Painter et al. 2012) developed an approach to reconstruct velocity fields from flow solutions obtained on unstructured control volume mesh. Using the flow solution provided by dfnFlow, cell-centered velocities are estimated by solving a overdetermined linear system for the Darcy velocity. The system is overdetermined because each control volume has more sides than the dimension of the problem, e.g., in two dimensions each control volume has a minimum of three sides. On cells in the interior of the domain an unconstrained least squares method is used, and a constrained least squares method used to reconstruct velocities on boundary cells to enforce Neumann boundary conditions along fracture walls.

This procedure creates piecewise constant flow velocity vectors at every vertex in the DFN mesh. Then barycentric interpolation (Coxeter, 1969) is used to determine a particle's velocity at any location within a cell at any point in the DFN. Using these velocities, an adaptive time stepping first-order predictor-corrector method is used to numerically integrate the trajectory equation. The semi-implicit nature of the predictor-corrector method prevents particles from reaching the edge of a fracture with no-flow boundary conditions.

Fracture Intersections

Simulating transport through fracture intersections is a principal challenge for modeling transport through a three-dimensional DFN. The control volume cells along fracture intersections are three-dimensional objects formed from the union of two polygons in different planes; control volume cells away from intersections are two-dimensional planar polygons. This peculiar shape at intersections results in more complicated flow behavior than elsewhere in the network. Flow can go through the intersection and continue onto the same fracture without changing directions, or it change direction and exit onto the intersecting fracture or, as is usually the case, the flow can split by some percentage between the fractures. The technique schematically presented in Fig. 9-6 was developed to provide the necessary information so that the number of particles dispersed at fractures intersections is representative of the percentage of flux outgoing onto each fracture at intersections. Figure 9-6.a shows a control volume along a line of intersection between two fractures. The control volume is a three-dimensional objects formed from the union of two polygons in different planes where the Darcy flux is defined along the boundaries of the control volumes. The first step is dividing the control volume into four sub-polygons using the line of intersection, this partition is shown in Fig. 9-6.b. Here, the green and orange sub-polygons are on one fracture and the blue and purple are on another. Then the flow velocities are reconstructed on each of the split polygons, where arrows indicate inflow/outflow. In the example shown in Fig. 9-6.c, the flux into the control volume occurs through the purple sub-volume and outflow occurs through the remaining sub-polygons; any combination of inflow/outflow can be accommodated. To determine how particles pass through intersections, probabilities proportional to the outgoing flux are assigned to each cell that borders the intersection. Then, the downstream cell is chosen randomly based on these probabilities. This method ensures that the percentage of particles exiting onto each cell is proportional to the flux exiting onto those cells.
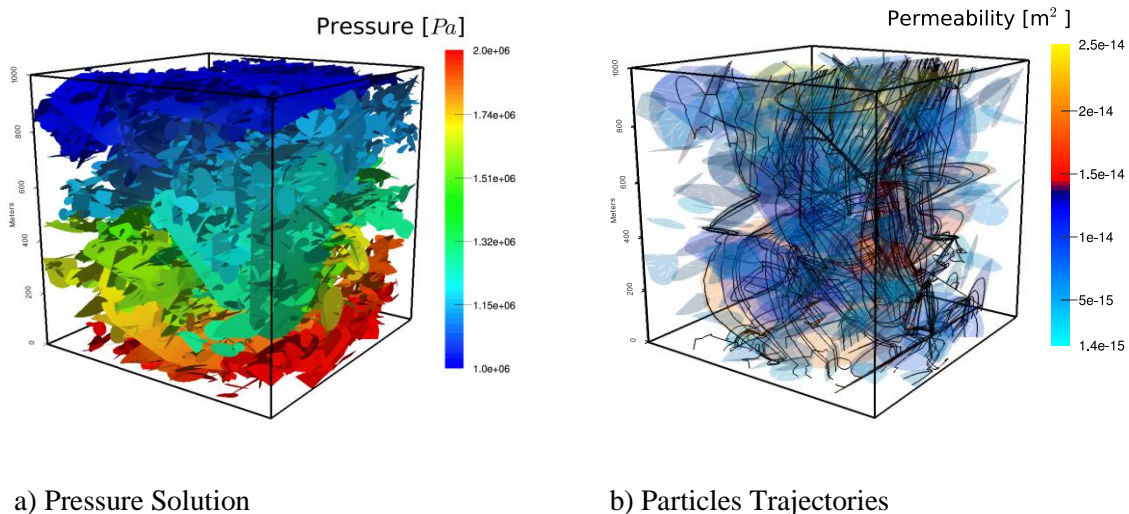
a) Pressure Solution   b) Particles Trajectories

Figure 9-7: a) A DFN realization based upon the fractured granite at the Forsmark, Sweden site in a 1 km^3 domain. The model consists of multiple sets of circular fractures whose orientations follow a Fisher distribution. The fracture diameters in each fracture set follow a truncated power-law distribution with lower cutoff at 15 meters. Fractures are colored by pressure. Dirichlet boundary conditions are imposed on he top (1 MPa) and bottom (2 MPa) of the domain to create a pressure gradient in the z direction, and no-flow boundary conditions are imposed along lateral boundaries. b) Two hundred particle trajectories within the DFN shown in Fig. 9-7. Particles are inserted uniformly along fractures on the bottom of the domain. Trajectories are overlaid on the networks shown in Fig. 9-7(a), but here fractures are colored by the permeability, to show how particles are drawn to larger fractures, which have higher permeabilities and offer less resistance than smaller fractures. Although particles are inserted uniformly along fractures in the inlet plane, they cluster on larger fractures as the exit the domain. This clustering suggests that transport only occurs within a small portion of the fracture network far away from the inlet plane.

Analysis of Trajectories

The information obtained using these particles is processed in a number of ways to characterize transport through these networks. Foremost, distributions of travel time and pathline length are constructed and their moments computed. In addition to these more common measurements, information about the location and velocity of the particles can be recorded throughout their journeys. This information can be sampled using two different methods, at a set of given times or at a set of given locations. The sampling at prescribed time increments can be used to determine key statistical features of the plume such as mean displacement and dispersion. Complimentary sampling information at a set of given location, e.g., at uniformly spaced control planes, creates a pseudo-time evolution of the plume with distance traveled. Regardless of which sampling method is used, information such as current fracture aperture, box-dimension of the plume, and number of fractures a particle has touched can be recorded and analyzed. Flow topology maps where the

particle trajectories are used to determine what percentage of the network contributes to transport can be also obtained using these particle trajectories.

The Swedish Nuclear Fuel and Waste Management Company (SKB) has undertaken a detailed investigation of the fractured granite at the Forsmark, Sweden site as a potential host formation for a subsurface repository for spent nuclear fuel (Hartley and Joyce, 2013, SKB, 2011). The Forsmark area is about 120 km north of Stockholm in northern Uppland, and the repository is proposed to be constructed in crystalline bedrock at a depth of approximately 500 m. Based on the SKB site investigation, a statistical fracture model with multiple fracture sets was developed; detailed parameters of the Forsmark site model are in (Hartley and Joyce, 2013). We adopt a subset of the model that consist of three sets of background (non-deterministic) circular fractures whose orientations follow a Fisher distribution, fracture radii are sampled from a truncated power-law distribution, the transmissivity of the fractures is estimated using a power-law model based on the fracture radius, and the fracture aperture is related to the fracture size using the cubic law (Adler et al. 2012). Under such a formulation, the fracture apertures are uniform on each fracture, but vary among fractures. The network is generated in a cubic domain with sides of length one-kilometer. Dirichlet boundary conditions are imposed on the top (1 MPa) and bottom (2 MPa) of the domain to create a pressure gradient aligned with the vertical axis, and no-flow boundary conditions are enforced along lateral boundaries.

A sample realization of the Forsmark DFN is shown in Fig. 9-7. The realization contains 4,934 fractures and the computational mesh consists of 7,731,299 cells. There are significantly more small, low permeability, fractures than larger fractures due to the power law distribution used to generate the network. The larger fractures act as conduits for flow, connecting numerous small fractures together in the network. Figure 9-7.a shows the steady state pressure solution. Fractures are colored by pressure, with warmer colors indicating higher values. A selection of two hundred particle trajectories passing through this network is shown in Fig. 9-7.b. The particles are inserted uniformly along fractures in the inlet plane (bottom), and the movement of the particles is determined by the local velocity. The permeability of the fractures is shown along with the trajectories to highlight that particles are attracted toward larger fractures. Because the fracture permeability is based upon the fracture radius, the largest fractures have the highest permeabilities. Although the particles are inserted uniformly, their trajectories cluster together onto larger fractures. This clustering suggests that transport only occurs within a small portion of the fracture network far away from the inlet plane.

Solute Transport with Sorption and Matrix Interactions

The particle trajectories generated by dfnWorks represent those of hypothetical groundwater tracers moving through complex DFNs. Although not strictly part of dfnWorks, the dfnWorks-generated trajectories may be used as transport pathway input to contaminant transport algorithms that use particle tracking in the time domain (Painter et al. 2008) to simulate transport of trace contaminants such as radionuclides. For example, groundwater tracer trajectories generated by dfnWorks may be used as input to the MARFA computer code (Painter and Mancillas, 2013) to simulate the migration of trace contaminants in DFNs taking into account diffusion into a matrix of limited or unlimited extent, sorption onto immobile minerals, longitudinal dispersion, and first-order transformations (decay and in-growth).

Remarks

DFNWORKS is a parallalized computational suite for simulating single/multiphase flow and transport in stochastically generated three-dimensional discrete fracture networks. We have described the pillars of DFNWORKS (DFNGEN, DFNFLOW, DFNTRANS) and provided several applications of the work flow to demonstrate its utility. The three applications we presented highlight various aspects of DFNWORKS including its ability to generate networks in accordance with geological data, match transport properties to data, and simulate multiphase flow.

We focused on the basic elements of the computational suite to provide a foundational understanding of the workflow. However, there are several extensions of the method that, while not being central to the workflow, increase its utility. These include: (i) in-fracture aperture/transmissivity variability; (ii) networks composed of multiple regions with variable fracture densities; (iii) mapping a DFN into a continuum for the inclusion of fracture-matrix interaction; (iv) multicomponent reactive transport; (v) integration uncertainty quantification and sensitive analysis suites such as MADS (Model Analysis and Decision Support) (Vesselinov and Harp, 2012); (vi) inclusion of large deterministic fractures for site specific studies.

9.3   INFLUENCE OF INJECTION MODE

9.3.1   Introduction

In low permeability fractured rocks, networks of fractures are typically the principal pathways for fluid flow and transport of dissolved contaminants. However, fractured rocks are difficult to characterize because their structural attributes, e.g., fracture orientations and apertures, exhibit anisotropy and heterogeneity on length scales that span several orders of magnitude (Neuman, 2005). The energy and engineering applications impacted by this uncertainty include hydrocarbon extraction, aquifer storage and management, geothermal energy extraction, environmental restoration of contaminated fractured rock, and the disposal of used nuclear fuel (Adler et al. 2012, Berkowitz, 2002, Faybishenko, 2005, Karra et al. 2015). In particular, the long term storage of used nuclear fuel in subsurface repositories requires a comprehensive understanding of the mechanisms governing transport in fractured media.

There exists a variety of models, both computational and theoretical, for the phenomena associated with transport in heterogeneous and fractured media (Berkowitz and Scher, 1997, Berkowitz, 2002, Cacas et al. 1990, Cvetkovic, 2011, Endo et al. 1984, Frampton and Cvetkovic, 2007, 2011, Long and Remer, 1982, Neuman and Tartakovsky, 2009, O'Malley and vesselinov, 2014, Painter and Cvetkovic, 2005, Painter et al. 2002, Smith and Schwartz, 1984, Schwartz and Smith, 1988, Tsang et al. 1988). However, a major obstacle in the successful application of these models in fractured media is the lack of field scale information that can be used to verify and validate them. This information gap is the result of physical limitations associated with *in situ* tracer experiments (Andersson et al. 2007). Computational simulations, such as those performed here, serve as a virtual laboratory to provide data which can be used to calibrate and validate analytical models, while also providing insights into transport through fractured media. The most common computational approaches to simulate flow and transport in fractured media are the stochastic continuum, dual/multiple continuum, and discrete fracture network (DFN) methodologies, each of which has its advantages and disadvantages (Neuman 2005, Lichtner and Karra 2014, Painter et al. 2002).

In general, the initial distribution of mass transport in fractured rock can be modeled using one of two injection methods. The first method, *flux-weighted injection*, mimics a solute that is released in proportion to the flux at the location of insertion, e.g., miscible gas released into a packed off borehole connected to hydraulically active fractures (Jankovic and Fiori, 2010). The second method, *resident based injection*, is designed to mimic a source that introduces a solute uniformly throughout the input zone, e.g., multiple leaking canisters within a buffer zone (Frampton and Cvetkovic, 2009). Studies concerning the influence of injection mode on solute transport date back to at least (Kreft and Zuber, 1978). They derived solutions to the advection-dispersion equation for various initial and boundary conditions in semi-infinite and infinite domains. Computational studies of transport through strongly heterogeneous and fractured media, e.g., two and three-dimensional porous media (Demmy et al. 1999, Gotovac et al. 2009, 2010, Jankovic and Fiori, 2010, Vanderborght 1998) and in two-dimensional DFN simulations (Frampton and Cetkovic, 2009), report that the choice of injection scheme influences key physical observables, namely the scaling of the moments of transport travel time with distance traveled. Many theoretical models of transport require these moments to scale linearly with distance; most notably Fickian dispersion (Frampton and Cvetkovic, 2011). These previous studies found that solutes inserted under flux-weighted conditions scales linearly with distance, while those obtained using resident injections display nonlinear behavior. In a computational study of transport through strongly heterogenous two-dimensional porous media, (Gotovac et al. 2010) found that all moments of travel time eventually scale linearly with distance, even those observed using resident based injection that initially displayed nonlinear behavior. In the context of DFN, (Frampton and Cvetkovic, 2009) observed non-linear scaling of travel time modes under resident conditions using in two-dimensional DFNs, and (Frampton and Cvetkovic, 2011) observed linear scaling of the first two moments of travel time obtained using flux-weighted injection in three-dimensional DFN, but they did not consider resident injection.

The contribution of this paper is testing the hypothesis that solute plumes injected under resident conditions evolve to behave similarly to solutes injected under flux-weighted conditions in terms of transport time, pathline tortuosity, and flow channeling. We test this hypothesis in large (km) three-dimensional DFN. Computational limitations have prohibited simulations sufficiently large enough to investigate this hypothesis previously. A new DFN methodology allows us to couple the DFN methodology with a Lagrangian approach to model transport through fractured media at the kilometer-scale and characterize the influence of injection mode, asymptotic behavior of the plumes, and the physical mechanisms at play. Statistically independent DFN realizations are generated in kilometer cubes based on site characterization data obtained from the Forsmark site in Sweden (SKB, 2011), a potential host repository for spent nuclear fuel. We selected this particular location due to the wealth of information available about the site that resulted from the Swedish Nuclear Fuel and Waste Management Company's (SKB) detailed investigation of the area. Even though the DFN are based on site-specific data, the presented results are general, not than site- specific. We use generic boundary conditions, do not include *site-specific features*, e.g., fracture zones, rock domains, topography, regional flow, and only use a subset of the site investigation data related to fracture statistics from the cited report. Although these large scale simulations are feasible using modern DFN capabilities, specifically the computational suite DFNWORKS that we utilize, they are still computationally demanding. Therefore, we limit the number of DFN samples to sixty. However, the domains sizes considered appear to be sufficiently large to provide informative statistics about the ensemble.

Each of the DFNs contains approximately five thousand fractures. A pressure gradient is imposed across the domain, the governing equations for flow are numerically integrated until steady state conditions are reached, and advective non-reactive particles are injected into the resulting flow

field to simulate solute transport through the networks. Approximately one hundred thousand advective particles are inserted into each DFN. In sum, over 5.5 million particle trajectories are considered. Our focus is on advection-dominated flows where the effects of matrix diffusion are small. We impose no-flow boundary conditions along fracture walls so that particles do not interact with the fracture walls or the surrounding, and do not consider processes such as absorption or precipitation. Spatial and temporal particle attributes are recorded at uniformly spaced control planes throughout the domain to observe the evolution of transport properties as functions of distance traveled. Both flux-weighted and resident injection methods are considered.

We observe that the mean value of travel time computed using advective particles inserted using flux-weighting scale linearly with distance traveled, and the tails of their cumulative distributions of travel time exhibit power-law scaling. In contrast, the mean travel time of particles inserted using resident injection initially scales non-linearly with distance and power-law scaling of the tail of the empirical cumulative distribution of travel times is not observed. However, after accounting for a pre-asymoptic region, the mean travel time of particles inserted using resident injection conditions also scales linearly, and the tails of their breakthrough curves exhibit power-law scaling with nearly the same exponent as that observed for particles inserted using flux-weighting. The physical mechanism behind this evolution appears to be the draw of mass into larger fractures, both network scale channeling and in-fracture channeling are observed.

We present a formal mathematical description of the problem in Sec. 9.3.2. Next, our adopted methodology for generating DFNs and therein simulating flow and transport is outlined in Sec. 9.3.3. We use the computational suite DFNWORKS, which combines the feature rejection algorithm for meshing (FRAM) (Hyman et al. 2014), the LaGriT meshing toolbox (LaGriT, 2014) the massively parallel flow and transport solver PFLOTRAN (Lichtner et al. 2015), and an extension of the WALKABOUT particle tracking method (Painter et al. 2012) to determine pathlines through the DFN and simulate conservative solute transport (Makedonska et al. 2015). In Sec. 9.3.4, we present and discuss the spatial and temporal Lagrangian observations. Final remarks are provided thereafter in Sec. 9.3.5.

9.3.2 Theory

The focus of this work is on the spreading of a nonreactive conservative solute in a three-dimensional discrete fracture network (DFN) represented by a cloud of passive tracer particles, i.e., using a Lagrangian approach. The imposed pressure gradient is aligned with the vertical axis, z, and thus the primary direction of flow is also in the vertical direction. Particles are released at an inlet plane of the domain, $z = 0$, at time $t = 0$.

Problem Statement

Let $\mathcal{X}$ denote a set of N particles with unique initial positions, $x_i = (x_i, \; y_i, \; 0)$ for $i = 1, \ldots$, on the fractures which intersect the inlet plane. The trajectory of the ith particle starting at x_i is defined by the pathline, p_i, which is the solution to initial value problem

$$\frac{dx}{dt} = v\big(x(t)\big), \qquad x(0) = x_i \qquad\qquad (9\text{-}1)$$

Here, v is the Eulerian velocity vector with components, $v = [u, \; v, \; w]$ defined at every point in the fracture network. The length of the pathline, ℓ, is used to parameterize the spatial and temporal coordinates of the particle. Explicitly, $p(\ell) = [x(\ell), \; y(\ell), \; z(\ell), \; t(\ell)]$ for $\ell > 0$ and

$p_i(0) = [x_i, \; y_i, \; 0, \; 0]$.   Under the assumptions of steady state flow and in the absence of local dispersion, particles move along their respective pathlines and arrive at a control plane, CP(z), at the point $p_i(\ell') = [x(\ell'), \; y(\ell'), \; z, \; t(\ell')]$, at a time $t(\ell') = \tau_i(z)$, the breakthrough time of particle i at CP(z). The Lagrangian integral along each trajectory can be used to compute $\tau_i(z)$ for each particle,

$$\tau_i(z) = \int_0^{l'(z)} \frac{d\xi}{w[x(\xi),y(\xi),z(\xi)]} \qquad (9\text{-}2)$$

to reach CP(z). In Eq. 9-2, w is the vertical Eulerian velocity along p_i. Our focus is on first passage time of pathlines through each CP, which we define as the travel time required for a particle to reach a CP for the first time. It is possible that multiple crossings at a CP occur due to local flow opposite the primary direction of flow, but these crossings are not considered in our analysis.

The two injection modes are distinguished from one another by the initial mass distribution along the inlet plane. Given a fixed total mass represented by the particles, M, the mass associated with each particle, m_i, is determined using the total area of the fractures, length times aperture, along the inlet plane, A, and, in the case of flux-weighted injection, the local flux associated with the particle's initial position, Q_i and the total flux, Q, across the inlet plane. Specifically,

$$m_i = M/A \qquad \text{resident injection,} \qquad (9\text{-}3a)$$
$$m_i = (M/A)(Q_i/Q) \qquad \text{flux-weighted injection.} \qquad (9\text{-}3b)$$

The mass represented by each particle and the breakthrough time at each control plane can be combined to compute the total solute mass flux $F(t, \; z)$ that has crossed CP(z) at a time t,

$$F(t,z) = \frac{1}{M} \int m_i \, H[t - \tau_i(z)] \, d\mathcal{X} \qquad (9\text{-}4)$$

Here, (t) is the Heavyside function where $(t) = 1$ for $t > 0$, and $(t) = 0$ otherwise, and integration is carried out using Lebesgue measure. Equation (9-4) is the integral form of the familiar cumulative distribution function (CDF) of solute passing through a control plane. We also consider the expression $1 - (t, \; z)$, the complementary cumulative distribution function (CCDF), which when plotted on a log-log scale can be used to determine power law scaling of the tail of the $(t, \; z)$ (Painter et al. 2002). The relevant solute flux through CP(z) is

$$F(t,z) = \frac{dF}{dt} = \frac{1}{M} \int m_i \, \delta[t - \tau_i(z)] \, d\mathcal{X} \qquad (9\text{-}5)$$

which is an integral form of the breakthrough curve. Placing (9-3) into (9-5) one obtains the distributions of travel time for both initial conditions:

$$f_R(t,z) = 1/A \int \delta \, [t - \tau_i(z)] \, d\mathcal{X} \qquad (9\text{-}6)$$
$$f_W(t,z) = 1/(AQ) \int Q_i \delta \, [t - \tau_i(z)] \, d\mathcal{X} \qquad (9\text{-}7)$$

For clarity, the quantities $f_R(t, \; z)$ and $f_W(t, \; z)$ denote the distributions of travel time τ at a control plane a distance of z away from the inlet plane for resident and flux-weighted injection schemes. We use the notation $F_R(t, \; z)$ and $F_W(t, \; z)$ for the cumulative distributions based on resident and flux-weighted injection that result from placing (9-3) into (9-4).

One of our major foci is how $(t,\ z)$ evolves with vertical distance traveled. This evolution is typically studied as the cloud evolves from the inlet plane. However, one may also study how the plume evolves between control planes. To do so, we introduce the following notation to aid in the isolation of the evolution of the particle cloud between control planes, not only from the inlet plane. Consider particle travel times at $\mathsf{CP}(z^1)$, $\tau_i(z^1)$, and at another control plane $\mathsf{CP}(z^2)$, τ_i (z^2), where $z^1 < z^2$. Then the CDF of the cloud between these two planes is given by

$$F(t, z^2, z^1) = \frac{1}{M} \int m_i\, H[t - \Delta\tau_i(z^{2,1})]\, d\mathcal{X} \qquad (9\text{-}8)$$

where $\Delta\tau_i(z^{2,1}) = \tau_i(z^2) - \tau_i(z^1)$. This expression $(t,\ z^2,\ z^1)$ eliminates the history of the particle travel times prior to arriving at $\mathsf{CP}(z^1)$, and allows for the isolation of the cloud evolution moving to $\mathsf{CP}(z^2)$. Placing (9-3) into (9-8) provides an expression for the difference CDF of both resident, $(t,\ z^2,\ z^1)$, and flux-weighted injection schemes, $(t,\ z^2,\ z^1)$.

9.3.3   Methods

In this section, we describe the methods used to generate and mesh three-dimensional discrete fracture networks (DFN), numerically integrate the governing equations for fully saturated flow, and track particles through the network. The DFNs in this study are based on the fractured granite at the Forsmark, Sweden site (a potential host formation for a subsurface repository for spent nuclear fuel (SKB, 2011, Cvetkovic 2013)) and we provide details of the site in the section below.

In the DFN approach, geologic field investigations are used to create a network of fractures where the geometry and properties of individual features (usually fractures) are represented explicitly, as lines in two dimensions or planar polygons in three dimensions. Fractures in the network are assigned a shape, location, aperture, and orientation based on distributions determined by the geological survey. To account for the uncertainty associated with these distributions, multiple independent DFN realizations are generated stochastically by sampling these distributions. Once a network is constructed, the individual fractures are meshed for computation and the flow equations are numerically integrated on the resulting computational mesh. Examples of the various DFN methodologies and their applications are found in (Cacas et al. 1990, Dreuzy et al. 2004, 2012, Dershowitz 2014, Erhel et al. 2009, Mustapha et al. 2007, Pichot et al. 2010, 2012, Xu et al. 2006). One advantage of DFN models over stochastic continuum models is that they can represent a wider range of transport phenomena (Painter and Cvetkovic, 2005, Painter et al. 2002), which makes them a preferred choice when investigating the influence of injection mode on transport. Additionally, DFN simulations are generally favorable when investigating sparsely fractured rock because heterogeneity and topology can be explicitly represented.

DFN Model: Forsmark, Sweden

The Swedish Nuclear Fuel and Waste Management Company (SKB) has undertaken a detailed investigation of the fractured granite at the Forsmark, Sweden site as a potential host formation for a subsurface repository for spent nuclear fuel (SKB, 2011, Hartley and Joyce, 2013). The Forsmark area is about 120 km north of Stockholm in northern Uppland. The repository is proposed to be constructed in crystalline bedrock at a depth of approximately 500 m. Based on the SKB site investigation, a statistical fracture model with multiple fracture sets was developed and the detailed parameters of the Forsmark site model are provided in (SKB, 2011). We adopt a

subset of the site investigation using three stochastic/statistical descriptions of background fractures. Our model consist of three sets of circular fractures whose orientations follow a Fisher distribution,

$$f(\mathrm{x}; \mu,) = \frac{\kappa \exp(\kappa \mu^T \mathrm{x})}{4\pi \sinh(\kappa)} \qquad (9\text{-}9)$$

Here, μ is the mean direction vector, which can be expressed in terms of spherical coordinates, θ' and φ', and $\kappa \geq 0$ is the concentration parameter that determines the degree of clustering around the mean direction. Values of κ approaching zero represent a uniform distribution on the sphere while larger values generate small average deviations from the mean direction.

Fracture radii r are sampled from a truncated power-law distribution with exponent α and upper and lower cutoffs $(ru; r0)$,

$$r = r0 \left[1 - u + u \left(\frac{\mathrm{r}_0}{\mathrm{r}_u}\right)^{\alpha}\right]^{-1/\alpha} \qquad (9\text{-}10)$$

where μ is a random number sampled from the continuous uniform distribution on the open interval (0,1). We assume that the transmissivity of the fractures, σ, is estimated using a deterministic power-law model based on the fracture radius,

$$\log(\sigma) = \log(\gamma \mathrm{r}^{\beta}) \qquad (9\text{-}11)$$

with parameters, $\gamma = 1.6 \times 10^{-9}$, and $\beta = 0.8$. Other relationships between the fracture radius and transmissivity have also been proposed. For example, there can be no correlation between the two, they can be perfectly correlated, or they can be semi-correlated. We adopted the second of these assumptions because (a) we believe that the assumption that larger fractures have high transmissivities is generally valid and are not concerned with site specific sensitivities, but (b) a systematic study concerning how variations in the semi-correlation between radius and transmissivity influence flow properties would be better performed using a simple DFN setting so the particular influences of the semi-correlation (and its strength) can be properly characterized. The fracture aperture, b, is related to the fracture transmissivity using the cubic law, $\sigma = b^3/12$ (Adler et al. 2012). Under such a formulation, the fracture apertures are uniform on each fracture, but vary between fractures. Values of the parameters used to generate the sample DFNs for all three fracture sets are provided in Table 9-1. The average surface area of fractures per unit volume of rock, denoted as P_{32} (m2/m3), computed using the entire DFN for the three different cutoffs are $r_0 = 15$ m : 0.048 m^{-1}, $r_0 = 20$ m : 0.056 m^{-1}, $r_0 = 25$ m : 0.057 m^{-1}.

Table 9-1: DFN parameters used in simulations of the Forsmark repository site, Sweden.

Set	Orientation Distribution: Fisher			Size Distribution: Power Law			Fracture Density
	Mean Trend	Mean Plunge	Conc. κ	α	r_u, m	r_0, m	Number of fractures in 1 km^3
1. (NS)	90.0°	0.0°	21.7	2.5	560	15	2093
						20	1019
						25	583
2. (NE)	135.0°	0.0°	21.5	2.7	560	15	2000
						20	919
						25	503
3. (HZ)	360.0°	90.0°	8.2	2.38	560	15	7711
						20	3887
						25	2285
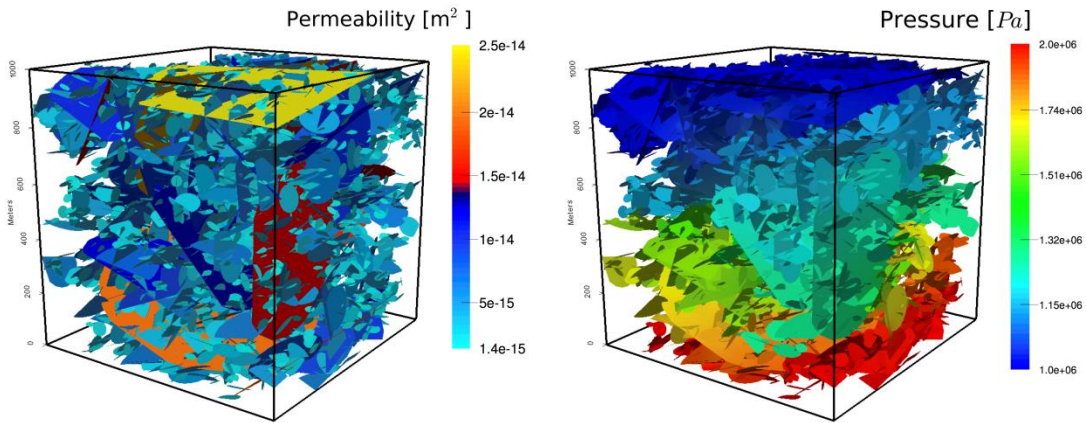
a) Permeability   b) Pressure Solution

Figure 9-8: a) A DFN realization based upon the fractured granite at the Forsmark, Sweden site in a 1 km^3 domain. The model consists of three sets of circular fractures whose orientations follow a Fisher distribution. The fracture diameters in each fracture set follow a truncated power-law distribution with lower cutoff at 15 m. Fractures are colored by permeability, which is based upon fracture radius. b) steady state pressure solution within the network shown in (a). Dirichlet boundary conditions are imposed on the top (1 MPa) and bottom (2 MPa) of the domain to create a pressure gradient in the *z* direction, and no-flow boundary conditions are imposed along lateral boundaries.
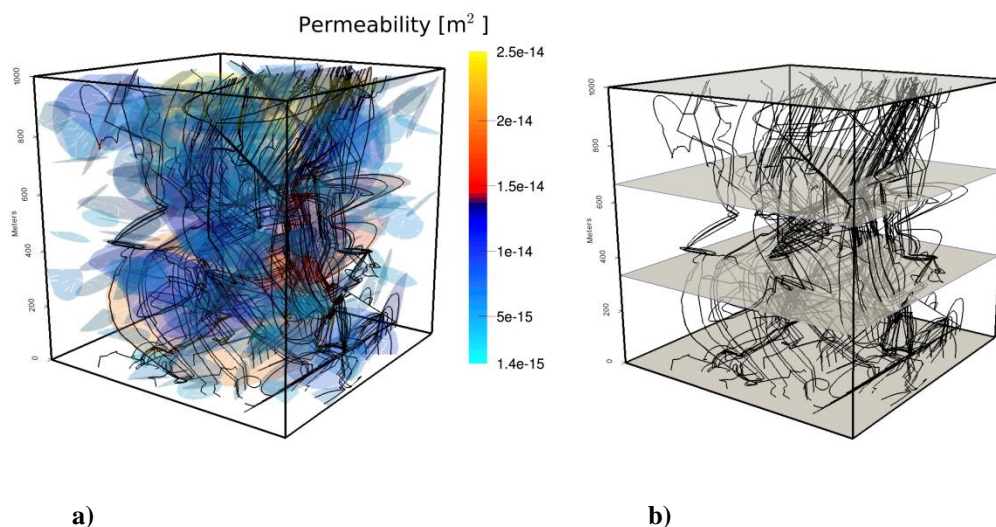
Figure 9-9: Two hundred particle trajectories within the DFN shown in Fig. 1-8. Particles are inserted uniformly along fractures on the bottom of the domain. a) Trajectories are overlaid on Fig. 1-8.a, fractures are colored by the permeability, to show how particles are drawn to larger fractures, which have higher permeabilities and offer less resistance than smaller fractures. Although particles are inserted uniformly along fractures in the inlet plane, they cluster on larger fractures as they exit the domain. This clustering suggests that transport only occurs within a small portion of the fracture network far away from the inlet plane. b) Trajectories with four example control planes, shown in grey. To quantify the visually observed clustering, particle attributes are recorded at uniformly spaced control planes throughout the domain.

Using this statistical model, sixty DFNs with three lower cutoffs in the truncated power-law distributions (15m, 20m, and 25m) and upper limit 560m are generated (twenty realizations are generated at each other lower cutoff values) in cubic domains with sides of length one kilometer. The upper limit of fracture size reflects a technical distinction between background and deterministic fractures in the SKB report. We note that these simulations are not meant to be site-specific and therefore inclusion of deterministic features (fractures larger than 560m) is not necessary. The DFN sets represent rock mass between larger deterministic fracture zones and should be thought of as a representation of a background/stochastic fractures. In a site-specific study, background fractures are typically incorporated stochastically, whereas features larger than this approximate threshold are included with assigned properties as fracture zones and do not vary between realizations. All other generation parameters, with the exception of the number of fractures, are fixed. For equivalency, the number of fractures in each realization is selected so that the fracture density is relatively constant between realizations. Dirichlet boundary conditions are imposed on the top (1 MPa) and bottom (2 MPa) of the domain to create a pressure gradient aligned with the vertical axis, and no-flow boundary conditions are enforced along lateral boundaries. Approximately one hundred thousand particles are inserted into each network, using uniform spacing across all fractures at the bottom of the domain.

A sample realization of the Forsmark DFN is shown in Fig. 9-8a. The realization contains 4,934 fractures and the computational mesh consists of 7,731,299 cells. Fractures are colored by permeability, with warmer colors indicating higher values. Because the fracture permeability is based upon the fracture radius, the largest fractures have the highest permeabilities. There are significantly more small, low permeability, fractures than larger fractures due to Eq. 9-10. Dirichlet pressure boundary conditions are applied to the z-faces of the 1 km $\times$ 1 km $\times$ 1 km domain of the network shown in Fig. 9-8a, and Fig. 9-8b shows the steady state pressure solution. The larger fractures act as conduits for flow, connecting numerous small fractures together in the network.

A selection of two hundred particle trajectories passing through this network is shown in Fig. 9-9. The particles are inserted uniformly along fractures in the inlet plane (bottom), and the movement of the particles is determined by the local velocity. In Fig. 9-9a, the permeability of the fractures is shown along with the trajectories to highlight that particles are attracted toward larger fractures. In Fig. 9-9b, four of the previously mentioned control planes are shown along with the trajectories. At each of these control planes, spatial and temporal attributes of the particles are recorded to provide a psuedo-temporal evolution of the solute plume. Although the particles are inserted uniformly, their trajectories cluster together onto larger fractures. This clustering suggests that transport only occurs within a small portion of the fracture network far away from the inlet plane. This observed clustering is investigated quantitatively in the next section where we report spatial and temporal particle attributes recorded at uniformly spaced control planes.

9.3.4   Lagrangian Based Observations

Spatial and temporal particle attributes are recorded at uniformly spaced control planes, CP, throughout the domain to observe the evolution of transport properties. The CP is perpendicular to the imposed pressure gradient in the z direction, the primary direction of flow, and spaced twenty five meters apart.

Three spatial traits are considered, each of which highlight different aspects of the solute plume. The first attribute is the aperture of the fractures on which a particle resides as it passes through a CP. At one control plane, the combination of these values shows the distribution of mass in the network. Placing these distributions into a sequence according to the vertical distance traveled shows how mass disperses or clusters as it moves through the network. The second trait we consider is the tortuosity of a trajectory. Tortuosity is the ratio of the length of a trajectory ℓ over the vertical distance traveled to reach the control plane z, $\mathcal{T} = \ell/z$, and measures the deviation of a trajectory from a straight-line path (Bear, 1988). Once pathlines are computed, determining tortuosity is a straightforward procedure. The tortuosity of the plume of particles can be related to the coefficient of hydrodynamic dispersion (Bear, 1988), and is an indicator of dispersion in high Pe´let number flows. The third trait we consider is the box-counting dimension of the cloud based on their $x - y$ spatial locations at each control plane computed according the techniques outlined in (Falconer, 2013). The box-counting dimension, box-dimension for short, is a computationally tractable upper bound on the Hausdorff dimension, which is a generalization of the notion of dimension in a real vector space, that we use to estimate the fractal dimension of the particle cloud at CPs. The fracture network has a Hausdorff dimension of one at CPs. Initially, the particles are uniformly spaced on these fractures and the plume also has a Hausdorff dimension of one. As the set of particles moves through the network it may evolve to have a fractal dimension that is less than one due to mechanical dispersion induced by the network; local in-fracture dispersion is not included in these simulations. A fractal dimension less than one indicates that the plume has clustered on individual fractures.

Particle travel time is computed according to Eq. (9-2) and is recorded at every control plane. The cumulative distribution function of travel time (t, z) Eq. (9-4), and the complement of the cumulative distribution function, $1 - (t, z)$, provide information regarding the distribution of trajectory times at a control plane. In sequence, they show how the plume evolves as the cloud moves through the domain. We also consider the travel times between CPs computed according to Eq. (9-8), as well as the mean of the plume at each of the CPs.

Comparisons of the influence of injection mode are performed for fracture aperture, tortuosity, and travel time by assigning the mass associated with each particle using Eq. (9-3). However, the adopted computation of the box-dimension only depends on the spatial distribution of particle trajectories, not upon the distribution of mass associated with each particle. Nonetheless, the box-dimension complements the other traits by measuring clustering of the plume.

Spatial Attributes

We begin by presenting the measurements of the spatially based attributes: fracture aperture, tortuosity, and box-dimension.

Fracture Aperture

Figure 9-10 shows heat maps of the mass distribution plotted as a function of fracture apertures (abscissa) and vertical distance traveled (ordinate) where colors indicate percent of mass. The plots are pro- vided for one realization, with a lower cutoff of fifteen meters. Across each vertical level in the domain, horizontal level in the graph, the sum of all the mass equals one. Figure 9-10a shows the mass distribution for resident injection and Figure 9-10b provides the same information for the flux-weighted injection. In the case of resident injection, the initial distribution of mass is relatively uniform across all apertures. As the particles move through the domain, the mass consolidates into fractures with larger apertures, indicated by the trend of increasingly warmer colors to the right with increasing distance traveled. In the case of flux-weighted injection, the initial distribution of mass is non-uniform; more mass is in fractures with larger apertures due to the reduced resistance to flow offered by the higher permeabilities. Recall that the aperture of the fracture depends on the radius of the fractures, larger fractures have larger radii. Similarly to the resident injection, the bulk of the mass is drawn into fractures with larger apertures as the particles move through the domain. After traveling approximately two hundred meters vertically, the distributions of mass for resident and flux-weighted injection resemble one another closely.

Figure 9-11 shows the same information as Fig. 9-10, but the values computed using all particles in all thirty realizations. Mass is more widely distributed under resident injection conditions than flux-weighted because of the abundance of small fractures in the networks. In particular, the initial distribution of mass favors small apertures due to their prevalence in the networks The observed trend of warmer colors up and right indicates that after an initial region, which depends upon the injection mode and the particular realization, the majority of mass is transported through larger fractures. Under flux-weighted conditions, more mass is initially placed into larger fractures due to the reduced resistance to flow, and higher flux, offered therein. As is the case in the resident injection, as the particle cloud moves through the domain, the majority of the mass migrates into the largest fractures in the networks. After this initial region, the distributions of mass for resident and flux-weighted injection resemble one another, with the majority of the mass in large fractures.a. Resident   b. Flux-weighted
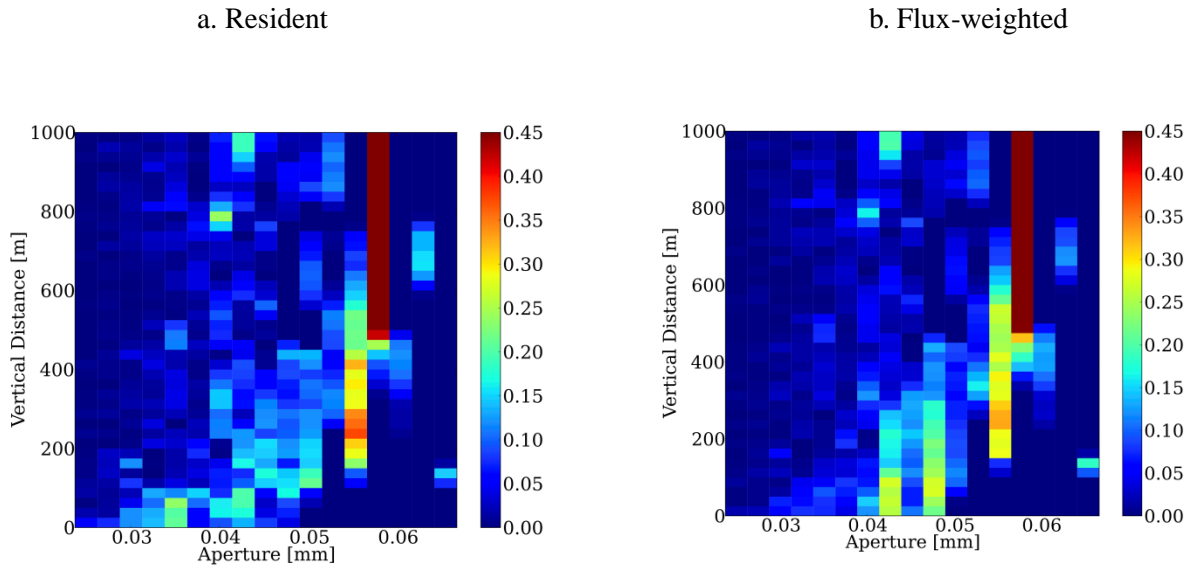
a. Resident   b. Flux-weighted
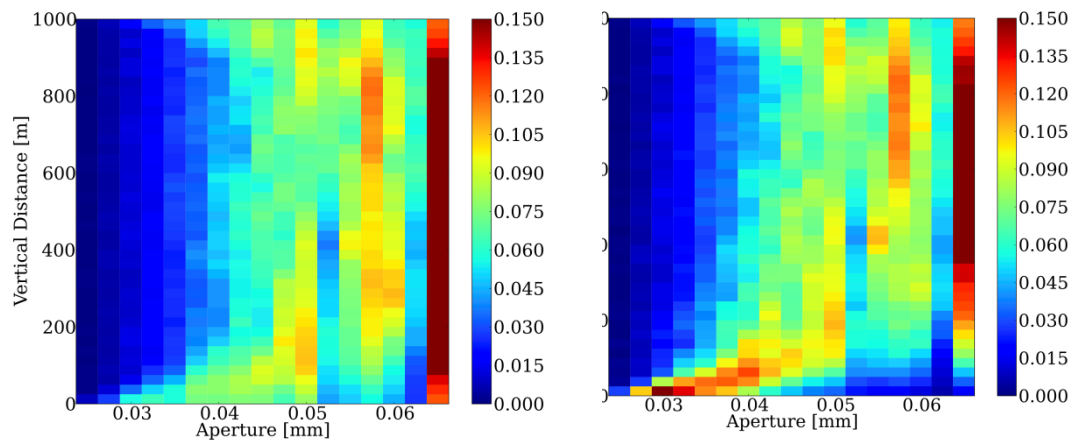

Figure 9-10: Heat map of mass distribution plotted as a function of fracture apertures (abscissa) and vertical distance traveled (ordinate) where colors indicate percent of particles for one realization. The primary direction of flow is from bottom, vertical distance equal to 0, to the top, vertical distance equal to 1000. (a) Resident injection: The initial distribution of mass is relatively uniform across all apertures, with slightly more weight at lower values due to larger numbers of small fractures in the network. As the particles move further through the domain, the bulk of the mass is drawn into fractures with larger apertures indicated by the trend of warmer colors up and right with increasing vertical distance traveled. (b) Flux-weighted injection: The initial distribution of mass is non-uniform across all apertures, with more mass being observed in fractures with larger apertures, compared to the resident injection. After traveling through a burn-in region, the distributions of mass for resident and flux-weighted injection resemble one another.

Tortuosity

The computed values of mean tortuosity are plotted as a function of travel distance in Fig. 9-12.a. Color indicates lower cutoff in the truncated power-law distribution of fracture size: $r_0 = 15$; blue, $r_0 = 20$; red, $r_0 = 25$; green. Dashed lines denote flux-weighted injection, and solid lines indicate resident based injection. The values of mean tortuosities computed for particles inserted under resident injection are consistently higher than those observed using flux-weighted injection. As the particles move through the domain, the difference between the two injection schemes decreases. This convergence appears more rapid for the two higher lower cutoffs, the red and green lines.

Figure 9-11: Heat map of mass distribution plotted as a function of fracture apertures (abscissa) and vertical distance traveled (ordinate) where colors indicate percent of particles for all realizations. The primary direction of flow is from bottom, vertical distance equal to 0, to top. (a) Resident injection: The initial distribution of mass favors small apertures due to their prevalence in the networks. As the particles move further through the domain, the bulk of the mass is drawn into fractures with larger apertures indicated by the observed trend up and right with increasing vertical distance traveled. (b) Flux-weighted injection: Compared to (a), more mass is initially placed into larger fractures due to the reduced resistance to flow, and higher flux, offered therein. As is the case in the resident injection, as the particle cloud moves through the domain, the majority of the mass migrates into the largest fractures in the networks. This clustering indicates large, fracture-to-fracture, flow channeling.

The difference between the mass inserted into small fractures and large fractures under resident and flux-weighted conditions is likely responsible for the observed differences in tortuosity. Under resident injection conditions mass is uniformly distributed regardless of the size of the fracture, cf. Fig. 9-10a. While under flux-weighting conditions, mass is disproportionally distributed into larger fractures whose wider apertures provide a decreased resistance to flow that results in higher flux, cf. Fig. 1-10b. Movement between small fractures at various orientations will result in longer trajectories when compared to the movement within larger fractures where the particle remains on a single plane when the same total vertical distance is covered. This additional fracture switching is likely the cause of the higher observed values for tortuosity in the resident injection mode. As particles move through the domain they are drawn towards larger fractures that offer reduced resistance to flow, as discussed in Sec. 9.3.4. Transport through these larger fractures results in straighter trajectories, because the particles do not have to switch fractures to enter the primary flow channels. These straighter trajectories are reflected in the lower values of tortuosity that are observed. Because tortuosity can be related to the coefficient of dispersion (Bear, 1988), these results indicate that the difference of dispersion under the two different injection conditions also diminishes with time.

A trajectory's length, and therefore its tortuosity, depends on the entire history of a particle's journey, as opposed to the aperture of the fracture on which a particle resides which is a local, in time, attribute. This hysteresis of tortuosity could be the reason that the initial difference between

the flux-weighted and resident particles' tortuosities persist as the plume moves through the domain, even though the distribution of mass appear similar.

Box-Dimension

The box-counting dimension of the particle plumes at every control plane is reported in Fig. 9-12b. Individual realizations are shown as semi-translucent lines, and thick lines indicate average values by lower cutoff. Color indicates lower cutoff, $r_0 = 15$; blue, $r_0 = 20$; red, $r_0 = 25$; green. Initially, all particles are evenly spaced on fractures and have a box-dimension of one, and the box-dimension of the DFN at CPs is constant with a value of one (details not shown). However, as the cloud moves through the domain, the mean box-dimension decreases and stabilizes at a values of ≈ 0.80. This value indicates that the particles are clustering within fractures; if the particles remained uniformly spaced on fractures they would retain a box-counting dimension of one. This in-fracture clustering can be observed using scatter plots of the particle locations overlaying the network at CPs. All thirty DFN realizations exhibit this behavior suggesting that the in-fracture channeling occurs regardless of realization.

In conjunction with the plots presented and discussed in Sec. 9.3.4, these results indicate that particle clustering occurs on two scales in these networks. There is a larger scale of mass moving into larger fractures indicated by the observed trend of mass into fractures with larger apertures (Fig. 1-11) and a smaller scale in-fracture channeling, particle trajectories clustering on a single fracture plane, which is indicated by the stabilization of the box-dimension to a value less than one. Both of these types of channeling are observed in Fig. 9-9. Variations between fracture apertures induce the network scale channeling, while the network topology induces the smaller scale of in-fracture channeling. Recall that fracture aperture varies from fracture to fracture, but not within a fracture in these simulations; in-fracture aperture variability has been shown to induce in-fracture channeling (Tsang and Neretnieks, 1988, Tsang and Tsang, 1989, Berkowitz, 2002, Berkowitz and Braester, 1991). This channeling influences mass transport times which can be linked to injection mode, as we discuss in the following section.

a. Tortuosity   b. Box-Dimension
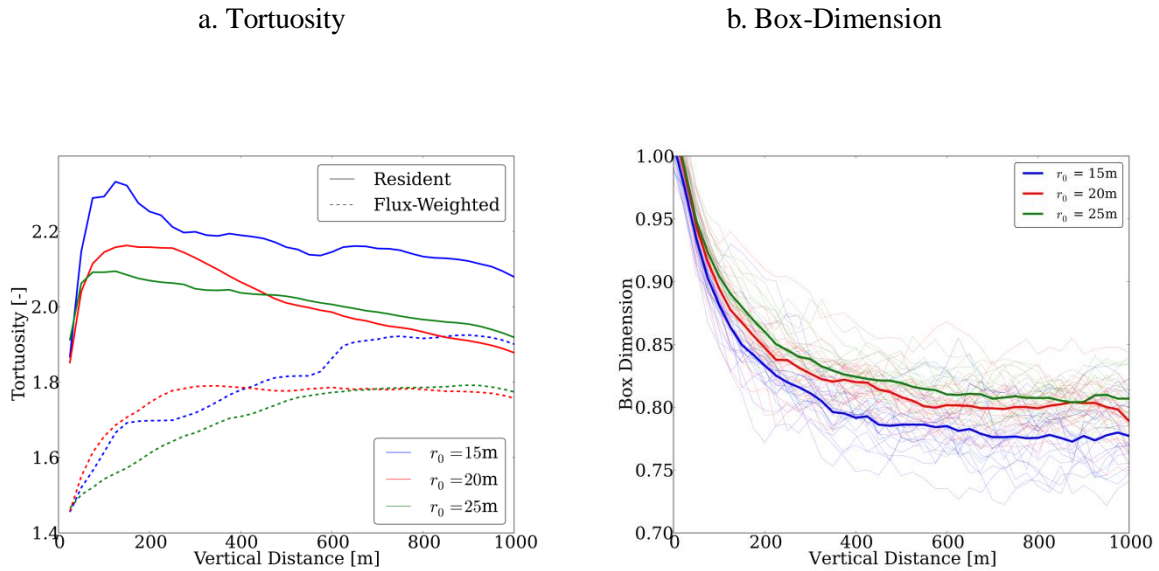
Figure 9-12: (a) Mean particle tortuosity plotted as a function of control plane distance. Averages are computed using all particles in each DFN at each of the lower cutoffs for the generation of the DFN. Solid lines indicate particles inserted under resident injection conditions and dashed lines indicate flux-weighted values. Color indicates lower cutoff, $r0 = 15$; blue, $r0 = 20$; red, $r0 = 25$; green. The computed mean tortuosities using resident injection are consistently higher than those observed using flux-weighted injection. As the particle clouds move through the domain the difference between the two injection schemes decreases. (b) Box-dimension of particle cloud plotted as a function of control plane distance. Color indicates lower cutoff, $r0 = 15$; blue, $r0 = 20$; red, $r0 = 25$; green. Semi-transparent lines are individual realizations and thick line indicate average values. The network of fractures has a box-dimension of one at each of the control planes. The box-dimension of the particle clouds start at one because they are uniformly distributed along fractures on the inlet plane. At they move through the domain, the box-dimension decreases with distance and stabilizes to a mean value near 0.80, which indicates in-fracture clustering.

Temporal Attributes

Particle travel times are recorded at every control plane, and their distributions are discussed in this section. We focus on the empirical cumulative distribution, the compliment of the empirical cumulative distribution, and the mean travel time. Particles are inserted at the bottom of the domain, $z = 0$. Empirical cumulative distributions of travel time, breakthrough curves, at CP(100) and CP(750) are shown in Fig. 9-13 for resident, (t, z); Fig. 9-13a, and flux-weighted, (t, z); Fig. 9b, injection modes. Line color indicate lower cutoffs, $r_0 = 15$; blue, $r_0 = 20$; red, and $r_0 = 25$; green. Line style indicates CP, $z = 100$; solid line, $z = 750$; dashed line. Individual realizations are semi-transparent, and thick lines are ensemble values. In the case of (t, z), variation in travel time within and between realizations is apparent. These variations are most prevalent for $r_0 = 15$ m. The initial portion of (t, z), values less than 0.6, are fairly uniform, but thereafter several of the realizations exhibit behavior that does not follow the general trend. The plotted values of (t, z), are more homogeneous than (t, z), but differences between realizations are still present. Steep segments of the curves are observed in $(t, 100)$, where a large

portion of the mass passes through CP(100) in a relatively short time period. Flux-weighting injection places more mass into larger fractures due to their higher transmissivities and that mass is transported at a uniform velocity with little mechanical dispersion for short distances; these sharp fronts are not observed in $(t, \ 100)$. (Frampton and Cvetkovic, 2011) observed similar behavior in smaller, $(100m)$, three-dimensional DFNs and reached a similar conclusion regarding the physical mechanisms that created this feature. As the plume moves further through the domain, mechanical dispersion induced by the network breaks this plume apart and particles travel at various speeds, and these sharp interfaces are not observed in $(t, \ 750)$.

Additional differences between travel times associated with resident and flux-weighted injection modes are observed by looking at the complement of the cumulative distributions, 1 - $(t, \ z)$; shown in Fig. 9-14, colloquially referred to as the survivor function. The survivor function can be used to determine power-law scaling in the tails of these distributions, if it exists. Fig. 9-14a shows the survivor function obtained using resident injection conditions, and no universal power-law scaling is observed. In the case of flux-weighted injection from the inlet (Fig. 9-14b), it is possible that the tails demonstrate power-law scaling. However, this behavior breaks down at longer time scales, possibly an artifact of the number of particles used in the simulations. This is expected in empirical distributions where the structure in tails suffers from small densities.

A black dotted line for a power-law with exponent of two is included in the plot for reference. Averaging over all realizations, the best fit for a power-law scaling is computed at every control plane and when plotted as a function of vertical distance from the inlet plane they display exponential convergence to an asymptotic value slightly greater than two, ≈ 2.07, (images not provided). The best fit for a power law in the tail of 1 - $(t, \ 750)$ is a value of ≈ 2.01.

Mean particle travel time for each plume is plotted as a function of vertical distance traveled in Figure 9-15; resident injection in Fig. 9-15.a and flux-weighted in Figure 9-15b. Line color indicate lower cutoffs, $r_0 = 15$; blue, $r_0 = 20$; red, and $r_0 = 25$; green. Individual realizations are semi-transparent, and thick lines are average values. Values based on resident injection initially scale nonlinearly, and after some vertical distance, which depends on the particular realization, the values scale linearly. In contrast, the mean value of travel time for particles inserted under flux-weighting conditions scales linearly with vertical distance traveled, although there is one outlier from the typical behavior. There are differences between realizations, but they are minor when compared to those observed in Fig. 1-15a.

By computing the second derivative of these curves as a function of vertical distance traveled, we determine a value of z such that thereafter the second derivative is within a user prescribed tolerance of zero, indicating linearity. The average mean values, standard deviations, minimum value, and maximum value for this value of z are reported in Table 9-2 for each of the three lower cutoffs in the generation of the DFN. Two hundred and fifty meters appears to be a sufficient distance for the first moment of travel time for clouds inserted using resident injection to scale linearly for most realizations. Below this value there is substantial variation, and above it the majority of the realizations exhibits mean values of travel time that scale linearly. In the case of resident injection conditions, the mean, standard deviations, and maximum values depend on the lower bound of the power-law. In the case of flux-weighted injection, no relationship between these values and the lower cutoff is observed. At all lower cutoff values, the mean values are near zero, indicating the first moment of travel time scales linearly when particles are inserted using flux-weighting.

Table 9-2: Values of vertical distance traveled such that linear scaling of the first moment of travel time is observed [All values are in meters]. In the case of resident injection conditions, the mean, standard deviations, and maximum values depend on the lower bound of the power-law, decreasing with increasing lower cutoff. In the case of flux-weighted injection, no statistically significant relationship between these values and the lower cutoff is observed. At all lower cutoff values, the mean values are near zero, indicating the first moment of travel time scales linearly when particles are inserted using flux-weighting.

	Resident				Flux			
r_0	Mean	Std. Dev.	Min	Max	Mean	Std. Dev.	Min	Max
15	180.0	67.36	100	325.0	21.25	55.49	0.0	250.0
20	130.0	66.59	50.0	300	6.25	15.56	0.0	50.5
25	143.75	43.92	75.0	225.0	2.50	7.5	0.0	25.0

To confirm this behavior we plot the mean travel time generated of $(t, z, 250)$, as defined in Eq. (1-8). This removes the particles history prior to reaching CP(250) to isolate how they advance beyond that control plane. These moments are shown in Figure 3.8.c, and they all scale linearly with distance as is the case for the flux-weighted particles.

Figure 9-16a shows $(t, 350, 250)$ and $(t, 1000, 250)$ after applying this 250 meter burn-in region. Here, blue lines correspond to $(t, 350, 250)$ and the red lines correspond $(t, 1000, 250)$. These CPs are selected so that the distance traveled from the burn-in plane is the same as those shown in Fig. 9-13a. After accounting for the burn-in region, the general behavior of the curves is more similar to those observed for the flux-weighted injection displayed in Fig. 9-13b than with Fig. 9-13a. Figure 9-16b. shows $1 - (t, 350, 250)$ and $1 - F_R(t, 1000, 250)$ for additional comparison. All realizations exhibit similar behaviors, and power-law scaling of the tails can been observed. A black dashed line for a power-law with exponent of two is included in the plot for reference. Averaging over all realizations, the best fit for a power-law scaling are computed at every control plane and when plotted as a function of vertical distance from the inlet plane they display stabilization to a value slightly greater than two, ≈ 1.94, which is remarkably close to the exponent observed under flux-weighted conditions.

These similarities suggest that after a burn-in region mass inserted under resident conditions evolves into a cloud that behaves in a manner similar to a cloud inserted under flux-weighted conditions. This trend was also observed when considering spatial attributes of the particles plumes. For example, the Kolmogorov-Smirnov test does not reject the null hypothesis that these empirical distributions are from the same underlying distribution after 250 meters, indicating the degree of similarity between the samples.

In the following and final section we provide remarks regarding this behavior, hypothesize about the physical mechanisms which induce it, and discuss its implications and applications.
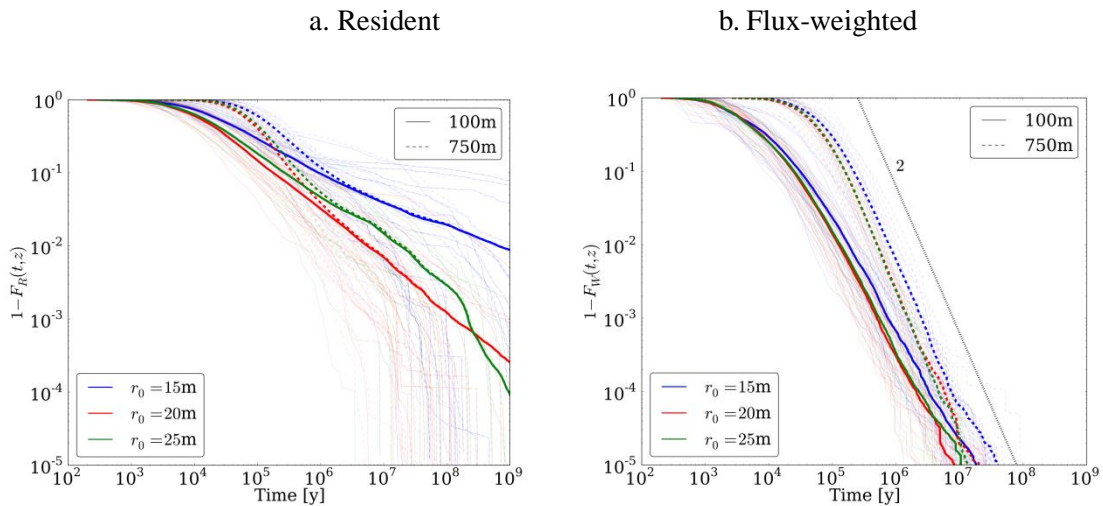
a. Resident   b. Flux-weighted
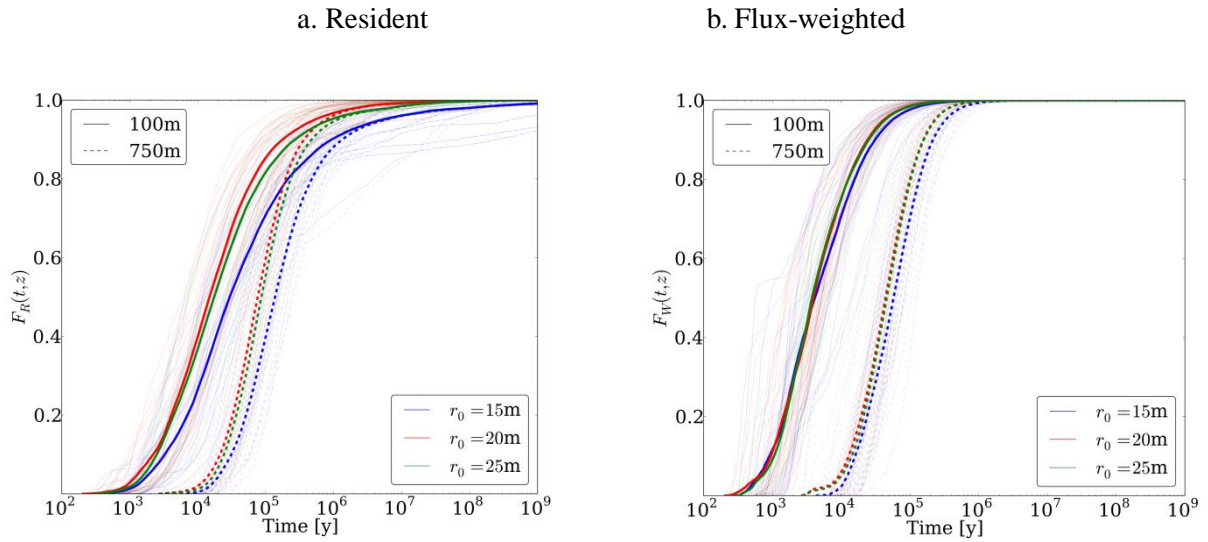
Figure 9-13: Cumulative distribution functions (t, z) of passage times. Line color indicate lower cutoffs, $r0 = 15$; blue, $r0 = 20$; red, and $r0 = 25$; green. Line style indicates CP, $z = 100$; solid line, $z = 750$; dashed line. Individual realizations are semi-transparent, and solid lines are average values. (a) (t, z) generated using resident based inject scheme. (b) (t, z) generated using flux-weighted injection scheme. The plotted values of (t, z), are more homogeneous than (t, z) due to the majority of the mass transporting through larger fractures.

a. Resident   b. Flux-weighted

Figure 9-14: Complement of the cumulative distribution function, $1 - F(t, z)$, of passage times. Line color indicate lower cutoffs, $r0 = 15$; blue, $r0 = 20$; red, and $r0 = 25$; green. Line style indicates CP, $z = 100$; solid line, $z = 750$; dashed line. Individual realizations are semi-transparent, and solid lines are average values.(a) $1 - F_R(t, z)$ generated using resident based inject scheme. Universal power-law scaling is not observed. (b) $1 - F_W(t, z)$ generated using flux-weighted injection scheme. It is possible that the tails demonstrate power-law scaling.

The dotted black line is a power law with exponent two. The best fit for a power law in the tail of $1 - F_W(t, \ 750)$ is a value of ≈ 2.01.

a. Resident
b. Flux-weighted

c. Resident with burn-in
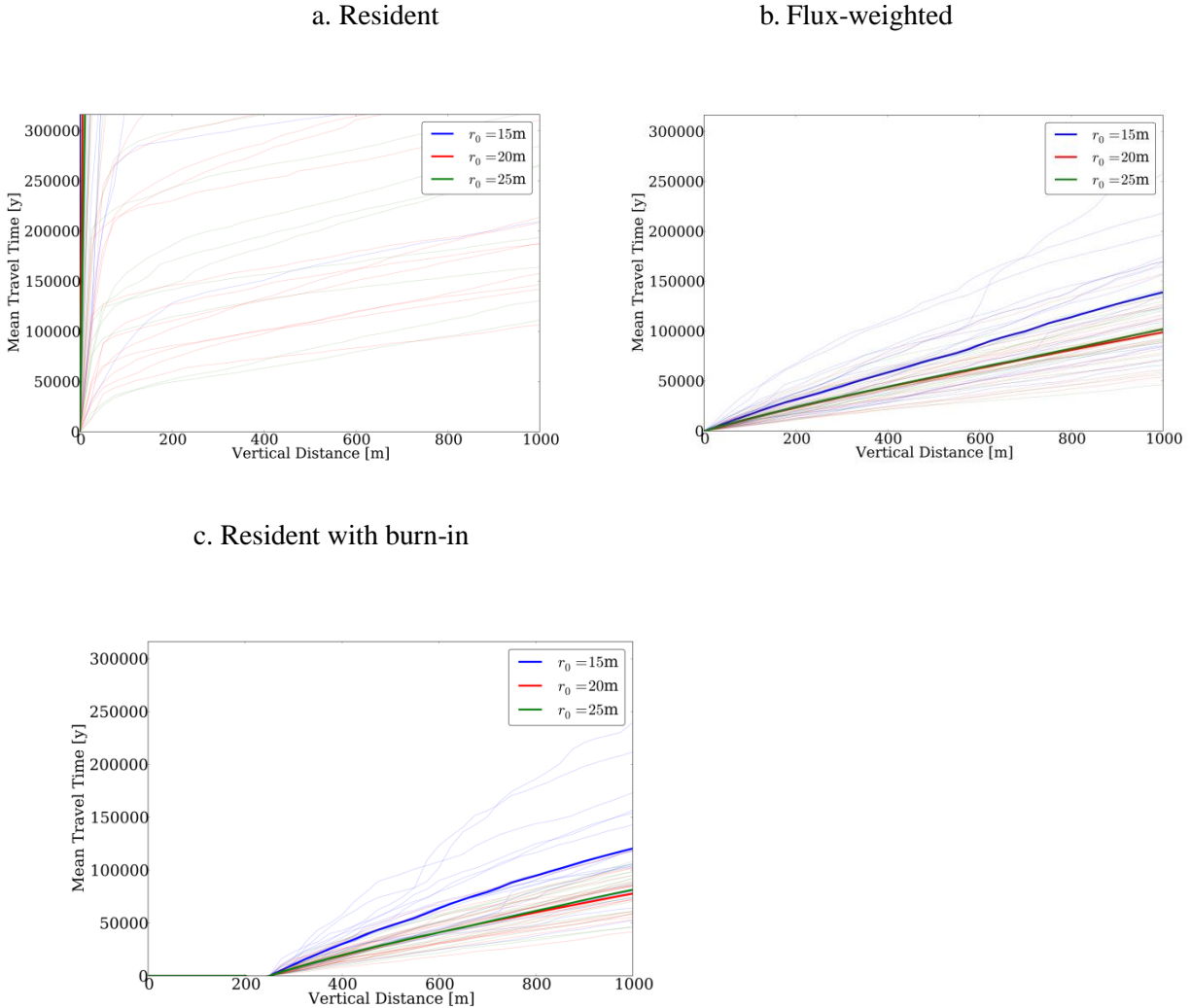
Figure 9-15: Mean travel time plotted as a function of longitudinal distance. Color indicates lower cutoff, $r0 = 15$; blue, $r0 = 20$; red, $r0 = 25$; green. Semi-transparent lines are individual realizations and thick lines are average values. (a) Resident injection mean travel times from inlet initially scale nonlinearly. After an initial distance, the mean travel time does scale linearly with distance. (b) Flux-weighted injection mean travel times scale linearly at all distances from the inlet. (c) Beyond a 250 meter burn-in region, mean travel times of particles inserted using resident injection scale linearly with distance.

a. CDF Resident   b. CCDF   Resident
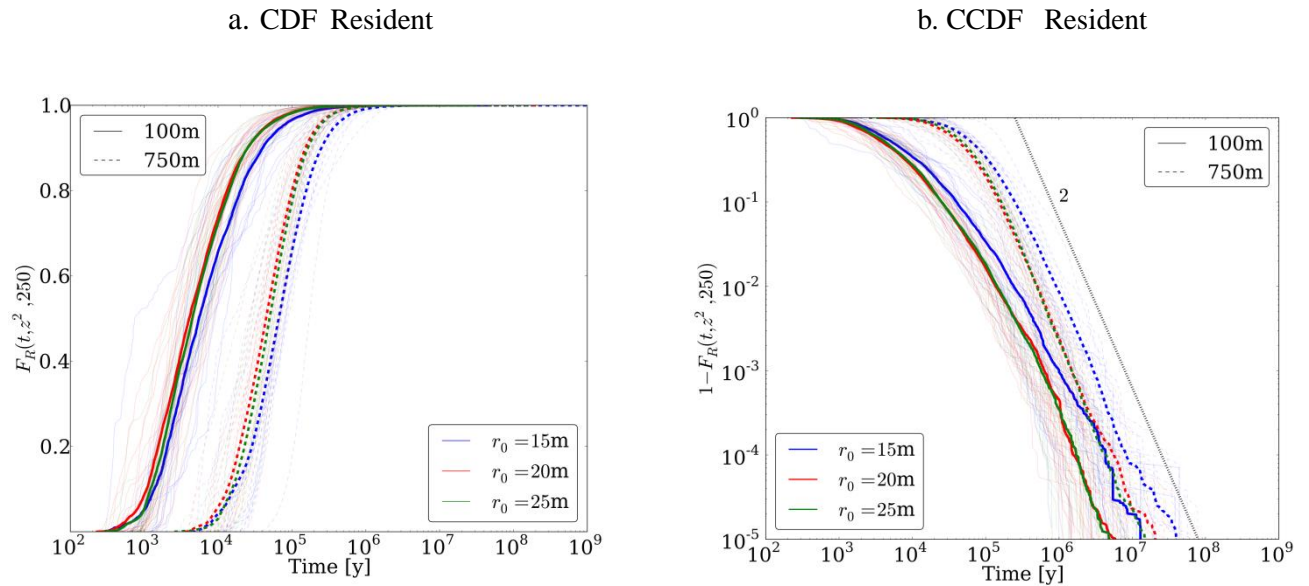
Figure 9-16: $F_R(t, \; z^2, \; 250)$ and $1 - F_R(t, \; z^2, \; 250)$ for particle travel time inserted using resident injection to account for a 250 meter burn-in region. Here, blue lines correspond to $(t, \; 350, \; 250)$ and the red lines correspond $(t, \; 1000, \; 250)$. Line color indicate lower cutoffs, $r0 = 15$; blue, $r0 = 20$; red, and $r0 = 25$; green. Line style indicates CP, $z = 100$; solid line, $z = 750$; dashed line. Individual realizations are semi-transparent, and thick lines are ensemble values. These distances are selected so that the distance traveled from the burn-in plane is the same as those shown in Fig. 9-13a. After accounting for the burn-in region, the general behavior of the curves is more similar to those observed for the flux-weighted injection displayed in Fig. 9-13b, although some differences are still present. After applying this burn-in region, it is possible that these tails exhibit power law scaling, which is clearly impossible in Fig. 9-14a. Averaging over all realizations, the best fit for a power-law tail of $1 - F_R(t, \; 1000, \; 250)$ is ≈ 1.94, which is remarkably close to the exponent observed under flux-weighted conditions.

9.3.5   Discussion

The observations of the particle trajectories and analysis of their behavior support the notion of a burn-in region in the context of fractured media, as well as providing a physical explanation for its occurrence. The existence of a burn-in region such that solutes inserted under resident conditions evolve into plumes that exhibit similar behavior to those inserted under flux-weighted conditions has been hypothesized but has never been observed before due to computational limitations. The major observations that support the existence of this burn-in region are the following:

1. Initially, the mean travel time of particle clouds inserted under resident injection conditions scale non-linearly with distance. After a burn-in region, however, they scale linearly, as does the first moment of the travel time for particle inserted under flux-

       weighted conditions, cf. Fig. 9-15.

2. Power-law scaling in the tail of the empirical distributions of travel time is observed for solutes inserted under flux-weighted conditions, Fig. 9-14b, and under resident injection conditions once accounting for this burn-in region, Fig. 9-16b. The best fit for the exponent of the power-laws for these distributions are close to one another.

3. After traveling through the burn-in region, the distributions of mass as a function of fracture aperture for resident and flux-weighted injection resemble one another closely, cf. Fig. 9-10 and Fig. 9-11. The Kolmogorov-Smirnof test does not reject the null hypothesis that these empirical distributions are from the same underlying distribution after this burn-in region.

4. The computed mean tortuosities using resident injection are consistently higher than those observed using flux-weighted injection, yet as the cloud moves through the domain the difference between the two injection schemes decreases, cf. Fig. 9-12a.

The physical mechanisms behind this evolution appear to be the combination of in-network channeling, mass moves into fractures with larger apertures because they offer less resistance to flow, and in-fracture channeling, particle trajectories cluster on single fracture planes, that results from the structure of the DFN. The strength of this flow channeling might be a result of the adopted correlation function between transmissivity and fracture radius. However, the assumption that larger fractures have larger transmissivities is generally valid and this flow channeling is likely to occur under other reasonable correlation assumptions between transmissivity and fracture radius. The stabilization of the distribution mass into larger fractures, Fig. 9-11, and stabilization of the box-counting dimension of the particles to a value less than one, Fig. 9-12b, occurs at roughly the same distance from the inlet where the mean travel time of particle clouds inserted using resident injection begins to scale linearly.

Under resident injection conditions, mass is inserted uniformly along the inlet plane, and as the plume moves through the DFN it is drawn into larger fractures, Fig. 9-10a and Fig. 9-10a. Retention of mass in these large fractures is observed after the cloud passes through this burn-in region. Flux-weighting inserts more mass into larger fractures and the mass remains there as the cloud moves through the domain. After this initial difference, the mass inserted under both conditions is primarily found in these larger fractures that act as principal pathways for flow and transport. Plots of the mean aperture of fractures on which mass resides show that the initial discrepancy between the resident and flux-weighted injection rapidly decreases and the two curves nearly overlay one another after approximately two hundred and fifty meters (images not shown).

In addition to the migration of mass into large fractures, mass clusters within individual fractures. This is evidenced by the stabilization of the particle cloud box-dimension to a value less than one, ≈ 0.80. This value indicates that the particles occupy a subspace of the fracture network at control planes which has a dimension of one. This in-fracture clustering is a result of the network topology and variability between fractures; there is no in-fracture aperture variability which would enhance in-fracture clustering (Tsang and Neretnieks, 1988, Tsang and Tsang, 1989, Berkowitz, 2002, Berkowitz and Braester, 1991).

Tortuosity retains information from all previous time steps, unlike mean aperture and box-dimension. Therefore it is more challenging to clearly see the evolution of the resident injected particles to the flux- weighted curves. However, the shape of the curve reporting the mean tortuosities rather than the actual values hints towards this convergence. Moreover, these results indicate that the difference in dispersion of the particle plumes inserted using the two different

injection conditions also diminishes with time because tortuosity can be related to the coefficient of dispersion. After a slightly longer burn-in region than that observed for mean aperture and box-dimension, the shape of the two curves match closely, suggesting that the particles are moving through similar regions in the network. There might be a dependence of tortuosity on fracture set orientation. However, a systematic study with a thoughtfully designed synthetic fracture set would be more appropriate to characterize this dependence rather than the adopted fracture set. Nonetheless, changes in the fracture set orientation will not change the presented results that the initial difference between the two computed values of tortuosity decreases with time because of channeling.

Significantly, the exponent in the power-law tail of mass breakthrough was found to be greater than 2 for both flux-weighted and resident injection, which suggests that with sufficiently long travel distances the central limit theorem will ensure that the travel time distribution approaches a normal distribution. In such a situation, transport may be described with conventional analytical techniques such as the advection dispersion equation, (e.g., Painter et al. 2002). This is in contrast to the results of numerical experiments on smaller two-dimensional networks, (Berkowitz and Scher, 1997, 1998) and using smaller three-dimensional networks with more approximate numerical approaches (Painter et al. 2002), which found evidence for anomalous (non-Fickian) transport using resident injection assumptions.

With larger fully three-dimensional networks and better numerical control for the particle tracking, and after accounting for a burn-in period in the resident-injection cases, we found evidence that the advection- dispersion equation might be an appropriate theoretical model for asymptotic behavior of transport in fractured media. The key factor for the asymptotic behavior of the plumes to be Fickian is that the velocity field must be fully sampled. One of the principal observations in this paper is that flow channeling occurs in these sparsely fractured networks. As noted above, this study suggest that particles spend the majority of their travel time in large fractures, which act as conduits through the domain rather than dispersing and sampling the entire network/velocity field. However, we only considered one fracture site characterization, which although generic, is insufficient to characterize how the geometry and connectivity of a DFN influence the time/domain size required for full sampling of a velocity field in a fracture dominated system. Moreover, the Forsmark site is extremely sparsely fractured, even in the context of sparsely fractured rock, and this might influence the ability of particles to sample the entire velocity field. Therefore, a separate study with a synthetic DFN where the geometry and connectivity of the network are designed to isolate and quantify this influence would be a more appropriate framework to determine how fracture connectivity influences the particles ability to sample the entire velocity field. The application of theoretical models to represent the transport simulations reported here will be the focus of future investigations.

With regard to the sensitivity of the measured particle attributes to different lower cutoffs in the truncated power-law distribution used to generate the DFN, the following observations can be made. In the case of flux-weighted injection, no significant dependence is observed for any of the particle based attributes on the lower bound. This is likely the result of mass being inserted and then transported through the larger fractures in the network, which are not influenced by the lower cutoff used in the generation. However, the dependence is observed in the case of resident based injection. In general, particles moving through DFNs generated with lower values of the cutoff require longer distances before their mean travel time scales linearly. This dependence is possibly the result of more small fractures with low flux receiving the same percentage of mass as larger fractures under resident injection conditions. Therefore it takes longer for all the mass inserted in these small fractures to reach the large high transmissivity fractures than in networks

generated with higher cutoff values. How this cutoff influences the distance required to reach an asymptotic state when resident injection conditions are employed requires further investigation.

9.3.6 Conclusions

We investigated the influence of injection mode on transport properties by coupling the DFN technique with a Lagrangian approach to model transport through stochastically generated representations of kilometer-scale fractured media. To simulate transport, passive advective particles were tracked through thirty independent DFN realizations generated according to site characterization data obtained from an extensive field investigation of the Forsmark site in Sweden. Spatial and temporal particle attributes were recorded at uniformly spaced control planes throughout the domain to observe the evolution of transport properties.

We observe that the mean value of travel time computed using particles inserted using flux-weighting scale linearly with distance traveled, and the tails of their cumulative distributions of travel time exhibit power-law scaling. In contrast, the mean travel time of particles inserted using resident injection initially scales non-linearly with distance and power-law scaling of the tail of the empirical cumulative distribution of travel times is not observed. However, after accounting for a pre-asymptotic region, the mean travel time of particles inserted using resident injection conditions also scales linearly, and the tails of their breakthrough curves exhibit power-law scaling with nearly the same exponent as that observed for particles inserted using flux-weighting. The physical mechanism behind this evolution appears to be the draw of mass into larger fractures, both network scale channeling and in-fracture channeling are observed.

9.4 EFFECT OF INTERNAL APERTURE VARIABILITY ON PARTICLE TRACKING IN DFN

9.4.1 Introduction

Aperture variability within individual fractures is usually neglected in fractured media modeling. In such case, individual fractures are assumed to be homogeneous. However, in reality, individual fractures are heterogeneous and have an effect on flow and transport properties. For example, the strong influence of fracture aperture variations on dispersion of contaminants was found by Keller et al. (Keller et al. 1999). In this study strong dependent of dissolved contaminants in fractured rocks from fracture aperture variability was established using 2D continuum model. It was shown that large fracture aperture regions result in significant channeling of the fluid flow, accelerating the movement of solute in particular direction (Keller et al. 1999). Dreuzy et al addressed effect of internal heterogeneity on flow properties in fractured media modeling using discrete fracture networks. Authors have shown that the distribution of local apertures effects on global fracture transmissivity field (Dreuzy et al. 2012). However, the importance of in-fracture variability in large-scale 3D discrete fracture network modeling on flow and solute transport is still poorly studied due to high computational cost.

The relative importance of in-fracture variability on solute transport is a long-standing scientific issue. Previous studies (e.g., Cvetkovic et al. 1999) of the transport effects of flow channeling in variable-aperture fractures typically considered a single fracture isolated from the rest of the network. Although these studies yield some clear insights into the process, the unrealistic boundary conditions for flow limit the usefulness of the results for field-scale applications. Flow in an individual fracture is controlled not only by the aperture variability, but also by the boundary conditions that are determined by connections with other fractures in the network. Fluid

may enter and leave a fracture only where the fracture intersects other fractures. Those connections may represent a relatively small fraction of the fracture surface. This limited connection to other fractures introduces a certain degree of flow channeling independent of that caused by aperture variability. The relative importance of the two channeling mechanisms – heterogeneity-induced or geometry-induced – cannot be investigated without considering heterogeneous fractures embedded in a three-dimensional network. Previous attempts to address that issue (Painter, 2006) were limited by lack of reliable numerical tools. The new DFN simulation capability, DFNWORKS, has been extended to incorporate both fracture-to-fracture and within-fracture variability, thus allowing the importance of single-fracture aperture variability to be reliably assessed at the field scale.

In order to investigate the importance of in-fracture variability on solute transport simulation in large-scale DFN we compute Lagrangian parameters τ and β. The role of the flow-dependent Lagrangian parameters τ and β in controlling transport and retention in heterogeneous fractures and fracture networks was established in previous studies (Cvetkovic and Frampton, 2012). The non-reacting travel time τ[T] and cumulative reactivity parameter β [T/L] (also referred to as transport resistance and denoted F) are cumulative parameters obtained by integrating along random streamlines. Once the probability distributions for these parameters are known, probabilistic simulation of transport can be performed with relatively little effort (Painter, 2006). Detailed analyses (Cvetkovic et al. 2004) of comprehensive discrete fracture network simulations using the FracMan platform (Outters, 2003) clearly demonstrate that the distributions of τ and β are highly non-Gaussian at the scales of interest, which is inconsistent with the results of continuum models and suggests that DFN simulation is a more reliable method for assessing transport in sparsely fractured rock. DFN-based simulation must adequately represent the transport processes at small scales. When aperture variability within individual fractures is neglected in DFN simulations, individual fractures are assumed to be homogeneous. The cumulative reactivity parameter β is then computed as a ratio of the "flow-wetted surface" and flow rate of an individual fracture. When individual fractures are heterogeneous, it may cause flow to be "channelized" in individual fractures. However, the importance of internal variability relative to other sources of variability in the flow system is not obvious. On the one hand, internal variability in aperture tends to be smaller than fracture-to-fracture variability, which would suggest that internal aperture variability is less important. On the other hand, flow channeling in heterogeneous fractures tends to cause flow lines to coalesce in high-velocity regions, which may introduce a systematic bias toward lower β and less retention (Painter, 2006).

The current study addresses the importance of internal fracture aperture variability in determining field-scale transport in large-scale discrete fracture network. Recently developed DFNWORKS software is used to generate large-scale DFN, to apply internal heterogeneity on every fracture, where each computational cell is given its own value of aperture and transmissivity, to simulate a particle tracking through DFN, and, as a result, to analyze statistics of Lagrangian parameters calculated for millions of particles.

9.4.2   State of the Art

The DFN modeling and transport simulation are the primary tools in the study of in-fracture variability effect. DFNWORKS software, described in Section "DFNWORKS", is used to model large scale DFN with following simulation of steady state flow and particle tracking. Once the DFN is generated, the in-fracture variability is applied to every single fracture of DFN. This procedure is described in Section "Representation of internal variability in DFN", which also includes simple example of transport simulation of one fracture problem, showing the transport

"channeling" in high variances. Section "Transport Lagrangian variables: β and τ is focused on the Lagrangian variables β and τ that are used to analyze the transport results in large scale discrete fracture networks.

Representation of Internal Variability in DFN

Once the DFN is generated and the computational mesh is produced, the value of aperture and transmissivity of each individual fracture can be calculated independently of each other. Fracture transmissivity is calculated as a function of fracture aperture using the cubic law (Adler et al. 2012), while aperture is semi-correlated to fracture size and estimated as $b=F \times R^k$, where R is a fracture radius and $0.5<k<2.0$ (Adler et al. 2012). This aperture value is used in our previous studies, when aperture and transmissivity remained constant along the fracture. In the case of in-fracture variability we use this value as a mean value for Gaussian distribution, which is applied to all fracture cells. GSTAT software is used to scatter aperture values to each computational cell along every fracture (Pebesma and Wesseling, 1998; Pebesma, 2004). It was found that the aperture distribution in the open part of the fracture in natural granite is well approximated by log-normal distribution. In the current study the aperture was modeled as having a log-normal distribution. The log-normal model for aperture is widely used in studies of transport in fractured rock. If aperture and transmissivity are related through cubic law, a log-normal distribution of aperture implies a log-normal distribution of transmissivity, albeit with different distribution parameters.

Applied spatial correlation length, λ, is a function of fracture size: $λ=c \times R$. We consider following values of coefficient *c*: *c*=0.1, 0.3, 0.5, and 0.7. Fig. 9-17 shows the example of one circular fracture with distributed aperture values according to different spatial correlation lengths.

Another parameter that is being varied is a variance. Since fracture transmissivity is calculated from aperture using cubic law, we refer to variance in transmissivity: $Var_2(σ)$, $Var_4(σ)$, and $Var_6(σ)$ correspond to 2, 4, and 6 orders of magnitude difference in DFN transmissivity, respectively.

Once aperture and transmissivity are defined for each computational cell on each fracture, the flow solution is obtained using DFNFLOW and transport is simulated using DFNTRANS.

Transport Simulation on Single Fracture Problem

Before we proceed to large scale DFN modeling we have tested our workflow on a single fracture problem. Effect of internal heterogeneity on transport on single fracture model is well studied (e.g., Moreno and Tsang, 1994). It's been shown that flow "channeling" takes place as a variance in permeability increases. Fig. 9-18 shows results of particle tracking through a single fracture. The pressure boundary conditions are applied on bottom (high pressure) and top (low pressure) boundaries of the fracture. Aperture is distributed according to spatial correlation length λ=0.1R, where R is an average of lengths of rectangular sides. Three cases are shown for different variance of transmissivity (from left to right): $Var_1(σ)$, $Var_2(σ)$, and $Var_4(σ)$, which correspond to 1, 2, and 4 order of magnitude difference in transmisivity value, respectively, shown on color patterns on the figure.
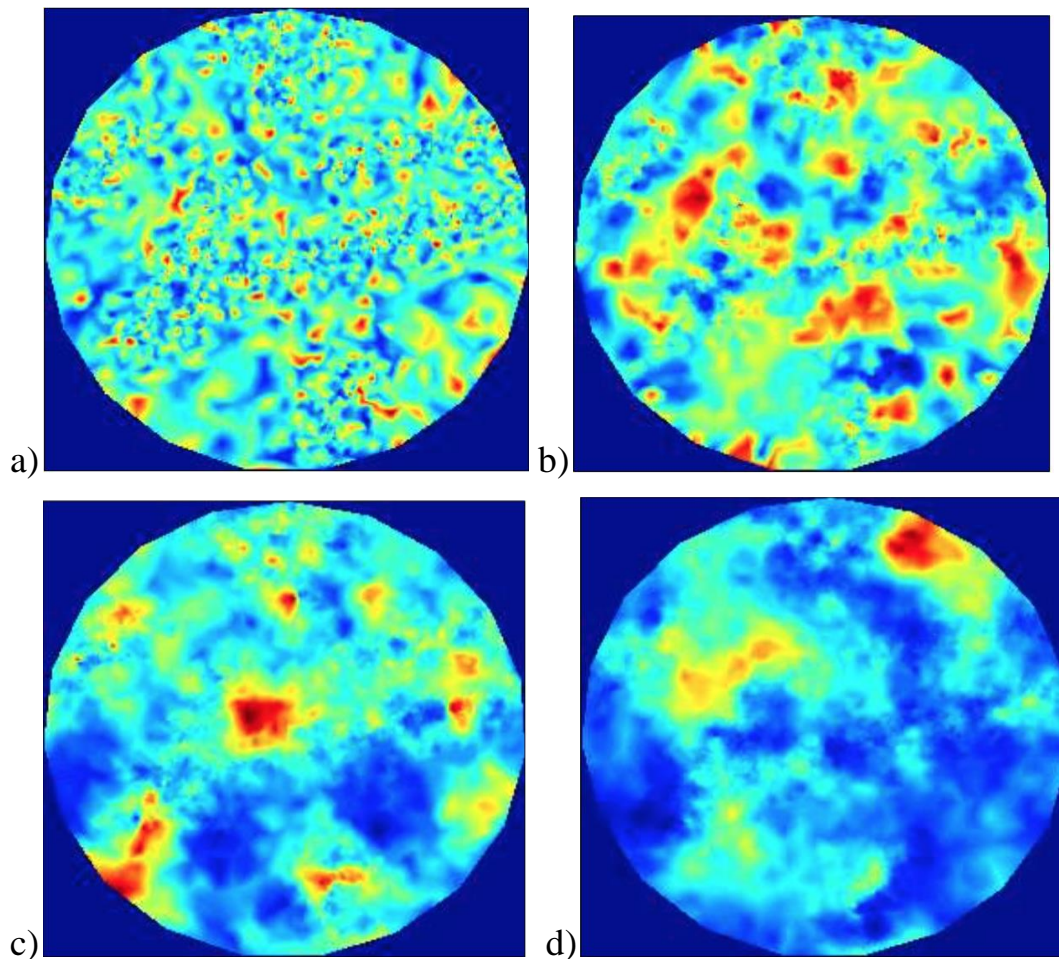
Figure 9-17: An example of one circular fracture with in-fracture variability. There are different spatial correlation lengths are applied: a) $\lambda=0.1R$, b) $\lambda=0.3R$, c) $\lambda=0.5R$, d) $\lambda=0.7R$. As correlation length increases, the zones of high and low aperture are observed clearer.

Initially particles are placed equidistant at bottom boundary of the fracture. Proceeding to the top out-flow boundary, the trajectories are pretty straight and tortuosity of paths is minimal in case of low variance. As variance of transmissivity is getting higher we can observe flow "channeling". Particles tend to move around zones with low transmissivity and keep motion towards higher transmissivity regions.
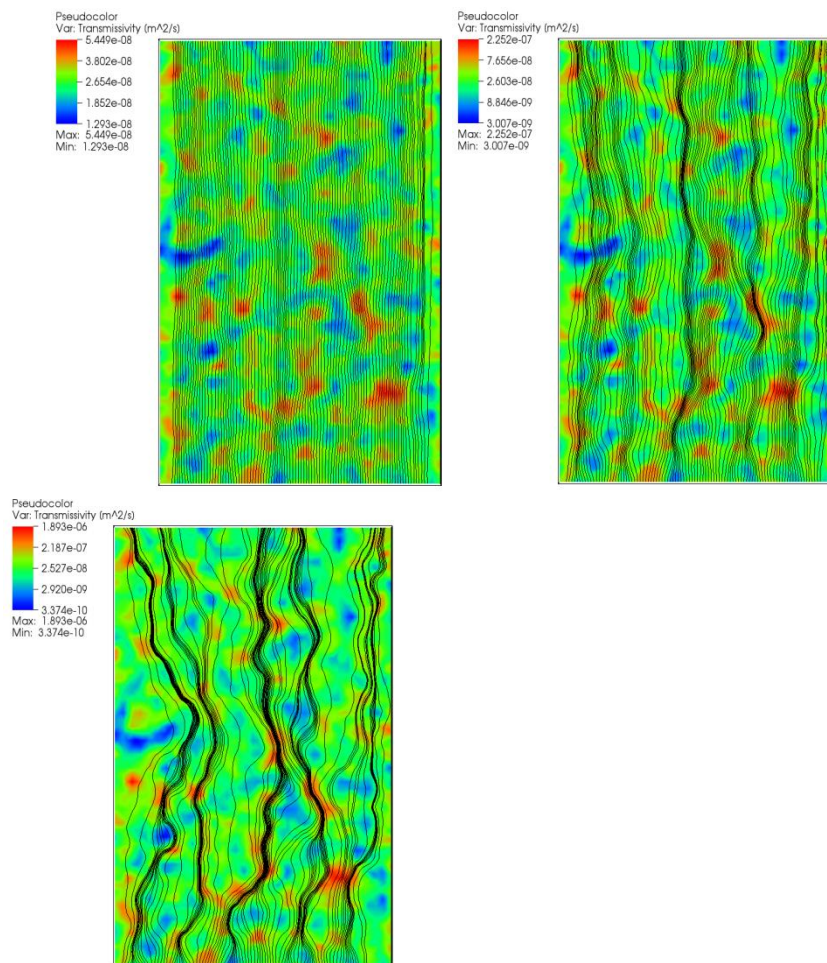
Figure 9-18: Single fracture configuration with three cases of particle trajectories are shown for different applied variances of transmissivity (from left to right): $Var_1(\sigma)$, $Var_2(\sigma)$, and $Var_4(\sigma)$, which correspond to 1, 2, and 4 orders of magnitude difference. Transmisivity distribution is shown by color patterns. Solid lines represent particles trajectories that are moving from bottom to top boundaries of the fracture. As variance in transmissivity increases the flow channeling is observed clearer, and the tortuosity of particles trajectories increases.

DFN with In-fracture Variability in Scale of 1 km

The discrete fracture networks, similar to those observed in natural repository cite Forsmark, Sweden, are generated to study the effect of in-fracture variability on a transport in large scale DFN. Details and input parameters for DFN generation are provided in Section "DFN Model: Forsmark, Sweden". In this study we use the version of DFN with highest density, where low cut-off radius of circular fractures is 15m (r_0=15m in Eq.9-10, Table 9-1). Ten independent DFN realizations were generated. The pressure boundary conditions are applied to top and bottom side of the domain, assuming fluid flow in vertical direction, from bottom to top. Example of steady state pressure solution in one of DFN realizations is shown in Fig. 9-19.
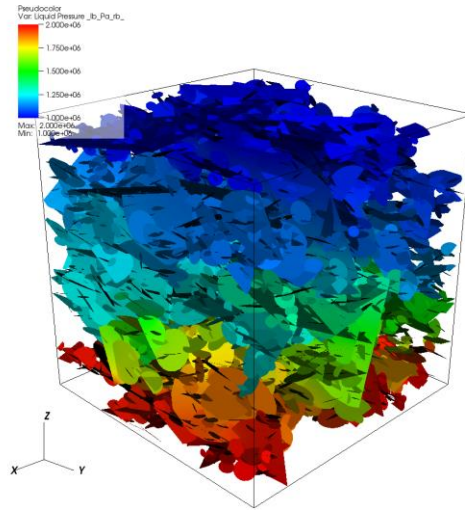
Figure 9-19: Example of steady state pressure solution in one of DFN realizations. The pressure boundary conditions are applied to top and bottom side of the domain, assuming fluid flow in vertical direction, from bottom to top. High pressure is shown by warm colors.
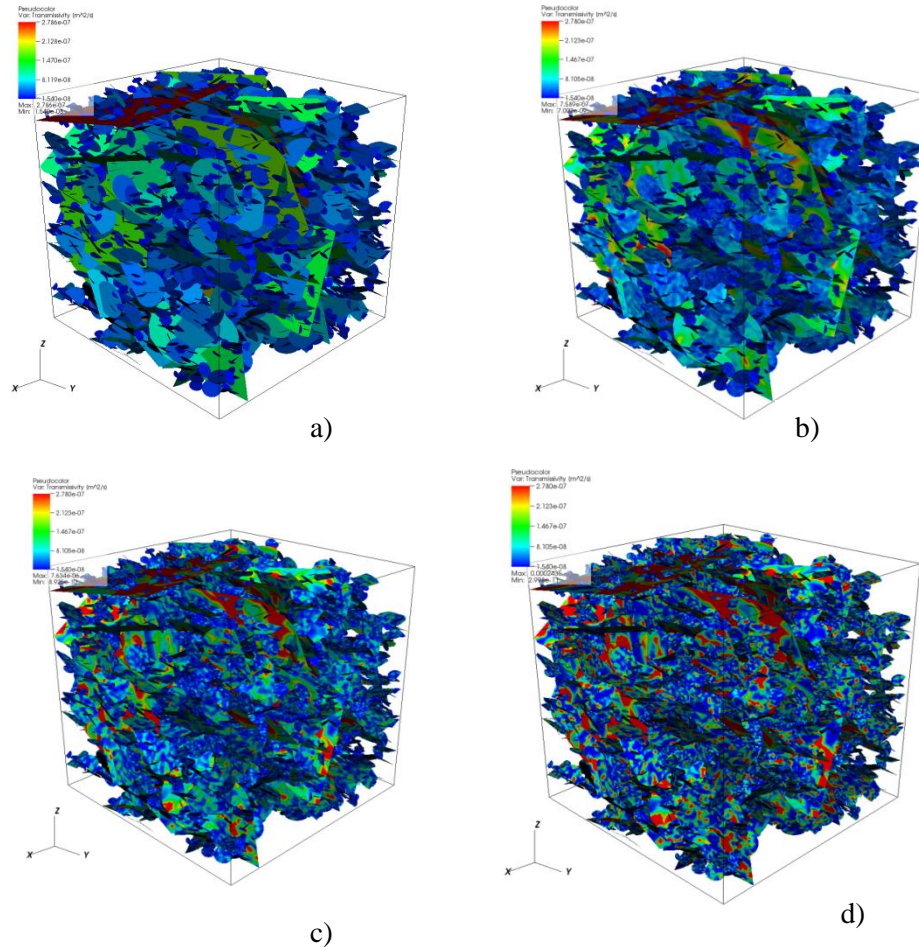
Figure 9-20: An example of DFN configuration with 4 cases of transmissivity distribution: a) transmissivity is constant along each fracture, but varies from fracture to fracture according to fracture size; b), c), d) show transmissivity distribution with $Var_2(\sigma)$, $Var_4(\sigma)$, and $Var_6(\sigma)$, respectively.

Figure 1-20 shows the transmissivity distribution over entire DFN. The constant transmissivity along each fracture is shown in Fig. 9-20a. The transport for this case is modeled for all 10 realizations and is used as a reference case. Fig.9-20 b, c, d show transmissivity distribution with $Var_2(\sigma)$, $Var_4(\sigma)$, and $Var_6(\sigma)$, respectively. The actual minimum and maximum of transmissivity values are show below the color legend, however colors are scaled according to the reference case (Fig.9-20a). This way, the smooth transition of transmissivity from cell to cell can be observed in case of low variance (Fig. 9-20b), and local sharp change of transmissivity is detected at high variance.

Transport Lagrangian Variables: β and τ

We are interested in the time required for a particle to be transported by advection with the water flowing in open fractures. The residence time is a random variable and is controlled by two Lagrangian variables: τ, the residence time for a particle moving with water from in-flow to out-

flow boundary, and β, a retention parameter related to the normalized surface area available for diffusional transfer to the rock matrix. These parameters are defined as integrals along the trajectory *x'*

$$\tau = \int_0^x \frac{1}{v(x')} dx' \cong \sum_{i=1}^n \frac{l_i}{v_i}$$

(1-12)

$$\beta = \int_0^x \frac{1}{v(x')b(x')} dx' \cong \sum_{i=1}^n \frac{l_i}{b_i v_i}$$

where the particle trajectory is a path through fractures in fracture network, passing through a series of *n* cells with a constant velocity and aperture in each cell n_i. Here b_i is a half-aperture of the current cell, v_i is a particle velocity in the cell, and l_i is a length of the *i*-th cell in the pathway. The total travel distance is through fracture network from in-flow to out-flow boundary is *x* (Painter et al. 2002). The Lagrangian variables are defined along the trajectories of particles, therefore they have the flow dynamics built in. Given statistics of τ and β and a model retention process, the distribution of residence time can be calculated.

Fig. 9-21 shows the cumulative and complementary cumulative distributions of calculated Lagrangian variables of advective transport in large scale DFN. Here τ (top panel) and β (bottom panel) are calculated for reference case, when the fracture transmissivity remains constant along each fracture but varies from fracture to fracture in the network.
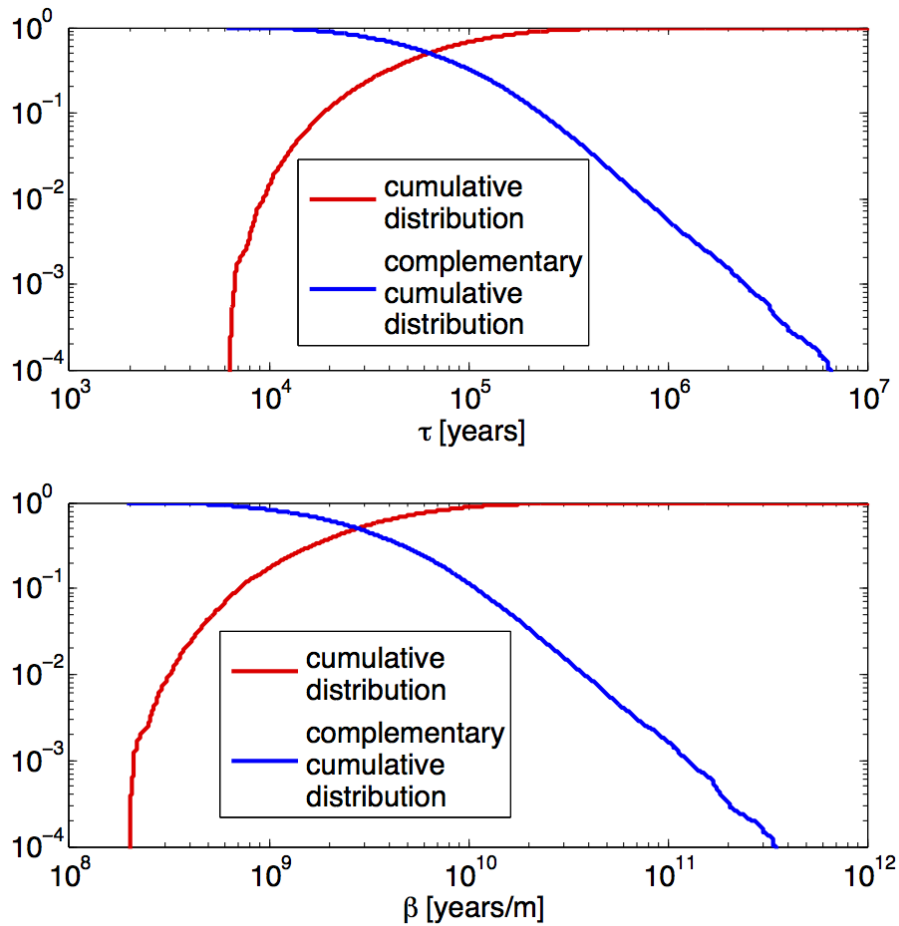
Figure 9-21: The cumulative and complementary cumulative distributions of calculated τ (top panel) and β (bottom panel) are calculated for transport in reference case.

9.4.3   Results and Discussion

Lagrangian parameters τ and β are computed during particles travel through fracture network. Initially particles are placed equidistant on in-flow boundary and followed to out-flow boundary accumulating τ and β in each computational cell. Statistics of τ and β are shown for 10^6 particles participated in 10 DFN independent realizations. The cumulative (CDF) and complementary cumulative (CCDF) distributions are plotted according to their flux weights, calculated by Eq.9-3b, showing statistics of earlier time on cumulative distributions (fastest particles) and longest travel time on tail of complementary cumulative distributions.

Fig. 9-22 and Fig.9-23 show CDF and CCDF of τ and β, respectively, comparing results of simulations with different correlation lengths, λat the same transmissivity variance. The in-fracture variability has an insignificant effect on both, τ and β, when the fracture transmissivity variance is little, $Var_2(\sigma)$. However, as variance increases, the tails of cumulative distributions of different spatial correlation lengths diverge from reference case (constant transmissivity along

each fracture) of both, τ and β. Thus, travel time of fastest particles is sensitive to transmissivity variation, and at longest spatial correlation length, λ=0.7R , the smallest travel time has been captured. Analyzing complementary cumulative distribution, no difference between spatial correlation lengths is observed at probability higher than 0.001. There is a little diverging of distribution tails (Probability<0.001) from the reference case, however no clear dependence on spatial correlation length is detected.

Fig. 9-24 and Fig.9-25 show CDF and CCDF of τ and β, respectively, comparing results of simulations with different variance of DFN transmissivity and plotted for the spatial same correlation length. As correlation lengths increases, the difference between reference case and largest transmissivity variance expands in cumulative distribution tails. Thus, the shortest travel time is sensitive to transmissivity variance at probability <0.1, however there is no difference is observed at probability higher than 0.1 at any considered variance of ttransmissivity. The longest time measured for particles (tails of complementary cumulative distribution) shows almost no divergence with reference case.

Scott Painter looked at the sensitivity of transport on in-fracture variability in previous study (Painter, 2006) for small scale DFN, comparing β for two different correlation length. Analyzing CDF and CCDF for particles under residence injection, no sensitivity to in-fracture variability was noticed (Painter, 2006). In our large-scale DFN simulations with flux-weighted particles, we observe a little sensitivity on transmissivity variations at earlier travel time. Also, no significant effect of spatial correlation length, λ, was detected.
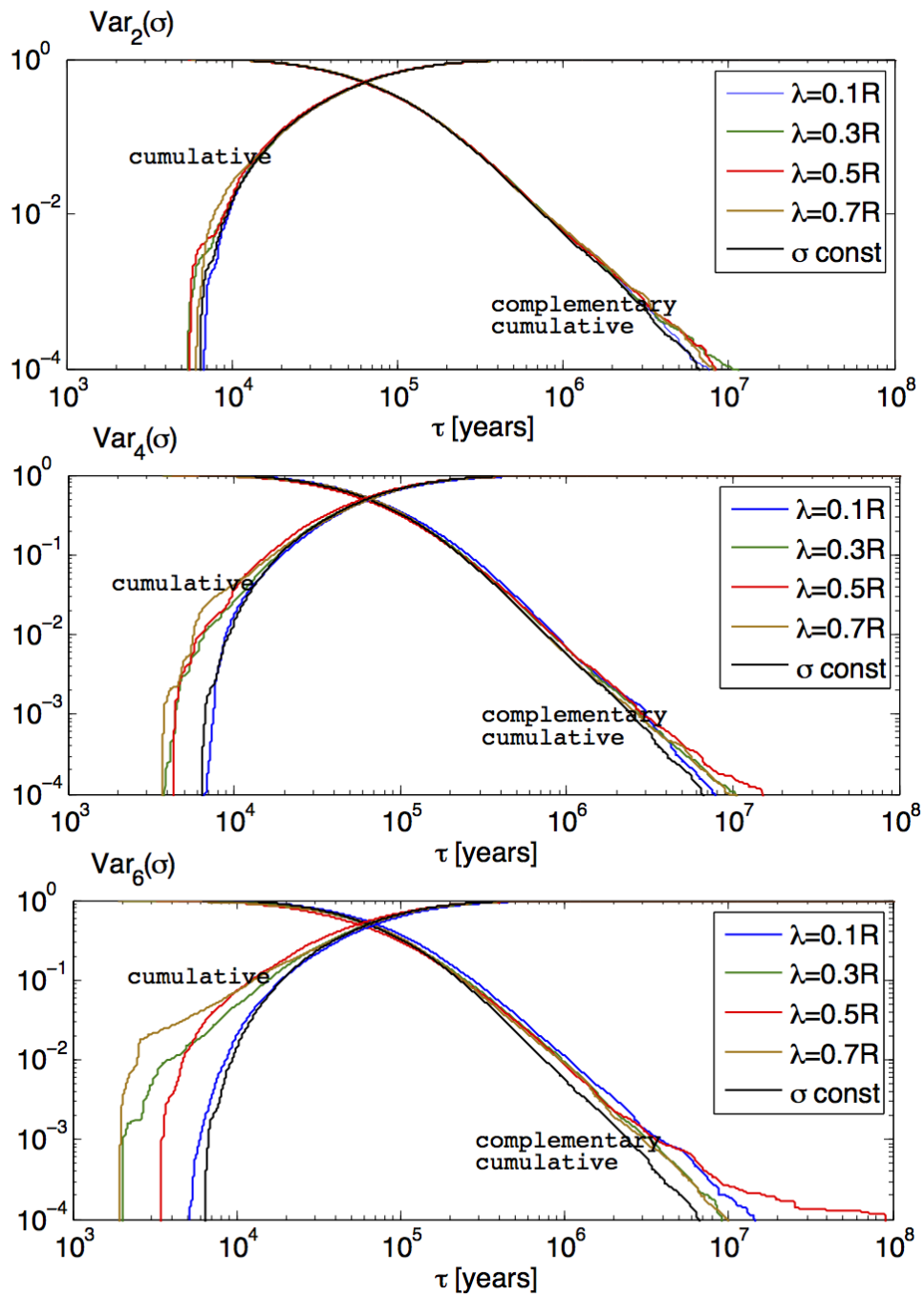
Figure 9-22: Cumulative and complementary cumulative distributions of τ for different variations of DFN transmissivity. Different correlation lengths, λ, compared to the reference case, when no in-fracture variability is implied.
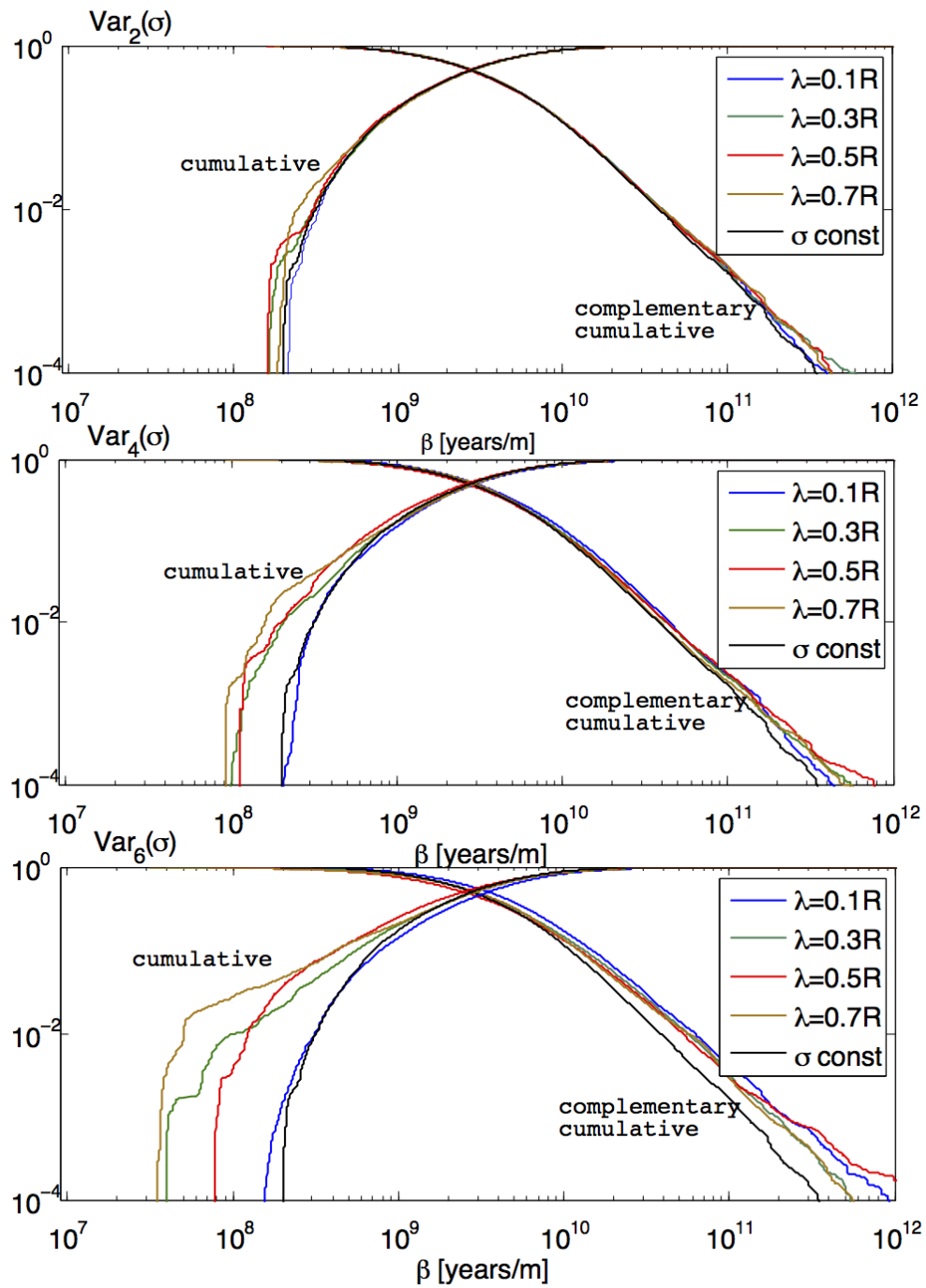
Figure 9-23: Cumulative and complementary cumulative distributions of β for different variations of DFN transmissivity. Different correlation lengths, λ, compared to the reference case, when no in-fracture variability is implied.
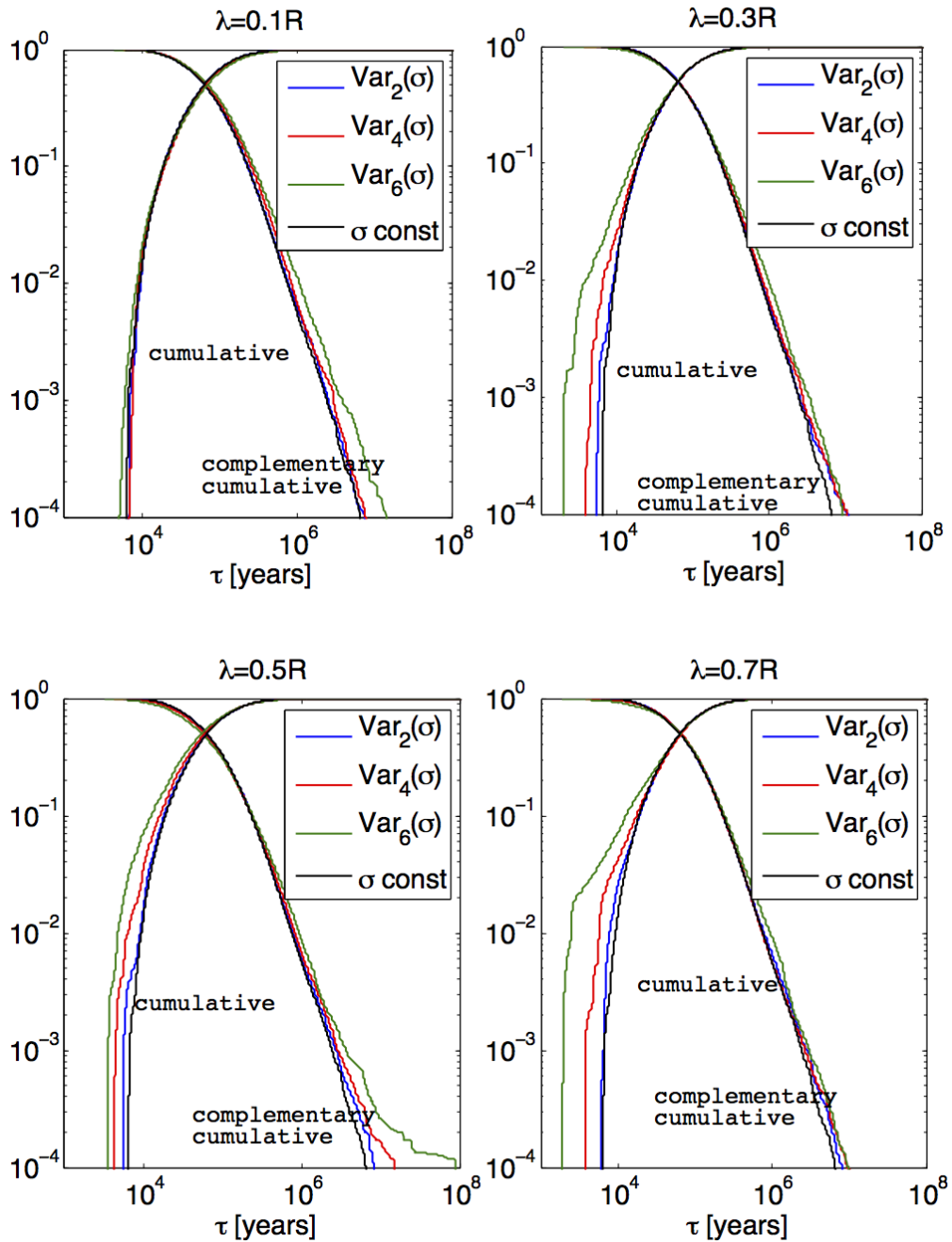
Figure 9-24: Cumulative and complementary cumulative distributions of τ for each considered correlation lengths, λ. Different variations of DFN transmissivity are compared to the reference case, when no in-fracture variability is implied.
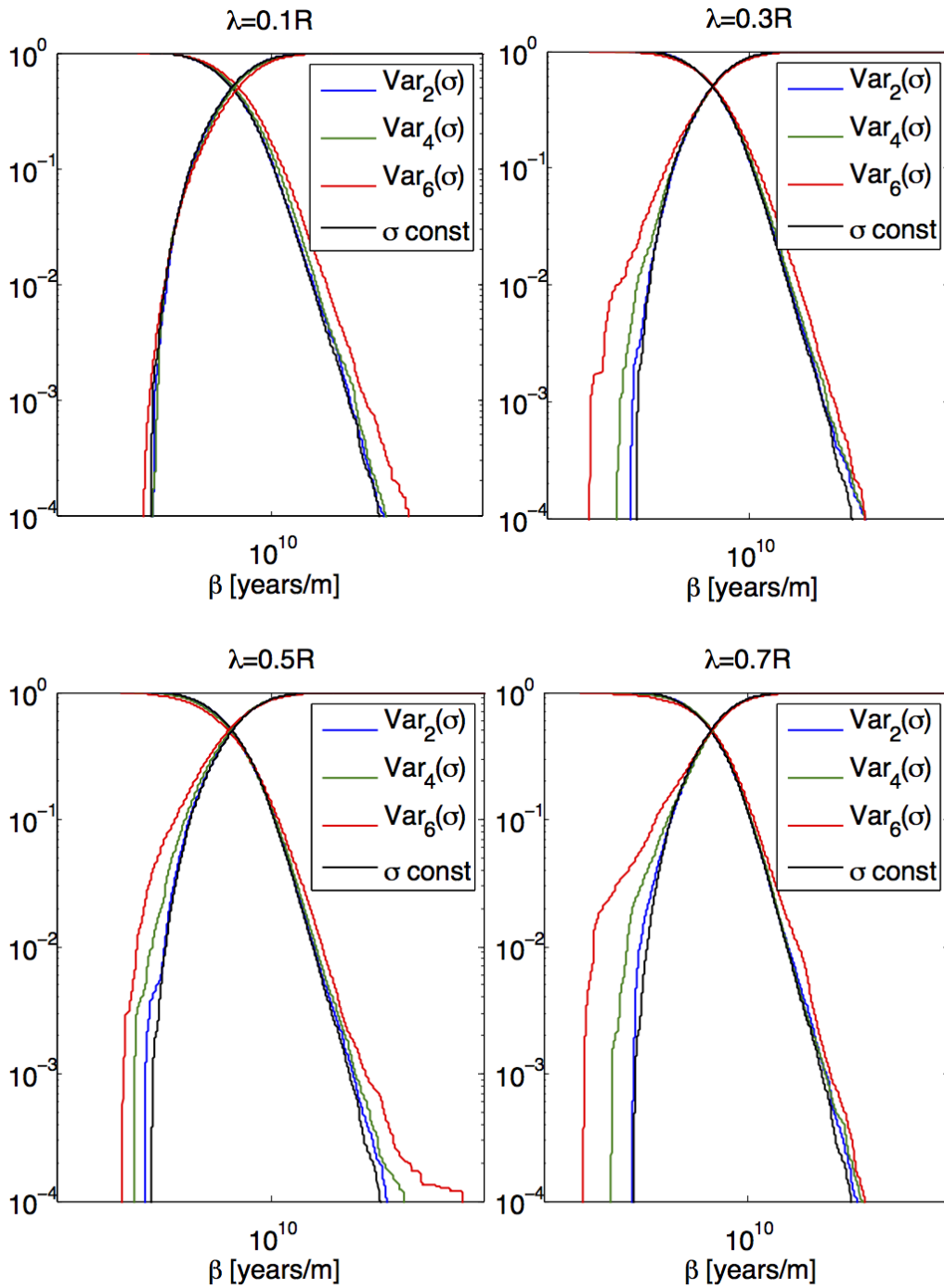
Figure 9-25: Cumulative and complementary cumulative distributions of β for each considered correlation lengths, λ. Different variations of DFN transmissivity are compared to the reference case, when no in-fracture variability is implied.

9.5   CONCLUDING REMARKS

We have provided a unified description of the dfnWorks suite that was developed over the past five years with significant contribution from the Used Fuel Campaign. The generation and meshing strategy are outlined, a description of the flow solver provided, and the pillars of the particle tracker presented. The ability to resolve flow and transport while retaining fracture geometry allowed for two unique studies of transport in large, kilometer-scale, DFN. The first study showed that after a pre-equilibrium region solutes injected under resident conditions evolve and behave similarly to that injected under flux-weighted conditions. The observation of this evolution was made feasible by the size of the DFN considered and characterizing the physical mechanisms that induced this phenomenon was made possible by retaining the geometry of the fractures rather than using a one-dimensional pipe-network approximation. Similarly, the second study was made possible because the fracture geometry was retained, so in-fracture variability could be incorporated. Other studies have used breakthrough times acquired from single fractures with internal aperture variability, but this study marks the first to resolve Lagrangian based transport in DFN where in-fracture variability is explicitly represented. We found that early breakthrough times and retention curves are influenced by in-fracture aperture variability but the tails of the breakthrough curves are insensitive to these variations.

Moving forward, we are utilizing the dfnWorks suite in a number of ways. First, a major question in DFN modeling is the relationship between fracture size and transmissivity. We are currently characterizing the impact of adopting different relationships between the two on transport by selecting three different models,: i) deterministic   correlation between fracture radius and transmissivity, ii) semi-determinnsitic correlation between fracture radius and transmissivity that includes a stochastic noise term, and iii) non-correlated where transmissivities are sampled from log normal distribution without regard for fracture size. This work is being done in collaboration with Andrew Frampton of the Stockholm University and Scott Painter of Oak Ridge National Laboratory. Second, we are moving beyond model development and towards model comparison in a co-operative venture with Sandia National Laboratory to compare our DFN model with their fractured continuum model (FCM). Preliminary results from a DFN/FCM comparison are presented in Sandia's Level 4 milestone. Using the same fracture site characterization, we are individually modeling transport using our unique models and comparing the results. We plan on using this collaboration to understand the transition between when continuum and DFN models are more appropriate when sites have varying degrees of fracture density. Finally, PFLOTRAN provides an efficient and scalable framework to capitalize on for upcoming performance assessment and uncertainty quantification studies that will be conducted under the Used Fuel Disposition Program. We are developing tools to run PFLOTRAN and then extract reduced order models that can be rapidly implemented in system-level and decision-making models.

In frame of SKB Task "Force on Modeling of Groundwater Flow and Transport of Solutes", Task 9A, LANL team can provide a significant contribution to a modeling of REPRO experiments WPDE-1&2 and TDE. Modeling the boreholes with diameter of 56 mm, leaving 1 mm gap between borehole walls and the filled inside dummy requires accurate computational mesh that can be produced by LaGriT (LaGriT, 2013). Modeling the water injection into the gap with a tracer pulse can be successfully driven by massively parallel flow solver, PFLOTRAN (Lichtner et al 2015), where the tracer diffusion into rock matrix can be accurately measured.

9.6   REFERENCES

Adler P. M., Thovert J. F. and Mourzenko V. V. (2012) *Fractured porous media*. Oxford University Press.

Andersson P., Byega˚rd J., Billaux D., Cvetkovic V., Dershowitz W., Doe T., Hermanson J., Poteri A., Tullborg E. L., and Winberg A. (2007) *TRUE block scale continuation project. final report.*, Technical report, Swedish Nuclear Fuel and Waste Management Co., Stockholm, Sweden.

Balay S., Abhyankar S., Adams M., Brown J., Brune P., Buschelman K., Eijkhout V., Gropp W., Kaushik D., Knepley M., et al. (2014) *PETSc users manual*, revision 3.5.

Bear J. (1988) *Dynamics of fluids in porous media*, Dover publications.

Benedetto M. F., Berrone S., Pieraccini S., and Scialo` S. (2014) The virtual element method for discrete fracture network simulations, *Computer Methods in Applied Mechanics and Engineering*, 280, 135–156.

Berkowitz B. (2002) Characterizing flow and transport in fractured geological media: A review, *Adv. Water Resour.*, 25(8-12), 861–884.

Berkowitz B. and Braester C. (1991) Solute transport in fracture channel and parallel plate models, *Geophys. Res. Lett.*, 18(2), 227–230.

Berkowitz B. and Scher H. (1997) Anomalous transport in random fracture networks, *Phys. Rev. Lett.*, 79(20), 4038.

Berkowitz B. and Scher H. (1998) Theory of anomalous chemical transport in random fracture networks, *Phys. Rev. E*, 57, 5858–5869.

Berrone S., Pieraccini S., and Scialo` S. (2013) A PDE-constrained optimization formulation for discrete fracture network flows, *SIAM Journal of Scientific Computing*, 35(2), B487–B510.

Cacas M. C., Ledoux E., De Marsily G., Tillie B., Barbreau A., Durand E., Feuga B., and Peaudecerf P. (1990) Modeling fracture flow with a stochastic discrete fracture network: Calibration and validation: 1. the flow model, *Water Resources Research*, 26(3), 479–489.

Coxeter H. S. M. (1969) *Introduction to geometry*, Vol. 6, Wiley New York.

Cvetkovic V. (2011) The tempered one-sided stable density: a universal model for hydrological transport? *Environ. Res. Lett.*, 6(3), 034008.

Cvetkovic V. (2013) How accurate is predictive modeling of groundwater transport? A case study of advection, macrodispersion, and diffusive mass transfer at the Forsmark site (sweden), *Water Resour. Res.*, 49(9), 5317–5327.

Cvetkovic V. and Frampton A. (2012) Solute transport and retention in three-dimensional fracture networks, *Water resources research*, 48(2).

Cvetkovic V., Selroos J. O. and Cheng H. (1999) Transport of reactive tracers in rock fractures, *Journal of Fluid Mechanics*, 378, 335-356.

Cvetkovic V., Painter S., Outters N. and Selroos J. O. (2004). Stochastic simulation of radionuclide migration in discretely fractured rock near the Äspö Hard Rock Laboratory, *Water resources research*, 40(2).

De Dreuzy J.-R., Darcel C., Davy P., and Bour O. (2004) Influence of spatial correlation of fracture centers on the permeability of two-dimensional fracture networks following a power law length distribution, *Water Resources Research*, 40(1).

Demmy G., Berglund S., and Graham W. (1999) Injection mode implications for solute transport in porous media: Analysis in a stochastic Lagrangian framework, *Water Resour. Res.*, 35(7), 1965–1973.

Dershowitz W. (2014) *Interactive discrete feature data analysis, geometric modeling, and exploration simulation: User documentation*, version 7.4, FracMan, http://fracman.golder.com/.

Dershowitz W. and Fidelibus C. (1999) Derivation of equivalent pipe network analogues for three-dimensional discrete fracture networks by the boundary element method, *Water Resources Research*, 35(9), 2685–2691.

Dreuzy J.-R., Me´heust Y., and Pichot v. (2012) Influence of fracture scale heterogeneity on the flow proper- ties of three-dimensional discrete fracture networks, *Journal of Geophysical Research - Solid Earth*, 117(B11).

Elsworth D. (1986) A hybrid boundary element-finite element analysis procedure for fluid flow simulation in fractured rock masses, *International Journal for Numerical and Analytical Methods in Geomechanics*, 10(6), 569–584.

Endo H., Long J., Wilson C., and Witherspoon P. (1984) A model for investigating mechanical transport in fracture networks, *Water Resour. Res.*, 20(10), 1390–1400.

Erhel J., De Dreuzy J.-R., and Poirriez B. (2009) Flow simulation in three-dimensional discrete fracture networks, *SIAM Journal of Scientific Computing*, 31(4), 2688–2705.

Falconer K. (2013)*Fractal Geometry: Mathematical Foundations and Applications*. John Wiley & Sons, 2013.

Faybishenko B. (2005) *Dynamics of fluids and transport in fractured rock*, Number 162, American Geophysical Union.

Frampton A. and Cvetkovic V. (2007) Upscaling particle transport in discrete fracture networks: 1. Nonreactive tracers, *Water Resour. Res.*, 43(10).

Frampton A. and Cvetkovic V. (2007) Upscaling particle transport in discrete fracture networks: 2. Reactive tracers, *Water Resour. Res.*, 43(10).

Frampton A. and Cvetkovic V. (2009)Significance of injection modes and heterogeneity on spatial and temporal dispersion of advecting particles in two-dimensional discrete fracture networks, *Adv. Water Resour.*, 32(5), 649–658.

Frampton A. and Cvetkovic V. (2011)Numerical and analytical modeling of advective travel times in realistic three-dimensional fracture networks, *Water Resour. Res.*, 47(2).

Geier J. (2011) *Investigation of discrete-fracture network conceptual model uncertainty at forsmark*, Tech. rep., Swedish Radiation Safety Authority, Stockholm, Sweden.

Gotovac H., Cvetkovic V., and Andricevic R. (2009) Flow and travel time statistics in highly heterogeneous porous media, *Water Resour. Res.*, 45(7).

Gotovac H., Cvetkovic V., and Andricevic R. (2010) Significance of higher moments for complete char- acterization of the travel time probability density function in heterogeneous porous media using the maximum entropy principle, *Water Resour. Res.*, 46(5).

Hammond G. E. and Lichtner P. C. (2010) Field-scale model for the natural attenuation of uranium at the Hanford 300 area using high-performance computing, *Water Resources Research*, 46(9), 2010.

Hammond G. E., Lichtner P. C., and Mills R. T. (2014) Evaluating the performance of parallel subsurface simulators: An illustrative example with PFLOTRAN, *Water Resources Research*, 50(1), 208–228.

Hammond G. E., Lichtner P. C., Lu C., and Mills R. T. (2012) PFLOTRAN: reactive flow & transport code for use on laptops to leadership-class supercomputers, *Groundwater Reactive Transport Models*, pages 142–160.

Hartley L. and Joyce S. (2013) Approaches and algorithms for groundwater flow modeling in support of site investigations and safety assessment of the Forsmark site, Sweden, *Journal of Hydrology*, 500, 200–216.

Hartley L., Cox I., Holton D., Hunter F., Joyce S., Gylling B., Lindgren M. (2004) *Groundwater flow and radionuclide transport modelling using CONNECTFLOW in support of the SR can assessment*, Tech. Rep. SKB Rapport R-04-61, Swedish Nuclear Fuel and Waste Management Co., Stockholm, Sweden.

Hyman J. D., Gable C. W., Painter S. L., and Makedonska N. (2014) Conforming Delaunay triangulation of stochastically generated three dimensional discrete fracture networks: A feature rejection algorithm for meshing strategy, *SIAM Journal of Scientific Computing*, 36(4), A1871–A1894.

Jankovic´ I. and Fiori A. (2010) Analysis of the impact of injection mode in transport through strongly heterogeneous aquifers, *Adv. Water Resour.*, 33(10), 1199–1205.

Joyce S., Hartley L., Applegate D., Hoek J., and Jackson P. (2014) Multi-scale groundwater flow modeling during temperate climate conditions for the safety assessment of the proposed high-level nuclear waste repository site at forsmark, Sweden, *Hydrogeology Journal*, 22(6), 1233–1249.

Karra S. and Kitay C. (2015) *PyFLOTRAN documentation release 1.0.0*, Technical Report LA-UR-15- 21189, Los Alamos National Laboratory.

Karra S., Painter S. L., and Lichtner P. C. (2014) Three-phase numerical model for subsurface hydrology in permafrost-affected regions (PFLOTRAN-ICE v1. 0), *The Cryosphere*, 8(5), 1935–1950.

Karra S., Bisht G., Lichtner P. C., and Hammond G. E. (2013) Coupling geomechanics with flow and reactive transport in PFLOTRAN for subsurface applications, *AGU Fall Meeting Abstracts*, 1, 1106.

Karra S., Makedonska N., Viswanathan H., Painter S. L., and Hyman J. D. (2015) Effect of advective flow in fractures and matrix diffusion on natural gas production, *Water Resources Research*, (under review).

Keller A. A., Roberts P. V. and Blunt M. J. (1999) Effect of fracture aperture variations on the dispersion of contaminants, *Water Resources Research*, 35(1), 55-63.

Kreft A. and Zuber A. (1978) On the physical meaning of the dispersion equation and its solutions for different initial and boundary conditions, *Chem. Eng. Sci.*, 33(11), 1471–1480.

LaGriT (2013) *Los Alamos Grid Toolbox, (LaGriT)*, http://lagrit.lanl.gov, Los Alamos National Laboratory.

Lichtner P. C. and Karra S. (2014) Modeling multiscale-multiphase-multicomponent reactive flows in porous media: Application to co2 sequestration and enhanced geothermal energy using PFLOTRAN. In *Al-Khoury R.and Bundschuh J. (eds.) Computational Models for CO₂ Geo-sequestration & Compressed Air Energy Storage (http://www.crcnetbase.com/doi/pdfplus/10)*, pages 81–136, CRC Press.

Lichtner P. C., Hammond G. E., Lu C., Karra S., Bisht G., Andre B., Mills R. T., and Kumar J. (2015) *PFLOTRAN user manual: A massively parallel reactive flow and transport model for describing surface and subsurface processes*, Technical report, Los Alamos National Laboratory.

Long J., Remer J., Wilson C., and Witherspoon P. (1982) Porous media equivalents for networks of discontinuous fractures, *Water Resour. Res.*, 18(3), 645–658.

Lu C. and Lichtner P. C. (2007) High resolution numerical investigation on the effect of convective instability on long term CO_2 storage in saline aquifers, *Journal of Physics: Conference Series*, 78, 012042, IOP Publishing.

Makedonska N., Painter S. L., Bui Q. M., Gable C. W., and Karra S. (2015)Particle tracking approach for transport in three-dimensional discrete fracture networks, *Computation Geosciences*, (under review).

Maryšˇka J., Severyˇn O., and Vohral´ık M. (2005) Numerical simulation of fracture flow with a mixed-hybrid fem stochastic discrete fracture network model, *Computational Geosciences*, 8(3), 217–234.

Middleton R. S., Carey J. W., Currier R. P., Hyman J. D., Kang Q., Karra S., Jime´nez-Mart´ınez J., Porter M. L., and Viswanathan H. S. (2015)Shale gas and non- aqueous fracturing fluids: Opportunities and challenges for supercritical CO_2, *Applied Energy*, 147, 500–509.

Mills R. T., Lu C., Lichtner P. C., and Hammond G. E. (2007) Simulating subsurface flow and transport on ultrascale computers using PFLOTRAN, *Journal of Physics: Conference Series*, 78, 012051, IOP Publishing.

Mills R. T., Bisht G., Karra S., Hoffman F. M., Hammond G. E., Kumar J., Painter S. L., Thornton P. E., and Lichtner P. C. (2012) Progress towards coupled simulation of surface/subsurface hydrologic processes and terrestrial ecosystem dynamics using the community models PFLOTRAN and CLM, In *AGU Fall Meeting Abstracts*, 1, 1426.

Moreno L. and Tsang C. F. (1994) Flow channeling in strongly heterogeneous porous media: A numerical study, *Water Resources Research*, 30(5), 1421-1430.

Mount D. M. and Gable C. W. (2001) A point-placement strategy for conforming Delaunay tetrahedraliza- tion, *International Journal of Computational Geometry & Applications*, 11(6), 669–682.

Mustapha H. and Dimitrakopoulos R. (2011) Discretizing two-dimensional complex fractured fields for incompressible two-phase flow, *International Journal for Numerical Methods in Fluids*, 65(7), 764– 780.

Mustapha H. and Mustapha K. (2007) A new approach to simulating flow in discrete fracture networks with an optimized mesh, *SIAM Journal of Scientific Computing*, 29, 1439.

Mustapha H., Dimitrakopoulos R., Graf T., and Firoozabadi A. (2011) An efficient method for discretizing 3D fractured media for subsurface flow and transport simulations, *International Journal for Numerical Methods in Fluids*, 67(5), 651–670.

National Research Council (1996) *Rock fractures and fluid flow: contemporary understanding and applications*, National Academy Press.

Neuman S. P. (2005) Trends, prospects and challenges in quantifying flow and transport through fractured rocks, *Hydrogeology Journal*, 13(1), 124–147.

Neuman S. P. and Tartakovsky D. M. (2009) Perspective on theories of non-Fickian transport in heterogeneous media, *Advances in Water Resources*, 32(5), 670–680.

O'Malley D. and Vesselinov V. V. (2014) Analytical solutions for anomalous dispersion transport, *Adv. Water Resour.*, 68, 13–23.

Outters N. (2003) *A generic study of discrete fracture network transport properties using FracMan/MAFIC*, Rep. R-03, 13.

Outters N., Shuttle D. (2000) *Sensitivity analysis of a discrete fracture network model for performance assessment of aberg*, Tech. rep., Swedish Nuclear Fuel and Waste Management Co., Stockholm, Sweden.

Painter S. (2006) *Effect of single-fracture aperture variability on field-scale transport*, Technical report, SKB.

Painter S. and Cvetkovic V. (2005) Upscaling discrete fracture network simulations: An alternative to continuum transport models, *Water Resources Research*, 41, W02002.

Painter S. and Mancillas J. (2013) *Marfa user's manual: migration analysis of radionuclides in the far field*, Posiva Working Report 1.

Painter S., Cvetkovic V., and Selroos J.-O. (2002) Power-law velocity distributions in fracture networks: Numerical evidence and implications for tracer transport, *Geophysical Research Letters*, 29(14), 20–1–20–4.

Painter S. L., Gable C. W., and Kelkar S. (2012) Pathline tracing on fully unstructured control-volume grids, *Computational Geosciences*, 16(4), 1125–1134.

Painter S., Cvetkovic V., Mancillas J. and Pensado O. (2008) Time domain particle tracking methods for simulating transport with retention and first-order transformation, *Water Resources Research*, 44 (1).

Pebesma E.J. (2004) Multivariable geostatistics in S: the gstat package, *Computers & Geosciences*, 30(7), 683-691

Pebesma E.J. and Wesseling C.G. (1998) Gstat, a program for geostatistical modelling, prediction and simulation, *Computers & Geosciences*, 24(1), 17-31.

Pichot G., Erhel J., and De Dreuzy J. R. (2010) A mixed hybrid mortar method for solving flow in discrete fracture networks, *Applicable Analysis*, 89(10), 1629–1643.

Pichot G., Erhel J., and De Dreuzy J. R. (2012) A generalized mixed hybrid mortar method for solving flow in stochastic discrete fracture networks, *SIAM Journal of Scientific Computing*, 34(1), B86–B105.

Pierre M. A., Jean-François T., and Valeri V. M. (2012) *Fractured Porous Media*, Oxford University Press.

Pruess K., Oldenburg C. M., and Moridis G. J. (1999) *TOUGH2 user's guide version 2*.

Ruppert J. (1995) A Delaunay refinement algorithm for quality 2-dimensional mesh generation, *Journal of Algorithms*, 18(3), 548–585.

Schwartz F. W. and Smith L. (1988) A continuum approach for modeling mass transport in fractured media, *Water Resour. Res.*, 24(8), 1360–1372.

SKB (2011) *Long-term safety for the final repository for spent nuclear fuel at Forsmark. main report of the SR-site project*, Technical Report SKB TR-11-01, Swedish Nuclear Fuel and Waste Management Co., Stockholm, Sweden.

Smith L. and Schwartz F. W. (1984) An analysis of the influence of fracture geometry on mass transport in fractured media, *Water Resour. Res.*, 20(9), 1241–1252.

Tsang C.-F. and Neretnieks I. (1998) Flow channeling in heterogeneous fractured rocks, *Reviews of Geo- physics*, 36(2), 275–298.

Tsang Y. W. and Tsang C. F. (1989) Flow channeling in a single fracture as a two-dimensional strongly heterogeneous permeable medium, *Water Resour. Res.*, 25(9), 2076–2080.

Tsang Y., Tsang C., Neretnieks I., and Moreno L. (1988) Flow and tracer transport in fractured media: A variable aperture channel model and its properties, *Water Resour. Res.*, 24(12), 2049–2060.

Vanderborght J., Mallants D., and Feyen J. (1998) Solute transport in a heterogeneous soil for boundary and initial conditions: Evaluation of first-order approximations, *Water Resour. Res.*, 34(12), 3255–3270.

Vesselinov V. and Harp D. (2012) Model analysis and decision support (mads) for comple physics models, In *XIX International conference on water resources-CMWR*.

Xu C., Dowd P. A., Mardia K. V., and Fowell R. J. (2006) A connectivity index for discrete fracture networks, *Mathematical Geology*, 38(5), 611–634.

Zyvoloski G. A. (2007) *FEHM: A control volume finite element code for simulating subsurface multi-phase multi-fluid heat and mass transfer*, Los Alamos Unclassified Report LA-UR-07-3359.

Zyvoloski G. A. and Vesselinov V. V. (2006) An investigation of numerical grid effects in parameter estimation, *Groundwater*, 44(6), 814–825.

10.0 FRACTURE CONTINUUM MODEL AND ITS COMPARISON WITH DISCRETE FRACTURE NETWORK MODEL

10.1 INTRODUCTION

Various fracture representations are used to allow modeling of fractured rock using numerical models. These representations are based on fracture characterization methods that depend on field data. Two of these methods are the Discrete fracture Network (DFN) and the Fracture Continuum Model (FCM). The DFN is based on characterization of individual fractures, while the FCM uses a geostatistical approach to assign fracture data to grid blocks. Details of the DFN approach can be found in Chapter 9 and Section 10.4.4. The FCM is described below in Section 10.2.

Both the DFN and FCM have been applied to flow and transport in granite rock for various applications. The objectives of this study are to evaluate both methods for use in flow and transport modeling of a generic deep geologic disposal of used fuel in crystalline rocks. As outlined in the 2014 report (Wang et al., 2014) this study is intended to support better characterization and understanding of the fractured media, and fluid and transport in such media. For this FY a preliminary benchmark testing of the fracture models with the use of synthetic data is presented.

10.2 STATE OF THE ART

10.2.1 Fracture Continuum Model

The FCM approach is a stochastic method for estimating fracture permeability. The model utilizes the advantages of discrete fracture network models and the speed of effective continuum representations of fracture permeability (McKenna and Reeves, 2005). The FCM maps the permeability of discrete fractures onto a regular grid using a continuum approach. This approach defines fracture sets using the strike, dip, aperture, and spacing of parallel fractures in the system. The method allows generation of permeability fields using field observations of fracture sets. The original method described in McKenna and Reeves (2005) was designed for vertical fractures. It has been applied to ground water flow and transport for different applications. The method has since then been extended to incorporate fully three-dimensional representations of anisotropic permeability, multiple independent fracture sets, and arbitrary fracture dips and orientations (Kalinina et al. 20012, 2014). The extended FCM method has successfully been applied to enhanced geothermal systems (EGS) applications. The computation speed and realistic representation of complex fracture systems (e.g. Figure 6.1) of the FCM approach is particularly appealing for EGS applications that typically cover large areas of interest.
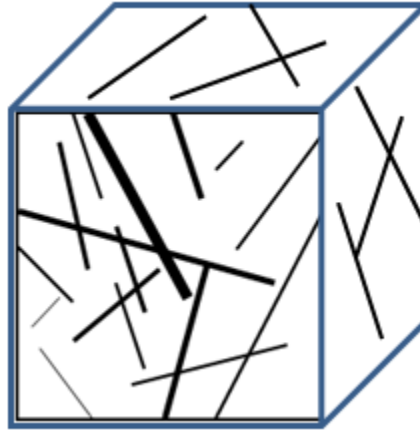
Figure 10-1: Schematic diagram showing fractures in three-dimensional space

The extended FCM approach incorporates the permeability tensor developed by Chen et al. (1999) which includes multiple fracture sets with arbitrary fracture orientations. Chen et al. (1999) developed analytical models for evaluating anisotropic permeability of fracture networks. The mathematical models use geometric considerations to allocate fracture permeability to fractures. The resulting permeability tensor can be applied to fractures of any orientations.

The FCM continuum approach computes permeability tensors for each grid block in the model domain. For one fracture set, the permeability tensor is defined in Equation (6.1) (Chen et al. 1999).

$$k_{ij} = \frac{b^3}{12d} \begin{bmatrix} (n_2)^2 + (n_3)^2 & -n_1 n_2 & -n_3 n_1 \\ -n_1 n_2 & (n_3)^2 + (n_1)^2 & -n_2 n_3 \\ -n_3 n_1 & -n_2 n_3 & (n_1)^2 + (n_2)^2 \end{bmatrix},$$

(10.1)

where k_{ij} is the permeability tensor in the $i = x,y,z$ and $j = x,y,z$ directions, b is fracture aperture, d is fracture spacing, and $n_{1,2,3}$ is the unit normal to the fracture plane in the x, y, and z direction, respectively.

The unit normal components to the fracture plane are defined in Equation (10.2).

$$n_1 = Cos\left(\alpha \frac{\pi}{180}\right) x Sin(\omega \frac{\pi}{180})$$

(10.2a)

$$n_2 = Cos\left(\alpha \frac{\pi}{180}\right) x Cos(\omega \frac{\pi}{180})$$

(10.2b)

$$n_3 = -Sin\left(\alpha \frac{\pi}{180}\right),$$

(10.2c)

where $\alpha = 90^0$ - dip and ω = strike - 90^0.

For multiple fracture sets the permeability tensor can be computed by summing the permeability tensors for individual fracture sets as shown in Equation 10.3. An illustration is shown in Figure 10.2.

$$k_{ij}^* = \sum_{m=1}^{N} k_{ij}^m,$$ (10.3)

where N is the number of fracture sets and k_{ij}^m is defined by Equation (6.1). The summation assumes that the total porosity within a grid-block changes very little, which is valid for most granite rock applications. Note that only k_{xx}^*, k_{yy}^*, and k_{zz}^* components of the permeability tensor are used for applications to ground water flow, mass and heat transport.

The k_{xx}^m, k_{yy}^m and k_{zz}^m values are calculated for each grid block based on the fracture aperture, spacing, strike, and dip probability distributions that are defined for the fracture set m.
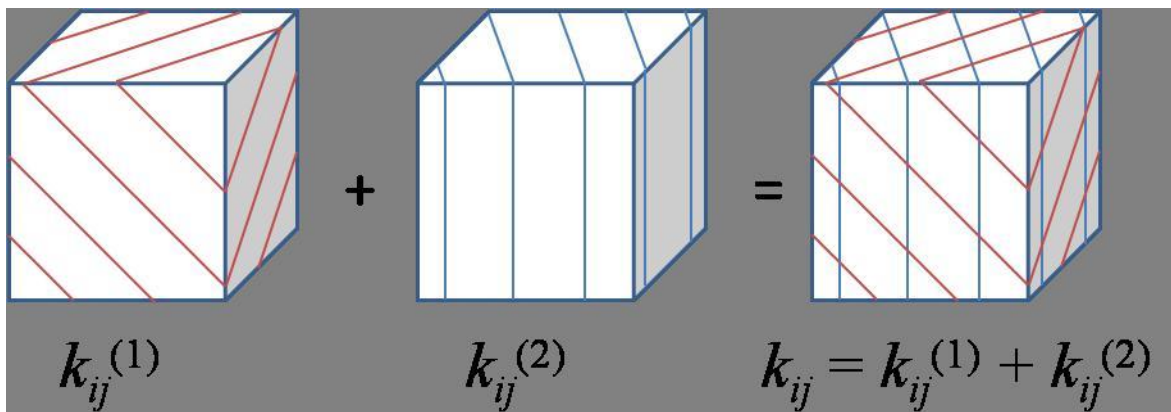
Figure 10-2: Schematic diagram showing the approach for the effective overall permeability calculation for multiple fracture sets

In the FCM approach two different Monte Carlo methods can be used to assign the fracture parameter value to a grid block. In the first method, a random number is generated for the block and the parameter value is drawn from the corresponding probability distribution at the probability value specified by this random number. In the second method, spatially correlated random numbers are generated by running the Sequential Gaussian Simulation (SGSIM) code (Deutsch and Journel 1998) for a selected mesh. The orientation of the desired spatial correlation can be specified in SGSIM by defining the correlation angles in x, y, and z directions. The spatial correlation distance can be specified by defining the correlation range in each direction. The output from the SGSIM simulation is a spatially correlated random number for each grid block. The SGSIM field is then normalized to values between 0 and 1 and used as input to select a value from the desired probability distribution. This provides the capability to create spatially correlated features with a specific distribution. Using these two methods, individual fracture sets can use

random or spatially correlated properties and can have different probability distributions for the fracture parameters. For applications where fracture density varies with depth the FCM can be applied to specified zones at different depth intervals. Thus, the permeability field would include anisotropic permeability representative of different depth intervals.

10.2.2 PFLOTRAN Flow and Transport Simulator

For this study the numerical code PFLOTRAN (Lichtner et al., 2015) has been used to model flow and transport in the far-field of a generic crystalline repository in granite host rock. PFLOTRAN solves a system of generally nonlinear partial differential equations describing multiphase, multicomponent and multiscale reactive flow and transport in porous materials. The code is designed to run on massively parallel computing architectures as well as workstations and laptops (e.g. Hammond et al., 2011). Parallelization is achieved through domain decomposition using the Portable Extensible Toolkit for Scientific Computation (PETSc) libraries for the parallelization framework (Balay et al., 1997). Simulations for this study were conducted using Sandia's high performance computing system. Thus, the parallel implementation of PFLOTRAN allowed efficient computations of different realizations.

10.3   TECHNICAL APPROACH

10.3.1 Comparison of DFN and FCM Fracture Representations

A study was carried out at Sandia National Laboratories (SNL) and Los Alamos National Laboratory (LANL) to compare the DFN and FCM approaches for modeling flow and transport in crystalline rock. The benchmark testing used representative synthetic data for the comparison. Future comparisons will include field data.

As described above, the FCM approach uses distributions of fracture spacing, aperture, strike and dip as input. These parameters are different from the input parameters used at LANL for the DFN approach. A list of the different DFN and FCM parameters are given below. To bridge the difference representations of fractured rock, code modifications were introduced at SNL to evaluate FCM parameters based on specified DFN parameter distributions.

The DFN parameters include:

- *λ - fracture density*
- *R- fracture radius*
- *Fracture Aperture*
- *Fracture Transmissivity (permeability)*
- *Fracture shape (elliptical or rectangular*
- *Fracture shape aspect ratio*
- *a,θ,κ - fracture orientation*

The FCM parameters include:

- *d – fracture spacing*
- *b – fracture aperture*
- *α – fracture plunge (90° – dip)*

- θ – *fracture trend (strike – 90°)*

10.3.2 Evaluation of FCM Parameters Based on DFN Representations

Chapter 9 discusses parameter representations of the DFN approach used at LANL for fracture network generation. Those representations were then used to obtain relationships for FCM parameters. The relationships for individual parameters are described below.

Fracture Spacing Calculation

In the DFN approach, number of fractures is used to compute fracture density for a given domain size. The number of fractures, N_f, in a grid block is calculated using a Poison distribution as follows:

$$Nf(x, \lambda) = \frac{\lambda^x \cdot e^{-\lambda}}{x!}; x\ in\ [0,1]$$ (10-4)

where λ is the sample mean. Fracture spacing is then calculated from:

$$d = \frac{\Delta l}{Nf}$$ (10-5)

where Δl is grid block size, and d is fracture spacing.

Fracture Aperture Calculation

In the DFN approach, aperture is computed based on fracture radius using Equation (6.6). The same method was adopted for the FCM method to obtain aperture values.

$$b = F.R^k$$ (10-6)

where b is the aperture, F and k are parameters, and R is radius of circular fracture, representing fracture size (in case of rectangular fractures, R is a minimum length). The fracture radius R is defined using truncated lognormal distribution.

Fracture orientation (strike and dip) calculation

In the DFN approach, fracture orientation is defined using a Fisher distribution. The Fisher distribution results in an angular deviation from mean orientation, as defined in Equation (10.7):

$$f(\phi', \theta') = \frac{\kappa \cdot Sin(\phi') \cdot e^{\kappa \cdot Cos(\phi')}}{2 \cdot \pi \cdot (e^\kappa - 1)}\ \ , 0 \leq \theta \leq 2\pi$$ (10.7)

where ϕ is the mean trend, θ is the mean plunge, and κ is a dispersion coefficient. The angular deviation is then used to assign the plunge and trend for each grid block in the FCM.

10.4   TECHNICAL RESULTS

For the benchmark comparison of the DFN and FCM approaches, typical generic DFN data was defined based on McKenna and Reeves (2005) and other sources from the literature. Code modifications were then made in the FCM codes to evaluate FCM parameters based on the relationships developed in Section 10.3.2.

10.4.1   FCM Input Parameters and Permeability Field

The number of fractures per grid cell is computed using a Poisson distribution that defines the number of fractures per grid cell using Equation (10-4). The Poisson distribution has a mean fracture spacing of 0.52 fractures per 2 m. The Poisson distribution is shown in Figure 10-3. Fracture spacing is then computed using Equation (10-5). For example, if 1 fracture is specified per 2m, then the fracture spacing is 0.5. As the number of fractures per grid cell increases, the fracture spacing decreases.
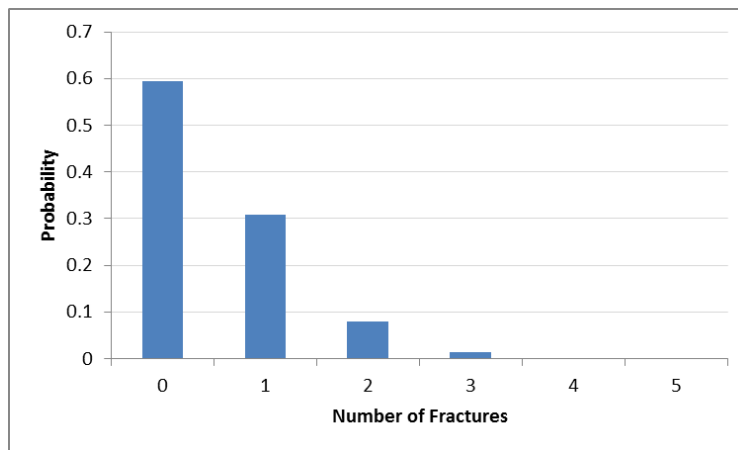
Figure 10-3: Number of fractures per grid cell distribution

Fracture radius is selected from a lognormal distribution with a mean value of 2 m and standard deviation of 1 m, as shown in Figure 10-4a. Equation (10.6) is then used to compute fracture aperture from fracture radius using parameter values of $F = 3.5*10^{-5}$ and $k = 1$. The resulting aperture distribution is shown in Figure 10-4b.
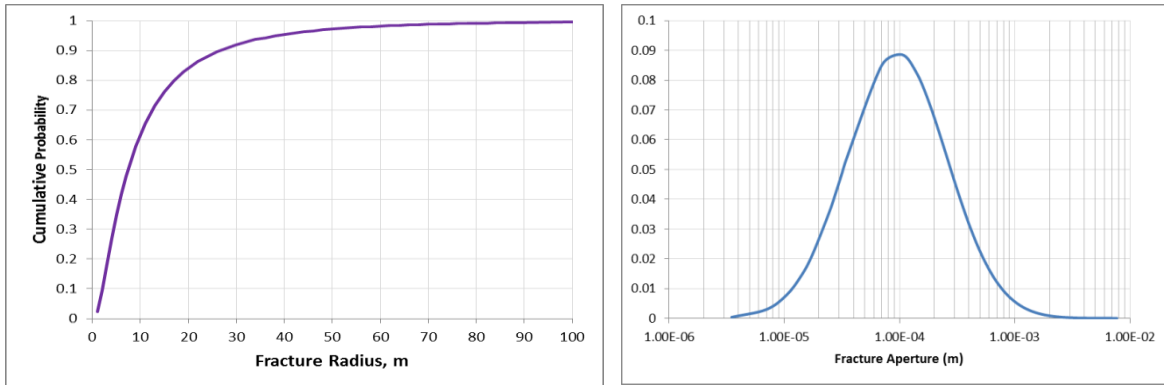
Figure 10-4: a) Fracture radius cumulative probability distribution and b) fracture aperture probability distribution

For the benchmark comparison, two fracture sets were defined. Set 1 has a mean trend of 90° and a mean plunge of 20°. Set 2 has a mean trend of 0° and a mean plunge of 20°. Both sets use a Fisher dispersion coefficient of 50. Equation (6.7) is used to compute fracture orientations for each grid cell. Resulting orientation distributions are shown in Figure 6.5.

Fracture Set 1:Mean trend 90°, mean plunge 20°, κ = 50	Fracture Set 2:Mean trend 0°, mean plunge 20°, κ = 50
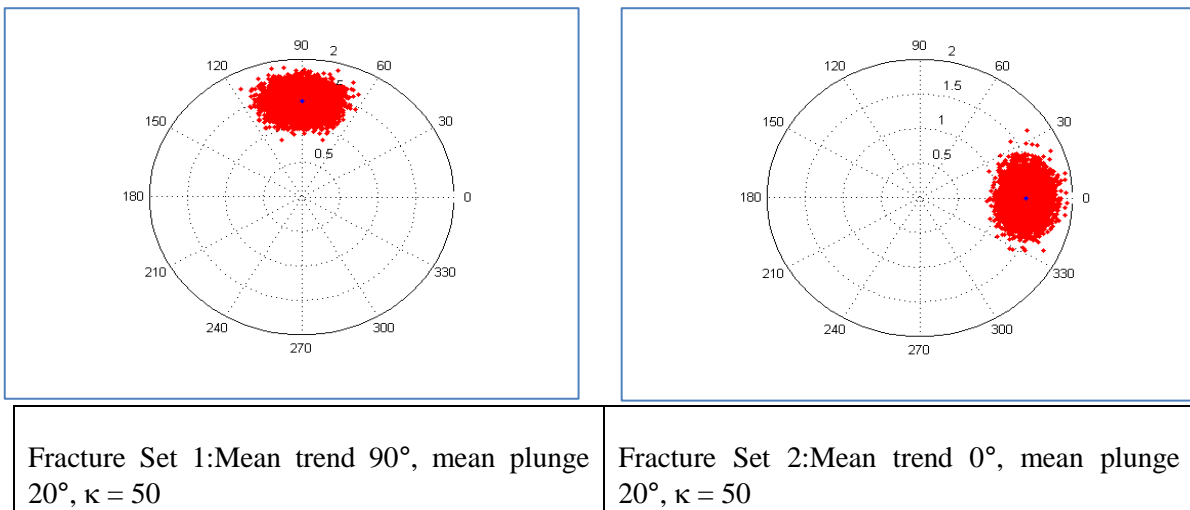
Figure 10-5: Fracture orientation distributions for two fracture sets

To include spatially continuous fractures in the FCM, spatial correlation was introduced by using spatially correlated random numbers generated using SGSIM code. To generate fractures that extend through multiple grid cells, fracture spacing is correlated in the direction of trend and plunge. The correlation length is set to 52 m, the radius of the circular fractures. For each fracture set, spatial correlation for spacing is aligned with the mean orientation of that set. For example, if the spatial correlation for spacing has a trend of 90° and a plunge of 20°, the mean value for trend should be 90° and the mean value for plunge should be 20°. The spatially corrected random variable is then used to select fracture radius for each grid cell, and subsequently compute fracture spacing. All other parameters (fracture trend, plunge, and aperture) are randomly selected from their corresponding distribution.

This process was used to generate 25 realizations for the FCM. The permeability tensor of Chen et al. (1999) was then used to evaluate the fracture permeability field for the FCM method. For the first set of calculations a 3-D domain with 100 m x 100 m x 100m and grid block size of 2 m x 2m x 2m were used. The resulting permeability field for a single realization (Realization 25) is shown in Figure 10.6. The corresponding permeability probability distribution for Realization 25 is shown in Figure 10.7.
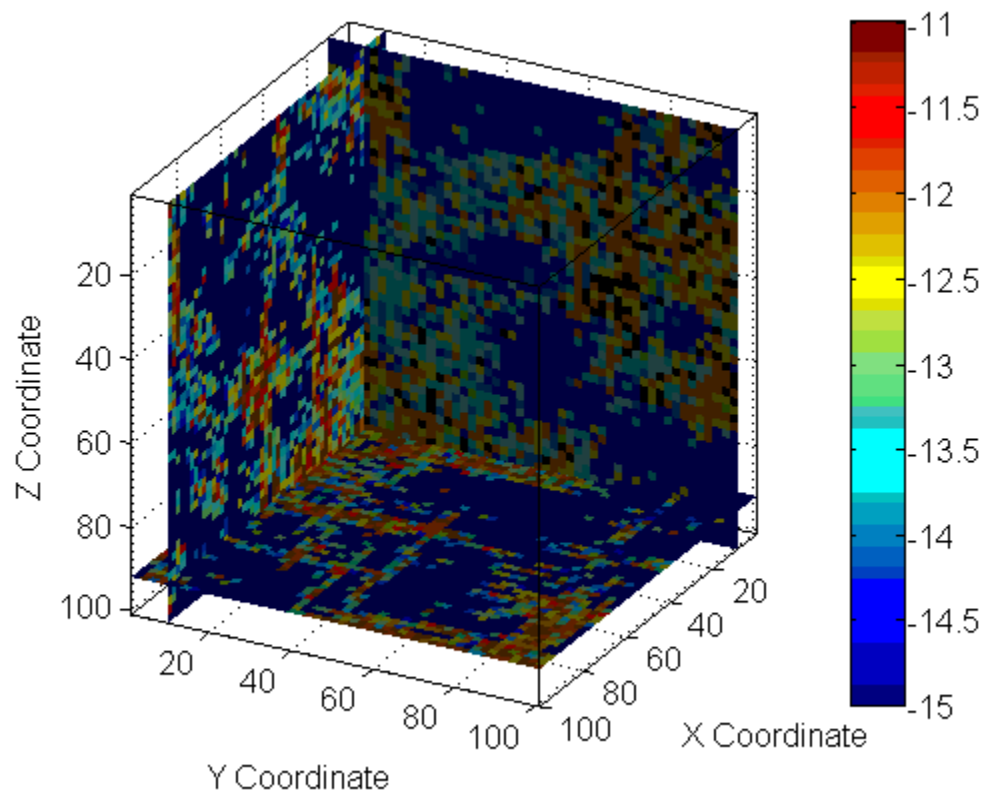
Figure 10-6: FCM fracture permeability field for a single realization
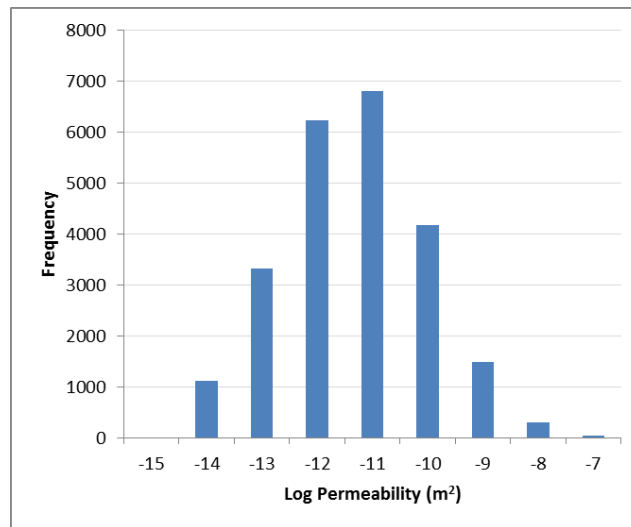
Figure 10-7: Simulated probability distribution for FCM fracture permeability field for Realization 25. Note that the background permeability of 10^{-15} m^2 is not included in the plot. It covers 60% of the permeability field.

10.4.2   Flow and Transport Simulation with FCM Fracture Representation Only

In this section, we describe flow and transport simulations conducted using the FCM approach. Comparison of the FCM and DFN approaches is described in Section 6.4.4.

Model setup

For the test problem, the domain is assumed to be at a depth of 500 m. The model geometry is 100 m x 100 m in the horizontal direction and 100 m in the vertical direction. The mesh consists of a structured grid with 125,000 elements (132651 nodes) and a constant grid block size of 2 m x 2 m x 2 m. The input data include porosity value of 0.01, tortuosity of 1.0, rock density of 2800 kg/m^3 and diffusion coefficient of 1 x 10^{-9} m^2/s. Permeability fields were calculated for 25 realizations as described in Section 10.4.2.

For the simulation, the system was assumed to be at hydrostatic pressure initial conditions. Regional ground water flow is represented by a pressure gradient from west to east. Boundary conditions include:

- Pressure of 5 MPa at top of domain
- Pressure at top of West Face: 5.1 MPa
- Pressure at top of East Face: 5.0 MPa

A source was also defined at a specified point in the domain. The tracer injection point is the location: X = 30 m, Y = 50 m, Z = 50 m. An injection rate of 1 x 10^{-4} m^3/s and tracer concentration of 1.0 M were defined.

FCM simulations were then made with the above data and the permeability fields using the PFLOTRAN code. The flow and transport simulations for the 25 realizations were carried out to

total time of 10^6 years. Simulation results are shown in Figures 10.8 to 10.12. The results include pressure and tracer distributions, tracer concentrations at selected observation points, and breakthrough curves for transport through the east face. Figure 10.8 shows distribution of pressure for Realization 25, indicating pressure gradient from west to east (x-axis). Figure 10-9 shows tracer transport for the same realization after 1 year of simulation. The contours are for different slices in the X, Y and Z planes, relative to the injection point. Figure 10-10 shows tracer concentration at the specified observation points as a function of time. The results show that very little tracer concentration is transported to the third observation point (i.e. at location X = 70 m, Y = 50 m, Z = 10 m) as it is at a much lower depth compared to the other two observation points. Figure 10-11 is for tracer concentration at Observation 1, which is at the center of the domain, for all realizations. As shown, some of the realizations have low tracer concentrations at this location, which is a result of the corresponding permeability fields. Figure 10-12 shows breakthrough curves for the east face of the domain, for all realizations. The breakthrough curves show minimal spread.
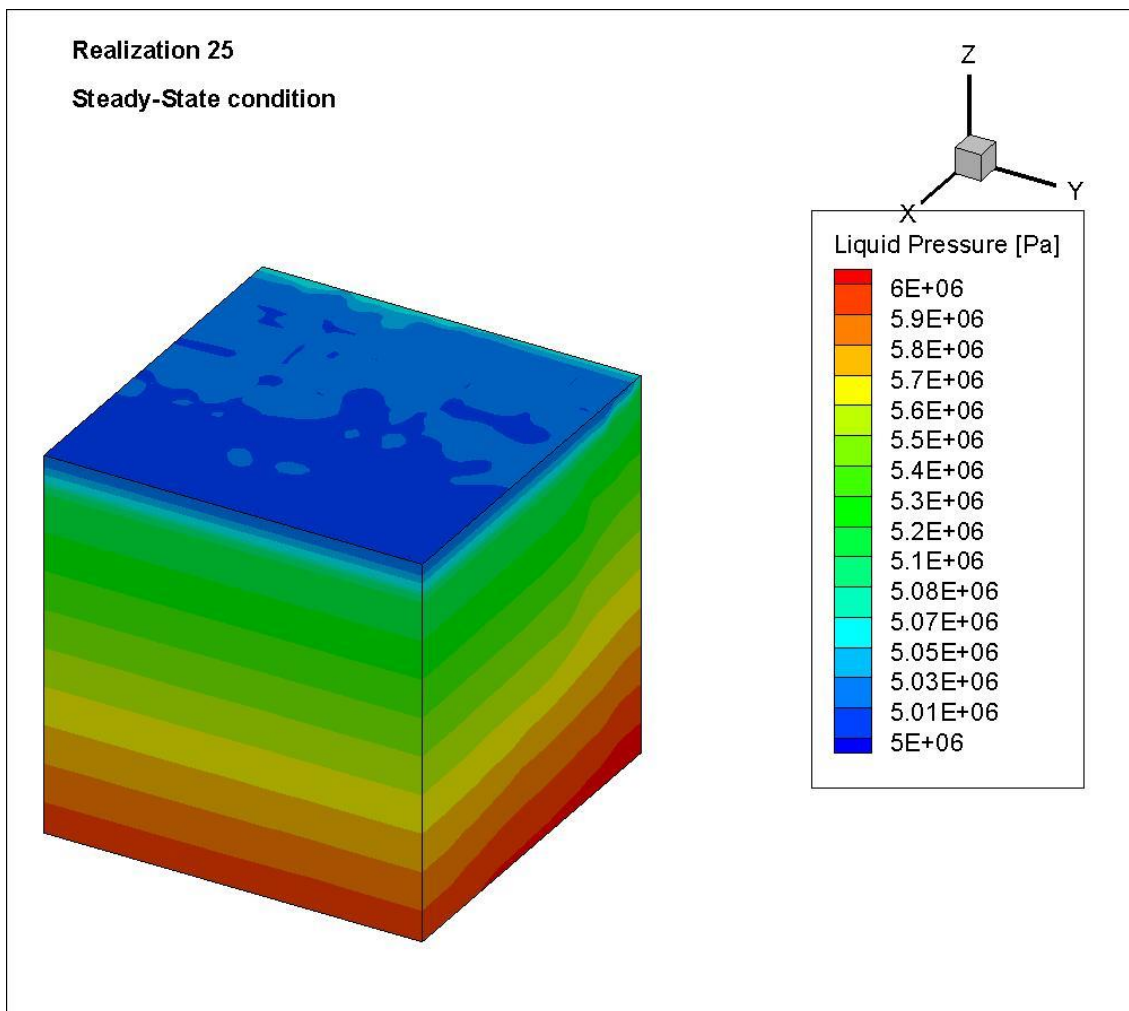
Figure 10-8: Steady state pressure distribution for Realization 25
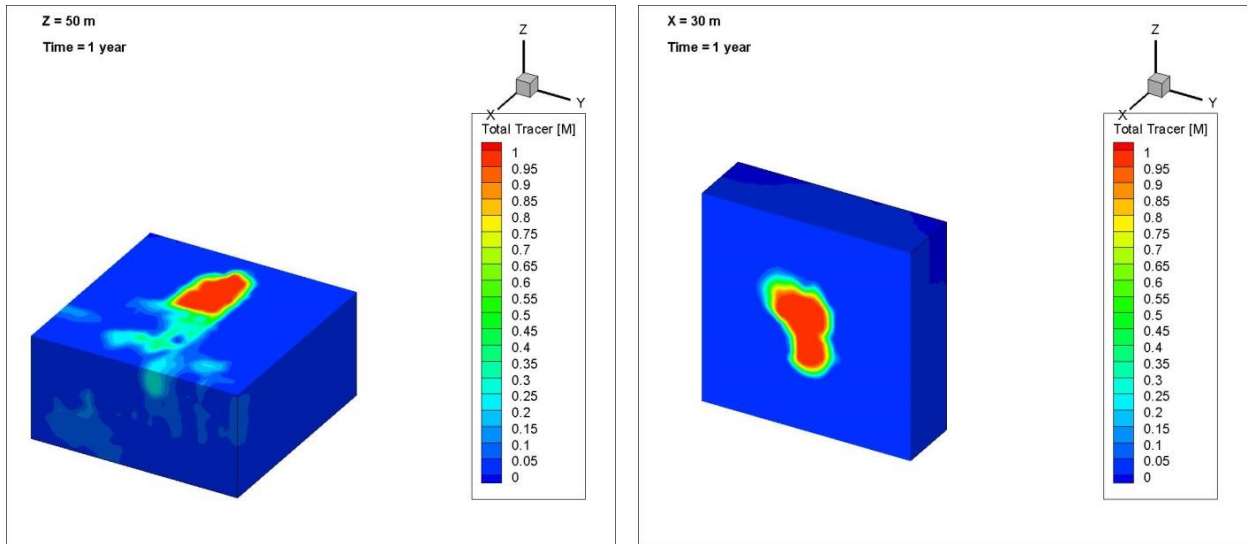
a)   b)
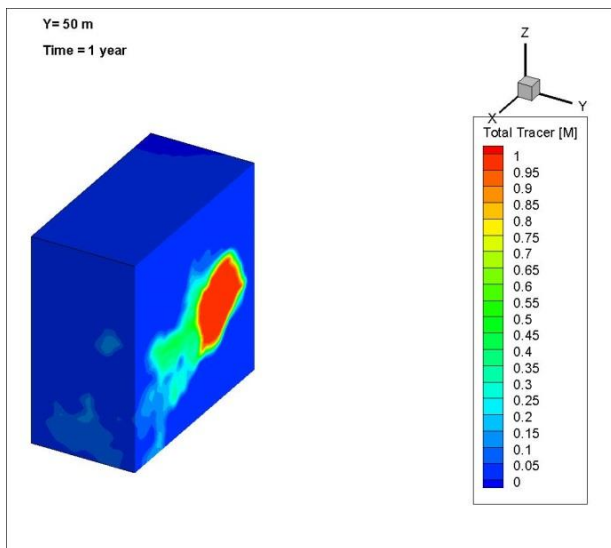
c)

Figure 10-9: Distributions of tracer transport for Realization 25 after 1 year simulation time. a) Z-plane at Z = 50m, b) X-Plane at X = 30 m, and c) Y-plane at Y = 50 m.
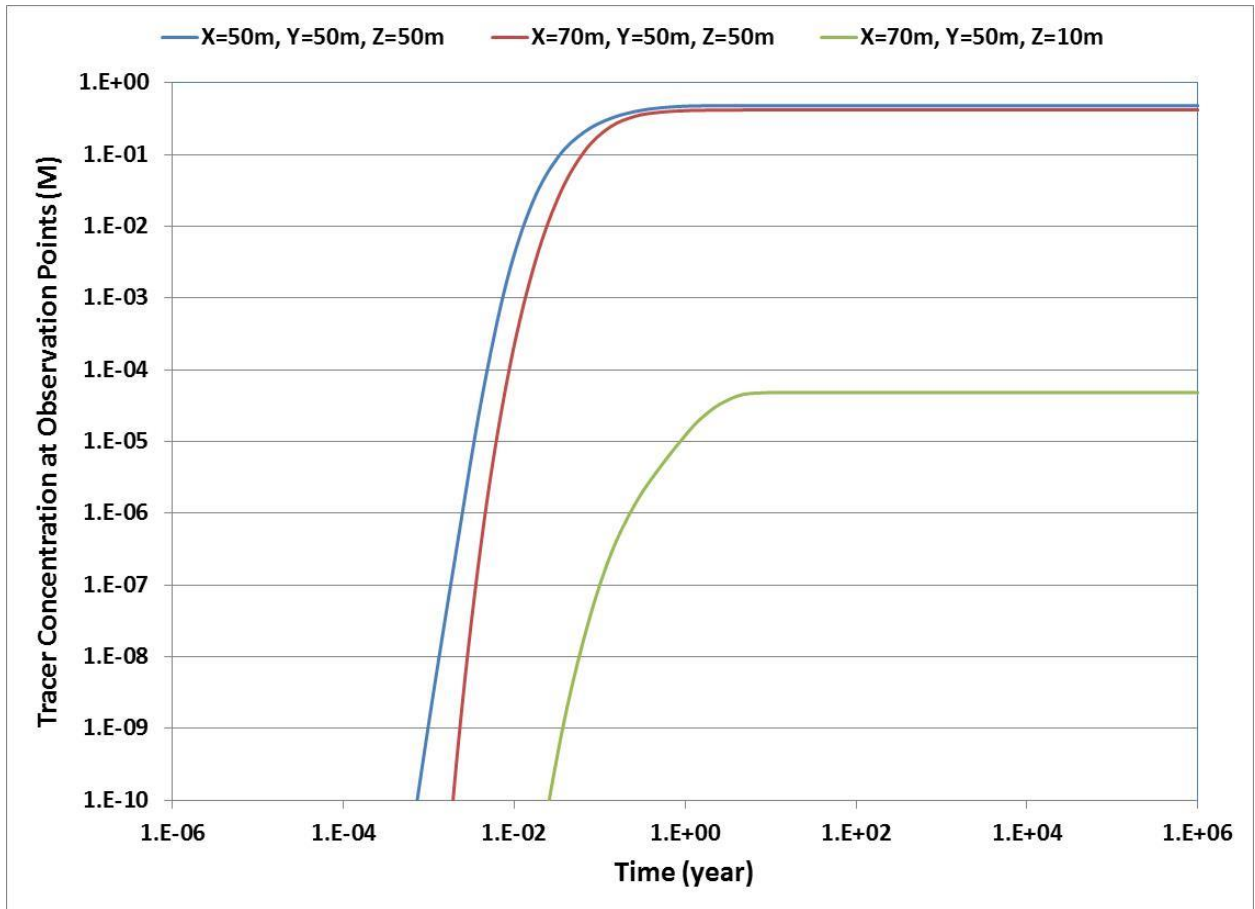
Figure 10-10: Plot of tracer concentration vs. time at selected observation points for Realization 25.
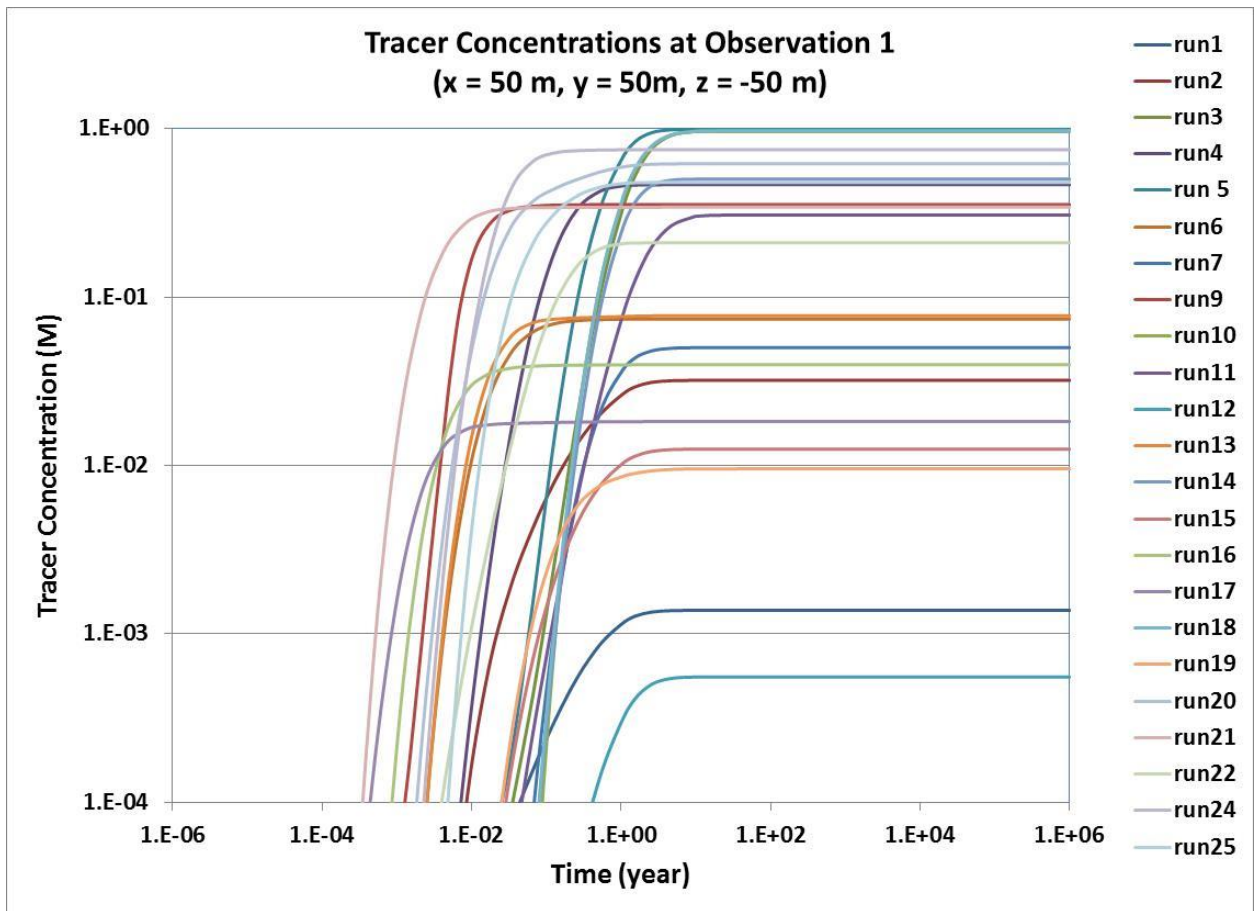
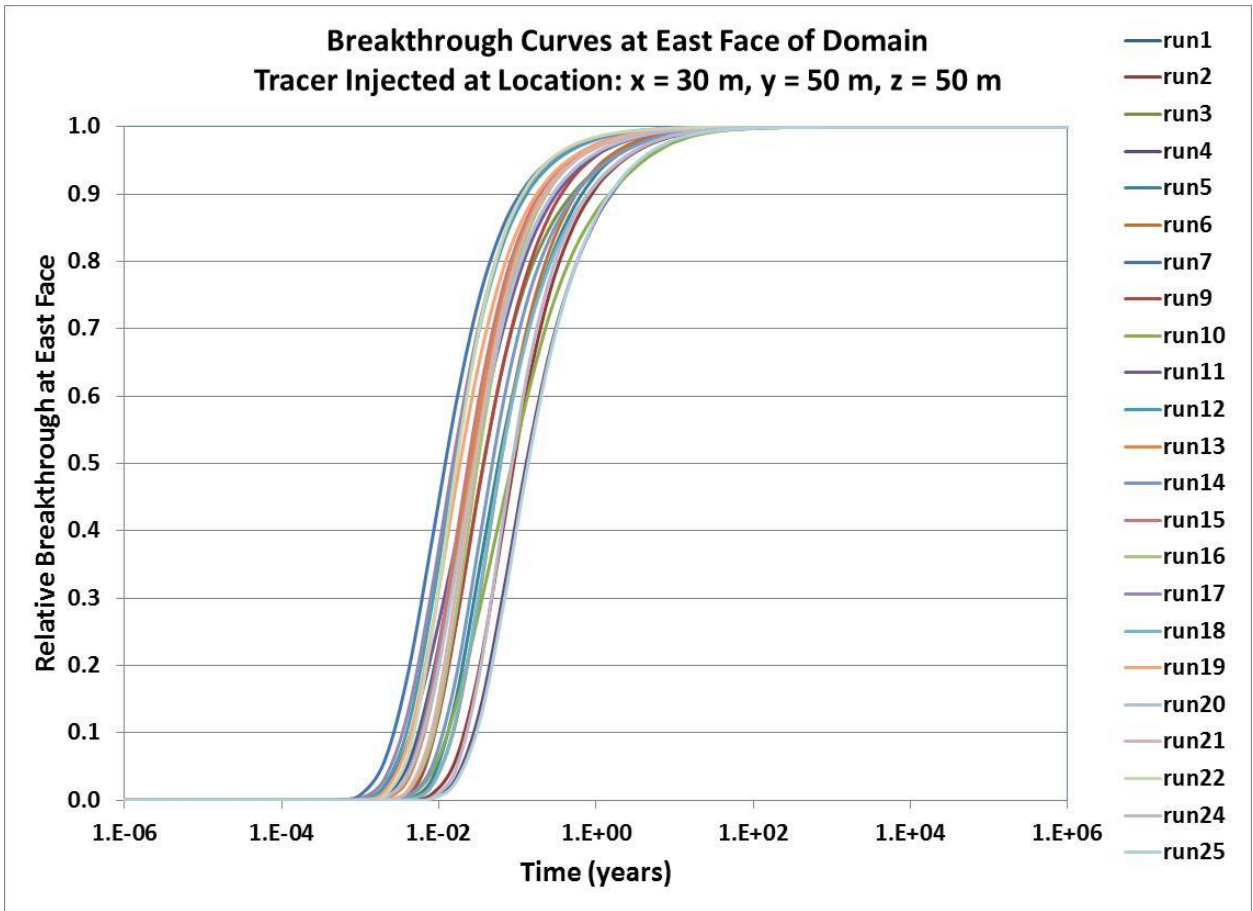**Figure 10-11:** Plot of tracer concentration vs. time at Observation Point 1 for all realizations.

Figure 10-12: Plot of tracer relative breakthrough curves vs. time at east face of domain.

10.4.3 Flow and Transport Simulations with DFN and FCM Fracture Representations

In this section we describe flow and transport simulations for the benchmark comparison conducted using both DFN and FCM approaches. FCM simulations are described below. DFN simulations are described below.
.

FCM Simulation for comparison with DFN

For the test problem the domain is assumed to be at a depth of 500 m, as in Section 10.4.3. In this case a smaller model geometry with 50 m x 50 m in the horizontal direction and 50 m in the vertical direction is used. For modeling with the FCM approach the mesh consists of a structured grid with 125,000 elements (132651 nodes) and a constant grid block size of 1 m x 1 m x 1 m. The input data include porosity value of 0.01, tortuosity of 1.0, rock density of 2800 kg/m^3 and diffusion coefficient of 1×10^{-9} m^2/s. Permeability fields were calculated for 25 realizations as described in Section 6.4.2 but for the new model geometry and grid block size.

For the simulations in this section the system was assumed to be at a constant pressure initial condition, with no hydrostatic pressure variations with depth. Regional ground water flow is represented by a pressure gradient from west to east. Boundary conditions include:

- pressure of 5 MPa initial condition (dirichlet)
- Pressure on West Face: 5.1 MPa (dirichlet)
- Pressure on East Face: 5.0 MPa (dirichlet)

For the test problem tracer was placed at the center of the west face and allowed to move to the east face due to advection as a result of the pressure gradient. FCM Simulations were then made with the above data and the permeability fields using the PFLOTRAN code. The flow and transport simulations for the 25 realizations were carried out to total time of 10^6 years. Simulation results are shown in Figures 10-13 to 10-16. The results show permeability, pressure and tracer distributions of selected realizations. The realizations were selected to represent fast (Realization 7) and slow (Realization 10) transport to the east face. The results also include breakthrough curves for transport through the east face. Realization 7 represents a higher permeability field (Figure 10-13). Figure 10-14 shows distribution of pressure for Realization 7 and Realization 10 with pressure gradient from west to east (X-axis). Figure 10-15 shows tracer distribution for the same realizations after 1 year of simulation. The figure on the left (for Realization 7) displays a wide tracer spread, indicating faster transport. The tracer spread for Realization 10 is not as wide because of the lower permeability (see Figure 10-13). Figure 10-16 shows breakthrough curves for the east face of the domain, for all realizations.
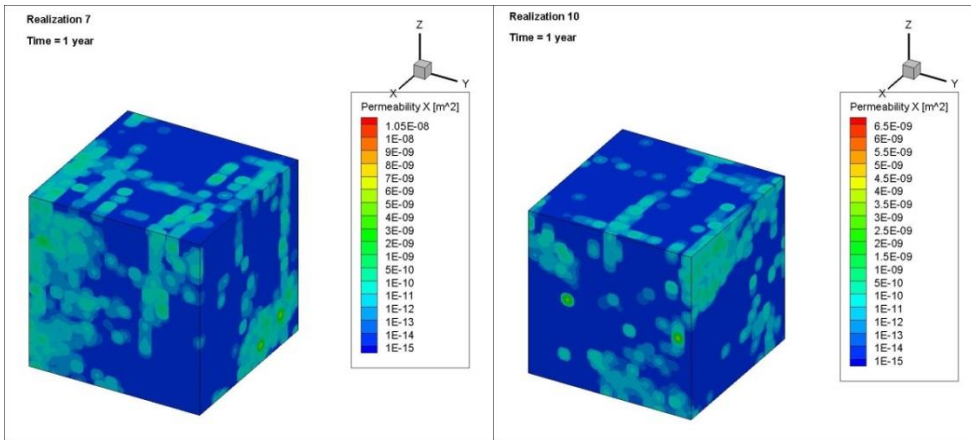
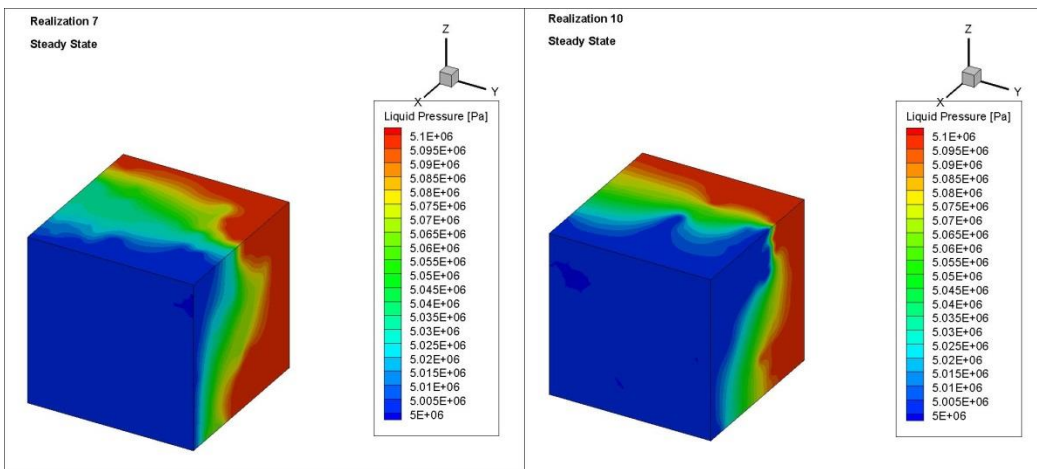**Figure 10.13:** Permeability distribution for Realization 7 (left) and Realization 10 (right)

Figure 10-14: Steady state pressure distribution for Realization 7 (left) and Realization 10 (right)
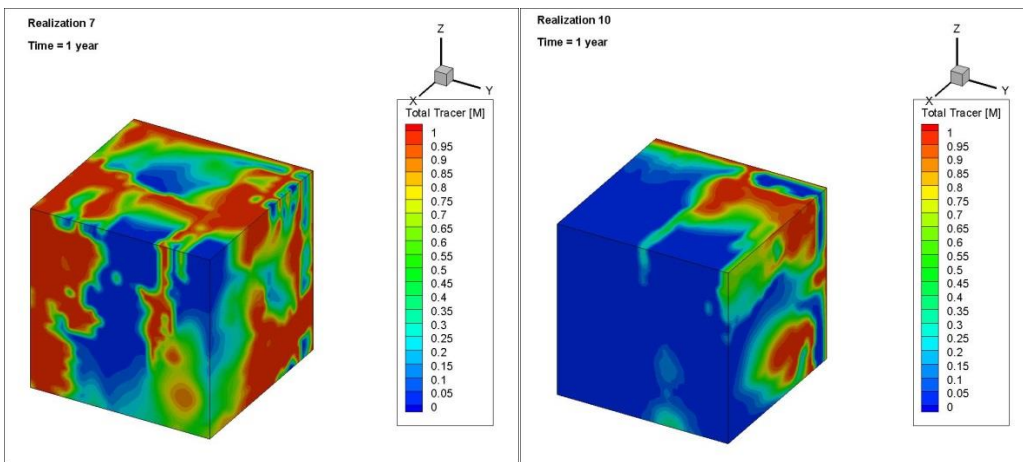

Figure 10-15: Tracer distribution after 1 year simulation time for Realization 7 (left) and Realization 10 (right)
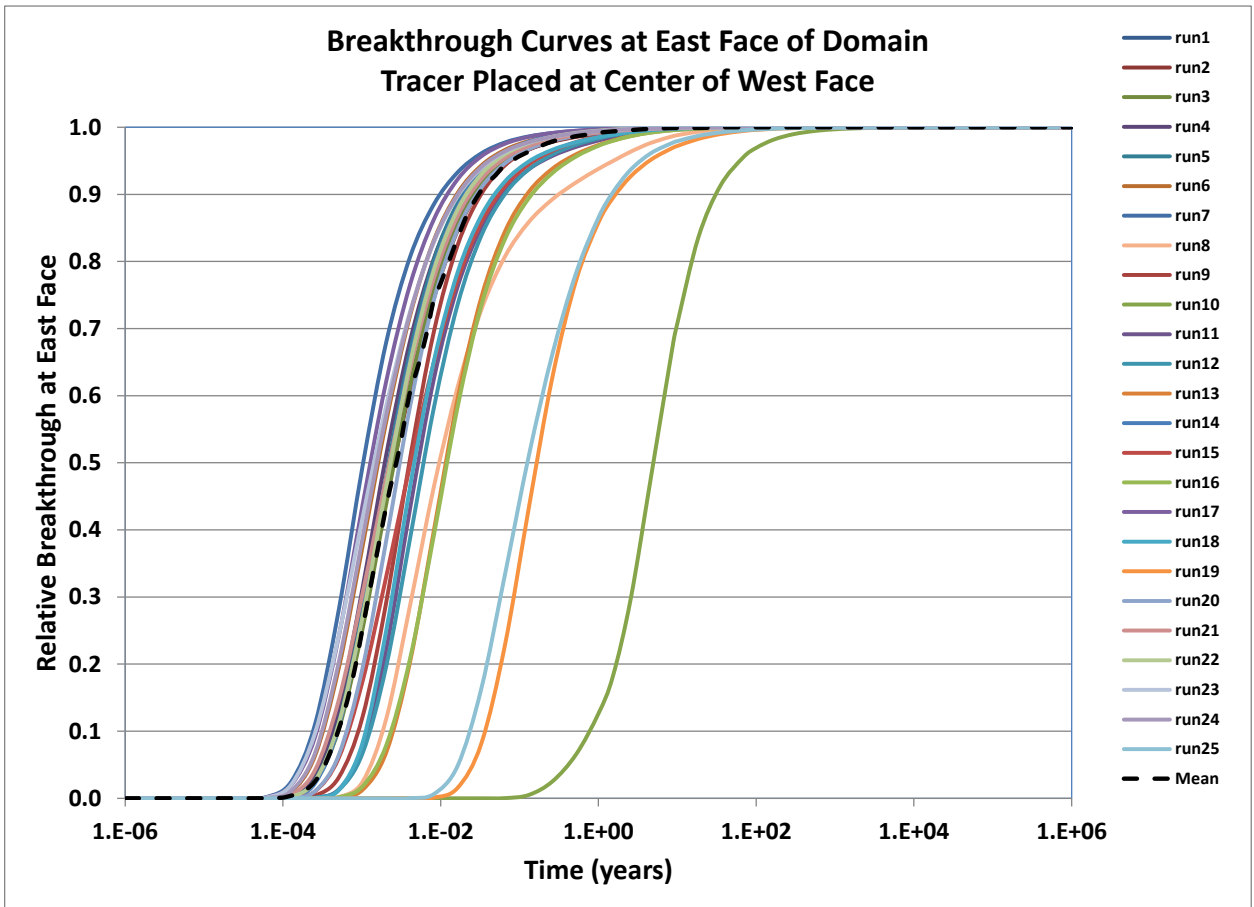
Figure 10-16: Plot of tracer relative breakthrough curves vs. time at east face of domain

Modeling Advective Transport in Discrete Fracture Network using dfnWorks

The three-dimensional DFN are generated and meshed for computation using the feature rejection algorithm for meshing (fram) introduced by Hyman et al. [2014]. The fractures are represented by two-dimensional planar objects, which are intersecting each other in three-dimensional domain. Each fracture is assigned its location, orientation, size, aperture and transmissivity. Once the fracture network is generated, the LaGriT meshing toolbox [LaGriT, 2013] is used to create a high resolution computational mesh representation of the DFN in an intrinsically parallel fashion where each fracture is meshed   individually and in parallel.

An algorithm for conforming Delaunay triangulation is implemented so that meshes on intersecting fractures coincide at the intersections [Mount and Gable, 2001] and Voronoi control volumes suitable for finite volume solvers such as   FEHM [Zyvoloski, 2007], TOUGH2 [Pruess et al., 1999], and PFLOTRAN [Lichtner et al., 2015] are produced. In the current simulations PFLOTRAN is used to obtain a steady-state pressure solution to the steady-state fully-saturated flow equations.

Flow solver provides flow fluxes on each face of control volume cells. We use reconstruction velocity method proposed in [Painter et al., 2012] to obtain Darcy velocities of flow on each cell center, on fracture intersections, and on fractures boundary cells. Given the reconstructed velocities, pathlines are determined via advective particles using the methods of Makedonska et al. [2014]. In short, the governing equations of particle movement, $\dot{\mathbf{x}}(t) = \mathbf{v}(\mathbf{x}(t))$, are numerically integrated using an adaptive time-step predictor-corrector method coupled with barycentric interpolation to obtain particle   velocities away from cell centers.

Discrete Fracture Network Parameters: synthetic data of simplified test: The following fracture parameters are used to generate 25 DFN independent realizations in the simulation for the DFN-FCM comparison:

- Domain size: 50m x 50m x 50m, with following axis coordination: -25<X<25; -25<Y<25; -25<Z<25.
- Minimum edge length of unstructured computational mesh is 0.3 m.
- The average fracture density over 25 independent DFN realizations) is P_{32}=0.74 (P_{32} is an area of fracture surface per unit volume).
- The average number of fractures is 6000, which is calculated according to FCM density, where the fracture frequency is described by a Poisson distribution with an expected value of 0.52 fractures per 2 m. One of DFN realizations is shown in Figure 10.17.
- The fractures shape is an elliptical with aspect ratio 2:1.
- The fracture radius distribution follows the lognormal distribution. The mean radius is 2 m and the standard deviation is 1 m. The fracture radius cumulative distribution of one DFN realizations shown in Figure 10.18.
- Fractures orientation follow Fisher Distribution with κ =50.
- There are two fracture sets:
  - Fracture set 1 is orientated north-south with mean trend (*Phi*) 90^0 and mean plunge (*Theta*) 20^0
  - Fracture set 2 is orientated east-west with mean trend (*Phi*) 0^0 and mean plunge (*Theta*) 20^0.

- The fracture aperture (*b*) is defined using the following relationship: $b = F \cdot R^k$ The parameters are defined as follows: F=3.5*10^{-5} and k=1. The distribution of fracture aperture is shown in Figure 10-19a.

- Fractures permeability is calculated according to cubic law [Adler et al., 2012]: $k = \frac{b^2}{12}$. The distribution of fracture permeability is shown in Figure 10-19b.
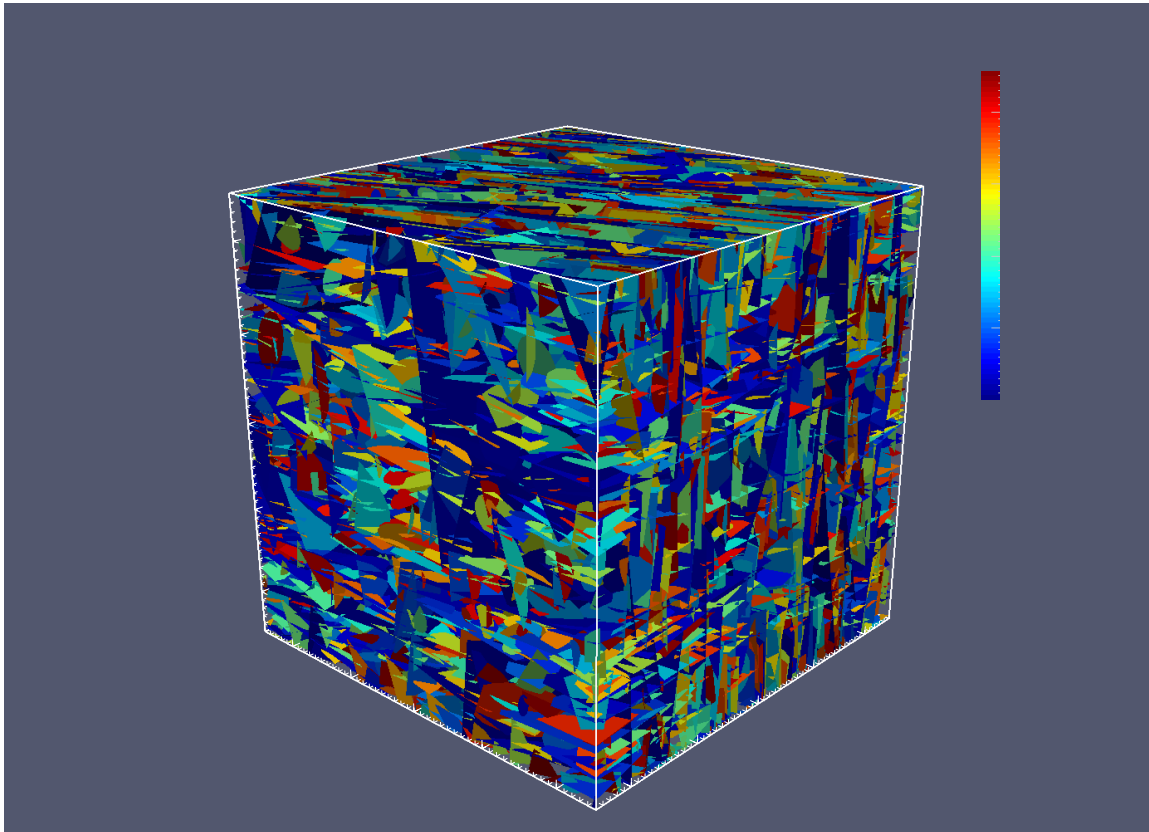

Figure 10-17: Example of one of DFN realizations. There are 6853 two-dimensional polygons, representing fractures, are placed in three-dimensional domain and colored individually by their material ID number.
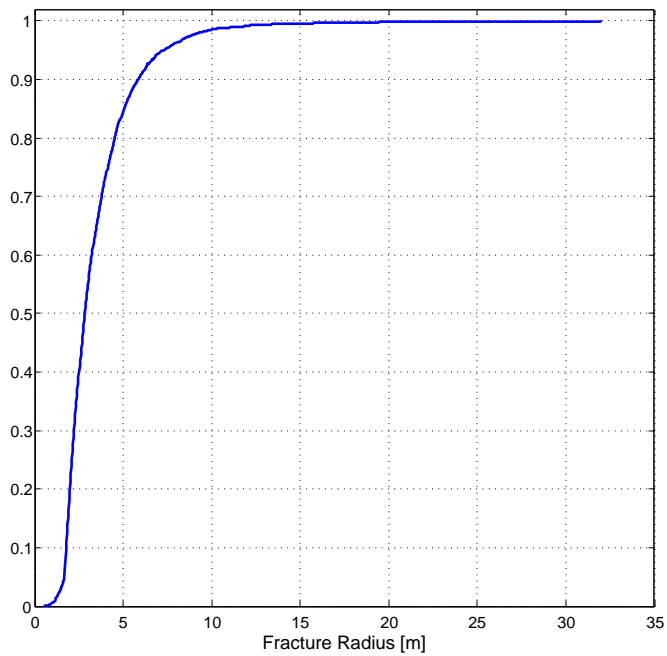
Figure 6-18: Cumulative distribution of fracture radii. Fracture radii follow lognormal distribution.
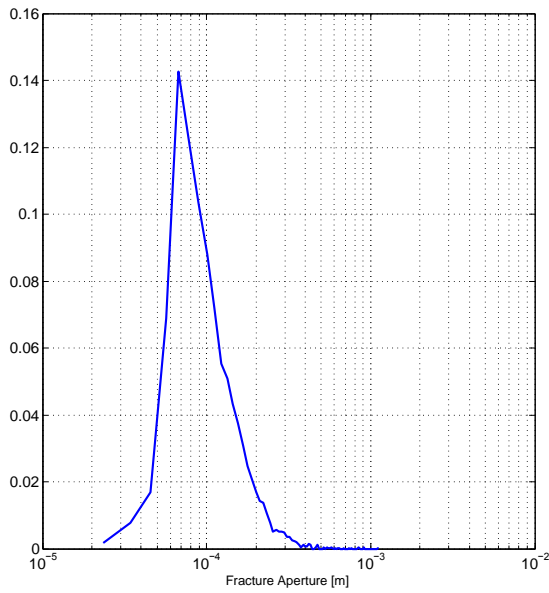
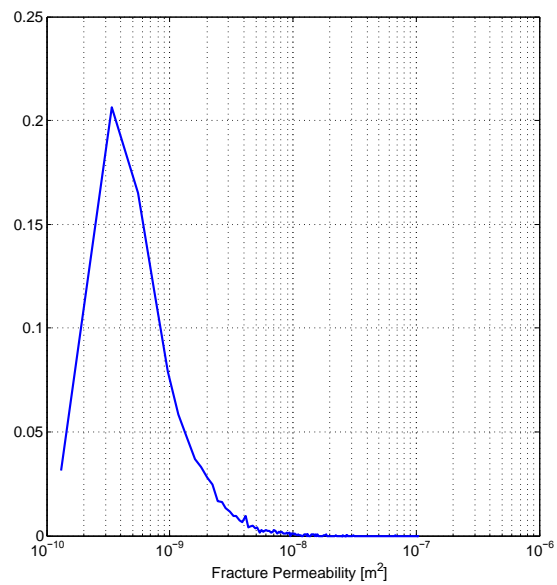**Figure 6-19a:** Fracture aperture distribution.

Figure 6-19b: Fracture permeability distribution.

Flow Parameters:

- The initial pressure is set to be 5 MPa, while west side of the domain is 5.1 MPa, Dirichlet boundary conditions.

- Assume there is no flow on top, bottom, front and back faces of the domain.
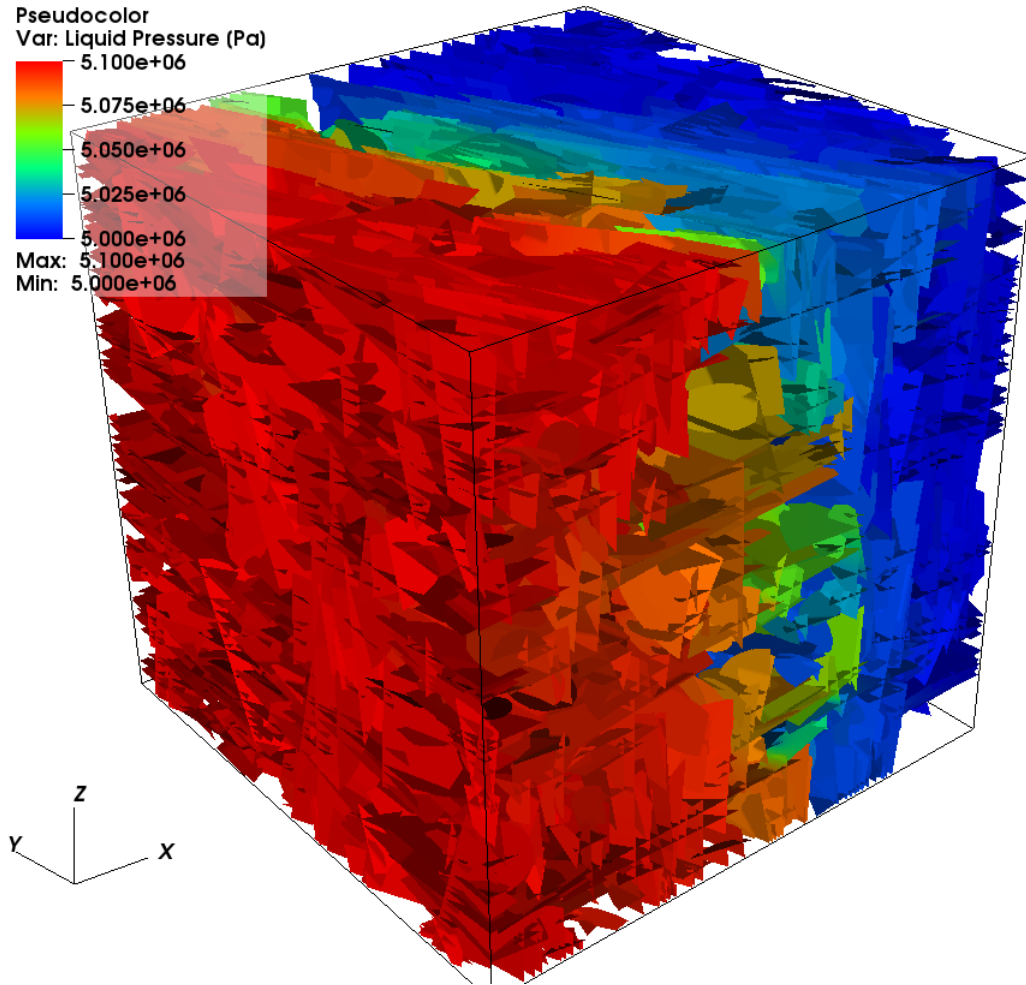
Steady state pressure solution for one of DFN realizations is shown in Figure 10-20.

Figure 10-20: Steady state pressure solution for one of DFN realizations is obtained. Worm red colors represent high pressure. Pressure gradient changes from left to right side of the domain, assuming fluid flow from West to East side.

First Numerical Transport Experiment: Particles Injection at a Center of West Face

In first numerical simulation of transport (Case 1) all particles are initially located in the center of West face. The location of injection region is: x=-25.0; -3.0< y <3.0; -3.0< z <3.0. Particles are placed on edges of fractures that cross the injection region. A total of 2.2 x 10^6 particles participated in the experiment in all 25 DFN realizations.

Figure 10-21 shows 4000 particles trajectories colored by the fracture aperture. Figure 10-22 shows the same particles trajectories colored by their velocity. High space dispersion is shown by particles paths: starting from the center of West face particles leaving the domain over whole East face.

Figure 10-23 shows Breakthrough Curves (BTC) for 25 realizations. The blue bold line represents the average of BTC over all 25 DFN realizations. The difference of BTC between realizations can be explained by complicated geometrical structure of fracture network in the domain. Particles tend to travel in the direction of flow, which is carried by big fractures with higher aperture and higher permeability. The injection region at the center of West face not necessary directly connected to big fractures, on the contrary, it may take a long path through small fractures with low permeability to reach the main flow or East face. In those cases, BTC are shifted to longer times. In other DFN realizations, when large fractures are crossing injection regions, or located close to it, particles need shorter time to reach East face of the domain.
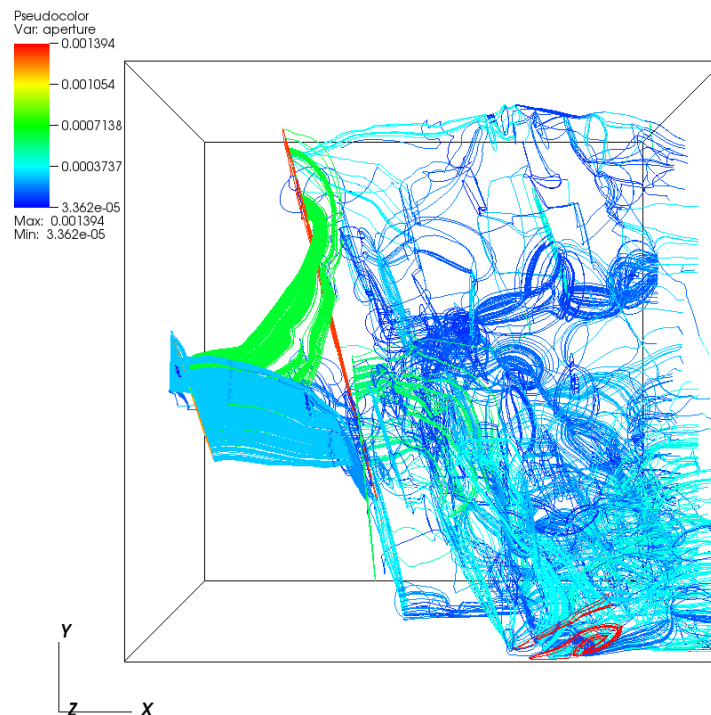

Figure 10-21: 4000 particles trajectories, initially placed on the center of West face, moving across domain size, showing high space dispersion. Trajectories are colored by fracture aperture – Case 1
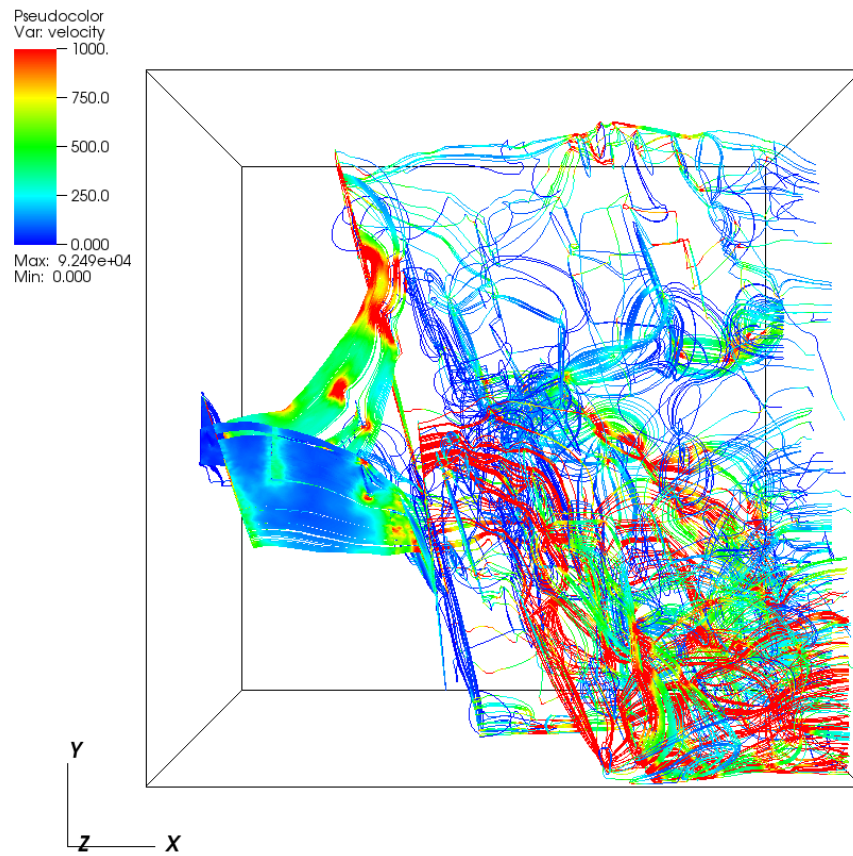
Figure 10-22: 4000 particles trajectories, initially placed on the center of West face, are colored by their instanteneous velocities – Case 1

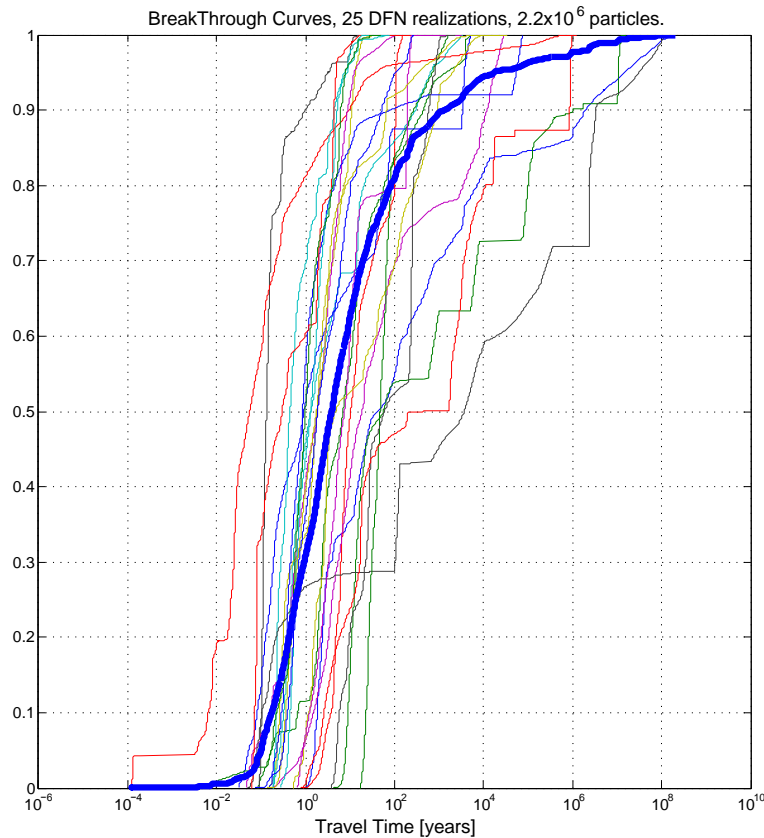BreakThrough Curves, 25 DFN realizations, 2.2x10^6 particles.

Figure 10-23: Breakthrough Curves of transport through 25 independent DFN realizations. Bold blue line shows an average BTC over all realizations – Case 1

Second Numerical Transport Experiment: Uniform Particles Injection over West Face

In second numerical simulation of transport (Case 2) all particles are initially uniformly distributed on all fracture edges at West face. There are 2.0 x 10^6 particles participating in the experiment in all 25 DFN realizations.

Figure 10-24 shows 3000 particles trajectories colored by the fracture aperture. Figure 10-25 shows the same particles trajectories colored by their velocity. Figure 10-26 shows Breakthrough Curves (BTC) for 25 realizations. Blue bold line shows an average BTC over all realizations. Less difference of BTC between realizations is observed in the experiment with uniform distribution of particle injections at West face. We speculate that this is a result of higher probability of connection to the main flow.
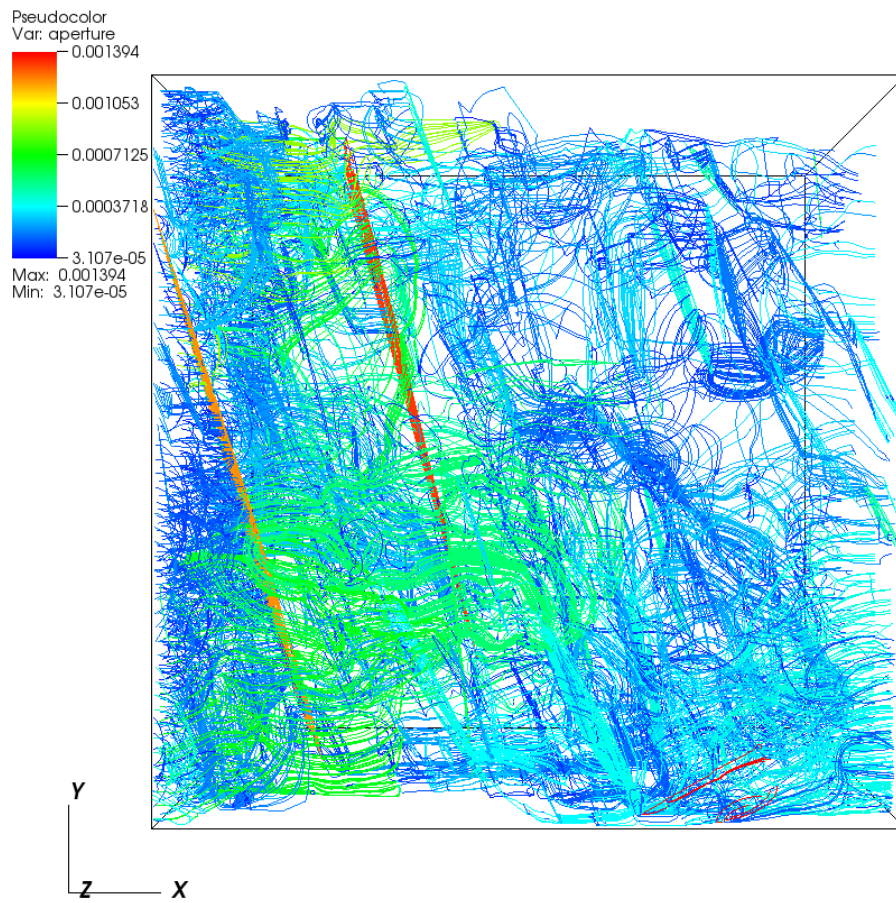
Figure 10-24: 3000 particles trajectories, initially uniformly distributed at West face, moving across domain size, showing high space dispersion. Trajectories are colored by fracture aperture – Case 2
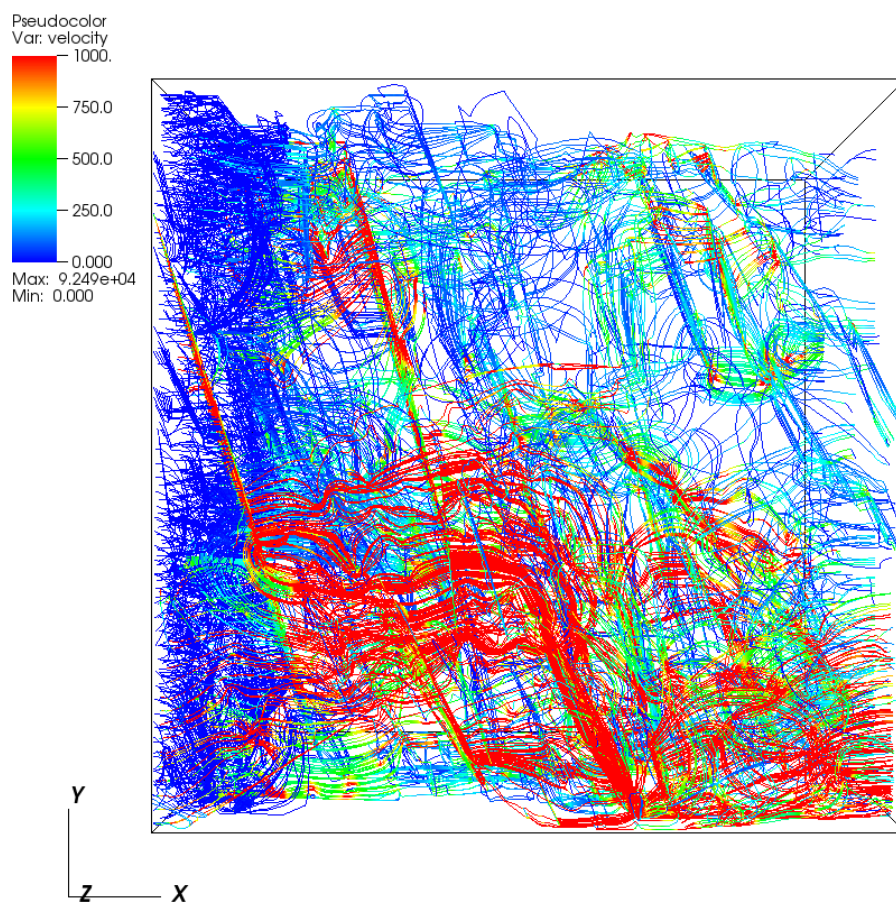
Figure 10-25: 3000 particles trajectories, are colored by their instanteneous velocities – Case 2
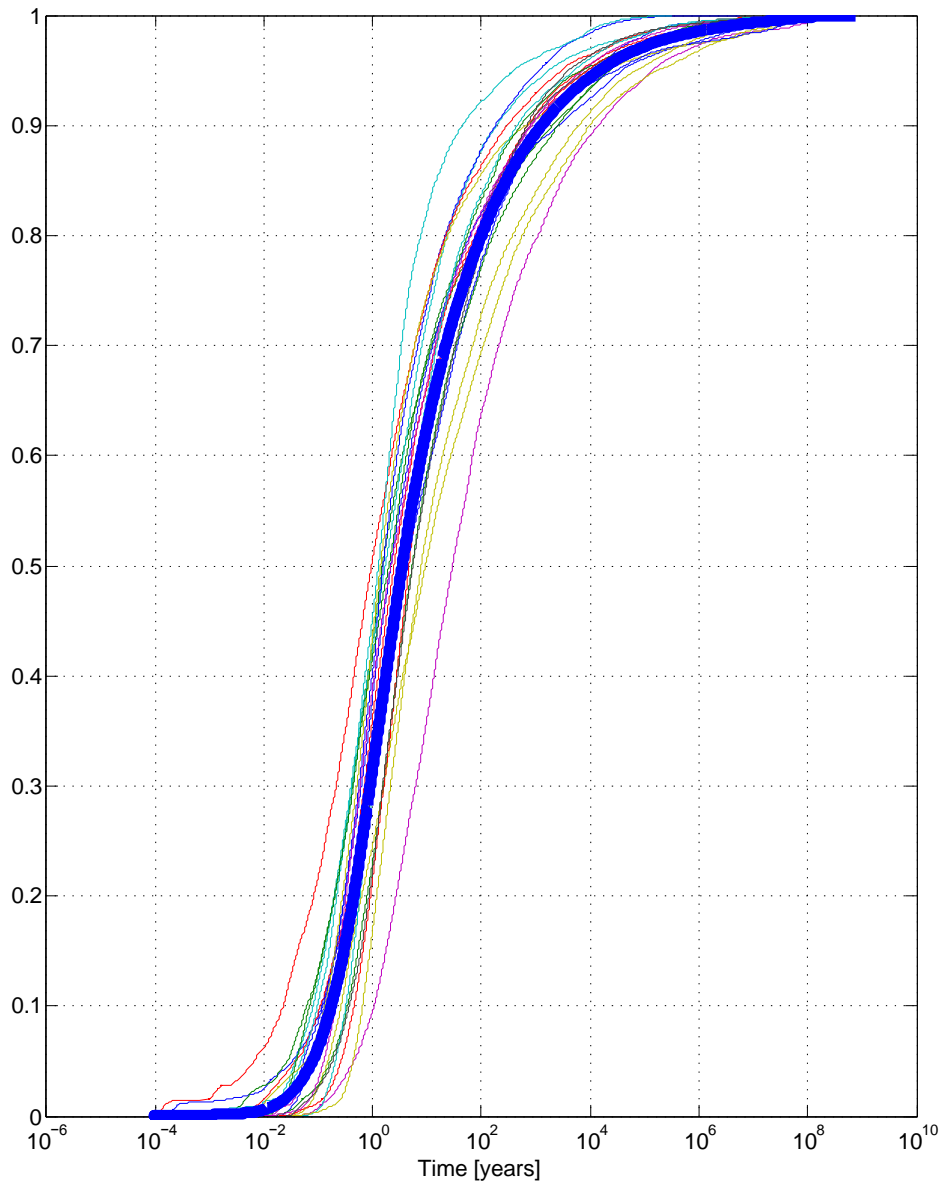
Figure 10-26: Breakthrough Curves of transport through 25 independent DFN realizations. Bold blue line shows an average BTC over all realizations – Case 2

Comparison of DFN and FCM simulation results

As shown above, both DFN and CFM simulation models used similar fracture data and problem definition. Both used the same domain geometry (50 m x 50 m x 50m), and boundary and initial conditions. In both cases tracer is placed at the center of the west face and advected to the east face due to the imposed pressure gradient. Breakthrough curves for tracer transport at the east face for both methods are shown in Figures 10-16 and10-23. Figure 10-16 (FCM) shows less spread compared to Figure 10-23 (DFN), with the exception of a few outliers. Figure 10-27 shows comparison of the average breakthrough curves from both the DFN and FCM modeling results. The average curves show similar trends, with a gap between the two. The bottom part shows the DFN breakthrough delayed by about two orders of magnitude. The middle and top parts show the DFN curve tailing over a much longer time than the FCM curve.

Although an effort was made to reduce differences between the modeling of the two approaches, there were still some differences. Both simulations used PFLOTRAN code for flow modeling. However, as indicated above two simulation methods and two codes were used for transport. For FCM transport the PFLOTRAN code was used, solving advection-diffusion equations. For DFN transport the particle tracking approach was used (Makedonska, 2014). The tailing at the top of the DFN curve could be attributed to the use of the particle tracking method. Another reason for the differences in the results might be due to the use of coarse discretization in solving the advection-diffusion equation for the FCM simulations causing numerical dispersion. However, as a relatively fine mesh (1m x 1m x 1m) was used the effect of numerical dispersion is expected to be minimal. Further study is needed for the interpretation of the DFN and FCM fracture representations. The study could include comparison of effective permeability of the two methods. The benchmark testing showed that both methods are suitable to model flow and transport in the far-field but can also be applied to thermal-hydrologic-chemical modeling. The experience of the use of the FCM approach to geothermal thermal-hydrology modeling can be leveraged.
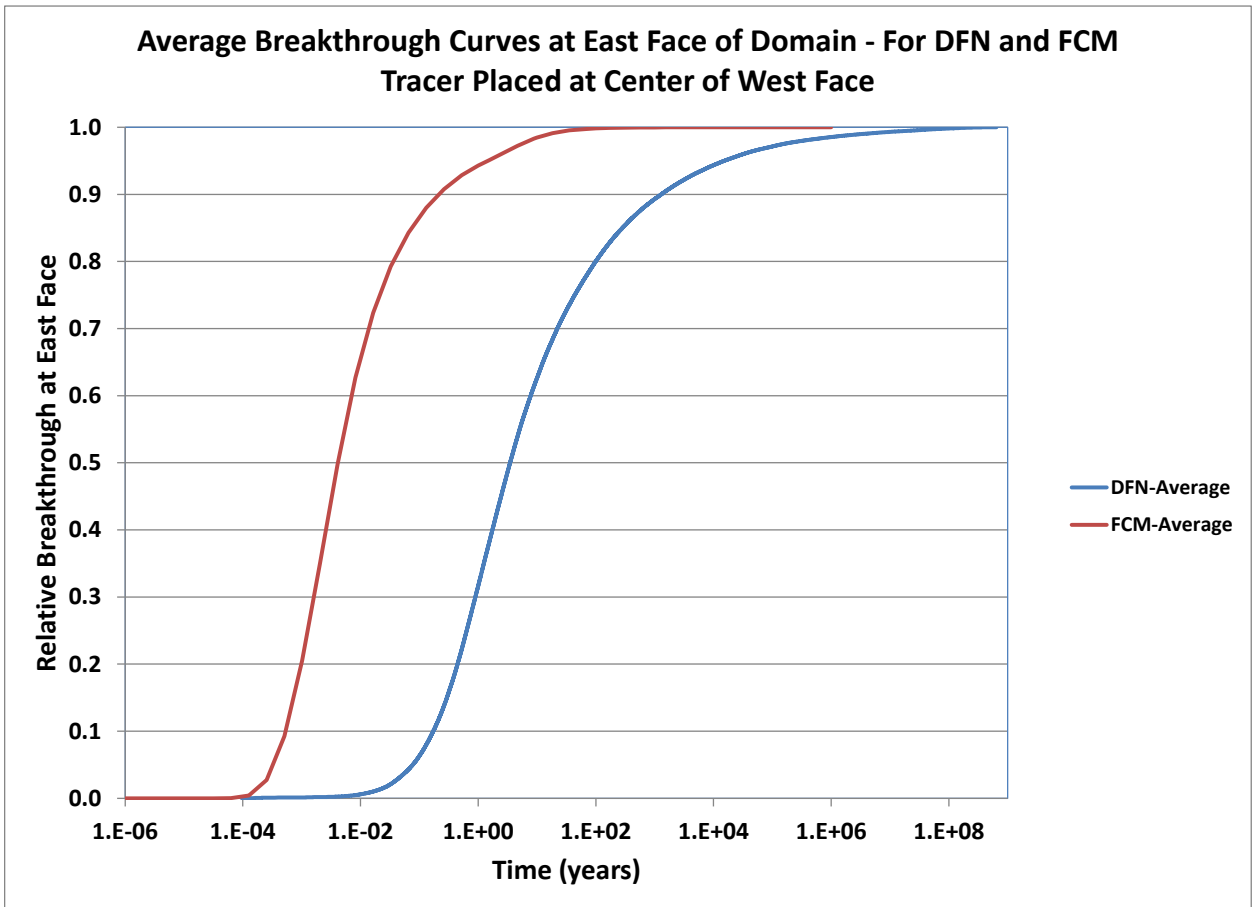
Figure 10-27: Comparison of DFN and FCM average tracer relative breakthrough curves vs. time at east face of domain (average of 25 Realizations)

10.5   CONCLUSIONS AND FUTURE WORK

The work documented in this chapter explores the use of the FCM approach to model flow and transport in a generic fractured crystalline nuclear waste repository. The FCM is a continuum representation of fractured rock using geostatistical simulations. The approach has been used in other applications such as groundwater flow and transport (McKenna and Reeves, 2005) and geothermal thermal-hydrology modeling (Kalenina et al., 2012, 2014). The method was developed based on the advantages of discrete fracture network and effective continuum approaches.

The chapter also evaluates the use of the FCM and DFN fracture characterization approaches for modeling of flow and transport in the host rock of a generic crystalline repository. The chapter shows development of one-to-one correspondence between DFN and FCM fracture parameters. Benchmark tests were developed for FCM-only modeling, and DFN-FCM modeling comparison using synthetic data. The results are encouraging and show that both the DFN and FCM methods can be used for modeling flow and transport in crystalline rocks. The results also indicate that further work is needed to bridge differences in results and to exercise both methods under different modeling conditions. Both fracture characterization methods are widely used and will be valuable for thermal-hydrologic-chemical modeling applied to geologic disposal of used fuel in crystalline rocks.

Recommendations for future work include further testing of DFN and FCM fracture representations, including comparison of effective permeability of the two methods. The methods can also be tested for different modeling conditions such as domain geometry and meshing. Suggestions for future work also include comparisons of DFN and FCM using the same modeling approaches applying the same or similar codes so that differences are minimized. For example particle tracking could be used for the FCM approach so that both approaches use the same transport method. Recommendations also include use of field data for the DFN-FCM comparison.

10.6   REFERENCES

Balay S, Eijkhout V, Gropp WD, McInnes LC and Smith BF (1997) Modern Software Tools in Scientific Computing, Eds. Arge E, Bruaset AM and Langtangen HP (Birkhaüser Press), pp. 163–202.

Chen, M., Bai, M., Roegiers, J.-C. (1999) Permeability Tensors of Anisotropic Fracture Networks, *Mathematical Geology*, **31**, No. 4.

Deutsch CV and Journel AG (1998) GSLIB Geostatistical software library and user's guide. 2nd ed. Oxford Univ. Press, New York

Hammond, G.E., P.C. Lichtner, C. Lu, and R.T. Mills (2011) PFLOTRAN: Reactive Flow & Transport Code for Use on Laptops to Leadership-Class Supercomputers, Editors: Zhang, F., G. T. Yeh, and J. C. Parker, Ground Water Reactive Transport Models, Bentham Science Publishers. ISBN 978- 1-60805-029-1.

Hyman, J. D., C. W. Gable, S. L. Painter, and N. Makedonska (2014) Conforming Delaunay triangulation of stochastically generated three dimensional discrete fracture networks: A feature rejection algorithm for meshing strategy, SIAM J. Sci. Comput., 36 (4), A1871–A1894.

Kalinina, E, McKenna, S.A., Klise, K., Hadgu, T., Lowry, T.S. (2012) Incorporating Complex Three-Dimensional Fracture Network into Geothermal Reservoir Simulations", *Geothermal Resources Council Transactions*, **36**,

Kalinina, Klise, K., E, McKenna, S.A., Hadgu, T., Lowry, T.S. (2014) Applications of Fractured Continuum Model to Enhanced Geothermal System Heat Extraction Problems", *SpringerPlus 2014,* **3**:110.

LaGriT, Los Alamos Grid Toolbox (2013) (LaGriT) Los Alamos National Laboratory, http://lagrit.lanl.gov.

Lichtner, P. C. and Hammond, G., Lu, C., Kara, S., Bisht, G., Andre, B., Mills, R., and Kumar, J., (2015) PFLOTRAN User Manual. A Massively Parallel Reactive Flow and Transport Model for Describing Surface and Subsurface Processes.

Makedonska, N., S. L. Painter, C. W. Bui, Q. M. Gable, and S. Karra (2014) Particle tracking approach for transport in three-dimensional discrete fracture networks, Computat. Geosci., Submitted, 2014.

McKenna, S. A. and P. C. Reeves (2005) Fractured Continuum Approach to Stochastic Permeability Modeling in T. C. Coburn, J. M. Yarus, and R. L. Chambers, eds., "Stochastic Modeling and Geostatistics: Principles, Methods, and Case Studies", **II**, 1–14.

Mount, D., and C. Gable (2001) A point-placement strategy for conforming Delaunay tetrahedralization, Int. J. Comput. Geom. Ap., 11 (6), 669–682.

Painter, S. L., C. W. Gable, and S. Kelkar (2012) Pathline tracing on fully unstructured control-volume grids, Computat. Geosci., 16 (4), 1125–1134.

Pruess, K., C. M. Oldenburg, and G. J. Moridis (1999) Tough2 user's guide version 2.

Y. Wang, E. Matteo, J. Rutqvist, J. Davis, L. Zheng, J. Houseworth, J. Birkholzer, T. Dittrich, C. W. Gable, S. Karra, N. Makedonska, S. Chu, D. Harp, S. L. Painter, P. Reimus, F. Perry, P. Zhao, J. Begg, M. Zavarin, S. J. Tumey, Z. Dai, A. B. Kersting , J. Jerden, K. Frey, J. M. Copple, and W. Ebert (2014) Used Fuel Disposal in Crystalline Rocks: Status and FY14 Progress, FCRD-UFD-2014-000060, SAND2014-17992 R (UUR).

Zyvoloski, G. (2007) FEHM: A control volume finite element code for simulating subsurface multi-phase multi-fluid heat and mass transfer, Los Alamos Unclassified Report LA- UR-07-3359.

11.0   RELEVANCE TO DOE-MANAGED HIGH LEVEL WASTE (HLW) AND SPENT NUCLEAR FUEL (SNF) RESEARCH

There has recently been an effort to develop a separate deep geologic repository for DOE managed high level waste (HLW) and spent nuclear fuel (SNF). This chapter will provide a brief description of the relevance and the applicability of the work documented in the previous chapters to the DOE-managed HLW and SNF research.

Table 11-1 shows both generated and projected disposal volumes of various waste types. It is clear that vitrified HLW dominates the total disposal volume of DOE managed waste. For this reason, our discussion in this chapter will focus on HLW glass.

Table 11-1: Disposal volume of U.S. SNF and HLW (SNL, 2014)

Waste	Present Volume (m³)	Additional Projected Volume in 2048 (m³)	Total Volume (m³)
Commercial SNF disposed of in dual-purpose canisters	90,299	93,597	183, 896
DOE-managed SNF	7,165	0	7,165
Savannah River Site vitrified HLW	2,969 (through macrobatch 8)	3,988	6,957
Hanford site vitrified HLW	0	14, 089	14, 089
Calcine waste after treatment by hot isostatic pressing	0	3,661	3,661
Sodium-bearing waste after treatment by fluidized bed steam reforming	0	721	721
Vitrified Cs/Sr capsules	0	453	453
West Valley Demonstration Project vitrified HLW	245	0	245
Treated sodium-bonded fuel (electrometallurgical treatment)	0	132	132
Federal Republic of Germany HLW glass	3	0	3
Total	100,681	116,641	217,332

Note: Table assumes constant nuclear power generation in commercial reactors. For simplicity, all DOE SNF is shown as "existing," although approximately 3,500 m³ of naval SNF remains to be generated. In addition, all the waste from electrometallurgical treatment of Na-bonded fuel is shown as "projected" even though a small quantity was generated during demonstration of the treatment process.
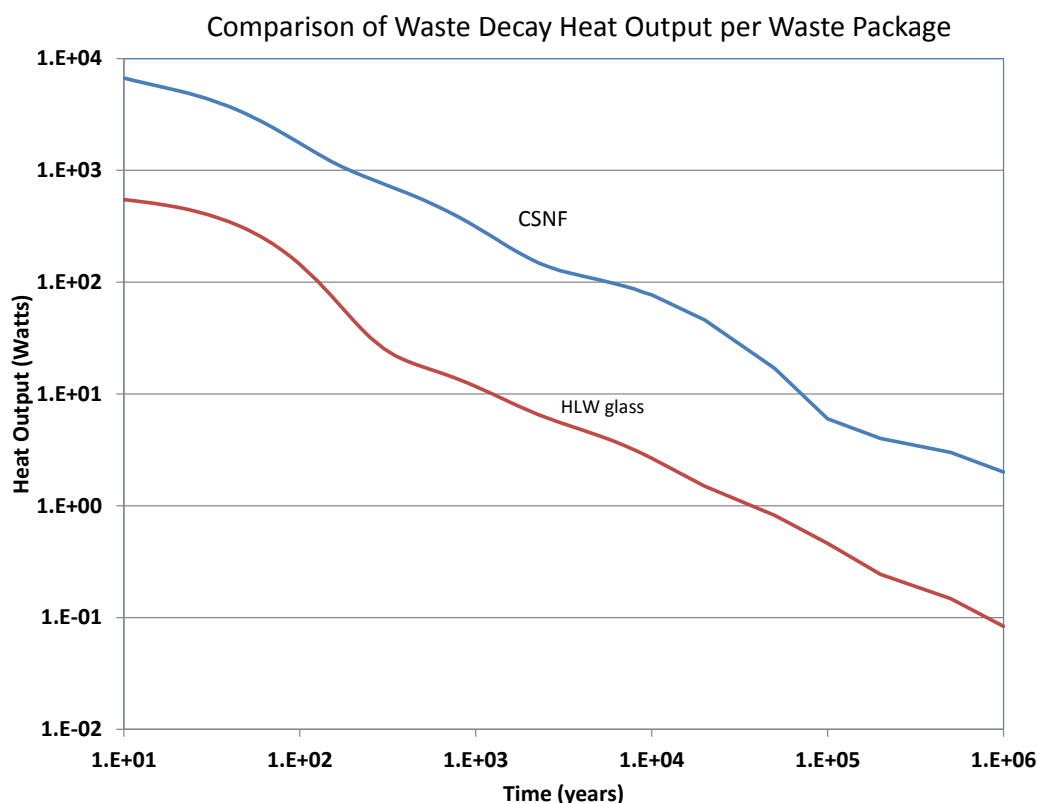
Comparison of Waste Decay Heat Output per Waste Package

Figure 11-1: Comparison of decay heat for commercial spent nuclear fuel (CSNF) and high level waste (HLW) glass

Compared to commercial spent nuclear fuel (CSNF), HLW glass has singficantly lower thermal loadings (Figure 11-1). Therefore, it is anticipated that the thermal perturbation due to radionuclide decay to a long-term repository performance can be negligible for DOE-managed HLW. In this sense, any work documented in chapters 2 through 10 that are not specifically on temperature effects can be directly applied to DOE-managed HLW (Table 11-2).

Table 11-2: Relevance of current work to DOE-managed SNF and HILW research

Existing R&D activity	Relevance
Development of Fuel Matrix Degradation Model (FMDM)	Yes
Thermal limit study of clay materials	No
Short-term (< 35 days) study of uranium sorption and diffusion in bentonite	Yes
Long-term (6 years) study of uranium diffusion in bentonite	Yes
Study of Pu sorption and desorption in bentonite	Yes
Colloid stability study	Yes, except temperature effects
Laboratory investigation of Cs colloid-facilitated transport	Yes
Development and demonstration of Discrete Fracture Network (DFN) model	Yes
Comparison of Fracture Continuum Model (FCM) with DFN model	Yes

REFERENCES

Sandia National Laboratories (2014) Evaluation of Options for Permanat Geologic Disposal of Spent Nuclear Fuel and High Level Radioactive Waste, Volume 1, FCRD-UFD-2013-000371.

12.0 SUMMARY AND PERSPECTIVES

Significant progress has been made in FY15 in both experimental and modeling arenas in evaluation of used fuel disposal in crystalline rocks. The work covers a wide range of research topics identified in the R&D plan. The major accomplishments are summarized below:

- *Development of Fuel Matrix Degradation Model (FMDM):* Completed a model validation study in which results from the state of the art FMDM were compared to experimental data from international geologic repository programs. Completed conversion of the state of the art FMDM (version 2.3) to Fortran to facilitate integration with the Generic Disposal System Analysis (GDSA) repository Performance Assessment (PA) code PFLOTRAN. Completed preliminary model runs focused on expanding the FMDM to account for corrosion of the used fuel steel canister. Completed scoping experiments investigating the possible poisoning of the Noble Metal Particles (NMP), which are known to catalyze the oxidation of H_2, thus shutting down the oxidative dissolution of used fuel.

- *Thermal limit study of clay materials:* Smectite and illite materials were heated up to 1300 ^{o}C over various time periods. Thermally treated materials were carefully caharacterized with X-ray diffraction (XRD), BET surface area measurments, cation exchange capacity measurements, and particle settling experiments. The results show that mineralogic alteration as a function of heat treatment exerts the greatest control on chemical and physical properties of both illite and smectite clays. Under dry heating, such alteration seems unlikely to occur below temperature 500 ^{o}C. However, thermal treatment under 500 ^{o}C does seem to change surface properties (e.g. surface area) and settling properties of clay particles.

- *Short-term (< 35 days) study of uranium sorption and diffusion in bentonite:* Experimental results from U(VI) sorption experiments with bentonite samples before and after heat treatments suggest a decrease in U(VI) sorption due to heat-induced mineral alterations. This effect could lead to lower U(VI) retardation in comparison to the pristine solids, and potential changes in diffusive U(VI) fluxes. The results from parallel U(VI) through-diffusion experiments in Na-montmorillonite at two alkaline pH conditions (pH 8.75 and 8.95), indicate a relevance of so-called anion exclusion effects, the full or partial exclusion of anionic U(VI) solution species from clay interlayer spaces. Such exclusion affects the diffusion-accessible porosity for U(VI) species predominant under these chemical solution conditions, as well as the resulting U(VI) diffusive fluxes.

- *Long-term (6 years) study of uranium diffusion in bentonite:* For a time period of six years, U(VI) diffusion through compacted MX-80 bentonite was investigated as a function of clay dry bulk density (ρ =1.3, 1.6, 1.9 g/cm^3). Speciation calculations revealed that independent of pore water type and water sampling time the $Ca_2UO_2(CO_3)_3$(aq) complex was always the dominant U(VI) species in solution (83-90%). U(VI) diffused about 2 mm, 1 mm, and 0.7 mm deep in the clay at ρ = 1.3, 1.6, and 1.9 g/cm^3, respectively. The distribution coefficients modeled are very low (K_d = 5.8-2.6$\times$10^{-3} m^3/kg). The K_d values obtained from the long-term experiment is one order of magnitude lower than those from batch sorption measurements. The apparent U(VI) diffusion coefficient determined from the long-term experiment is about two orders lower than obtained from short-term experiments, which may be attributed to a reduction of clay porosity.

- *Study of Pu sorption and desorption in bentonite:* Pu(IV) sorption to industrial grade FEBEX bentonite was studied over the concentration range 10^{-7}–10^{-16} M. Pu(IV)

sorption was broadly linear over the 10^{-7}–10^{-16} M concentration ranged during the 120 d experimental period; however, it took up to 100 d to reach sorption equilibrium. A flow cell experiment with Pu(IV) loaded on FEBEX bentonite demonstrated continued desorption of Pu over a 12 day flow period. Comparison with a desorption experiment performed with SWy-1 montmorillonite showed a strong similarity and suggested the importance of montorillonite phases in controlling Pu sorption/desorption reactions on FEBEX bentonite.

- *Colloid stability study:* A study of the dissolution of intrinsic colloids in the presence of montmorillonite at different temperatures was successfully accomplished using a novel experimental setup containing a dialysis device. We showed that the kinetic constants for dissolution were one to two orders of magnitude lower than the apparent diffusion rates across the dialysis membranes. Therefore the dissolution process was the rate-limiting step. Although the presence of clay changes neither the colloids dissolution nor diffusion rates, it can stabilize dissolved Pu species and drive intrinsic Pu colloid dissolution and the formation of more stable pseudo-colloids. Temperature enhances dissolution of intrinsic Pu colloids with activation energy of 28 kJ/mol. Our thermodynamic study shows that the sorption of Pu to montmorillonite is endothermic as a positive change in enthalpy for the sorption has been obtained. The affinity of Pu for montmorillonite increases with increasing temperature and resulting in higher K_ds. Although the fact that intrinsic Pu colloids tend to dissolve in the presence of montmorillonite may limit the migration of intrinsic colloids, the subsequent formation of thermodynamically more stable pseudo-colloids can play important role in Pu transport in the environment over significant temporal and spatial scales.

- *Laboratory investigation of Cs colloid-facilitated transport:* The work demonstrated that a combination of batch sorption/desorption experiments and column transport experiments could be used to effectively parameterize a model describing the colloid-facilitated transport of Cs. Cs partition coefficient estimates onto both the colloids and the stationary media obtained from the batch experiments were used as initial estimates of partition coefficients in the column experiments, and then the column experiment results were used to obtain refined estimates of the number of different sorption sites and the adsorption and desorption rate constants of the sites. The desorption portion of the column breakthrough curves highlighted the importance of accounting for adsorption-desorption hysteresis (or a very nonlinear adsorption isotherm) of the Cs on the fracture filling materials (FFM) in the model, and this portion of the breakthrough curves also dictated that there be at least two different types of sorption sites on the FFM. The two-site model parameters estimated from the column experiments provided excellent matches to the batch adsorption/desorption data, which provided a measure of assurance in the validity of the model. It was also demonstrated that a relatively simple retardation factor expression could be used to provide a good approximation of colloid-facilitated solute transport under conditions of near-constant mobile colloid concentrations and rapid and reversible solute sorption/desorption onto both the colloids and immobile surfaces.

- *Development and demonstration of Discrete Fracture Network (DFN) model:* A unified description of the dfnWorks suite was developed over the past five years with significant contribution from the Used Fuel Disposition Campaign. The generation and meshing strategy were outlined, a description of the flow solver provided, and the pillars of the particle tracker presented. The ability to resolve flow and transport while retaining fracture geometry allowed for two unique studies of transport in large, kilometer-scale

DFN. The first study showed that after a pre-equilibrium region solutes injected under resident conditions could evolve and behave similarly to that injected under flux-weighted conditions. The observation of this evolution was made feasible by the size of the DFN considered and characterizing the physical mechanisms that induced this phenomenon was made possible by retaining the geometry of the fractures rather than using a one-dimensional pipe-network approximation. Similarly, the second study was made possible because the fracture geometry was retained, so in-fracture variability could be incorporated. Other studies have used breakthrough times acquired from single fractures with internal aperture variability, but this study marks the first to resolve Lagrangian based transport in DFN where in-fracture variability is explicitly represented. We found that early breakthrough times and retention curves are influenced by in-fracture aperture variability but the tails of the breakthrough curves are insensitive to these variations.

- *Comparison of Fracture Continuum Model (FCM) with DFN model:* We evaluated the use of the FCM and DFN fracture characterization approaches for modeling of flow and transport in the host rock of a generic crystalline repository. The methodology to establish one-to-one correspondence between DFN and FCM fracture parameters was developed. Benchmark testing was performed for FCM-only modeling, and DFN-FCM modeling comparison using synthetic data. The results were encouraging and showed that both the DFN and FCM methods could be used for modeling flow and transport in crystalline rocks. The results also indicated that further work was needed to bridge differences in results and to exercise both methods under different modeling conditions.

Based on the work accomplished in FY15 and the prior years, the future work is recommended to:

- Focus on two key topics related to deep geologic disposal of used fuel in crystalline rocks: (1) better characterization and understanding of fractured media and fluid flow and transport in such media, and (2) designing effective engineered barrier systems (EBS) for waste isolation. Specific attention will be given to the development of scientifically sound thermal limits for various buffer materials.
- Explore various disposal concepts, for example, borehole disposal vs. drift emplacement, regular waste packages vs. dual purpose canisters (DPCs). Especially, the work will explore potential advantages of crystalline media for the disposal of DPCs, given the high mechanical strength of the rocks.
- Move more towards model demonstrations and applications using data obtained from international collaborations.
- Continue international collaborations, especially with Korea Atomic Research Institute (KAERI), and Sweden Underground Research Lab and through Development of Coupled models and their validation against Experiments (DECOVALEX).
- Closely coordinate with the deep borehole disposal control account. The data obtained and the tools developed in this control account may be transferable to the deep borehole disposal, or vice versa.
- Continue to work with the generic disposal system analysis control account to refine the reference safety case for crystalline media and help to develop a performance assessment model for the reference case.

.